



U.S. Department of Energy

National Virtual Biotechnology Laboratory

Technical Report



U.S. DEPARTMENT OF
ENERGY

Office of
Science

June 2022

U.S. Department of Energy

National Virtual Biotechnology Laboratory

Technical Report

DOE Office of Science

Executive Oversight: Harriet Kung, Harriet.Kung@science.doe.gov
Michelle Buchanan, Michelle.Buchanan@science.doe.gov
Ashley Predith, Ashley.Predith@science.doe.gov

Co-Directors

Stephen Streiffer, Argonne National Laboratory
Marianne Walck, Idaho National Laboratory

Project Leads

Molecular Design for COVID-19 Therapeutics: Martha Head, Oak Ridge National Laboratory
COVID-19 Testing: Patrick Fitch, Los Alamos National Laboratory
Epidemiological Modeling: Budhendra Bhaduri, Oak Ridge National Laboratory
Viral Fate and Transport: Katrina Waters, Pacific Northwest National Laboratory
Materials and Manufacturing of Critical Supplies: Lonnie Love, Oak Ridge National Laboratory

Disclaimer: This report was prepared as an account of work sponsored by an agency of the United States government. Neither the United States government nor any agency thereof, nor any of their employees, makes any warranty, express or implied, or assumes any legal liability or responsibility for the accuracy, completeness, or usefulness of any information, apparatus, product, or process disclosed, or represents that its use would not infringe privately owned rights. Reference herein to any specific commercial product, process, or service by trade name, trademark, manufacturer, or otherwise does not necessarily constitute or imply its endorsement, recommendation, or favoring by the United States government.

Funding: The research and development activities described in this document were supported by the U.S. Department of Energy (DOE) Office of Science through the National Virtual Biotechnology Laboratory, a consortium of DOE national laboratories focused on response to COVID-19, with funding provided by the CARES Act. Note: In addition to the 10 national laboratories participating in the COVID-19 Testing project, the National Renewable Energy Laboratory was an active participant throughout all processes and Brookhaven National Laboratory was active in the proposal development and review processes.

Suggested citation: U.S. DOE. 2022. U.S. Department of Energy National Virtual Biotechnology Laboratory: Technical Report. U.S. Department of Energy Office of Science. DOI: 10.2172/1871217

U.S. Department of Energy

National Virtual Biotechnology Laboratory

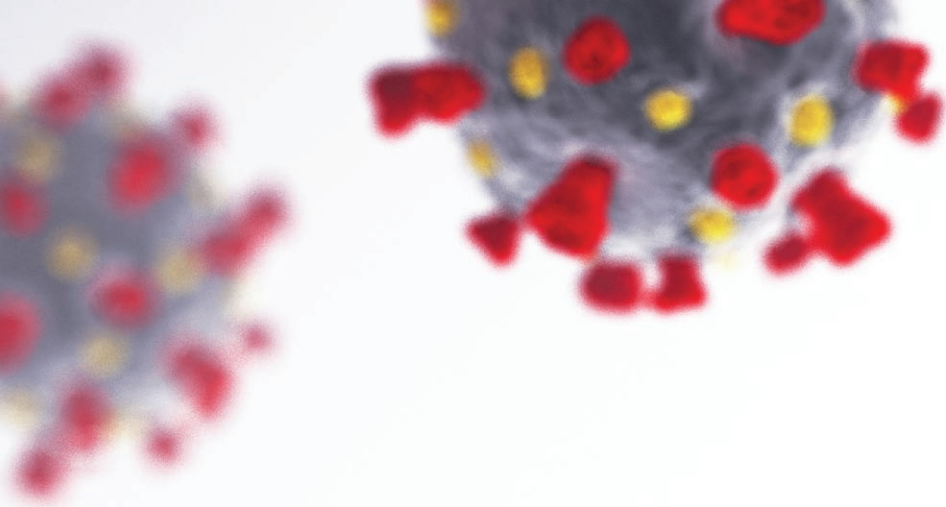
Technical Report

Published June 2022



U.S. DEPARTMENT OF
ENERGY

Office of
Science



Contents

| | |
|---|-----|
| Executive Summary | iii |
| Chapter 1: Molecular Design for COVID-19 Therapeutics | 1 |
| Chapter 2: COVID-19 Testing..... | 36 |
| Chapter 3: Epidemiological Modeling..... | 97 |
| Chapter 4: Viral Fate and Transport..... | 155 |
| Chapter 5: Materials and Manufacturing of Critical Supplies | 211 |
| Appendix A: Research Team | 267 |
| Appendix B: Acronyms and Abbreviations | 283 |

Executive Summary

With funding from the CARES Act, the U.S Department of Energy (DOE) established the National Virtual Biotechnology Laboratory (NVBL) in March 2020 to address key challenges associated with the COVID-19 crisis. The NVBL brought together the broad scientific and technical expertise and resources of DOE's 17 national laboratories to help tackle medical supply shortages, discover potential drugs to fight the virus, develop and validate COVID-19 testing methods, model disease spread and impact across the nation, and understand virus transport in buildings and the environment. National laboratory resources leveraged for this effort include a suite of world-leading user facilities broadly available to the research community, such as light and neutron sources, nanoscale science research centers, sequencing and biocharacterization facilities, and high-performance computing facilities.

As part of the NVBL framework, DOE rapidly assembled five project teams to (1) identify new targets for medical therapeutics; (2) develop innovations in testing capabilities; (3) provide epidemiological and logistical support; (4) understand viral fate and transport in the environment; and (5) address supply chain bottlenecks by harnessing extensive additive manufacturing capabilities. Each research team was charged with defining high-impact projects that could be completed in a 6-month sprint while coordinating their developments with academia, other government agencies, and the private sector.

Within months, NVBL teams used DOE's high-performance computers and light and neutron sources to identify promising candidates for antibodies and antivirals that universities and drug companies are now evaluating. NVBL researchers also developed new diagnostic targets and sample collection approaches, and supported efforts by the U.S. Food and Drug Administration,

FOR MORE ON NVBL

- **Website**
science.osti.gov/nvbl
- **Accomplishments Brochure**
science.osti.gov/-/media/nvbl/pdf/NVBL_Brochure.pdf
- **Summary Report**
science.osti.gov/-/media/nvbl/pdf/NVBL_report_021822.pdf



Centers for Disease Control and Prevention, and U.S. Department of Defense to establish national guidelines used in administering millions of tests. Researchers used artificial intelligence and high-performance computing to produce near-real-time data analysis to forecast disease transmission, stress on public health infrastructure, and economic impact, which supported decision-makers at the local, state, and national levels. To minimize virus uptake and protect human health, NVBL teams studied how to control indoor virus movement. Researchers also produced innovations in materials and advanced manufacturing that mitigated shortages in test kits and personal protective equipment, creating nearly 1,000 new jobs.

Through its NVBL framework, DOE has contributed significantly to the nation's COVID response, demonstrating in only a few months the critical impact of its national laboratories. NVBL's accomplishments demonstrate not only the powerful

resource represented by DOE's national laboratories working together to meet national needs, but also the effectiveness of the integrated NVBL framework for rapidly responding to emergencies with research and development solutions. Going forward, the NVBL is poised to apply the unique capabilities and expertise of the national laboratory complex to future national and international emergencies, both natural and engineered. Through this framework, DOE will continue to be an integral component of agency-wide efforts to prepare for and respond to biorisks and other crises.

This technical report describes the goals, progress, and results of NVBL's five project teams—Molecular Design for COVID-19 Therapeutics, COVID-19 Testing, Epidemiological Modeling, Viral Fate and Transport, and Materials and Manufacturing of Critical Supplies—and lists each team's publications and research output.

CHAPTER 1

Molecular Design for COVID-19 Therapeutics

| | |
|---|-----------|
| 1.1 Project Overview | 2 |
| 1.2 Key Outcomes and Impact | 2 |
| 1.2.1 Antibody Discovery | 2 |
| 1.2.2 Inhibitors of Viral Cysteine Proteases | 3 |
| 1.2.3 Computational Antiviral Screening | 4 |
| 1.3 Crosscutting Tasks | 4 |
| 1.3.1 Crosscutting Deliverable 1: Data Infrastructure and Dashboard | 6 |
| 1.3.2 Crosscutting Deliverable 2: High-Performance Computational Campaign and Infrastructure | 9 |
| 1.4 Task 1: Elucidation and Structural Biology of Viral and Human Targets for Therapeutic Intervention | 13 |
| 1.4.1 Task 1 Deliverable 1: Identify Potential Therapeutic Targets | 14 |
| 1.4.2 Task 1 Deliverable 2: Determine Key Protein Structures | 14 |
| 1.5 Task 2: Discovery and Optimization of Small-Molecule, Vaccine, and Antibody Therapeutics | 16 |
| 1.5.1 Task 2 Deliverable 1: Interactively Design and Optimize Small-Molecule Modulators | 17 |
| 1.5.2 Task 2 Deliverable 2: Develop Covalent Modeling Pipeline..... | 18 |
| 1.5.3 Task 2 Deliverable 3: Iteratively Design Vaccines and Antibodies..... | 20 |
| 1.6 Task 3: Experimental Validation and Characterization of Small Molecules, Vaccines, and Antibodies | 21 |
| 1.6.1 Task 3 Deliverable 1: Small-Molecule Synthesis | 24 |
| 1.6.2 Task 3 Deliverable 2: Assays to Inform Computational Models of Target Therapeutics | 27 |
| 1.7 Publications and Research Output | 34 |

Team Leadership

Marti Head (Team Lead), Oak Ridge National Laboratory; **Paul Adams**, Lawrence Berkeley National Laboratory; **Jim Brase**, Lawrence Livermore National Laboratory; **Tom Brettin**, Argonne National Laboratory; **Stephanie Galanie**, Oak Ridge National Laboratory; **Srinivas Iyer**, Los Alamos National Laboratory; **Kerstin Kleese Van Dam**, Brookhaven National Laboratory; **Neeraj Kumar**, Pacific Northwest National Laboratory; **Felice Lightstone**, Lawrence Livermore National Laboratory; **Joe Schoeniger**, Sandia National Laboratories; **Rick Stevens**, Argonne National Laboratory; **Soichi Wakatsuki**, SLAC National Accelerator Laboratory; **Bobbie-Jo Webb-Robertson**, Pacific Northwest National Laboratory

1.1 Project Overview

At the start of the COVID-19 pandemic, there were no approved therapeutic options beyond treating the symptoms of disease. In the months since, only a few medicines have received U.S. Food and Drug Administration (FDA) Emergency Use Authorization (EUA) for treating COVID-19. To accelerate discovery of potential treatments and identify small molecules and antibodies that interact with key viral targets, the Molecular Design team leveraged DOE national laboratory capabilities and analytical resources in high-performance computing, artificial intelligence (AI), structural biology, and chemistry. Even with the rapid development of several vaccines that recently received FDA approval or EUA, ongoing therapeutics development remains an important component of an integrated pandemic response as well as strategies to prepare for future viral challenges. To that end, the Molecular Design team continues to apply DOE capabilities to accelerate discovery of medical therapeutics targeting the virus responsible for the current pandemic—severe acute respiratory syndrome coronavirus 2 (SARS-CoV-2). Their work continues to complement other public and private-sector activities.

The goal of the Molecular Design project has been to focus on viral proteins and find small molecules and antibodies that inhibit all parts of the viral life cycle, capitalizing on an integrated computational and experimental platform that has been funded over time through DOE, the U.S. Department of Defense (DoD), the Defense Advanced Research Projects Agency, and other funding sources (see Fig. 1.1, p. 3).

The design platform's starting point includes structures of viral proteins, multiple antibody templates developed for earlier coronaviruses, and databases of chemical structures of small molecules that can be purchased for experimental confirmation. These inputs feed into a computational approach that combines simulation and machine learning (ML) methods, along with structure- and

sequence-driven models, to iteratively design, make, and test new molecules. Data from experimental assays and structural characterization are then fed back into the computational methods for multiple design rounds. Platform outputs include identification of small molecules and antibodies with confirmed inhibition of a viral protein and predicted probability for good physical and safety parameters. All project data will be made public, and team members are partnering with public and private organizations to further advance these discoveries along the pathway to clinical impact.

1.2 Key Outcomes and Impact

1.2.1 Antibody Discovery

The starting points for antibody design involved three antibodies known to bind to the spike protein of SARS-CoV-1 (the virus that caused the 2003 SARS outbreak) but not to the spike of SARS-CoV-2. The Molecular Design team's goal was to modify these existing antibody scaffolds to create new antibodies that effectively bind to and neutralize SARS-CoV-2. The team used AI methods to sample more than 10^{40} possible antibody variations, and they made and experimentally screened about 300 designed antibodies. Using this combined computational and experimental approach, the team identified experimentally confirmed hits for all three antibody scaffolds. After two rounds of optimization for antibody scaffold 1, they identified an antibody that has been experimentally confirmed to disrupt binding of the SARS-CoV-2 spike to the human ACE2 cell receptor at ~100 nM potency and neutralize cell entry of a vesicular stomatitis virus (VSV) pseudovirus. For scaffold 2, the team identified four antibodies, one of which binds to the SARS-CoV-2 spike at 2.5 nM potency. None of the scaffold 2 antibodies neutralized viral entry, so subsequent rounds of design will focus on improving neutralization. For the final scaffold, the team completed an initial round of design, from which they identified antibodies that show evidence of binding to the SARS-CoV-2 spike protein.

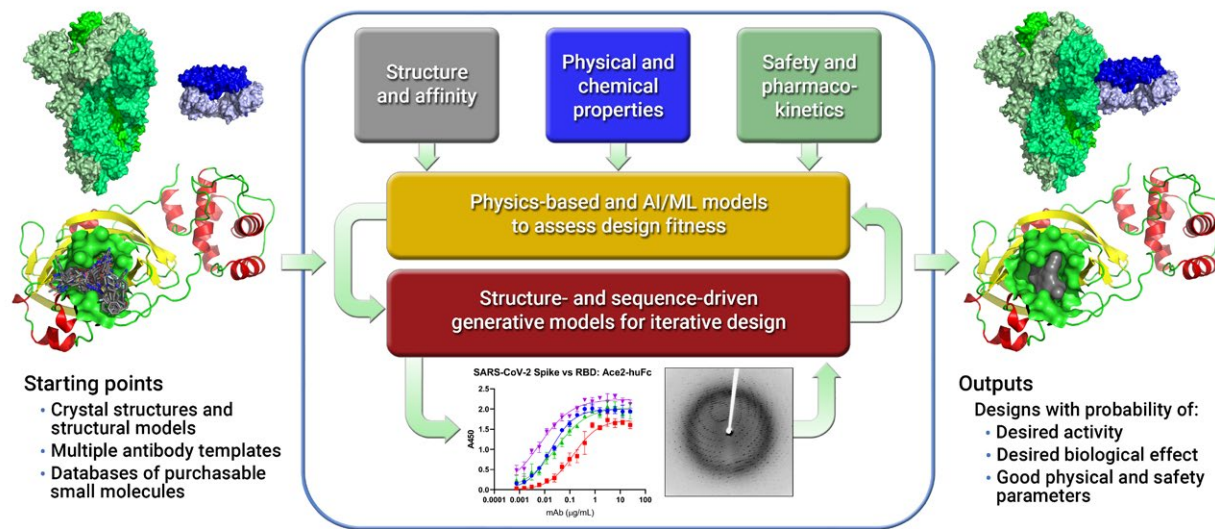


Fig. 1.1. Integrated computational and experimental platform for designing COVID-19 therapeutics. [Courtesy Oak Ridge National Laboratory]

1.2.2 Inhibitors of Viral Cysteine Proteases

Two viral proteases, 3 chymotrypsin-like protease (3CLpro) and papain-like protease (PLpro), are essential for SARS-CoV-2 replication and thus are important targets for pharmaceutical drug design and discovery. Both belong to the cysteine protease family, a structural family not amenable to traditional docking-based modeling pipelines, which use computational approaches to characterize and predict the atomic-level interactions of small molecules in a target protein's binding site. The team therefore created an integrated comprehensive docking, molecular dynamics, and quantum mechanics workflow and used it to design and optimize small-molecule inhibitors, resulting in the identification of two experimentally confirmed protease inhibitors: one for 3CLpro, the main protease (also called Mpro), and one for PLpro.

A series of covalent inhibitors of PLpro was computationally designed by introducing a linker and warhead into a previously reported noncovalent inhibitor. The computationally designed PLpro

inhibitor binds to the protein and then reacts to form a chemical bond with the cysteine residue that is vital for enzyme activity. A subset of these designed inhibitors was sent to external groups for screening against structurally related human proteins and for measuring metabolic stability of the molecules. The most promising covalent inhibitor is potent and selective for PLpro and displays antiviral activity in cell-based assays rivaling that of the RNA-dependent RNA polymerase inhibitor remdesivir in a side-by-side comparison. In addition, the team's collaborators at SLAC National Accelerator Laboratory have determined an X-ray crystal structure of this compound bound to PLpro (see Fig. 1.2, p. 4). This promising lead molecule displayed sufficient metabolic stability in mouse liposomes to enable a small efficacy study in mice. In the experiment, run by collaborators at the University of Tennessee Health Sciences Center, the molecule improved outcomes for mice infected with COVID-19. A larger, more extensive mouse study is underway. A manuscript describing these findings is in preparation, a patent covering the lead molecule and a set of structurally similar compounds has been submitted, two National Institutes of

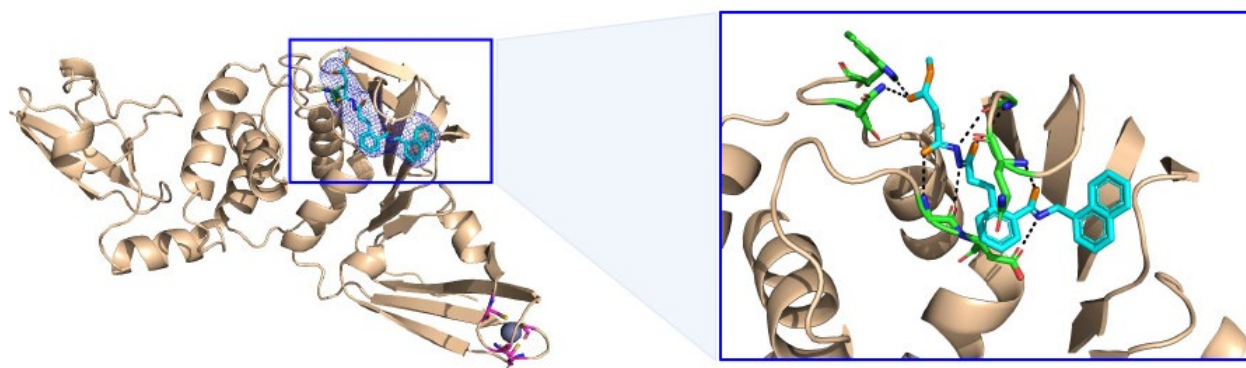


Fig. 1.2. Crystal structure of computationally designed covalent inhibitor of SARS-CoV-2 papain-like protease (PLpro). [Courtesy SLAC National Accelerator Laboratory]

Health (NIH) grant proposals have been submitted, and the team is exploring a possible licensing opportunity with a small biotechnology company.

A high-throughput virtual screening workflow was used to identify a small molecule that inhibits 3CLpro; this confirmed hit binds to the protein but does not form a chemical bond with the cysteine of 3CLpro. An X-ray crystal structure has been solved and reveals important atomic-level details of how the molecule interacts with the protein. Based on this structural information, the computational workflow has been used to design molecules with improved properties; a set of about 50 closely related, purchasable molecules have been ordered for experimental testing, and additional new molecules have been synthesized and experimentally validated. Two manuscripts were published: one describing the computational discovery and experimental validation of a noncovalent small-molecule inhibitor, MCULE-5948770040 (Clyde et al., 2022), and a second describing the activity of structurally related analogs of MCULE-5948770040 (Kneller et al., 2021; see Fig. 1.3, p. 5). This set of molecules will be transferred to Accelerating Therapeutic Opportunities for Medicine (ATOM), a public-private partnership among DOE, the National Cancer Institute, GlaxoSmithKline Pharmaceuticals, and the University of California, San Francisco. ATOM will use these molecules as

a starting point for molecule synthesis enabled by AI and ML, with improved activity for the SARS-CoV-2 3CLpro and broad-spectrum activity for the Middle East respiratory syndrome-related coronavirus (MERS-CoV) 3CLpro.

1.2.3 Computational Antiviral Screening

The Molecular Design team used the power of DOE's leadership computing facilities for computational docking calculations and AI methods that enabled the team to computationally screen tens of millions of small molecules against more than 100 binding sites of the SARS-CoV-2 viral proteins. Larger databases (on the order of 50 to 100 million molecules) were docked against a subset of the 100 binding sites. From these computational screens, more than 2,000 small molecules were purchased for experimental validation in an antiviral screen, and 56 of these show some inhibition of viral infection in a cell-based assay. The 56 hits are being confirmed in an independent antiviral screen, and experiments are ongoing to elucidate which parts of the viral lifecycle are being inhibited by each confirmed hit.

1.3 Crosscutting Tasks

The response to COVID-19 has necessarily been fast-moving and involved numerous components

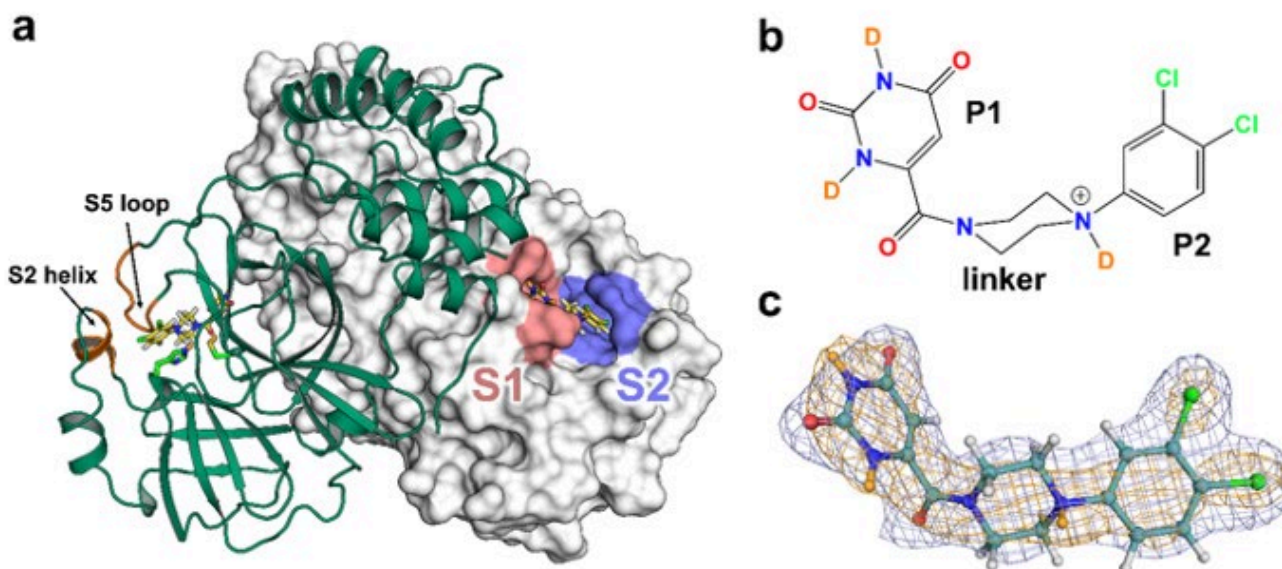


Fig. 1.3. A competitive noncovalent inhibitor MCULE-5948770040 binds to the S1 and S2 subsites of 3CLpro. (a) Dimer of 3CLpro-1 is represented with one protomer as cartoon (green) and the other as surface (white). The locations of subsites S1 (pink) and S2 (purple) are highlighted. The S2 helix and S5 loop are labeled in orange. The Cys145 and His41 catalytic dyad are shown as sticks. PDB ID 7N8C. (b) Chemical structure of MCULE-5948770040 as observed in 3CLpro-1. (c) MCULE-5948770040 from 3CLpro-1 shown in a ball-and-stick representation (teal carbons). H/D-exchanged D atoms are colored in orange. The electron density $2F_o - F_c$ map (blue mesh) and nuclear density $2F_o - F_c$ map (orange mesh) contoured to 1σ . [Reprinted by permission from the American Chemical Society from Kneller, D.W., et al. Structural, Electronic, and Electrostatic Determinants for Inhibitor Binding to Subsites S1 and S2 in SARS-CoV-2 Main Protease, *Journal of Medicinal Chemistry* **2021**, 64 (23), 17366–17383. Copyright 2021.]

across multiple organizations in the government, public, and private sectors. Within Molecular Design research activities, there were touchpoints with other NVBL teams, along with multiple external and internal partnerships and similar research across other labs. In support of NVBL coordination efforts, the Molecular Design team was tasked with two deliverables that aligned activities within the team, maintained awareness of other NVBL teams, and captured knowledge, results, and outcomes for broad use now and in the future.

Crosscutting tasks focused on two deliverables:

1. Developing an open repository of computational and experimental results, sequence and mutational analyses, molecular designs, publications, and reports. The team set up a public, open-source, scalable tool that enables users to

curate, link, and publish digital content, data, and software in one integrated archive. This public archive captures all materials created by the team or relevant to its work and serves as a central point for dissemination of team information and results.

2. Integrating team capabilities into a cohesive discovery platform. As Molecular Design projects were launched, the team developed a clear plan to coordinate and direct all efforts to achieve the maximum impact possible across all DOE resources it brought to bear as part of NVBL. They envisaged this plan to be living and adaptable as new results emerged from the team, its partners, and researchers worldwide, enabling them to target DOE resources in the most impactful way and to create an enduring,

integrated platform capability for response to COVID-19 and future crises.

1.3.1 Crosscutting Deliverable 1: Data Infrastructure and Dashboard

During times of crisis, such as the COVID-19 pandemic, researchers may be called upon to work together and across institutions for a common purpose in ways beyond normal scientific collaboration regarding number of collaborators, complexity of data streams, and pace. A key challenge faced by NVBL and the Molecular Design project was the need to rapidly share complex heterogeneous data and knowledge arising in real time from distributed *in vitro* and *in silico* experiments, such as the team's information about molecular entities and their viral targets. This section describes the challenges, what the team was able to achieve during the project, and how these challenges could be addressed more effectively in the future.

The key finding is that a data infrastructure across the entire DOE national laboratory system that could be easily integrated with resources at other government agencies would be a tremendous advantage in times of crisis, enabling teams to launch projects faster and be better informed and prepared. In this context, the Molecular Design team identified three main tasks that a collaborative data infrastructure would need to accomplish to make teams more effective:

- Provide immediate access and search capabilities to all existing relevant data, software, and documents to kick-start a project.
- Provide a dashboard-like capability that helps track and coordinate project activities across many different labs and other organizations.
- Preserve and publish results to support faster solution development during the crisis, enable training and further research after the crisis, and prepare for possible future crises that could benefit from the collection of data, software, and documents (see first point).

Access to Prior Knowledge

While each crisis is unique in its specific details, most bear some similarities to past events, so knowledge about those events can be helpful as a starting point to understand the current crisis better in a shorter period of time. As an example, initial research in the COVID-19 crisis built on past results of SARS and MERS outbreaks that provided a general understanding of this type of virus, including its structure, properties, and infection mechanisms. This type of information is found in a variety of different forms such as experimental structures, computer simulations, government reports, and scientific publications. At the same time, scientists need a set of tools to investigate the challenge at hand, including experimental capabilities, computational modeling software at different scales, data analysis tools, and AI methods that support the discovery process in various ways. The often-complex processes need to interact with each other seamlessly, so computational workflows that integrate a variety of tools in the most efficient way are also needed. In the case of computational tools, finding the ones best suited to a task can be very time consuming, especially when it is necessary to include scientific assessments of their accuracy. The following sections discuss the challenges encountered in accessing pre-existing knowledge and suggest alternative approaches to mitigate some of these challenges.

Prior data accessible to researchers can generally be grouped into experimental, observational, and computational scientific data. Data sources with restricted access are excluded here. Such sources include health data (e.g., from emergency services) and proprietary data (e.g., from industry), which are always protected and only accessible on a case-by-case basis. Experimental and observational data access varies widely by scientific discipline and the size of the facility where the data is collected. For example, new protein structures are always available in Protein Data Bank ([www.wwpdb.org](http://www wwpdb.org)) because experimental results cannot be published without depositing the structure in this worldwide

database. In the United Kingdom, data collected at the ISIS Neutron and Muon Source (isis.stfc.ac.uk/) is made openly accessible after an initial proprietary phase. However, these are exceptions. In many cases, experimental data is collected in small- to medium-sized laboratories and captured in spreadsheets with little or no metadata attached. At larger facilities, data are collected in instrument-specific data formats, with users taking the data home on hard drives. Some of this data is later made available through small public databases, but many of the databases are not computationally searchable due to their different data and metadata formats, making discovery and analysis extremely difficult. Supported by DOE's Office of Biological and Environmental Research, the DOE Systems Biology Knowledgebase (KBase) aims to help by providing analytical access to a large set of integrated experimental results (www.kbase.us/). While substantial in its data collection, KBase only covers a small fraction of available biological data. In the future it would be extremely beneficial in times of national need to have computationally searchable and accessible repositories of experimental data for DOE user facilities. This project leveraged pre-existing and contemporaneous experimental results from the Protein Data Bank and light sources around the world to access the latest virus structures.

Scientific publications are a tremendous source of prior knowledge and, in the case of the COVID-19 pandemic, contemporaneous information. A 2020 *Nature* article¹ reported that well over 100,000 articles were published on SARS-CoV-2 in 2020 alone, amounting to 4% of the world's scientific output. Many additional papers were published through preprint services such as medRxiv, bioRxiv, SSRN, ResearchSquare, and others. This is in addition to the articles that already existed on previous SARS and MERS outbreaks. It would have been impossible for researchers to survey the entire volume of

¹ Else, H. 2020. How a Torrent of COVID Science Changed Research Publishing – In Seven Charts. *Nature* **588**, 553.

publications and extract useful leads and key data points without computational support.

In response, this project focused on developing literature services based on Natural Language Processing (NLP) that enabled researchers to quickly find relevant publications in the fast-growing collections related to COVID-19. The team assembled a comprehensive dataset of about 50,000 articles that was continually updated with more than 2,000 articles per week, including both open- and restricted-access publications of interest. The NLP methods not only extract information from text, but also from tables, figures, and graphics. The service offers both automated annotation and advanced search capabilities. In addition, an Explorer feature provides an initial question answering service. Both services are available online using InCommon identities for authentication. Access restrictions were necessary due to the inclusion of restricted articles from a wide range of publishers (e.g., American Association for the Advancement of Science, Elsevier, Nature Publishing Group, Royal Society of Chemistry, and PubMed Central). The work was presented at the 2020 International Conference on Intelligent Systems for Molecular Biology. Information from the literature was used to identify new possible target compounds and to evaluate the efficacy of leads identified by the project against results from other studies.

Project Data Collection

Datasets were generated by various teams at all nine DOE laboratories involved in the project. The datasets had different rates, sizes, formats, descriptive metadata, and more. Adding further complexity, they differed in who they could be shared with—ranging from a specific team to the full public—and were sometimes stored in multiple locations (e.g., Box, Google Drive, or Globus). The project established a single key data collection point at one of the DOE laboratories (see Fig. 1.4, p. 8) where project teams could deposit their key experimental and computational data, as well as information needed to coordinate the overall project such as next targets, target evaluation

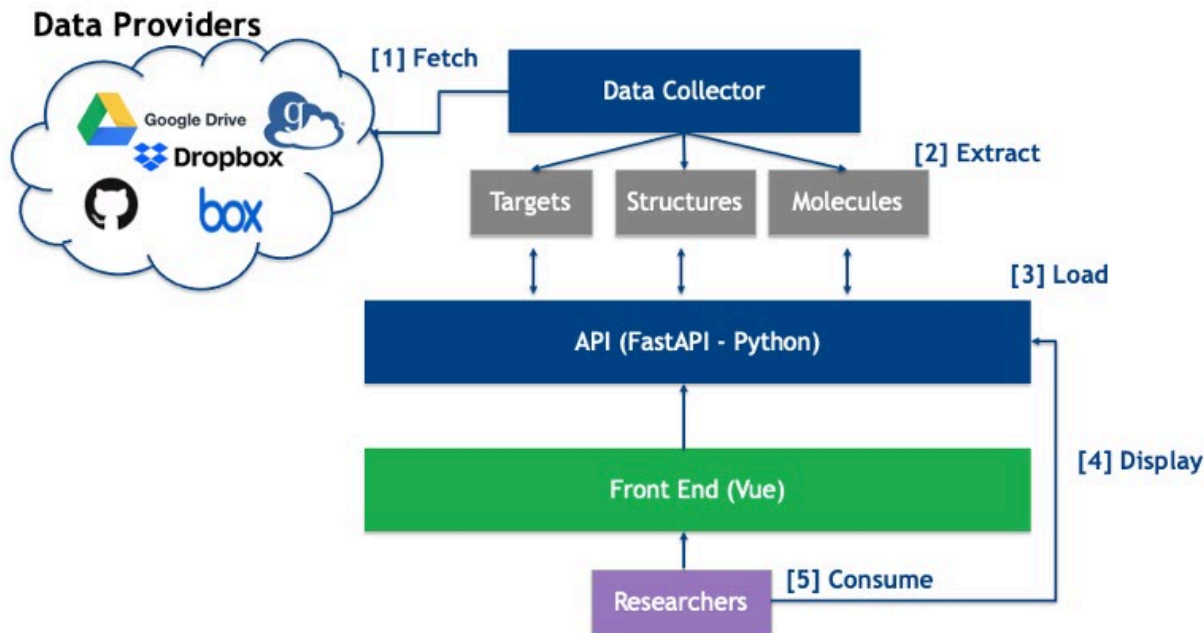


Fig. 1.4. Architecture overview diagram. An infrastructure was built to collect data from several data providers, extract molecular data into a common format, load the data into a database, serve the data via API, and display a dashboard of results. [Courtesy Brookhaven National Laboratory]

progress, leads, compound order status, and experimental validation results. Other sites at the participating labs stored more detailed and extensive experimental and computational results. One lab had already set up a limited infrastructure to capture both experimental and computational results, but it was not possible to expand the infrastructure to serve the entire project.

The following recommendations may facilitate simplified data collection in the future:

- A primary data contact should be designated to help coordinate data sharing with other parts of the team.
- Data storage locations should be pre-specified by the team and accessible through a programmatic interface, such as a Python client or representational state transfer (REST) application programming interface (API).
- Data formats should be well defined. If data are easy to access, but their origin and meaning are

unclear, their value is diminished, and automatically linking them with other collected data will be difficult.

- Terms used in the collected data should be well defined. For example, a dataset may contain a simplified molecular-input line-entry system (SMILES) string describing a molecule. In such a case, specifying the generating software (e.g., RDKit version release_2020.09.5) is recommended.

Data Access and Display

One of the key challenges encountered in the project was coordination among the different partners and activities, as all tasks were interconnected and interdependent. For the basic and summary data being collected, the pace of the project (e.g., billions of calculations during just a few months) made it very challenging to keep track of progress. For this reason, the project developed an initial dashboard that enabled the team to view and

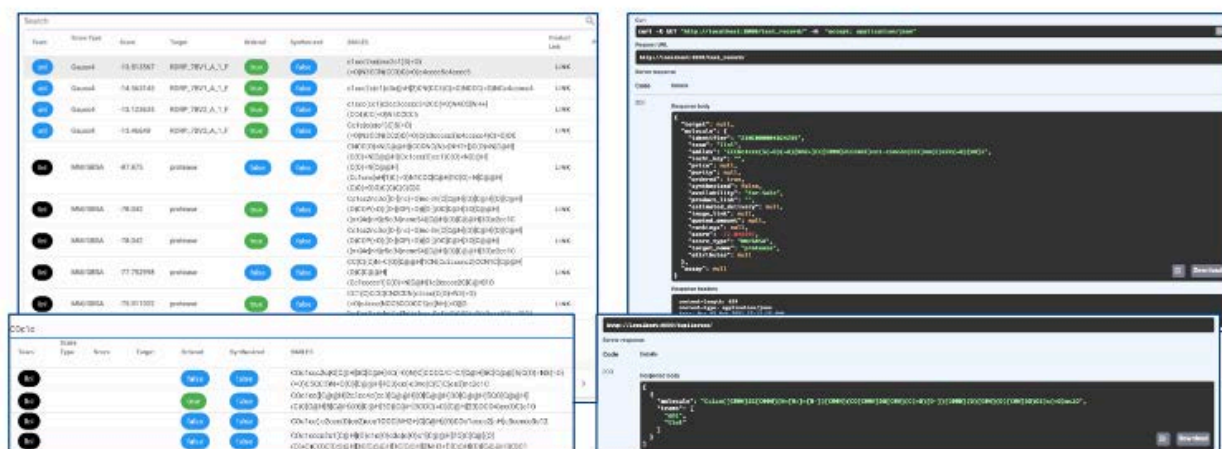


Fig. 1.5. Dashboard overview showing molecular screening data collected from teams at Argonne National Laboratory and Lawrence Berkeley National Laboratory. The displayed fields include the SMILES representation of the molecule, the target, the team that generated the data, and a simulation score (left). Accessing collected molecular data via a REST API (right). [Courtesy Brookhaven National Laboratory]

compare key data such as molecules computationally assessed, docking score, docking methods, overall ranking in the lead table, and experimental validation. The dashboard offered two principal methods of access (see Fig. 1.5, this page) enabling computational evaluation: a web interface and a REST API. Future deployments would need additional functionalities, specifically to track molecules through the processing pipeline from proposal to final validation, including responsible project partners for each step.

1.3.2 Crosscutting Deliverable 2: High-Performance Computational Campaign and Infrastructure

The drug discovery process currently employed in the pharmaceutical industry typically requires about 10 years and \$2–3 billion to deliver one new drug. This is both too expensive and too slow, especially in emergencies like the COVID-19 pandemic. *In silico* methodologies need to be improved to select better lead compounds that will improve the efficiency of later stages in the drug discovery protocol and to identify those lead compounds more quickly.

With the sudden onset of COVID-19 and the need for an immediate response, several DOE national laboratories—primarily Argonne and Brookhaven—came together to develop a computational infrastructure supporting a high-throughput virtual screening pipeline capable of synergizing with DOE experimental facilities. The project developed an end-to-end computational campaign and the enabling computational infrastructure to support methodological innovations at scale, across a range of computing platforms. The resulting infrastructure evolved to become the workhorse of the Molecular Design team and came to be known as Integrated Modeling PipEline for COVID Cure by Assessing Better LEads (IMPECCABLE). The pipeline embodies multiple methodological and infrastructural innovations to overcome fundamental challenges of virtual screening. It brings together hybrid ML-physics methods, as well as ML-based surrogates, to both supplement and substitute traditional stages of virtual drug screening. It employed these novel methods at scale on leadership-class computing facilities to rapidly screen an adequate number of drug-like candidates with sufficient accuracy.

The following sections provide technical details of the infrastructure used to stand up IMPECCABLE, which leveraged RADICAL Cybertools (RCT) to support needs of scale, portability, and workload and platform heterogeneity. In essence, IMPECCABLE is comprised of multiple distinct and heterogeneous workflows coupled together—offline and online—to improve the collective capability to screen drug candidates better, faster, and larger.

The specific capabilities of the infrastructure, as measured by the metrics of throughput, peak performance, and number of nodes, are provided in Lee et al. (2020) and Saadi et al. (2020), with additional updates occurring later in the project. Individual workflow components delivered 100 to 1,000 times improvement over traditional methods, and the integration of methods, supported by scalable infrastructure, sped drug discovery by orders of magnitude. IMPECCABLE has screened more than 1,000 ligands and discovered promising drug candidates. The fact that IMPECCABLE was functionally ready and was gradually scaled to meet the scientific and computational requirements in a matter of months is a direct consequence of the design and implementation details of RCT.

Infrastructure Background and Development for NVBL Projects

The design and development of middleware to support scientific computing is a challenging undertaking due to the unprecedented complexity arising from diverse application requirements and disruptive changes in resource and technology landscapes, all intermixed with new discovery modalities and the need for scalable computing. RCT addresses two critical challenges: (1) How can middleware be designed and implemented to meet the collective challenges of scale, new and diverse functionality, and usability? (2) How can critical middleware components be designed as sustainable software implementations that also enable innovative capabilities? RCT addresses these challenges by providing the necessary abstractions and systems. RCT comprises building blocks that can be used as a stand-alone system or integrated

with other RCT or third-party tools to enable diverse functionalities. Further details can be found in Lee et al. (2020), Saadi et al. (2020), Bhati et al. (2021), and Clyde et al. (2021).

Despite the many important, necessary, and powerful capabilities that already existed in RCT at the onset of the project, several additional properties were needed to provide a full range of capabilities to support the heterogeneous and diverse workloads of the Molecular Design project. Specifically, the ability to execute high-throughput function calls reliably and in a scalable way on leadership-class high-performance computing (HPC) platforms without degrading system performance required the *ab initio* development of RADical-Pilot Task OverLay (RAPTOR). Further, the need to sustain the Molecular Design project on a wide range of platforms—DOE, National Science Foundation, and international systems—required performance and functionality enhancements to RCT. Some highlights are outlined below, and full details can be found in Lee et al. (2020), Saadi et al. (2020), Bhati et al. (2021), and Clyde et al. (2021).

RAPTOR: The RADical-Pilot Task OverLay

RAPTOR (Merzky et al. in review) is a master/worker framework for the execution of function and executable tasks on HPC platforms. Specifically, RAPTOR is designed to enable high-rate task execution at extreme scale. RAPTOR is tightly integrated with RADICAL-Pilot (RP) (Merzky et al. 2022), relying on that system to acquire and manage resources and to schedule and launch its masters and workers on those resources.

RAPTOR was designed to offer capabilities missing in RP: executing both function and executable tasks, achieving high-throughput and high-resource utilization with arbitrary short running tasks, arbitrary partitioning of resources and tasks, multilevel scheduling in which workloads are partitioned and then subsets of tasks are locally scheduled to a subset of resources, and partitioning tasks across multiple independent executors. Conversely, RAPTOR imposes some limitations on the size of tasks

that can be executed compared to RP. RAPTOR executes only tasks that can fit within a single compute node of the target platform. This means that each executor has, at most, the resources of one compute node. The size of the compute node depends on the architecture of the target HPC platform. Thus, there is no intrinsic limitation in RAPTOR regarding the size of the task; rather, it is a platform-dependent limitation.

RAPTOR was key to performing an aggregated (estimate) of > 1,011 docking calculations (Lee et al. 2020; Saadi et al. 2020; Merzky et al. in review) at approximately twice the speed of any other high-throughput docking capability, including cloud computing. As an example of extending and hardening existing capabilities for RCT, the sections below describe advances in using lower-level software capabilities such as Process Management Interface for Exascale (PMIx) and Flux.

RADICAL-PMIx Integration

PMIx is an open-source standard that extends previous PMI version 1 and version 2 interfaces that were used to launch tasks on compute resources. PMIx provides a method for tools and applications to interact with system-level resource managers and process launch mechanisms. PMIx provides a bridge between such clients and underlying execution services (e.g., process launch, signaling, event notification). The clients communicate with PMIx-enabled servers, which may support different versions of the standard. PMIx is also a coordination and resource discovery mechanism (e.g., machine topology information). The OpenPMIx project provides an implementation of the PMIx standard as a software library containing the programming interfaces needed to use the standard. The OpenPMIx project also provides a reference implementation of a PMIx reference runtime environment called PRRTE.

RP uses both PRRTE and PMIx (Merzky et al. 2022) to partition pilot resources. In turn, this enables scheduling and use of very large pilot jobs on Oak Ridge National Laboratory's (ORNL) Summit

supercomputer, Lawrence Livermore National Laboratory's Lassen, and Argonne National Laboratory's Theta. This is fundamental to executing AI-enabled workflows in which heterogeneous tasks must execute concurrently on different portions of the pilot job's resources.

Additionally, the Molecular Design team interfaced with Flux, a hierarchical workload manager for HPC. Flux enables scheduling of heterogeneous and dynamic processes at DOE national laboratories. Its hierarchical capabilities improve scalability and flexibility through a divide-and-conquer approach; jobs and resources are divided among the schedulers in the hierarchy and managed in parallel. This approach increases the scalability of Flux over traditional schedulers that rely on a centralized scheme. Flux and RCT were integrated to enable efficient scheduling of very large workloads on HPC resources, enabling the team to achieve higher efficiency and reliability compared to the previously used native scheduler.

IMPECCABLE Developments

IMPECCABLE leveraged existing tools and technologies to an extent. This section discusses advances in two areas of needed development and significant extensions to base capabilities. Four molecular design workflows were built to work independently of other workflows yet be easily integrated in a scalable way into the pipeline. Also discussed below are specific customizations on a range of DOE computing resources that were needed to meet workflow demands and requirements.

Molecular Design Workflows

Workflow 1: Ensemble Docking

High-throughput docking was implemented using RAPTOR. The runs used between 128 and 8,000 concurrent nodes. For each run, throughput (the number of docking calls per hour) and resource utilization (the fraction of time that acquired nodes were kept busy) were measured. Resource utilization depended on the size of the run (number of compounds to dock and number of nodes to use)

and was typically above 90%. Details can be found in Lee et al. (2020) and Clyde et al. (2021).

Workflow 2: DeepDrive Molecular Dynamics (DDMD)

The AI-driven ensemble execution framework DDMD and resulting adaptive sampling methods were integrated into the IMPECCABLE campaign to support the exploration of protein-ligand bound states. Several developments were made to enable heterogeneity and scalability in HPC platforms: (1) extension of the type of tasks and nodes supported to manage, for example, parallel task executions on a single graphics processing unit (GPU), multiple GPUs, or a mixture of central processing units (CPUs) and GPUs; (2) optimization of resource assignments of heterogeneous tasks for higher utilization; (3) extension of DDMD to adopt the PyTorch distributed data parallel module; (4) optimization of the communication protocol between RADICAL-Ensemble Toolkit (EnTK) and a message broker (RabbitMQ) and reduction of the communication latency by eliminating the number of multiple concurrent connections and reusing communication channels among EnTK threads.

Workflows 3 and 4: Binding Free Energies

Two important protocols used to estimate binding affinities of protein-ligand complexes are the enhanced sampling of molecular dynamics with approximation of continuum solvent (ESMACS) and thermodynamic integration with enhanced sampling (TIES). Experimentally, ESMACS and TIES are computationally intensive methods that compute binding free energies but have workloads composed of different heterogeneous tasks: GPU-based OpenMM tasks and CPU-based nanoscale molecular dynamics tasks, respectively, which run on different components of heterogeneous nodes within HPC facilities. Merging both workloads into a single hybrid workflow enabled improved resource utilization of HPC facilities by employing RCT's unique capabilities of concurrently executing heterogeneous tasks on CPU cores and GPUs.

Based on the task launch method, the RCT pilot job manager (i.e., RP) places tasks on specific

compute nodes, CPU cores, and GPUs. This placement enables efficient scheduling of tasks on heterogeneous resources. When scheduling tasks that require different numbers of cores and/or GPUs, RP tracks the available slots on each compute node of its pilot. Depending on availability, RP schedules CPU tasks (e.g., message passing interface tasks) within and across compute nodes and reserves a CPU core and a GPU for each GPU task. By leveraging the capability of placing tasks on heterogeneous components within a compute node, the two workflows utilizing CPU and GPU individually were merged into an integrated hybrid workflow with heterogeneous tasks utilizing CPU and GPU concurrently.

Specific Developments on DOE Computing Resources

To meet the challenge of sustained throughput, RCT had to be deployed on several HPC platforms that had not been used previously, including Theta and Lassen. Development was undertaken to support the Molecular Design campaign on these platforms.

RCT deployment and testing on Theta/ThetaGPU (www.alcf.anl.gov/alcf-resources/theta/) required solving the following tasks: (1) installing and configuring MongoDB; (2) setting up resource configuration (Theta/ThetaGPU descriptions); (3) fixing implementations of RP and SAGA components (interfaces to corresponding services), including resource manager Cobalt (Cobalt Job Scheduler, xgitlab.cels.anl.gov/aig-public/cobalt) and launch method APRUN; (4) fixing the procedure of launching RP processes on Theta (RP creates new sessions for its running components that are not supported by the APRUN management process); and (5) validating the correctness of RP deployment with integration testing that used synthetic payloads.

On Lassen, the team deployed on-premise MongoDB and RabbitMQ services with transport layer security/secure sockets layer support (github.com/radical-cybertools/radical.entk/issues/577) to optimize the communication protocol and provide

a secure connection. The ability to use nonvolatile memory express node-local storage was added and tested (github.com/DeepDriveMD/DeepDriveMD-pipeline/blob/main/test/bba/lassen-integration.yaml). As a result, input/output on the parallel file system was reduced and the team achieved scalable runs for workloads, including the full spike protein system.

Even though Summit had been extensively used, the scale and novelty of methods and resulting workloads required enhancing Summit's existing capabilities. Bugs were fixed in jsrun to facilitate parallel task executions at scale (github.com/radical-cybertools/radical.pilot/pull/2420, <https://github.com/radical-cybertools/radical.pilot/issues/2419>). In addition, the team responded to upgrades of Summit's operating system to Red Hat Enterprise Linux 8, and the PyTorch Conda environment for DDMD was refreshed. Dozens, if not hundreds, of issues were reported at multiple levels of the stack and system to sustain the scale and diversity of the campaigns across multiple distinct and heterogeneous platforms.

Summary

The Molecular Design team's computational campaigns, supported by high-performance infrastructure, were significant in achieving NVBL scientific goals. The team estimates that the IMPECCABLE campaign supported ~1,011 docking calculations, ~10³ ML-driven molecular dynamics workflows (where each workflow involved on the order of hundreds of molecular dynamics ensemble members) and ~10⁴ binding free energy calculations. Together, these workflows consumed upwards of 2.5 x 10⁶ node-hours across different DOE computing platforms. The peak scale/performance reached more than 8,000 nodes on Frontera (Intel Cascade Lake-based system) and more than 4,000 nodes on Summit, and at least a half-dozen distinct supercomputers supported the campaign. Finally, the peak performance of ~150 x 10⁶ docks per hour represents a high water mark for any published docking campaign.

Of significance, project functionality and scale were essentially rolled out in four to six weeks, with subsequent incremental improvements, extensions, and performance optimization. In addition to validating RCT design and implementation, the campaign's successful evolution is a testimony to strong collaborations within an interdisciplinary team of domain scientists (consumers) and computer scientists/engineers (producers) responsible for the IMPECCABLE infrastructure.

Innovations and enhancements continue, with IMPECCABLE impacting the original scientific objectives. These capabilities are in active consideration by projects such as ATOM. In general, IMPECCABLE and its enabling technologies represent a new and increasingly important infrastructural capability that DOE will want and need to deploy in other domains and problem spaces, such as support for future beamline experimental analysis at facilities like the National Synchrotron Light Source II (NSLS-II). Thanks to the powerful multistage, multifidelity/component filtering motif, IMPECCABLE will support the design and selection of more than drug candidates. The ability to compose sophisticated and scalable computational campaigns in synergy and collaboration with experiments and user facilities is paramount and requires base solutions to be grown and made sustainable.

1.4 Task 1: Elucidation and Structural Biology of Viral and Human Targets for Therapeutic Intervention

The computational biology expertise and world-leading light source, neutron, and cryo-EM capabilities of the national laboratories enabled an integrated understanding of which viral proteins are most promising as targets for therapeutic intervention, where to intervene in the interconnected network of human and viral interactions to identify the most effective treatments for viral infection and human inflammatory and immunological response, and where viral mutational patterns might lead to

the development of resistance. Structural biology was tightly coupled to computational Task 2 activities to ensure that computations used the most reliable structural information available to support the iterative design of small molecules, antibodies, and vaccines.

Task 1 focused on two deliverables:

1. Developing a prioritized list of viral and human targets and protein complexes based on network analysis of interacting viral and human genes and evolutionary and mutational analysis of viral variability.

The team applied AI-enabled sequence analysis, co-evolution analysis, hypergraph analytics, and causal reasoning methods in a holistic, comprehensive approach to identify and prioritize viral and human proteins and protein complexes that are viable targets for therapeutics discovery. These efforts incorporated and supplemented public target identification results.

2. Using structural biology approaches to characterize viral and human therapeutic targets. Light source, neutron, cryo-EM, cryo-tomography, and computational methods were applied to generate structural information suitable to guide iterative design efforts for small-molecule, antibody, and vaccine therapeutics. High-resolution structures and dynamics provided critical information to validate and improve promising computational and experimental hits.

1.4.1 Task 1 Deliverable 1: Identify Potential Therapeutic Targets

Researchers from Lawrence Berkeley National Laboratory (LBNL) and Pacific Northwest National Laboratory (PNNL) worked to integrate publicly available COVID-19 data to accelerate discovery for COVID-19 response. They applied the Knowledge Graph (KG) COVID-19 framework (Reese et al. 2021), developed separately with LBNL's laboratory-directed research and development funding, to generate a knowledge graph that integrated data relevant to COVID-19 including drug, drug target, protein-protein interactions, scientific literature,

human and viral gene/protein information, and human phenotypes and diseases (see Fig. 1.6, p. 15). This knowledge graph harmonized information about SARS-CoV-2 cleavage products for Task 1 structural biologists to prioritize host and viral drug targets in Deliverable 2. Additionally, in collaboration with ORNL, graph machine algorithms were applied to the KG COVID-19 knowledge graph to identify existing drugs that might be repurposed for COVID-19 and drugs that might negatively affect COVID-19 outcome. A partnership with colleagues in the N3C Consortium, another large COVID-19 research consortium, has been used to further validate these drug candidates using patient-level data. The team also collaborated with Ben Brown (LBNL) to apply its graph ML results to help guide Brown's Graph Convolutional Policy Network strategy for COVID-19 drug design.

1.4.2 Task 1 Deliverable 2: Determine Key Protein Structures

As part of the collaboration among the structural biology teams, a variety of biophysical and structural studies were performed to understand the viral proteins. The primary targets based on the prioritization performed in Task 1 Deliverable 1 were: PLpro, 3CLPro, ADP ribose phosphatase (ADRP), and the SARS-CoV-2 endoribonuclease (Nsp15). Priority lists of computationally designed compounds were purchased and screened in crystallization trials for each protein. In total, nearly 20,000 crystallization trials were performed and nearly 1,000 datasets collected, resulting in more than 100 structures. In some cases (ADRP and Nsp15), no binding of the designed molecules was observed despite some encouraging biochemical data from Task 3 and extensive crystallographic trials. However, for both proteases it was possible to obtain complexes with molecules (see "Inhibitors of Viral Cysteine Proteases," p. 3).

Inhibitor Against SARS-CoV-2 PLpro

In collaboration with an ORNL team that designed covalent inhibitors against SARS-CoV-2 and teams at light source facilities, including Brookhaven

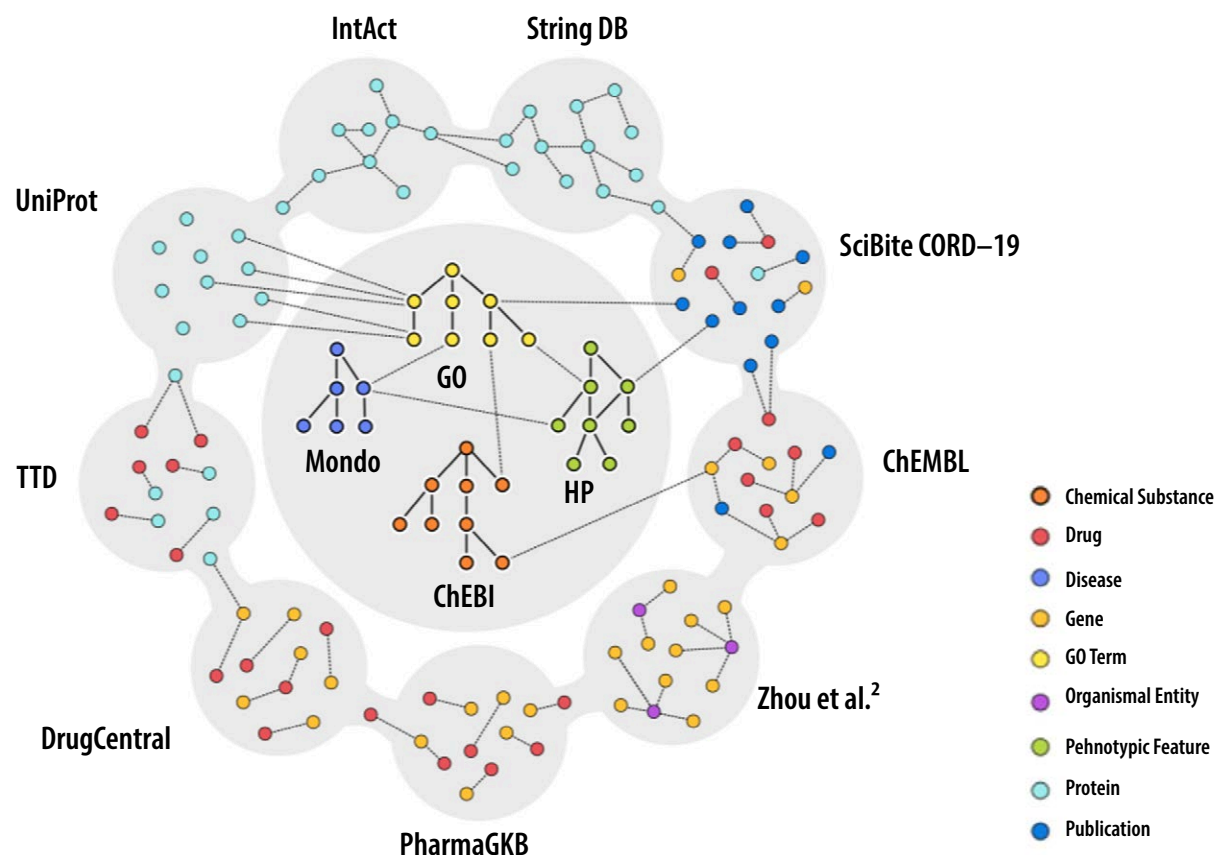


Fig. 1.6. KG-COVID-19: A knowledge graph to integrate publicly available data for COVID-19 response, for drug target prioritization and dissemination of up-to-date COVID-19 information. Labels indicate the sources of data, and types of data for each source are indicated by colored circles. [Reprinted under a Creative Commons License (CC BY 4.0) from Reese, J.T., et al. KG-COVID-19: A Framework to Produce Customized Knowledge Graphs for COVID-19 Response, *Patterns* **2021**, 2 (1).]

National Laboratory, LBNL, and Argonne National Laboratory, the SLAC team solved the structure of PLpro complexed with one of the best inhibitors at 3.1 Å resolution (see Fig. 1.7, p. 16). The structure shows the intricate interactions between the inhibitor compound and the active site residues of PLpro, confirming the novel design concept of the covalent inhibitor. Structure comparisons of this complex with human deubiquitinating enzymes (such as ubiquitin specific proteases and ubiquitin C-terminal hydrolases) demonstrate how this²

² Zhou, Y., et al. 2020. Network-based drug repurposing for novel coronavirus 2019-nCoV/SARS-CoV-2. *Cell Discov.* **6**(14).

compound does not inhibit human deubiquitinating enzymes, an important design criterion of SARS-CoV-2 molecular therapeutics developments (manuscript to be submitted).

3CLpro Complexes

The NSLS-II team solved the structure of 3CLpro in complex with commercially available protease inhibitors (including boceprevir, telaprevir, and narlaprevir) (see Fig. 1.8, p. 16). Crystallographic data revealed the modes of binding for these compounds, and the models and data were deposited in the Protein Data Bank. The SLAC team solved the crystal structure of SARS-CoV-2 3CLpro in

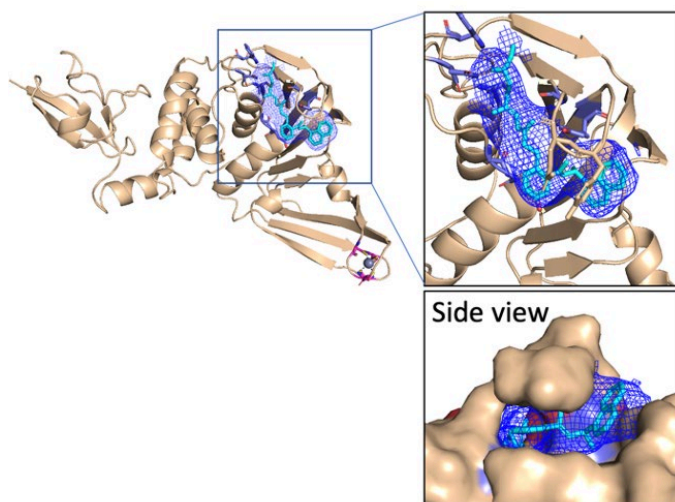


Fig. 1.7. Covalent inhibitor designed by Oak Ridge National Laboratory bound to the SARS-CoV-2 papain-like protease (PLpro). Overall PLpro structure (teal) and the inhibitor (cyan) with its electron density (left). The compound and the density in the active site residues in purple (inset, top right). Surface of PLpro showing how tightly the inhibitor compound is surrounded by the enzyme (bottom, side view of the inset). [Courtesy SLAC National Accelerator Laboratory]

complex with a human NF- κ B essential modulator (NEMO) (see Fig. 1.8). This provides a structural basis of human protein substrates as targets of SARS-CoV-2 3CLpro, which could lead to a disruption of the human NF- κ B pathway. Molecular dynamics, quantum mechanics/molecular mechanics, and AI/ML binding studies by the ORNL team provided extensive comparisons of the binding and cleavage activities of 3CLpro enzymes from various viruses and several host protein substrates (manuscript in preparation).

Cryo-EM Structures of SARS CoV-2 Components

The NSLS-II team determined a structure of the human cell junction protein PALS1 and SARS-CoV-2 viral envelope (E) protein. The structure shows that an E protein C-terminal motif recognizes a pocket formed exclusively by hydrophobic residues from PALS1 and provides novel targets for peptide and

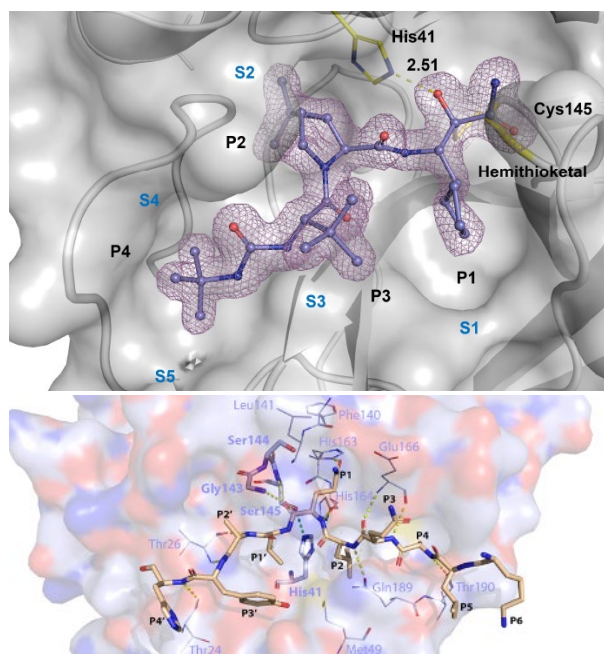


Fig. 1.8. SARS-CoV-2 3CLpro structure in complex with small molecule and protein substrates. Complex between 3CLPro and boceprevir (top). NEMO peptide interactions with the active site residues of SARS-CoV-2 3CLpro (bottom). [Courtesy SLAC National Accelerator Laboratory]

small-molecule inhibitors that could block the PALS1-E interactions to reduce E-mediated virulence.

The SLAC team led by Wah Chiu and Stanford University scientists determined the structure of a frame shift stimulation element from the SARS-CoV-2 RNA genome using cryo-EM. The frame shift is one of the critical processes in viral replication, producing different sets of viral proteins. The high-resolution cryo-EM structure provides a way to target the common RNA feature as robust molecular therapeutics, which would be less prone to virus mutations.

1.5 Task 2: Discovery and Optimization of Small-Molecule, Vaccine, and Antibody Therapeutics

The Molecular Design team used a multi-pronged computational approach to identify

small-molecule therapeutics and design vaccines and antibodies. This research used the horsepower of DOE's leadership computing facilities for computational docking and AI-based screening of millions of small molecules, vaccines, and antibodies; development of technologies to support unique challenges for inhibitors of cysteine proteases; detailed simulations of the most promising hits; and iterative optimization to improve the predicted efficacy and safety of designed therapeutics.

Task 2 focused on three deliverables:

1. Iteratively designing and optimizing small-molecule modulators of SARS-CoV-2 proteins.

The team used AI/ML models and probabilistic generative AI design, along with mechanistic molecular dynamics and quantum mechanics rescoring, to tightly couple computation with Task 3 experimental measurements. This approach drove optimal design of successive rounds of computation and experimentation and provided feedback for iterative design of small-molecule therapeutics.

2. Developing a novel covalent modeling pipeline to build advanced lead sets for viral and host cysteine proteases.

The viral proteases 3CLpro and PLpro both belong to the cysteine protease family, a structural family that is not amenable to traditional docking-based modeling pipelines. Comprehensive molecular dynamics and quantum mechanics approaches were implemented and applied to the design and optimization of covalent small-molecule inhibitors of 3CLpro and PLpro.

3. Iteratively designing vaccines and antibodies.

A suite of structural biology capabilities were utilized for simultaneous optimization of efficacy and developability of protein-based therapeutics using integrated ML and mechanistic models. Experimental evaluation of proposed designs fed back into the optimization process to improve predictive models. Engaged facilities included DOE light and neutron sources.

1.5.1 Task 2 Deliverable 1: Iteratively Design and Optimize Small-Molecule Modulators

Graph Neural Fingerprint Docking Models

Docking is a first step in screening libraries of drug-like molecules as candidates against protein targets. In this process, an algorithm works through a collection of molecules trying different positions, orientations, and conformations looking for a good fit to a cavity or pocket in a protein's structure. A good fit is found when the molecule shows a significant binding energy. In practice, highly approximate expressions are used for the binding energy. Even then, docking screens are expensive because of the tremendous scale of the molecule libraries and the many energy evaluations needed for each molecule. Significant progress can be made by reducing the resources needed for docking screens.

In principle, once a pocket in a protein has been identified and a drug-like molecule selected, the factors that determine how well the complex will bind are fixed. This suggests that it is possible to build a ML model that directly predicts how well a molecule will bind to a particular pocket. Unlike a docking model, such a ML model would not predict the binding pose, but that information can easily be obtained from regular docking codes for the top candidates once they have been established. Based on these ideas, a ML approach that uses graph neural networks to predict binding energies was developed. Specifically, different approaches were compared to encode the molecule and pocket properties so that separate encodings for the molecule and pocket properties could be built, with the aim of building target-agnostic models. Such models should be applicable to different future targets, rather than being target specific and requiring retraining for every protein pocket. A paper was published in the *Journal of Chemical Information and Modeling* (Clyde et al., 2021).

Additional details about high-throughput virtual screening (HTVS) workflows and specific

computational campaigns are included in the “Crosscutting Deliverable 2” section (see p. 9). HTVS workflows were used to screen a targeted compound library of over 6.5 million molecules that could be readily ordered against all SARS-CoV-2 viral proteins; multiple docking sites for each protein and protein-protein interfaces were screened, resulting in more than 100 HTVS campaigns.

3CLpro: Main Protease

For the viral 3CLpro, a noncovalent small-molecule inhibitor, MCULE-5948770040, was identified and experimentally validated as a 3CLpro inhibitor with an inhibitor constant (K_i) of 2.9 μM potency. The molecule binds to the primary active site of 3CLpro. The ML-based analyses of these simulations demonstrate quantitatively that the bound ligand alters the conformational states accessed by 3CLpro, involving motions both proximal and distal to the binding site. Neutron and room-temperature crystallographic studies were carried out, and a structure of the molecule bound to the 3CLpro active site is shown in Fig. 1.3, p. 5.

Together, the results provide insights into how even smaller, targeted compound libraries can be used to discover novel validated inhibitors for 3CLpro, while also providing mechanistic insights into how such inhibitors may provide starting points for further therapeutic design. Two manuscripts were published, one describing the computational discovery and experimental validation of MCULE-5948770040 (Clyde et al., 2022) and a second describing the activity of structurally related analogs of MCULE-5948770040 (Kneller et al., 2021). This set of molecules were transferred to ATOM, a public-private partnership among DOE, the National Cancer Institute, GlaxoSmithKline Pharmaceuticals, and the University of California San Francisco; ATOM will use these molecules as a starting point for AI/ML-enabled synthesis of molecules with improved activity for SARS-CoV-2 3CLpro and broad-spectrum activity for MERS-CoV 3CLpro.

Non-Protease Viral Proteins

DOE computing resources and AI methods were used to conduct computational docking calculations and screen tens of millions of small molecules against more than 100 binding sites of the SARS-CoV-2 viral proteins. Larger databases (on the order of 50-100 million molecules) also were docked against a subset of the 100 binding sites. From these computational screens, more than 2,000 small molecules were purchased for experimental validation in an antiviral screen, and 56 of those molecules showed some inhibition of viral infection in a cell-based assay. The 56 hits are being confirmed in an independent antiviral screen, and experiments are ongoing to elucidate which parts of the viral lifecycle are being inhibited by each confirmed hit.

1.5.2 Task 2 Deliverable 2: Develop Covalent Modeling Pipeline

Computational high-throughput screening on high-performance supercomputers shows great promise to expedite the identification of promising drug compounds in a computational workflow. However, the computational prediction of covalent inhibitors is severely hampered by the shortcomings of commonly employed methods based on molecular mechanics or empirical scoring function, which are unable to accurately describe the formation of the covalent bond. Quantum mechanics has the potential to quantitatively describe covalent docking in computational drug discovery due to its native ability to describe chemical bond formation and breaking. In this task a linear scaling version of an approximate, yet remarkably accurate, density functional theory method called fragment molecular orbital density-functional tight-binding was employed in a supercomputer pipeline for the quantum mechanics-based refinement and re-evaluation of potential COVID-19 drug inhibitors. As a first use case, compounds from a molecular library containing mild electrophilic inhibitor candidates were computationally screened, revealing potential covalent binders to the 3CLpro and PLpro of SARS-CoV-2. The inclusion of quantum mechanics-based methods in the

computational drug discovery workflow will allow for more accurate predictions of strong covalent inhibitor drug candidates in the future.

The Automated Modeling Engine for Covalent Docking (AMECovDock), using AutoDockFR docking³, was developed and contains all the pieces needed to automate covalent docking of specified electrophilic warheads to a receptor cysteine sidechain of the protein target. Given a prepared receptor and a list of SMILES, the pipeline forms a covalent bond between the cysteine sidechain and the appropriate functional groups. Using AME-CovDock and a recently developed deep-learning 3D-scaffold model (Joshi et al. 2021) to generate warhead-based covalent candidates, the team screened for covalent small-molecule inhibitors targeting SARS-CoV-2 3CLpro based on their binding affinity as an indicator of their potential effectiveness as dimer inhibitors. Several potential candidates were identified and further tested experimentally using native mass spectrometry and fluorescence resonance energy transfer (FRET)-based screening assays. Four of the AI-generated compounds with chloroacetamide warheads were hits with high functional activities. (Half maximal inhibitory concentration, or IC₅₀, ranged from 0.02-2 μM). These hits were further confirmed to be covalently bound using time-dependent experiments. To elucidate the molecular basis of 3CLpro inhibition and covalent binding by chloroacetamide warheads compounds, an X-ray crystal structure of 3CLpro in complex with these compounds was determined to 1.80 Å at near-physiological (i.e., room) temperature. A comparison of the computationally predicted (pink carbons) and experimentally determined (purple carbons) pose of C_Z2799209083 bound to 3CLpro is shown in Fig. 1.9, this page. Atomistic molecular dynamics simulations were used to characterize the mechanism by which this inhibitor interacted and bound to the 3CLpro active

³ Ravindranath, P. A.; Forli, S.; Goodsell, D. S.; Olson, A. J.; San-ner, M. F., AutoDockFR: Advances in Protein-Ligand Docking with Explicitly Specified Binding Site Flexibility. *Plos Computational Biology* **2015**, 11.

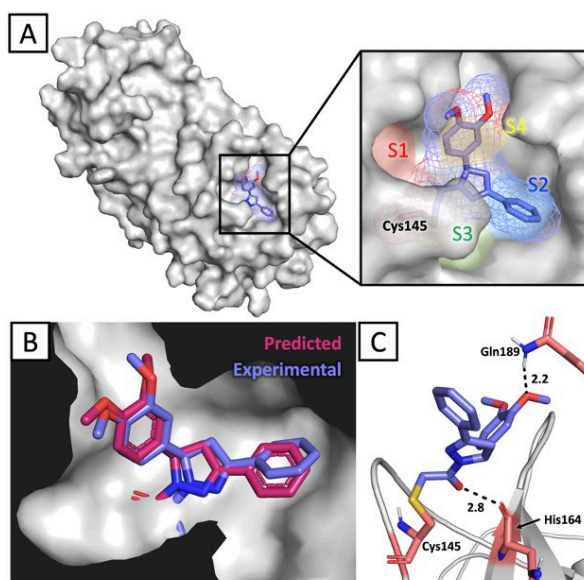


Fig. 1.9. (A) Single subunit of SARS-CoV-2 3CLpro shown with predicted binding pose of ligand C_Z2799209083. Subsites are labelled S1-S4 binding pockets. (B) Sectional view of the binding pocket occupied by the predicted ligand pose superimposed with the experimentally determined crystal structure. (C) Polar contacts between the binding pocket residues and C_Z2799209083. [See Clyde, A., et al. High-Throughput Virtual Screening and Validation of a SARS-CoV-2 Main Protease Noncovalent Inhibitor, *J. Chem. Inf. Model.* **2022**, 62 (1) 116–128.]

site, while altering the enzyme's overall conformational dynamics.

A series of covalent inhibitors of PLpro was computationally designed by introducing a linker and a warhead into a previously reported noncovalent inhibitor. The computationally designed PLpro inhibitor binds to the protein and then reacts to form a chemical bond with the cysteine residue that is vital for enzyme activity. A subset of these designed inhibitors was sent to external groups for screening against structurally related human proteins and for measuring their metabolic stability. The most promising covalent inhibitor was potent and selective for PLpro and displayed antiviral activity in cell-based assays rivaling that of the RNA-dependent RNA polymerase inhibitor

remdesivir in a side-by-side comparison. In addition, collaborators at SLAC determined an X-ray crystal structure of the compound bound to PLpro (see Fig. 1.7, p. 16). This promising lead molecule has sufficient metabolic stability in mouse liposomes to enable a small study of efficacy in mice; the experiment was conducted by collaborators at the University of Tennessee Health Sciences Center. A manuscript describing these findings is in preparation, a patent covering the lead molecule and a set of structurally similar compounds was submitted, two NIH grant proposals were submitted, and the team is exploring a possible licensing opportunity with a small biotechnology company.

1.5.3 Task 2 Deliverable 3: Iteratively Design Vaccines and Antibodies

Viral neutralizing antibodies, specifically humanized single-domain heavy chain antibodies (nanobody-huFc antibodies), represent a promising therapeutic tool to help mitigate the progression of patients with COVID-19 to severe disease. Several antibody therapies have been approved for emergency use authorization by the FDA; however, SARS-CoV-2 glycoprotein variants pose a significant risk to successful intervention by these antibody therapies and vaccine-driven immunity. Having multiple therapeutic options combined with information about their success against specific SARS-CoV-2 variants is critical to overcoming the current pandemic. Using a high-diversity (3.24×10^{10}) single-domain (nanobody) library (see Fig. 1.10A, p. 21), multiple nanobodies that strongly bind SARS-CoV-2 spike protein and the receptor binding domain (RBD) were identified (see Fig. 1.10B, p. 21).

These nanobodies, also known as V_H Hs, are the variable region of heavy chain only antibodies (HcAbs). They are highly soluble, stable, versatile, and contain unique structural attributes in their complementarity determining region 3 (CDR3) loop, which can facilitate binding to antigen sites inaccessible to traditional immunoglobulin G (IgG) antibodies. To increase the half-life of

the nanobody candidates and take advantage of the effector functions of human IgG, each top candidate was produced as a fusion to the hinge region and crystallizable fragment (Fc) domain of a human IgG1 (V_H H-huFc) (see Fig. 1.10C, p. 21). Nanobody-huFc antibody constructs are half the size of a conventional antibody, making them easier to produce and better able to circulate to and penetrate target body tissues. Each of these nanobody-based huFc antibodies was characterized in biochemical, biophysical, and cell-based assays to determine their *in vitro* efficacy (see Fig. 1.11, p. 22).

Using a pseudotyped SARS-CoV-2 virus, next-generation sequencing, and biophysical methods, the viral epitopes targeted by these antibodies were identified and the means by which the virus escapes neutralization were determined (see Fig. 1.12, p. 23).

Next, a robust animal model was used to determine the efficacy of top candidates both prophylactically and as a treatment. Two of the candidates showed great preclinical potential (see Fig. 1.13, p. 24). The work (Stefan et al. 2021) is described in Fig. 1.10, p. 21.

After the Stefan et al. (2021) publication, multivalent anti-SARS-CoV-2 nanobodies were constructed with two distinct antigen binding sites linked to human IgG Fc. Although the V_H H-huFc antibodies identified by Sandia National Laboratories (SNL) in the initial screen bound to a single epitope, the U nanobody described in Koenig et al. (2021) targeted a distinct epitope and was used in combination with the SNL-identified nanobodies resulting in a synergistic neutralization increase up to levels comparable to currently deployed therapeutics (see Fig. 1.14, p. 25).

Studies are underway to determine the efficacy of these constructs against VSV-SARS-CoV-2-green fluorescent protein pseudoviruses expressing the spike protein from circulating variants of SARS-CoV-2, including Alpha, Beta, Delta, Gamma, and Lambda. Based on the results, their efficacy will be

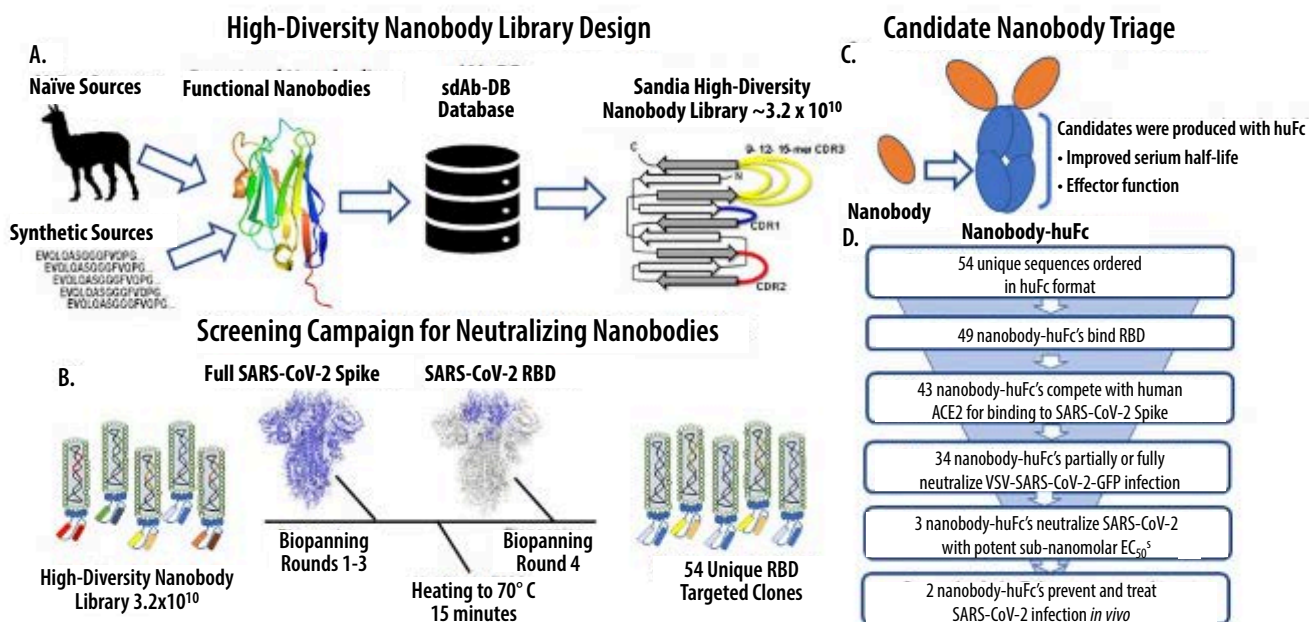


Fig. 1.10. Development and screening of high-diversity nanobody library to identify and characterize anti-SARS-CoV-2 nanobody-based humanized antibodies. **(A)** Nanobodies are the variable antigen binding fragment of heavy chain antibodies found in camelids. The proprietary synthetic high-diversity nanobody library includes a humanized nanobody framework, and complementary determining regions (CDR) were designed using sequences from the single domain antibodies database (sdAb-DB) to determine optimal CDR length and amino acid prevalence at each amino acid position within each respective CDR. **(B)** Schematic for the screening (biopanning) approach used to identify neutralizing nanobodies directed to the SARS-CoV-2 RBD. **(C)** Selected SARS-CoV-2 nanobodies were produced as nanobody-based humanized heavy chain antibodies (nanobody-huFc) by fusing the nanobodies to the hinge region and crystallizable fragment (Fc) domain of a human immunoglobulin G (IgG)1. **(D)** Triage flowchart for selection of top nanobody-huFc candidates, from production as nanobody-based huFc antibodies to characterization of top nanobody-based huFc antibodies *in vivo*. [Reprinted under a Creative Commons License (CC BY-NC 4.0) from Stefan M.A., et al. 2021. Stefan M. A., et al. Development of potent and effective synthetic SARS-CoV-2 neutralizing nanobodies, *mAbs* **2021**, 13 (1).]

evaluated *in vivo* using a mouse model of severe SARS-CoV-2 disease and the wildtype version of these SARS-CoV-2 variants.

In addition, a high-diversity (3.24×10^{10}) single-domain (nanobody) library is being screened against seven variant RBDs to discover specific broad-spectrum nanobodies that work against the SARS-CoV-2 variants. Biopanning against the Alpha, Beta, Epsilon, and Kappa SARS-CoV-2 RBDs was carried out and the phages screened for neutralization of VSV-SARS-CoV-2 pseudoviruses

with spike mutations from the Beta, Delta, Gamma, and Wuhan strains. The top 40 candidates from the screen were ordered as nanobody-huFc constructs for validation.

1.6 Task 3: Experimental Validation and Characterization of Small Molecules, Vaccines, and Antibodies

National laboratory and DOE user facility capabilities in small-molecule synthesis and biochemical,

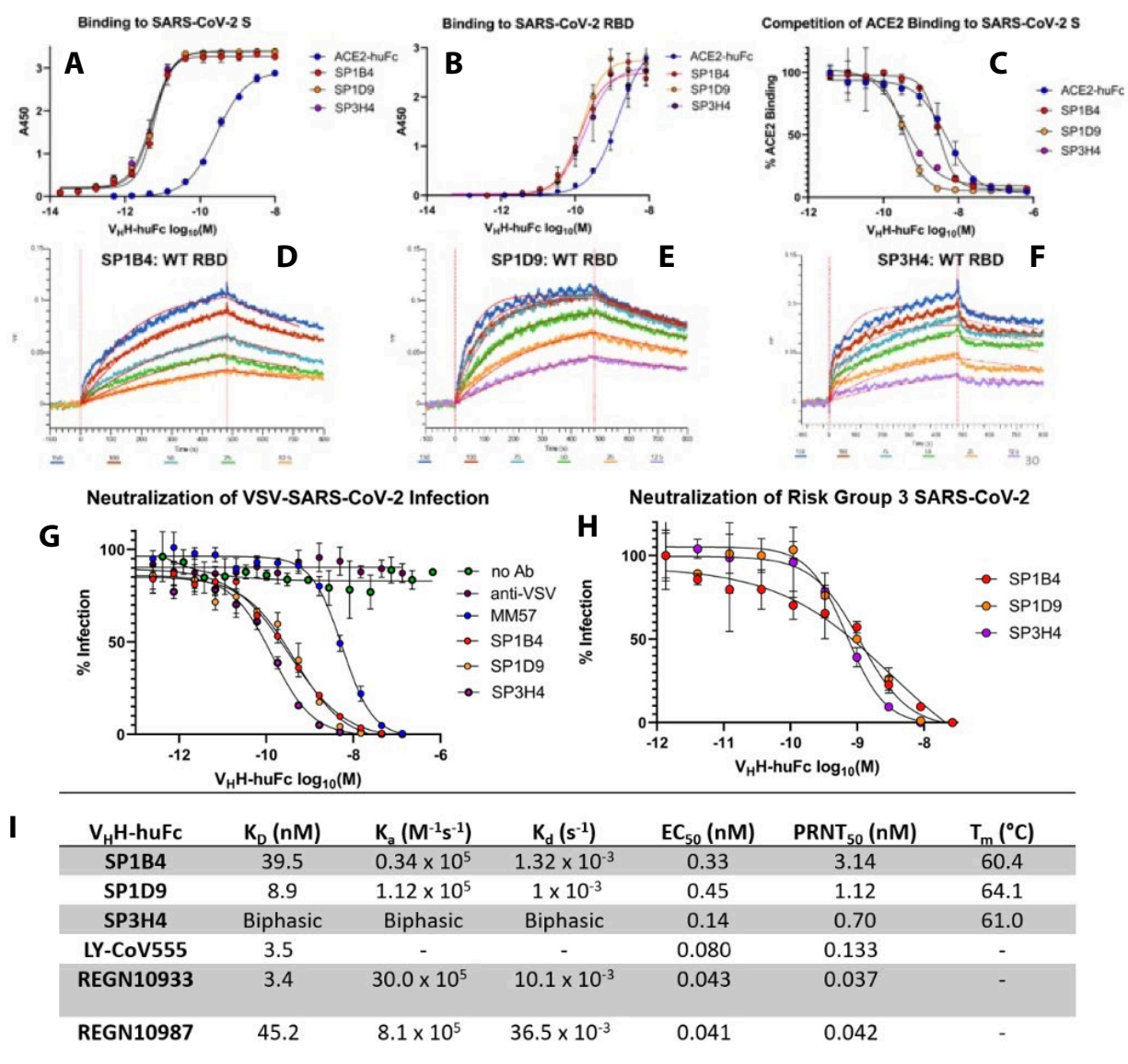


Fig. 1.11. *In vitro* characterization of top nanobody-huFc candidates. Reconfirmation ELISA of top three candidates binding to (A) SARS-CoV-2 S and (B) SARS-CoV-2 RBD. (C) Top candidate V_HH -huFcS compete with ACE2-huFc for binding to SARS-CoV-2 S by competition ELISA. BLI sensorgrams show binding to SARS-CoV-2 RBD by SP1B4 (D), SP1D9 (E), and SP3H4 (F). At least 5 concentrations were used for global fit analysis. (G) SP1B4, SP1D9, and SP3H4 all neutralize VSV-SARS-CoV-2 GFP infection of Vero cells. The data for A-F are from experimental conditions performed in triplicate, the error is the standard deviation from the mean. (H) All three V_HH -huFcS also neutralize wt SARS-CoV-2 in a plaque reduction neutralization assay. The data from this is the mean of the plaque assay performed in duplicate, the error is the standard deviation from the mean. (I) Table summarizing kinetic properties, neutralizing efficacy, and thermal stability properties for SP1B4, SP1D9, and SP3H4. Melting temperatures from DSF were determined from two independent experiments each performed in triplicate. [Reprinted under a Creative Commons License (CC BY-NC 4.0) from Stefan M.A., et al. 2021. Stefan M. A., et al. Development of potent and effective synthetic SARS-CoV-2 neutralizing nanobodies, *mAbs* 2021, 13 (1).]

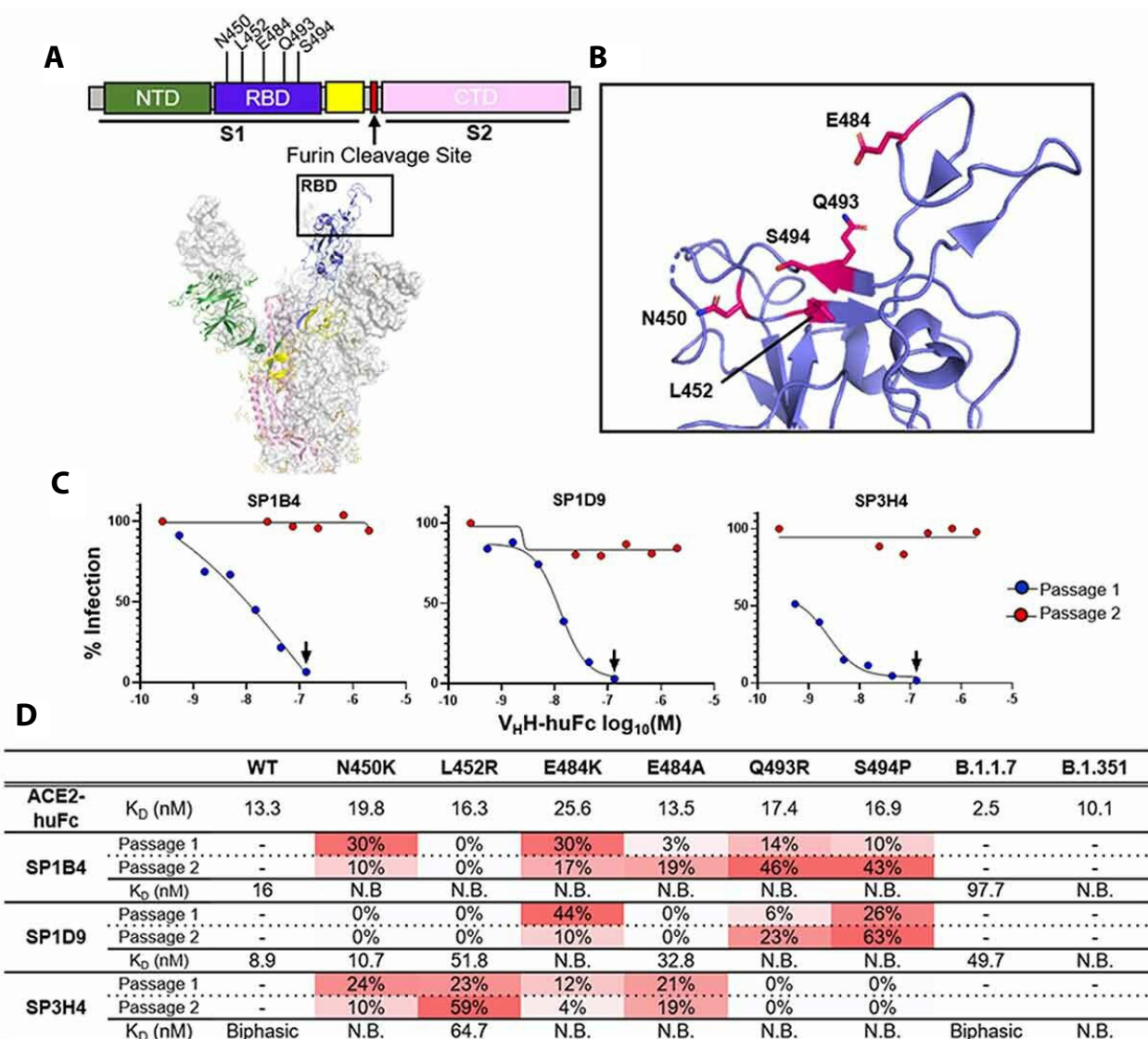


Fig. 1.12. Generation and characterization of V_HH -huFc neutralization escape mutants. **(A)** Subdomains of the SARS-CoV-2 S gene are color coded with corresponding structural context (PDB: 7CAK). Loci of mutations on S gene from NGS evaluation of virus supernatant from virus infected cells passaged in the presence of V_HH -huFc antibodies. In this structure the RBD is in the up position. **(B)** The RBD is designated with the dominant mutations characterized in this study (magenta). **(C)** VSV-SARS-CoV-2-GFP neutralization escape occurs in a single passage. VSV-SARS-CoV-2-GFP neutralization is recorded 12 hpi. The black arrow designated the well from which the virus-containing supernatant was taken and diluted for the second passage. Data for this is from a single replicate. **(D)** NGS and kinetic summary of each of the neutralization escape mutant profiles for SP1B4, SP1D9, and SP3H4. Dissociation constants for each individual RBD mutation with ACE2-huFc and V_HH -huFc antibodies. N.B. = no binding observed at 150 nM SARS-CoV-2 RBD by BLI. Sensorgrams were designated biphasic if they did not agree with a global 1:1 fit analysis. The prevalence of each escape mutation is presented as a percentage at that amino acid position and is conditionally colored with increasing intensity of red. [Reprinted under a Creative Commons License (CC BY-NC 4.0) from Stefan M.A., et al. 2021. Stefan M. A., et al. Development of potent and effective synthetic SARS-CoV-2 neutralizing nanobodies, *mAbs* **2021**, 13 (1).]

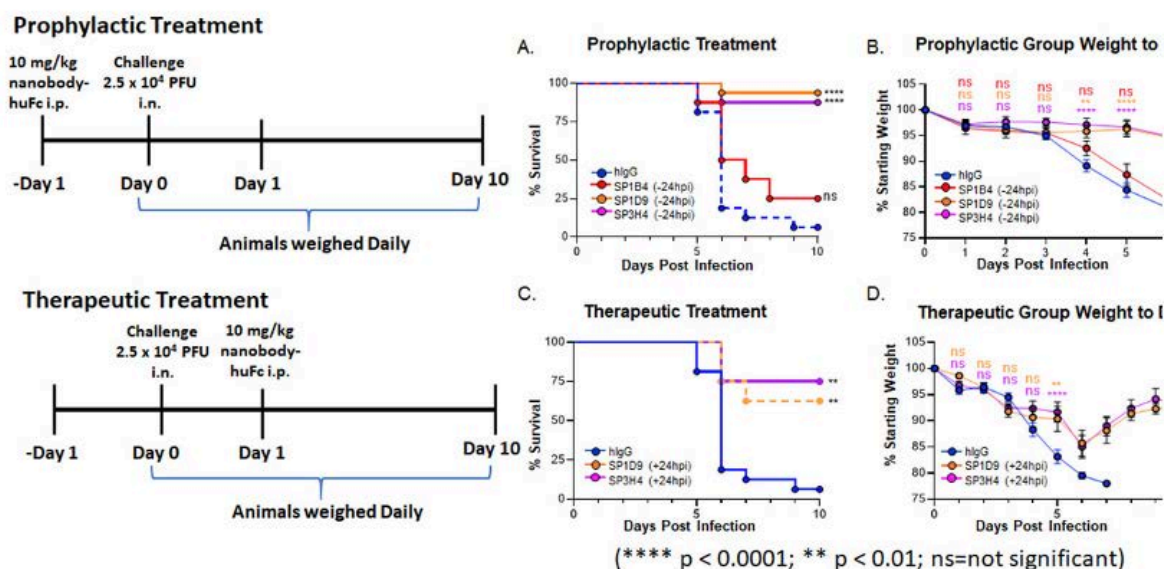


Fig. 1.13. Top nanobody-huFc candidates provide protection from lethal SARS-CoV-2 infection *in vivo*. Kaplan-Meier curve illustrating percentage survival of K18-hACE2 mice infected intranasally with 2.5 x 10⁴ PFU SARS-CoV-2 and dosed with 10 mg/kg nanobody-huFc via intraperitoneal injection prophylactically (A) at 24 hours prior to infection or therapeutically (C) at 24 hpi. A log rank test was performed with Bonferroni multiple comparison correction applied. (B) Percentage weight loss for mice in (A). (D) Percentage weight loss for mice in (C). For (B) and (D), statistical analyses were performed at time points when all mice were alive to avoid survivor bias. Data displayed are the mean +/- standard error of the mean. [Reprinted under a Creative Commons License (CC BY-NC 4.0) from Stefan M. A., et al. 2021. Stefan M.A., et al. Development of potent and effective synthetic SARS-CoV-2 neutralizing nanobodies, *mAbs* 2021, 13 (1).]

biophysical, and cell-based assays bridged the computational and structural biology power of Tasks 1 and 2 with an immediate, integrated approach to validating computational models and characterizing designed molecules. The goal was to derive potential therapeutics for further development by academic, government, biomedical, and pharmaceutical partners.

Task 3 deliverables included:

1. Synthesizing small molecules. Task 3 scientists performed rapid synthesis of small molecules to support active learning feedback into AI/ML models and iterative design cycles for potential therapeutics. Additionally as-needed, labeled versions of selected molecules were synthesized to support design and mechanistic understanding

for covalent inhibitors of the viral cysteine proteases.

2. Performing biochemical and biophysical assays to enable construction and validation of computational models for small molecules, antibodies, and vaccines. Plate-based enzymatic assays, binding assays using mass spectrometry, surface plasmon resonance, other relevant methodologies, and encoded library technology selections were carried out to generate data for training AI/ML models and to activate learning feedback and iterative design of small molecules, vaccines, and antibodies.

1.6.1 Task 3 Deliverable 1: Small-Molecule Synthesis

The Task 3 team reviewed hitlists from colleagues in Task 2 and prioritized molecules based

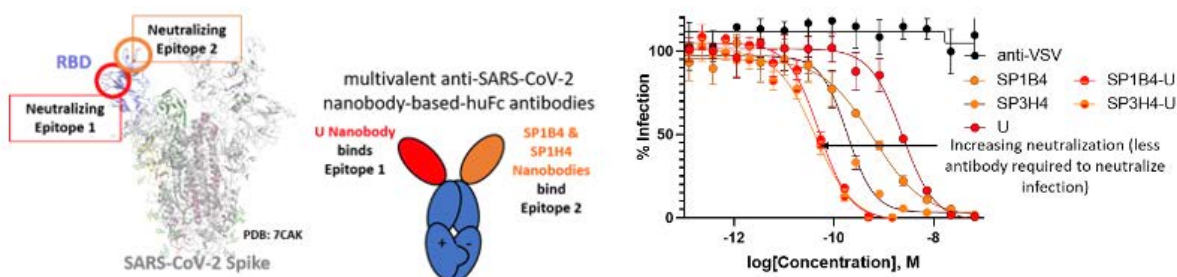


Fig. 1.14. Improving therapeutic potential by targeting multiple non-overlapping epitopes. Construction of multivalent anti-SARS-CoV-2 nanobodies with two distinct antigen binding sites on RBD, shown in orange and red circles, linked to human IgG Fc (blue) resulted in a synergistic increase in neutralization to levels comparable to currently deployed therapeutics. [See Stefan, M. A., et al. Development of Potent and Effective Synthetic SARS-CoV-2 Neutralizing Nanobodies, *mAbs* **2021**, 13 (1) 1958663.]

on: (1) optimal synthesis routes, (2) solubility, (3) potential toxicity based on known motifs, and (4) availability of these molecules from commercial sources. During the project, the team synthesized close to 100 compounds that supported the experimental validation and exploration of computationally designed molecules. The class of compounds synthesized, analyzed, and advanced for bioassay validation spanned a wide range of molecular scaffolds. The following text provides selected examples of the compounds that were synthesized *de novo*. Most of the molecules were novel molecular entities. However, the pandemic resulted in serious limitations with acquiring globally sourced pharmacores. In addition to stay-at-home mandates for resource providers, supply chain constraints made sourcing materials time consuming. Consequently, the team deployed DOE resources to synthesize entities and chemical intermediates that were no longer commercially available or on backorder due to pandemic supply shortages.

A key outcome of this NVBL project was the rapid mobilization of biochemical synthesis capabilities at national laboratories. In addition to providing support for the project, this demonstration of advanced biochemical synthesis points to an available national resource for therapeutic design projects.

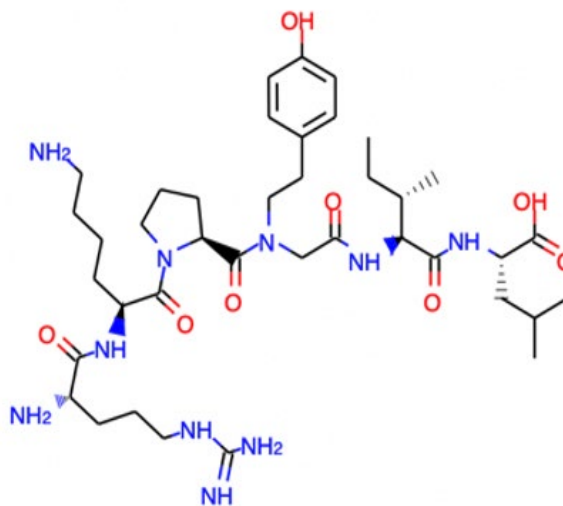


Fig. 1.15. Peptidomimetic structure as 3CLpro inhibitor. [Courtesy Los Alamos National Laboratory]

Peptidomimetics as Protease Inhibitors

All peptides and peptidomimetics were derived from automated solid phase syntheses. Syntheses followed general peptide synthetic protocols, and all compounds were purified using HPLC and confirmed by mass spectrometry.

SARS-CoV strains engage in protein processing for cell entry using SARS-CoV viral proteases, such as SARS-CoV-1 3CLpro. These proteases are ideal targets to interfere with and prevent host cell entry.

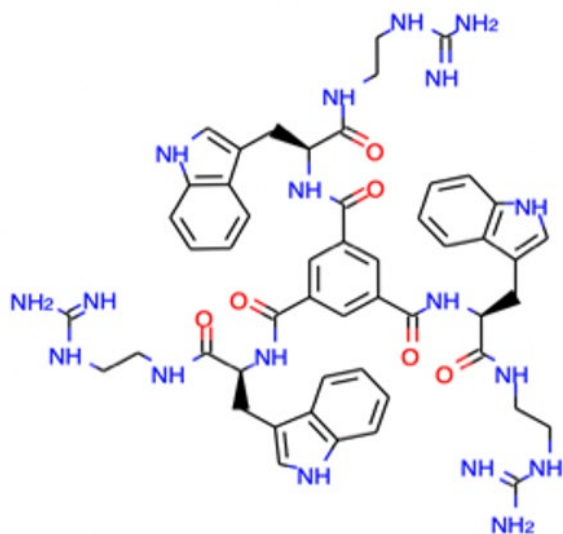


Fig. 1.16. Tridentate molecule to bridge spike protein helical bundles. [Courtesy Los Alamos National Laboratory]

Thus, synthesized peptidomimetic small molecules were designed to interfere with and inhibit these viral enzymes. An example is shown in Fig. 1.15, p. 25. This structure contains common structural features that mimic the natural peptide substrate but enable substitutions that make the molecule more stable towards cleavage by the enzyme (peptide to peptoid substitution) while increasing its affinity to compete with the natural peptide target. More than 30 compounds, peptide mimetics, and small molecules were synthesized as protease inhibitors. Typical quantities synthesized and shipped to sister laboratories were in the range of 100-1,000 mg and included enantiomers.

Spike Structure Disruptors

The SARS-CoV-2 spike protein makes initial contact with the host cell. Disrupting the structure of the spike protein may therefore reduce host-cell docking and consecutive host-cell docking. Model structures that interact with the helical spike protein structure were synthesized. One example (see Fig. 1.16, this page) is a tridentate bridging molecule found to connect helical bundles of spike protein and slow the folding necessary for infection. Eight such compounds were synthesized.

Nucleoside Analogs

Viral replication, once infection cycles commence, is significantly dependent on the processing of DNA and RNA to produce proteins for the viral capsid, the Nsp15 protein for nucleoside turnover, and the synthesis of viral progeny genomes.

Nucleoside antivirals, such as remdesivir, are thus attractive target compounds for disrupting viral replication. From computational leads of potential nucleoside analogs, 39 nucleoside mimics were synthesized including a small combinatorial library. Two examples are illustrated by their chemical structures in Fig. 1.17, p. 27.

Substrates for Bioassays

Assay Substrates and Peptides for Substrate Selections

To support bioassay selection of the inhibitors, more than 25 peptides (in significant quantities) were designed and synthesized to be used in fluorescent assays, stable isotope assisted mass spectrometry quantification, and the design of new assay formats by screening substrate candidates. This included PLpro/3CLpro, Nsp15 assay substrates delivered, and an ADRP substrate. Examples shown in Fig. 1.18, p. 27, include a peptide substrate labeled with a stable isotope and two fluorescent substrates that became commercially unavailable during the pandemic. The substrates, although expensive, are normally commercially available. During the COVID-19 pandemic these SARS-CoV-2 substrates were on indefinite back-order due to high demand. Use of microwave syntheses for peptide syntheses is very efficient but leads to reaction of the EDANS amines with the incoming amino acids. The overall reaction thus failed under standard conditions as double derivatized EDANS cannot be removed from the resin. Optimization included attachment of the first residue to the EDANS resin with HATU at room temperature, followed by chain elongation at 500°C for 5 minutes to reduce this side reaction. While substrate synthesis was not in the original plan, this capability enabled the assay teams to

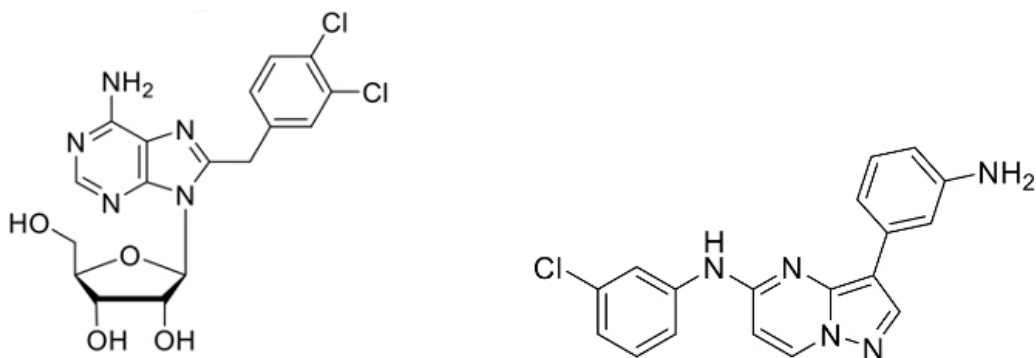


Fig. 1.17. Nucleoside analog examples. [Courtesy Los Alamos National Laboratory]

proceed quickly and was another key outcome of this project.

Synthesis Support in Scaling Reactions for Toxicity and Efficacy Studies

Leads identified for further development were scaled to gram quantities necessary for biological testing in toxicity and efficacy studies. Multiple samples of > 200 milligrams for the targets were prepared and sent to sister labs. Further, grams of the intermediates before final attachment of a suicide inhibitor group are currently awaiting the final down selection of the pharmacophores. The compounds are currently being experimentally evaluated and potential intellectual property protection does not allow their inclusion in this report. At the time of writing, multiple compound syntheses are ongoing, including substrates for the ADRP assay (see “Screening of ADRP Inhibitors,” p. 32).

1.6.2 Task 3 Deliverable 2: Assays to Inform Computational Models of Target Therapeutics

The assay component of the Task 3 effort encompassed the entire team, with each laboratory taking responsibility for a single or set of viral targets. Targets identified and prioritized by Tasks 1 and 2 teams were discussed, and the Task 3 team decided on a path forward based on assay availability. In some cases, the team decided to

Dabcyl-KLAQLQVAYHQE-EDANS

Dabcyl-KLAQLQAAYHQE-EDANS

Cbz-RLRGG-AMC

(A+7)VLQSGFRKK

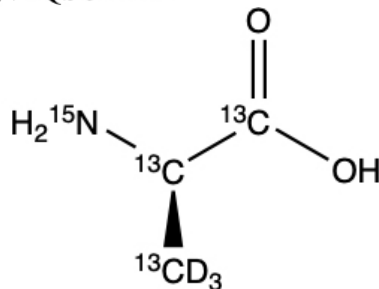


Fig. 1.18. Examples of synthesized assay substrates. [Courtesy Los Alamos National Laboratory]

develop an entirely new assay when a commercial option was not available. The coordinated approach to establishing assays, ordering compounds, and performing the assays resulted in a cumulative set of data captured in a master sheet (not presented here). Briefly, plate-based enzymatic assays; binding assays using mass spectrometry, surface plasmon resonance, and other relevant methodologies; and encoded library technology selections were carried out to generate data needed for training AI/ML models and to activate learning feedback and iterative design of

small molecules, vaccines, and antibodies. The initial data from these assays enabled decisions on a path forward for these molecules. So far, four compounds have met the stringent criteria of $IC_{50} < 10 \mu M$. This key outcome is shown in Table 1.1, this page.

Screening of Viral PLpro Inhibitors

Computationally predicted inhibitors against the PLpro SARS-CoV-2 target were obtained from Enamine and Mcule, Inc., or provided by the Task 3 synthesis team. The assays were optimized with commercial substrates for both targets. During later campaigns, the substrate provided by the Task 3 synthesis team was used successfully.

A PLpro assay was established using a commercial substrate from Bachem, Inc., in the early phase of the project (125 nM enzyme, 50 μM substrate, 50 μM compound, 20 mM Tris pH 8.0, 5 mM NaCl, 5 mM DTT, 0.1 mg/ml BSA). In a later phase of screening and inhibitor characterization, the substrate provided by the Task 3 synthesis team (Z-RLRGG-AMC) was used. The list of potential inhibitors was provided by the Task 2 team. During the first campaign, a set of 190 compounds was obtained from Enamine. The dry compounds were used to create 10 mM DMSO stocks. Several of the compounds were insoluble and excluded from downstream analyses. One of the compounds displayed inhibition at the 50 μM concentration. Upon further inspection it was revealed that the compound, GRL0617, is a well-characterized inhibitor of SARS-CoV-2 PLpro and a structure of the enzyme/

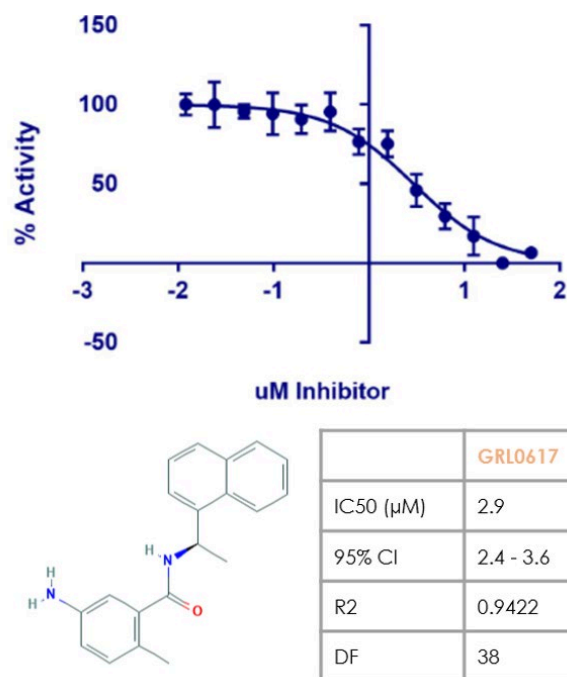


Fig. 1.19. Characterization of GRL0617 inhibitor. [Courtesy Oak Ridge National Laboratory]

inhibitor complex was already deposited into the Protein Data Bank (see Fig. 1.19, this page).

The synthesis team synthesized the two different enantiomer forms of this inhibitor but only the R-enantiomer was active as predicted (5-amino-2-methyl-N-[(1R)-1-naphthalen-1-ylethyl]benzamide). The compounds for the next two screening campaigns were purchased from Mcule and provided by synthesis teams. Unfortunately, none of the screened compounds displayed inhibitory activity.

Table 1.1. Hits with $IC_{50} < 10$ micromolar

| Target | Area 3 ID | Assay | Results |
|---------------|-----------|-------|--|
| 3CLpro (Mpro) | A81 | FRET | $IC_{50} < 20 \mu M$ in primary screen, $IC_{50} = 5 \mu M$ in curve in triplicate, crystal structure solved |
| PLpro | B8 | FRET | IC_{50} , $\mu M = 2.70$, 95% CI = 2.12 to 3.43 |
| PLpro | B214 | FRET | IC_{50} 0.08 μM (30 min preinc.); kinact/ Kiapp 0.6 min ⁻¹ μM ⁻¹ |
| PLpro | B219 | FRET | IC_{50} 0.07 μM (30 min preinc. similar IC_{50} and time dependence to BCS071) |

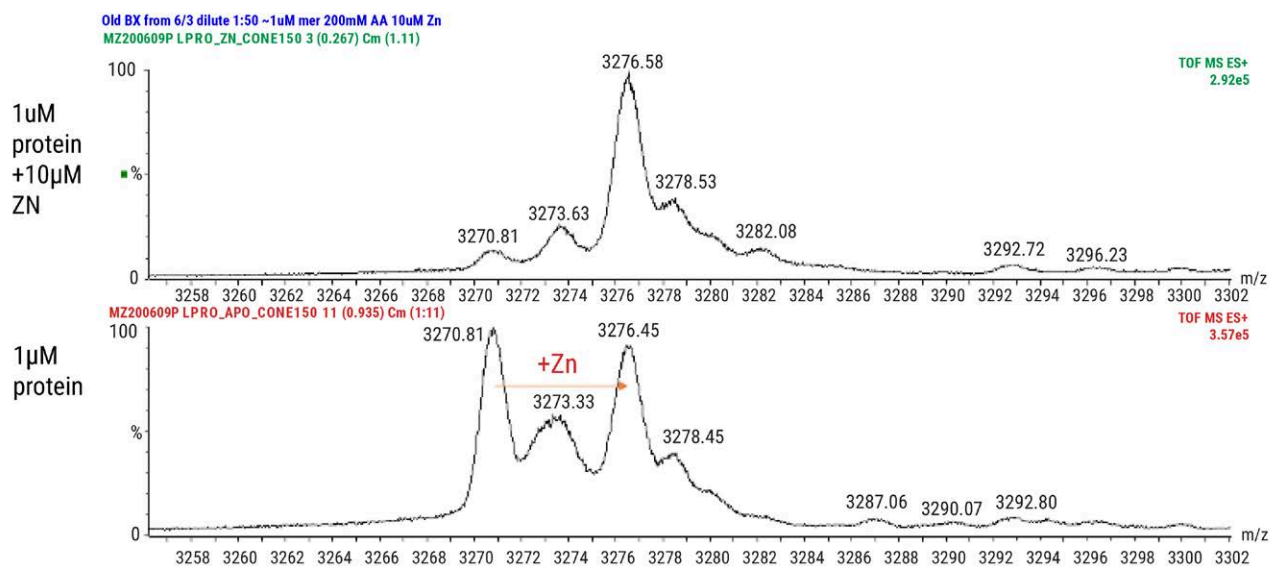


Fig. 1.20. Demonstration of PLpro saturation with Zn^{2+} supplementation using native mass spectrometry. [Courtesy Oak Ridge National Laboratory]

Overall, more than 290 compounds were tested in assays, and 190 compounds were tested using differential scanning fluorimetry for thermal shift. Since the enzyme is stored in a buffer supplemented with Zn^{2+} , native mass spectrometry was used to see if the enzyme was still saturated in diluted form. An aliquot of the protein was sent to PNNL for analysis, and it was revealed that adding $10 \mu M$ Zn^{2+} to PLpro at $1 \mu M$ concentration shifted the m/z peak of the complex, suggesting that Zn-supplementation was necessary in the assays (see Fig. 1.20, this page). A subset of compounds was re-tested with the new buffer recipe, but no significant changes were observed in either the control or screening activities.

Screening of Viral 3CLpro Inhibitors

3CLpro is an attractive drug target mainly because it plays a critical role in viral replication and does not have any closely related homologs within the human genome. Drug discovery efforts have resulted in discovering or repurposing small molecules based on their ability to inhibit 3CLpro from other coronaviruses such as MERS-CoV and SARS-CoV-1. However, it has been a challenge to identify noncovalent inhibitors for SARS-CoV-2

3CLpro, mainly due to the intrinsic flexibility of the primary binding site. From a Mcule library consisting of 6.5 million in-stock compounds, the team selected 116 for experimental screening, using the top 20 from different 3CLpro crystal structures. Of these 116 compounds, five were not available for ordering, 15 were excluded due to pan assay interference compounds violations, and 72 were ultimately delivered. The compounds were subjected to a primary SARS-CoV-2 3CLpro activity inhibition screen in which they were pre-incubated with the enzyme and the initial velocities of FRET peptide cleavage were determined. The Z' -factor of the assay was 0.65, and Fig. 1.21, p. 30, shows the distribution of the compounds' z-scores and the positive (no inhibitor) and negative (no enzyme) controls. At least 25% inhibition was observed for seven compounds, with MCULE-5948770040 resulting in the lowest residual activity at $20 \mu M$. The assays pointed to one molecule that inhibits 3CLpro with a K_i of $2.9 \mu M$; its room-temperature X-ray crystallographic structure was determined to 1.8 \AA resolution. Microsecond-timescale atomistic molecular dynamics simulations were used to characterize the binding mechanism to the 3CLpro active site while altering the enzyme's overall

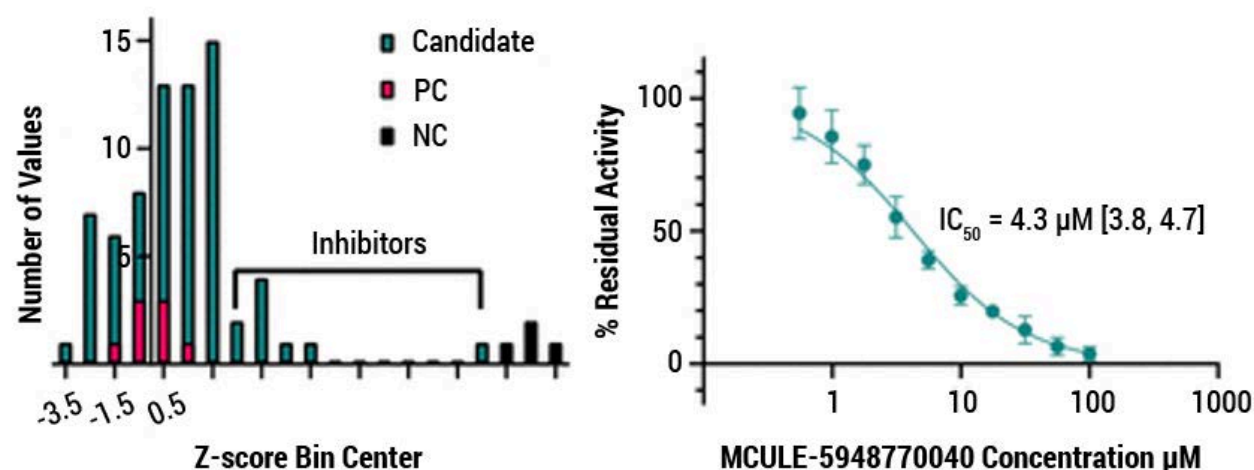


Fig. 1.21. Plate-based 3CLpro activity inhibition screening and hit confirmation. A histogram of z-scores of candidate inhibitors, no-enzyme negative controls (NC), and no inhibitor positive controls (PC) (left). Inhibition of 3CLpro activity *in vitro* with increasing concentrations of MCULE-5948770040 (right). [Courtesy Oak Ridge National Laboratory]

conformational dynamics. The workflow provides a scalable framework for the rapid discovery of viable lead molecules against SARS-CoV-2.

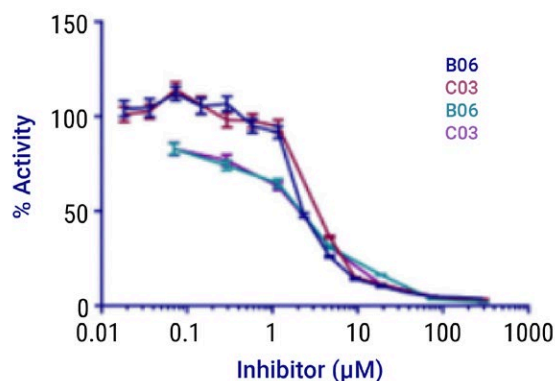
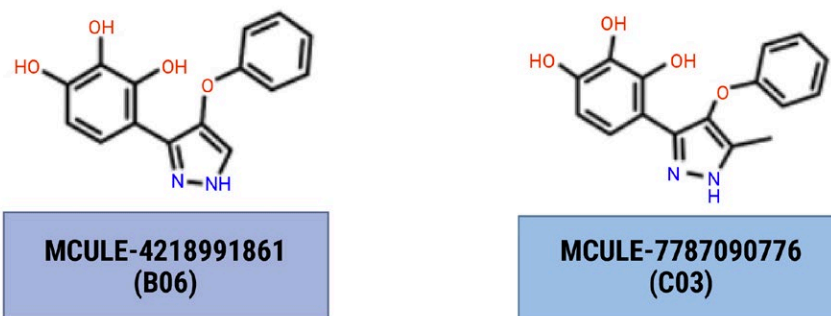
Screening of Nsp15 Inhibitors

A previously published Nsp15 assay was modified after testing different variants of the published substrate (5'- /56-FAM/ArUAA/3BHQ_1/ -3'). Up to two extra rU residues were added, which increased the observed signal. The screening campaigns were performed with the 5'- /56-FAM/ArUrU rUAA/3BHQ_1/ -3' substrate in the published condition (200 nM enzyme, 2 µM substrate, 50 µM Mcule compound, 20 mM HEPES pH 7.8, 100 mM NaCl, 5 mM MnCl₂). More than 200 compounds were screened for inhibition at 50 µM final concentrations. Two of the compounds displayed significant inhibition at this concentration and were used to measure half maximal effective concentration (EC₅₀) values (see Fig. 1.22, p. 31). The compounds were tested in cell assays at Argonne National Laboratory's High-Throughput Research Laboratory and displayed no inhibition of viral entry. The assay was not optimized for the screening of protease inhibitors, nor for the immune response elicited

when Nsp15 is inhibited. In addition to activity assays, more than 100 compounds were tested using differential scanning fluorimetry for thermal shift. The active compounds (B06 and C03) displayed lowered thermal melt points, suggesting a destabilizing effect.

The active compounds were sent for measurement of apparent binding affinity (K_d) using native mass spectrometry. The Nsp15 protein exists as a hexamer when tagged with a C-terminal His6-tag (see Fig. 1.23, p. 31). This form was used both in assays and structural studies. Once the C-terminal His6-tag is removed, the protein loses its activity and does not form the hexamer. It was apparent that when the ligand was added, the hexameric form was disrupted and the ligand bound to the monomeric form. This finding can explain the apparent enzyme inhibition observed with these inhibitors.

Structural studies are ongoing with these compounds. To date, no co-crystal structures have been obtained. This is not an unusual behavior of this enzyme, as many other inhibitors, except for tipiracil, fail to co-crystallize with the protein.



| | B06 | C03 |
|--------------------------|---------|---------|
| IC ₅₀ (μM) | 3.0 | 3.9 |
| IC ₅₀ (95%CI) | 2.0-4.6 | 2.5-5.7 |
| DF | 14 | 13 |
| R2 | 0.95 | 0.96 |

Fig. 1.22. Characterization of two identified Nsp15 inhibitors. [Courtesy Pacific Northwest National Laboratory]

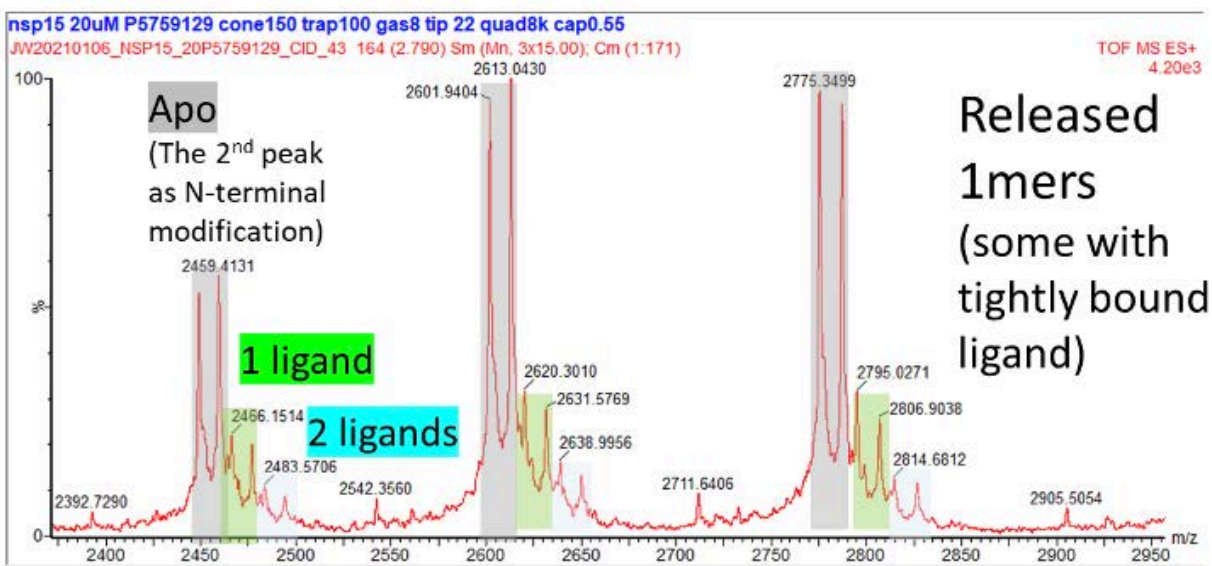


Fig. 1.23. Characterization of two identified Nsp15 inhibitors. [Courtesy Pacific Northwest National Laboratory]

Screening of ADRP Inhibitors

ADP-ribosylation is a post-translational protein modification important in cellular regulation and defense, especially in eukaryotic defense against viral infection. SARS-CoV-2 Mac1 is a macro-domain of the viral non-structural protein 3 (Nsp3), which is also referred to as ADRP. An inhibitor of the viral ADRP would therefore offer potential as a therapeutic for COVID-19 by blocking the hydrolysis of mono-ADP-ribose and thereby maintaining the human host-defense response. For such an inhibitor to have real potential as a drug, the discovered molecule would need to effectively inhibit ADRP without inhibiting host macrodomain proteins. Microscale thermophoresis was used to assay binding of small molecules to the ADRP protein. However, due to the lack of commercially available and/or established activity assays, the Task 3 team worked towards building biochemical and biophysical assays to test whether ADRP inhibition is indeed the mechanism of action for antiviral activity of candidate molecules. The development of this assay is another key outcome of this project.

Two approaches were developed to screen potential ADRP inhibitors in microtiter plate format:

- 1. A binding assay with fluorescent readout.** An as-yet-unpublished competition binding assay was developed in the United Kingdom and the details shared with the Task 3 team. This assay uses a synthetic peptide with ADP-ribose and biotin attached and measures the competition of potential inhibitors for displacement of the peptide-ADP-ribose-biotin conjugate; Task 3 synthetic teams synthesized the peptide to develop the assay. Members of the team were completing screening of target molecules at the time of writing this report.
- 2. An activity assay with mass spectrometric readout.** The activity assay uses either an ADPr-protein or peptide as a substrate and detects ADRP activity via ADP-ribose release. The team successfully auto-ADP-ribosylated a protein substrate, the PARP10 catalytic domain (PARP10cd), and detected ADRP-catalyzed ADPr hydrolysis by

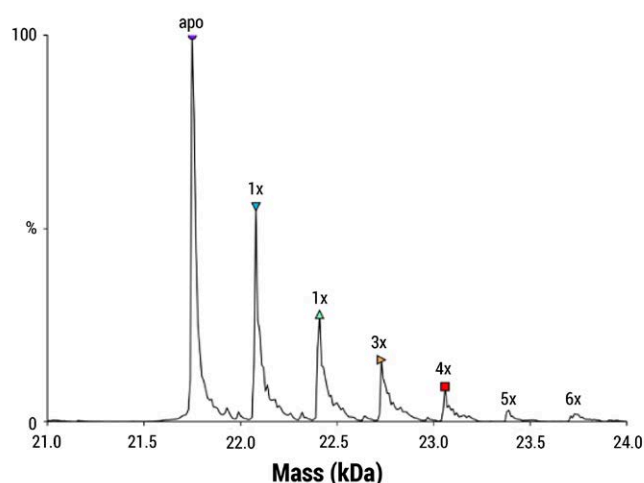


Fig. 1.24. A representative deconvoluted mass spectrum of ADRP mixed with 10 μ M compound (MCULE-4420815181). The intensities for apo (21.75 kDa) and first binding (1x, 22.08 kDa) peaks were used to estimate K_d . More than one compound bound to the protein, as labeled by 2x – 6x in the spectrum. [Courtesy Pacific Northwest National Laboratory]

mass spectrometry. As an alternative assay format, a smaller peptide substrate would improve the dynamic range of the assay over the current assay that uses protein substrate. Test peptides were synthesized and a new synthetic route to produce ADPr-peptides was designed. In addition, a proteomics study identified 10 peptides from human lung cell proteins that are ADP-ribosylated by PARP10cd and then hydrolyzed by SARS-CoV-2 ADRP to inform future peptide designs. In lower throughput, thermophoresis was used to characterize binding.

For the mass spectrometry assays, ADRP was mixed with individual compounds and electrosprayed under non-denaturing conditions. The apoproteins and holo-proteins were mass resolved and quantified by mass spectrometry, giving an estimated K_d for the compound. The best hits were in the 20-30 μ M range for the first binding event. Interestingly, multiple binding on the protein was always observed (e.g., 1, 2, 3 compound per protein monomer detected at the same time, Fig. 1.24, this page). This potentially suggests

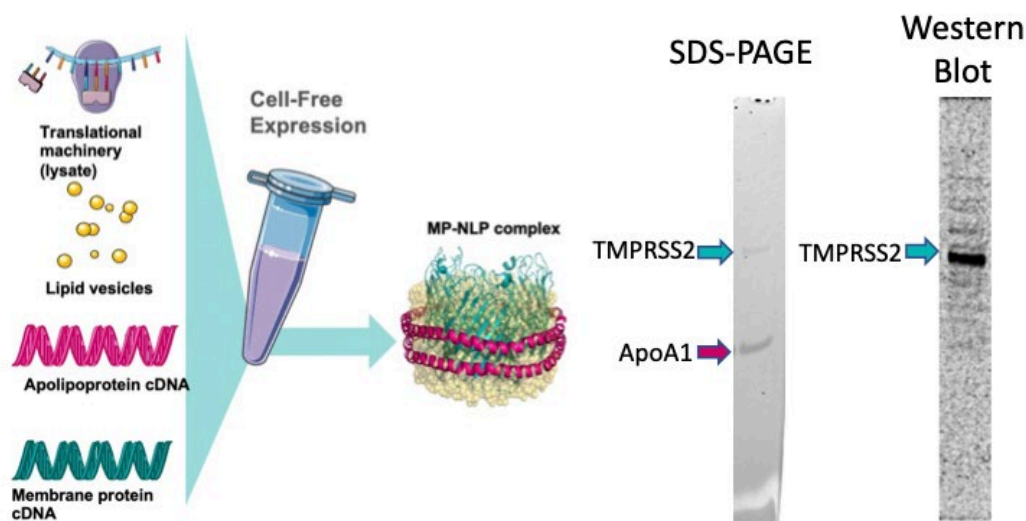


Fig. 1.25. Cell-free expression of full-length TMPRSS2 using lipid nanoparticles to stabilize the protein. [Courtesy Lawrence Livermore National Laboratory]

some level of nonspecific binding. The two batches of 86 and 94 compounds were performed at different times using different instrument setups. Robotic systems were used to automate data collection, but the precision was lower than manual operation (due to variation in electrospray that needs further optimization for improved stability). Average K_d was reported. The absolute K_d values may change slightly depending on different instrument conditions, but the qualitative differences (or ranking) should be reliable.

Other Targets

Transmembrane serine protease 2 (TMPRSS2) is a critical host protease responsible for SARS-CoV-2

activation and represented the only host protein target that had been prioritized. Members of the Task 3 team worked extensively on developing an assay for TMPRSS2, as well as E, M, and N proteins. The team used a novel lipid nanodisc-based cell-free expression of the full-length TMPRSS2 membrane protein (see Fig. 1.25, p. 33) in a fluorescence-based peptide cleavage assay, a key outcome of this project. With additional funding support from other sources, the team is actively screening molecules against TMPRSS2 and E, M, and N proteins using this approach. The screening data was not available at the time of writing this report.

1.7 Publications and Research Output

Publications

Bhati, A. P.; Wan, S.; Alfè, D.; Clyde, A. R.; Bode, M.; Tan, L.; Titov, M.; Merzky, A.; Turilli, M.; Jha, S.; Highfield, R. R.; Rocchia, W.; Scafuri, N.; Succi, S.; Kranzlmüller, D.; Mathias, G.; Wifling, D.; Donon, Y.; Di Meglio, A.; Vallecorsa, S.; Ma, H.; Trifan, A.; Ramanathan, A.; Brettin, T.; Partin, A.; Xia, F.; Duan, X.; Stevens, R.; Coveney, P. V. Pandemic Drugs at Pandemic Speed: Infrastructure for Accelerating COVID-19 Drug Discovery with Hybrid Machine Learning- and Physics-Based Simulations on High Performance Computers. *Interface Focus* **2021**, 11 (6), 20210018. DOI: 10.1098/rsfs.2021.0018

Chai, J.; Cai, Y.; Pang, C.; Wang, L.; McSweeney, S.; Shanklin, J.; Liu, Q. Structural Basis for SARS-CoV-2 Envelope Protein Recognition of Human Cell Junction Protein PALS1. *Nat. Commun.* **2021**, 12 (1), 3433. DOI: 10.1038/s41467-021-23533-x

Cho, H.; Gonzales-Wartz, K. K.; Huang, D.; Yuan, M.; Peterson, M.; Liang, J.; Beutler, N.; Torres, J. L.; Cong, Y.; Postnikova, E.; Bangaru, S.; Talana, C. A.; Shi, W.; Yang, E. S.; Zhang, Y.; Leung, K.; Wang, L.; Peng, L.; Skinner, J.; Li, S.; Wu, N. C.; Liu, H.; Dacon, C.; Moyer, T.; Cohen, M.; Zhao, M.; Lee, F. E-H.; Weinberg, R. S.; Douagi, I.; Gross, R.; Schmaljohn, C.; Pegu, A.; Mascola, J.R.; Holbrook, M.; Nemazee, D.; Rogers, T.F.; Ward, A. B.; Wilson, I. A.; Crompton, P. D.; Tan, J. Bispecific Antibodies Targeting Distinct Regions of the Spike Protein Potently Neutralize SARS-CoV-2 Variants of Concern. *Sci. Transl. Med.* **2021**, 13 (616). DOI: 10.1126/scitranslmed.abb5413

Clyde, A.; Galanie, S.; Kneller, D. W.; Ma, H.; Babuji, Y.; Blaiszik, B.; Brace, A.; Brettin, T.; Chard, K.; Chard, R.; Coates, L.; Foster, I.; Hauner, D.; Kertesz, V.; Kumar, N.; Lee, H.; Li, Z.; Merzky, A.; Schmidt, J. G.; Tan, L.; Titov, M.; Trifan, A.; Turilli, M.; Van Dam, H.; Chennubhotla, S. C.; Jha, S.; Kovalevsky, A.; Ramanathan, A.; Head, M. S.; Stevens, R. High Throughput Virtual Screening and Validation of a SARS-CoV-2 Main Protease Non-Covalent Inhibitor. *J. Chem. Inf. Model.* **2022**, 62 (1) 116–128. DOI: 10.1021/acs.jcim.1c00851

Joshi, R. P.; Gebauer, N. W. A.; Bontha, M.; Khazaieli, M.; James, R. M.; Brown, B.; Kumar, N. 3D-Scaffold: Deep Learning Framework to Generate 3D Coordinates of Drug-like Molecules with Desired Scaffolds. *J. Phys. Chem. B* **2021**, 125 (44), 12166–12176. DOI: 10.1021/acs.jpcc.1c06437

Kneller, D. W.; Li, H.; Galanie, S.; Phillips, G.; Labbé, A.; Weiss, K.L.; Zhang, Q.; Arnould, M. A.; Clyde, A.; Ma, H.; Ramanathan, A.; Jonsson, C. B.; Head, M. S.; Coates, L.; Louis, J. M.; Bonnesen, P. V.; Kovalevsky, A. Structural, Electronic, and Electrostatic Determinants for Inhibitor Binding to Subsites S1 and S2 in SARS-CoV-2 Main Protease. *J. Med. Chem.* **2021**, 64, 23, 17366–17383. DOI: 10.1021/acs.jmedchem.1c01475

Koenig, P.-A.; Das, H.; Liu, H.; Kümmerer, B. M.; Gohr, F. N.; Jenster, L.-M.; Schiffelers, L. D. J.; Tesfamariam, Y. M.; Uchima, M.; Wuerth, J. D.; Gatterdam, K.; Ruetalo, N.; Christensen, M. H.; Fandrey, C. I.; Normann, S.; Tödtmann, J. M. P.; Pritzl, S.; Hanke, L.; Boos, J.; Yuan, M.; Zhu, X.; Schmid-Burgk, J. L.; Kato, H.; Schindler, M.; Wilson, I. A.; Geyer, M.; Ludwig, K. U.; Hällberg, B. M.; Wu, N. C.; Schmidt, F. I. Structure-Guided Multivalent Nanobodies Block SARS-CoV-2 Infection and Suppress Mutational Escape. *Science* **2021**, 371 (6530), eabe6230. DOI: 10.1126/science.abe6230

Lee, H.; Merzky, A.; Tan, L.; Titov, M.; Turilli, M.; Alfe, D.; Bhati, A.; Brace, A.; Clyde, A.; Coveney, P.; Ma, H.; Ramanathan, A.; Stevens, R.; Trifan, A.; Van Dam, H.; Wan, S.; Wilkinson, S.; Jha, S. Scalable HPC and AI Infrastructure for COVID-19 Therapeutics. In *PASC '21: Proceedings of the Platform for Advanced Scientific Computing Conference*, Geneva, Switzerland, **2021**; Association for Computing Machinery: New York, NY, USA, 2021; Article 2, pp 1–13. DOI: 10.1145/3468267.3470573

Merzky, A. T. M.; Titov, M.; Saadi, A. A.; Jha, S. Design and Performance Characterization of RADICAL-Pilot on Leadership-Class Platforms. *IEEE Transactions on Parallel and Distributed Systems* **2022**, 33 (4), 818–829. DOI: 10.1109/TPDS.2021.3105994

Merzky, A.; Turilli, M.; Jha, S. "RAPTOR: Ravenous Throughput Computing." *Cluster Computing*. Manuscript submitted.

Reese, J. T.; Unni, D.; Callahan, T. J.; Cappelletti, L.; Ravanmehr, V.; Carbon, S.; Shefchek, K. A.; Good, B. M.; Balhoff, J. P.; Fontana, T.; Blau, H.; Matentzoglou, N.; Harris, N. L.; Munoz-Torres, M. C.; Haendel, M. A.; Robinson, P. N.; Joachimiak, M. P.; Mungall, C. J. KG-COVID-19: A Framework to Produce Customized Knowledge Graphs for COVID-19 Response. *Patterns* **2021**, 2 (1), 100155. DOI: 10.1016/j.patter.2020.100155

Saadi, A. A.; Alfe, D.; Babuji, Y.; Bhati, A.; Blaiszik, B.; Brace, A.; Brettin, T.; Chard, K.; Chard, R.; Clyde, A.; Coveney, P.; Foster, I.; Gibbs, T.; Jha, S.; Keipert, K.; Kranzlmüller, D.; Kurth, T.; Lee, H.; Li, Z.; Ma, H.; Mathias, G.; Merzky, A.; Partin, A.; Ramanathan, A.; Shah, A.; Stern, A.; Stevens, R.; Tan, L.; Titov, M.; Trifan, A.; Tsaris, A.; Turilli, M.; Van Dam, H.; Wan, S.; Wifling, D.; Yin, J. IMPECCABLE: Integrated Modeling Pipeline for COVID Cure by Assessing Better LEads. In *ICPP 2021: Proceedings of the 50th International Conference on Parallel Processing*, Chicago, IL, USA, 2021; Association for Computing Machinery: New York, NY, USA, **2021**; Article 40, pp 1–12. DOI: 10.1145/3472456.3473524

Stefan, M. A.; Light, Y. K.; Schwedler, J. L.; McIlroy, P. R.; Courtney, C. M.; Saada, E. A.; Thatcher, C. E.; Phillips, A. M.; Bourguet, F. A.; Mageeney, C. M.; McCloy, S. A.; Collette, N. M.; Negrete, O. A.; Schoeniger, J. S.; Weilhammer, D. R.; Harmon, B. Development of Potent and Effective Synthetic SARS-CoV-2 Neutralizing Nanobodies. *mAbs* **2021**, 13 (1), 1958663. DOI: 10.1080/19420862.2021.1958663

Zhang, K.; Zheludev, I. N.; Hagey, R. J.; Haslecker, R.; Hou, Y. J.; Kretsch, R.; Pintilie, G. D.; Rangan, R.; Kladwang, W.; Li, S.; Wu, M. T.-P.; Pham, E. A.; Bernardin-Souibgui, C.; Baric, R. S.; Sheahan, T. P.; D'Souza, V.; Glenn, J. S.; Chiu, W.; Das, R. Cryo-EM and Antisense Targeting of the 28-kDa Frameshift Stimulation Element from the SARS-CoV-2 RNA Genome. *Nat. Struct. Mol. Biol.* **2021**, 28 (9), 747–754. DOI: 10.1038/s41594-021-00653-y

Presentations

NIH-DOE Meeting: IMPECCABLE-DOE-NIH-Workshop

Intel Performance User Group (IXPUG)

Case Western Reserve University

ATOM Technical Team Meeting

IEEE HPC-Cloud, Washington, D.C.

Institute for Computation and Data Sciences, Penn State

UK ESPRC Excalibur Project

PASC21: AI-HPC-Infrastructure-PASC21

ICPP21: IMPECCABLE-ICPP21

Patent

Non-provisional patent filed 15639: Highly effective SARS-CoV-2 neutralizing humanized nanobodies

Media Mentions

Chhui, G. A Fast, Accurate System for Quickly Solving Stubborn RNA Structures from Pond Scum, the SARS-CoV-2 Virus and More. *SLAC Today* (Menlo Park, CA), August 11, 2021. www6.slac.stanford.edu/news/2021-08-11-fast-accurate-system-quickly-solving-stubborn-rna-structures-pond-scum-sars-cov-2 (accessed 2022-06-10).

CHAPTER 2


COVID-19 Testing

| | |
|---|-----------|
| 2.1 Project Overview | 38 |
| 2.2 Introduction | 39 |
| 2.3 Task 1: Establish Alternative Instruments/Reagents and Reachback/Validation | 39 |
| 2.3.1 Evaluating Three Extraction Kits with a 2019-n-CoV Assay | 40 |
| 2.3.2 Evaluating Abbott ID NOW and the CDC 2019-n-CoV Assay | 42 |
| 2.3.3 Evaluating the Thermo Fisher Scientific TaqPath COVID-19 Combo and CDC 2019-n-CoV Assay | 43 |
| 2.3.4 Testing Assay Efficacy of COVID-19 Commercial Kits | 44 |
| 2.3.5 Testing Clinical Sample Stability | 44 |
| 2.3.6 Testing Alternative Virus Inactivation Protocols | 45 |
| 2.3.7 Identifying Alternative RNA Extraction Technologies | 46 |
| 2.3.8 Identifying Alternative RNA Extraction Technologies for Saliva-Based Diagnostics | 53 |
| 2.4 Task 2: Develop Affinity Reagents and Novel Platform Approaches | 54 |
| 2.4.1 Antibody Selection and Characterization | 54 |
| 2.4.2 Diagnostic Potential of Antibodies | 57 |
| 2.4.3 Therapeutic Potential of LANL Antibodies | 57 |
| 2.4.4 Conclusions | 58 |
| 2.5 Task 3: Droplet Digital Microfluidic Platforms for Detection of COVID-19 | 59 |
| 2.5.1 Disposable Device | 60 |
| 2.5.2 Current Project Status | 60 |
| 2.6 Task 4: Integrated Data Science and Genomic-Guided Approaches | 60 |
| 2.6.1 Phase 1: Integrated Data Science Approach to Support COVID Detection and Diagnosis | 60 |

Continued on next page

Team Leadership

Pat Fitch (Team Lead), Los Alamos National Laboratory; **Marit Nilsen-Hamilton**, Ames Laboratory; **Dion Antonopoulos**, Argonne National Laboratory; **Andrzej Joachimiak**, Argonne National Laboratory; **Rebecca Abergel**, Lawrence Berkeley National Laboratory; **Blake Simmons**, Lawrence Berkeley National Laboratory; **Adam Arkin**, Lawrence Berkeley National Laboratory; **Nigel Mouncey**, Lawrence Berkeley National Laboratory; **Dave Rakestraw**, Lawrence Livermore National Laboratory; **Crystal Jaing**, Lawrence Livermore National Laboratory; **Elizabeth Hong-Geller**, Los Alamos National Laboratory; **Geoff Waldo**, Los Alamos National Laboratory; **Michael Guarnieri**, National Renewable Energy Laboratory; **Scott Retterer**, Oak Ridge National Laboratory; **Malin Young**, Pacific Northwest National Laboratory; **Kristin Omberg**, Pacific Northwest National Laboratory; **Anup Singh**, Sandia National Laboratories; **Robert Meagher**, Sandia National Laboratories; **Marc Salit**, SLAC National Accelerator Laboratory



Continued from previous page

| | |
|---|-----------|
| 2.6.2 Phase 2: Using Genomics-Guided Approaches to Improve Testing Effectiveness..... | 63 |
| 2.7 Task 5: Structure-Based Protein Design for Diagnostics | 66 |
| 2.7.1 Task 5: Research and Approach..... | 66 |
| 2.7.2 Antibodies | 68 |
| 2.7.3 Repurposing Existing Antibodies for SARS-CoV-2 RBD..... | 68 |
| 2.7.4 Structural Studies of SARS-CoV-2 Nonstructural Proteins (Nsps) | 69 |
| 2.8 Task 6: Next-Generation Rapid Testing..... | 79 |
| 2.8.1 Highlights | 79 |
| 2.8.2 Interlab Collaborations | 80 |
| 2.8.3 Impacts and Follow-On Work..... | 80 |
| 2.8.4 Breath Sampling Whistle (Aim 1)..... | 80 |
| 2.8.5 Reveal-CoV Instrument for Point-of-Care Diagnostics (Aim 2)..... | 80 |
| 2.8.6 Stabilization of RT-LAMP Reagents (Aim 2)..... | 82 |
| 2.8.7 Alternative Molecular Diagnostics and Protein Reagents (Aims 1 and 2) | 84 |
| 2.8.8 Aptamer Magnetic Nanoparticle Assay (Aims 1 and 2)..... | 84 |
| 2.8.9 Nanoporous Alumina Sensor (Aim 2)..... | 87 |
| 2.9 Publications and Research Output | 90 |
| 2S. Task 2 Supplementary Information and Graphics..... | 92 |

2.1 Project Overview

The DOE National Virtual Biotechnology Laboratory has proven to be an exceptionally effective contributor to the nation's COVID-19 response, quickly marshaling unique national laboratory expertise and capabilities to meet critical needs. Working closely with other federal agencies and state and regional decision-makers, NVBL provided solutions across a range of COVID-19 challenges, including the need for new testing methods, approaches, and instrumentation (see Fig. 2.1, this page).

In March 2020, researchers from 10 DOE national laboratories came together to form the NVBL Testing team to address significant R&D gaps in COVID-19 testing. The team developed an R&D agenda, worked with DOE and other agencies to set priorities, and collaborated to deliver timely results.

Priority was given to developing and quickly implementing novel capabilities for immediate and evolving pandemic needs without placing additional burden on operational performers. Priority activities capitalized on DOE national laboratory strengths and expertise in areas such as chemical and biological analysis. The team delivered (1) testing and evaluation that enabled decisions on testing options, (2) forward-leaning approaches to prepare for future scale-up needs, and (3) models and experiments that supported prioritization of diagnostic and therapeutic candidates.

Highlights of the COVID-19 Testing Team's R&D activities include:

- Collaborating with the U.S. Department of Defense (DoD), the Centers for Disease Control and Prevention (CDC), and the U.S. Food and Drug Administration (FDA) to provide experimental data that (1) enabled national testing guidelines, (2) assessed potential contamination in commercial kits, (3) evaluated sample pooling approaches, (4) examined viral transport media and protocols, and (5) evaluated virus inactivation and extraction methods to assure test efficacy and safety for frontline health care workers. This R&D impacted millions of tests.



Fig. 2.1. National laboratory scientists with expertise in chemical and biological analysis developed new methods and instrumentation for COVID-19 testing as part of the NVBL Testing Team. [Courtesy Los Alamos National Laboratory]

- Developing analysis tools to assess global evolution of the SARS-CoV-2 RNA genome, as it relates to nucleic acid-based assays. For example, the team provided an automatic *in silico* platform for evaluating diagnostic assays that has been used around the world for over two years (covid19.edgebioinformatics.org/#/home).
- Identifying distinguishing signatures in the SARS-CoV-2 RNA genome that can be used to rapidly detect this and other co-infecting pathogens in multiplexed assays. For example, this advance identified potentially significant relationships of co-infections with *Streptococcus pneumoniae* and *Streptococcus pyogenes* in positive COVID-19 samples. Co-infections with other pathogens were also evaluated.
- Developing Reveal-CoV, a small instrument to rapidly detect SARS-CoV-2 nucleic acid with

high sensitivity. The instrument uses a one-step amplification process followed by heat inactivation and lysis and employs a colorimetric change for detection.

- Devising a COVID Whistle Breath Collector that incorporates sample collection media to simplify both collection of exhaled breath and extraction of virus. The device is being evaluated by a university collaborator.

Contributing to NVBL and Testing Team success were productive collaborations with federal, state, and local government stakeholders as well as experts in academia and industry. The team's contributions demonstrated the ability of the integrated NVBL framework to effectively provide R&D and technological solutions that support rapid response to such events. Going forward, the NVBL can bring these resources to bear on future national and international needs and emergencies.

2.2 Introduction

In March and April 2020, DOE received a concept paper titled "Scientific Data to Enhance Situational Awareness and Decision-Making" jointly submitted by eight DOE national laboratories (Argonne, Lawrence Berkeley, Lawrence Livermore, Los Alamos, Oak Ridge, Pacific Northwest, Sandia, and SLAC) and two user facilities (the Environmental Molecular Sciences Laboratory and Joint Genome Institute). This paper summarized the collective capabilities of these resources for addressing the threats posed by COVID-19, from near-term responses to longer-term R&D opportunities. To address the nation's testing challenges, DOE requested that experts in chemical and biological analysis at the laboratories develop a proposal for new COVID-19 testing methods and instrumentation.

To assist and complement operational testing activities across the country, the Testing Team launched critical collaborations in March 2020 with (1) several DOE national laboratories that stood up and conducted COVID-19 tests and with (2) a subcommittee of the Diagnostic Task Force that

included the Centers for Disease Control and Prevention (CDC), U.S. Food and Drug Administration (FDA), and Department of Defense (DoD).

By the end of the first week in April 2020, DOE had approved Phase 1 of the COVID-19 Testing project, and account codes were open at several labs. To build on initial success and address remaining R&D gaps, DOE requested and approved Phase 2 of the project that began in June 2020.

Six tasks were funded and integrated across both phases of the project:

- **Task 1:** Establish alternative instruments/reagents (Phase 1) and reachback/validation (Phase 2).
- **Task 2:** Develop affinity reagents and novel platform approaches.
- **Task 3:** Droplet digital microfluidic platform.
- **Task 4:** Integrated data science (Phase 1) and genomic-guided approaches (Phase 2).
- **Task 5:** Structure-based protein design for diagnostics.
- **Task 6:** Next-generation rapid testing (Phase 2 – Next-generation Task 1).

Project goals and accomplishments across the six tasks are summarized in Fig. 2.2., p. 40, along with the team's canonical testing protocol. The sections that follow detail the team's contributions for each task and include a complete list of team publications and presentations.

2.3 Task 1: Establish Alternative Instruments/Reagents and Reachback/Validation

Phase 1 of this task addressed the need to provide validated alternatives to the instruments and reagents used for currently approved diagnostics. The main goal was to normalize sample testing across available RNA extraction kits, instrumentation, and other high impact test protocols using a common RNA standard across the labs.

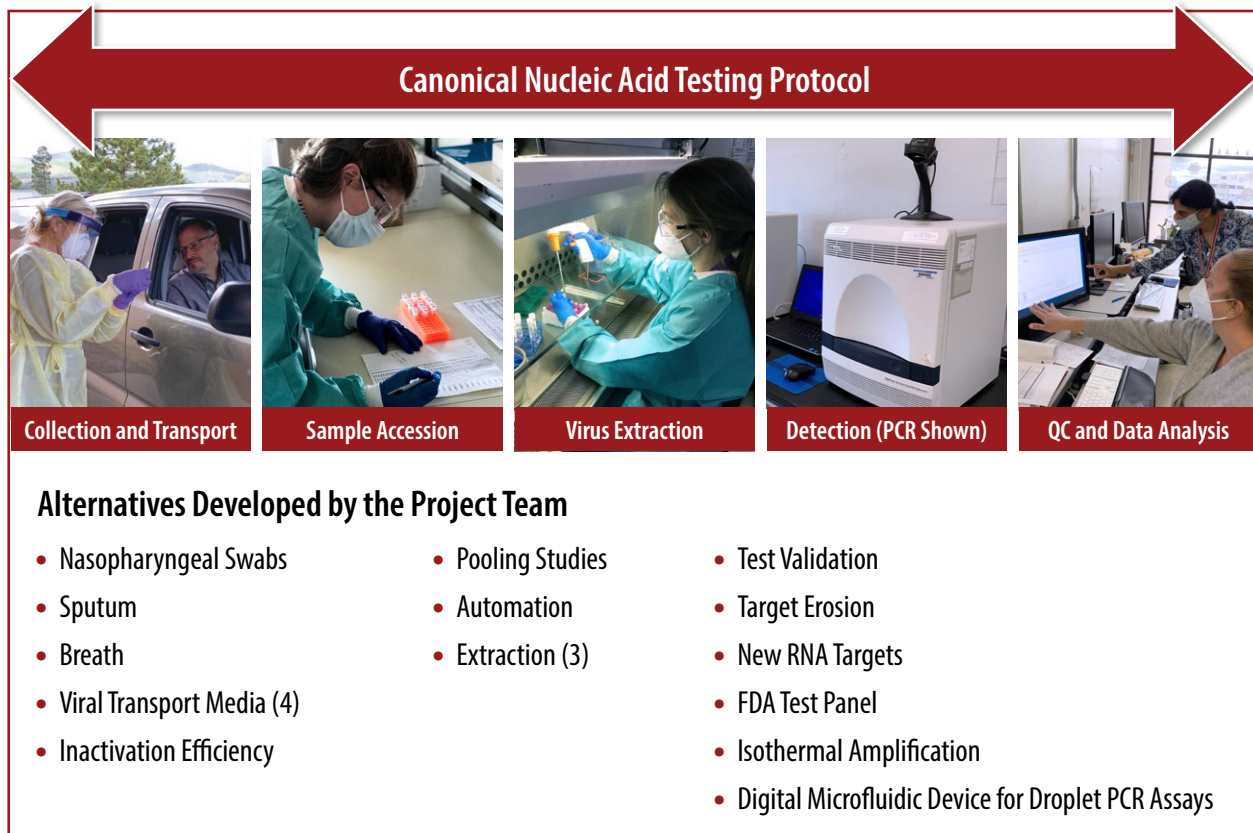


Fig. 2.2. The Testing Team’s canonical nucleic acid testing protocol involved five phases, outline above. [Courtesy Los Alamos National Laboratory]

Phase 2 of this task addressed the need to continue reach-back and validation capabilities to support priorities of the FDA, CDC, and DoD representatives of the Laboratory Diagnostics Task Force, led by the U.S. Department of Health and Human Services (HHS) and the Federal Emergency Management Agency (FEMA). The task group performed analysis of clinical sample stability and alternatives to RNA extraction methods, reverse transcription polymerase chain reaction (RT-PCR) assays, and other test protocols compared to the CDC-approved diagnostics that were in use at the time.

2.3.1 Evaluating Three Extraction Kits with a 2019-n-CoV Assay

The COVID-19 pandemic and associated increase in clinical testing produced a sharp rise in demand

for RNA extraction kits. Laboratories reported issues with receiving extraction kits in a timely manner, resulting in subsequent delays in test results. To help alleviate these issues, Pacific Northwest National Laboratory (PNNL) assisted the HHS/FEMA Laboratory Diagnostics Task Force by evaluating three Task Force-identified RNA extraction kits: (1) the Norgen Biotek Total RNA Purification Kit, (2) the Bioneer AccuPrep® Viral RNA Extraction Kit, and (3) the Promega Maxwell® High-Throughput (HT) Viral Total Nucleic Acid (TNA) Kit (Omberg et al. 2020). PNNL’s evaluation focused on the following characteristics:

- Limits of detection for quantitative synthetic RNA using the CDC’s 2019-Novel Coronavirus (2019-nCoV) Real-Time RT-PCR Diagnostic Panel and the Applied Biosystems 7500 Fast Dx system;

Table 2.1. Performance of RNA Extraction Kits*

| Kit | Concentration copies/mL | Positive Replicates / Total Replicates | N1 | | N2 | |
|----------|-------------------------|--|--------|-----|--------|-----|
| | | | Avg Ct | SD | Avg Ct | SD |
| Norgen | 0.3 | 20/20 | 35.8 | 1.0 | 36.4 | 0.7 |
| Bioneer | 0.3 | 18/20 | 36.4 | 1.0 | 36.6 | 0.7 |
| Promega | 0.3 | 20/20 | 32.0 | 1.2 | 31.4 | 2.1 |
| Qiagen** | 0.3 | 24/24 | 33.7 | 1.9 | 34.4 | 2.2 |
| Norgen | 1 | 20/20 | 31.9 | 1.3 | 32.2 | 0.6 |
| Bioneer | 1 | 20/20 | 34.5 | 0.8 | 35.2 | 0.6 |
| Promega | 1 | 20/20 | 31.8 | 0.6 | 31.5 | 0.3 |
| Qiagen** | 1 | 24/24 | 31.7 | 1.1 | 32.7 | 1.2 |
| Norgen | 3 | 20/20 | 32.3 | 0.8 | 33.3 | 0.4 |
| Bioneer | 3 | 20/20 | 33.0 | 0.4 | 33.8 | 0.4 |
| Promega | 3 | 20/20 | 30.0 | 0.6 | 30.2 | 0.5 |
| Qiagen** | 3 | 24/24 | 30.6 | 0.9 | 31.7 | 2.5 |

* Norgen Biotek Total RNA Purification Kit (#17200), Bioneer AccuPrep Viral RNA Extraction Kit (#K-3033), Promega Maxwell HT Viral TNA Kit (#AX2340) and Qiagen QIAamp Viral RNA Mini Kit (#52906) at approximately 0.3 copy, 1 copy, and 3 copies per microliter of virus in positive clinical specimen.

** Results shown are the average and standard deviation of eight replicates performed on three separate days.

- Limits of detection for positive clinical specimen using the CDC's 2019-Novel Coronavirus (2019-nCoV) Real-Time RT-PCR Diagnostic Panel and the Applied Biosystems 7500 Fast Dx system; and
- Ability to inactivate the virus as measured by a cell-based infectivity assay.

The three RNA extraction kits were selected for evaluation based on commercial availability. The QIAGEN QIAamp® Viral RNA Mini Kit, which was already approved for use with the CDC 2019-nCoV assay, was used as reference. All kits were run using the manufacturer's instructions.

To evaluate limits of detection (LOD), first, quantitative synthetic RNA from SARS-Related Coronavirus 2 was spiked into a diluent consisting of a suspension of human A549 cells and viral transport medium (VTM).¹ The LOD of the CDC assay was evaluated by performing 20 extraction replicates using each kit.

¹ VTM was prepared using the CDC's Standard Operating Procedure, "Preparation of Viral Transport Medium," #DSR-052-03.

Next, positive clinical specimen was diluted to concentrations that approximated the cycle threshold (Ct) values obtained with synthetic RNA at 3, 1, and (estimated) 0.3 genome copies per microliter. The LOD of the CDC assay was evaluated by performing 20 extraction replicates with each kit.

To evaluate inactivation efficiency, the lysis buffers from each kit were mixed with the CDC reference strain, SARS-CoV-2 USA-WA1/2020, at various ratios in serum-free media. Suspensions were incubated at room temperature for 10 minutes then added to confluent Vero cell (ATCC CCL-81) monolayers in 96-well plates. The monolayers were incubated at 37°C for four days then scored for cell death by microscopic observation.

A summary of the limit of detection for each kit with clinical specimen is shown in Table 2.1, this page.

All four lysis buffers inactivated SARS-CoV-2 USA-WA1/2020 at the concentrations recommended in the kit instructions. All four also

Table 2.2. Lysis Buffer Failure Points for Inactivation of SARS-CoV-2*

| Manufacturer | Point of failure Virus : Buffer | Kit Instructions Sample : Buffer | Fold-increase of Buffer Above Point of Failure |
|-----------------------------|--|---|---|
| Norgen Buffer RL | 2 : 1 | 100 uL : 350 µL (1 : 3.5) | 7 |
| Bioneer VB Buffer | 1 : 1 | 200 uL : 300 µL (1 : 1.5)* | 1.5* |
| Promega Lysis Buffer MC5018 | 2 : 1 | 200 uL : 200 µL (1 : 1) | 2 |
| QIAGEN Buffer AVL | 2 : 1 | 140 uL : 560 µL (1 : 4) | 8 |

*Only the lysis buffer was tested in this experiment. The Bioneer kit instructions include a 60°C 10-minute incubation, which was not performed and could change the results.

demonstrated similar patterns of cytopathic effect (CPE) at high concentrations of lysis buffer followed by decreasing CPE at lower concentrations and returning CPE at the point of failure where the virus was no longer inactivated. A summary of the point of failure for each of the buffers is presented in Table 2.2, this page.

After reviewing the PNNL results, the FDA listed two additional kits options that labs can consider using in the fight against COVID-19, thereby boosting the supply of chemicals and supplies linked to a critical step in the testing process.

2.3.2 Evaluating Abbott ID NOW and the CDC 2019-n-CoV Assay

On May 14, 2020, the FDA issued an alert due to “early data that suggest potential inaccurate results from using the Abbott ID NOW point-of-care test to diagnose COVID-19. Specifically, the test may return false negative results.”² To assist the FDA in making decisions about the Abbott ID NOW, PNNL verified the performance of its COVID-19 assay in comparison to the CDC 2019-nCoV assay. The Abbott ID NOW COVID-19 assay targets a unique region of the ORF1ab/RdRp gene.

² U.S. Food and Drug Administration. 14 May 2020. “Coronavirus (COVID-19) Update: FDA Informs Public About Possible Accuracy Concerns with Abbott ID NOW Point-of-Care Test.” www.fda.gov/news-events/press-announcements/coronavirus-covid-19-update-fda-informs-public-about-possible-accuracy-concerns-abbott-id-now-point.

The CDC assay targets two regions of the SARS-CoV-2 nucleocapsid (N) gene (N1 and N2). The performance of the two assays had not previously been compared.

Two positive specimens in VTM were obtained from the Washington State Department of Health. The specimens were previously analyzed using the CDC assay and determined to be positive with Ct values <24 for N1 and N2. Conversations with Abbott’s technical support indicated that the presence of VTM in the specimens should not impact results.

The evaluation was performed over two separate days. One day prior to each evaluation day, a specimen was thawed and the concentration of virus in the specimen was estimated using the CDC 2019 n-CoV panel with Biodefense and Emerging Infections (BEI) Resources’ Quantitative Synthetic RNA as the reference. On the day of the experiment, the specimen was serially diluted to working concentrations based on concentrations calculated from the prior day’s PCR results. Each working concentration suspension was vortexed and split into two tubes. One split was used to perform 20 replicates of the Abbott ID NOW test (10 replicates on each of two instruments). The other split was used to perform between 3 and 20 replicates of the CDC assay.

For the Abbott ID NOW test, the suspension was vortexed and 5 µL of suspension was spiked into 2.5 mL Abbott elution buffer. Results were

recorded and the process was repeated for a total of 20 replicates at each concentration. The final suspensions had approximately 312.5 (Abbott 1X LOD), 625 (Abbott 2X LOD), 1250 (Abbott 4X) and 2500 (Abbott 8X LOD) genome copies in 5 μ L.

For the CDC assay, the suspension was vortexed and 5 μ L of suspension was spiked into a vial containing 3 mL VTM. Each vial was treated as one specimen for analysis by the CDC assay. 20 replicates of the CDC assay were performed at each concentration.

Results indicated that the Abbott ID NOW assay was less sensitive than the CDC assay. In parallel with this study, FDA developed a live virus reference panel that was provided to all 2019-nCoV diagnostic test manufacturers. The results provided by Abbott and CDC similarly indicated an approximately twofold difference in sensitivity. Based on an aggregate set of data that included PNNL's results, Abbott submitted a request to amend its Emergency Use Authorization (EUA) to indicate that the test is approved only for specimens collected from individuals suspected of having COVID-19 by their healthcare provider within the first seven days of symptom onset. Specimens collected within the first seven days of symptoms typically contain larger concentrations of virus than those collected pre-symptomatically or at later times. The revision of the labelling was intended to mitigate the sensitivity issues observed by restricting test use to specimens with presumed high virus concentrations.

2.3.3 Evaluating the Thermo Fisher Scientific TaqPath COVID-19 Combo and CDC 2019-n-CoV Assay

The PNNL Medical Test Site (PNNL-MTS) routinely performs the CDC assay using the IDT 2019-nCoV CDC qPCR Probe Assay (#10006606, #0000510344) with the Thermo Fisher Scientific TaqPath™ 1-Step RT-qPCR Master Mix, CG (#A15299) on the Applied Biosystems 7500 Fast Dx. The PNNL-MTS verified the performance

characteristics of the CDC assay using Quantitative Synthetic RNA from SARS-Related Coronavirus 2 (BEI Resources, NR-52358) and successfully reproduced CDC's LOD data as reported in the CDC's *2019-Novel Coronavirus (2019-nCoV) Real-Time RT-PCR Diagnostic Panel*.³ The CDC reported that the LOD of their assay with the Qiagen Viral RNA Mini Kit was 1 RNA copy per microliter. The CDC assay targeted two regions of the N gene.

The Testing Team was interested in verifying the Thermo Fisher TaqPath COVID-19 Combo kit, which was being used by Lawrence Livermore National Laboratory (LLNL). The Thermo Fisher assay's reported LOD is slightly higher than the CDC's. In addition, concerns have been raised about potential erosion of performance of the Thermo Fisher assay because it targets both the N, ORF1ab, and spike (S) genes; mutations of the S gene have been observed in recent variants.

To compare LOD for the CDC and Thermo Fisher assays, first, quantitative synthetic RNA from SARS-Related Coronavirus 2 was spiked into a diluent consisting of a suspension of human A549 cells and VTM.⁴ Each assay's LOD was evaluated by performing 20 extraction replicates using each kit. PNNL confirmed that the manufacturers' reported LODs are correct; that is, the Thermo Fisher assay does have an LOD of 10 RNA copies per reaction, which is about twice the LOD of the CDC assay.

To compare LOD with recent variants, PNNL sequenced positive clinical specimens obtained between January 1, 2021, and March 31, 2021, from PNNL employees that were released for research. The sample sequences indicate the presence of the B.1.1.7 variant of SARS-CoV-2, first detected in California. However, none of the

³ Centers for Disease Control and Prevention. 2020. *CDC 2019-Novel Coronavirus (2019-nCoV) Real-Time RT-PCR Diagnostic Panel*. CDC-006-00019, Revision: 03. <https://www.fda.gov/media/134922/download>

⁴ VTM was prepared using the CDC's "Preparation of Viral Transport Medium," #DSR-052-03.

specimens contained variants with S gene mutations that might impact assay performance.

2.3.4 Testing Assay Efficacy of COVID-19 Commercial Kits

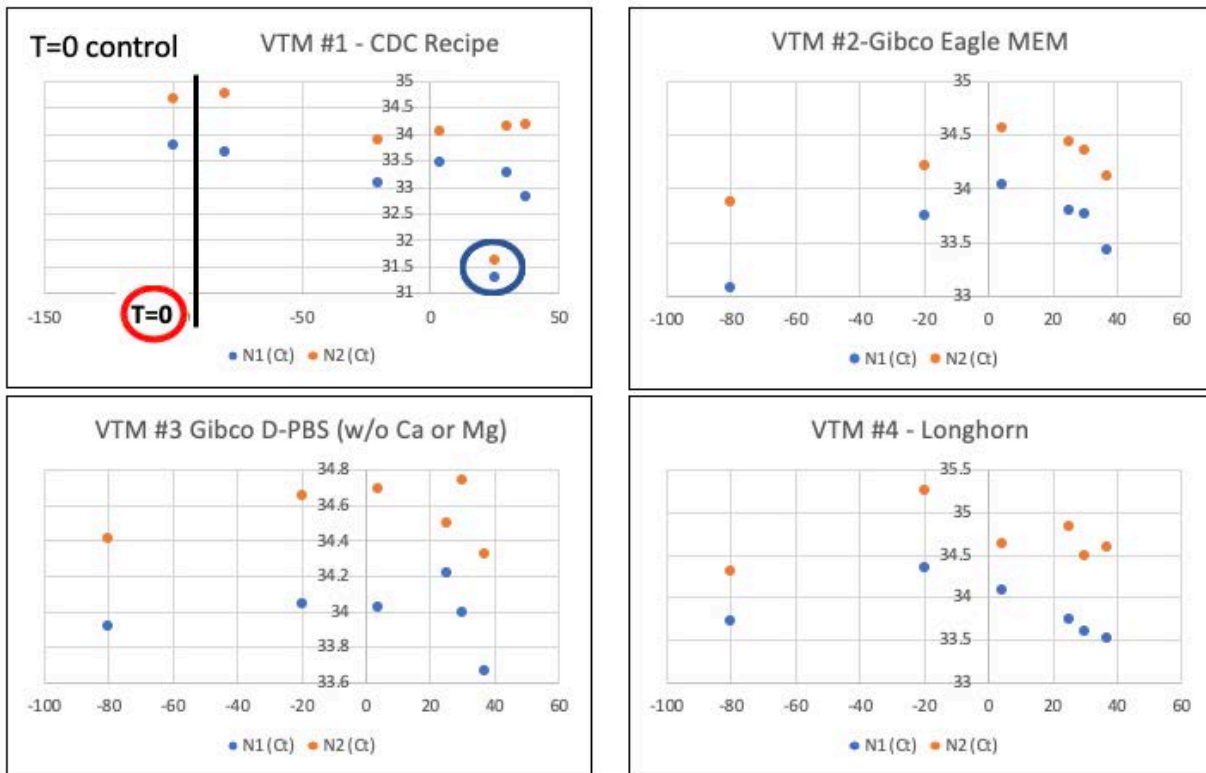
Together with PNNL, Los Alamos National Laboratory (LANL) tested a specific commercial kit for diagnostic assay efficacy. Initial results seemed to indicate that the kit was not working correctly. Negative controls using just plain water as the test substance yielded a positive COVID-19 signal with the RT-PCR assay across 10 different lot numbers. At the time, the cause of the false positive tests was unclear. The Testing Team speculated that contamination in the kits might be the reason: the positive control used in the kits may have been inadvertently packaged with the other kit components during manufacturing, thus yielding false positive signals. To determine whether this scenario could be an explanation, the Genomics Team at LANL sequenced the false positive amplicon products from the RT-PCR reaction to examine at their genetic sequence. The team's examination revealed genetic sequences in the false positive amplicons that exactly matched the positive control sequences included in the kit, suggesting that our hypothesis of contamination was likely the case. Based on these results, the decision was made to pull the diagnostic kits from national distribution. This work was essential to preventing millions of contaminated COVID-19 tests from nation-wide distribution, which could potentially have led to false positive diagnoses and greater distrust in U.S. testing capabilities at a particularly sensitive time early in the pandemic.

2.3.5 Testing Clinical Sample Stability

At the beginning of the pandemic, many questions emerged regarding how to keep clinical samples stable and ensure viral stability prior to lab testing. In April 2020, supply chain issues occurred for all materials and supplies needed for Lab Testing, including VTM. We performed evaluations of several different VTMs—including a commercially-available VTM, basic buffers such as

phosphate-buffered saline (PBS), and a VTM recipe made with components available in a standard research lab—to see if there was a difference in VTMs for sample stability. We performed systematic studies using positive clinical nasopharyngeal (NP) samples acquired from the New Mexico Department of Health and determined that NP samples were stable and were detected at the same levels using any of the VTMs tested, including the basic buffers (see Fig. 2.3, p. 45) This determination was particularly useful information for the Diagnostics Task Force, since a basic buffer, such as PBS, is cheap and easy to acquire. Thus, if supply chain proved to be an issue, diagnostic labs did not need to use hard-to-find or expensive VTMs for sample storage.

The team also tested sample storage at different temperatures as another stability parameter. At the time, the Task Force was looking at the possibility of self-sampling with NP swabs during the summer months if extremely long lines and significant wait times continued at testing facilities across the nation. However, questions about the reliability and usability of self-samples arose. For example, if individuals self-sampled and then left their sample in a hot car for several days, how would that affect reliability of sample stability? Our team performed systematic experiments to test clinical sample stability at different temperatures across a range between -80°C to $+37^{\circ}\text{C}$ (human body temperature). Surprisingly, the efficiency of virus detection in samples incubated for 3 days was similar across the entire temperature range (see Fig. 2.3, p. 45) We had speculated that virus at 37°C for 3 days might have undergone degradation and would no longer be detectable. However, our results indicated that samples left in a hot car for 3 days would likely be just as accurate compared to storage at room temperature or in the refrigerator. These analyses provided the Task Force with a valuable risk assessment of clinical sample handling and accuracy of diagnostic testing. Self-swabbing combined with mail-in testing became an option for the public at local pharmacies last year.



- 4 VTMs
- 6 temps (-80, -20, 4,25,30, 37°C)
- Starting material Ct ~30 – clinical sample
- 1:5 dilution with VTM for 72 hrs
- Added T=0 sample
- CDC-approved assay

Maybe of note:
•VTM1: 25°C

Conclusions:

- Incubation at higher temperatures (30, 37) do not seem to affect assay
- Not much difference between the temperatures
- Not much difference between VTMs. Note #1-3 all have FBS, gentamicin and amphotericin

Fig. 2.3. Results of Los Alamos National Laboratory study to test SARS-CoV-2 in different VTMs and storage temperatures. [Courtesy Los Alamos National Laboratory]

In addition to the two examples described above, the LANL team also led studies for the Task Force on (1) sample pooling strategies to combine individual samples for testing in communities with low disease prevalence to save reagents and labor; (2) saliva studies using spiked samples to examine heterogeneity of assay efficacy in a small population; and (3) LOD studies of a heat-inactivated SARS-CoV-2 standard for the FDA. These multiple efforts provided government agency stakeholders with the data and information needed to make

timely decisions and offer validated lab testing guidance to the diagnostic community.

2.3.6 Testing Alternative Virus Inactivation Protocols

During Phase 1 testing activities, Lawrence Berkeley National Laboratory (LBNL) tested alternative virus inactivation protocols to enable automation methods for both RNA extraction and reverse transcription quantitative polymerase chain reaction (RT-qPCR) analysis to ultimately accelerate the

testing process. Two virus inactivation tests were initiated under biosafety level 3 (BSL-3) protocols at PNNL. These tests aimed to (1) evaluate the potency of DNA/RNA shield (Zymo research) at inactivating viral samples prior to RNA extraction and (2) demonstrate inactivation by Proteinase K in both nasal fluids and saliva samples (University of California–Berkeley Tijan-Darzacq protocols).

Each step was part of a different protocol that has been evaluated for reproducibility, stability, and subsequent automation. The Zymo DNA/RNA shield inactivation buffer had been implemented in testing standard operating protocols for surveillance at UC Berkeley in April 2020, and the methods were transferred to LBNL after inactivation efficiency was confirmed for safe handling under BSL-2 conditions. Automation processes and laboratory information management system (LIMS) protocols were developed for the following steps: (1) virus inactivation (Hamilton Microlab STARlet liquid handlers), (2) RNA extraction and purification (KingFisher Flex), (3) RT-qPCR dispensing and readout (Hamilton Vantage and 7500 Fast Dx RT-qPCR). The protocols were implemented in LBNL's newly established Berkeley Lab Automated Diagnostics Extension (BLADE) facility.

2.3.7 Identifying Alternative RNA Extraction Technologies

Testing supply manufacturers have struggled to keep up with demand, leading to shortages of commercially available RNA extraction reagents. The Testing Team identified four potential alternate RNA extraction methods—two lysis buffers and two PCR purification methods—comprised of readily available reagents and materials. These methods produce extraction yields that range in comparability with reagents currently authorized for use in testing, with the most promising method producing statistically equivalent PCR Ct values to the EUA Qiagen Viral RNA extraction kit.

Sample Preparation

Alternative RNA extraction methods were tested on simulated clinical samples containing a surrogate virus or synthetic RNA. These artificial samples were created using human nasal cavity swabs (provided by Lee Biosolutions, Maryland Heights, MO) mixed with VTM (provided by Teknova, Hollister, CA). The frozen nasal cavity swab was added to 3 mL of VTM and used fresh. Bovine coronavirus (BCoV), Mebus (NR-445) (provided by M. Borucki, LLNL) or SARS-CoV-2 synthetic RNA encapsulated in phage protein (provided by Microbiologics, St. Cloud, MN) was then added to the nasal sample and VTM background. Additionally, RNA extraction performance was evaluated for five clinical samples supplied by the California Department of Public Health (CDPH). The samples had been previously confirmed as positive or negative for SARS-CoV-2. Of the five samples, four were confirmed by the CDPH as positive with N gene and Orf1ab RT-qPCR assays (see Table 2.3, p. 47).

RNA Extraction

Extractions were carried out in triplicate using 140 μ L of simulated clinical sample for each extraction method. Control extractions were performed using the Qiagen Viral RNA extraction kit, with the addition of RNA carrier as described by the manufacturer and eluted in 60 μ L of elution buffer. For CDPH clinical samples, both the control and alternative RNA extractions were performed using 100 μ L of sample as input and eluted in 100 μ L.

Alternate methods for RNA isolation were carried out in two stages: lysis and PCR inhibition removal. Two lysis buffers were used:

- Lysis Buffer A (2 M guanidinium thiocyanate, 80 mM DTT, 25 mM sodium citrate, 20 μ g/mL glycogen, pH 6.9)⁵
- Lysis buffer B (25 mM DTT, 1.25 mM sodium citrate, pH of 6.8)

⁵ He, H. et al. "Integrated DNA and RNA Extraction Using Magnetic Beads from Viral Pathogens Causing Acute Respiratory Infections." *Science Report* 7, 45199 (2017). DOI: 10.1038/srep45199

Table 2.3. Clinical Samples from California Department of Public Health

| Sample Name | Specimen Source | Date Collected | CDPH Result | Mean CDPH Ct Value* |
|-------------|-----------------|----------------|-------------|---------------------|
| LLNL_166 | NP Swab | 8/21/20 | Positive | 14.0 |
| LLNL_167 | NP Swab | 8/21/20 | Positive | 22.0 |
| LLNL_168 | NP Swab | 8/24/20 | Positive | 30.9 |
| LLNL_169 | NP Swab | 8/24/20 | Positive | 36.4 |
| LLNL_170 | NP Swab | 8/25/20 | Negative | Not Detected |

* CDPH Ct values were determined by RT-qPCR of N gene and Orf1ab regions tested at CDPH.

Buffers were combined with either a magnetic bead-based or column-based clean-up procedure, for a total of four potential alternative RNA isolation methods. One of the two lysis buffers was added to each sample, followed by incubation for 10 minutes:

- Buffer A was incubated at 65°C.
- Buffer B was incubated at 80°C.

Heat-lysed samples were purified with one of two methods:

- 1.8X Beckman Coulter RNA Clean magnetic beads (Beckman Coulter, Pasadena, CA) and eluted in 100 µL of nuclease-free water.
- Zymo RNA Clean and Concentrator 25 columns (Zymo Research, Irvine, CA), and eluted in 50 µL of nuclease-free water.

BCoV RT-qPCR Amplification

Bovine coronavirus (BCoV) RT-qPCR amplifications were run for each sample using 1X TaqPath 1-Step RT-qPCR Master Mix reagents (Life Sciences Corporation, Grand Island, NY) and custom primers and probes targeting the BCoV strain Mebus polymerase gene as previously described (Borucki et al, 2013). The assay contained 250 nM probe (/56-FAM/CCGTGTTAG/ZEN/GATGGTATGGCATACTCCAGTG/3IABkFQ/) and 500 nM of forward and reverse primers (5'-CCATGTGTCATGCATTGGATT-3' and 5'-CACCGATCATCCTGACAATCA-3'). Standard curves were generated by amplifying tenfold serial dilutions of 10⁹ to 10² copies of synthetic Mebus BCoV strain polymerase

gene. 5 µL of extracted RNA samples were added to each RT-qPCR reaction in a final reaction volume of 20 µL.

SARS-CoV-2 RT-qPCR Amplification

Synthetic and clinical SARS-CoV-2 amplifications were run for each sample, following protocols described in the CDC's *2019-Novel Coronavirus (2019-nCoV) Real-Time RT-PCR Diagnostic Panel*. 1X TaqPath 1-Step RT-qPCR Master Mix reagents and SARS-CoV-2 (2019-nCoV) CDC qPCR Probe Assay primers and probes (Integrated DNA Technologies, Coralville, IA) were used for the N1, N2, and human RNase P (RP) assays. For SARS-CoV-2 synthetic RNA extractions, standard curves were generated for the N1 and N2 assays by adding 10⁷ to 10² copies of SARS-CoV-2 N gene synthetic RNA (Microbiologics, St. Cloud, MN) diluted tenfold, serially. Human RNase P positive DNA controls and Hs_RPP30 Positive Control (Integrated DNA Technologies, Coralville, IA) were included in each RP assay. Only the N1 and N2 assays were performed for RNA extracted from CDPH clinical samples. These assays were not run with standard curves, but with 10⁷ copies of synthetic SARS-CoV-2 RNA as positive controls. RNA volumes were normalized to the Qiagen extraction elution volume and 5 µL was added to each 20 µL PCR reaction. No template controls were included with each assay. RT-qPCR reactions for all samples, standards curves, and controls were performed in triplicate.

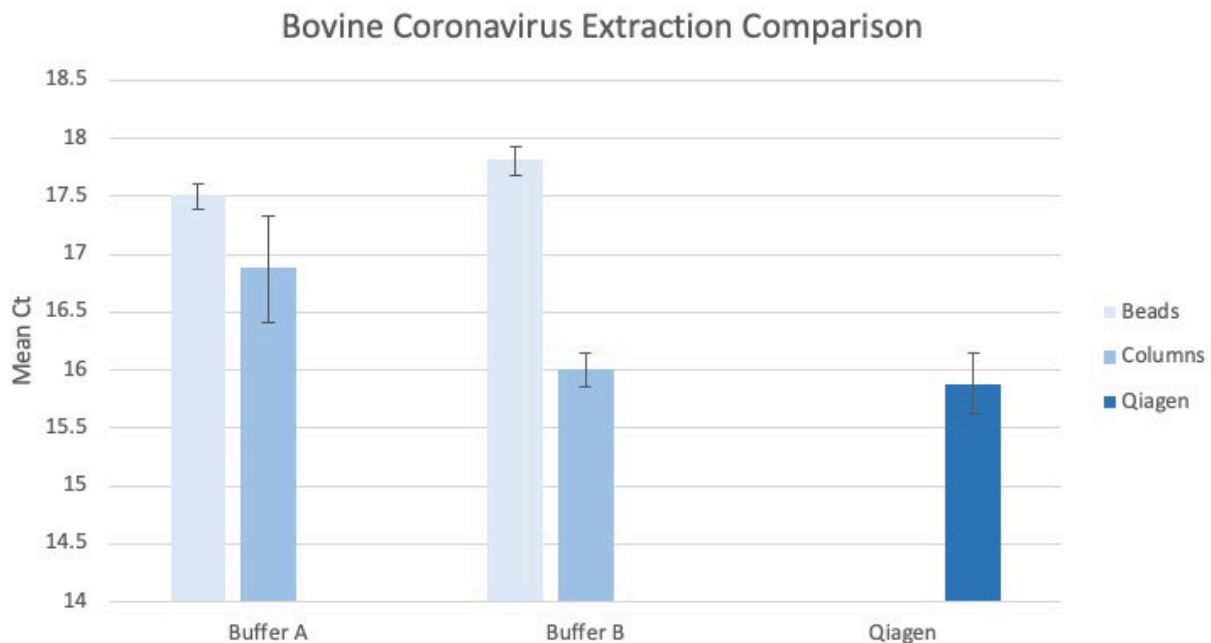


Fig. 2.4. RT-qPCR of bovine coronavirus extraction methods. [Courtesy Lawrence Livermore National Laboratory]

RT-qPCR was performed on an Applied Biosystems 7500 Fast Real Time System with the following parameters: 2-minute hold at 25°C, 15-minute hold at 50°C, 2-minute hold at 95°C, and 45 cycles of 95°C for 15 seconds followed by 55°C for 30 seconds.

Bovine Coronavirus and Synthetic SARS-CoV-2 RNA Samples

Two lysis buffers and two purification methods were tested as four total extraction comparisons against the Qiagen Viral RNA extraction method. The RNA extraction efficiencies of these four methods were evaluated by comparing the differences of the average cycle threshold (Ct) values between each procedure and the Qiagen extraction method.

For the extractions of the BCoV strain Mebus virus, a single RT-qPCR assay amplifying the Mebus coronavirus polymerase gene was run using each of the four alternate extraction methods. Figure 2.4, this page, shows the average of these Ct values for Buffer A and B lysis buffers, in combination with

the magnetic bead and Zymo column purifications. The Qiagen standard extraction produced a mean Ct of 15.9 ± 0.3 , while Buffer A yielded a mean Ct of 17.5 ± 0.1 and 16.9 ± 0.5 when purified by magnetic bead or column. Buffer B produced a Ct value of 17.8 ± 0.1 for the magnetic bead purification and produced the highest average extraction efficiency at a Ct of 16.0 ± 0.2 using column purification.

The synthetic SARS-CoV-2 RNA sample extractions were evaluated by amplification of the N1 and N2 regions, which target the SARS-CoV-2 nucleocapsid (N) gene, and by amplification of the RP assay, which is used as an RNA extraction control in clinical sample testing and maps to human RNase P. Buffer A lysis amplified the N1 and N2 assays at Ct values of 29.6 ± 0.4 to 30.6 ± 0.2 for bead and column purification, whereas Qiagen amplified at 28.7 ± 0.4 to 29.0 ± 0.4 (see Fig. 2.5, p. 49).

When purified via magnetic beads, Buffer B produced average Ct values of 27.5 ± 0.1 and 29.1 ± 0.3 for the N1 and N2 assays, while the

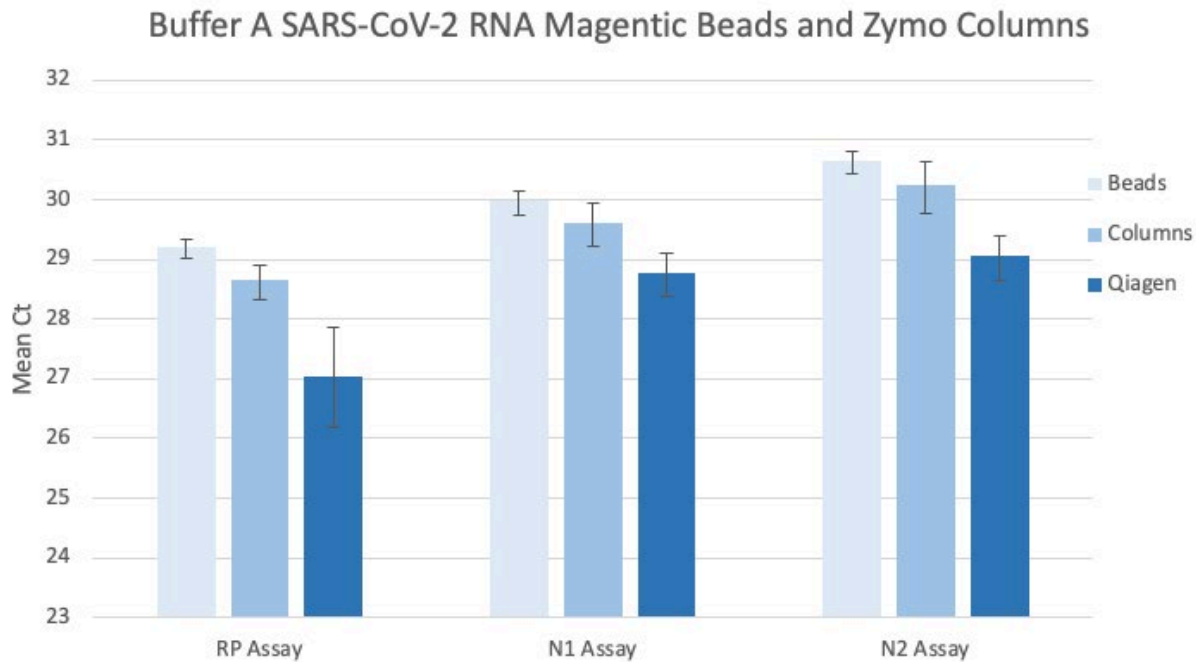


Fig. 2.5. RT-qPCR of SARS-CoV-2 synthetic RNA buffer B extractions. [Courtesy Lawrence Livermore National Laboratory]

Qiagen extractions amplified at 26.9 ± 0.2 and 28.4 ± 0.1 Cts (see Fig. 2.6, p. 50). For lysis followed by Zymo column clean up, the N1 and N2 average Cts were at 28.8 ± 0.2 and 30.3 ± 0.3 , compared with the Qiagen amplification of 28.6 ± 0.1 and 29.9 ± 0.2 (see Fig. 2.7, p. 50).

The average Ct value of each alternate extraction method was compared to the Qiagen extraction method average Ct value. These comparisons are presented as mean Ct differences in Table 2.4, p. 51. The alternate extractions yielded efficiencies that were dependent upon the template used, as well as on the RT-qPCR assay amplified. The first method, which consisted of a Buffer A lysis followed by a magnetic bead clean up, yielded the lowest average extraction efficiency for the N1 and N2 assays when compared to the Qiagen standard kit, giving mean Ct differences of 1.2 and 1.6 (see Table 2.4, p. 51). However, for both the SARS-CoV-2 RP assay and for the bovine coronavirus RNA extraction, the most significant

Ct change was seen with Buffer B lysis and bead clean up, with delta Ct values of 1.9 and 3.8. Interestingly, the N1 and N2 assays for this method had smaller Ct delays of 0.6 and 0.7, on average. Buffer A purified by column yielded an average amplification that was 1.0 Cts later for the bovine coronavirus assay and between 0.8 and 1.6 Cts later for the SARS-CoV-2 synthetic RNA. As with the Buffer B/Bead extraction, the SARS-CoV-2 N1 and N2 assays aligned more closely with the Qiagen extraction, with 0.8 and 1.2 Ct value delays, respectively.

Overall, all four of the RNA extraction methods performed better for the N1 and N2 assays as compared with the RP assay. The highest extraction efficiency overall gave a mean delta Ct of just 0.1 ($p=.24$). This was accomplished through extraction of the bovine virus using Buffer B and column purification. Indeed, extraction of SARS-CoV-2 RNA with this combination yielded Ct values closest to the Qiagen for the RP, N1 and N2 assays as well.

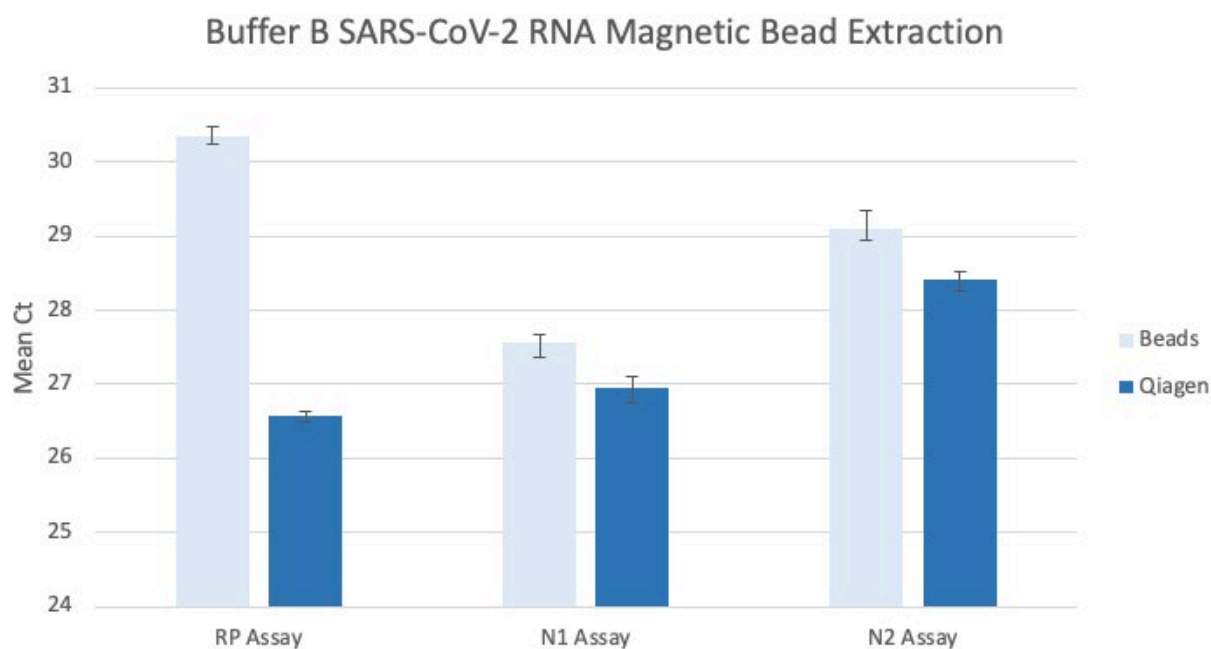


Fig. 2.6. RT-qPCR of SARS-CoV-2 synthetic RNA magnetic bead extraction. [Courtesy Lawrence Livermore National Laboratory]

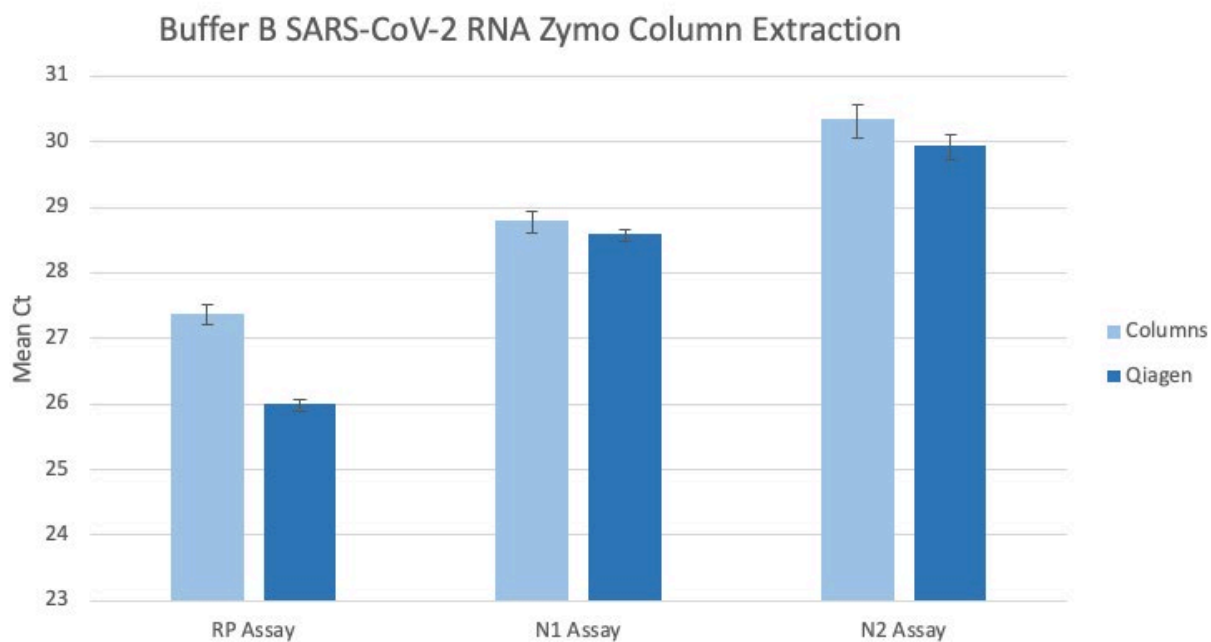


Fig. 2.7. RT-qPCR of SARS-CoV-2 synthetic RNA Zymo column extraction. [Courtesy Lawrence Livermore National Laboratory]

Table 2.4. Mean Synthetic SARS-CoV-2 and BCoV Ct Increase*

| RT-qPCR Assay | Buffer A | | Buffer B | |
|------------------------|-----------|-----------|-----------|-------------|
| | Beads | Column | Beads | Column |
| RP | 2.2 **** | 1.6 **** | 3.8 **** | 1.4 **** |
| N1 | 1.2 **** | 0.8 **** | 0.6 **** | 0.2 ** |
| N2 | 1.6 **** | 1.2 **** | 0.7 **** | 0.4 *** |
| BCoV | 1.6**** | 1.0 **** | 1.9 **** | 0.1 (p=.24) |
| Overall Mean Ct Change | 1.7 ± 0.4 | 1.1 ± 0.4 | 1.8 ± 1.5 | 0.5 ± 0.6 |

*Mean increase in synthetic SARS-CoV-2 and Bovine coronavirus alternative extraction RT-qPCR Ct values compared to Qiagen extraction. Two tailed Welch's t-test

**significant at $p < .05$,

***significant at $p < .005$

****significant at $p < .001$

SARS-CoV-2 Clinical Samples

Buffer B paired with a Zymo column clean up produced extraction yields most closely resembling the Qiagen extractions for both the Mebus virus surrogate and for the simulated SARS-CoV-2 samples. This combination was used as the sole alternate extraction method tested with clinical samples. Five SARS-CoV-2 clinical samples, which were previously tested by the CDPH and ranged in Ct values of 14 to not detected after 40 cycles, were evaluated with the alternate extraction and Qiagen extraction methods. These samples represented the high, medium, low, and very low levels of viral RNA that may be present in clinical samples.

The negative CDPH sample, LLNL_170, was not detected with the Buffer B/Zymo nor with the Qiagen extraction methods in the N1 or N2 assay. Sample LLNL_169, with an original CDPH average Ct of 36.4, was not detected with N1 or N2 assays following extraction with BufferB/Zymo. However, this sample yielded a mean Ct value of 35.3 ± 1.54 for the N1 assay and a single replicate amplification of Ct 36.6 for the N2 assay when extracted with the Qiagen kit. Furthermore, LLNL_169 was only detected in one of the three

RT-qPCR replicates within two of the three Qiagen RNA extraction replicates, demonstrating how this level of virus within a sample may only be detected intermittently. Samples LLNL_166, LLNL_167, and LLNL_168 amplified with Ct values ranging from 13.8 ± 0.2 to 32.5 ± 0.3 for the N1 and N2 assays following extraction by Qiagen. When extracted using Buffer B/Zymo column, they amplified at Ct values of 13.9 ± 0.3 to 33.4 ± 1.4 (see Fig. 2.8 and 2.9, p. 52). The mean Ct differences between the alternate method and Qiagen for the sample with the highest level of detected virus were 0.1 and 0.4 for the N1 and N2 assays. As the CDPH Ct values within the clinical samples increased, the mean Ct delay for the alternate method increased (see Table 2.5, p. 53). This relationship between increased Ct delay as a factor of increased Ct value may reflect how RNA extraction efficiency declines with lower levels of viral RNA input.

In this project, the Testing Team evaluated two lysis buffers and two PCR purification methods as alternate RNA extraction protocols for SARS-CoV-2 detection by PCR. These reagents do not depend on commercially available kits, which alleviates kit dependency when reagents are in shortage. The two lysis buffers can be made in a laboratory using

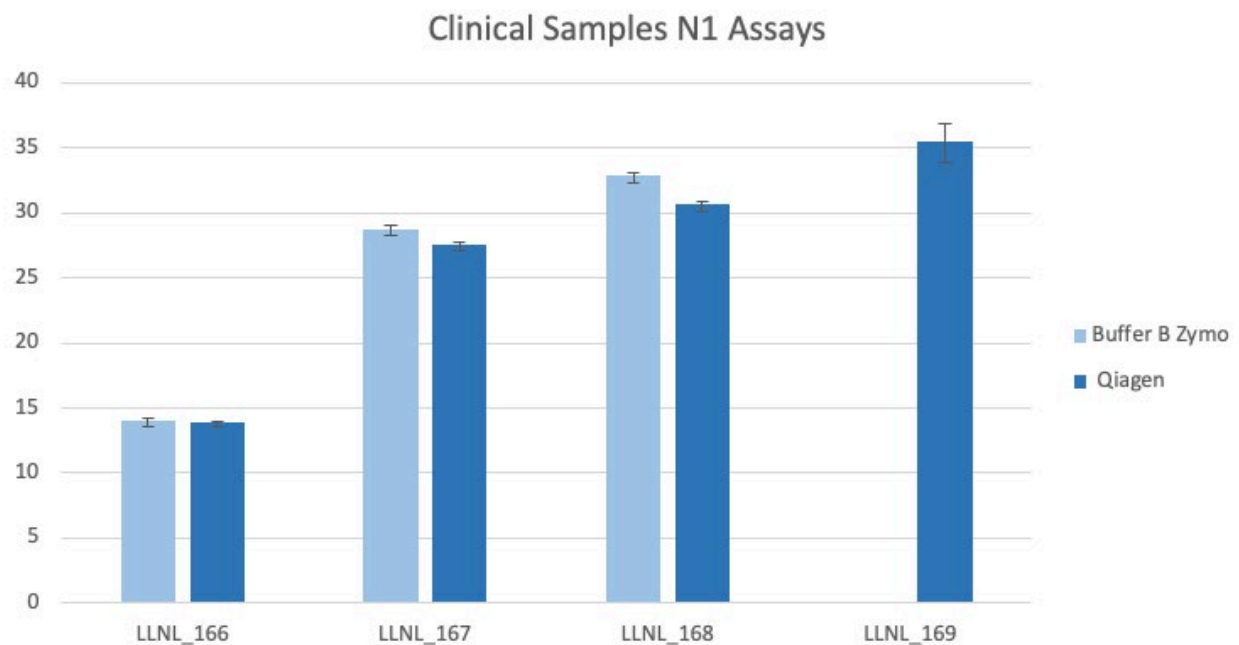


Fig. 2.8. N1 assay RT-qPCR of SARS-CoV-2 clinical samples. [Courtesy Lawrence Livermore National Laboratory]

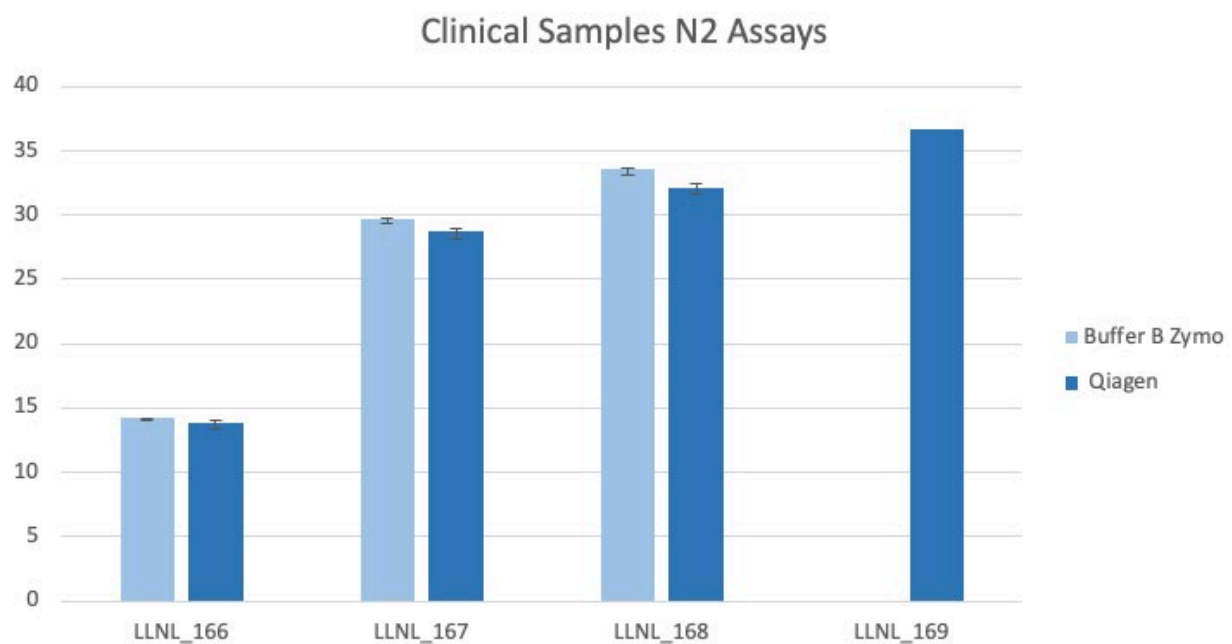


Fig. 2.9. N2 assay RT-qPCR of SARS-CoV-2 clinical samples. [Courtesy Lawrence Livermore National Laboratory]

Table 2.5. Mean Clinical Sample SARS-CoV-2 Ct Increase*

| CDPH Sample | Sample Virus Level | N1 Assay Mean Ct Delay | N2 Assay Mean Ct Delay |
|-------------|--------------------|------------------------|------------------------|
| LLNL_166 | High | 0.1 (p=.49) | 0.4*** |
| LLNL_167 | Medium | 1.2**** | 1.0**** |
| LLNL_168 | Low | 2.2**** | 1.4**** |
| LLNL_169 | Very Low | Not Detected | Not Detected |
| LLNL_170 | Negative | Not Detected | Not Detected |

*Mean increase in SARS-CoV-2 clinical sample alternative extraction RT-qPCR Ct values compared to Qiagen extraction. Two tailed Welch's t-test

**significant at $p < .05$

***significant at $p < .005$

****significant at $p < .001$

standard reagents. The two purification methods are not part of any extraction kits and can be purchased separately. We compared the extraction efficiency against the EUA Qiagen viral RNA extraction kit using bovine coronavirus, synthetic SARS-CoV-2, and archived clinical samples from the CDPH. Our results showed that lysis Buffer B (25 mM DTT, 1.25 mM sodium citrate, pH of 6.8) paired with the Zymo column produced extraction yields very comparable to the Qiagen extraction methods. This alternate extraction protocol will be valuable for future nucleic acid needs when commercially available kits are scarce.

2.3.8 Identifying Alternative RNA Extraction Technologies for Saliva-Based Diagnostics

During Phase 1 testing activities, Oak Ridge National Laboratory (ORNL) identified alternative RNA extraction technologies, optimized saliva-based diagnostics, and created allele-specific RT-qPCR methods to rapidly detect SARS-CoV-2 and its variants. These alternatives safeguarded a robust clinical testing program at ORNL that could have been derailed by supply chain shortages. Technologies and capabilities developed at ORNL in consultation with the multi-laboratory NVBL Testing Team can be applied to future biosecurity,

biosurveillance, and healthcare diagnostics programs to rapidly respond to emerging threats.

We demonstrated that a non-EUA-approved RNA purification system, NucleoSpin RNA Plus isolation kit (produced by Macherey-Nagel), efficiently extracted viral RNA from the SARS-CoV-2 surrogate bacteriophage MS2. This system worked efficiently in saliva matrices, including artificial saliva (Pickering Laboratories) and frozen, multiple donor human saliva (Innovative Research). RNA recoveries from fresh saliva were lower and were not significantly improved by the addition of sample stabilizers or nuclease inhibitors. The addition of dithiothreitol (DTT) to samples increased assay signal strength by almost sixfold. Thus, fresh saliva samples could be stored cold without additives for rapid processing—a practice now applied by many community surveillance programs.

To evaluate the potential for test methods that did not require RT-qPCR, we compared the CDC EUA method with a commercial colorimetric Loop-mediated isothermal AMplification (LAMP) assay (New England Biolabs). Both assays readily detected SARS-CoV-2 N gene transcripts spiked in pooled saliva, and RNA was immediately extracted. However, samples spiked with N gene transcript and added directly to the LAMP assay mixture were not

detected, demonstrating a requirement for sample purification and concentration. We also evaluated the Yale-developed Saliva Direct assay that does not require RNA purification. Several common beverages were observed to interfere with saliva-based detection results, emphasizing the importance of supervised saliva collection and abstinence from food and beverage before sample collection.

Clinical diagnostic tests at ORNL were accelerated by automating RNA extraction procedures and implementing saliva-based diagnostics. Together with ORNL Health Services, The Testing Team implemented KingFisher Flex automation for RNA extraction from nasopharyngeal swab samples in a Clinical Laboratory Improvement Amendments (CLIA)-certified testing lab that used the multiplex Thermo COVID-19 TaqPath assay. This advance amplified ORNL's testing capabilities, enabling rapid diagnostic testing of swab samples from UT-Battelle staff and contractors and making continuous and safe on-site operations possible during Phase 1 of the return-to-work process. We also collaborated on the implementation of the Saliva Direct assay that was made available to staff under that EUA. Although this simple assay was used less frequently due to the additional time required for sample collection compared to swab sampling, it provided a valuable alternative test in case swabs or molecular reagents would become unavailable.

New SARS-CoV-2 variants have emerged globally and spread rapidly in the U.S., creating a need for rapid diagnostics that identify variants of concern in clinical samples in time for medical or public health response. To address this problem, the team developed an allele-specific RT-qPCR method to rapidly distinguish between RNAs from reference and variant SARS-CoV-2 in COVID-19 samples. While next generation sequencing provides exceptionally detailed data for biosurveillance, new methods are required to distinguish strains in a clinically relevant timeframe. A rapid *in vitro* transcription system was developed to produce full-length RNA transcripts of the SARS-CoV-2 N and S genes. These standards were valuable for

the development of rapid diagnostic methods and could be stored without degradation, shared freely, and used safely in BSL1 environments. Subsequently, we used site-directed mutagenesis to modify the S gene reference sequence in a plasmid vector, introducing characteristic mutations found in B.1.1.7, B.1.351, and P.1 variants of concern. These variant templates were used to develop an allele-specific RT-qPCR method that blocks the reference gene sequence and preferentially amplifies variant sequences with 4-8 exponential cycles of discrimination.

2.4 Task 2: Develop Affinity Reagents and Novel Platform Approaches

The overarching goal of this project was to develop antibodies for sensitive and selective detection of SARS-CoV-2, the causative agent of COVID-19. The Testing Team chose the ACE2 receptor-binding domain (RBD) of viral spike protein as the target antigen. In addition to the descriptions and images in this section, see Task 2 Supplementary Information and Graphics at the end of this chapter, beginning on p. 92.

2.4.1 Antibody Selection and Characterization

Selection was performed by *in vitro* evolution of a human single chain antibody (scFv) library, synergizing phage, and yeast display technologies (see Fig. 2.10, p. 55). Additionally, to select antibodies targeting precisely the receptor binding motif of RBD [i.e., the region of RBD with the most sequence variation between SARS-CoV-2 RBD (RBD2) and SARS-CoV RBD (RBD1)], some of our selections included RBD1 as a counter selector. As a result, we obtained a set of 18 anti-RBD antibodies (see Fig. 2S.1, p. 92), mostly selective for RBD2 (see Fig. 2.11, p. 56) except for antibody R04, which binds more strongly to RBD1. Remarkably, this antibody was obtained from selections not including counter selector RBD1. Yeast-displayed scFv's affinities (K_{Ds}) for RBD2 were determined by flow cytometry (see Fig. 2S.2A and Table 2S.1, p. 93 and p. 95). To

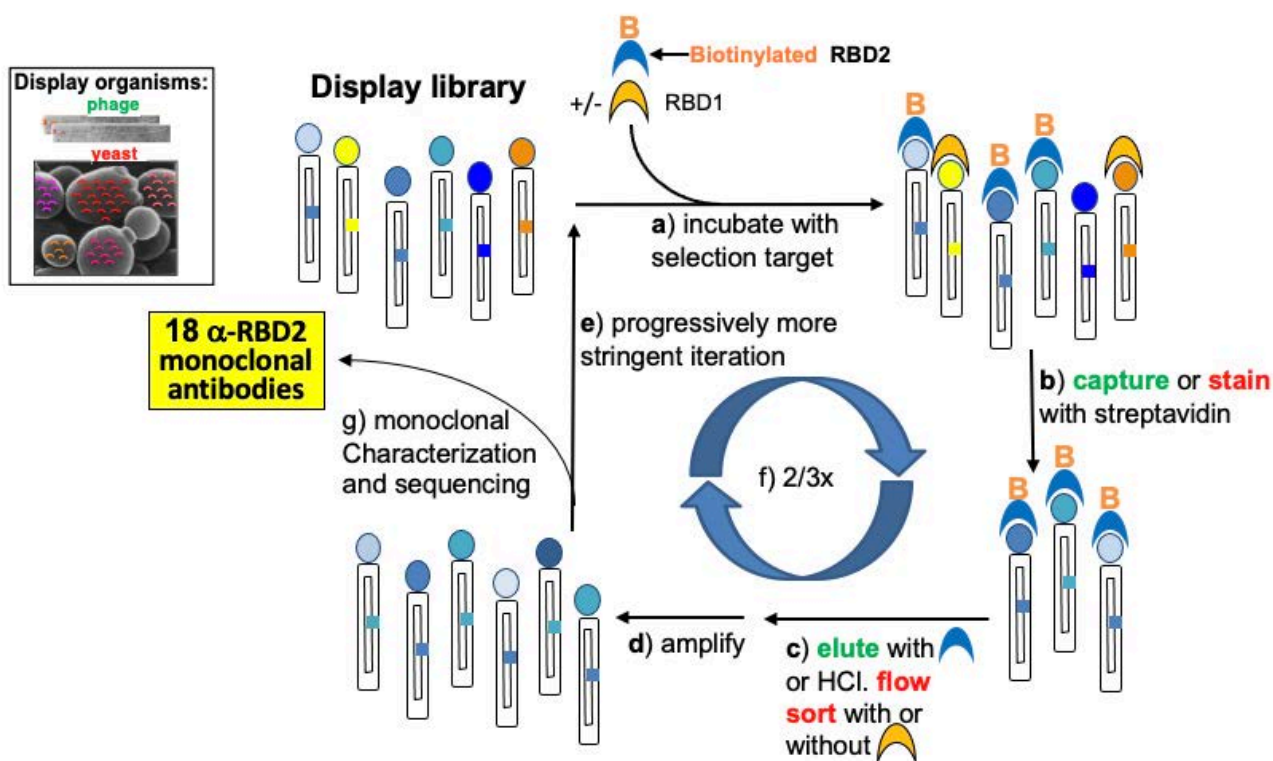


Fig. 2.10. Selection of monoclonal antibodies by *in vitro* evolution of display libraries. Phage and yeast display technologies were used in tandem for selection of 18 anti-SARS-CoV-2 spike protein RBD (RBD2). Selection steps **a** through **g** are indicated. Actions color-coded in blue and purple pertain to phage and yeast sections, respectively. Subtractive selection strategies included: (1) the use of non-biotinylated SARS-CoV RBD (RBD1) during the incubation step (**a**); and (2) elution with excess unbiotinylated RBD2 during the phage display elution step (**c**). [Courtesy Los Alamos National Laboratory]

obtain soluble antibodies (i.e., free of the display organism) resembling full-length immunoglobulin G (IgG), we produced minibodies [molecules containing two copies of scFv held together by rabbit or human fragment crystallizable (Fc) receptors]. Antibodies in this format behaved similarly to yeast-displayed scFvs (see Fig. 2.11B and C) and allowed us to perform some preliminary experiments for identification of non-competitive RBD2 binders (“antibody pairs,” data not shown). Minibodies’ affinity for RBD2 were determined by surface plasmon resonance (SPR; see Table 2S.1, p. 95). Based on affinity measurement and likelihood of forming pairs, we selected antibody B04, E01, E08, F07, G07, H01, H05 and S01 for conversion to IgGs.

We also converted R04 because of its unique preference for RBD1 over RBD2. IgG’s affinity for RBD2 were determined by SPR (see Fig. 2S.2B and Table 2S.1, p. 93 and p. 95). For those antibodies available in multiple formats, we noticed that duplication of the variable region (i.e., conversion to minibodies and/or IgG) resulted mostly (82%) in decrement of affinity [increment of binding affinity (K_D)]. The remainder of the clones were equally split in those with same affinity (same K_D) and those with higher affinity (lower K_D ; see Fig. 2S.3, p. 94). IgG’s ability to specifically recognize RBD2, even in the context of spike S1 portion, was confirmed by fluorescence-linked immunosorbent assay (FLISA; see Fig. 2S.4, p. 94).

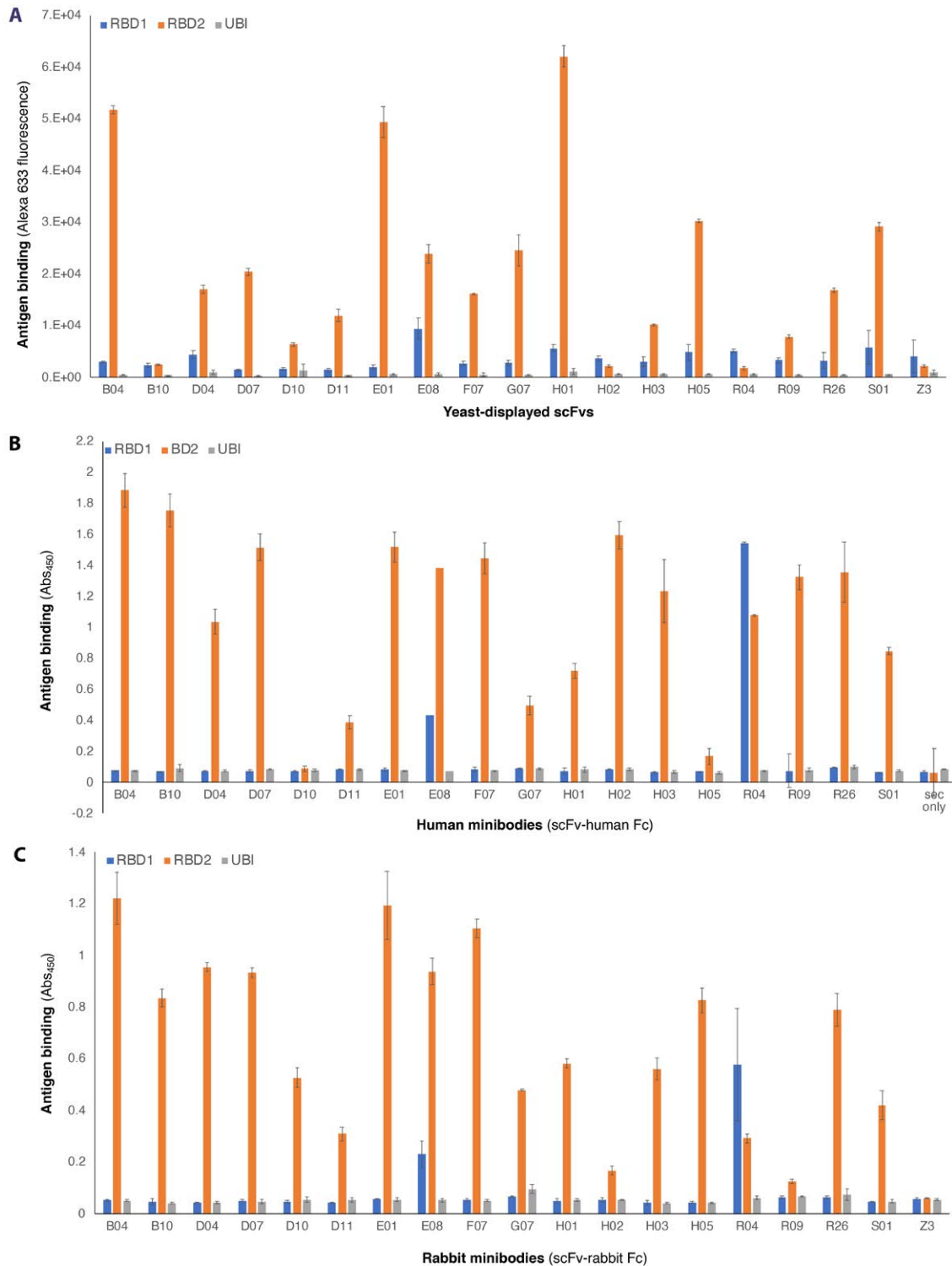


Fig. 2.11. Affinity and specificity of selected antibodies. Relative affinity of **(A)** monoclonal yeast-displayed scFvs, **(B)** human minibodies (i.e., scFv-human Fc), and **(C)** rabbit minibodies (scFv-rabbit Fc) for 3 antigens. The orange and blue bars indicate binding to RBD2 and RBD1 respectively. Data include a negative control antigen (ubiquitin, UBI, grey bars) and a negative control antibody (human anti-influenza M2, called Z3). This control antibody was used either as yeast displayed scFv **(A)** or as rabbit minibody **(C)**. The height of each bar is an average of three measurements, and the error bars correspond to the standard deviations of each set of three measurements. [Courtesy Los Alamos National Laboratory]

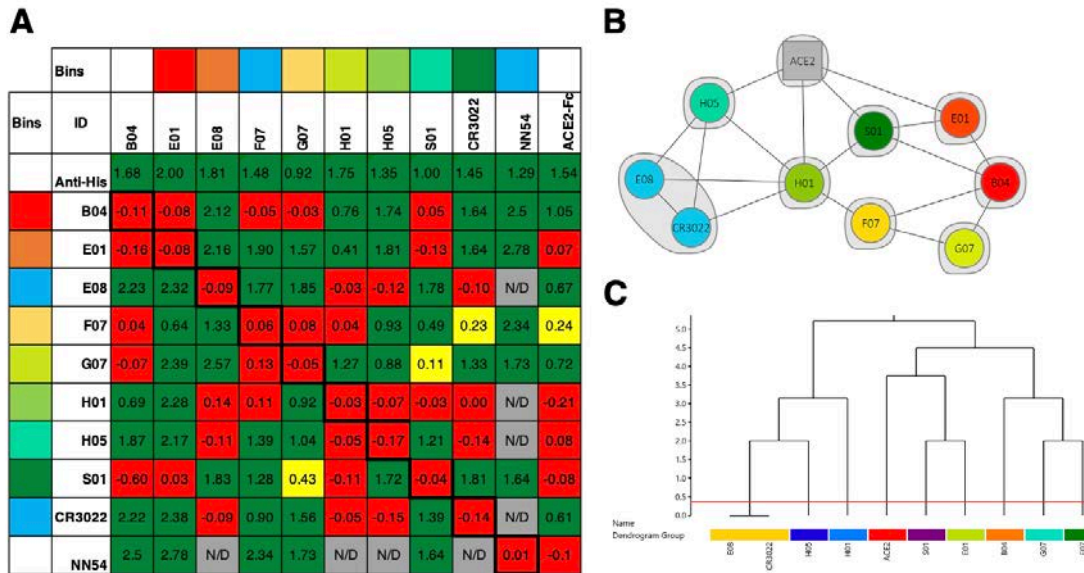


Fig. 2.12. Antibody epitope binning by surface plasmon resonance (SPR). IgGs were tested for their ability to bind SARS-CoV 2 spike protein's receptor binding domain (RBD2, histidine tagged) by SPR. Antihistidine tag IgG was used as a positive control non-competitive RBD2 binder. And commercial gold standards anti-RBD2 antibody NN54 was included in the analysis. (A) The green and red cells in the heat map rendition of the SPR data indicate the intersection of two non-competing and competing IgGs, respectively. The network plot rendition of the SPR data (B) indicate competing IgGs connected by a line, whereas all the non-competing igGs are isolated. The dendrogram rendition of the SPR data (C) shows the relatedness of the competition profiles across the clones. This can be then used to create cut-offs to group similar epitope clusters together. [Courtesy Los Alamos National Laboratory]

2.4.2 Diagnostic Potential of Antibodies

Immunoassays are much more specific and sensitive when pairs of antibodies recognizing two distinct regions of the target antigen are used rather than single antibodies. Therefore, we screened our IgGs for their ability to bind non-competitively to the antigen (epitope binning) by both SPR (see Fig. 2.12, this page) and sandwich enzyme-linked immunosorbent assay (ELISA; see Fig. 2S.5, p. 96).

A set of four IgG pairs were identified: E1/F07; E1/G07; S1/F07 and S1/G07. These pairs were tested for LOD of spike protein and whole SARS-CoV-2 virus (see Fig. 2.13, p. 58). Results from the sandwich ELISA showed:

- Pairs E01/F07 and S01/F07 detected wild type spike at ≤ 3.4 pM (see Fig. 2.13A).
- Pairs S01/F07 detect spike mutant D614G at a minimum of 3.4 pM (see Fig. 2.13B).

- Pairs E01/F07 and E01/G07 detected whole heat inactivated SARS-CoV-2 virus at a concentration of $1.25\text{E}+3/\text{mL}$ (see Fig. 2.13D).

Results from Sandia National Laboratories' (SNL) SpinDx™ diagnostic platform showed the best performing IgG pairs were S01/F07 and S01/G07 (see Fig. 2.13C), which detected spike protein at 0.16 and 9.6 pM, respectively.

2.4.3 Therapeutic Potential of LANL Antibodies

Although discovery of therapeutic antibodies was not part of our proposal, we were able to explore the therapeutic potential of our antibodies through collaborations with the University of New Mexico (Steven Bradfute) and with LANL coworkers (Sofiya Micheva-Viteva). SPR analysis revealed that all of our IgGs (including B04, which does not form pairs, see Fig. 2.12, this page) compete with ACE2 for

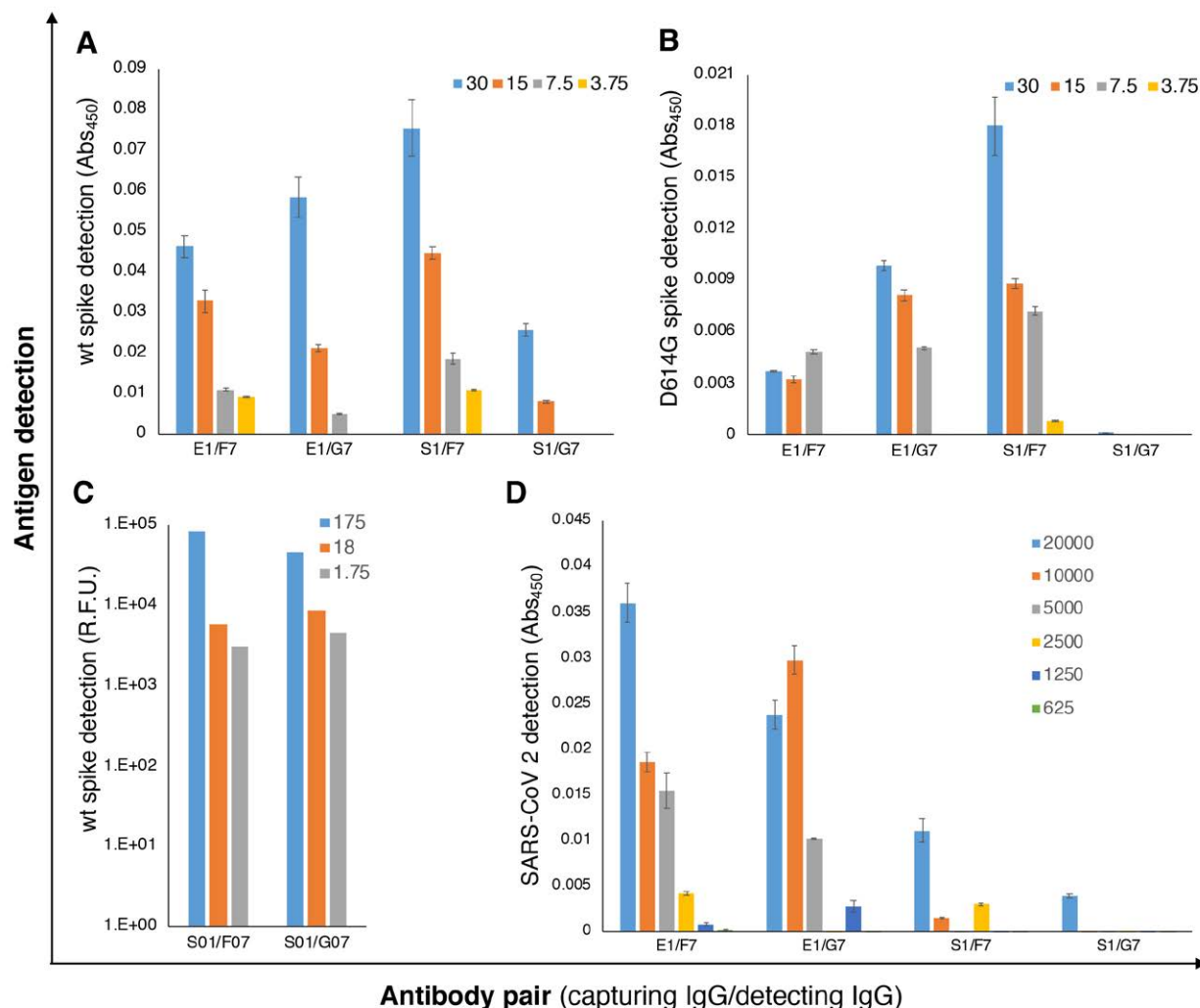


Fig. 2.13. Limit of detection of trimeric spike by whole SARS-CoV-2. Detection of wild type spike (A) and D614G mutant spike (B) by sandwich ELISA. Detection of wild type spike by SpinDX™ (C). Detection of heat inactivated whole SARS-CoV-2 virus by sandwich ELISA (D). Binding to negative control antigen myoglobin (A and B) and beta coronavirus (D) have been subtracted from reported data. Signal detected in the absence of antigen (noise) has been subtracted from data reported in C. [Courtesy Los Alamos National Laboratory]

binding to RBD2 (see Fig. 2.14A, p. 59), suggesting that they could be used as a therapeutic cocktail. These results were partially corroborated by immuno-cytochemistry analysis (see Fig. 2.14B).

Finally, *in vitro* study of human embryonic kidney (HEK) cells viral infection demonstrated that all our IgGs, except G07, neutralize the live virus (see Fig. 2.15A, p. 60) and that antibody pairs S01/F07 and E01/F07 outperform the most active member of each pair (see Fig. 2.15B).

2.4.4 Conclusions

We selected and characterized a set of 18 antibodies recognizing SARS-CoV-2 spike protein's receptor binding domain (RBD2). Four of these antibodies (E01, F07, G07 and S01) form four pairs of noncompetitive RBD2 binders (E01/F01; E01/G07; S01/F07; and S01/G07). These same antibodies plus antibodies B07, E08, H01, and H05 compete with recombinant ACE2 for binding to RBD2 and neutralize viral infection of HEK cells. Antibody pair S01/F07 can

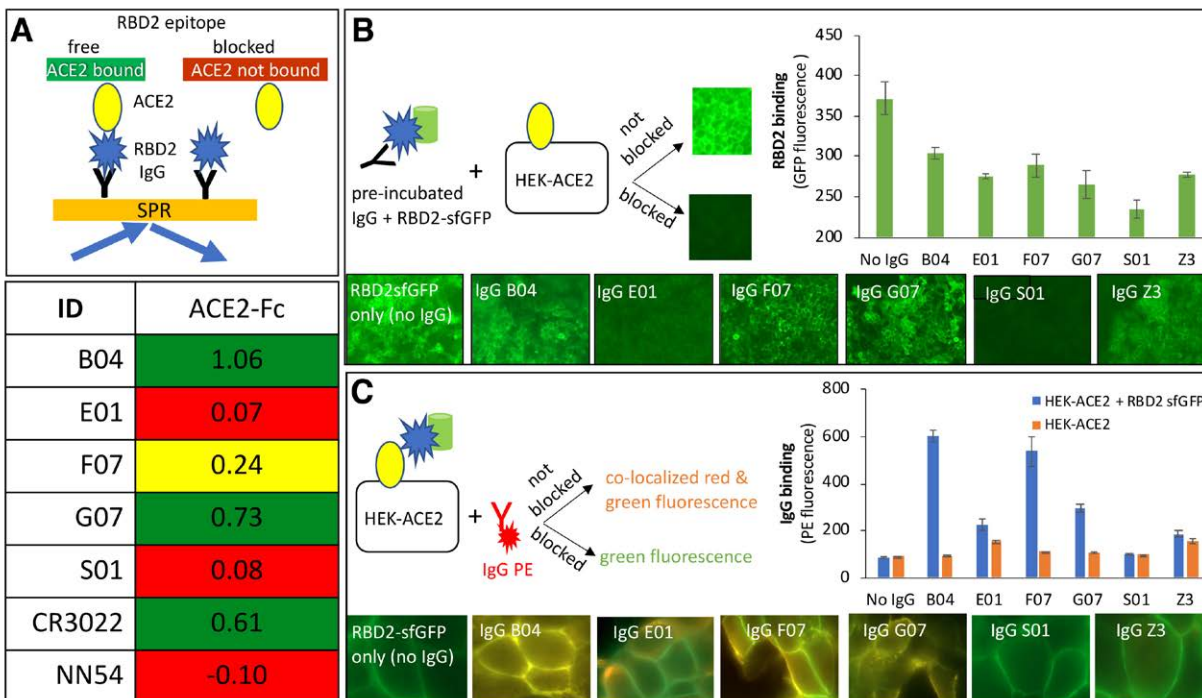


Fig. 2.14. Antibody interference with binding of SARS-CoV-2 spike protein's receptor-binding domain (RBD2) to ACE2. Presented are data for five anti-RBD2 antibodies (B04, E01, F07, G07 and S01) along with controls. A heat map plot of SPR data (**A**) depicts normalized ACE2-Fc binding to RBD2 captured by immobilized antibodies. The green, red and yellow cells indicate non-competing, competing and mildly competing binding relationships, respectively. Antibodies CR3022 and NN54, known to not compete and compete with ACE2, respectively, were included as controls. (**B and C**) Evaluation of the effect of the antibodies on interaction between HEK cells constitutively expressing ACE2 (HEK-ACE2) and RBD2-sfGFP chimera (green fluorescence). Both panels provide three pieces of information: a graphical representation of the experimental design, quantitative fluorescence data in bar graph format (error bars show standard deviation of triplicate experiment) and representative microscopy images for each of the antibodies. Data obtained without IgGs (only RBD2sfGFP) and anti-influenza M2 IgG Z3 were used as a positive control for absence of inhibition (B) and binding (C). [Reprinted under a Creative Commons Attribution License (CC BY 4.0) from Velappan, N., et al. *Healthy Humans Can be a Source of Antibodies Countering COVID-19. Bioengineered* **2022**, 13(5), 12598-12624, DOI: 10.1080/21655979.2022.2076390]

detect as little as 160 femtomolar spike by SpinDx™, and pair E01/F07 can detect as little as 1.25E+3/mL viral particles by sandwich ELISA.

In addition to fulfilling the main objective of this proposal (i.e., developing high-selectivity and high-sensitivity assays for detecting SARS-CoV-2), the team has obtained potentially therapeutic antibody cocktails.

Finally, this project has allowed the Testing Team to explore collaborative side projects with LANL coworkers (B and T divisions) and form

collaborations with the University of New Mexico, Carterra Inc., LBNL, and Argonne National Laboratory (ANL). This network will be a solid foundation for future proposals on COVID-19 research and obtainment of additional funding.

2.5 Task 3: Droplet Digital Microfluidic Platforms for Detection of COVID-19

The goal of this task was to develop a proof-of-concept microfluidic platform for SARS-CoV-2 nucleic acid detection using a synthetic RNA standard for testing. The platform allows for a

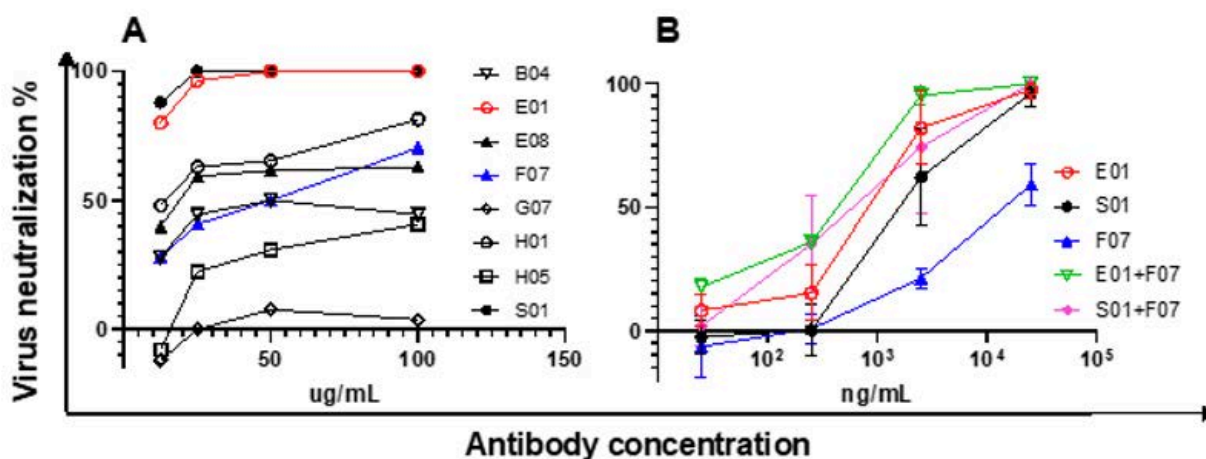


Fig. 2.15. Antibody neutralization of SARS-CoV-2 infection HEK cells expressing ACE2. Single antibody analysis (A) and pairs versus single antibody analysis (B). Data reported in B are averages of 3 measurements plus corresponding standard deviations (error bars). [Courtesy Los Alamos National Laboratory]

hundredfold reduction in reagent consumption per test, with an inherently scalable design that would allow for multiplexing and low production cost.

2.5.1 Disposable Device

The disposable digital microfluidic (DMF) device (see Fig. 2.16, p. 61) transports, mixes, and splits small 'digitized' packets of aqueous droplets submerged in an immiscible oil phase. The device generates movement by electrostatic force through electrode pads. The proof-of-concept DMF device is designed to mix droplets containing PCR or LAMP reagents and SARS-CoV-2 samples generated from their respective reservoirs. The resultant mixed droplet is then moved to on-board resistive heating locations that enable the various enzymatic reactions required for reverse transcription, PCR, or LAMP. During the amplification steps, fluorescence data are periodically collected to provide real-time data.

2.5.2 Current Project Status

We have built a device with a scalable and low-cost production design that successfully performs droplet generation, mixing, and transportation of reagents and RNA standards. Material compatibility at elevated temperatures was one of the

largest hurdles in this project, requiring an array of different materials used for various components of the device to be tested. At the end of the project's budget and timeline, a successful combination of materials was determined.

Remaining steps required to complete the project include (1) refinement of data acquisition controls, (2) fabrication of new devices for testing, and (3) completion of an experimental matrix showing successful nucleic acid detection of SARS-CoV-2 of via PCR or LAMP.

2.6 Task 4: Integrated Data Science and Genomic-Guided Approaches

2.6.1 Phase 1: Integrated Data Science Approach to Support COVID Detection and Diagnosis

As part of the COVID-19 Testing Team, LLNL performed research for Task 4: Integrated Data Science Approach to Support COVID Detection and Diagnosis. We focused our bioinformatics research on two areas: (1) analysis of SARS-CoV-2 proteomics structures and mutations; and (2) analysis of all available SARS-CoV-2 genomes and design

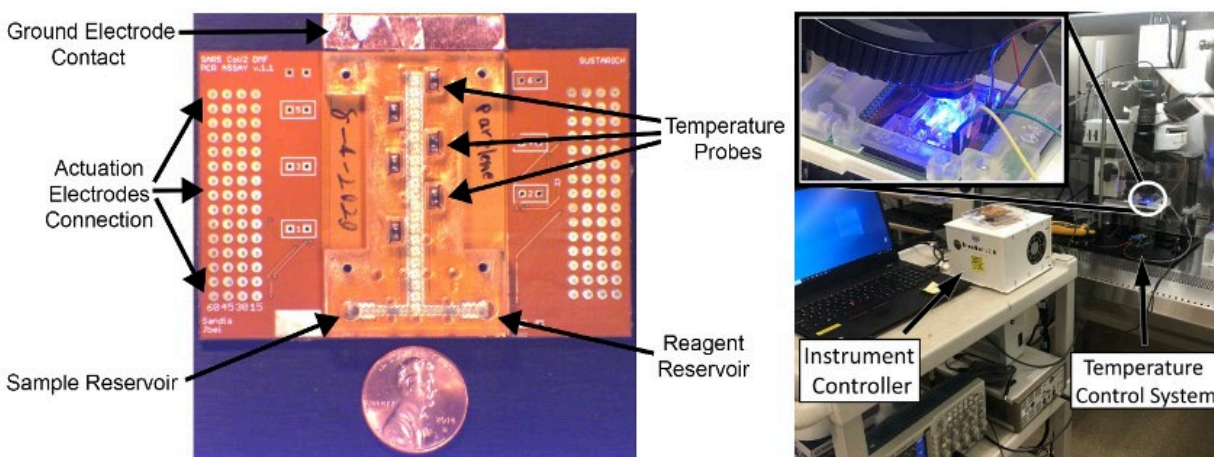


Fig. 2.16. Disposable digital microfluidic device. [Courtesy Sandia National Laboratories and Lawrence Berkeley National Laboratory]

signatures on consensus regions that can capture SARS-CoV-2 variants.

SARS-CoV-2 Proteomic Mutation Analysis

Mutation analysis in various SARS-CoV-2 proteins was performed to support future applications for discovering compounds for therapeutic use. We created a pipeline that can rank viral protein candidates as drug targets by comparing the frequency of mutations between binding sites and surrounding regions, classifying mutations by the type of secondary structure in which they are found, and evaluating the solvent accessibility of a mutation based on whether it is exposed or buried within Protein Data Bank (PDB) models. Future work also aims to use this pipeline to explain differences in mutation rates between geographic regions that favor different drug therapies by examining the same mutation characteristics.

Technical Details

Tens of thousands of protein sequences from GISAID and the Virus Pathogen Database and Analysis Resource (ViPR) were processed for identifying mutations. Sequences that were too short (missing more than ten amino acids compared to the maximum length sequence), or contained undertermined amino acids were filtered out. To access

the same position on all available sequences for a protein, the sequences must be aligned first so that deletions can be represented by gaps. Each multiple sequence alignment (MSA) was generated using Multiple Sequence Comparison by Log-Expectation (MUSCLE) software, version 3.8.1441. This tool allows a maximum of 500 sequences to be included per run. Many MSAs were generated per protein to be able to align all available sequences.

Mutations across all 20 amino acids were counted for drug binding pockets of interest (see Fig. 2.17, p. 62). A similar analysis was performed in pockets of interest in proteins: Nsp1, Nsp3, Nsp4, Nsp5, Nsp7, Nsp8, Nsp9, Nsp10, Nsp12, Nsp13, Nsp14, Nsp15, Nsp16, Orf3A, Orf7A, Spike, E, S, and N.

Using the approach outlined in Zemla, et al. 2014⁶ the team used closely matched PDB models for each position in a drug binding site, to determine the secondary structure the position is most likely found in. The PDB models also determined if the amino acid at the site was pointing in towards the protein, stabilizing it, or pointing outside the protein, more likely to interact with other proteins and solvent.

⁶ Zemla, A., et al. "GeneSV – An Approach to Help Characterize Possible Variations in Genomic and Protein Sequences." *Bioinformatics and Biology Insights* **8**, 1-16 (2014). DOI: 10.4137/BBI.S13076

| Residue | A | R | N | D | C | G | Q | E | H | I | L | K | M | F | P | S | T | W | Y | V |
|---------|---|-------|-------|-------|-------|-------|-------|-------|-------|-------|---|-------|---|-------|-------|-------|-------|-------|---|-------|
| T24 | | 1 | 0 | 0 | 0 | 0 | 0 | 0 | 0 | 0 | 2 | 0 | 0 | 0 | 0 | 0 | 0 | 0 | 0 | 0 |
| T25 | | 0 | 0 | 0 | 0 | 0 | 0 | 0 | 0 | 0 | 0 | 0 | 0 | 0 | 0 | 0 | 0 | 0 | 0 | 0 |
| T26 | | 0 | 0 | 0 | 0 | 0 | 0 | 0 | 0 | 0 | 0 | 0 | 0 | 0 | 0 | 0 | 0 | 0 | 0 | 0 |
| L27 | | 0 | 0 | 0 | 0 | 0 | 0 | 0 | 0 | 0 | 0 | 74603 | 0 | 0 | 0 | 0 | 0 | 0 | 0 | 0 |
| H41 | | 0 | 0 | 0 | 0 | 0 | 0 | 0 | 0 | 74602 | 0 | 0 | 0 | 0 | 0 | 1 | 0 | 0 | 0 | 0 |
| M49 | | 0 | 0 | 0 | 0 | 0 | 0 | 0 | 0 | 0 | 4 | 0 | 0 | 74599 | 0 | 0 | 0 | 0 | 0 | 0 |
| Y54 | | 0 | 0 | 0 | 0 | 0 | 0 | 0 | 0 | 0 | 0 | 0 | 0 | 0 | 0 | 0 | 0 | 0 | 0 | 74603 |
| F140 | | 0 | 0 | 0 | 0 | 0 | 0 | 0 | 0 | 0 | 0 | 0 | 0 | 0 | 74603 | 0 | 0 | 0 | 0 | 0 |
| L141 | | 0 | 0 | 0 | 0 | 0 | 0 | 0 | 0 | 0 | 0 | 74603 | 0 | 0 | 0 | 0 | 0 | 0 | 0 | 0 |
| N142 | | 0 | 0 | 74593 | 0 | 0 | 0 | 0 | 0 | 0 | 0 | 5 | 0 | 0 | 0 | 0 | 0 | 5 | 0 | 0 |
| G143 | | 0 | 0 | 0 | 0 | 0 | 74597 | 0 | 0 | 0 | 0 | 0 | 0 | 0 | 0 | 0 | 0 | 6 | 0 | 0 |
| S144 | | 0 | 0 | 0 | 0 | 0 | 0 | 0 | 1 | 0 | 0 | 1 | 0 | 0 | 0 | 0 | 74601 | 0 | 0 | 0 |
| C145 | | 0 | 0 | 0 | 0 | 74602 | 0 | 0 | 0 | 0 | 1 | 0 | 0 | 0 | 0 | 0 | 0 | 0 | 0 | 0 |
| H163 | | 0 | 0 | 1 | 0 | 0 | 0 | 0 | 0 | 74602 | 0 | 0 | 0 | 0 | 0 | 0 | 0 | 0 | 0 | 0 |
| H164 | | 0 | 0 | 0 | 0 | 0 | 0 | 0 | 0 | 74603 | 0 | 0 | 0 | 0 | 0 | 0 | 0 | 0 | 0 | 0 |
| M165 | | 0 | 0 | 0 | 0 | 0 | 0 | 0 | 0 | 0 | 2 | 1 | 0 | 74600 | 0 | 0 | 0 | 0 | 0 | 0 |
| E166 | | 0 | 0 | 0 | 0 | 0 | 0 | 0 | 74601 | 0 | 0 | 0 | 0 | 0 | 0 | 0 | 0 | 0 | 0 | 2 |
| P168 | | 0 | 0 | 0 | 0 | 0 | 0 | 0 | 0 | 0 | 0 | 0 | 0 | 0 | 0 | 74597 | 6 | 0 | 0 | 0 |
| H172 | | 0 | 0 | 0 | 0 | 0 | 0 | 0 | 0 | 74603 | 0 | 0 | 0 | 0 | 0 | 0 | 0 | 0 | 0 | 0 |
| D187 | | 0 | 0 | 0 | 74602 | 0 | 1 | 0 | 0 | 0 | 0 | 0 | 0 | 0 | 0 | 0 | 0 | 0 | 0 | 0 |
| R188 | | 0 | 74595 | 0 | 0 | 0 | 0 | 0 | 0 | 0 | 0 | 0 | 7 | 0 | 0 | 0 | 0 | 1 | 0 | 0 |
| Q189 | | 0 | 0 | 0 | 0 | 0 | 0 | 74602 | 0 | 0 | 0 | 0 | 1 | 0 | 0 | 0 | 0 | 0 | 0 | 0 |
| T190 | | 1 | 0 | 0 | 0 | 0 | 0 | 0 | 0 | 0 | 4 | 0 | 0 | 0 | 0 | 0 | 0 | 74598 | 0 | 0 |
| A191 | | 74520 | 0 | 0 | 0 | 0 | 0 | 0 | 1 | 0 | 0 | 0 | 0 | 0 | 0 | 0 | 0 | 2 | 0 | 80 |
| Q192 | | 0 | 0 | 0 | 0 | 0 | 0 | 74603 | 0 | 0 | 0 | 0 | 0 | 0 | 0 | 0 | 0 | 0 | 0 | 0 |

Fig. 2.17. Residues in drug binding pocket of interest in protein Nsp5 and corresponding amino acid counts in GISAID sequences for Nsp5. The 'Residue' column shows the wild type amino acid and the position of a ligand binding residue. The rest of the columns are counts for the amino acid indicated in the column header. [Courtesy Lawrence Livermore National Laboratory]

In addition to mutations in the binding sites, mutations in amino acids near binding sites were examined, as well as mutations further from the binding sites, to score proteins by the conservation of their drug binding sites.

The result is a pipeline that will prioritize proteins and their drug binding sites in drug discovery pipelines and help researchers understand the selection pressures against various drugs.

SARS-CoV-2 Genomic Signature Analysis

Finding regions in SARS-CoV-2 that distinguish it from all other viruses is the key to designing molecular detection assays. Ideal signature regions are highly conserved across most isolates of the virus. Multiple signatures that span across the entire genome are needed for multiplexed assays that have high sensitivity in degraded samples where parts of the genome may be missing.

Technical Details

All possible 60-mers from 41,540 SARS-CoV-2 genomes were generated using Jellyfish 2.2.10 for

evaluation as signatures. Only complete, medium-, or high-coverage genomes from GISAID were included for this analysis. Any genome with over 3,000 Ns or genomic length below 28,000 were filtered out. Only viruses isolated from human hosts were included. To find unique 60-mers, the 60-mers were mapped with the Basic Local Alignment Search Tool (BLAST) against an anti-target sequence set consisting of all virus families other than Coronaviridae from the National Center for Biotechnology Information (NCBI) and SARS-CoV-1, as well as the human genome. A hybridization probability score based on entropy, BLAST bit score, guanine-cytosine (GC) content, and number of mismatches was computed for every BLAST hit. 60-mers with a probability of over 20% to any anti-target genome was filtered out, leaving 365,292 unique k-mers.

The next step was to determine which of the unique k-mers were also highly conserved among the SARS-CoV-2 genomes. 42 BLAST databases were created out of the genomes to parallelize the

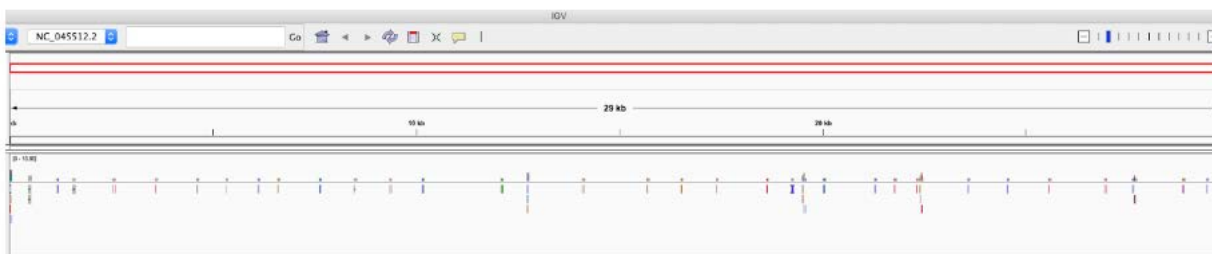


Fig. 2.18. Microarray probes distributed across the SARS-CoV-2 genome (reference sequence NC_045512.2), shown using Integrative Genomics Viewer (IGV) from the Broad Institute. The top panel shows the 29kb reference. The bottom panel shows where in the reference each 60 mer probe maps. Locations that are highly conserved show multiple probes at the same location. [Courtesy Lawrence Livermore National Laboratory]

conservation analysis. After the unique 60-mers were BLASTED to the target genomes, the same hybridization probability score was calculated for each BLAST result. This time 60-mers that had at least 95% probability of mapping to any of the target genomes were kept. High scoring 60-mers were split into several categories. 60-mers that map to almost all target genomes and those that are less conserved were separated, since the less conserved 60-mers may be useful in distinguishing isolates in different samples. Next, each of those two groups of 60-mers were split by genomic location to make it easier to select signature regions across the genome for assay design.

The signature regions generated using the technique described above can now be incorporated into multiple existing pipelines for different types of assay design. A total of 78 microarray probes were downselected from the set of signature regions to span the SARS-CoV-2 genome (see Fig. 2.18, this page) and included in the Lawrence Livermore Microbial Detection Array (LLMDA) microarray, which is being used to test SARS-CoV-2 positive samples for co-infection. The LLMDA can detect up to 20,000 species, including viruses, bacteria, archaea, protozoa, and fungi in one run.

2.6.2 Phase 2: Using Genomics-Guided Approaches to Improve Testing Effectiveness

The novel coronavirus SARS-CoV-2 and other respiratory viruses are known to modify their surface proteins through nucleic acid mutations that result in changes in protein structure and content. These changes influence immune recognition and, hence, the effectiveness of serological tests. Furthermore, the impact of these mutations and the resulting SARS-CoV-2 variants on the nasal microbiome in patients with and without co-infections is not known. In this task, genomics-guided approaches were used to perform correlative analyses between the viral sequence with protein structure, immune recognition, nasal microbiome, and co-infections, both experimentally and computationally.

Population Genomics of SARS-CoV-2

Quasispecies Analysis of SARS-CoV-2 Genomes

Approximately 100 nasopharyngeal samples that had previously tested positive for SARS-CoV-2 viral RNA were obtained from the California Department of Public Health (CDPH) via collaboration with Drs. Debra Wadford and Sharon Messenger. The samples that were available for analysis were collected throughout California between late February 2020 to mid-July. Metadata available for each sample included age and geographic region; however,

no symptomatic data was available for most samples. For each sample, SARS-CoV-2 RNA was amplified using the ARTIC v3 protocol⁷ in which primer sets that span the genome amplify the genome in two highly multiplexed PCR reactions. The RT-PCR products were sequenced at the DOE Joint Genome Institute (JGI) using the Illumina NovaSeq platform to ensure the error rate was low enough to allow sensitive detection of emerging variants. Due to the SARS-CoV-2 genome size and depth of coverage achieved with the NovaSeq platform, the resulting sequence data files were very large, with an average compressed Fastq file size of about 1 GB each. The large file size has necessitated building a higher-throughput pipeline for data analysis and visualization. In particular, Mappgene, (<https://github.com/LLNL/mappgene>) was established on an LLNL high-performance computing (HPC) platform, as part of an internally funded Laboratory Directed Research and Development (LDRD) project. This pipeline enabled the samples to run in parallel on multiple nodes, allowing rapid processing of large datasets. This capability will be leveraged to allow the remainder of the samples to be analyzed.

Preliminary data analysis of the spike protein data from a subset of samples indicated that indels leading to frameshifts were very common and generally occurred at low frequency (<1%). Missense mutations were also detected, generally at much lower frequency as compared to synonymous mutations. We also observed that minor variants present at low frequency in a subset of the CADPH samples were sometimes seen as consensus changes that later emerged during the pandemic, including some mutations that are present in the genotypes of variants of concern and/or variants of interest. Preliminary analysis also indicated that mutation patterns may differ significantly among individual patient samples and between the timepoints in which samples were collected. The Illumina reads for each sample and available

metadata were deposited in GenBank SRA database. The results of the sequence data analysis will be published in an open-source journal.

Genome Analyses of SARS-CoV-2 Sequences

Clinical diagnostic and surveillance testing of samples is currently one of the many critical fronts to containing and monitoring SARS-CoV-2 spread. Capitalizing on over 100,000 sequenced and publicly available SARS-CoV-2 genomes, we developed a computational pipeline to detect conserved regions across the available SARS-CoV-2 diversity. Once detected, these conserved regions were used as potential target sites for diagnostic and surveillance testing. Using this approach, we identified 65 sites of lower variance than sites currently used in CDC protocols for testing. We further prioritized these conserved sites to design primers and probes for nucleic acid amplification tests that take in consideration thermodynamic properties of qPCR amplification and viral secondary RNA structure into 12 primer pairs and their corresponding probes for testing in the lab.

Using a standard qPCR assay with carboxy-rhodamine (ROX) dye, we investigated the performance of the 12 primer sets using synthetic RNA of the Wuhan-Hu-1 strain from Twist Bioscience. Results showed that while the 12 pairs of primer sets worked as expected, seven in particular had low background noise and performed better than the current CDC 2019-nCoV-N1 and 2019-nCoV-N2 primer sets. The set of seven primers performed well to detect >100 copies of SARS-CoV-2 template. We are currently further developing these seven sets of primers into full TaqMan assays to increase their sensitivity and specificity with the goal of making these available for diagnostic testing and generating a peer-reviewed publication.

With the availability of more viral sequences from global sequencing efforts, combined with the rise in the number of variants of concerns, we modified the analysis pipeline to process a larger set of viral sequences. As a result, the pipeline is currently analyzing up to 700,000 available

⁷ Freed, N. E., et al. "Rapid and Inexpensive Whole-Genome Sequencing of SARS-CoV-2 Using 1200 bp Tiled Amplicons and Oxford Nanopore Rapid Barcoding." *Biology Methods and Protocols* 5(1), bpaa014 (2020). DOI: 10.1093/biomethods/bpaa014

genome sequences from NCBI and GISAID. Further, we incorporated a lineage sorting function using existing tools to separate the genomes into their respective lineages with emphasis on current variants of concern. The sorted lineages then undergo entropy analysis to detect conserved and slow mutating sites per lineage. This information is then collated and used to design lineage-specific primers and probes that can provide discriminating power between different variants of concern, such as the B.1.1.7 or B.1.351 strains, while still maintaining overall specificity.

Analysis of SARS2 Genome and Proteome Sequence Variation

Monitoring genomic and proteomic sequence variation of a pathogen during an outbreak may signal turning points, such as appearance of variants with increased or decreased (attenuated) virulence. It may also reveal when therapeutics, vaccines, and diagnostics begin to fail. We created a system to develop an all-coronavirus genome sequence database and automate its updating as much as possible. This system addressed the challenges of (1) cross-referencing identical samples from the two main data sources (GenBank and GISAID) that did not coordinate their efforts, and (2) treating the high frequency of samples with blocks of uncertain nucleotide sequence. Variations in genome and proteome sequences were identified and monitored. Findings were as follows:

1. A subset of coronavirus proteins was identified that were sufficiently conserved for broad phylogenetic analysis.
2. Regions of the SARS2 genome were identified where variations occurred from 10-50-fold higher than the background level of variation. One high-variation region was within the spike gene, but others were found in accessory protein and polyprotein genes. A small number of exceptionally frequent variations, such as spike D614G, were also identified.
3. SARS2 ORF9c and ORF3a showed high levels of missense variation, and ORF9c also had

significant levels of gross variation (frameshifts, nonsense, or unstop).

4. Spike phylogeny and receptor-binding motif sequence alignment among the SARS genus showed four main insertion/deletion types: BatA, SARS1, BatB, and SARS2.
5. Analysis of the binding sites for nucleic acid-based SARS2 diagnostics, such as the CDC PCR tests and Sandia LAMP assays, showed that, as of October 1, these tests were not seriously compromised (variations detected in <0.04 % of the genomes).

Genomics-Guided Antibody-Epitope Interactions

SARS-CoV-2 Antibody-Binding Capacity Prediction

We assessed multiple methods to separate intact mass recombinant spike receptor binding domain (RBD) proteins. The methods tested were (1) capillary electrophoresis (CE), (2) reverse phase (C2), and (3) hydrophilic liquid interaction chromatography (HILIC). Our HILIC method outperformed CE and C2. Previous research has shown the SARS-CoV-2 spike RBD to be heavily glycosylated. Our mass spectrometry analysis indicated substantial heterogeneity in glycosylation, leading to a diversity of protein glycoforms. Our current method can robustly generate analyses of spike RBD glycoforms and will allow for rapid characterization of spike RBD mutants. Finally, we have initiated development of mass spectrometry methods for assessing antibody binding to SARS-CoV-2 spike recombinant RBD proteins.

Effects of Viral Sequence on the Nasal Microbiome and Co-Infections

The presence of co-infections in COVID-19 and the nasal microbiome affects not only disease severity and morbidity but also SARS-CoV-2 diagnostic assay sensitivity and specificity. In this task, we analyzed 201 retrospective COVID-19 samples to identify co-circulating viral, bacterial, and fungal pathogens using a comprehensive microarray technology, the Lawrence Livermore Microbial Detection Array (LLMDA). We conducted bioinformatics

analysis to identify (1) pathogens whose presence is correlated or anti-correlated with COVID-19 infection and (2) nasal microbial communities that could affect the susceptibility or resilience to COVID-19.

We found that the LLMDA is sensitive to detect SARS-CoV-2. When compared to PCR, the array detected 92% of the PCR positive samples. The nine samples that were not detected by LLMDA had a range of PCR Ct values, and the negative detection could be related to sample processing or degradation. The correlation of sensitivity of more comprehensive technology like the LLMDA to PCR was found in another study⁸ using Nanopore sequencing. In this study, SARS-CoV-2 were confirmed by nanopore sequencing in 77.5% (31/40) of samples positive by RT-PCR, correlating with lower Ct values and fewer days from symptom onset. In the same study, possible bacterial or viral co-infections were detected in 12.5% of SARS-CoV-2 positive samples, and a decrease of microbiome diversity was observed in patients with confirmed COVID-19.

LLMDA identified other viruses and bacteria from both COVID-positive and COVID-negative samples. *Streptococcus*, *Prevotella*, *Haemophilus*, *Mycoplasma*, and *Veillonella*—all considered commensal microbiome—were detected in both positive and negative samples. *Flavobacterium* was only detected in COVID-positive samples, while *Lactococcus* was only detected in COVID-negative samples. In a recent study⁹ of 40 COVID-19 samples, five phyla—Firmicutes, Bacteroidetes, Proteobacteria, Actinobacteria, and Fusobacteria—were detected by 16S rRNA sequencing. The microbiota of the nasopharynx was not different in patients positive for SARS-CoV-2 RNA compared to the microbiota of patients negative for SARS-CoV-2 RNA. Our study provided species level detection

⁸ Mostafa H. H., et al. "Metagenomic Next-Generation Sequencing of Nasopharyngeal Specimens Collected from Confirmed and Suspect COVID-19 Patients." *mBio Clinical Science and Epidemiology* 11(6), e01969-20 (2020). DOI: 10.1128/mBio.01969-20

⁹ De Maio F., et al. "Nasopharyngeal Microbiota Profiling of SARS-CoV-2 Infected Patients." *Biological Procedures Online* 22, 18 (2020). DOI: 10.1186/s12575-020-00131-7

and differences in microbiome are observed in COVID-negative vs COVID-positive samples. Overall, additional bacteria and viruses were detected in 16% of all samples, and 17% of COVID-positive samples.

2.7 Task 5: Structure-Based Protein Design for Diagnostics

The multi-laboratory working group for the Testing Research and Development (R&D) Team identified opportunities where additional R&D would assist with response to the COVID-19 public health emergency. Priority emphasis was given to quick implementation as well as development of novel capabilities for current and evolving pandemic needs without placing any additional burden on current reagent demand. Priority elements capitalized on DOE national laboratory strengths and expertise, and also provided a forward-leaning posture to prepare for future scale-up needs, multi-element testing, and prediction for testing elements for diagnostics or therapeutics.

2.7.1 Task 5: Research and Approach

Task 5 activities focused on the topic of structure-based protein design for diagnostics. An integrated approach for utilizing emerging structural data (e.g., the surface spike glycoprotein and new high-resolution crystal structures) was applied to address essential targets and demonstrate high-affinity reagents for non-nucleic acid-based detection systems. This work leveraged and complemented existing efforts on high-resolution structural characterization of viral proteins and variants. Participating national laboratories coordinated their activities as follows.

Argonne National Laboratory

The ANL team helped provide proteins for affinity reagent development for COVID-19 diagnostics. As part of the structural characterization effort conducted by the Center for Structural Genomics of Infectious Diseases (CSGID), the ANL/University of Chicago team had previously cloned and purified more than 50% of the SARS-CoV-2 proteome. The

ANL team could produce proteins in affinity tagged or free form that would enable the identification of high-affinity reagents and provide new constructs targeting regions of the spike protein amenable for HTP studies.

ANL also provided expression of key viral proteins in mammalian cells. The spike protein variants were cloned and expressed as described previously.¹⁰ Similarly, human ACE2 (wild type and variants identified by recent GWAS study)^{11,12} were expressed in a C-terminal fusion form. Other SARS-CoV-2 surface proteins requiring glycosylation were expressed and purified similarly.

The ANL team also used the Advanced Protein Characterization Facility (APCF) to produce antibodies developed through collaborations, and optimized these antibodies (i.e., affinity, specificity, stability) for diagnostic purposes. Mutants of SARS-CoV-2 proteins could be rapidly developed and used to monitor virus evolution. We worked closely with modelling efforts at ANL, LBNL and PNNL to predict mutations that may help the virus avoid detection. New reagents could be developed to monitor and detect this evolution and track down new versions of virus. Crystal X-ray and cryo-EM structures were determined for selected complexes to confirm key interactions and aid design of specific high affinity reagents. Argonne's Advanced Photon Source Structural Biology Center (SBC) beamlines were used for this project.

Lawrence Berkeley National Laboratory

The LBNL team performed high-throughput small angle X-ray scattering (HT-SAXS) experiments at the Advanced Light Source (ALS), using proteins

¹⁰ Wrapp, D., et al. "Cryo-EM structure of the 2019-nCoV spike in the prefusion conformation." *Science* **367**(6483), 1260–1263 (2020). DOI: 10.1126/science.abb2507

¹¹ Horowitz, J. E., et al. "Genome-Wide Analysis in 756,646 Individuals Provides First Genetic Evidence that ACE2 Expression Influences COVID-19 Risk and Yields Genetic Risk Scores Predictive of Severe Disease." *medRxiv* (2020), 2020.12.14.20248176. DOI: 10.1101/2020.12.14.20248176

¹² Suryamohan, K., et al. "Human ACE2 Receptor Polymorphisms and Altered Susceptibility to SARS-CoV-2." *Communications Biology* **4**, 475 (2021). DOI: 10.1038/s42003-021-02030-3

provided by ANL. These studies (1) provided biologically-relevant information about the conformation, oligomeric state, and flexibility of the targets in solution; (2) provided experimental distance data to help constrain our *ab initio* structure prediction calculations, in particular for those targets recalcitrant to other structural solution methods; (3) identified viral protein variants that alter the conformation, which might indicate changes in functionality or detectability; and (4) were used to screen for changes in protein conformation in the presence of candidate high-affinity reagents once they are available.

Located at ALS beamline 12.3.1, the Structurally Integrated Biology for the Life Sciences (SIBYLS) beamline is the leading U.S. beamline for mail-in HT-SAXS and size-exclusion chromatography-SAXS (SEC-SAXS) data collection. In high-throughput mode, data can be collected on hundreds of samples in one day, with samples loaded on 96 well plates. Structure prediction calculations made use of the ASCR-supported NERSC supercomputing center at LBNL.

Oak Ridge National Laboratory

The ORNL team contributed to neutron protein crystallography (NPX) studies and structure-based development of diagnostics. Prior to the project, the structure of the main protease from SARS-CoV-2 had been solved with X-ray diffraction to a resolution of 1.31 Å, indicating its viability as a target for NPX studies. The determination of neutron crystal structures at ORNL provided a detailed description of potential ligand binding sites, including the positions of all hydrogen atoms and associated hydrogen bond networks. The resulting structures can be used to guide the development of rapid, small-molecule-based viral diagnostics, bypassing the need for PCR-based approaches. Specifically, ORNL performed high-throughput, supercomputer-based virtual screening on the Summit supercomputer to identify small molecule ligands that bind the protease with high affinity. Understanding the molecular details of these interactions is expected to provide

new routes for diagnostics that reveal the presence of coronavirus infections.

Los Alamos National Laboratory

The cryo-EM structure of SARS-CoV-2 surface spike glycoprotein (S-protein) interaction with human Angiotensin-converting enzyme 2 (ACE2) had been published prior to the start of the project (PDB 6M17). Based on this info, LANL used Rosetta protein design and high-throughput screening to develop affinity reagents for diagnostic tests. The binding affinity between these proteins is ~35 nM. Learning from the interface, they selected a peptide motif from ACE2 and redesigned around it into small globular proteins (of ~40 amino acids). They then created a library of these small globular proteins (~10,000), displayed them on yeast surface, and screened for binding activity. The top binders were selected, sequenced, and the beneficial mutations incorporated into the next cycle of Design-Build-Test-Learn. The main goal was to achieve a binding affinity that is tenfold stronger than the native RBD and ACE2 interaction and could potentially be used for diagnostics. LANL researchers also docked ACE2 in RBD in the near native conformation, while redesigning the RBD surface, to be able to predict the mutational landscape. The knowledge gained from this research will be useful for creating diagnostics for evolved strains in the future.

A summary of key findings from this project are outlined below according to the main activities conducted during the funding period.

2.7.2 Antibodies

Monoclonal antibodies (mAbs) are the basis of treatments and diagnostics for pathogens and other biological phenomena. We characterized several mAbs specific for several SARS-CoV-2 proteins. Collaboration with Patrick Wilson's lab at the University of Chicago resulted in isolation of specific human mAbs. Complexes were prepared and crystallized, and five structures of human antigen-binding fragments (Fabs) with the N-nucleocapsid RNA binding domain were solved at 1.50, 1.82, 2.41 Å and two

at 2.70 Å resolution. The overall conformations of the N-nucleocapsid RNA binding domain in the complexes were quite similar. However, the orientations of the N-nucleocapsid RNA binding domain in the complexes relative to Fabs were different. In particular, N-protein bound by one Fab complex had a more divergent epitope than the others. We also obtained crystal of human IgG with N-nucleocapsid RNA binding domain. The best crystals diffracted to about 3.8 Å. These structures revealed that complement-determining regions (CDR1-3) of these Fabs are distinct but bind to mostly similar epitopes of N-nucleocapsid RNA binding domain.

We also conducted a structural characterization of commercial mAbs against the N-nucleocapsid RNA binding domain from SARS-CoV-2 using SAXS and transmission electron microscopy (TEM). Our solution-based results distinguished the mAbs' flexibility and how this flexibility affects the assembly of multiple mAbs on an antigen (see Fig. 2.19, p. 70). By pairing two mAbs that bound different epitopes on the N-nucleocapsid RNA binding domain, we showed that flexible mAbs formed a closed sandwich-like complex. With rigid mAbs, a juxtaposition of the antigen-binding fragments was prevented, enforcing a linear arrangement of the mAb pair, which facilitated further mAb polymerization. In a modified sandwich enzyme-linked immunosorbent assay, we showed that rigid mAb-pairings with linear polymerization led to increased nucleocapsid protein (NPNTD) detection sensitivity. These enhancements can expedite the development of more sensitive and selective antigen-detecting point-of-care lateral flow devices, which are critical for early diagnosis and epidemiological studies of SARS-CoV-2 and other pathogens.

2.7.3 Repurposing Existing Antibodies for SARS-CoV-2 RBD

An antibody, CR3022, which could be effective against SARS-CoV-2 was identified very early during the COVID-19 pandemic. CR3022, originally isolated from a patient convalescing from the 2003 SARS-CoV outbreak, binds to the RBD of the spike protein. While CR3022 has potential to become a

diagnostic reagent as well as a promising therapeutic and prophylactic agent against SARS-CoV-2, poorer binding affinity compared to SARS-CoV would have restricted its application. The comparison of the binding affinities of the CR3022 Fab with the RBD and spike protein of SARS-CoV and SARS-CoV-2 showed greater than a hundredfold difference in dissociation constant in favor of SARS-CoV.

While leveraging various crystal structures of the CR3022, the RBD of SARS-CoV-2 (henceforth called RBD2) and SARS-CoV (henceforth called RBD1) and the complex between the CR3022 Fab and RBD2, we pursued computational and experimental analysis with a goal to improve the binding affinity of CR3022 for SARS-CoV-2. We extracted the light and heavy chains from the complex structure (PDB 6YLA). Concurrently, we also extracted the coordinates of CR3022 from the apo structure (PDB 6W7Y) and of RBD2 from another complex between RBD2 and the human receptor ACE2 (PDB 6M0J). In our analysis, we performed protein-protein docking between CR3022 (VL-VH) and RBD1 and RBD2. Three poses of the CR3022 VL-VH with RBD were then relaxed using the ROSETTA fastrelax protocol to remove any clashes introduced due to overlaying or crystal structure imperfections, which were then used as an input for the docking studies. Using the RosettaDock protocol, the VL-VH dimer was randomly perturbed around the starting conformation, followed by low resolution centroid mode, and finally high-resolution all-atom refinement stage to predict a bound pose. The interface score calculated by subtracting the energy of each partner in isolation from the score of the complex was then plotted against the RMSD of the new complex from the input structure. While the input structures derived from the bound complex (6YLA) showed stems of the funnel around low RMSD, the other input poses derived from unbound 6W7Y CR3022 and 6M0J RBD2 or 6WAQ RBD1 only showed very weak funnels and pointed to relatively high RMSD. To further analyze the interface, we performed a more rigorous docking study. SnugDock has been specifically developed for antigen/antibody docking. The

protocol aggressively samples the CDR loops from the structural database, hence a larger conformational space search is possible.

Starting with the structure of the complex (6YLA), we performed RosettaDesign to create a library of ~10,000 different variants of CR3022. The sequences were constructed in the format of single chain variable fragment (scFv), where VL-VH domains were linked with a well-established cre-lox linker. After four rounds of sorting in the presence of RBD2 (0.5 – 5 nM), variants of CR3022 with 4 mutations in CDRL1 and CDRH3 that showed improved binding to RBD2 were isolated. The mutant CR3022 showed improvement in binding affinity well above the native one. While antibody modeling has remained challenging, rationally designed libraries accompanied by high-throughput screening can help rapidly engineer variants with gain-of-function.

2.7.4 Structural Studies of SARS-CoV-2 Nonstructural Proteins (Nsps)

Main Protease—3CLpro

The main protease for SARS-CoV-2 is 3 chymotrypsin-like protease (3CLpro). It is indispensable for viral replication and thus is an important target for the design of specific protease inhibitors. Detailed knowledge of the structure and function of 3CLpro (also called Mpro) is crucial to guide structure-aided and computational drug-design efforts.

Oxidation and reactivity of the cysteine residues of the protease were reported using room-temperature X-ray crystallography, revealing that the catalytic Cys145 can be trapped in the peroxysulfenic acid oxidation state at physiological pH, while the other surface cysteines remained reduced. Only Cys145 and Cys156 reacted with the alkylating agent N-ethylmaleimide. It was suggested that the zwitterionic Cys145-His45 catalytic dyad is the reactive species that initiates catalysis, rather than Cys145-to-His41 proton transfer via the general acid-base mechanism upon substrate

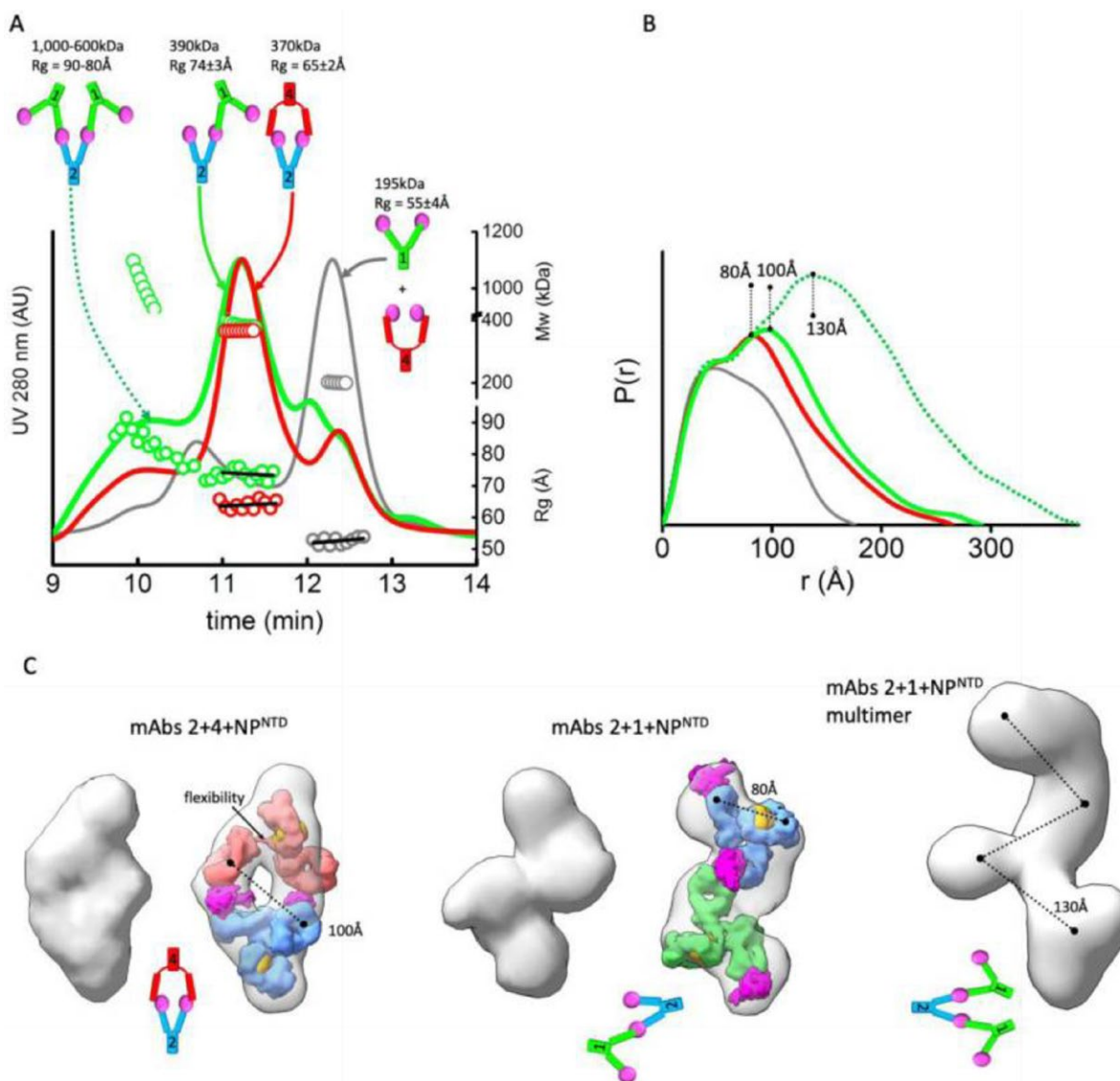


Fig. 2.19. mAb linear or sandwich pairing depends on inherent flexibility. **(A)** SEC-MALS-SAXS chromatograms for the mAb1-2-NPNTD (green), mAb2-4-NPNTD (red) and mAb1-4-NPNTD (gray) samples. Solid lines represent the UV 280 nm signal in arbitrary units, while symbols represent molecular mass (top) calculated from multi-angle light scattering (MALS) and Rg values (bottom) for each collected SAXS frame versus elution time. **(B)** P(r) functions calculated for the experimental SAXS curves for the main SEC peak of mAb1-2-NPNTD (green), mAb2-4-NPNTD (red), mAb1-4-NPNTD (gray), and early SEC shoulder of mAb1-2-NPNTD (green dots). The P(r) functions are normalized at the $r = 40$ Å. The P(r)-maxima peaks are indicated. **(C)** Average SAXS envelopes obtained for mAb2-4-NPNTD, mAb1-2-NPNTD complexes were calculated using a P2 symmetry operator. A single representative envelope was manually superimposed with compact conformers of mAb1 (red), mAb2 (blue), and mAb4 (green) taken from the two-state model of free mAbs. The structure of NPNTD (magenta; PDB ID: 6VY0) was manually docked at the proximity of the CRD3 -Fab region. Additionally, the SAXS envelope obtained for the larger multimer of mAb1-2-NPNTD determined in P1 symmetry is shown. [Reprinted under a Creative Commons Attribution License (CC BY 4.0) from Hodge, C. D., et al. Rigid Monoclonal Antibodies Improve Detection of SARS-CoV-2 Nucleocapsid Protein. *mAbs* **2021**, 13 (1), 1905978.]

binding (see Fig. 2.20, this page). The structures also provided insight into the design of improved 3CLpro inhibitors.

Papain-Like Protease—PLpro

Papain-like protease (PLpro) is one of two SARS-CoV-2 proteases potentially targetable with antivirals. PLpro is an attractive target because it plays an essential role in cleavage and maturation of viral polyproteins, assembly of the replicase-transcriptase complex, and disruption of host responses. We reported a substantive body of structural, biochemical, and virus replication studies that identified several inhibitors of the SARS-CoV-2 enzyme. We determined the high-resolution structure of wild-type PLpro, the active site C111S mutant, and their complexes with inhibitors (see Fig. 2.21, p. 72). This collection of structures details inhibitors recognition and interactions providing fundamental molecular and mechanistic insight into PLpro. All compounds inhibited the peptidase activity of PLpro *in vitro*, and some blocked SARS-CoV-2 replication in cell culture assays. These findings will accelerate structure-based drug design efforts targeting PLpro to identify high-affinity inhibitors of clinical value.

Nsp15 Endoribonuclease

SARS-CoV-2 Nsp15 is a uridine-specific endoribonuclease with a C-terminal catalytic domain belonging to the EndoU family that is highly conserved in coronaviruses. As endoribonuclease activity seems to be responsible for the interference with the innate immune response, Nsp15 emerges as an attractive target for therapeutic intervention.

We reported the first structures with bound nucleotides and showed how the enzyme specifically recognizes uridine moiety. In addition to a uridine site, we presented evidence for a second base binding site that can accommodate any base. Our structures were consistent with the binding of single stranded nucleic acids, such as loops or bulges. The structure with a transition state analog, uridine vanadate, confirmed interactions key to catalytic

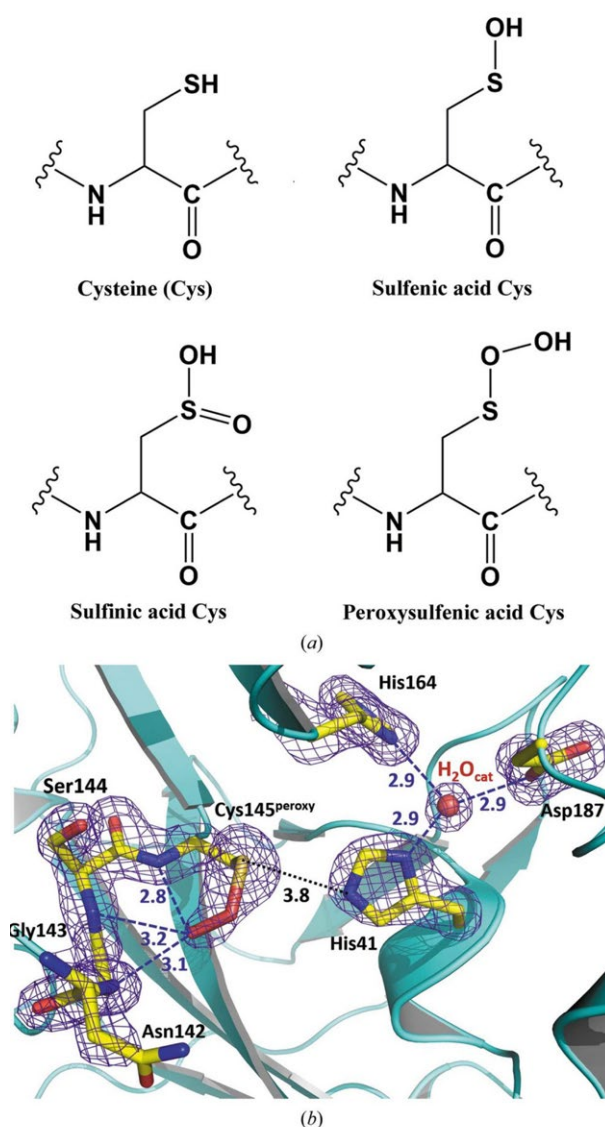


Fig. 2.20. Chemical diagrams of possible oxidation states of a cysteine sidechain (a). The catalytic site of SARS-CoV-2 3CLpro structure I (b). Possible hydrogen bonds are shown as blue dashed lines. The distance between Cys145 and His41, which is too long for a hydrogen bond, is shown as a black dotted line. The 2Fo - Fc electron-density map contoured at the 1.5 Å level is shown as a purple mesh. All distances are given in Å. [Reprinted under a Budapest Open Access Initiative License (BOAI-20) from Kneller, D. W., et al. Room-Temperature X-ray Crystallography Reveals the Oxidation and Reactivity of Cysteine Residues in SARS-CoV-2 3CL M^{pro}: Insights into Enzyme Mechanism and Drug Design. *International Union of Crystallography Journal (IUCrJ)* 2020, 7 (6), 1028–35.]

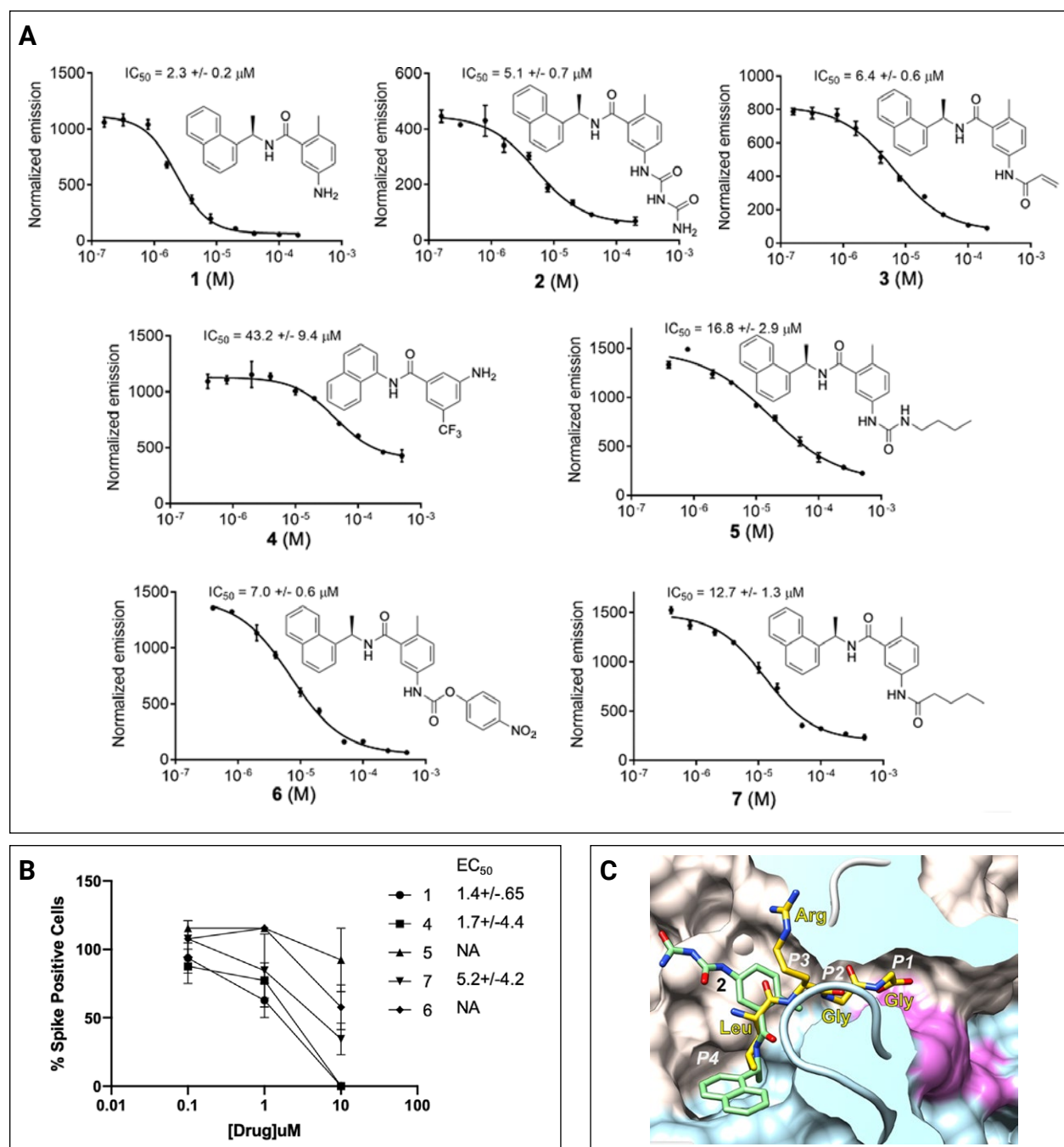


Fig. 2.21. Binding inhibitors to PLpro. **(A)** Biochemical activity assays for compounds 1–7. Activity assays were performed using fluorophore substrate. **(B)** Virus inhibition in whole cell assay. Virus replication activity assays for compounds 1, 4, 5, 6, and 7. Data are mean % percent spike positive cells relative to dimethyl sulfoxide (DMSO) treated cells \pm SEM of three biological replicates. **(C)** Compound 2 (green sticks) binds to a groove on the surface of PLpro protein (surface of palm subdomain is in white and thumb subdomain is in light blue) with the active site catalytic triad surface shown in red in the end of a slender tunnel. Peptide LRRG from ubiquitin structure in complex with SARS PLpro (PDB 4MOW) is shown in yellow and peptide positions corresponding to P1–P4 sites are marked in white. [Reprinted under a Creative Commons Attribution License (CC BY 4.0) from Osipiuk, J., et al. Structure of Papain-like Protease from SARS-CoV-2 and its Complexes with Non-covalent Inhibitors. *Nature Communications* **2021**, *12* (1), 743.]

mechanisms. In the presence of manganese ions, the enzyme cleaved unpaired RNAs.

This acquired knowledge was instrumental in identifying Tipiracil, an FDA-approved drug used in the treatment of colorectal cancer, as a potential anti-COVID-19 drug. Using crystallography, biochemical, and whole-cell assays, we demonstrated that Tipiracil, an uracil derivative, inhibits SARS-CoV-2 Nsp15 by interacting with the uridine binding pocket in the enzyme's active site (see Fig. 2.22, this page). It inhibited Nsp15 RNA nuclease activity *in vitro* and showed modest inhibition of CoV-2 virus replication in the whole cell assay. While the compound itself is not optimal for the therapeutic applications, our work shows that uracil and its derivatives may represent a plausible starting point for nucleotide-like drug development. Moreover, interaction of Trp333 with bases may provide additional site to build much higher affinity inhibitors. Our findings provide new insights for the development of uracil scaffold-based drugs.

Nsp7/Nsp8/Nsp12 RNA-Dependent RNA Polymerase Complex

The RNA transcription complex (RTC) from the virus, SARS-CoV-2, is responsible for recognizing and processing RNA for two principal purposes. The RTC copies viral RNA for propagation into new virus and for ribosomal transcription of viral proteins. To accomplish these activities the RTC mechanism must also conform to a large number of imperatives, including (1) RNA over DNA base recognition, (2) base pairing, (3) distinguishing viral and host RNA, (4) production of mRNA that conforms to host ribosome conventions, (5) interface with error checking machinery, and (6) evading host immune responses. In addition, the RTC will discontinuously transcribe specific sections of viral RNA to amplify certain proteins over others. Central to SARS-CoV-2 viability, the RTC is therefore dynamic and sophisticated.

We conducted a systematic structural investigation of three components that make up the RTC: Nsp7, Nsp8, and Nsp12 (also known as RNA dependent RNA polymerase [RdRp]; see Fig. 2.23,

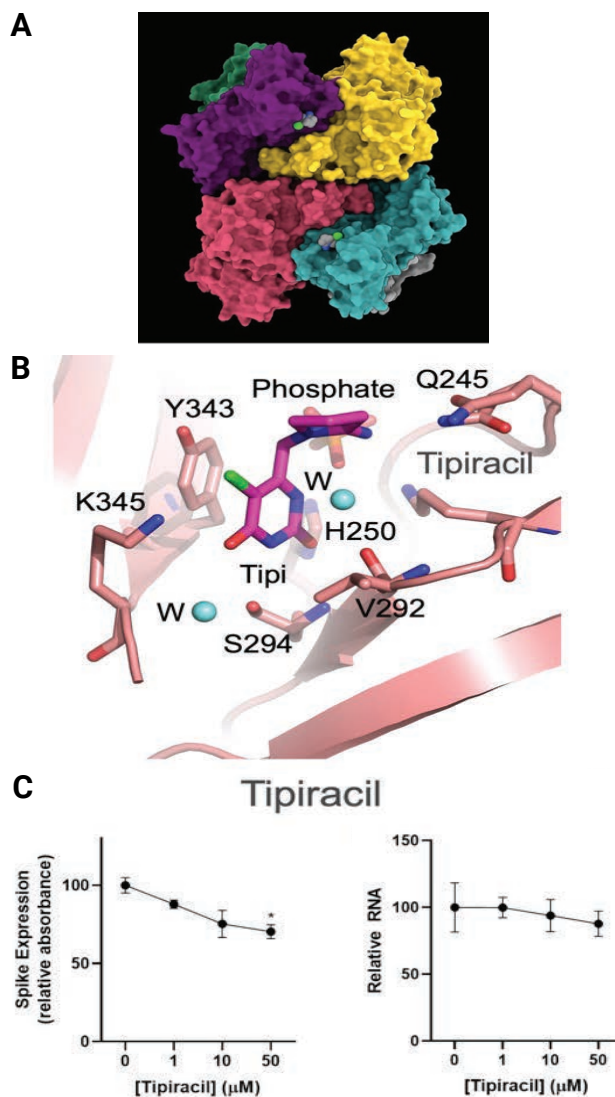


Fig. 2.22. Binding of Tipiracil to Nsp15. **(A)** Structure of SARS-CoV-2 hexamer with the bound Tipiracil in surface representation. Tipiracil bound to each subunit active site is shown with all atoms in color spheres (carbon, chlorine, nitrogen, oxygen in white, green, blue, and red, respectively). **(B)** Binding Tipiracil to Nsp15 endoribonuclease active site, Tipiracil in magenta. **(C)** Inhibition of SARS-CoV-2 coronavirus by Tipiracil in whole-cell assays. A549-hACE2 cells were pre-treated with Tipiracil or carrier (0 mM) for 2 h and infected with CoV-2 at MOI 1. After 48 h, cells were harvested to check (1) spike protein and (2) viral RNA expression. [Reprinted under a Creative Commons Attribution License (CC BY 4.0) from Kim, Y., et al. Tipiracil Binds to Uridine Site and Inhibits Nsp15 Endoribonuclease NendoU from SARS-CoV-2. *Communications Biology* 2021, 4, 193.]

p. 75). We solved high resolution crystal structures of the Nsp7/8 complex, providing insight into the interaction between the proteins. We used small angle X-ray and neutron solution scattering (SAXS and SANS) on each component individually as pairs and higher order complexes and with and without RNA. Using size exclusion chromatography and multi-angle light scattering coupled SAXS (SEC-MALS-SAXS), we defined which combination of components form transient or stable complexes. We used contrast matching neutron scattering to mask specific complex forming components to test whether components change conformation upon complexation. Altogether, we found that individual Nsp7, Nsp8, and Nsp12 structures varied based on whether other proteins in their complex were present. Combining our crystal structure, atomic coordinates reported elsewhere, SAXS, SANS and other biophysical techniques, we provided greater insight into the RTC assembly, mechanism, and potential avenues for disruption of the complex and its functions.

Serial Crystallography Studies of Nsp10/Nsp16 Methyltransferase

The genome of the SARS-CoV-2 coronavirus has a capping modification at the 5' UTR to prevent its degradation by host nucleases. These modifications are performed by the Nsp10/14 and Nsp10/16 heterodimers using S-adenosylmethionine as methyl donor. Nsp10/16 heterodimer is responsible for the methylation at the ribose 2'-O position of the first nucleotide. To investigate the conformational changes of the complex during 2'-O methyltransferase activity, we used a fixed-target serial synchrotron crystallography method at room-temperature. We determined crystal structures of Nsp10/16 with substrates and products that revealed the states before and after methylation, occurring within the crystals during the experiments (see Fig. 2.24, p. 76). Here we report the first crystal structure of Nsp10/16 in complex with Cap-1 analog (m7GpppAm2'-O). Inhibition of Nsp16 activity may reduce viral proliferation, making this protein an attractive drug target. The 2'-O methyl group in Cap-1 is essential to protect viral RNA from host interferon-induced

response. We determined crystal structures of SARS-CoV-2 Nsp10/16 heterodimer in complex with substrates (Cap-0 analog and S-adenosyl methionine) and products (Cap-1 analog and S-adenosyl-L-homocysteine) at room-temperature using synchrotron serial crystallography. Analysis of these structures will aid structure-based drug design against 2'-O-methyltransferase from SARS-CoV-2.

Modeling RBD2 Spike Protein Interaction with Human ACE2 Receptor

This activity was conducted to gain insights into hotspot residues on the spike protein that can be targeted.

Key Residues at RBD2-ACE2 Interface

To rank the relative importance of each residue at the interfaces of RBD1 and RBD2 with ACE2, we computed the bound probability of each pair at the interfaces during the 5- μ s equilibrium simulations. Figure 2.25, p. 77, shows a relative ranking of residues at the interface: high probabilities indicate highly interactive pairs, while low probabilities indicate weakly interacting pairs. To the best of our knowledge, such a complete ranking has not been reported in previous studies, even though calculations of relative changes of interaction energies or free energies were done for some of the pairs and mutations. Figure 2.25 shows that both RBD1-ACE2 and RBD2-ACE2 interfaces have almost the same number of interacting pairs. However, if counting stable pairs that have a probability larger than 60% (i.e., in close contact 60% of the total simulation time), there are only 22 ± 2 pairs in the RBD1-ACE2 interface, while RBD2-ACE2 showed substantially higher with 35 ± 1 stable pairs at the interface. Among these stable pairs, the mutations from RBD1 to RBD2, namely, Y455L, L456F, Y498Q, T501N and L486F appear to noticeably enhance the probabilities of interaction with the residues of ACE2 with multiple pairs having probabilities close to 100%. The brackets in Fig. 2.25 indicate two groups of neighboring residue clusters that have a substantial increase in interactions in the

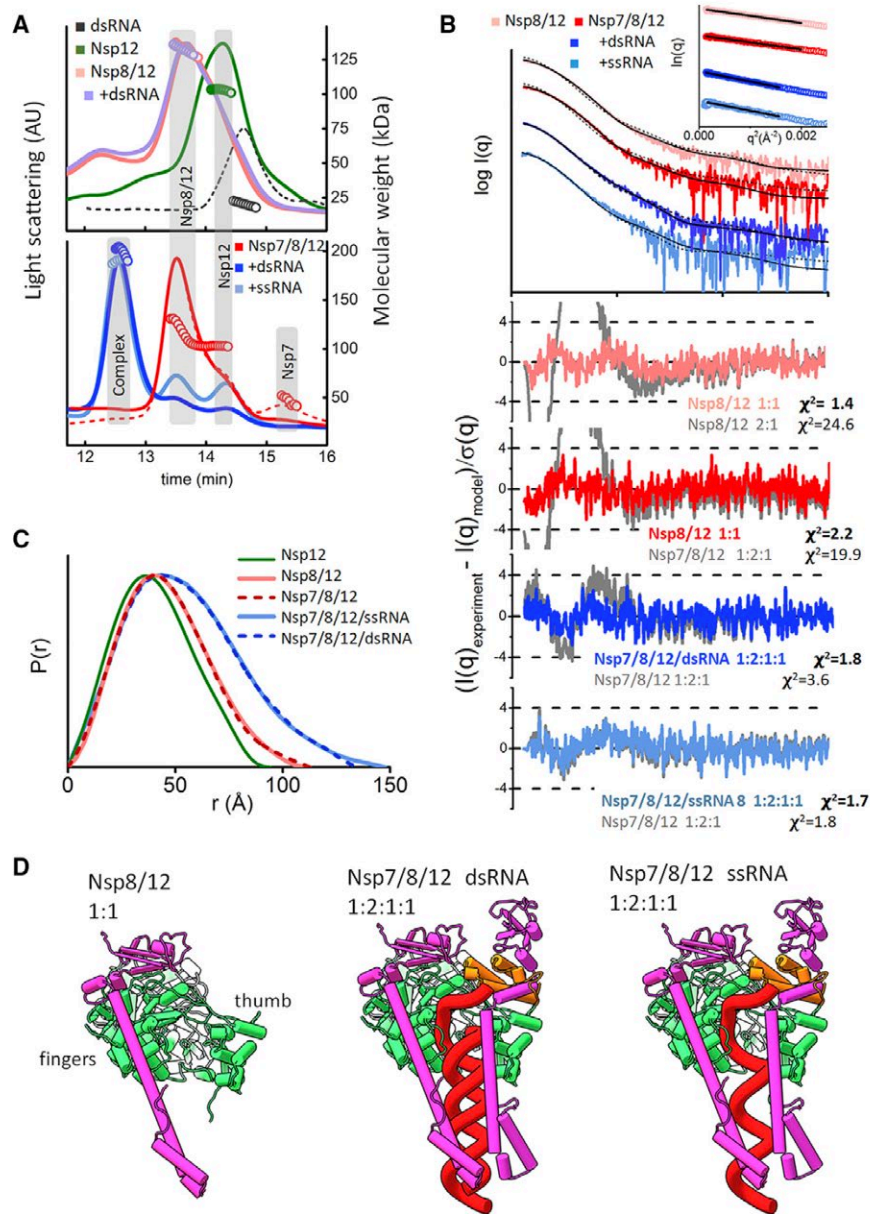


Fig. 2.23. RNA stabilized Nsp7/8/12 complex. **(A)** SEC-MALS chromatograms for Nsp12, Nsp8/12, Nsp8/12+dsRNA, dsRNA (top), and Nsp7/8/12, Nsp7/8/12+dsRNA, Nsp7/8/12+ssRNA (bottom) are colored as indicated. Solid lines represent the light scattering detector units, while symbols represent molecular mass versus elution time. **(B)** Experimental SAXS profiles for Nsp8/12, Nsp7/8/12, Nsp8/12+ dsRNA, and Nsp7/8/12 + ssRNA collected at the SEC peak are shown together with the theoretical SAXS profiles for best fitting models (black line) and alternative models (dash line). SAXS fits are shown together with the fit residuals for the solution-state model (colored as indicated), alternative model (gray), and goodness of fit values (χ^2). Guinier plots for experimental SAXS curves are shown in the inset. **(C)** Normalized $P(r)$ function for Nsp12, Nsp8/12, Nsp7/8/12, Nsp7/8/12+dsRNA, and Nsp7/8/12+ssRNA. The similarity of $P(r)$ functions between Nsp8/12 and Nsp7/8/12 further confirms the absence of Nsp7 and one Nsp8 in the Nsp7/8/12 mixture. **(D)** Solution state models for Nsp8/12, Nsp7/8/12+dsRNA, and Nsp7/8/12+ssRNA were used to fit experimental data shown in panel B. [Reprinted under a Creative Commons Attribution License (CC BY 4.0) from Wilamowski M, et al. "Transient and Stabilized Complexes of Nsp7, Nsp8, and Nsp12 in SARS-CoV-2 Replication." *Biophysical Journal* **2021**, 120 (15), 3152–65.]

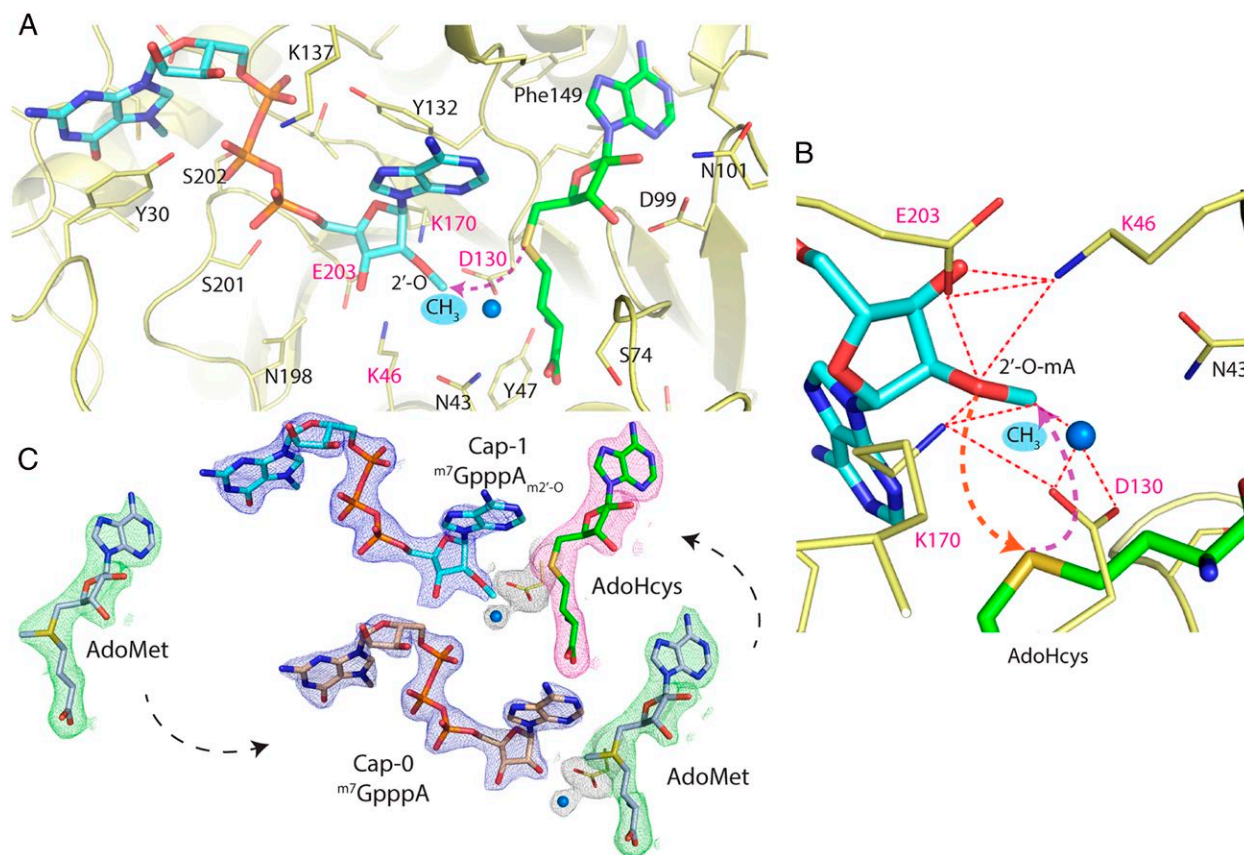


Fig. 2.24. Methylation of the 2'-O-ribose of the m⁷GpppA catalyzed by Nsp10/16 from SARS-CoV-2. **(A)** Active site of Nsp16 2'-O methyltransferase (yellow) in complex with m⁷GpppA_{m²'-O} (Cap-1) as aquamarine sticks and AdoHcys as green sticks. **(B)** Magnification of the active site depicts key residues Lys46-Asp130-Lys170-Glu203 essential for the 2'-O MTase activity shown as yellow sticks. Red dashed lines show close distances between residues, arrows depict simplified nucleophilic attack and subsequent movement of methyl group to the 2'-O position. The water molecule represented as a blue sphere. **(C)** The 2mFo-DFc maps contoured at 1.2 σ around ligands of the structures determined by SSX, cap analogs in blue, AdoHcys in pink, and AdoMet in green. [Reprinted under a Creative Commons Attribution License (CC BY 4.0) from Wilamowski M., et al. 2'-O Methylation of RNA Cap in SARS-CoV-2 Captured by Serial Crystallography. *Proceedings of the National Academy of Sciences of the United States of America* **2021**, 118 (21), e2100170118.]

RBD2-ACE2 interface compared to the similar clusters in the RBD1-ACE2 interface. This suggests that they are key residues that differentiate the RBD2-ACE2 binding interface from the RBD1-ACE2 binding interface.

To probe whether use of a different force field (FF) may change the outcomes of key residues

in the interfaces, we compared the probabilities with those obtained from the simulations using modified AMBER ff99SB FF performed by the Shaw group. We found that regardless of the FFs, the RBD2-ACE2 interface showed stronger inter-molecular interactions than the RBD1-ACE2 interface involving the same group of residue

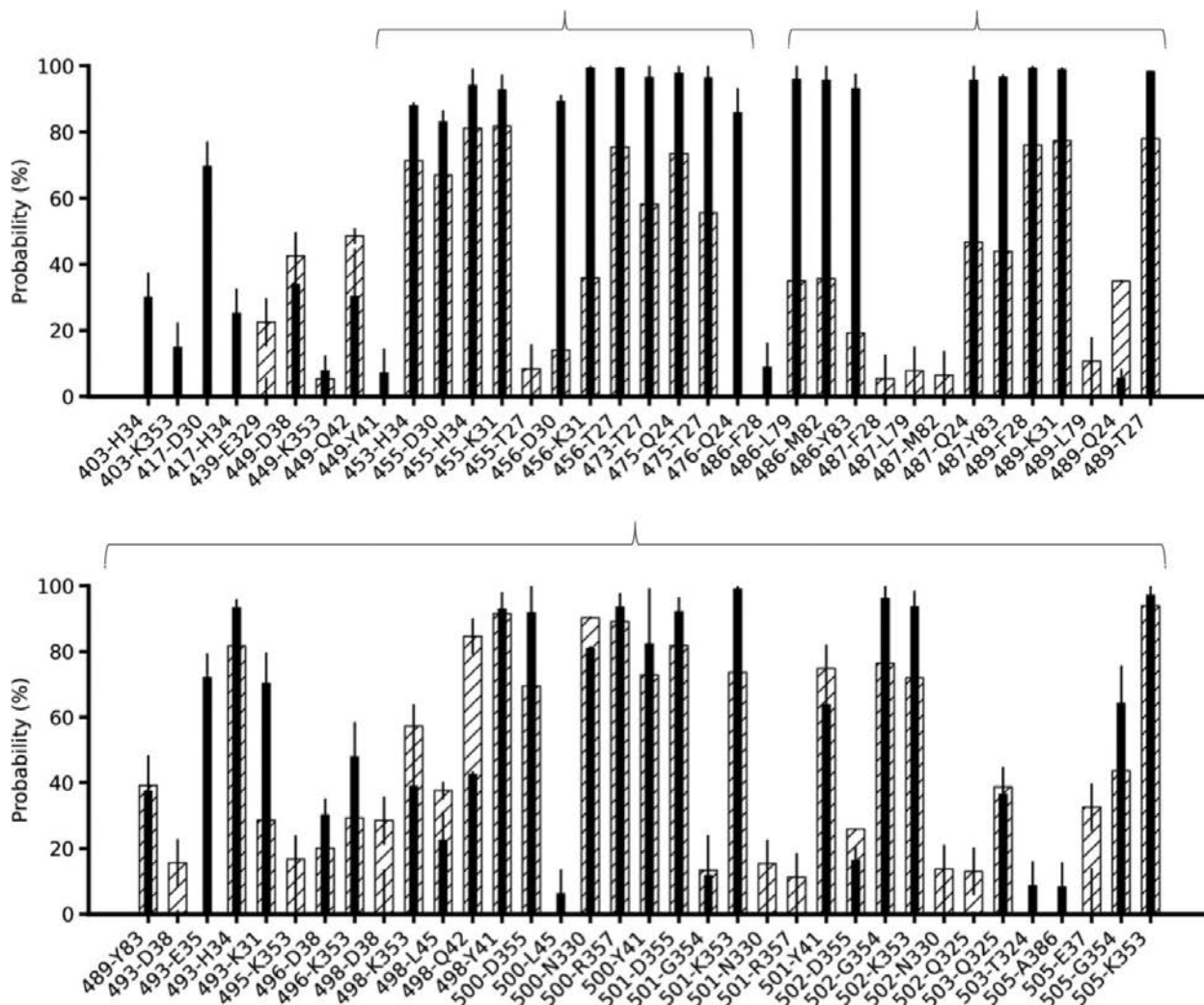


Fig. 2.25. Probability of aligned pairs of residues found within 3.5 Å at the RBD1-ACE2 (shaded bars) and RBD2-ACE2 (black bars) interfaces using C36 FF. The first number corresponds to RBD2 numbering and corresponding residue on RBD1 is used based on sequence alignment. A stable pair is defined to have a probability larger than 60% during the simulation times. The clusters of improved interactions in RBD2-ACE2 are marked with braces. [Reprinted under a Creative Commons Attribution License (CC BY 4.0) from Ngo, V. A. and Jha, R. K. Identifying Key Determinants and Dynamics of SARS-CoV-2/ACE2 Tight Interaction. *PLOS ONE* **2021**, 16 (11), e0257905.]

positions (see Fig. 2.25). The clusters of the important residues were consistent with the finding that residues L455, F486, and N501 of SARS-CoV-2 are perhaps the most critical residues that increase the interactions between RBD2 and ACE2 in comparison with the interactions between RBD1 and ACE2 with Y455, L486 and T501 residues on

RBD1. New residues, such as K417, Y473, and A475, which were not reported earlier but proposed to be important in others' work, emerged to be important for RBD2-ACE2 interface and enhanced the interaction compared to RBD1-ACE2 with V417 and P475 residues. Particularly, the V417K mutation created a salt-bridge with D30

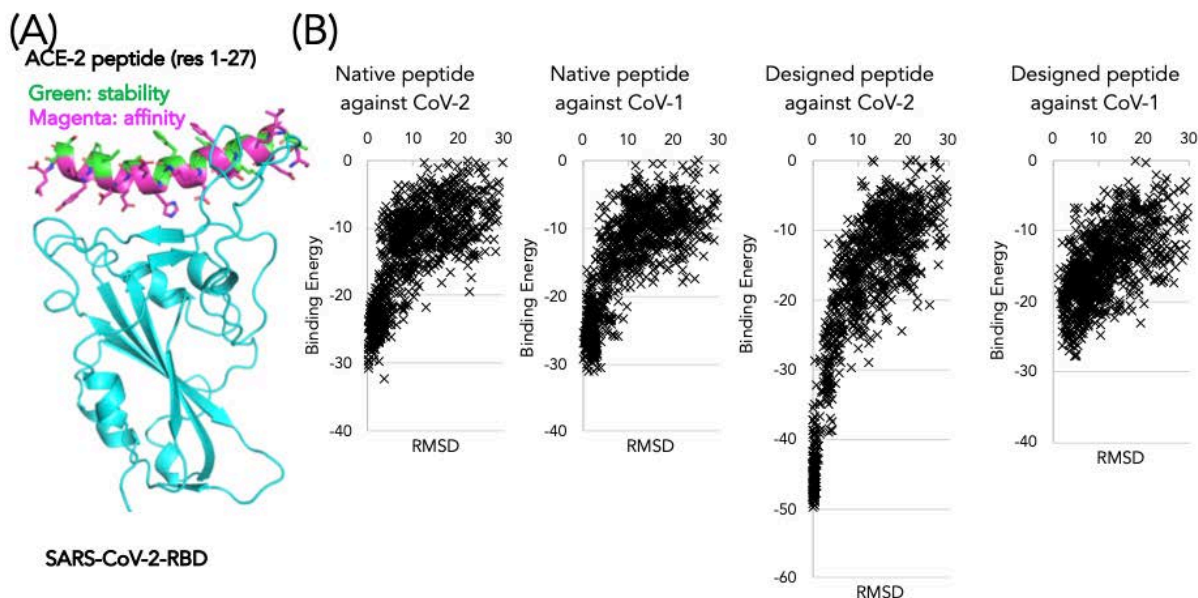


Fig. 2.26. ACE2 derived peptide redesigned for stability and binding affinity. **(A)** Truncated ACE2 showing first 27 amino acids bound to SARS-CoV-2 RBD (RBD2). The magenta surface was mutated for improved affinity and green surface for improved stability, to retain the curvature of the helix. **(B)** Docking of native and a designed peptide on RBD1 (RBD from SARS-CoV) and RBD2. Designed peptide show deeper energy funnel with RBD2. [Courtesy Los Alamos National Laboratory]

(on ACE2), thus contributing to an increase in the electrostatic interactions and compensating for coulomb energy due to mutation R439N and loss of distal R439-E329 electrostatic interaction (seen in RBD1-ACE2 interface).

Explore and Design Novel Binders for RBD

With an available crystal structure of ACE2 and RBD2, an approach was to design and test a minimal sized peptide that could bind to the RBD2 and block interaction with the ACE2 receptor. Our preliminary study using molecular dynamics simulation showed that the peptide consisting of the first 30 amino acids was unstable and would collapse or unfold. Using Rosetta, we took the first 27 amino acids (even smaller than our previously chosen sequence) and redesigned for higher affinity (magenta surface; see Fig. 2.26A, this page) and improved stability (green surface, Fig. 2.26). The redesigned peptides were then tested for binding energy funnel and showed improved

binding only for RBD2 (Fig. 2.26B). Binding affinity for RBD1 was, in fact, marginally disrupted in some of the designed peptides, hence improving the specificity of the designed peptides. Further, the peptides were also evaluated for stability using long timescale molecular dynamics simulations. The native peptide (res 1-27) showed very low stability. Contrary to that, the designed peptides showed high stability and retained helical structure (see Fig. 2.27, p. 79). A total of 66 peptides were displayed on a yeast cell surface and tested for binding to RBD2-sfGFP. While we were able to show display of the peptides on the yeast surface using c-myc tag expressed at the C-terminus of the peptide, we failed to see any binding at a low micromolar concentration range of the target RBD2-sfGFP. While it is very likely that the stability of the designed peptides improved, it is also very likely that the peptide does not preserve the right curvature/conformation to present interfacial residues to the RBD2. Further work will be needed

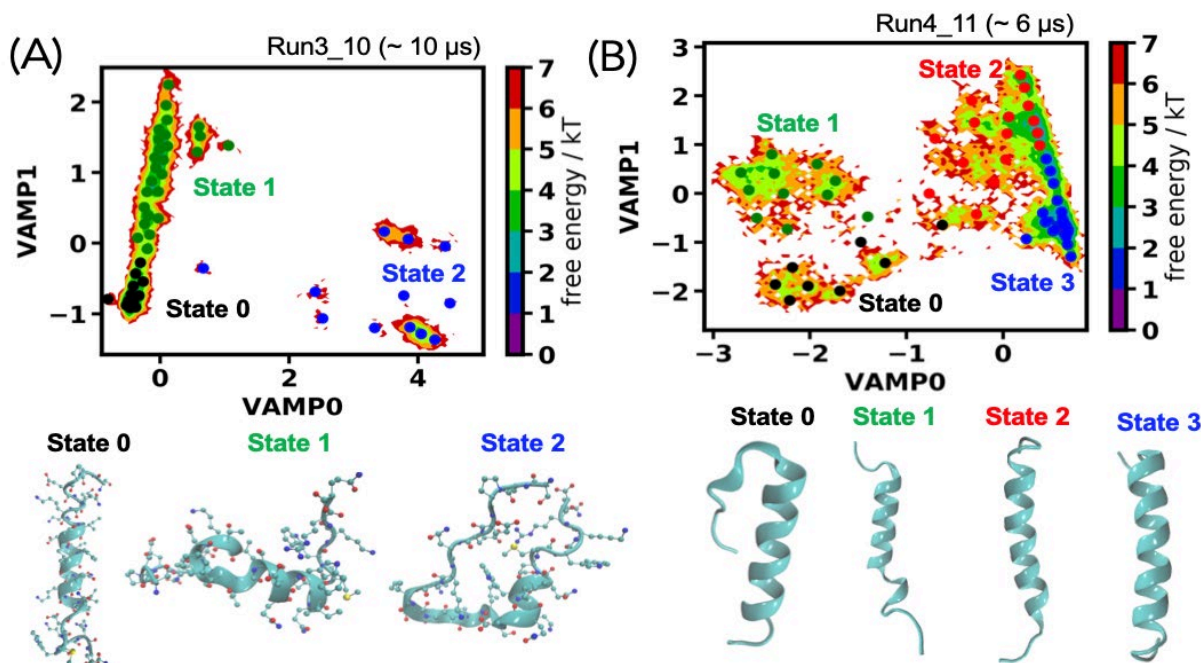


Fig. 2.27. Clustering of conformational macrostates of the simulated peptides in a transformed space obtained from variational approaches for Markovian processes (VAMP). **(A)** A designed peptide with three macrostates. **(B)** Another promising peptide with four macrostates. VAMP0 and VAMP1 of the VAMP space are principal components having the slowest timescales. A lag time=100 steps (100 ns) was used for the VAMP transformations, and the k-means clustering algorithm to distribute 100 clusters (microstates) in the transformed space to build a Markovian matrix M . A fuzzy spectral clustering, PCCA+, was applied to the matrix M to coarse-grain the 100 microstates into a few macrostates. [Courtesy Los Alamos National Laboratory]

to understand the structural perturbation in a single helical peptide, which can have a detrimental effect on the binding affinities. We also expect that use of RBD2 at higher concentrations (>20 μM) could show detectable binding affinities and would help compare the designed peptides with the native one.

2.8 Task 6: Next-Generation Rapid Testing

The next-generation testing R&D team performed research pertaining to the following two aims:

1. Developing novel methods for concentrating viruses from dilute sample matrices.
2. Developing highly sensitive and specific assays that would be suitable for rapid screening outside a laboratory setting.

2.8.1 Highlights

- ORNL developed a novel breath sampling device for noninvasive COVID-19 sampling and concentration of virus from breath.
- LLNL developed a portable reader for colorimetric RT-LAMP assays for COVID-19.
- SNL piloted freeze-drying of RT-LAMP reagents and tested methods for virus concentration from dilute samples.
- PNNL and AL worked on aptamer-based detection assays.
- LANL tested methods for developing ultrasensitive quantum dot-based immunoassays.
- ANL tested protocols for RT-LAMP detection in droplets and provided key reagents to other laboratories.

2.8.2 Interlab Collaborations

- SNL, LLNL, and SLAC collaborated on a review article on point-of-care diagnostics using LAMP, with a special focus on COVID-19 LAMP assays (Moehling et al. 2021).
- ORNL shared protocols for agarose gel matrices as a substrate for other laboratories to test detection assays.
- ANL shared reagents including anti-RBD antibodies with PNNL and SNL.
- PNNL and AL shared knowledge on aptamer-based assays.
- SNL, LLNL, and ANL shared knowledge on LAMP assays.

2.8.3 Impacts and Follow-On Work

- ORNL has filed a joint invention disclosure on the breath sampling whistle device.
- SNL's reagent stabilization work helped inform an NIH RADx-sponsored CRADA project with a small business (VIC Foundry) to develop a home-based molecular COVID-19 test.
- LLNL has received inquiries for licensing the Reveal-CoV instrument.
- ANL's Spike-RBD and antibody work continues in the National Institute of Allergy and Infectious Disease (NIAID) structural biology center (CSGID).

2.8.4 Breath Sampling Whistle (Aim 1)

ORNL's work evolved to focus on using a whistle to capture viral particles from aerosols in exhaled breath. The whistle is loaded with a hydrogel material designed to capture aerosol as a patient blows into it for a set duration and volume (see Fig. 2.28, p. 81). To date, ORNL produced hundreds of whistles using 3D printers within the Nanofabrication Research Lab and Macromolecular Nanomaterials groups at the Center for Nanophase Materials Science. Manufactured whistles were sent to the University of Tennessee Health Science Center (UTHSC) for testing with patients. Approvals from the UTHSC Institutional Review Board (IRB) are in

progress for a joint invention disclosure, as the IRB conducts on-site work to analyze the hydrogels as they are used alongside nasal swab tests.

The whistles have a tone and volume that modulate based on breathing rate, making it possible to consistently monitor duration and rate of exhalation. Loading agarose hydrogels into the bottom portion of the whistle did not negatively impact the whistle's tone or volume during operation. It was determined that a 4% agarose solution (~400 microliters) could be readily added to the bottom of the whistle and easily rinsed with buffer to remove adequate amounts of virus for analysis by PCR or sequencing. These agarose hydrogels were used in all patient testing.

Engineering and optimization of structured hydrogels was a primary focus. The ORNL team expanded beyond the basic agarose hydrogels used in the UTHSC partnership and determined how the topography, porosity, and surface chemistry of captured material could be tuned to improve capture and release of breath-generated aerosols for introduction into a lateral flow assay or another analytical platform. The material's geometry, topography, and chemistry can be tuned to optimize capture and subsequent release. Due to limits in printing resolution and stability of available formulations of hydrogels, the team determined that using a conventional 3D printing resin to print the lattice and using a hydrogel formulation as a lattice coating were the most cost effective and flexible approaches for introducing highly structured hydrogels into the whistle (see Fig. 2.29, p. 81). A laboratory system for testing the flow and capturing particles in the whistle was implemented and is being used to test aerosol capture in different designs (see Fig. 2.30, p. 81).

2.8.5 Reveal-CoV Instrument for Point-of-Care Diagnostics (Aim 2)

LLNL designed and built a rapid RT-LAMP-based molecular diagnostics platform as a potential tool to quickly diagnose COVID-19 in under one hour. This point-of-care testing approach involves an initial high temperature swab sample inactivation

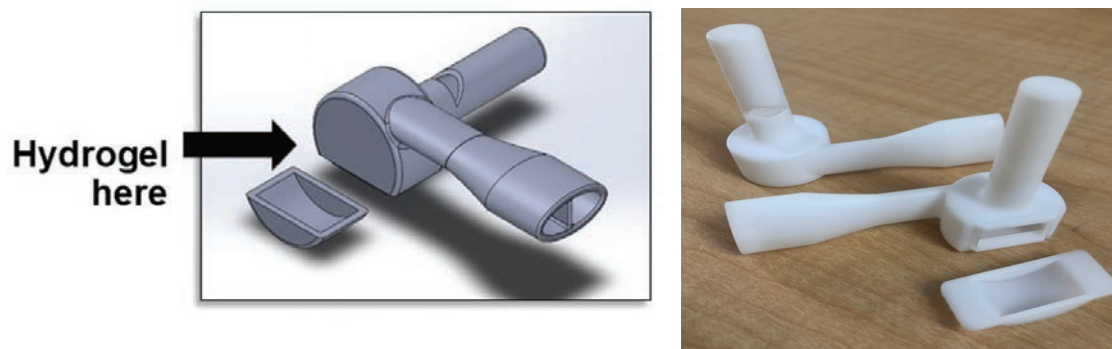


Fig. 2.28. A 3D CAD rendering of the whistle shows the location where the hydrogel is added (left). The hydrogel can be readily removed for testing. Whistles were 3D printed for testing, with modifications being made to improve ease of use and handling based on feedback during patient testing (right). [Courtesy Oak Ridge National Laboratory]

step followed by amplification of viral RNA using up to five control and pathogen-specific assays. Results are determined based on a discreet reaction color change from red to yellow but can also be determined using fluorescence detection. Testing of this prototype platform was conducted with synthetic viral RNA and dried, stabilized reagents. Buffer systems, swab selection, and assay stabilization formulations were evaluated for performance. LOD was determined using RNA; however, testing was not performed with viable SARS-CoV-2 virus or clinical samples.

Figure 2.31, p. 82, shows the prototype instrument (left) developed to inactivate a sample in the Stage 1 heater and test for viral RNA with a single, pathogen-specific assay in Stage 2. The Stage 1 heating cycle required ~12 minutes to heat from RT to 95°, maintain 95° for the required five minutes, and then cool to a safe handling temperature below 45°. Stage 2 heating is isothermal at 65° for 30 minutes and requires ~40 minutes from heat up to cool down to safe handling temperature.

A redesigned instrument concept model is shown on the right side of Fig. 2.31. The redesign incorporates a 5-tube heating block in Stage 2. This design change was pursued to allow us to incorporate additional assays into testing for improved specificity and potentially reduced LOD. Additionally, this

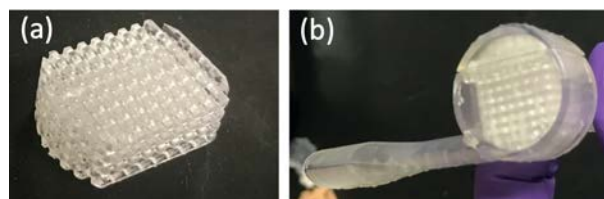


Fig. 2.29. Lattice structures of printed hydrogels and solid supports coated with hydrogels were created (a) and placed within the whistle (b). Lattices did not interfere with the operation of the whistle. Ongoing modeling and testing are in progress to determine the impacts of surface topography, chemical composition, and airflow on pathogen capture. [Courtesy Oak Ridge National Laboratory]

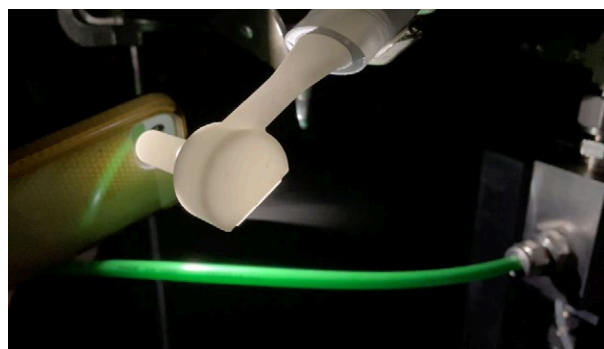


Fig. 2.30. Laboratory testing using an atomizer was initiated to visualize flow and particle capture was initiated and is still underway. Laboratory testing was performed using aqueous aerosols with colored and fluorescent dyes or particles in water. [Courtesy Oak Ridge National Laboratory]



Fig. 2.31. Reveal-CoV instrument development. First unit build of prototype single assay instrument consisting of two single-tube heaters for sample inactivation (Stage 1) and detection assay amplification (Stage 2) [left]. CAD model of five assay instrument concept consisting of a sample inactivation heater (Stage 1) and a 5-tube detection assay heater (Stage 2) [right]. [Courtesy Lawrence Livermore National Laboratory]

redesign could allow testing against other pathogens, using independent control reactions, and, potentially, incorporating fluorescence detection.

Several key test parameters were studied to demonstrate improved test sensitivity and performance. Heat lysis and viral inactivation of samples were incorporated into the testing scheme based on testing performed on a surrogate human coronavirus, NL63. A five-minute hold at 95° improved colorimetric detection ~tenfold (see Fig. 2.32, left, p. 83). Sampling swab selection is critical; the swab material must not interfere with the initial or final reaction color (see Fig. 2.32, center). Finally, the use of positive and negative controls along with three virus-specific assays provides added confidence that the testing performed as expected (see Fig. 2.32, right).

2.8.6 Stabilization of RT-LAMP Reagents (Aim 2)

SNL performed work related to Aim 1 to concentrate virus from dilute samples, although that work

is ongoing and data is not presented in this report. Pursuant to Aim 2, the goal of this work was to determine the stability of RT-LAMP reagents, lyophilized by a commercial service provider. Our goal was to provide a data set and recommendations that would be generally useful to the LAMP developer community, since reagent stabilization is critical to point-of-need assays, but is rarely described in any detail in open literature. The RT-LAMP assay was designed at SNL and consists of three primer sets: two targeting distinct genes in the SARS-CoV-2 genome and one targeting human genomic DNA (assay control). The assay incorporates SNL's patented end-point fluorescence detection mechanism called quenching of unincorporated amplification signal reporters (QUASR). This method incorporates a dye-labeled primer and a quencher-tagged probe. After the 45-minute reaction, the solution is cooled to ambient temperature, resulting in dark quenching of fluorescent primers in negative samples and highly fluorescent amplicons in positive samples. We also tracked amplification in real-time by adding an intercalating dye.



Fig. 2.32. Reveal-CoV test parameter development. A pre-amplification heat lysis/sample inactivation step improves colorimetric endpoint detection ~tenfold (left). Commercial swabs were evaluated to identify products with minimal effect on reaction color (center). A panel of five assays, including positive and negative controls and three virus-specific assays, were selected for optimal test performance (right). [Courtesy Lawrence Livermore National Laboratory]

RT-LAMP reagents were lyophilized, or freeze-dried, by our collaborator BIOLYPH and packaged with desiccant in airtight pouches. BIOLYPH used three proprietary excipients to stabilize the enzymes during the freeze-drying process. First, we tested the sensitivity of the lyophilized samples (three excipient groups for each primer set) using various concentrations of RNA and compared the results to freshly prepared reagents. After analyzing the data for all three primer sets, two excipients enabled the lyophilized samples to perform similarly to the fresh reagents. Moving forward, we only utilized samples lyophilized with these two excipients. We then evaluated the lyophilized reagents using inactivated SARS-CoV-2 virus as template and saw excellent amplification even at low concentrations of virus. Finally, we explored the performance of the lyophilized samples using inactivated virus spiked in 10% human saliva to better mimic a clinical diagnostic test. Our sample pretreatment process included chemical inactivation (using Tris(2-carboxyethyl)phosphine [TCEP] and ethylenediamine tetra-acetic acid [EDTA]) of RNases commonly found in saliva and a heating step (95°C for five minutes) to promote viral lysis.

The sensitivity with the lyophilized reagents (both excipients) coincided with the results from the fresh controls.

In the next portion of the project, we assessed the long-term stability of lyophilized RT-LAMP reagents. Lyophilized samples (two excipient groups for each primer set) were stored in airtight pouches containing desiccant at both 22°C and 45°C. After one month, the lyophilized reagents were reconstituted with RNA template and compared to freshly prepared samples. At the lower storage temperature (22°C), lyophilized reagents behaved similarly to the fresh controls (see Fig. 2.33A, p. 85). We noticed slower amplification in real-time for the lyophilized samples stored at the elevated temperature (45°C; see Fig. 2.33B) but this did not seem to affect end-point fluorescence measurements. We repeated this experiment after three months of storage. The lyophilized reagents were able to successfully detect target RNA even after extended storage at 22°C. Alternatively, lyophilized samples held at 45°C for three months showed very little amplification, even at high RNA concentrations. This indicates that there was significant loss in enzyme activity, and the lyophilized reagents cannot tolerate 45°C for more than one

month. It is worth noting that it is unlikely that lyophilized samples would experience temperatures as high as 45°C for any length of time.

2.8.7 Alternative Molecular Diagnostics and Protein Reagents (Aims 1 and 2)

During this project, the ANL team focused on developing alternative molecular diagnostic tools and providing reagents to collaborators.

Alternative RT-qPCR Protocol

The mainstream SARS-CoV-2 RT-qPCR-based diagnostic protocol uses predefined primer sets and associated TaqMan probe. The ANL team developed alternative primer sets using the nsp1 and nucleocapsid (N) genes and identified several primer sets that can be used with conventional intercalating dyes to obtain similar sensitivity and specificity to the commercial TaqMan-based method. The assay price is significantly lower, and the freedom of selecting alternative primer sets avoids restrictions that DNA oligo synthesis companies placed on sequences that were highly similar to the commercially-used probe sets. The ANL team also demonstrated the feasibility of obtaining high-quality RNA standards for the RT-qPCR assays using a plasmid template and the NEB HiScribe® T7 High Yield RNA Synthesis Kit. The ANL RNA standard was calibrated against the commercial RNA standard and used in all assay development efforts. The in-house generated RNA is <10,000 times cheaper than the commercial one.

LAMP Assay

The ANL team tested the LAMP assay with probe sets described in the literature for SARS-CoV-2 detection.¹³ Both the fluorophore and colorimetric dyes were tested for detection using the in-house RNA standard. The ideal temperature and reaction times were optimized using a BioRad CFX-384

¹³ Zhang, Y., et al. "Enhancing Colorimetric Loop-Mediated Isothermal Amplification Speed and Sensitivity with Quinidine Chloride." *BioTechniques* 69 (3), 178-185 (2020). DOI: 10.2144/btn-2020-0078

touch instrument. The optimized assay was then tested with a low-cost Mini-PCR instrument and demonstrated that the assay was able to confidently detect ~100 copies of RNA per reaction using the colorimetric substrate. The RNA was also detected from saliva when an intermediate purification process was employed. The LAMP assay was tested in microfluidic droplets. Several surfactant and fluorinated combinations were tested, which were used in the laboratory for droplet PCR, droplet assays, and other biological experiments. Unfortunately, the droplets were unstable when using the commercial LAMP reagents (New England BioLabs). The reaction optimization with lowered detergent concentrations was not pursued.

Protein Reagents

The ANL team expressed the SARS-CoV-2 Spike-RBP protein in HEK-293 cells and purified it for high homogeneity for distribution to many labs and local ANL efforts. In addition to the pure protein, biotinylated forms were also distributed for other users. The biotinylated form was used at ANL for characterization of mAbs, Fabs, and nanobodies. The team also purified and distributed the CR3022 mAbs to the NVB network.

2.8.8 Aptamer Magnetic Nanoparticle Assay (Aims 1 and 2)

PNNL's work toward developing a next generation Covid-19 test focused on using a single-stranded DNA aptamer (COV2-RBD-1C) to recognize and bind the receptor binding domain (RBD) of the SARS-CoV-2 Spike glycoprotein.

The first aim was to capture and concentrate the virus from saliva samples using magnetic nanoparticles (MNPs; see Fig. 2.34A, p. 86). PNNL made progress toward this goal by capturing RBD protein from aqueous solution. First, PNNL functionalized the surface of commercially available MNPs with aptamers using streptavidin-biotin chemistry and characterized the aptamer loading using flow cytometry to show successful co-localization of the

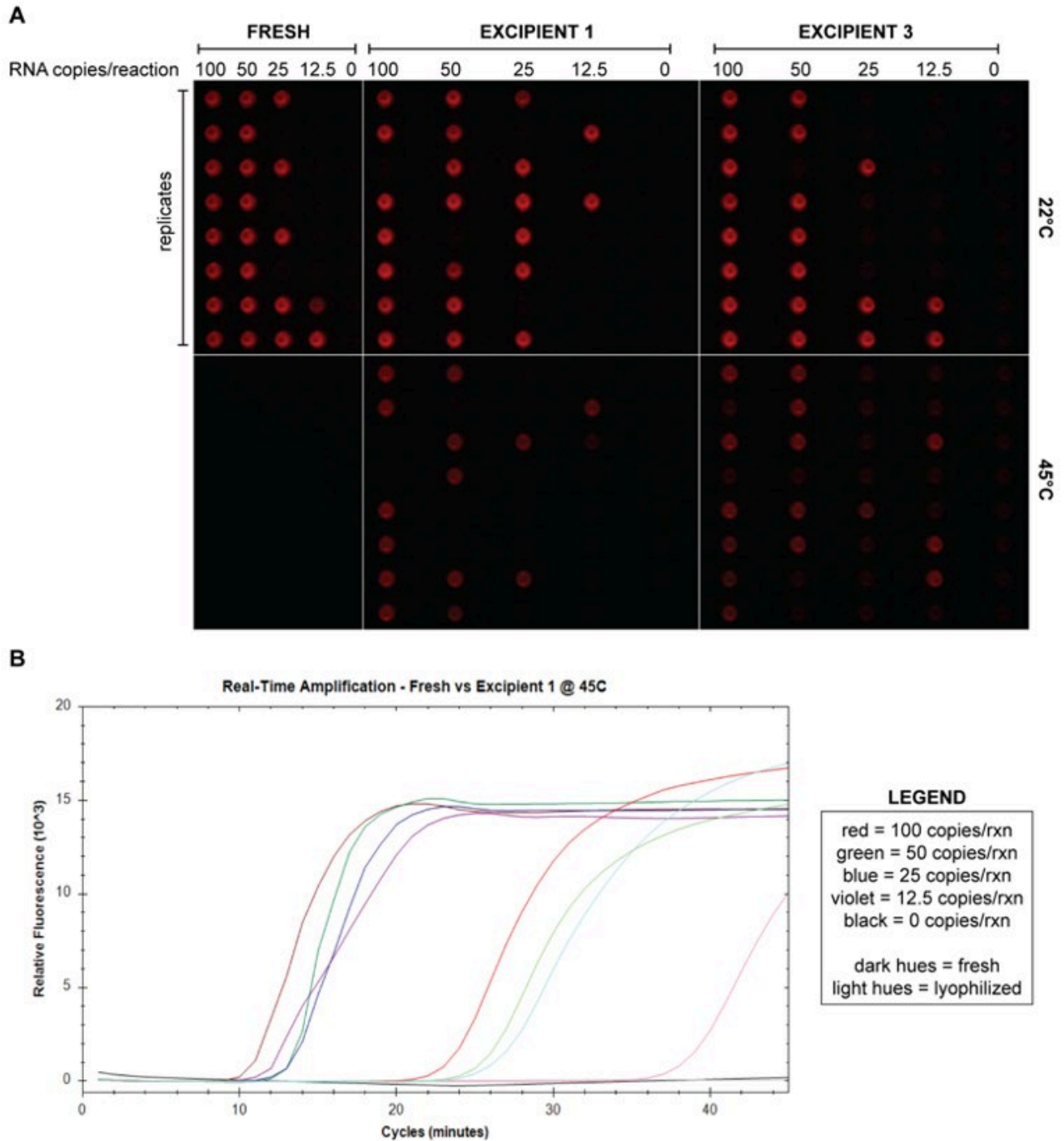


Fig. 2.33. Storage of lyophilized reagents for one month. **(A)** End-point fluorescence demonstrates that reagents lyophilized with both excipients amplify RNA template comparably to fresh controls when stored at 22°C; however, when stored at an elevated temperature (45°C), fewer of the replicates amplify. **(B)** Real-time fluorescence of representative replicates for both fresh controls and lyophilized reagents with excipient 1 stored at 45°C. There is a clear delay in time to amplify for the lyophilized reagents (light hues) when compared to the fresh controls (dark hues). [Courtesy Sandia National Laboratories]

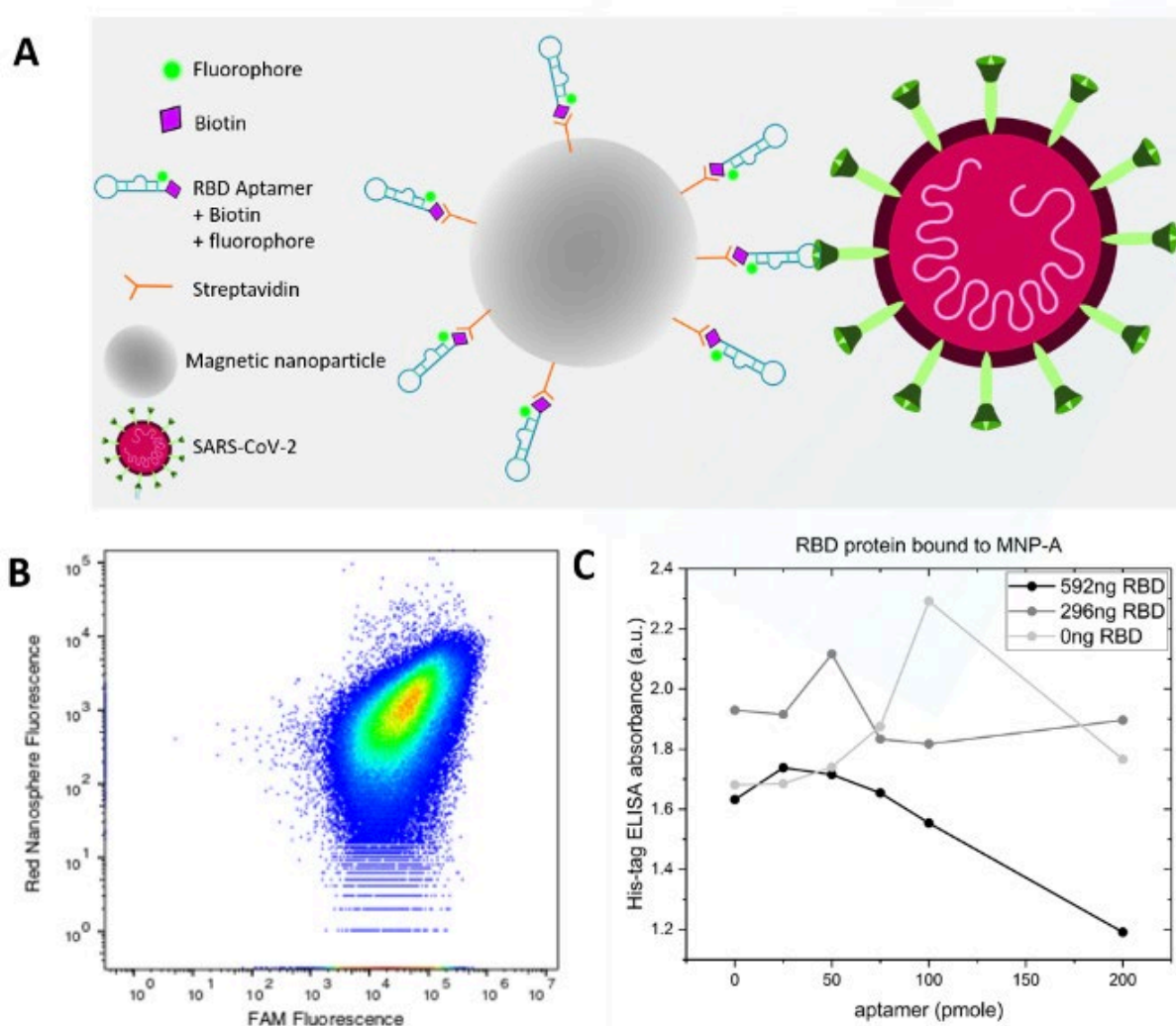


Fig. 2.34. (A) An illustration shows the mechanism behind aptamer-functionalized MNP capture of SARS-CoV-2. (B) Flow cytometry confirmed successful MNP surface functionalization with aptamer. (C) Results from his-tag ELISA show decreasing absorbance with increased aptamer loading for the highest tested concentration of RBD (592ng or 1.48 μ g/mL), suggesting RBD was captured by the MNPs. [Courtesy Sandia National Laboratories]

MNP fluorescence and the fluorophore-conjugated aptamer (see Fig. 2.34B). Next a polyhistidine-tagged RBD protein (produced and purified by Dr. Babnigg at ANL) was incubated in a solution of aptamer-functionalized MNPs. The MNPs were pulled from the solution using an externally applied magnet, redispersed in fresh buffer, and then tested for RBD protein using a his-tag competitive ELISA kit. Results from the his-tag ELISA suggest that

increasing the aptamer bound to the surface of the MNPs increases the amount of RBD detected in the assay (as indicated by a decrease in absorbance) for larger quantities of protein (592ng or 1.48 μ g/mL, Fig. 2.34C). Due to the nonlinear standard curve for RBD protein from the ELISA, an absolute quantity of RBD captured could not be determined. A micro-bicinchoninic acid test was tried as a secondary method for quantifying captured RBD, but

the streptavidin-coated MNPs interfered with this method's results.

The second aim of PNNL's work was to develop a colorimetric assay to detect SARS-CoV-2 using the COV2-RBD-1C aptamer for SARS-CoV-2 molecular recognition and gold nanoparticles (AuNPs) as a peroxidase enzyme mimic. The theory behind this assay (previously demonstrated for norovirus detection) is that, in the presence of H₂O₂, AuNPs catalyze the oxidation of a 3,3',5,5'-Tetramethylbenzidine (TMB) substrate to create a blue-colored solution. This reaction can be prevented by passivating the surface of the AuNPs with the aptamers, which cling to the gold surface via static interaction. When the SARS-CoV-2 virus is introduced, the aptamer can bind to the Spike glycoprotein RBD, and free the surface of the AuNP to catalyze the TMB oxidation (see Fig. 2.35, p. 88) PNNL optimized the peroxidase ability of citrate-capped AuNPs (see Fig. 2.35B) and achieved a 37% reduction in TMB oxidation by passivating the surface of the AuNPs with up to 200pmole of aptamer (see Fig. 2.35C). The colorimetric assay was then tested with gamma-irradiated inactive SARS-CoV-2 (BEI Resources) and the Vero E6 cell lysate control (BEI Resources).

Both virus and cell lysate samples were dialyzed to prevent salt-induced AuNP aggregation from the background cell culturing media. For non-passivated AuNPs (no aptamer), the assay's 655nm absorbance peak was not significantly different before or after the addition of cell lysate control or virus samples (see Fig. 2.35D). For passivated AuNPs (1uM aptamer) only a modest increase (5.2%) in absorbance was observed for the highest concentration of virus tested (2.8×10^5 TCID₅₀ per mL), which was not visible by eye (see Fig. 2.35E). Further optimization would be required to lower the detection limit and increase the colorimetric response; however, future work should focus on detecting active SARS-CoV-2 or pseudovirus, as it is possible that the Spike glycoprotein RBD could have been damaged in the viral inactivation process, making binding and detection by aptamer less effective.

2.8.9 Nanoporous Alumina Sensor (Aim 2)

With the purpose of developing a sensor to detect SARS-2 virions, Ames Laboratory (AL) researchers started with an available model system and, in parallel, tested the components necessary to detect SARS-2 virions. The model system was vesicular stomatitis virus (VSV) virions tagged (pseudo-typed) with the Ebola virus glycoprotein (GP1,2). An electrochemical sensor consisting of a nanoporous alumina membrane functionalized with an aptamer that recognizes GP1,2 with high affinity was tested for its ability to detect virions using ebola glycoprotein labeled VSV virions (EBVSV).

To develop the sensor, anodized alumina membranes with nominal pore-size of 20 nm were coated with gold films and thiolated aptamers were immobilized on the gold-coated alumina membranes. A thus functionalized membrane was mounted in an electrochemical cell filled with phosphate saline as electrolyte. A four-electrode configuration was used to monitor the impedance changes across the membrane during exposure to different densities of suspended virions. Two sets of experiments were performed: (1) to determine the minimum particle density detected by the sensor and (2) to determine the ability to selectively detect the targeted virion (in this case EBVSV) in the presence of other virions, with the total virion density being constant.

The first set of experiments showed that the sensor can detect densities higher than 500 virions/ml. Specificity was demonstrated because membrane impedance decreased on exposure to EBVSV virions but exposure to VSV virions produced either no-change or an increase in membrane impedance. The second set of experiments showed that with densities of 1000 virions/ml, a specific sensor response was recorded with EBVSV virions as 12% of the total. These results demonstrated that the aptamer-functionalized sensor could detect virions in the presence of higher concentrations of similar

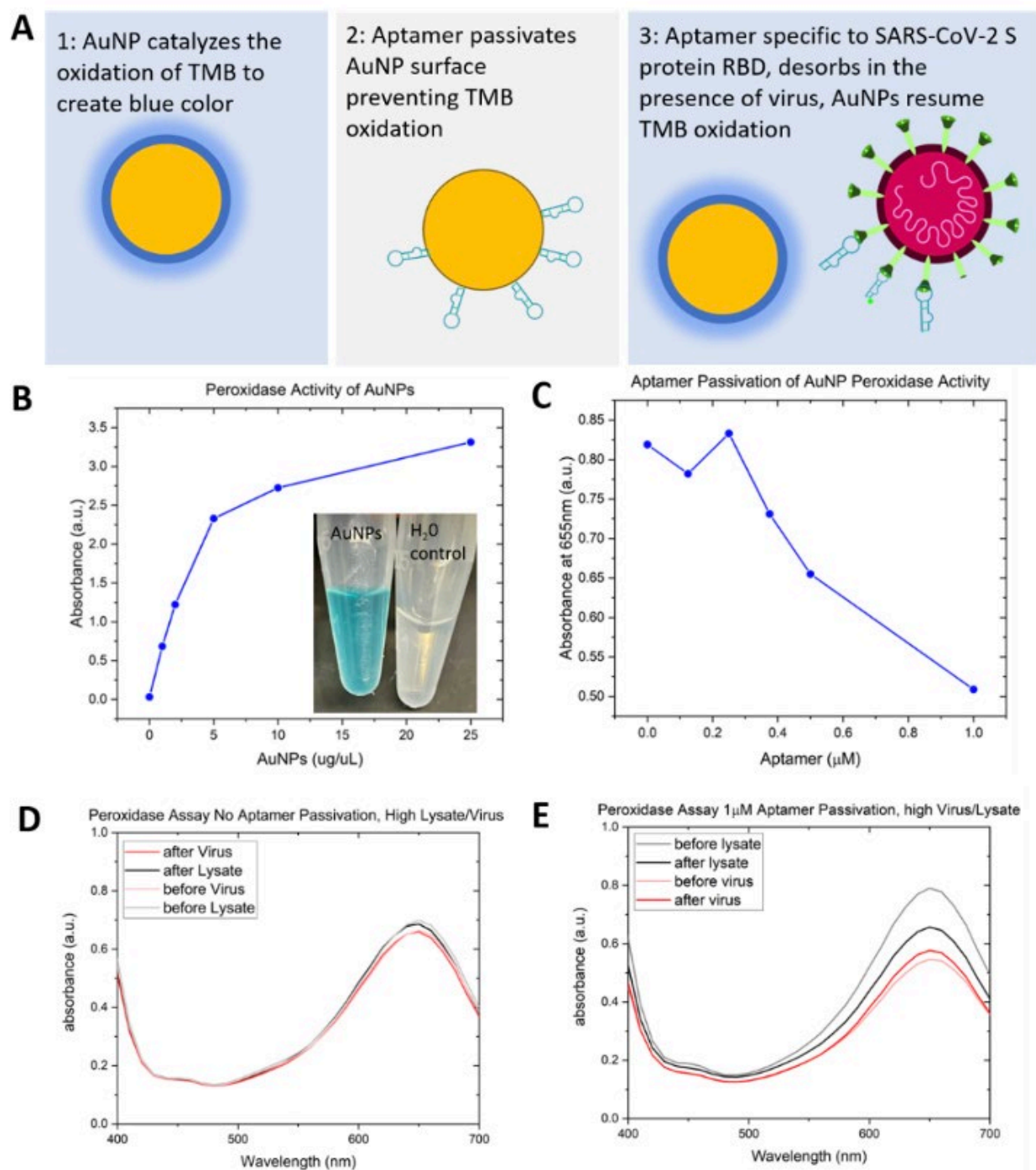


Fig. 2.35. (A) Schematic describing theory behind colorimetric detection assay. (B) Peroxidase activity of AuNPs was optimized to create a strong colorimetric response. (C) A 37% reduction in peroxidase activity was achieved by passivating the AuNP surface with aptamer. (D) No change in 655 nm absorbance was observed before or after lysate or virus addition for the zero-aptamer passivation experiment. (E) A modest 5.2% increase in 655 nm absorbance was observed after adding inactivated SARS-CoV-2 to the 1 μ M aptamer passivated assay. [Courtesy Pacific Northwest National Laboratory]

particles, but it lacked the Ebola GP1,2 protein for which the aptamer is specific.

In addition to the sensing experiments, we designed a frequency analyzer chip-based reader for continuous monitoring of membrane impedance. The chip-based reader replaces laboratory potentiostat in the sensing experiments and can reduce the sensing system cost from \$15,000 to a few hundred dollars.

In parallel with development of the sensor for detecting virions using the surrogate Ebola aptamer, we tested the affinities of aptamers

isolated to the SARS-2 receptor binding domain to bind the SARS-2 spike protein and identified one aptamer with high affinity. In preparation for testing this aptamer on the electrochemical device for its ability to recognize the SARS-2 virions, we tested various methods of purifying the virions from the large amount of contaminating membranous and other cellular materials. We have come to what appears to be the most effective separation, which involves a filtration step followed by a sucrose gradient. These conditions will be used to fractionate recently received SARS-2 virions for testing on the sensor with the identified SARS-2 aptamer.

2.9 Publications and Research Output

Publications

- Adikari, S. H.; Alipio Lyon, E. Z.; Hollander, A. D.; Deshpande, A.; Hong-Geller, E. Investigation of Pooling Strategies Using Clinical COVID-19 Samples for More Efficient Diagnostic Testing. *medRxiv* **2020**. Preprint. DOI: 10.1101/2020.08.10.20171819
- García, M.; Fares-Gusmao, R.; Lien, C.; Subramaniam, S.; Liu, S.; Dey, R.; Adikari, S. H.; Lovell, S.; Scherf, U.; Hong-Geller, E.; Wang, T.; McGivern, D.; Stenzel, T. SARS-CoV-2 Reference Panel for Molecular-Based Diagnostic Devices as an FDA Response Tool to a Public Health Emergency. **2020**. Manuscript submitted.
- Hodge, C. D.; Rosenberg, D. J.; Grob, P.; Wilamowski, M.; Joachimiak, A.; Hura, G. L.; Hammel, M. Rigid Monoclonal Antibodies Improve Detection of SARS-CoV-2 Nucleocapsid Protein. *mAbs* **2021**, *13* (1), 1905978. DOI: 10.1080/19420862.2021.1905978
- Jha, R. K.; Yankey, A.; Shabazz, K.; Naranjo, L.; Shin, S.-M.; Velappan, N.; Bradbury, A. R. M.; Strauss, C. E. M. Engineered pH-Sensitive Protein G/IgG Interaction. *ACS Chem. Biol.* **2021**, *16* (7), 1142–1146. DOI: 10.1021/acscchembio.0c00943
- Kim, Y.; Wower, J.; Maltseva, N.; Chang, C.; Jedrzejczak, R.; Wilamowski, M.; Kang, S.; Nicolaescu, V.; Randall, G.; Michalska, K.; Joachimiak, A. Tipiracil Binds to Uridine Site and Inhibits Nsp15 Endoribonuclease NendoU from SARS-CoV-2. *Commun. Biol.* **2021**, *4*, 193. DOI: 10.1038/s42003-021-01735-9 (Article in collection “Advances in SARS-CoV-2 Biology”).
- Kneller, D. W.; Galanie, S.; Phillips, G.; O’Neill, H. M.; Coates, L.; Kovalevsky, A. Malleability of the SARS-CoV-2 3CL Mpro Active-Site Cavity Facilitates Binding of Clinical Antivirals. *Structure* **2020**, *28* (12), 1313-1320.e3. DOI: 10.1016/j.str.2020.10.007
- Kneller, D. W.; Phillips, G.; Kovalevsky, A.; Coates, L. Room-Temperature Neutron and X-ray Data Collection of 3CL M(pro) from SARS-CoV-2. *Acta Crystallogr., Sect. F: Struct. Biol. Commun.* **2020**, *76* (Pt. 10), 483–487. DOI: 10.1107/S2053230X20011814
- Kneller, D. W.; Phillips, G.; O’Neill, H. M.; Tan, K.; Joachimiak, A.; Coates, L.; Kovalevsky, A. Room-Temperature X-ray Crystallography Reveals the Oxidation and Reactivity of Cysteine Residues in SARS-CoV-2 3CL M(pro): Insights into Enzyme Mechanism and Drug Design. *IUCrJ* **2020**, *7* (Pt. 6), 1028–1035. DOI: 10.1107/S2052252520012634
- Kneller, D. W.; Phillips, G.; Weiss, K. L.; Pant, S.; Zhang, Q.; O’Neill, H. M.; Coates, L.; Kovalevsky, A. Unusual Zwitterionic Catalytic Site of SARS-CoV-2 Main Protease Revealed by Neutron Crystallography. *J. Biol. Chem.* **2020**, *295* (50), 17365–17373. DOI: 10.1074/jbc.AC120.016154
- Li, P.-E.; Myers y Gutiérrez, A.; Davenport, K.; Flynn, M.; Chien-Chi Lo, B.-H.; Player Jackson, E.; Shakya, M.; Xu, Y.; Gans, J. D.; Chain, P. S. G. A Public Website for the Automated Assessment and Validation of SARS-CoV-2 Diagnostic PCR Assays. *Bioinformatics* **2021**, *37* (7), 1024–1025. DOI: 10.1093/bioinformatics/btaa710
- Moehling, T. J.; Choi, G.; Dugan, L. C.; Salit, M.; Meagher, R. J. LAMP Diagnostics at the Point-of-Care: Emerging Trends and Perspectives for the Developer Community. *Expert Rev. of Mol. Diagn.* **2021**, *21* (1), 43-61. DOI: 10.1080/14737159.2021.1873769
- Ngo, V. A.; Jha, R. K. Identifying Key Determinants and Dynamics of SARS-CoV-2/ACE2 Tight Interaction. *PLoS One* **2021**, *16* (11), e0259705. DOI: 10.1371/journal.pone.0259705
- Nguyen, K.; Chakraborty, S.; Mansbach, R. A.; Korber, B.; Gnana-karan, S. Exploring the Role of Glycans in the Interaction of SARS-CoV-2 RBD and Human Receptor ACE2. *Viruses* **2021**, *13* (5), 927. DOI: 10.3390/v13050927
- Omberg, K.; Engelmann, H.; Hutchison, J.; Melville, A.; Oxford, K.; Victry, K. Evaluation of Three Extraction Kits with a 2019-n-CoV Assay, PNNL-3008. **2020**. DOI: 10.2172/1833861
- Osipiuk, J.; Azizi, S.-A.; Dvorkin, S.; Endres, M.; Jedrzejczak, R.; Jones, K. A.; Kang, S.; Kathayat, R. S.; Kim, Y.; Lisnyak, V. G.; Maki, S. L.; Nicolaescu, V.; Taylor, C. A.; Tesar, C.; Zhang, Y.-A.; Zhou, Z.; Randall, G.; Michalska, K.; Snyder, S. A.; Dickin-son, B. C.; Joachimiak, A. Structure of Papain-Like Protease from SARS-CoV-2 and Its Complexes with Non-Covalent Inhibitors. *Nat. Commun.* **2021**, *12* (1), 743. DOI: 10.1038/s41467-021-21060-3
- Velappan, N., et al. Healthy Humans Can be a Source of Antibodies Countering COVID-19. *Bioengineered* **2022**, *13* (5), 12598–12624. DOI: 10.1080/21655979.2022.2076390
- Wilamowski, M.; Hammel, M.; Leite, W.; Zhang, Q.; Kim, Y.; Weiss, K. L.; Jedrzejczak, R.; Rosenberg, D. J.; Fan, Y.; Wower, J.; Bierma, J. C.; Sarker, A. H.; Tsutakawa, S. E.; Pingali, S. V.; O’Neill, H. M.; Joachimiak, A.; Hura, G. L. Transient and Stabilized Complexes of Nsp7, Nsp8, and Nsp12 in SARS-CoV-2 Replication. *Biophys. J.* **2021**, *120* (15), 3152–3165. DOI: 10.1016/j.bpj.2021.06.006
- Wilamowski, M.; Sherrell, D. A.; Minasov, G.; Kim, Y.; Shuvalova, L.; Lavens, A.; Chard, R.; Maltseva, N.; Jedrzejczak, R.; Rosas-Lemus, M.; Saint, N.; Foster, I. T.; Michalska, K.; Satchell, K. J. F.; Joachimiak, A. 2'-O Methylation of RNA Cap in SARS-CoV-2 Captured by Serial Crystallography. *Proc. Natl. Acad. Sci. U. S. A.* **2021**, *118* (21), e2100170118. DOI: 10.1073/pnas.2100170118
- Wilson, J. W.; Bilbao, A.; Wang, J.; Liao, Y.-C.; Velickovic, D.; Wojcik, R.; Passamonti, M.; Zhao, R.; Gargano, A. F. G.; Gerbasi, V. R.; Pasa-Tolić, L.; Baker, S. E.; Zhou, M. Online Hydrophilic Interaction Chromatography (HILIC) Enhanced Top-Down Mass Spectrometry Characterization of the SARS-CoV-2 Spike Receptor-Binding Domain. *Anal. Chem.* **2022**, *94* (15), 5909–5917. DOI: 10.1021/acs.analchem.2c00139

Presentations

- COVID-19 Diagnostic and Next Generation Lab Testing. Sequencing, Finishing and Analysis to the Future (SFAF) 15th Annual Virtual Conference, December 1–3, 2020.

COVID-19 Diagnostic and Next Generation Lab Testing. Director's Colloquium, Los Alamos National Laboratory, November 2020.

Hura, G. Diagnostics and Therapeutic Efforts of Task 5. Molecular Biophysics and Integrated Bioimaging (MBIB) Seminar Series, Lawrence Berkeley National Laboratory, December 2020.

Hura, G. Structural Studies of the SARS-CoV-2 RNA Transcription Complex. COVID-19 Seminar Series, Lawrence Berkeley National Laboratory, March 2021.

Joachimciak, A. Task 5 NVBL Presentation. Structure-Based Protein Design for Diagnostics, June 30, 2020.

Joachimciak, A. Crystallography of SARS-CoV-2 Non-structural Proteins. American Crystallographic Association (ACA) Annual Virtual Meeting, August 2–7, 2020. *Acta Cryst.* **2020**, A76 (a217). DOI: 10.1107/S0108767320097858

Joachimciak, A. COVID-19 Research Update. Biological and Environmental Research Advisory Committee (BERAC) Fall Remote Access Meeting, October 22–23, 2020. science.osti.gov/-/media/ber/berac/pdf/202010/Joachimciak_BERAC_202010.pdf (accessed 24 March 2022).

Joachimciak, A. Structural Studies of SARS-CoV-2 Proteins and Their Complexes. Florida Institute of Technology, October 29, 2020.

Joachimciak, A. Structural Studies of SARS-CoV-2 Proteins and Their Complexes. Rensselaer Polytechnic Institute, November 20, 2020.

Joachimciak, A. Structural Studies of SARS-CoV-2 Proteins and their Complexes. SARS-CoV-2 Weekly Investigators Meeting, National Institutes of Health (NIH) National Institute of Allergy and Infectious Diseases (NIAID), November 10, 2020.

Joachimciak, A. Progress in Structural Characterization of SARS-CoV-2 Proteins. Critical Assessment of Techniques for Protein Structure Prediction (CASP) 14, Annual Virtual Meeting, November 30–December 4, 2020. *Proteins: Structure, Function, and Bioinformatics* **2021**, 89 (12), 1647-1672. <https://onlinelibrary.wiley.com/toc/10970134/2021/89/12> (accessed 24 March 2022).

Patents and Invention Disclosures

Non-provisional patent filed 15639: Highly Effective SARS-CoV-2 Neutralizing Humanized Nanobodies.

Provisional patent for entire suite of 18 antibodies. EIDR S133918.

Joint invention disclosure submitted for COVID Whistle.

2S. Task 2 Supplementary Information and Graphics

B04
 SYVLTQPPSVSVAPGKARITCGGNNIGIRSVHWHYQKPGQAPVLVIYDSDRPSGIPERFSGSKSGNTATLTISRVEAGDEADYYCQVWDSDDHPVFGGDKLTVL
 LSGGGTITSYNYVYTKLSSSGTQVQLVESGAEVKKPGASVKVCKASGFTFTRYYMHVWRQAPGGQLEWMMIINPSSGTTSYAQKFGQGRVTMTDTRTSTSTVYMELS
 SLRSEDATVYYCAR**SFGELTSFDY**WGGGLTVTVSS

B10
 OSVVTQPPSVSAGPQRTVITISCTGSSSNIGSRVNYWYQQLPGTAPKLLIYANNORPSGVPDRFSGSKSGTASLAISGLQSEDEADYYCAAWDDSLNGYVFGTGK
 LTVLSSGGTITSYNYVYTKLSSSGTQVQLVESGAEVKKPGASVKVCKASGFTFSSYAIWWRQAPGGQLEWMMIINPSSGTTSYAQKFGQGRVTMTDTRTSTSTVYMELS
 LHLNPTVPEDTAVYYCAR**GRSYAFD**IWGGGTMVTVSS

D04
 SYVLTQPPSVSVAPGKARITCGGNNIGWKSVMHWHYQKPGQAPVLVYDNDORPSGVPDRFSGSKSGNTATLTISRVEAGDEADYYCQVWDSDDHVLFGGDKLTVL
 LTVLSSGGTITSYNYVYTKLSSSGTQVQLVESGAEVKKPGASVKVCKASGFTFSSYAIWWRQAPGGQLEWMMIINPSSGTTSYAQKFGQGRVTMTDTRTSTSTVYMELS
 SLRSEDATVYYCAR**ASGRWLQF**WHYGYMDVWGGGTTVTVSS

D07
 SYELTQPPSVSVAPGETARITCGGNNIGTKGVHWHYQKPGQAPVLVYDSDRPSGIPERFSGSNAGNTATLTISRVEAGDEADYYCQVWDSRSDQYVFGTRTKLTVL
 LSGGGTITSYNYVYTKLSSSGAQVTLKESGVLVLPKPTETLTLCTVSGFSLNARMGVSWIRQPPGKALEWLAHIFSNGEKSYSTSLKRLTISKDTSKQVLLTMT
 NMDPVDATVYYCAR**LDYDSSGYLVGGAFD**IWGGGTMVTVSS

D10
 OSVVTQPPSVSAGPQRTVITISCTGSSSNIGGNPNVNYWYQQLPGTAPKLLIYANNORPSGVPDRFSGSKSGISASLAISGLQSEDEADYYCAAWDDSLNGVIFGGDKLTVL
 LSGGGTITSYNYVYTKLSSSGTQVQLVESGAEVKKPGESLKISCKSGSYSTFYWGWWRQMPGKLEWMMIIPGSDTRVYSPFQGVQVITISADKISSTAYLQW
 SSLKASDAMYYCAR**HRSGSYSGAFD**IWGGGTMVTVSS

D11
 SYELTQPPSVSVAPGQARITCGGNNIGSKSVHWHYQKPGQAPVLVYDSDRPSGIPERFSGSNAGNTATLTISRVEAGDEADYYCQAWDSSTAYVFGSGTKLTVL
 LSGGGTITSYNYVYTKLSSSGTQVQLVESGGLVQPGSLRLSCAASGFTFSNYAMSWWRQAPGKLEWVSAISGGGATFHADSVKGRFTISRDNKNTLYLQMN
 SLRAEDTAVYYCAR**RVGYDSSGYWSDAFD**IWGGGTMVTVSS

E01
 SYELTQPPSVSVAPGETARITCGGNNIGRRVHWHYQKPGQAPVLVYDSDRPSGIPDRFSGSNAGNTATLTISRVEAGDEADYYCQVWSSNDPHVFGTGKTLTVL
 LSGGGTITSYNYVYTKLSSSGTQVQLQWGAAGLLKPKSETLSLCKAVYGGSFSGYIYWGWRQSPGKLEWMMIINRSGGNTNYPFLSKSRVITISVDTSKQFSLKLS
 VTAADTAVYYCAR**GGARYYGGSGYRSTPRPYFD**IWGGGTLTVTVSS

E08
 SYVLTQPPSVSVAPGKARITCGGNNIGWKSVMHWHYQKPGQAPVLVYDSDRPSGIPERFSGSNAGNTATLTISRVEAGDEADYYCQVWDSDDLVVFGGDKLTVL
 LTVLSSGGTITSYNYVYTKLSSSGTQVQLVESGAEVKKPGASVKVCKASGFTFSSYAIWWRQAPGGQLEWMMIINPSSGTTSYAQKFGQGRVTMTDTRTSTSTVYMELS
 LRSEDATVYYCAR**ASGRWLQFVHYGYMDV**WGGGTTVTVSS

F07
 SYVLTQPPSVSVAPGQARITCGGNNIGSKSVHWHYQKPGQAPVLVYDSDRPSGIPERFSGSNAGNTATLTISRVEAGDEADYYCQVWDSVVHYVFGTGKTLTVL
 LSGGGTITSYNYVYTKLSSSGTQVQLVESGAEVKKPGASVKVCKASGFTFSGYIYWGWRQAPGGQLEWMMIINPSSGTTSYAQKFGQGRVTMTDTRTSTSTVYMEL
 SSLRSEDATVYYCAR**RVGASDAFD**IWGGGTMVTVSS

G07
 OSVLIQPPSVSAGTPGQRTVITISCTGSSSNIFGNSVNYWYQQRPGTAPKLLIYANNORPSGVPDRFSGSKSGTASLAISGLQSEDEADYYCASWDDSLNAFVFGPGTK
 LTVLSSGGTITSYNYVYTKLSSSGTQVQLVESGAEVKKPGESLKISCKSGSYSTFYWGWWRQMPGKLEWMMIIPGSDIRYSPFQGVQVITISADKISFSSAYLQ
 WSSLKASDAMYYCAR**LATGAFD**IWGGGTTVTVSS

H01
 QPGLTQPPSVSLAPGQARITCGGNNIGSKSVHWHYQKPGQAPVLVYDSDRPSGIPERFSGSNAGNTATLTISRVEAGDEADYYCQVWDSRSDQYVFGTRTKLTVL
 LSGGGTITSYNYVYTKLSSSGAQVTLKESGVLVLPKPTETLTLCTVSGFSLNARMGVSWIRQPPGKALEWLAHIFSNGEKSYSTSLKRLTISKDTSKQVLLTMTN
 MDPVDATVYYCAR**LDYDSSGYLVGGAFD**IWGGGTMVTVSS

H02
 OSVVTQPPSVSAAAPGQKVTITISCTGSSSNIGNNYVNYWYQQLPGTAPKLLIYANNORPSGVPDRFSGSKSGTASLAISGLRSEDEADYYCATWDDKSLGVPVFGGDKTVL
 LTVLSSGGTITSYNYVYTKLSSSGTQVQLQSGPGLVKPQSLTLCTCAISGDSVSSNAAWWRQAPGGQLEWMMIINPSSGTTSYAQKFGQGRVTMTDTRTSTSTVYMELS
 QLNSTVPEDTAVYYCAR**QDNNPYGLD**VWGGGTTVTVSS

H03
 SYELTQPPSVSVAPGQARITCGGNNIGSKSVHWHYQKPGQAPVLVYDSDRPSGIPERFSGSNAGNTATLTISRVEAGDEADYYCQVWDSSSALYVFGTRTKVTVL
 LSGGGTITSYNYVYTKLSSSGTQVQLVESGGLVQPGSLRLSCAASGFTFDYAMHWRQAPGKLEWVSGIWSNNGSADSVKGRFTISRDNKNTLYLQMN
 SLRAEDTAVYYCAR**ELVGTTSPTDAFD**IWGGGTMVTVSS

H05
 SYVLTQPPSVSVAPGQARITCGANNIGRISVHWHYQKPGQAPVLVYDSDRPSGIPERFSGSNAGNTATLTISRVEAGDEADYYCQVWDSYSDHVFVFGGDKLTVL
 LSGGGTITSYNYVYTKLSSSGTQVQLVESGAEVKKPGASVKVCKASGFTFSSYAIWWRQAPGGQLEWMMIINPSSGTTSYAQKFGQGRVTMTDTRTSTSTVYMELS
 RSEDATVYYCAR**SIFGVIIHADGYGYMDV**WGGGTTVTVSS

R04
 EIVMTQSPSSLSASVGDRTVITICQASQDISNYLWYQKPGKAPKLLIYDANLETVGVPDRFSGSGSGTFTTISLQPEDATYYCQSYSTPYTFGGTKVDEIKS
 GGGTITSYNYVYTKLSSSGAQVQLQSGPGLVKSSQTLTLCTCAISGDSVSSNGAAWWRQAPGGQLEWMMIINPSSGTTSYAQKFGQGRVTMTDTRTSTSTVYMELR
 NSVTPEDTAVYYCAR**EGGGGRMDV**WSQGTTVTVSS

R09
 QPGLTQPPSVSVAPGQASITCSDGKLGKYYSVWHYQKPGQAPVLVYEDTKRPSGIPKRFSGSNAGNTATLTISRVEAGDEADYYCQAWDSVVFGGDKLTVL
 LSGGGTITSYNYVYTKLSSSGTQVQLVESGAEVKKPGASVKVCKASGFTFSSYAIWWRQAPGGQLEWMMIINPSSGTTSYAQKFGQGRVTMTDTRTSTSTVYMELR
 LRSDTAVYYCAR**MELRPPFD**IWGGGTLTVTVSS

R26
 SYELTQPPSVSVAPGQATITCGGKNIESKSVHWHYQKPGQAPVLVSDDDTRASGIPERFSGSNAGNTATLTISRVEAGDEADYYCQVWDSDDHYVFGPGTKLTVL
 LSGGGTITSYNYVYTKLSSSGTQVQLVESGGVQPGSLRLSCAASGFTFSSYAMHWRQAPGGQLEWVAVISYDGSNKYADSVKGRFTISRDNKNTLYLQMN
 NSLRGEDTAVYYCAR**ELSYDSSGYLRGDVYFDL**WGRGTLTVTVSS

S01
 EIVMTQSPSSLSASVGDVITICQASQDISNYLWYQKPGKAPKLLIYDANLETVGVPDRFSGSGSGTFTTISLQPEDATYYCQYDNPFTYFGPGTKVDIKS
 GGGTITSYNYVYTKLSSSGAQVQLVESGGVQPGSLRLSCAASGFTVGSNYMSWWRQAPGGQLEWVSVYSGGTTAYADSVKGRFTISRDNKNTLYLQMNLSRA
 EDTAVYYCAR**GSSGAWYFDL**WGRGTLTVTVSS

Fig. 2S.1. Sequences of unique antibodies derived from all selections. Single chain antibodies (scFvs) B04 through H05 were obtained by competitive selections using chemically biotinylated RBD2 as a target. scFvs R04 through S01 were obtained by non-competitive selections using AviTagged-biotinylated RBD2 as a target. The three complementarity-determining regions (CDRL1, 2, and 3) in each scFv's variable light regions (VL) are indicated in red; the linker between the VL and the scFv's variable heavy portion (VH) is indicated in gray; the CDRH1, 2, and 3 are indicated in green. The sequences differ the most in the CDRH3 regions. Sequences obtained from competitive selections (B04 through H05) are more similar to each other than sequences obtained from non-competitive selection (R04 through S01). [Courtesy Los Alamos National Laboratory]

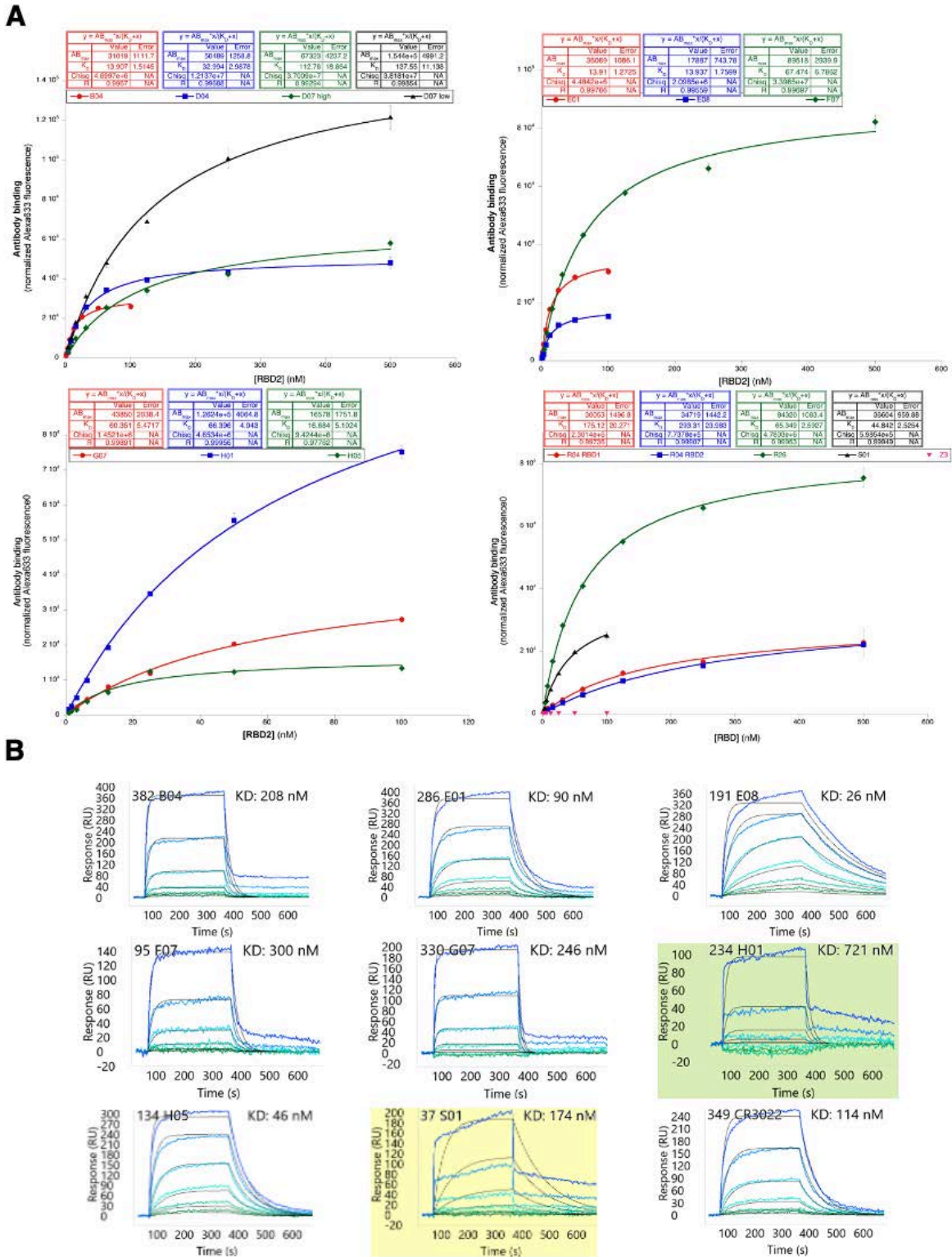


Fig. 2S.2. Kinetic data. **(A)** Graphs from flow cytometry-based kinetic measurements of yeast-displayed single chain antibodies (scFv). The upper two graphs are kinetics of RBD2 binding. The lower graph contains kinetics of scFv R01 binding to RBD1 and kinetics of scFv F07 binding to RBD2 at two different yeast densities. The minimal K_D differences of measured in these two conditions shows that yeast density does not affect kinetic measurements. **(B)** Representative sensograms from surface plasmon resonance (SPR)-based kinetic measurements. [Courtesy Los Alamos National Laboratory]

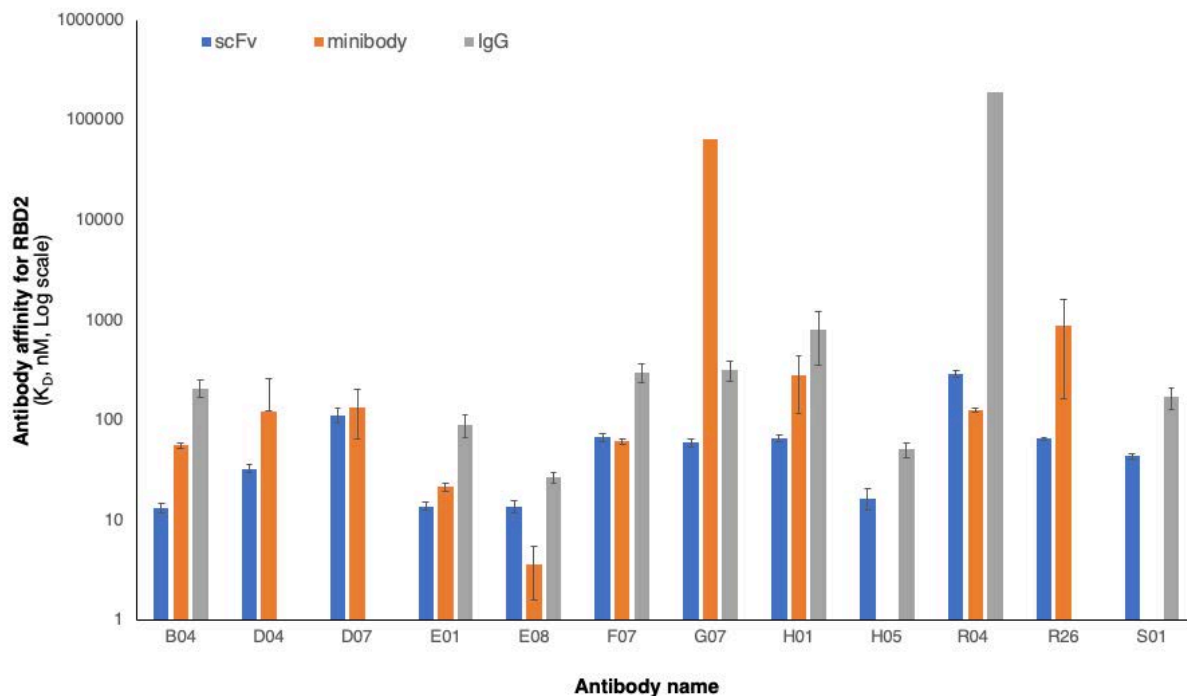


Fig. 2S.3. Affinity variations depending on antibody format. Affinities of antibodies for SARS-CoV-2 spike protein's receptor-binding domain (RBD2) are reported as dissociation constants (KD, lower KD → higher affinity) for: (1) single chain (scFv, blue bars); (2) minibody (orange bars); or (3) igG (grey bars) format. For affinity measurements repeated multiple time, K_D averages and corresponding standard deviations are reported. [Courtesy Los Alamos National Laboratory]

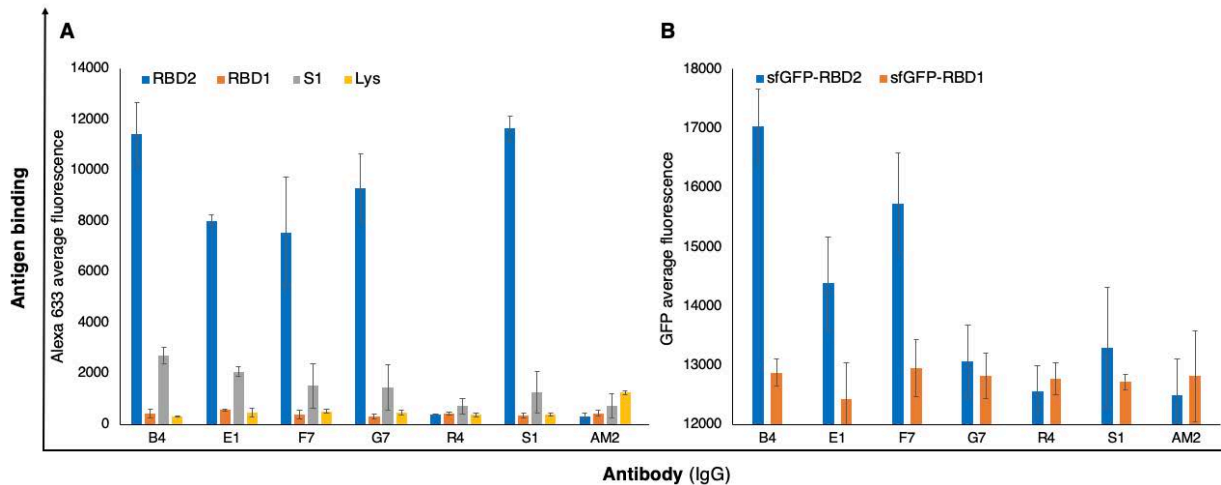


Fig. 2S.4. Specificity of IgG interactions. IgGs were immobilized on plastic and tested for recognition of either **(A)** chemically biotinylated SARS-CoV-2 RBD (RBD2, blue bars) and SARS-CoV RBD (RBD1, orange bars) and AviTag-biotinylated SARS-CoV-2 spike subunit 1 (S1, grey bars), subsequently stained with streptavidin-Alexa 633), or **(B)** super folded GFP-RBD2 (RBD2, blue bars) and super folded GFP-RBD2 (RBD2 orange bars) chimeras. Antigen Y pestis F1V (F1V) and anti-F1 antibody aF1Ig Am2 (AM2) were used as negative controls. Average or three measurements plus standard deviations (error bars) are reported. [Courtesy Los Alamos National Laboratory]

Table 2S.1. Affinity of All Selected Antibodies

| | Antibody Name | Affinity for RBD2 (kD, nM) ^a | | |
|----------------------------|---------------|---|------------------|------------------|
| | | scFv | Minibody | IgG |
| Competitive Selections | B04 | 13.9 ± 1.5 | 56.8 ± 3.5 | 99.0 ± 35.6 |
| | B10 | N/D ^f | 343.5 ± 99.7 | N/A ^c |
| | D04 | 33.0 ± 3.0 | 123.5 ± 139.3 | N/A ^c |
| | D07 | 112.8 ± 18.9 | 134.5 ± 68.6 | N/A ^c |
| | D10 | N/D ^b | N/D ^b | N/A ^c |
| | D11 | N/D ^b | 798.5 ± 567.8 | N/A ^c |
| | E01 | 13.9 ± 1.3 | 21.5 ± 2.12 | 48.3 ± 7.4 |
| | E08 | 13.9 ± 1.8 | 3.6 ± 2.0 | N/D ^b |
| | F07 | 67.5 ± 6.8 | 61.5 ± 3.5 | 151.8 ± 30.5 |
| | G07 | 60.3 ± 5.5 | 63900 | 1966.7 ± 503.3 |
| | H01 | 66.4 ± 5.1 | 281.0 ± 162.6 | N/D ^b |
| | H02 | N/D ^b | 15.5 ± 7.8 | N/A ^c |
| | H03 | N/D ^b | 117.0 ± 52.3 | N/A ^c |
| | H05 | 16.7 ± 4.0 | N/D ^b | N/D ^b |
| Non-competitive Selections | R04 (RBD2) | 293.3 ± 24.0 | 127.5 ± 7 0.0 | 190000 |
| | R04 (RBD1) | 175.1 ± 20.3 | N/D ^b | N/A ^c |
| | R09 | N/D ^b | 539.0 ± 223.4 | N/A ^c |
| | R26 | 65.3 ± 2.6 | 887.5 ± 724.78 | N/A ^c |
| | S01 | 44.1 ± 2.5 | 227000 | 293.0 ± 74.3 |

^a Determined either by flow cytometry (scFvs) or by surface plasmon resonance, SPR (minibodies or IgGs)

^b Not Determined

^c Not available in IgG format

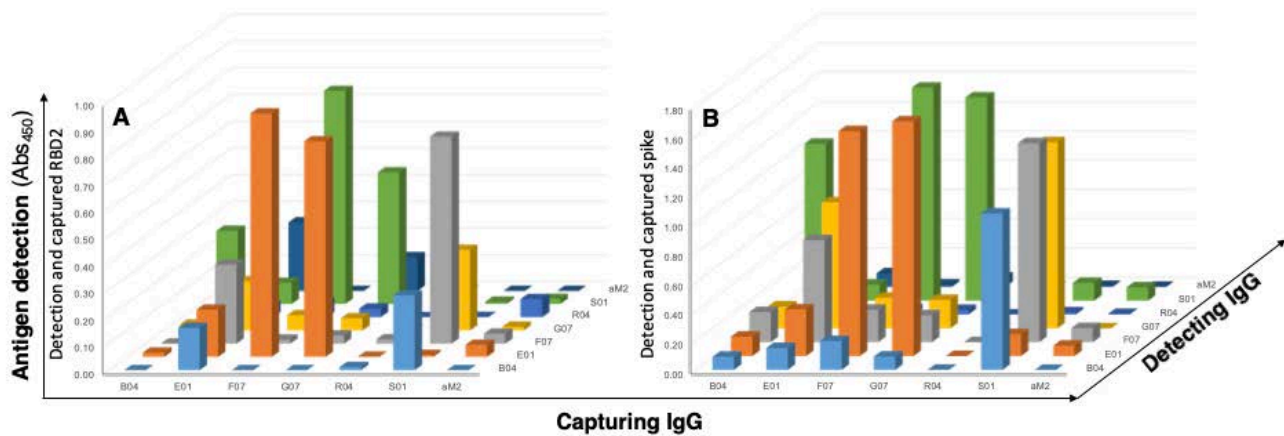


Fig. 2S.5. Epitope binning by sandwich ELISA. Identification of antibody pairs (capturing and detecting IgG) capable of binding to distinct regions (epitopes) of SARS-CoV-2 spike protein receptor binding domain (RBD2, **A**) and SARS-CoV-2 whole spike protein (**B**). Plastic bound capturing IgG (x axis) immobilize the antigen, and HRP-conjugated detecting IgG (z axis) reports the captured antigen. Anti-influenza M2 antigen (aM2) antibody was used as a negative control IgG. Signals above aM2-mediated antigen detection (noise) reveal antibody pairs noncompetitively binding to the antigen. [Courtesy Los Alamos National Laboratory]

CHAPTER 3

Epidemiological Modeling

| | |
|--|------------|
| 3.1 Project Overview | 98 |
| 3.2 Task 1: Near-Real-Time Situational Awareness | 98 |
| 3.2.1 Data Curation | 98 |
| 3.2.2 Curve Analytics | 99 |
| 3.2.3 Mobility and Community Detection | 102 |
| 3.3 Task 2: Predictive Analytics | 105 |
| 3.3.1 Statistical Modeling | 107 |
| 3.3.2 Multiscale Agent-Based Modeling | 111 |
| 3.3.3 Systems-Level Modeling of Economics and Public Health Response Strategies | 114 |
| 3.4 Task 3: COVID-19 Pandemic Modeling and Analysis Platform Development | 121 |
| 3.4.1 Architecture | 123 |
| 3.4.2 Roles and Credentials | 126 |
| 3.4.3 Release Plan | 126 |
| 3.4.4 Hotspot Detection | 126 |
| 3.4.5 DOE COVID-19 Situational Awareness Dashboard | 128 |
| 3.4.6 National, State, and County Report Cards | 129 |
| 3.5 Task 4: COVID-19 Transportation Modeling | 136 |
| 3.5.1 Chicago Transportation Analysis | 139 |
| 3.5.2 New York City Transportation Analysis | 141 |
| 3.5.3 Road and Air Travel Trends and Vaccine Administration Siting Analysis | 146 |
| 3.6 Publications and Research Output | 152 |

Team Leadership

Budhu Bhaduri (Team Lead), Oak Ridge National Laboratory; **Supriya Chinthavali**, Oak Ridge National Laboratory; **Robert Stewart**, Oak Ridge National Laboratory; **Rich Davies**, Oak Ridge National Laboratory; **Charles Macal**, Argonne National Laboratory; **Jonathan Ozik**, Argonne National Laboratory; **Aymeric Rousseau**, Argonne National Laboratory; **Benjamin McMahon**, Los Alamos National Laboratory; **Sara Del Valle**, Los Alamos National Laboratory; **Mark Rintoul**, Sandia National Laboratories; **Sean DeRosa**, Sandia National Laboratories; **Patrick Finley**, Sandia National Laboratories; **Stanley Young**, National Renewable Energy Laboratory; **Andrew Duvall**, National Renewable Energy Laboratory; **Thomas Kirchstetter**, Lawrence Berkeley National Laboratory; **Thomas Wenzel**, Lawrence Berkeley National Laboratory

3.1 Project Overview

To assist decision-makers in understanding COVID-19 spread and impact across the nation, NVBL's Epidemiological Modeling team brought together experts in spatial demography and human dynamics research; agent-based modeling systems; and transportation, infrastructure, economic, and risk modeling. Comprising researchers from six national laboratories, the team coupled its extensive expertise with DOE's powerful supercomputers and data capabilities. Building on prior work with the Centers for Disease Control and Prevention (CDC), National Institutes of Health, U.S. Department of Defense, and Federal Emergency Management Agency (FEMA), the team created a data platform that forecasts (1) disease transmission, (2) stress on public health infrastructure, and (3) U.S. economic outlook. The following accomplishments illustrate team-developed capabilities that provided unrivaled understanding of COVID-19 impacts.

- Officials in Chicago, New York City, and the states of Illinois, New Mexico, and Tennessee, among others, used the team's data and modeling efforts to illustrate county-level trends and forecasts, pinpoint locations (such as bars and restaurants) significant to SARS-CoV-2 transmissions, and identify the importance of contact tracing.
- The Chicago Transit Authority (CTA) and the New York Metropolitan Transportation Authority (MTA) used the team's transportation modeling to forecast ridership under various economic reopening scenarios.
- Decision-makers at DOE, the National Nuclear Security Administration, and FEMA used results from the team's COVID-19 data and visualization platform. The team shared findings from its economic impact modeling with the U.S. Bureau of Economic Analysis.
- The CDC's modeling group used the team's ensemble dashboard to visualize output data from forecast models. In addition, CDC Minority

and Rural Health groups benefitted from the team's efforts to (1) identify communities most vulnerable to K-12 school reopening disruptions (including specific geographic locations), (2) determine states with high vs. low COVID-19 burden, and (3) compare urban vs. rural COVID-19 mobility and burden.

The COVID-19 data and visualization platform included comprehensive data access and visualization capabilities to process near-real-time, multi-modal, and multi-source data to support informed decision-making and monitor potential recovery efforts. In addition, the epidemiological team delivered comprehensive weekly reports that included analytical results coupled with subject matter expertise interpreting the data-driven observations and modeling results in the context of COVID-19 transmission and recovery dynamics at county, regional, and national scales.

3.2 Task 1: Near-Real-Time Situational Awareness

This section discusses data curation, curve analytics, and methods for mobility and community detection used for Task 1 of this project.

3.2.1 Data Curation

New Case Curation

As the COVID-19 pandemic was gaining steam in 2020, major case-reporting outlets quickly coalesced around two primary vendors: Johns Hopkins University and *The New York Times*. They focused primarily on three major attributes: number of new cases, deaths, and recovery. The team curated these reports daily, creating weekly national status maps on the county-level progression of the disease (see discussion of curve analytics in Section 3.2.2, p. 99, and predictive analytics in Section 3.3, p. 105).

County Public Health Data

The team recognized that many states were reporting very detailed datasets (e.g., hospital beds) at

the county level or finer and embarked on a major data curation effort from March to June 2020 to capture this wealth of detailed data. The number of attributes reported by the states increased nearly every week. States also routinely shifted their web tool platforms. This growth in the number of attributes, combined with unpredictable shifts in data format, meant an aggressive and agile combination of automated scripting and manual scraping was required to capture new daily streams.

In capturing the raw data, each state followed its own naming conventions, often evolving over time, making direct comparisons of the raw data impossible. A substantial and ongoing harmonization effort was required to merge and link the data. To keep up with the data volume, the team scaled up staff and widened its approach for capture and storage to ultimately collect more than 11 million data points.

The details of this curation and harmonization effort can be found in the project report *DOE COVID-19 Data Curation Effort: Overview of Data Collection Coverage* (Piburn et al. 2020). A related manuscript by Kaufman et al. is in preparation.

Mobility and Community Data

Data on aggregate mobility patterns at the county level were produced by Descartes Labs and used to generate a weekly report on changes in mobility patterns; patterns were assessed for the U.S. as a whole, for each of the four major U.S. regions, for urban counties, and for rural counties. Data on visits to points of interest (e.g., restaurants, hotels, bars, schools, and other public venues) was collected from SafeGraph, a commercial data aggregator that made their data available for the COVID-19 response through the SafeGraph Data Consortium. Data on county-level shelter-in-place orders, county-level school closures, and city-level mask mandates were also collected from primary news sources and news aggregators. News reports across a wide range of media were tracked to generate a county-level estimate

of when shelter-in-place orders were issued and relaxed. Primary and secondary news sources and educational news aggregators were used to create a city-level estimate of when public schools were closed in response to the initial wave of closures and shelter-in-place orders. Primary and secondary news sources were tracked to create a comprehensive measure of if and when mask mandates were implemented and lifted in each U.S. metropolitan statistical area (MSA), in addition to identifying state-level mask mandates.

Epi Package

Oak Ridge National Laboratory (ORNL) previously developed a series of thematic dataset packages within a population database called the “UrbanPop 2017 High-Resolution and Demographically Detailed Population Database for the United States” (Moehl et al. 2020). The UrbanPop framework was modified to include variables for large-scale analysis of U.S. populations at high risk to COVID-19 in terms of household composition and employment sector. These variables included race, age, household income, occupation, presence of youth (ages 18 and younger) in the household, and presence of seniors (ages 60 and older) in the household. The new epidemiology data package and documentation was shared with Argonne National Laboratory (ANL) and Los Alamos National Laboratory (LANL) for analysis.

3.2.2 Curve Analytics

Several curve analytics approaches were applied to the national new case count data, detailed county-level data, and mobility data. In the case of the national new case count data, Susceptible-Infections-Recovered (SIR)-type models were struggling due to the scarcity of data in an uncertain data environment. The team responded by introducing and evolving a set of data-driven tools over the course of the project. The tools were initially aimed at understanding the COVID-19 case landscape but ultimately became the basis for predictive analytics as well (Section 3.3, p. 105). In the case of the detailed county-level data, the team engaged in

exploratory analysis and demonstrated how these data could be further examined for deeper insights. Finally, in the case of the mobility data, a wide range of analytics was performed and is discussed below.

COVID County Situational Awareness Tool

The ability to monitor and forecast disease progression both near term and long term was critical to effective situational awareness and decision support. Scientists traditionally rely on well-grounded mechanistic models such as the SIR model to characterize current conditions and forecast disease progression days or weeks ahead of time. These models require data on susceptible and recovered populations as well as reliable infection rate information. Unfortunately, this type of data was missing, especially early on, severely hampering efforts to reliably use traditional mechanistic models.

Still, a pressing need remained for reliable situational awareness at the federal, state, and local levels. The team responded to this need by developing the COVID County Situational Awareness Tool (CCSAT). CCSAT is a data-driven, statistical approach designed to provide critical stopgap, near-term monitoring and prediction in the limited and uncertain data environment that persisted during the first months of the pandemic. With a focus on near-term analysis, CCSAT leverages spatiotemporal techniques in statistics, visualization, and decision support to provide county-level characterization of COVID-19 progression over the previous seven days, a forecast of progression in the upcoming seven days, and the ability to observe progression trends back to the beginning of the pandemic. This approach helped support agile decision-making occurring on a one- to two-week timescale at the federal, state, and county levels.

CCSAT results enabled weekly updates about COVID-19 progression during the pandemic. Figure 3.1, p. 101, shows two CCSAT example outputs. The top panel shows the predicted velocity and acceleration (V&A) of the magnitude and growth in new county-level cases and the bottom panel

shows the observed V&A map. County-level new case growth and magnitude dynamics were obtained by observing the lower-, middle-, and upper-quartile (i.e., low, medium, high) distribution of new cases compared with counties designated as accelerating (reporting greater than 1.1 times more cases than the week before), constant (0.9-1.1 times the week before), or decelerating (0.9 times the week before), respectively. These data reveal the counties in which case numbers are (or will be) high and increasing, low and increasing, high and flattening, and so forth.

Figure 3.2, p. 102, shows the growth rate in COVID-19 cases related to the three conditions (accelerating, constant, decelerating) by population and county from March to June 2020. The graphs pose interesting hypotheses of seasonal and policy effects that can be further explored.

The underlying Bayesian model that performed the prediction is discussed in the Predictive Analytics section (3.3, p. 105). The underlying Bayesian model used to carry out the observations (V&A maps) and prediction (Bayesian Nowcast Model) is documented in “The COVID County Situational Awareness Tool: COVID-19 Near-Term Monitoring and Forecasting for Decision Support” (Stewart et al., manuscript submitted).

Harmonized Space-Time Cube Analysis

Following the collection of the harmonized data, the findings were explored using the World SpatioTemporal Analytics and Mapping Project (WSTAMP). WSTAMP is a major space-time analysis and visualization tool developed at ORNL for the National Geospatial-Intelligence Agency specifically for this kind of exploratory analysis. WSTAMP offers a rich analytical and graphical environment consisting of a wide range of analytics including time series plots, statistical summaries, data-mining techniques, trend and pattern detection, and hypothesis generation. WSTAMP provided a first deep look at the data and enabled the discovery of several critical findings that would not have been possible without it. The findings included

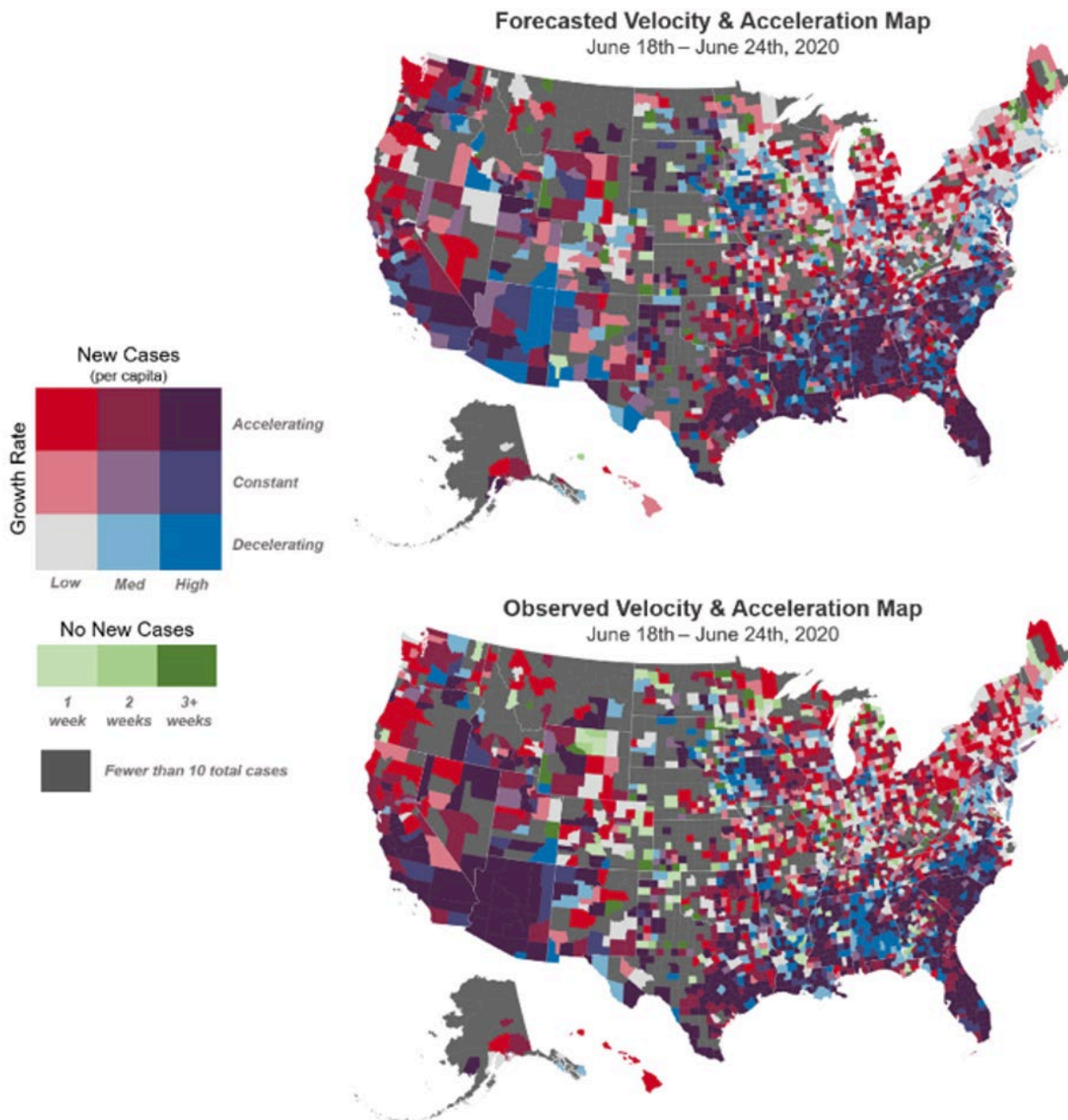


Fig. 3.1. Predictions (top) and observations (bottom) of the magnitude and growth in new county-level COVID-19 cases. [Courtesy Oak Ridge National Laboratory]

quality assurance/quality control issues requiring further attention, including point-wise curation errors requiring mitigation and harmonization decisions requiring review. A first detailed look at attribute trends revealed that many were agreeably continuous while some were fragmented and short

lived. For the most complete attributes, a series of data-mining exercises were conducted that surfaced the most common multivariate trends, revealing the presence of correlations among many of the data. The study explored the data across three scales of analysis: within-state county level,

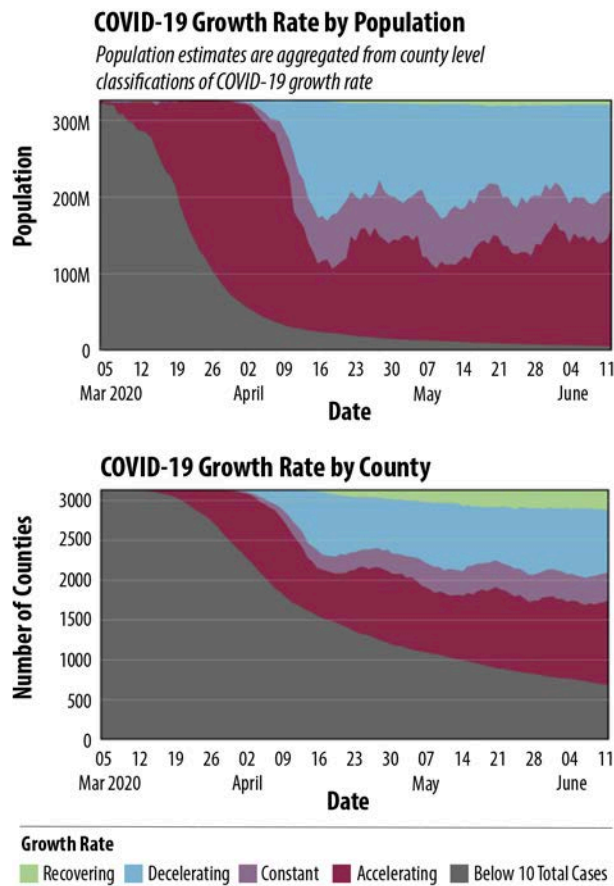


Fig. 3.2. COVID-19 growth rate by population and county. [Courtesy Oak Ridge National Laboratory]

within-state state level, and between-state. Florida and Ohio served as exemplar use cases for within-state county and within-state state-level analyses, respectively, due to their relatively rich and consistent set of attributes at those scales. A full discussion of the results can be found in the report *DOE COVID-19 Data Curation Effort: An Initial Analysis of the Data* (Piburn et al. 2020).

3.2.3 Mobility and Community Detection

Mobility was examined by region and activity type. Results from these analyses were updated weekly and submitted to DOE.

Mobility by Region

Figure 3.3a, p. 103, shows changes in typical U.S. mobility patterns between March 12, 2020, and January 8, 2021. A substantial decline in typical mobility across the entire U.S. began on March 12. Between April 1 and April 15, 95% of the U.S. population lived in a county where typical mobility was less than half the pre-COVID-19 level. Figure 3.3b shows the wide variability in mobility patterns across the four major U.S. regions. The Northeast saw the most dramatic decline in mobility, with 95% of the population reducing travel by 90% during the first wave of the pandemic. The South saw the smallest mobility declines, but even this pattern was significant: 95% of the population in the South lived in a county where mobility reduced to less than half the prepandemic normal, while half of the population lived in a county where mobility reduced to a quarter of the prepandemic normal. Figure 3.3c compares urban and rural counties. The U.S. census describes urban counties as those where 90% or more of residents are living in an urban environment and rural counties as those where 90% or more of residents are living in a rural environment. Throughout the pandemic, residents of urban counties responded much more dramatically to COVID-19 (i.e., decreased their mobility behavior) than residents of rural counties.

Mobility by Destination

Figure 3.4a, p. 104, compiled using SafeGraph data, compares the number of bar visits from the 7-day period ending January 3, 2021, relative to the weekly average number of visits to bars in a county during all of 2019. Each week's standard deviation relative to the 2019 distribution was calculated. Values near 0 indicate similar bar visitation in January 2021 compared to the 2019 weekly average. Values above 1 indicate much higher visitation than normal and values below -1 indicate much lower visitation than normal. Bar visitation rates were well below normal for major urban areas, the Northeast, and the West but approached typical levels in parts of the South and Midwest.

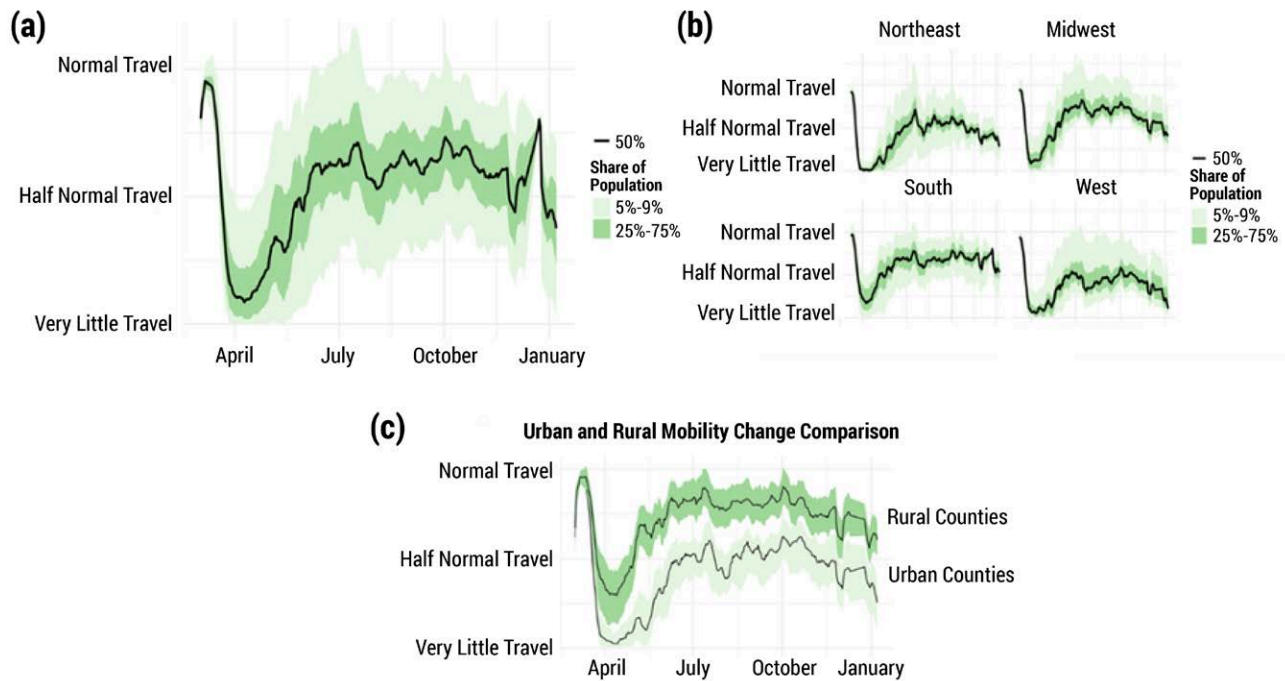


Fig. 3.3. Studies in U.S. population mobility by region: (a) all areas, (b) four major U.S. regions, and (c) rural vs. urban residents. [Courtesy Oak Ridge National Laboratory]

Figure 3.4b shows the number of visits to schools and other educational facilities during the week ending December 4, 2020, relative to the weekly average number of school visits from all of 2019, calculated using the same metrics as for bar visits. The week ending December 4 would typically be a fully attended school week, as it fell between the Thanksgiving and winter holidays. Nonetheless, school visits measured well below normal for urban and coastal areas. In several primarily rural counties in the South and Midwest, visits to schools approached normal levels.

Co-Evolution of COVID-19 Attention, Mitigation Behavior, and Cases

This research effort explored the co-evolution of COVID-19 attention, mitigation behavior, and case incidences through the 2020 waves of U.S. COVID-19 cases. The team used three strategies to describe associations between these factors:

(1) a narrative description drawing from quantitative measures of attention, mitigation behavior, and cases; (2) associations between the signs of changes in these factors; and (3) a Lotka-Volterra system dynamics model casting mitigation effort as predator and cases as prey. The team found that the model reproduced waves observed in the narrative and empirical analysis, and extensions reproduced the observed increases in wave amplitude. These results helped the team to begin developing an empirical and mathematical strategy for exploring the co-evolution of social and ecological processes, in a context in which a great deal of poor-quality data is available. The dynamics of behavior and disease ecology described here highlight the potential for cyclical patterns of vulnerability in other important social and ecological systems and processes. The details can be found in “Co-evolution of COVID-19 Attention, Mitigation Behavior, and Cases” (Brelsford et al., manuscript in preparation).

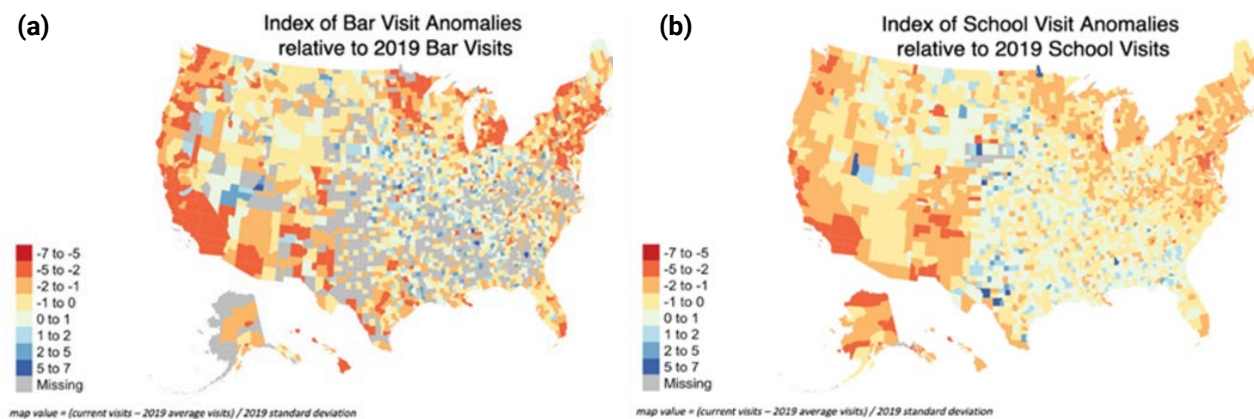


Fig. 3.4. Mobility by destination: **(a)** Change in the number of bar visits from the 7-day period ending January 3, 2021, relative to the weekly average number visits from all of 2019. **(b)** Change in the number of visits to schools and other educational facilities from the week ending December 4, 2020, relative to the weekly average number of school visits from all of 2019. [Courtesy Oak Ridge National Laboratory]

Spatial and Temporal Measurements of the Shopper-Worker Ratio

The team examined data that characterize spatial and temporal variation in the ratio of shoppers to workers in public places (i.e., points of interest) in the U.S. between 2019 and 2020. The underlying data on foot traffic to public places was collected by SafeGraph, a commercial data aggregator. The team estimated the ratio of shoppers to workers based on recorded visit duration. These data may be useful for understanding how use of public spaces changed during the COVID-19 pandemic and, more generally, for understanding activity patterns in public. The details of this work can be found in “Spatial and Temporal Characterization of Activity in Public Space, 2019–2020” (Brelsford et al., in review).

School Closures Associated with COVID-19 in U.S. Counties

The team collected data on district-level school closures in response to the COVID-19 pandemic in Spring 2020; the data were compiled from primary sources such as news media and district-level announcements. The data were validated against cell phone-based movement data and

aggregated to the U.S. County level for ease of incorporation with other tools for assessing the effectiveness of nonpharmaceutical interventions on mitigation strategies. This work is detailed further in “COVID-19 Associated School Closures in U.S. Counties” (Brelsford et al., unpublished manuscript).

Bayesian NowCast Model

Early in the pandemic, the combination of an uncertain and evolving data environment and a pressing demand for usable predictions motivated the development of a forecasting model based solely on the underlying population and the temporal progression of new cases. Because of the tight linkage between COVID-19 and population as both a target and mode of transmission, the team reasoned that a model based on these two inputs might quickly produce and operationalize viable near-term estimates. The goal of the NowCast model was to estimate the total number of new cases in the upcoming week for each U.S. County and classify the results as a V&A map. The NowCast model was implemented in the CCSAT with remarkable efficacy of prediction. The method, accuracy, and next steps are documented in “The COVID County Situational Awareness Tool: COVID-19 Near-Term

Monitoring and Forecasting for Decision Support” (Stewart et al., manuscript submitted).

Bayesian State Space Modeling for COVID-19

The team developed a Bayesian inferential framework for the spread of COVID-19 using mechanistic epidemiological models, such as SIR or Susceptible-Exposed-Infectious-Removed (SEIR), and allowed the effective contact rate to vary in time. A novel aspect of the team’s approach was the incorporation of a time-varying reporting rate, accounting for the initial phase of the pandemic before testing was widely available. By varying both the reporting rate and the effective contact rate in time, the team’s models captured changes in the data induced by external influences such as public health intervention measures. The model views COVID-19 incidence data as the observed measurements of a hidden Markov model, with latent space represented by the underlying epidemiological model, and employs a particle Markov chain Monte Carlo (PMCMC) sampling scheme for Bayesian inference. Parameter inference is performed via PMCMC on incidence data collated by *The New York Times* from the states of New York and Tennessee from March 1 to August 30, 2020. The team reported on its work performing Bayesian model selection on the different formulations of the epidemiological models, making predictions from their fitted models, and validating predictions against the true incidence data for August 31 to September 7, 2020, in “Bayesian State Space Modelling for COVID-19: With Tennessee and New York Case Studies” (Spannaus et al., manuscript submitted).

Spatiotemporal Ensemble Tools for COVID-19 Analysis

The team developed a set of statistical tools for near-real-time situational awareness and predictive analytics to provide critical guidance for policymakers and health care professionals on best actions to decrease the spread of COVID-19 in the U.S. As part of the ensemble of tools, a semi-Bayesian probabilistic bias analysis was used to estimate

the incomplete testing correction factor, and the team proposed a clustering algorithm as well a principal component analysis–based analysis to detect states with similar growth trend to guide policymakers in the allocation of resources. The ensemble tools were built on a discrete Weibull distribution framework with focus on real-time monitoring of the outbreak via a change point detection analysis, the evaluation of nonpharmaceutical intervention measures, and short-term future time predictions. All the proposed tools are generalizable at a finer scale (e.g., county level), while various effect terms can be included in the modeling framework, leading to accurate predictions to support policymakers.

3.3 Task 2: Predictive Analytics

The predictive analytics task was created to answer questions such as:

- When will the infection curve peak?
- What is the duration (i.e., time extent) of the overall curve?
- Can the case fatality rate (CFR) for each age stratum be estimated?
- What is the estimated need for hospital beds, intensive care units (ICUs), and ventilators?
- How much testing capacity is needed?
- Where is testing capacity needed?

Answering these questions during the project period of performance—late March through September 2020—required multiple modeling efforts, each evolving over the course of the project according to the needs of the national response. Predictive analytics task activities occurred at all five participating laboratories: LANL, Sandia National Laboratories (SNL), ORNL, ANL, and, for the latter half of the project, the National Renewable Energy Laboratory (NREL).

Figure 3.5, p. 106, shows that the predictive modeling effort required recalibrating models, reworking algorithms at the core of the modeling

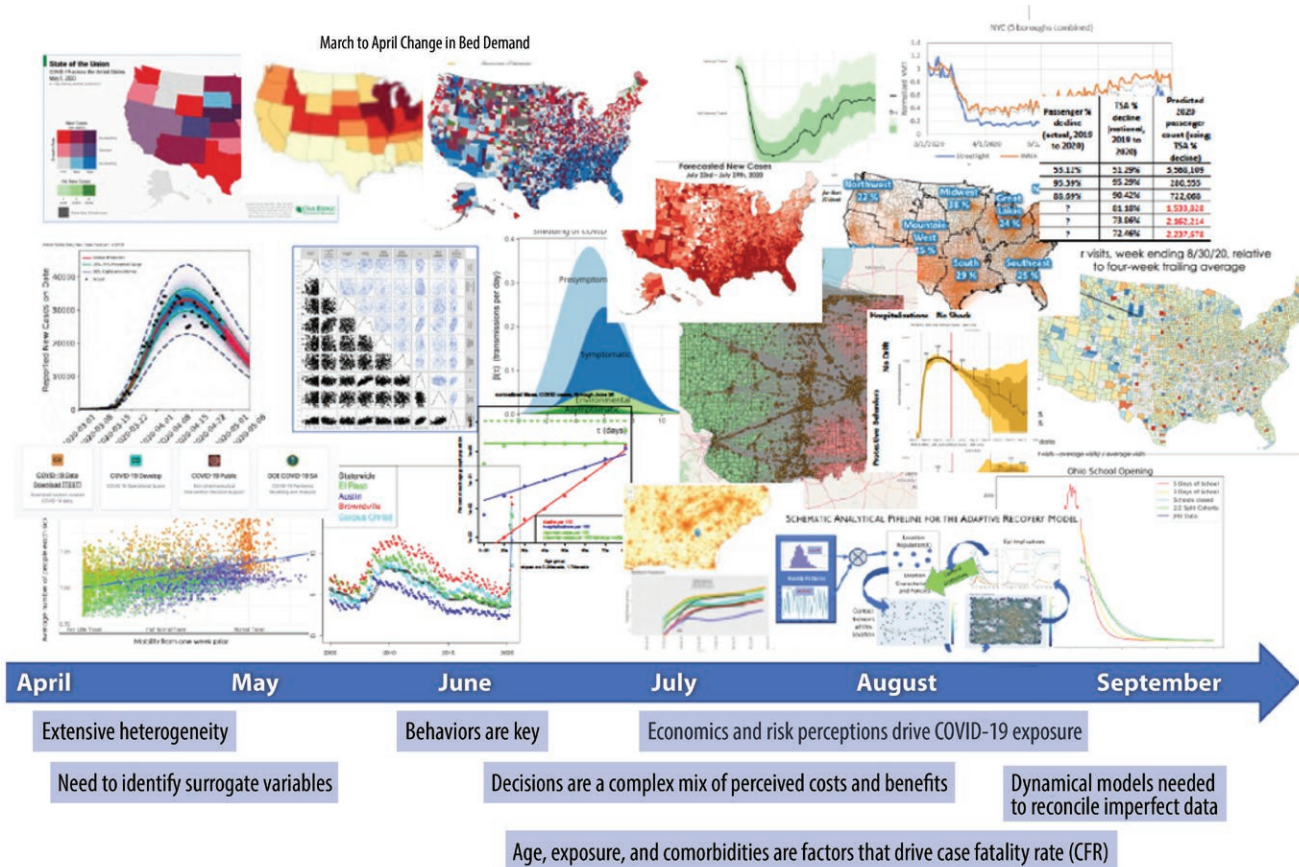


Fig. 3.5. Predictive modeling effort. A variety of analyses were produced by the predictive modeling task, including risk maps, correlations derived from statistical models, timelines of mobility patterns and assay sensitivities, uncertainties in projections, correlations in parameter uncertainties involving the various modeling efforts, and logic models describing newly created models (top panel). Key lessons drove model development (bottom panel). Initial efforts highlighted the spatial extent and heterogeneity of disease spread and the need to identify surrogate variables to characterize the spread. By early summer 2020, behavioral choices by the public had become key to understanding disease spread (e.g., filled hospitals promote behavior changes that reduce disease spread), while age, exposure levels, and comorbidities were driving CFR. By late summer 2020, it became clear that economics and risk perceptions were driving COVID-19 exposure and that decisions were a complex attempt to balance perceived costs and benefits. By the end of the project, the Epidemiological Modeling team built a new generation of more accurate dynamical models needed to reconcile a variety of imperfect data. [Courtesy Argonne, Los Alamos, Oak Ridge, and Sandia national laboratories]

tools, and developing new tools when necessary. These efforts connected with capabilities housed at the laboratories rooted in biosecurity, disaster planning, high-performance computing (HPC), and simulation science. Many, but not all, of the efforts resulted in publications or follow-on projects from a variety of sponsors.

Two example publications illustrate the depth of science and multidisciplinary collaborations on which the project drew. Although much of the work predated the earliest stages of the NVBL effort, the all-hands-on-deck approach to meeting national needs during the pandemic resulted in significant collaboration and sharing of staff across projects.

- “Tracking Changes in SARS-CoV-2 Spike: Evidence that D614G Increases Infectivity of the COVID-19 Virus” by Bette Korber et al. (LANL) appeared in *Cell* in August 2020 and had 1,737 citations as of April 2022. This article was the first to highlight the emergence of increasingly transmittable strains of SARS-CoV-2, with potential repercussions for virulence, diagnostics, and vaccine susceptibility.
- “High Contagiousness and Rapid Spread of Severe Acute Respiratory Syndrome Coronavirus 2” by Steven Sanche et al. (LANL) appeared in *Emerging Infectious Diseases* in July 2020 and had 704 citations as of April 2022. This article included a careful examination of the spatiotemporal spread of COVID-19 in China and estimated its contagion to be characterized by a replicative number, R_0 , of 5.7. This was much higher than estimates found in the literature early in the pandemic and required a much more active policy response for effective control.

This section describes the Predictive Analytics task in three parts:

- Statistical modeling
- Multiscale agent-based modeling
- Systems-level modeling of economics and public health response strategies

3.3.1 Statistical Modeling

Early in the pandemic, a strong need existed for statistical models capable of reconciling incomplete and underreported case counts and using these time series for short-term resource requirement estimations and statistical identification of the waxing and waning pandemic waves. Three instances of forecasting models illustrate these efforts.

LANL COVID-19 Cases and Deaths Forecasts Model

The LANL COVID-19 Cases and Deaths Forecasts were updated weekly from April 2020 through September 2021 for all 50 states and most

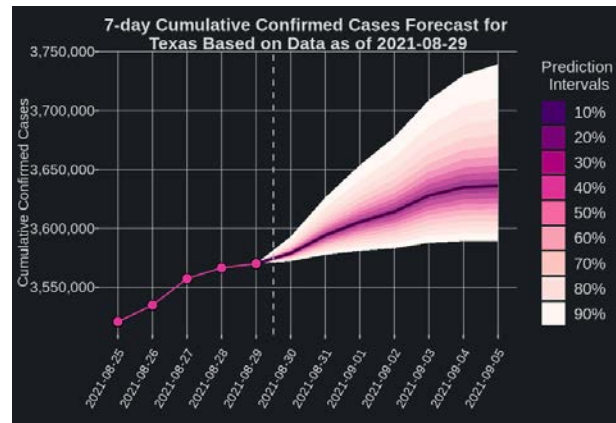


Fig. 3.6. Example forecast from the Los Alamos National Laboratory COVID-19 Cases and Deaths Forecasts tool. [Courtesy Los Alamos National Laboratory]

countries around the world and posted publicly at covid-19.bsvgateway.org. The tool projects case counts forward in time, with uncertainty bands derived from past data and benchmarked against data as time passes. Modeling details are provided on the website and were published in “How New Mexico Leveraged a COVID-19 Case Forecasting Model to Preemptively Address the Health Care Needs of the State: Quantitative Analysis” (Castro, 2021). Figure 3.6, this page, shows an example forecast from this tool.

Using systematized modeling tools such as this, it is possible to create estimations of resource requirements. The team met weekly with public health workers and hospital system administrators to define analytical tools required for planning, review the current week’s predictions, and evaluate the accuracy and appropriateness of predictions from previous weeks.

Figure 3.7, p. 108, shows actual case count data and hospital usage information for three of the most important projections needed for the public health response to COVID-19: hospital beds required, ICU beds required, and ventilators required during the three weeks following the forecast date. Iterative prediction, comparison to actual

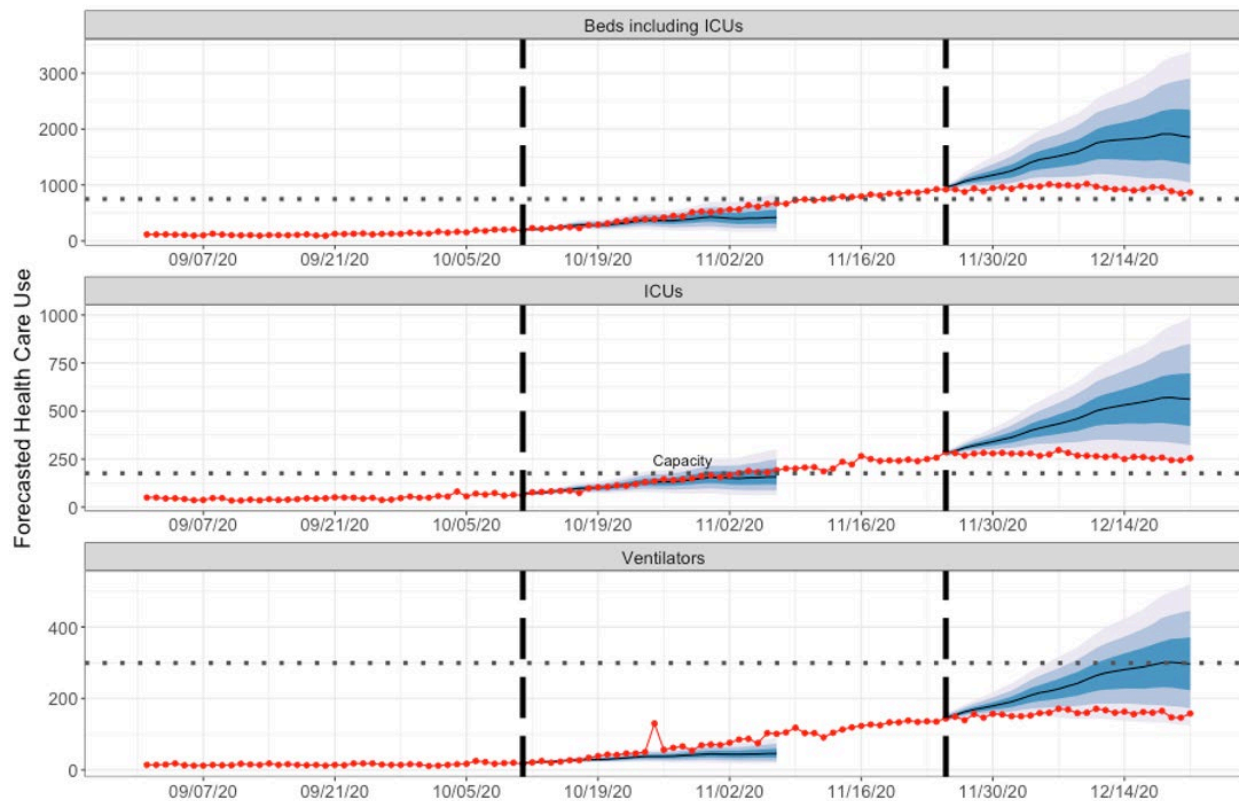


Fig. 3.7. Reported and forecasted use of concurrent hospitalization beds, ICU beds, and ventilators by New Mexico hospitals. The forecasts in October and November 2020 (black lines and blue shaded prediction intervals) are based on reported usage from September 1 to December 29, 2020 (dotted red lines). Forecasts are day-ahead predicted medians (black line), with 50% (dark blue), 80% (medium blue), and 95% (light blue) prediction intervals for 28 days (4 weeks). Two example forecasts are shown: the first beginning on October 11, 2020, and the second beginning on November 25, 2020. [Reprinted under a Creative Commons License (CC BY 4.0) from Castro, L. A., et al. How New Mexico Leveraged a COVID-19 Case Forecasting Model to Preemptively Address the Health Care Needs of the State: Quantitative Analysis. *JMIR Public Health & Surveillance* 2021, 7 (6), e27888. Copyright 2021 the Authors.]

events, and discussion of reasons for discrepancies occurred on a weekly basis throughout the project and greatly informed model formation and parameterization and ensured information was presented in a way that was most valuable to decision-makers. Complete details of the model and lessons learned from the model production and evaluation task are described in Castro et al. (2021).

While the LANL COVID-19 Cases and Deaths Forecasts model incorporates some information about COVID-19 disease progression, it is almost

completely statistical in nature and does not enable much mechanistic insight. The period during project execution was when basic information about the determinants of disease progression and epidemiological spread were unknown. In response to the need for mechanistic insight, the team developed and deployed a mechanistically based forecasting model run nightly throughout the project execution period. The results were ultimately displayed in the project information portal. Details of the model and examples of its use are published in Lin et al. (2021).

Mechanistically Based Forecasts Model

The mechanistically based forecasting model produces banded forecasts and undergoes continuous benchmarking and assessments like the LANL COVID-19 Cases and Deaths Forecasts model, but also incorporates a physically interpretable model of mixing, partially protected, and quarantined populations, as well disease progression parameters indicating rates of progression, effectiveness of medical interventions, and explicit couplings of disease states to the level of contagious spread. The model estimates seven location-dependent parameters to characterize the wave or pandemic propagation of cases:

- Time of transmission introduction
- Time of social distancing implementation
- Social distancing setpoint
- Social distancing rate
- Fraction of active cases reported
- Dispersal parameter characterizing disease spread

Details are provided in Lin et al. (2021). Iterative application of this model provided insight not only into the early detection of future waves of infection, but also into the possible range of parameter values and how these parameters played against one another.

Analysis using the mechanistically based model drove technological development in several ways. First, it rapidly provided data for the 15 most populous U.S. MSAs using a consistent model that could be related back to mechanistic parameters. Such models, although far less complex than the multiscale, mechanistic models described in the next section (3.3.2, p. 111), still pose significant and novel visualization challenges for the project's data portal, including real-time updates and accurate communication of statistical and model form uncertainties to users.

Another aspect of this model, developed and implemented but not described in Lin et al. (2021),

was its ability to apply statistically valid model selection procedures to case count data from particular cities to determine whether the data were best explained by a single process with slightly mis-estimated parameters or whether something about the situation had qualitatively changed, such as people's behavior, implementation of contact tracing or improved testing regimes, reporting processes, or attributes of disease progression or contagious spread. Figure 3.8, p. 110, shows Bayesian predictive inferences for daily new case counts in the 15 most populous MSAs between March 1 and June 21, 2020.

PRIME Model

A third statistical model is PRIME (Partially observed epldeMics – Bayesian Inference), which is an open-source software package for computing short-term (7-10 days) forecasts of COVID-19 morbidity using time-series data on detected COVID-19 cases that are now publicly available (github.com/nytimes/covid-19-data/). Developed by SNL researchers, PRIME was tested on wild-type COVID-19 data but should work for all variants. The forecasts it produces are a lower bound on the morbidity. The PRIME model does not need any user-supplied assumptions/information on the effects of countermeasures on COVID-19 spread or any changes in the mixing of people; instead, it infers effects of countermeasures and/or changes in mixing from data when they become evident. PRIME's model has been applied to entire countries and U.S. states (Safta et al. 2020) as well as to cities (Lin et al. 2021). It also accommodates multiple surges/waves of infection and detects the arrival of new waves using information-theoretic criteria (Blonigan et al. 2021).

PRIME's underlying technology is Bayesian inference, which infers key characteristics of the latent infection rate of COVID-19 in a population, given a time series of daily detected cases in a region. The infection rate is assumed to vary in time and is modeled using a series of Gamma functions, with each function serving as a new wave. The inference problem is conditioned on a COVID-19

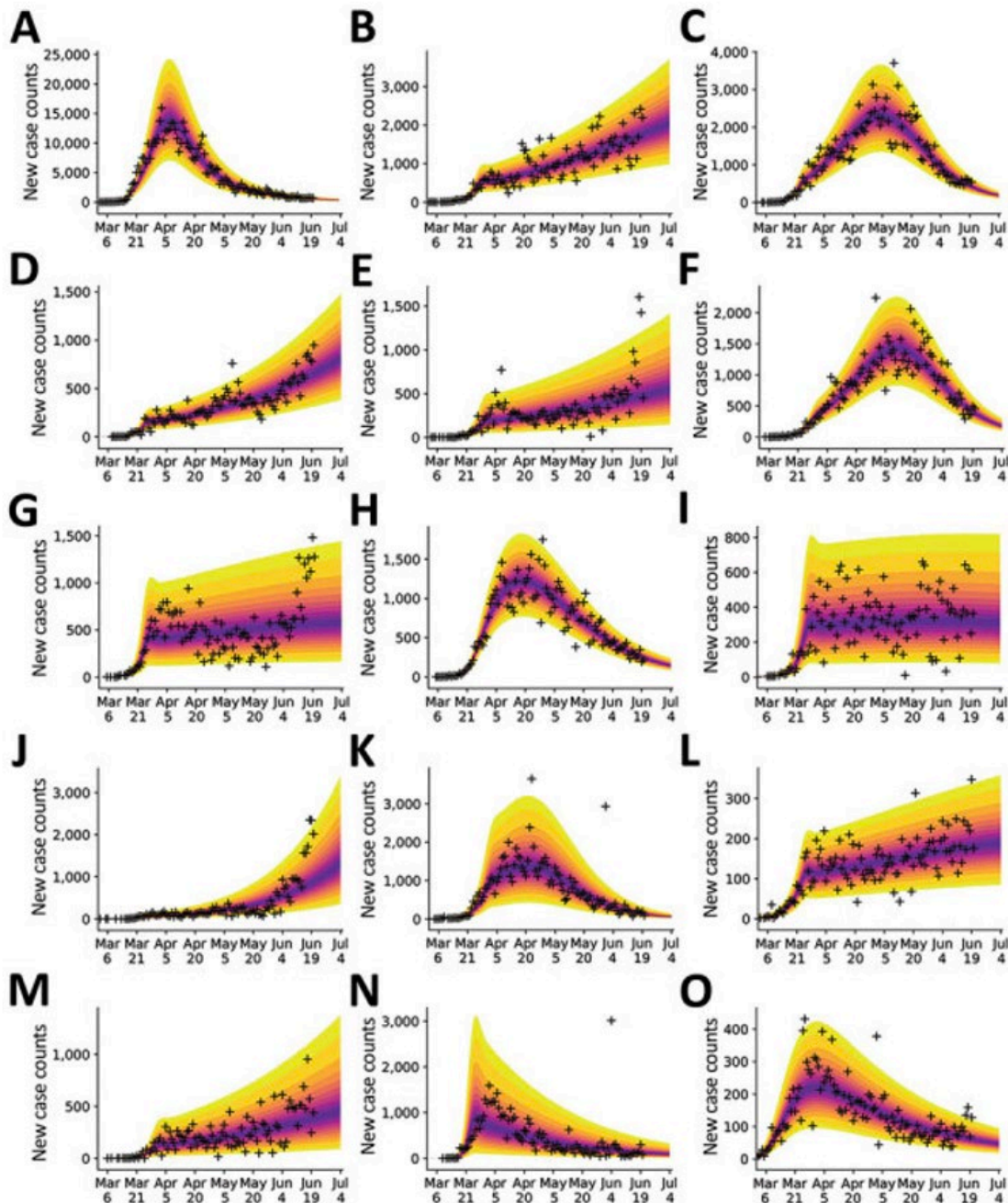


Fig. 3.8. Bayesian predictive inferences for daily new case counts of COVID-19 in the 15 most populous MSAs, U.S., March 1–June 21, 2020. Predictions were conditioned on the compartmental model with structure defined by $n = 0$, which accounts for a single initial period of social distancing. Inferences are shown for the following cities' MSAs: (A) New York City, (B) Los Angeles, (C) Chicago, (D) Dallas, (E) Houston, (F) Washington, D.C., (G) Miami, (H) Philadelphia, (I) Atlanta, (J) Phoenix, (K) Boston, (L) San Francisco, (M) Riverside, California, (N) Detroit, and (O) Seattle. Cross symbols indicate observed daily case reports. The shaded region indicates the 95% credible interval for predictions of daily case reports. The color-coded bands within the shaded region indicate alternate credible intervals. The model was parameterized with uncertainty quantification using data from January 21–June 21, 2020. The uncertainty bands/inferred model was used to make predictions for 14 days after the last observed data; the last prediction date was July 5, 2020. [Reprinted from Lin, Y., et al. Daily Forecasting of Regional Epidemics of Coronavirus Disease with Bayesian Uncertainty Quantification, United States. *Emerging Infectious Diseases* **2021** [cited May 2022], 27 (3), 767–778. Available from: wwwnc.cdc.gov/eid/article/27/3/20-3364_article.]

disease model, represented as a convolution of the infection-rate model by the incubation-period distribution, modeled as a lognormal distribution. The parameters of the Gamma functions, lognormal distribution, and the sizes of the individual waves are the objects of inference. The inference is performed via Markov-chain Monte Carlo sampling using Adaptive Metropolis¹ and a joint posterior distribution is developed over all the parameters. Forecasting is performed by sampling the posterior distribution and running the disease model with the samples. Uncertainties in the parameters of COVID-19 incubation-period distribution (i.e., bounds on the parameters of the lognormal distribution) can also be accommodated. In case a new wave is suspected, the infection-rate model is augmented with an additional surge model (i.e., a new Gamma function) and the new, augmented model is fitted to the data. The two competing models are then assessed using information-theoretic criteria (Akaike and Bayesian information criteria) to choose one of the models. If the new infection-rate model is chosen, it also yields the date of arrival of the new surge. For details, see Blonigan et al. (2021).

PRIME was used to detect the effects of lockdown on the number of new COVID-19 cases in California in spring 2020 (see Fig. 3.9. p. 112). Lockdowns were instituted in mid-March, though it took a week to affect population mixing. Forecasts generated using data on April 1 show a steadily increasing outbreak for the next two weeks; in contrast, the actual data showed that the outbreak had plateaued. By April 5, PRIME had inferred that the infection rate had modulated and adjusted its forecasts accordingly.

Fig. 3.10, p. 113, shows PRIME fitting a 2-wave model to data from Florida in October 2020 and providing forecasts; the data in the ensuing weeks are close to the median predictions and bracketed by the bounds on the predictions. PRIME fit a 3-wave model to data from New Mexico in

the winter of 2020; the initial, summer, and winter waves are clearly visible and captured by the model.

The project delivered open-source code, available on [github.com \(sandialabs.github.io/PRIME/description.html\)](https://github.com/sandialabs.github.io/PRIME/description.html); github.com/sandialabs/PRIME/. It also delivered two journal publications showing model performance for large populations with multiple waves (Blonigan et al. 2021; Safta et al. 2020) and its usefulness in urban regions (Blonigan et al. 2021). Note that PRIME was not used for urban populations; rather, a similar model was used and re-implemented by LANL in a different codebase.

3.3.2 Multiscale Agent-Based Modeling

Previous experience with other decision support applications combined with the obvious complexity of characterizing the variety of effects occurring in the evolution of COVID-19 across the U.S. over the project execution period prompted the team to apply three separate agent-based modeling schemes, summarized below.

EpiGrid

EpiGrid, developed by LANL researchers, is a SEIR-based model of disease progression with vaccination and early and late treatments applied to a gridded population database, which for the U.S. is derived from 5-km-resolution LandScan data. It is primarily designed for flexibility in developing models across all pathogen types causing outbreaks anywhere in the world. It explicitly models real-world mitigations that depend arbitrarily on time and geography, including short- and long-distance movement controls, vaccination, culling (for livestock diseases), early and late disease treatments, and nonspecific alterations of the force of infection. Although typically used interactively (runtimes < 1 minute) on ~200-mile regions, it was scaled up to compute COVID-19 simulations across the entire eastern U.S. with runtimes of two hours on a single desktop processor.

Sponsorship: Original development began with the U.S. Department of Homeland Security (DHS)

¹ Haario, H. et al. An adaptive Metropolis algorithm. *Bernoulli* **2001**, 7 (2), 223–242. DOI: 10.2307/3318737.

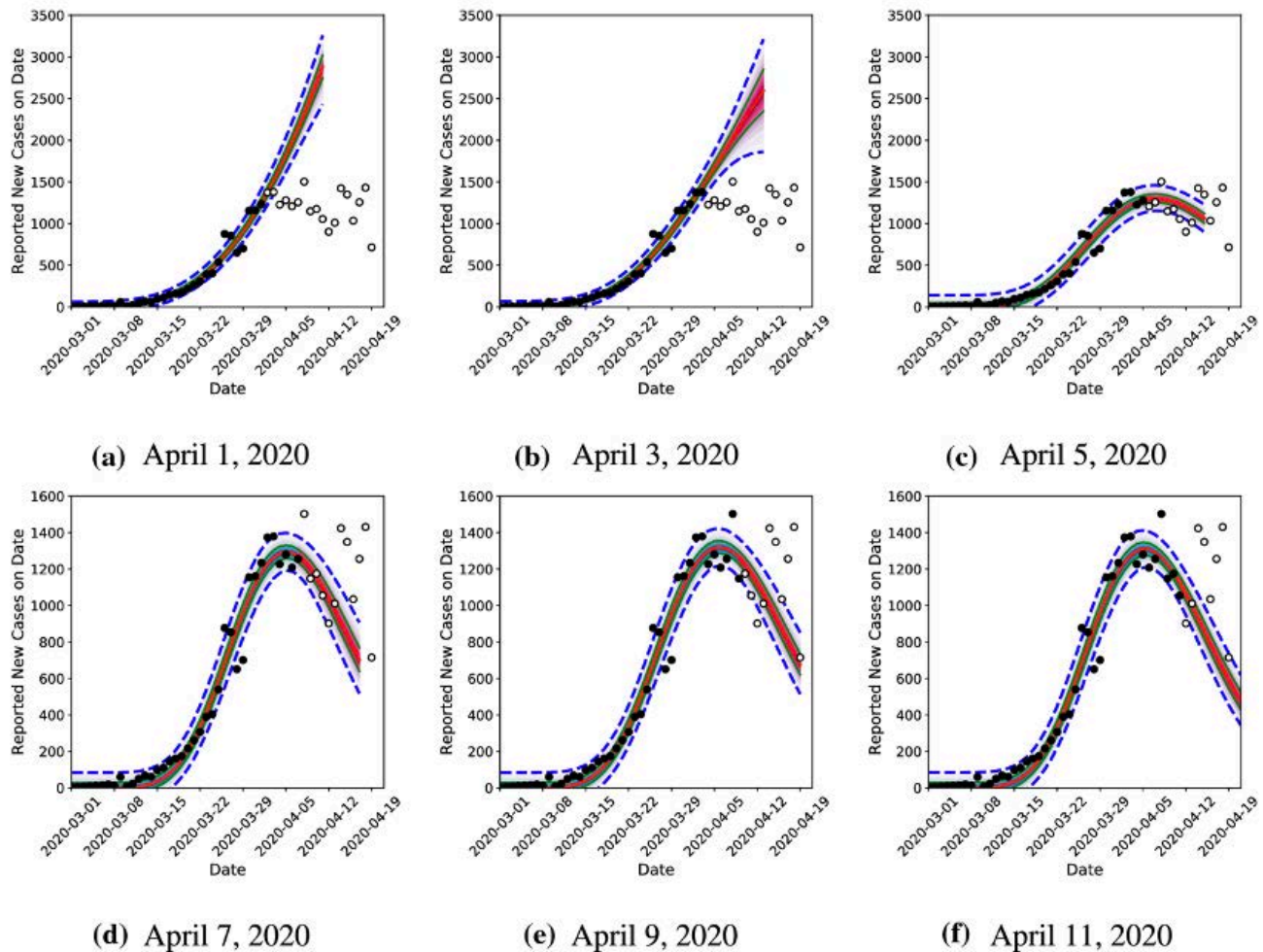


Fig. 3.9. PRIME forecasts of COVID-19 morbidity in California during spring 2020. Black dots represent the data used to train PRIME, solid lines are median predictions of the model, shaded regions are the inter-quartile range, and dashed lines are the 5th and 95th percentile predictions. The open circles are the actual data corresponding to predictions. [Reprinted with permission from Springer Nature from Safta, C., et al. Characterization of Partially Observed Epidemics Through Bayesian Inference—Application to COVID-19. *Computational Mechanics* **2020** 66, 1109–1129. Copyright 2020.]

sponsorship in 2003 and subsequently included funding from the Defense Threat Reduction Agency and Laboratory Directed Research and Development (LDRD).

EpiCast

Developed at LANL, Epidemiological Forecasting (EpiCast) is an agent-based model designed to simulate community-level influenza transmission

in the United States. The national-scale simulation model, which can incorporate a variety of disease, mitigation, and economic data, consists of ~300 million individuals distributed among ~65,000 census tracts to closely represent the actual population demographics (i.e., age and household size distributions) and commuting patterns. Daytime and evening contact networks represent potential contacts in schools, workplaces, households,

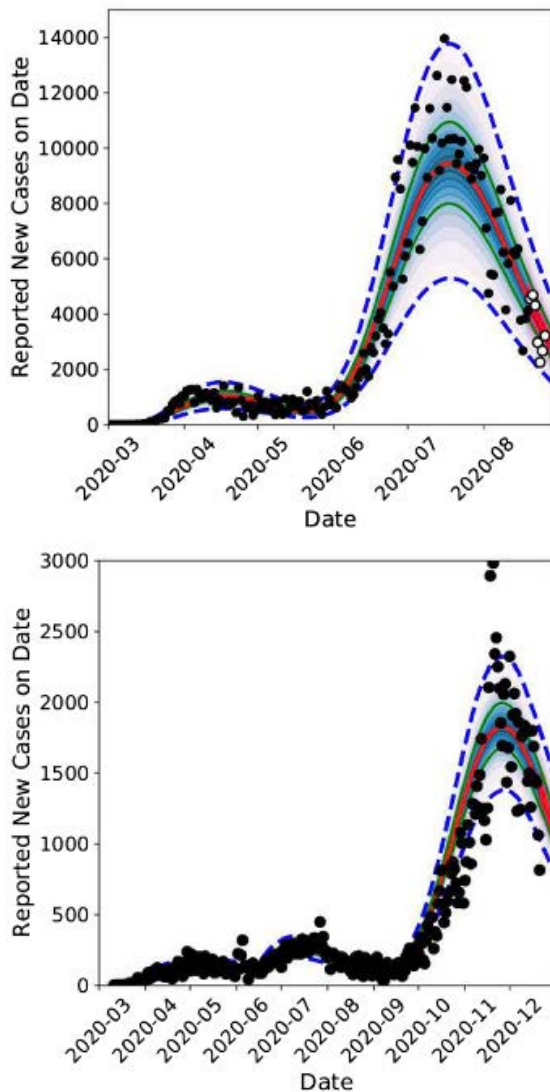


Fig. 3.10. Fitting a 2-wave model and forecasts to data from Florida in October 2020 (top); fitting a 3-wave model to New Mexico data in the winter of 2020 (bottom). The figures show posterior-predictive distributions with darker shades near the median and lighter shades towards the 2.5 and 97.5 quantile levels marked with dashed lines. The 25–75 interquartile range is marked with green lines. The blue shades correspond to hindcast dates along with black symbols marking the data used for model calibration. The red shades correspond to forecast and the white circles mark the data collected after the forecasts were made. [Reprinted by permission from Springer Nature from Blonigan, P., et al. Forecasting Multi-Wave Epidemics Through Bayesian Inference. *Archives of Computational Methods in Engineering* **2021**, 28, 4169–4183. Copyright 2021.]

neighborhoods, and communities. EpiCast now also stratifies workplaces using the North American Industry Classification System at the three-digit level, resulting in 99 sectors with appropriate county-level workforce levels. EpiCast was designed as a distributed-memory parallel code and is scalable and reproducible (for a given random number generator seed and processor count).

Sponsorship: Original development was supported by DHS. Subsequent EpiCast developments and applications were supported primarily by DHS and the Centers for Disease Control and Prevention.

CityCOVID

CityCOVID is an agent-based model developed at ANL that explicitly models individuals moving from actual individual locations on an hourly basis over a year or more. CityCOVID uses active learning Bayesian estimation algorithms to estimate key model parameters by fitting model outputs to actual data on deaths and hospitalizations as described in Ozik et al. 2021. CityCOVID considers details of the population in terms of individual characteristics (e.g., age, preexisting conditions, household/school/workplace locations) and behavior. The model's dynamic nature and hourly time steps enable the gaming of public policy interventions by predicting the effects of nonpharmaceutical interventions and other policy levers. It is currently implemented for the City of Chicago, Ill., via a distributed agent-based model built on the Argonne Recursive Porous Agent Simulation Toolkit (Repast) HPC toolkit and run on the Theta Supercomputer and other relevant HPC resources.

Sponsorship: Original development supported by the National Institutes of Health, followed by the National Science Foundation and ANL LDRD.

Modeling Constraints

Although the three models operate on distinct codebases with considerably different modeling approaches, they share a common challenge of identifying and capturing the complexity of

COVID-19 spread. Early in the project, eight key variables were identified to systematically define and constrain results across the three models.

- Level of reported cases, hospitalizations, and mortalities constrained by aggregated data sources such as USAFacts or the COVID Tracking Project.
- Characterization of COVID-19 testing, including positivity rate, testing strategy, and the timeliness of results. Some of this is available from the COVID Tracking Project, but some will likely need to be obtained where available and extrapolated by as-yet-undetermined methods.
- Effectiveness of contact tracing and social isolation or quarantine following positive test results. This will likely be obtained through detailed analysis of special cases in which data is available and extrapolated through careful perusal of news reports.
- Level of adherence to social isolation measures, including masking and reduction of mobility, and measures derived from nontraditional sources (e.g., social media). Mobility measures are systematically available; others will need to be obtained.
- Timeliness and effectiveness of COVID-19 hospitalizations, together with patient medical risk factors (e.g., immunity, age, gender), treatments, and indirect contributions to morbidity and mortality, that determine outcome.
- Level of protection afforded to vulnerable populations, such as those in long-term medical care, the homeless, or prison populations. This will likely be constrained by contact tracing listings, where available, and extrapolated with unstructured data.
- Level of economic activity or school reopening, and degree of protection available to workers in different sectors. This will likely be constrained by geospatial datasets and aggregated COVID-19 data sources, such as the COVID Tracking Project.

- Vaccination incorporated in a manner that is constrained by preliminary reports.

Figs. 3.11–3.13, beginning on p. 115, capture representative interfaces and assumptions by which EpiGrid, EpiCast, and CityCOVID incorporated the above constraints into their respective modeling architectures.

3.3.3 Systems-Level Modeling of Economics and Public Health Response Strategies

Whereas mechanistic models provide a level of detail and prediction accuracy requisite to the COVID-19 pandemic, systems-level models can cost-effectively target economic questions and general questions of public health strategy. With appropriate access to subject matter experts, these models can be used to develop and capture logic models describing a situation and to elucidate cost-benefit tradeoffs needing optimization.

Median Model

This LANL-led project developed, parameterized, and applied a systems-level model of the public health response, which was described in Fair et al. (2021). This work estimated the best strategies for COVID-19 testing and diagnostics, contact tracing, and quarantine, subject to the constraint of data characterizing the sensitivity, specificity, cost, and logistics of diagnostic tests. It also estimated the best scientific understanding of case presentation, disease progression, and mitigation effectiveness (see Fig. 3.14, p. 118). The work leveraged a decade of experience modeling critical infrastructures of the U.S. government as part of the National Infrastructure Simulation and Modeling Center, which was centered at LANL and SNL.

The starting point of the Median model, developed to model the New Mexico health care system during the pandemic, provided a systems-level description of how testing, contact tracing, and isolation of people with confirmed or suspected COVID-19 infections influence how individuals impact and

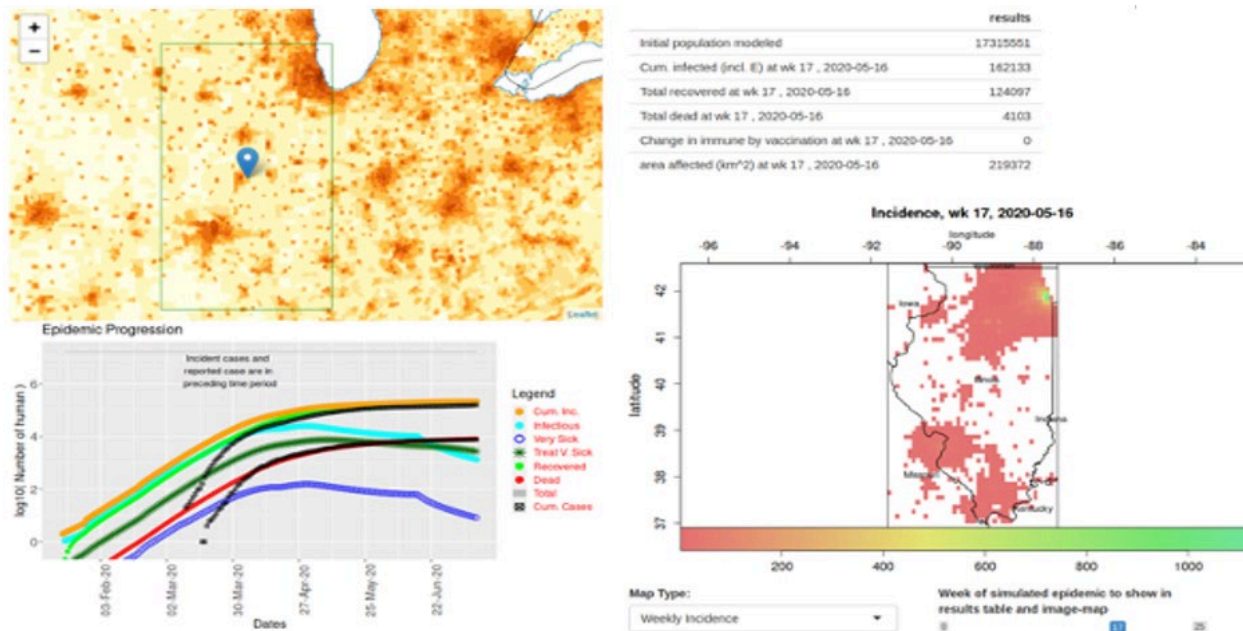


Fig. 3.11. EpiGrid simulation interfaces. Screenshot of an EpiGrid simulation of a rectangular region surrounding the state of Illinois, reproducing reported case counts and mortalities (black symbols in the graphed time series). Cases and deaths are reproduced with a single point introduction in Cook County, and transmissibility is derived from cell phone mobility data. As such, this algorithm can be extended throughout the U.S. Note that this simulation does not attempt to model undercounting. In addition, the by-county comparison of case counts essential to validating the simulation were performed but are not shown. The interface is written as a reactive interface in R Shiny, although a command-line interface has also been written, and the tool has been applied to the eastern half of the U.S. in a single simulation of ~200 million people, requiring ~2 hours of clock time to perform a six-month simulation. The various model parameters available in the EpiGrid model are visible in the screenshot each as an explicit function of time and administrative region down to county-level resolution, including disease progression parameters; spatiotemporal aspects of disease introduction to a region; the ability to mitigate disease progression (medical) and spread (vaccination); contact tracing; isolation-, short-, and long-range movement restriction; and social distancing. A variety of model outputs can be compared to case-count data, with the time course of cases and deaths most useful as model constraints. Hospital loadings and numbers of asymptomatic or contagious people are also available for follow-on analysis. [Courtesy Los Alamos National Laboratory]

propagate through the health care system. As shown in Fig. 3.15, p. 119, newly infected patients can flow through one of three pathways, depending on whether they are spreading disease symptomatically, asymptotically, or after being tested, traced, and isolated. The process of testing, contact tracing, and isolation costs a predictable amount of money for specified system performance, while also enabling reductions in contagious spread and improvements in patient outcomes through earlier and better-targeted health care.

The demographic groups used in the model are as follows:

- Young (ages 0–19)
- Young adults (ages 20–49)
- Adults (ages 50–69)
- Older adults (ages 70–79)
- Elderly (ages 80+)
- Responders

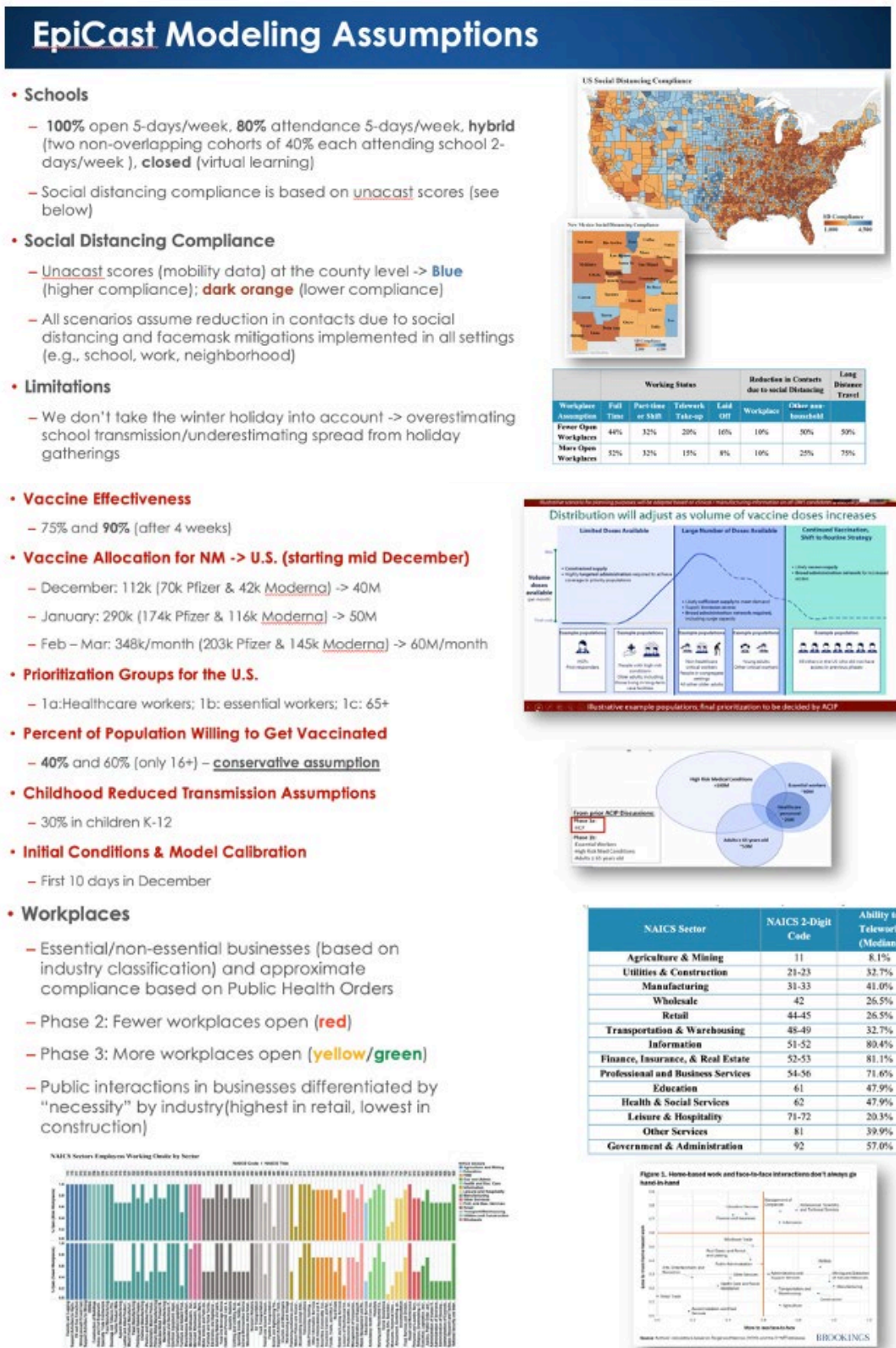


Fig. 3.12. Typical modeling assumptions used in the EpiCast epidemiological simulation model. [Courtesy Los Alamos National Laboratory]

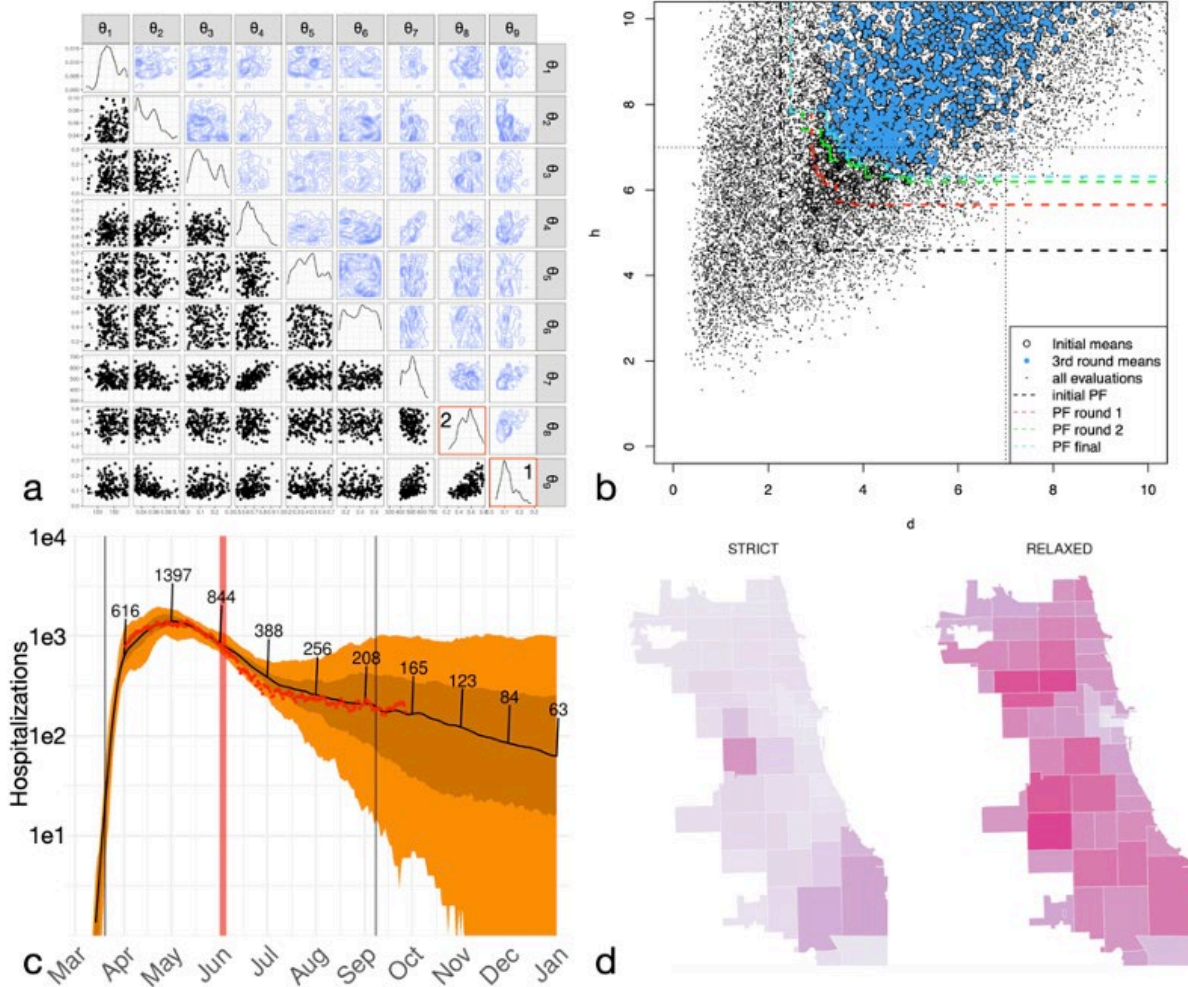


Fig. 3.13. CityCOVID simulation interfaces. [Reprinted under a Creative Commons License (CC BY-NC 4.0) from Ozik, J., et al. A Population Data-Driven Workflow for COVID-19 Modeling and Learning. *International Journal of High Performance Computing Applications* **2021**, **35** (5) 483–499.]

Model parameters described the baseline use of the health care system: 85.1% of the U.S. population saw a physician in 2019, with 8.7% admitted to a hospital for an average of 3–4 days, with 2–4 hours spent in an emergency department, with 0.0028 beds per person and an average occupancy rate of 66%. Additional model parameters developed during close consultation with Presbyterian Hospital Systems of New Mexico describe the resource usage and effectiveness of hospital care for COVID-19 patients during summer 2020.

Additional parameters described not just the mean values, but the full distribution of possibility space (i.e., mean, standard deviation, upper and lower cutoffs) for testing attributes such as the fraction contact traced and quarantined; false negative values for cohort testing (e.g., hospital workers, school children, shelter residents) by particular methods; and turnaround times for testing, contact tracing, and isolation.

The tool's flexibility enabled a wide variety of consequence metrics to be quantified as a function

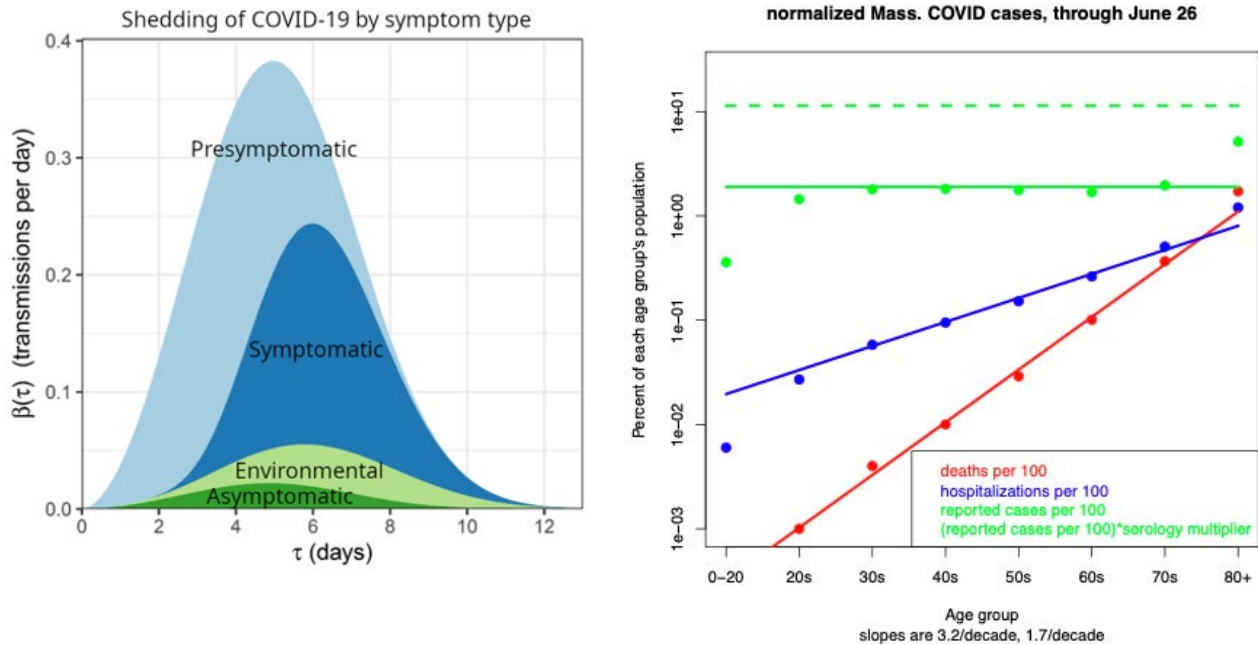


Fig. 3.14. Two examples of critical aspects of COVID-19 are shown incorporated into a systems-level model of public health interventions. Schematic distributions of four types of contagious disease spread across time after infection were taken from the literature (left). Immediately obvious is the importance of pre-symptomatic (but not asymptomatic) spread. Models of the relative importance of testing, contact tracing, and isolation processes depend critically on these distributions; the Median model of COVID-19 spread and its mitigation was built in part on these distributions. Near-raw age-dependent case data from the state of Massachusetts and serology data from the Centers for Disease Control and Prevention are shown for June 26, 2020 (right). Even at the time, it was possible to estimate the age dependence of COVID-19 mortality, hospitalization rates, and under-reporting levels. Such distributions were critical to estimating the direct and indirect economic impacts of COVID-19 as it spread across the country. [Left: Adapted from Ferretti, L., et al. Quantifying SARS-Cov-2 Transmission Suggests Epidemic Control with Digital Contact Tracing. *Science* **2020**, 368, eabb6936. Reused under a Creative Commons License (CC BY 4.0). Right: Courtesy Los Alamos National Laboratory.]

of system performance and COVID-19 disease attributes, including:

- Total COVID-19 cases, hospitalizations, and deaths
- Total outbreak duration
- Total cases and attack rate
- Total deaths (direct and indirect)
- Age breakdowns of the above consequences

Figure 3.16, p. 120, shows the number of cumulative cases as a function of the fraction of COVID-19 cases diagnosed, contact traced, and quarantined

for two different assumptions of the level of asymptomatic spread: 10% and 30%. For the lower level of asymptomatic spread, a relatively low rate of early isolation of cases results in relatively good control of the pandemic consequence, whereas even a 50% rate of contact tracing and isolation at the higher level of asymptomatic spread still results in 1,400 hospitalizations.

By providing salient sensitivities and a well-defined model, the Median model can aid decision-makers in responding to COVID-19, even in the face of changing boundary conditions such as increasing contagiousness of the virus, the presence of

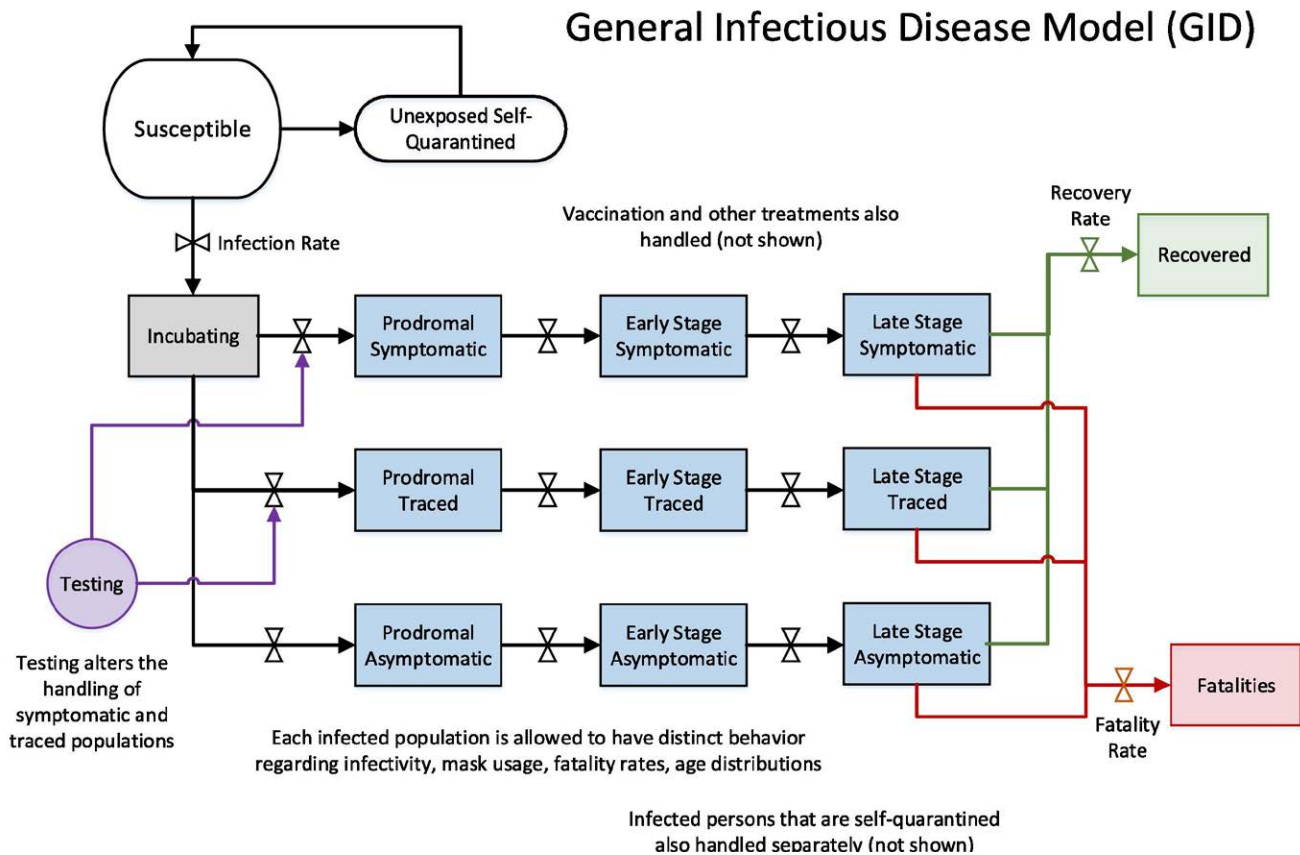


Fig. 3.15. Representation of the multistage SEIR general infectious disease model developed as part of the Median model. [Reprinted under a Creative Commons License (CC BY-NC-ND 4.0) from Fair, J. M., et al. *Systems Dynamics and the Uncertainties of Diagnostics, Testing and Contact Tracing for COVID-19. Methods* **2021**, 195, 77–91.]

vaccines of a specified efficacy, or an evolving understanding of the difficulty of maintaining a suitable level of economic activity and participation in normal life events. This work was possible only through extensive interaction of the project team with other modelers, disease progression experts, decision-makers, and frontline workers in hospital management, public health, economic analysis, and diagnostic testing.

Adaptive Recovery Model

Developed by SNL researchers, the Adaptive Recovery Model (ARM) represents a new approach to designing disease control policies by allocating scarce testing, contact tracing, and vaccination

resources to reduce community transmission of COVID-19 and similar diseases (see Fig. 3.17, p. 121). ARM combines a deterministic compartmental disease model with a stochastic network disease propagation model to enable simulation of COVID-19 community spread through the lens of two complementary modeling motifs. ARM contact networks are derived from cell-phone location data that have been anonymized and interpreted as individual arrivals to specific public locations. Modeling disease spread over these networks allows the identification of locations within communities conducive to rapid disease spread. ARM applies this model- and data-derived abstraction of community transmission to evaluate the effectiveness

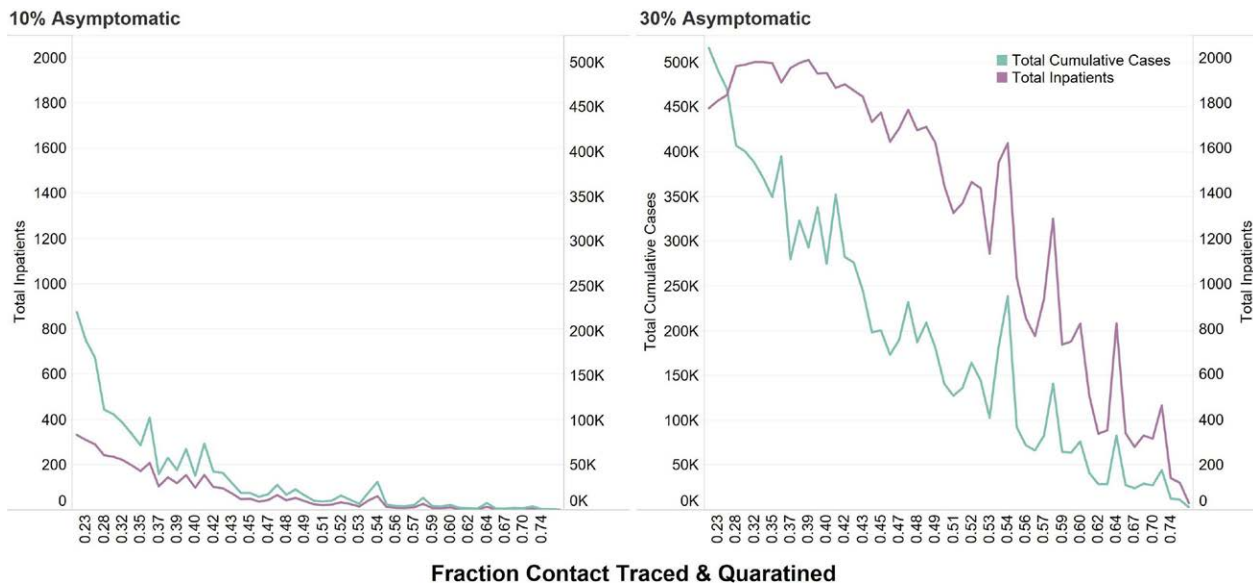


Fig. 3.16. Total inpatient COVID-19 hospitalizations and total cases as a function of the fraction of cases contacted, traced, and quarantined for two different assumptions of the level of asymptomatic spread: 10% (left) and 30% (right). [Reprinted under a Creative Commons License (CC BY-NC-ND 4.0) from Fair, J. M., et al. Systems Dynamics and the Uncertainties of Diagnostics, Testing and Contact Tracing for COVID-19. *Methods* **2021**, 195, 77–91.]

of disease control measures including targeted social distancing, contact tracing, testing, and vaccination. The ARM architecture provides a unique capacity to help decision makers understand how best to deploy scarce testing, tracing, and vaccination resources to minimize disease-spread potential in a community. In addition to providing optimal control strategies across a range of potential interventions, ARM has been applied to designing vaccine distribution strategies for multi-dose formulations across multiple viral variants.

Medical Resource Demand Model

Sandia's Medical Resource Demand (MRD) model calculates resource demands for treating COVID-19 patients based on disease spread projections from epidemiological models. The MRD model is a detailed healthcare-facility treatment model coupled with an AI-derived estimate of location-specific comorbidities to generate high-precision estimates of each patient's care trajectory and eventual outcome. Medical resources, defined as

personnel (physicians, nurses, techs, housekeeping), consumables (sedatives, analgesics, PPE, cleaning products), and committed resources (hospital beds, ventilators, ICU beds, metered-dose inhalers) are accurately determined for each patient's probable facility stay, yielding daily resource utilization metrics on a facility, county, or statewide level (see Fig. 3.18, p. 121). By comparing computed resource demands to near-real-time estimates of real-world availability, the MRD model predicts times and locations of medical resource shortfalls throughout an outbreak.

Uniquely, the MRD model is epi-agnostic in that it can utilize outputs from a range of epi models to generate corresponding resource demand estimates, thus enabling planners to contrast the logistics implications of different epidemiological model derived scenarios. The model applies state-of-the-art uncertainty quantification methods to provide decision makers with rigorously derived uncertainty metrics for each defined medical resource category (e.g., gloves, beds,

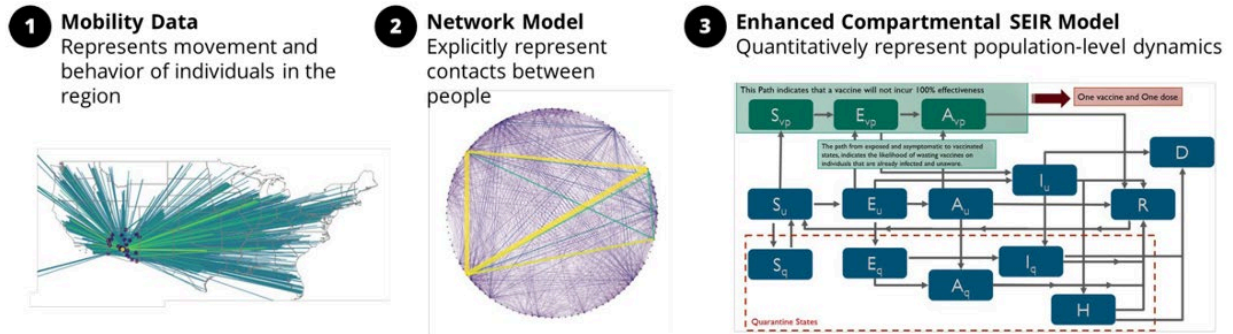


Fig. 3.17. Main components of the hybrid Adaptive Response Model (ARM) which enables decision makers to optimally balance supply-limited outbreak control resources most effectively. [Courtesy Sandia National Laboratories]

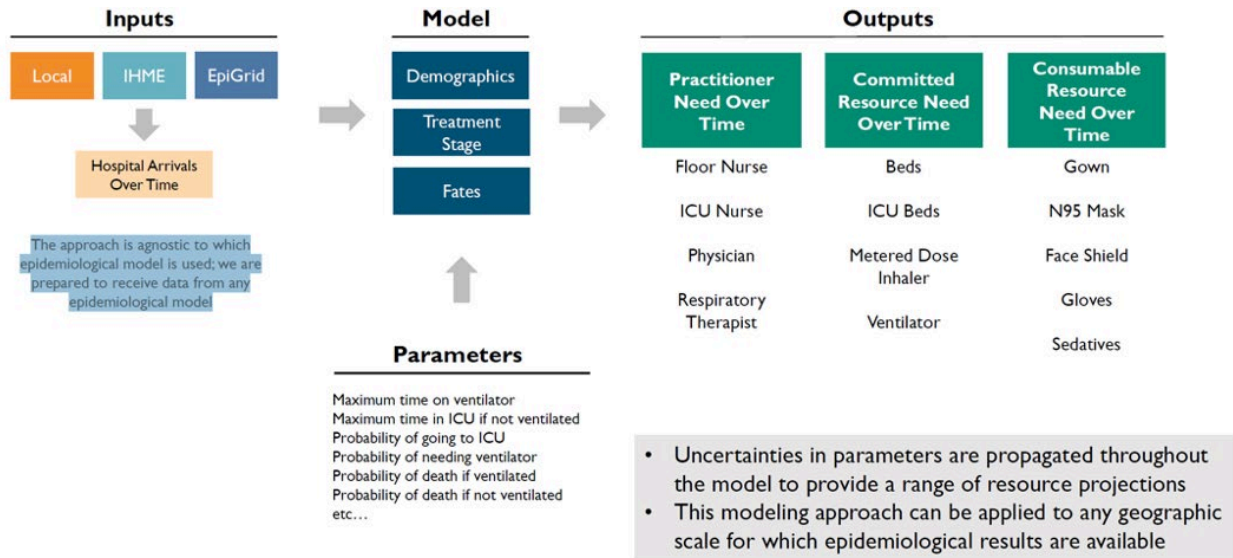


Fig. 3.18. Schematic of the Medical Resource Demand (MRD) model, which enables incorporation of epidemiological modeling outputs from varied sources and representative medical resource categories. [Courtesy Sandia National Laboratories]

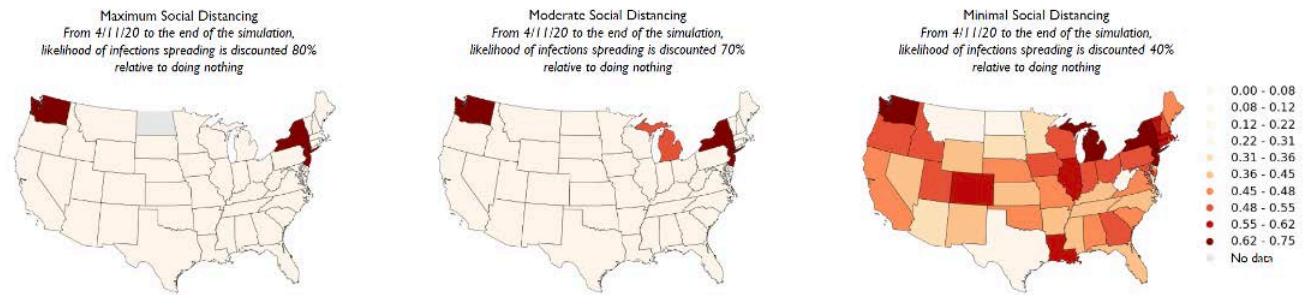
pulmonologists) to aid in evaluating options for resupply and shifting of resources in response to disease spread dynamics (see Fig. 3.19, p. 122). During 2020, the MRD model generated demand estimates at county and state-level granularity, along with maps of anticipated resource shortfalls. Additionally, the system generates optimal resource reallocation strategies to assess the cost and time required to address anticipated resource

shortfalls by transporting resources in critically short supply from regions of relative abundance.

3.4 Task 3: COVID-19 Pandemic Modeling and Analysis Platform Development

Availability of nonpharmaceutical interventions to reduce the impact and spread of COVID-19 requires collaborative development of policies and guidance

Probability of Exceeding ICU Bed Capacity



Note that with decreasing degree of social distancing (from left to right in above maps), the probability of exceeding capacity of ICU beds across the country increases significantly.

Fig. 3.19. Example outputs of the Medical Resource Model (MRM) in April 26 2020, based on patient loads calculated by Los Alamos National Laboratory's EpiGRID epidemiological model for three specified social distancing scenarios. [Courtesy Sandia National Laboratories]

among government, academia, the medical establishment, and the public. To operationalize this effort, the team developed an all-encompassing situational awareness platform (see Section 3.4.5, p. 128) that can process multimodal and multi-source data, enabling informed decision-making. In addition to showing the current spread of infection, the platform also captures the impact of human dynamics on infection spread and the location and availability of critical infrastructure, prediction, and HPC-driven simulation. The platform is extensible, allowing third-party integration and services to consume the curated data and analytics in near-real time. The platform is expected to augment critical decision-making for reducing the impact and spread of the pandemic.

The main objective of this task was to develop an integrated COVID-19 pandemic monitoring, modeling, and analysis capability that includes: (1) historical and current spatiotemporal trends of disease spread; (2) estimates of required hospital beds, ICU beds, and ventilators; (3) needed testing capacity. The capability must also quantify the effectiveness of implemented interventions and

mitigation strategies. To address these challenges, the team developed and operationalized an agile, online COVID-19 platform for integrating, synthesizing, analyzing, and visualizing geographically resolved data (collected as part of this effort) and for conveying modeling and simulation results that anticipate future COVID-19 transmission dynamics.

The COVID-19 Pandemic Modeling and Analysis platform was built by hybridizing Lambda and hyperscale architectures to achieve real-time analytics and visualization of spatiotemporally disparate datasets through load-aware vertical and horizontal scaling of available infrastructure with zero downtime. The platform offers two key application-level functions:

- Ability to ingest and merge structured and unstructured data sources curated in support of the COVID-19 platform from multiple sources, including hospitals, regional governments, social media, and other crowdsourced outlets, related to the spread of COVID-19 and other infectious diseases.

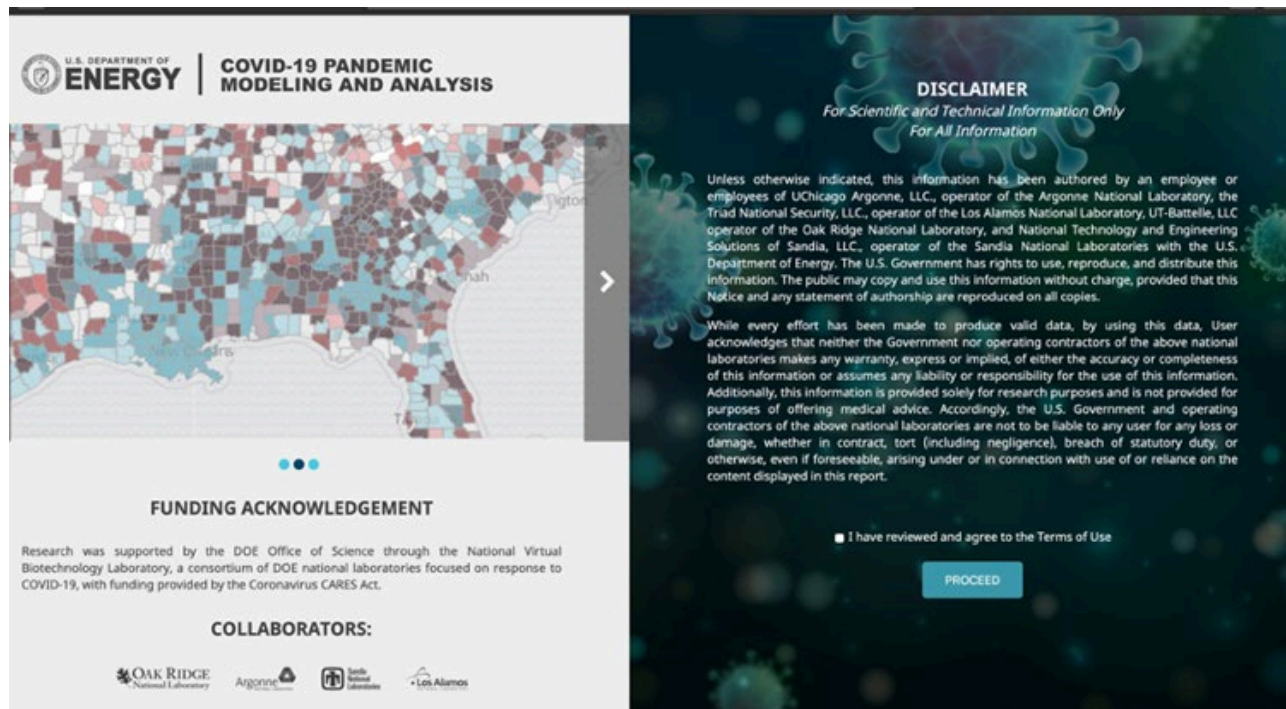


Fig. 3.20. COVID-19 Pandemic Modeling and Analysis platform landing page. [Courtesy Sandia National Laboratories]

- A substantive system for merging and scientifically analyzing multiple, disparate open-source data streams (e.g., COVID-19 cases, Twitter content, quarantine maps, demographic context, and news feeds); physical data (e.g., temperature, precipitation); and modeling and simulation outcomes. The work leverages hyperscale architecture for data curation, analysis, and visualization of a range of curated and modeled data.

The platform includes eight dashboards.

- DOE COVID-19 Situational Awareness Dashboard
- National, State, and County–level Report Card
- DOE Predictive Analytics Visualization Dashboard
- Testing Dashboard
- Three model-specific dashboards: EpiCast, EpiGrid, CityCOVID
- Ensemble Visualization

3.4.1 Architecture

The COVID-19 Pandemic Modeling and Analysis platform was built on the principles of Lambda and hyperscale architectures to address the challenges of combining disparate data sources and dynamically scaling them to address computational challenges. Figure 3.20, this page, shows the platform's landing page. The architecture benefits from using widely available off-the-shelf servers and computational equipment. The platform can be scaled as a function of load and latency to accommodate additional users and requests, and the architecture can be scaled both vertically and horizontally, maximizing in-built fault tolerance and cost-effectiveness.

Figure 3.21, p. 124, shows the platform architecture components including data collection and processing, a distributed data grid to expedite data transfer and reduce latency, an application server interface, machine learning, and data quality

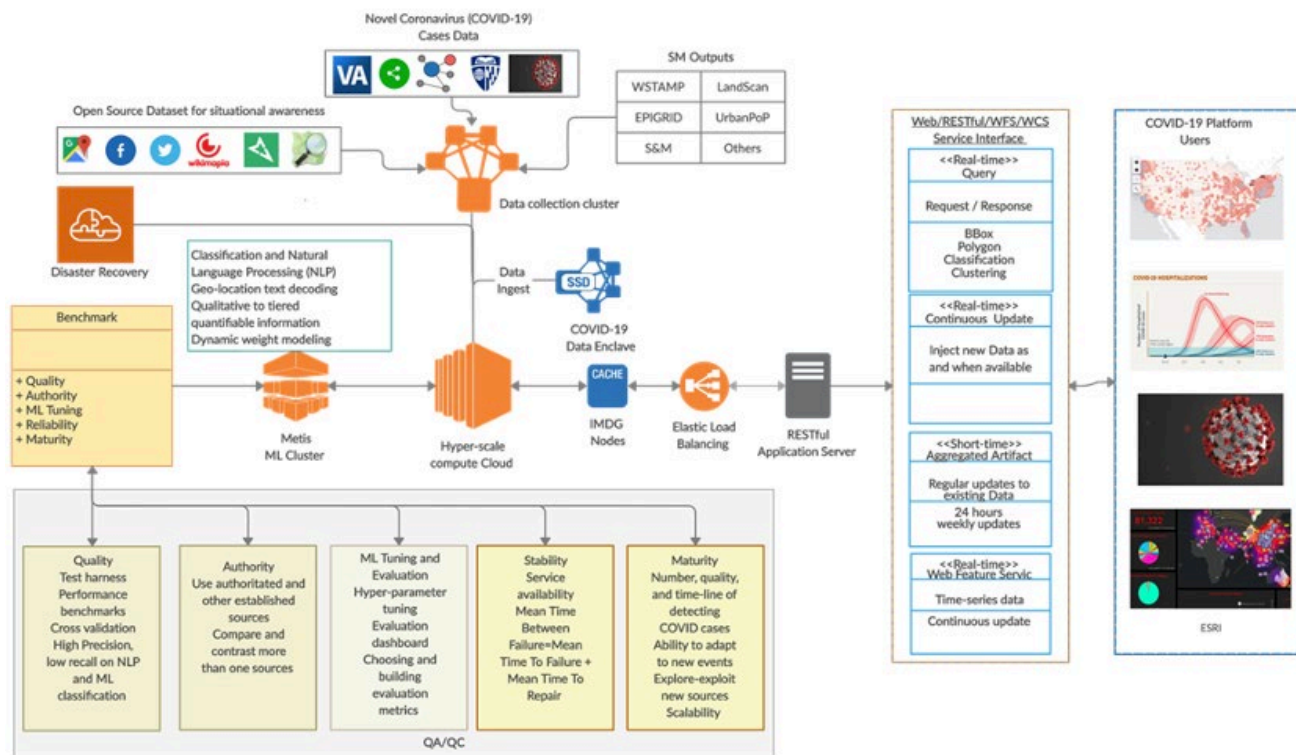


Fig. 3.21. COVID-19 Pandemic Modeling and Analysis platform architecture. [Reprinted from Thakur, G., et al. COVID-19 Joint Pandemic Modeling and Analysis Platform. *Proceedings of the 1st ACM SIGSPATIAL International Workshop on Modeling and Understanding the Spread of COVID-19 (COVID-19)*. 2020, Association for Computing Machinery, New York, 43–52. DOI: 10.1145/3423459.3430760.]

evaluation. Each component is discussed in the next sections.

Data Collection

The team collected and curated high-quality authoritative data to build the platform. This phase involved discovering relevant data sources, sanitizing and transforming the new data, and deduplicating and semantically conflating the data with other existing data sources. The data collection's geographic coverage is the entire planet, and the spatial granularity goes to the county or even census block group levels. Data gathering should be performed continuously and in real time to ensure insights are current. On average, over 100 data sources were searched daily and several million records were collected in an automated effort that included a human in the loop only when necessary.

The team's approach to conflate multiple data sources is shown in Fig. 3.22, p. 125.

Data Processing and Analytics

The team used RESTful APIs (application processing interfaces) to access the data for processing and analytics. Boilerplate templates were made available for developers to generate analytics via natural language processing and machine learning. In addition to authoritative data, the platform harvests social media data (e.g., tweets) to gather information about infection spread and response. Classification models can be built to evaluate communication and assess the impact of disease on health. Rigorous benchmarks that include quality control, tuning, and maturity of results are evaluated before releasing the results.

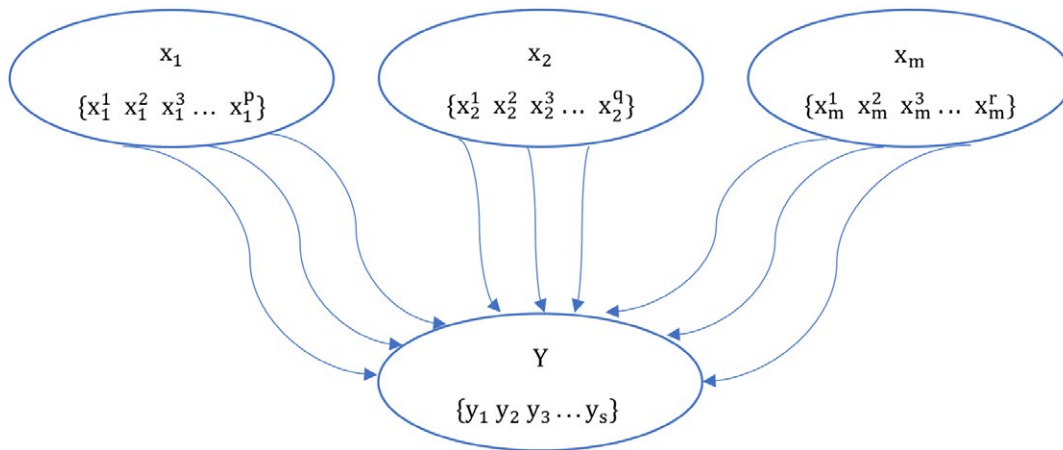


Fig. 3.22. Unified mapping format for disparate data sources. [Reprinted from Thakur, G., et al. COVID-19 Joint Pandemic Modeling and Analysis Platform. *Proceedings of the 1st ACM SIGSPATIAL International Workshop on Modeling and Understanding the Spread of COVID-19 (COVID-19)*. 2020, Association for Computing Machinery, New York, 43–52. DOI: 10.1145/3423459.3430760.]

Quality Assurance and Quality Control

A suite of spatiotemporal and statistical data processing templates was developed to gather insights from the data. In addition, visualization packages such as Vega and custom ensemble visualization have been integrated into the platform to allow for development of interactive dashboards and report processing. At times, the platform ingests direct results of simulation or predictive models for the purpose of visualization.

Distributed HyperCache

Developing elastic architectures that scale as a function of an evolving computing workload is essential for real-time applications. Significant advances have been made in hyperscalable storage, data centers, and cloud computing infrastructure to accommodate the exponential increase of such workloads. This architecture utilizes the distributed memory of nodes to improve storage latency that simultaneously processes and retrieves a large amount of disparate data for real-time analysis. HyperCache was implemented in the form of an In-Memory Distributed Grid built on top of the direct-attached storage computing cluster running simultaneous applications. These

applications communicate with HyperCache via client–server architecture for maximum compatibility. A monitoring system is developed and deployed for performance benchmarking and to provide essential support during exponential data compute workloads. A simple representation of adding/updating and removing the element in HyperCache is shown in Fig. 3.23, p. 126.

Replicated Data Management

This section addresses fault tolerance and approaches taken to ensure the platform remains accessible and robust. The platform manages data integrity through replication across multiple servers. As shown in Fig. 3.24, p. 127, a database index is broken down into four primary shards (i.e., pieces) and four replicated shards in the platform’s release plan workflow. The shards are distributed across six nodes in such a way that if any machine is down or data corruption takes place, the database can still be rebuilt, and no data loss occurs. The platform maintains global consistency by frequently broadcasting updates and propagating them on all the nodes (see Fig. 3.25, p. 127). In addition to replicating the data across the cluster, a remote disaster recovery site was also deployed

Algorithm 1: Algorithm for server-side HyperCache

```

Function Remove(key) return value
  Data: Distributed map
  Result: value of element to be removed
  acquire_lock();
  value ← remove(hmap, key);
  if value != null then
    return value;
    sync_cache();
    wait();
  else
    return null;
  release_lock();

Function Update(key, value) return result
  Data: Distributed map
  Result: value of element to be updated
  acquire_lock();
  result ← update(hmap, key);
  if result != 1 then
    return false;
  else
    return true;
  sync_cache();
  wait();
  release_lock();

```

Fig. 3.23. HyperCache algorithm. [Reprinted from Thakur, G., et al. COVID-19 Joint Pandemic Modeling and Analysis Platform. *Proceedings of the 1st ACM SIGSPATIAL International Workshop on Modeling and Understanding the Spread of COVID-19 (COVID-19)*. 2020, Association for Computing Machinery, New York, 43–52. DOI: 10.1145/3423459.3430760.]

to keep operations running in case of major failures (e.g., natural disaster). The team utilized the Google Cloud Platform as DRaaS (Disaster Recovery as a Service) to snapshot and back up the status of the database every four hours (see Fig. 3.21, p. 124). Because the snapshots are not instantaneous and are asynchronous with respect to time and data integrity, this approach uses incremental backup strategies to save changes quickly and efficiently. The cloud serves only as a backup and remote location to store data. When the snapshot

is in progress, new data can be added and other requests can be made of the cluster.

3.4.2 Roles and Credentials

Two sets of roles were released to enable proper authorization and authentication for end users. The roles include (1) DOE headquarters, national laboratories, and collaborators and (2) other federal agencies.

Spaces were created for containing visualization dashboards. Role-based access to spaces dictate what logged-in users can and cannot see. DOE-affiliated users can access interactive situational awareness and predictive analytics, model-specific dashboards, and ensemble visualizations.

3.4.3 Release Plan

The onset and rapid spread of COVID-19 created an immediate need to deploy a reliable and stable situational awareness platform accommodating inputs generated by several research entities. It was critically important that this platform display key scientific findings for policy guidance and informed decision-making within schedule, quality, and effort constraints. This led the team to formalize a systematic release plan workflow for the selection and development of features and their incremental release at regular intervals. Each release addresses the production of meaningful insights and new features developed by the participating research entities. This also allowed all the moving parts of the collaboration to work in sync toward a common goal and enabled end users to anticipate changes and updates. The release plan workflow is shown in Fig. 3.26, p. 128. The platform also monitors use of its services, detection of spurious activities, report generation, and allocation of resources to allow a third-party application to utilize the analytics and data stream. The post-deploy release step is useful for extending the platform and measuring use.

3.4.4 Hotspot Detection

Spatial hotspot analysis can identify clustering areas of a spatial phenomenon. To help

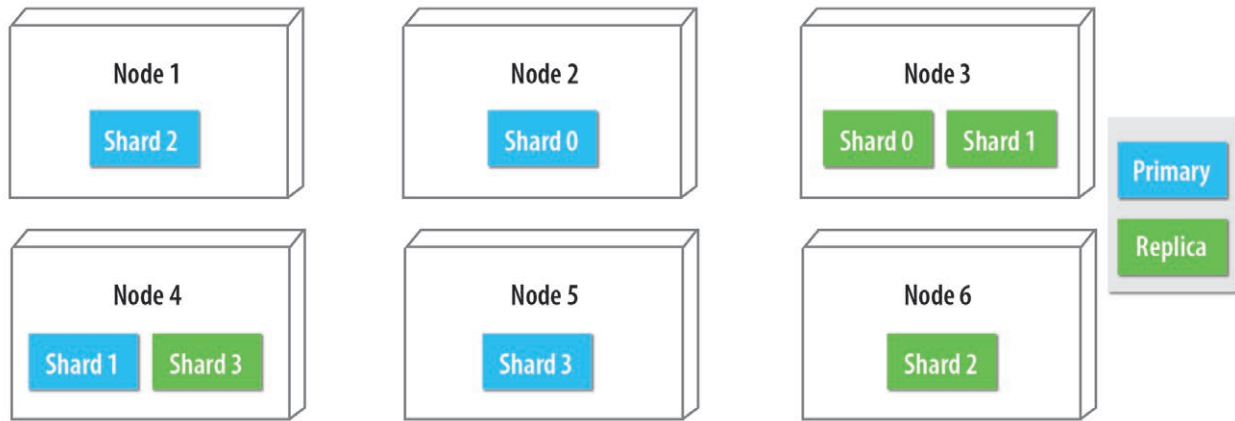


Fig. 3.24. Replicated data management. [Reprinted from Thakur, G., et al. COVID-19 Joint Pandemic Modeling and Analysis Platform. *Proceedings of the 1st ACM SIGSPATIAL International Workshop on Modeling and Understanding the Spread of COVID-19 (COVID-19)*. 2020, Association for Computing Machinery, New York, 43–52. DOI: 10.1145/3423459.3430760.]

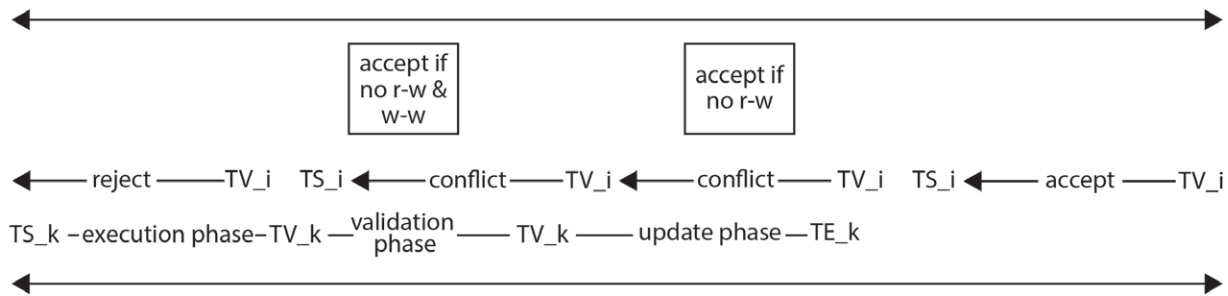


Fig. 3.25. Optimistic concurrency control to store integrity of the database records. [Reprinted from Thakur, G., et al. COVID-19 Joint Pandemic Modeling and Analysis Platform. *Proceedings of the 1st ACM SIGSPATIAL International Workshop on Modeling and Understanding the Spread of COVID-19 (COVID-19)*. 2020, Association for Computing Machinery, New York, 43–52. DOI: 10.1145/3423459.3430760.]

decision-makers better understand the U.S. geographic patterns associated with COVID-19, the team developed a hotspot detection module for the platform. For the initial version, the team selected two metrics (i.e., cases per 100k population and deaths per 100k population) that capture the prevalence and seriousness of COVID-19 in a region. In the future, the hotspot detection module can easily be extended to detect hotspots for other types of metrics (e.g., positive rate of testing, hospitalization). The raw data for hotspot detection is collected from the Johns Hopkins University

Data Archive, which provides daily updates of confirmed positive U.S. cases and deaths at the county level. The raw data is cleaned and then joined with census data to provide population data, with U.S. county shape files providing spatial information. For each county, the number of confirmed COVID-19 cases per 100k population and deaths per 100k population were calculated.

The hotspot detection algorithm uses the Getis-Ord G_i^* statistic, which looks at each county within the context of neighboring counties and against the

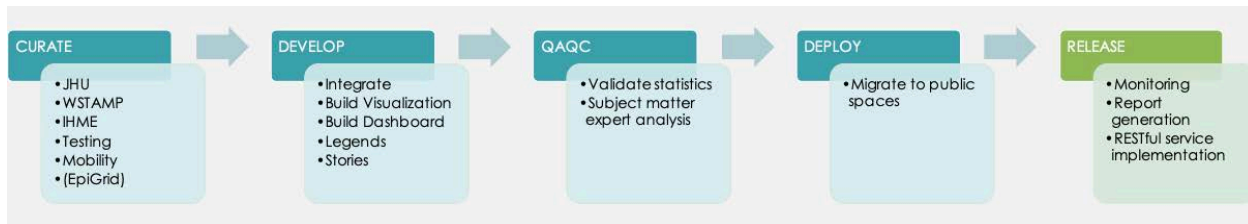


Fig. 3.26. COVID-19 Pandemic Modeling and Analysis Platform release plan workflow. [Reprinted from Thakur, G., et al. COVID-19 Joint Pandemic Modeling and Analysis Platform. *Proceedings of the 1st ACM SIGSPATIAL International Workshop on Modeling and Understanding the Spread of COVID-19 (COVID-19)*. 2020, Association for Computing Machinery, New York, 43–52. DOI: 10.1145/3423459.3430760.]

national average to determine whether a county is a hotspot or not. In the equation in Fig. 3.27, this page, n is the total number of features, x_j is the attribute value of the target feature, and w_{ij} is the spatial weight between features i and j . The G_i^* statistic accounts for both national average and neighborhood average. A county that has a high value and is surrounded by other counties with high values is a statistically significant hotspot.

The G_i^* statistic calculated for each county is a z-score. If the z-score is statistically significant, the larger the z-score is, the higher the confidence that high values will cluster (i.e., a hotspot). Because the significance of each county is tested individually during hotspot detection, there could be false positives due to multiple testing instances. Therefore, the corrected p -value cutoff must be calculated to correct the bias of multiple testing. The corrected p -value is used for hotspot visualization in the platform. Figure 3.28, p. 129, shows hotspot visualizations for cases per 100k population and deaths per 100k population.

3.4.5 DOE COVID-19 Situational Awareness Dashboard

The DOE COVID-19 Situational Awareness dashboard (see Fig. 3.29, p. 130) integrates several capabilities developed by various national laboratories to serve as a situational awareness and analytics platform enabling users to (1) assess the dynamic nature of the curve (i.e., cases and deaths; trends; and growth rates at global, state,

$$G_i^* = \frac{\sum_{j=1}^n w_{i,j} x_j - \bar{X} \sum_{j=1}^n w_{i,j}}{S \sqrt{\frac{n \sum_{j=1}^n w_{i,j}^2 - \left(\sum_{j=1}^n w_{i,j}\right)^2}{n-1}}}$$

$$\text{where } \bar{X} = \frac{\sum_{j=1}^n x_j}{n} \text{ and } S = \sqrt{\frac{\sum_{j=1}^n x_j^2}{n} - (\bar{X})^2}$$

Fig. 3.27. Hotspot detection. [Reprinted from Thakur, G., et al. COVID-19 Joint Pandemic Modeling and Analysis Platform. *Proceedings of the 1st ACM SIGSPATIAL International Workshop on Modeling and Understanding the Spread of COVID-19 (COVID-19)*. 2020, Association for Computing Machinery, New York, 43–52. DOI: 10.1145/3423459.3430760.]

and county levels), (2) measure mitigation policies against the curve, (3) anticipate future curve states, (4) evaluate impacts to health care infrastructure, and (5) use space and time analytics to assess impact and monitor potential recovery efforts. Twenty-three unique layers were created within the situational awareness dashboard.

- Dynamic growth maps at country, state, and county resolutions
- COVID-19 cases and deaths maps and temporal trend charts at country, state, and county resolutions
- COVID-19 testing data
- Mobility reduction maps and trend charts

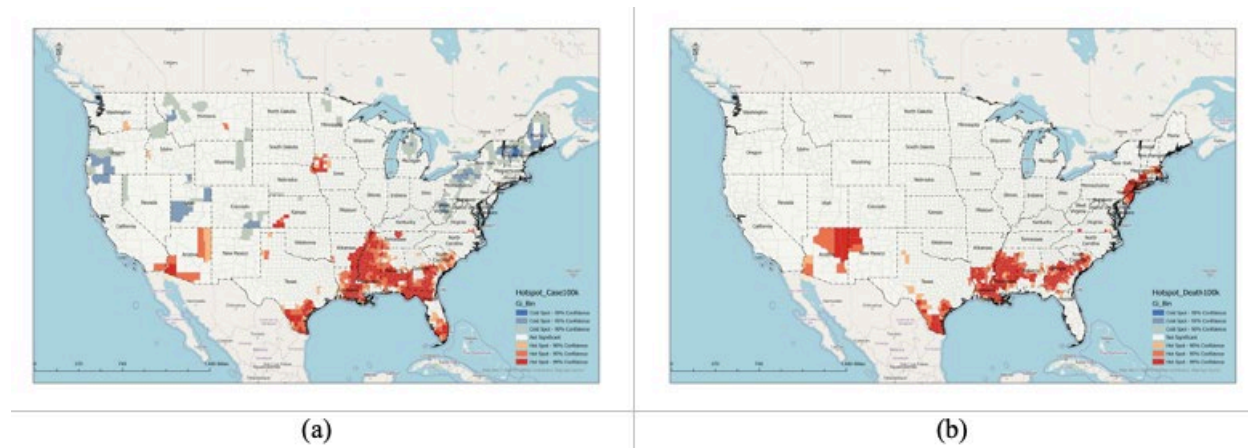


Fig. 3.28. Hotspot visualization for (a) cases per 100k population and (b) deaths per 100k population. [Reprinted from Thakur, G., et al. COVID-19 Joint Pandemic Modeling and Analysis Platform. *Proceedings of the 1st ACM SIGSPATIAL International Workshop on Modeling and Understanding the Spread of COVID-19 (COVID-19)*. 2020, Association for Computing Machinery, New York, 43–52. DOI: 10.1145/3423459.3430760.]

- R_0 trend charts
- Infrastructure layers
- LandScan population
- Hospitals

3.4.6 National, State, and County Level Report Cards

The COVID-19 Pandemic Modeling and Analysis platform contains a reporting capability to provide national-, state-, and county-level report cards as downloadable PDFs with accelerating, decelerating, and constant growth county names, growth rates, new cases in the previous seven days, R_0 , and mobility curves. Figure 3.30, p. 131, shows output from the platform's national-, state-, and county-level report cards. Output from the platform's DOE predictive analytics visualization dashboard is shown in Fig. 3.31, p. 132.

Short-Term Forecast Models with Daily Updates

Institute for Health Metrics and Evaluation (IHME)

IHME's COVID-19 projections were developed in response to requests from the University of

Washington School of Medicine and other U.S. hospital systems and state governments working to determine when COVID-19 would overwhelm their ability to care for patients. The forecasts showed demand for hospital services, including ventilators, general hospital beds, and ICU beds, as well as daily and cumulative deaths due to COVID-19 (<http://www.healthdata.org/covid>). Figures 3.32 and 3.33, p. 133, show visualizations of IHME data.

COMBO Model Predictions at MSA Level and LANL Mechanistic Model Predictions at State Level and MSA Level

To increase situational awareness and support evidence-based policymaking, LANL formulated two types of mathematical models for COVID-19 transmission within a regional population. One is a fitting function that can be calibrated to reproduce an epidemic curve with two timescales (COMBO Model). The other is a compartmental model (LANL Mechanistic Model) that accounts for quarantine/self-isolation, social distancing, a nonexponentially distributed incubation period, asymptomatic individuals, and mild and severe forms of symptomatic disease. Using Bayesian methods, LANL recalibrates both models daily

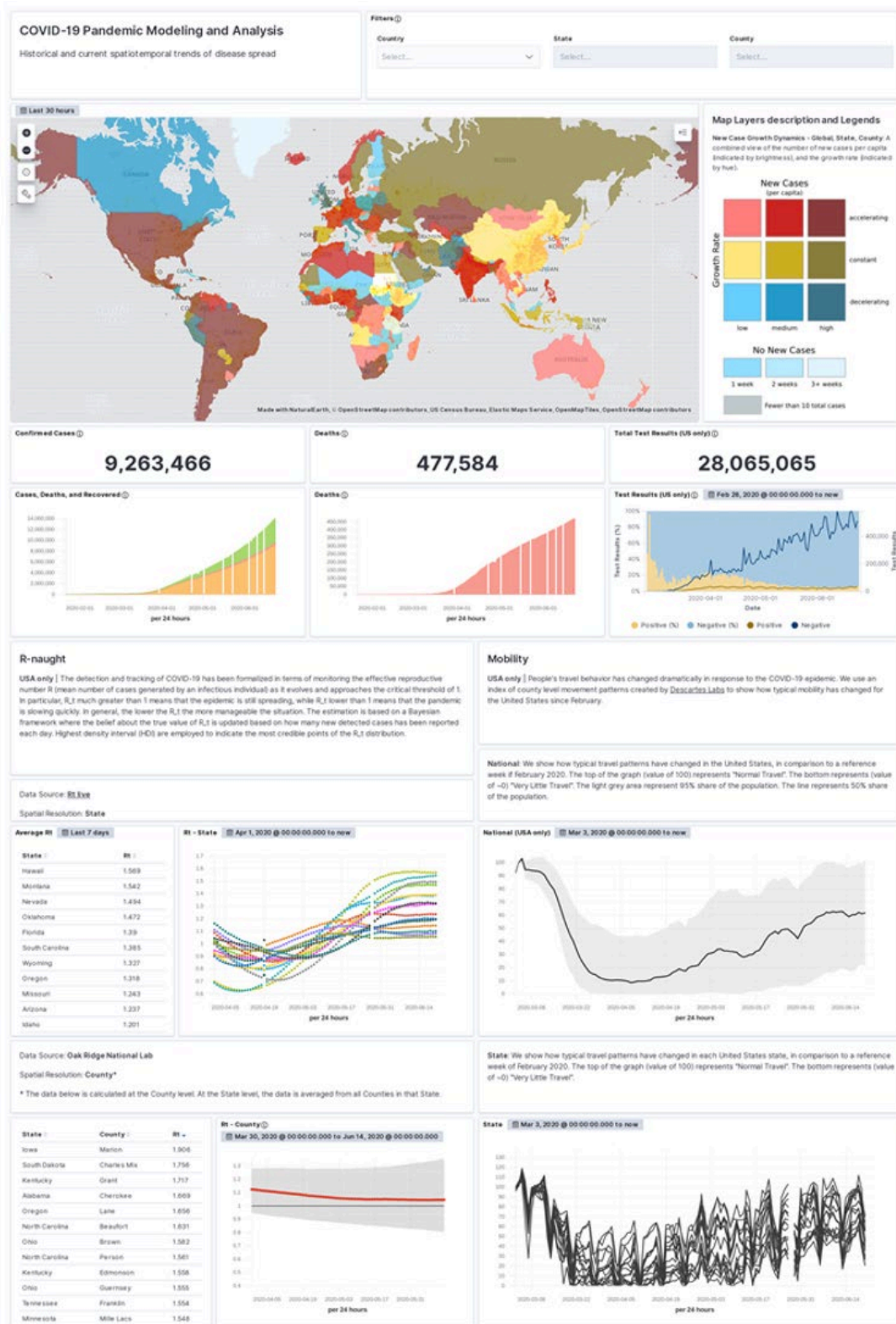


Fig. 3.29. Real-time COVID-19 Situational Awareness dashboard. [Reprinted from Thakur, G., et al. COVID-19 Joint Pandemic Modeling and Analysis Platform. *Proceedings of the 1st ACM SIGSPATIAL International Workshop on Modeling and Understanding the Spread of COVID-19 (COVID-19)*. 2020, Association for Computing Machinery, New York, 43–52. DOI: 10.1145/3423459.3430760.]

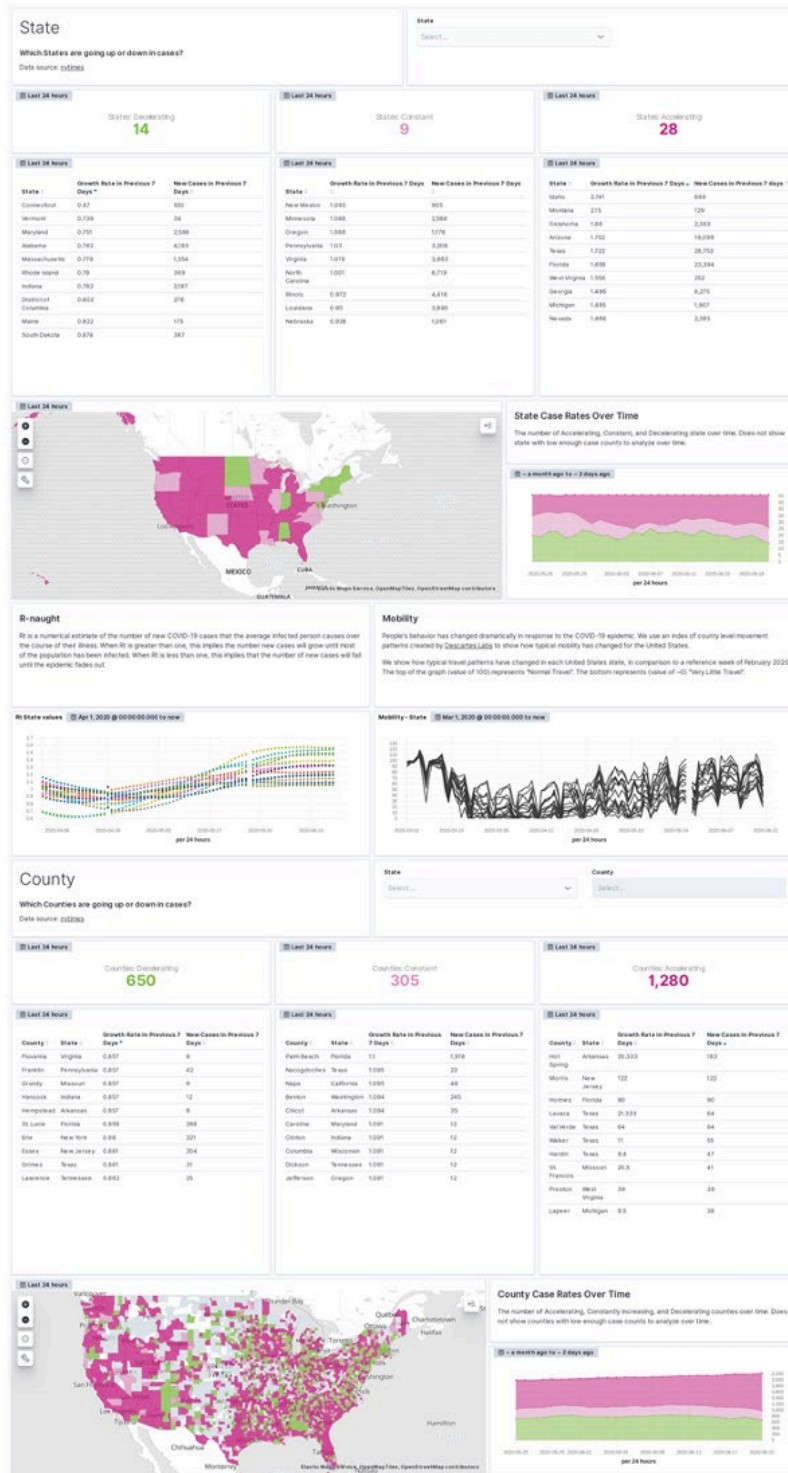


Fig. 3.30. Output from the COVID-19 Pandemic Modeling and Analysis platform, which provides report cards at the national, state, and county levels. [Courtesy Oak Ridge National Laboratory]

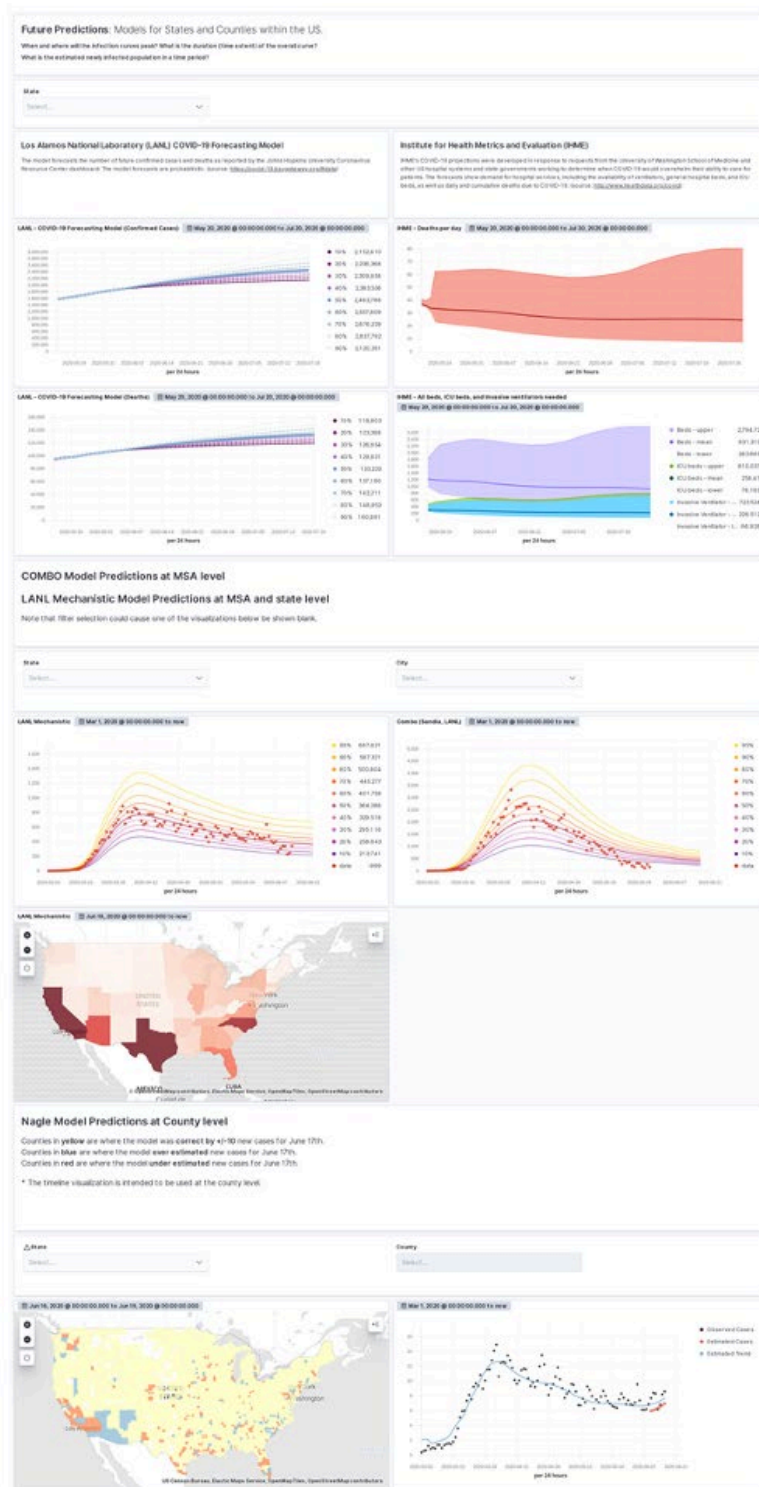


Fig. 3.31. DOE COVID-19 predictive analytics visualization dashboard. [Courtesy Oak Ridge National Laboratory]

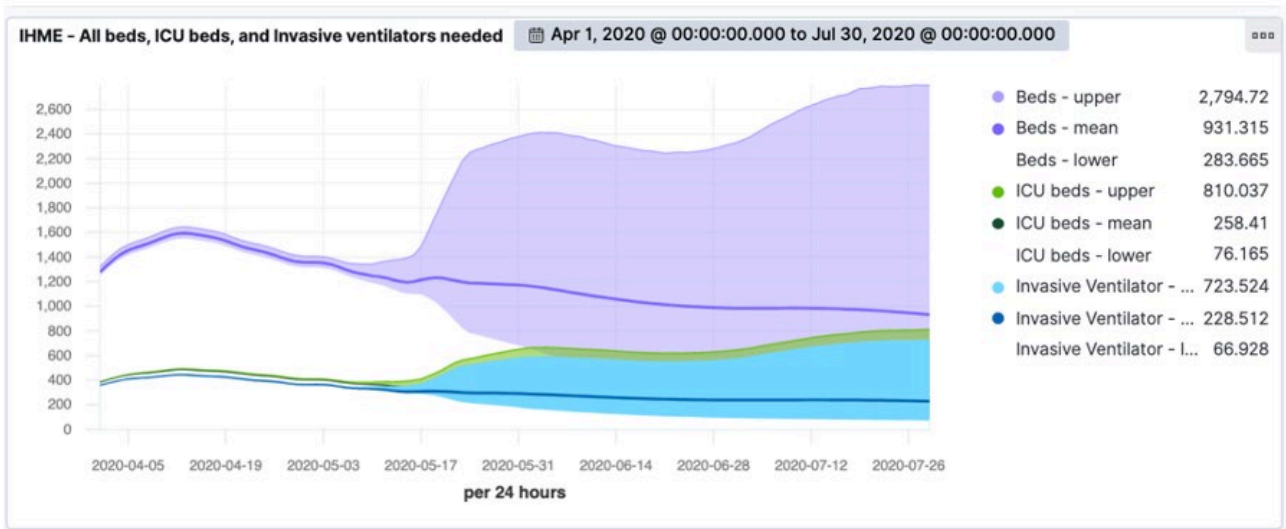


Fig. 3.32. IHME data visualization showing the needed number of general hospital beds, ICU beds, and invasive ventilators during spring and summer 2020. [Courtesy Oak Ridge National Laboratory]

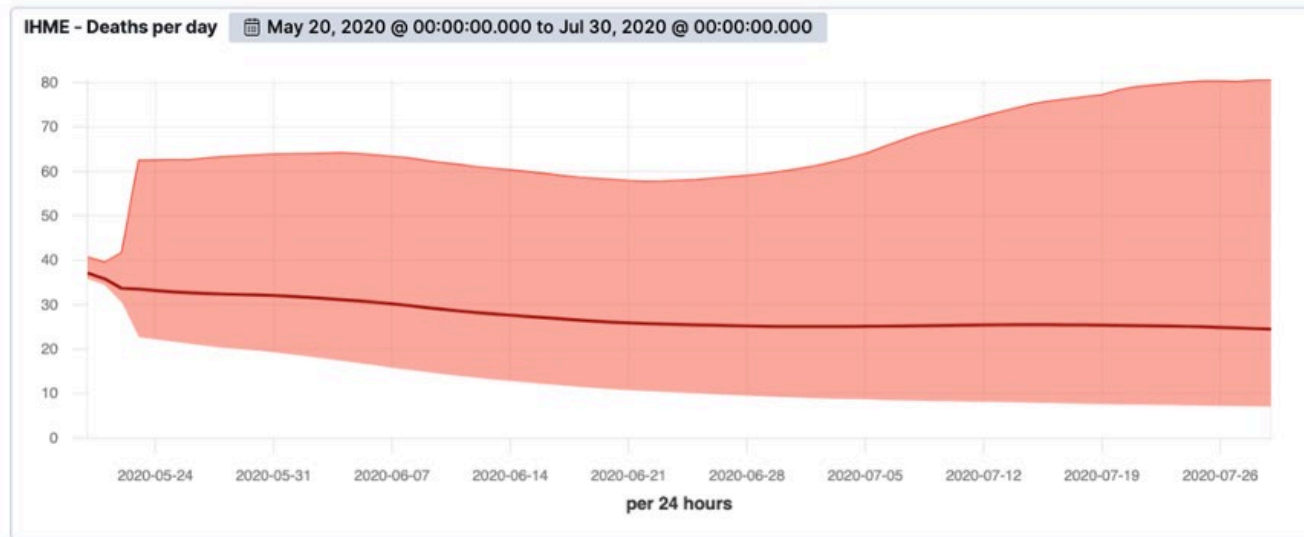


Fig. 3.33. IHME data visualization showing deaths per day during spring and summer 2020 due to COVID-19. [Courtesy Oak Ridge National Laboratory]

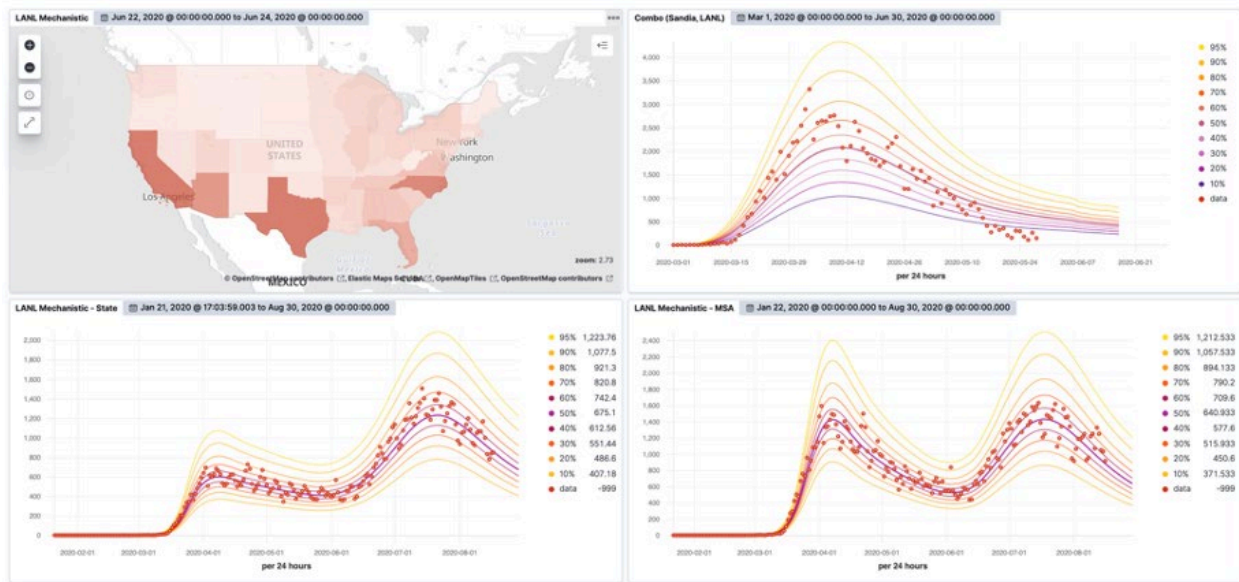


Fig. 3.34. Data visualizations using COMBO Model Predictions, a mathematical model for COVID-19 transmission within a regional population. [Courtesy Oak Ridge National Laboratory; See also: Thakur, G., et al. COVID-19 Joint Pandemic Modeling and Analysis Platform. In Proceedings of the 1st ACM SIGSPATIAL International Workshop on Modeling and Understanding the Spread of COVID-19 (COVID-19). *Proceedings of the 1st ACM SIGSPATIAL International Workshop on Modeling and Understanding the Spread of COVID-19, 2020*. 43–52.]

for consistency, adding new reports of confirmed cases from the 15 most populous MSAs in the U.S. and quantifies uncertainty in future new case report predictions. This online machine learning approach allows for identification of surveillance data anomalies in the face of case reporting variability. Filter selection is required to ensure the visualization displays appropriate data. Figure 3.34, this page, shows visualizations of the COMBO Model Predictions data.

LANL COVID-19 Forecasting Model

This model forecasts the number of future confirmed cases and deaths using data reported by the Johns Hopkins University Coronavirus Resource Center dashboard. The model forecasts are probabilistic (<https://covid-19.bsvgateway.org/#data>). Fig. 3.35, p. 135, shows visualizations of LANL COVID-19 Forecasting Model data.

Long-Term Forecast Models with Updates Every Few Weeks

EpiCast

EpiCast, an epidemiological model developed at LANL, uses a variety of inputs (e.g., age structure at census tract level) and can be configured to represent a variety of COVID-19 mitigation rules implemented in different areas around the United States. Data for the visualizations in Fig. 3.36, p. 135, were aggregated to the county level. The map includes layers related to the number of cumulative cases, symptomatic individuals (i.e., active cases), hospitalized individuals, individuals in an ICU, and individuals on ventilators. It should be noted that the model output does not account for resource availability (e.g., shortages in hospitals); it simply provides the amount of each resource needed. Users can choose map layers using a dropdown menu and select a subset of days or counties

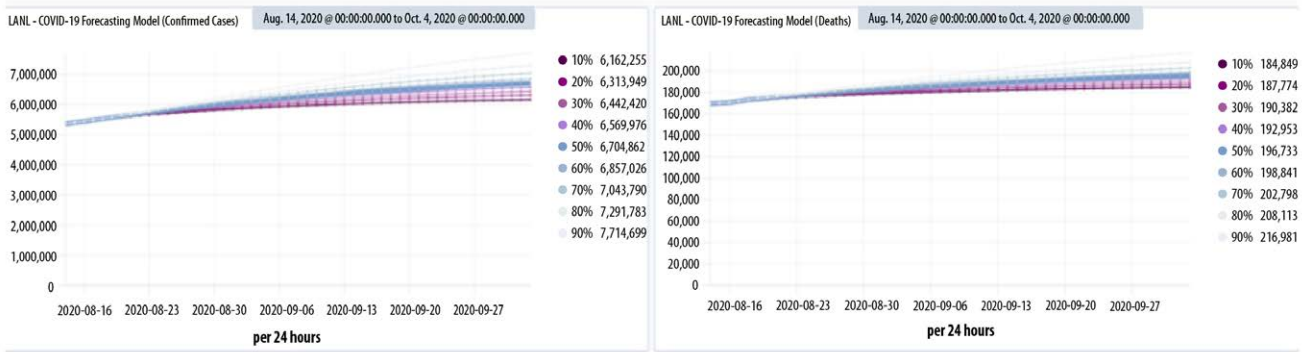


Fig. 3.35. Visualizations using Los Alamos National Laboratory COVID-19 Forecasting Model data. [Courtesy Oak Ridge National Laboratory]

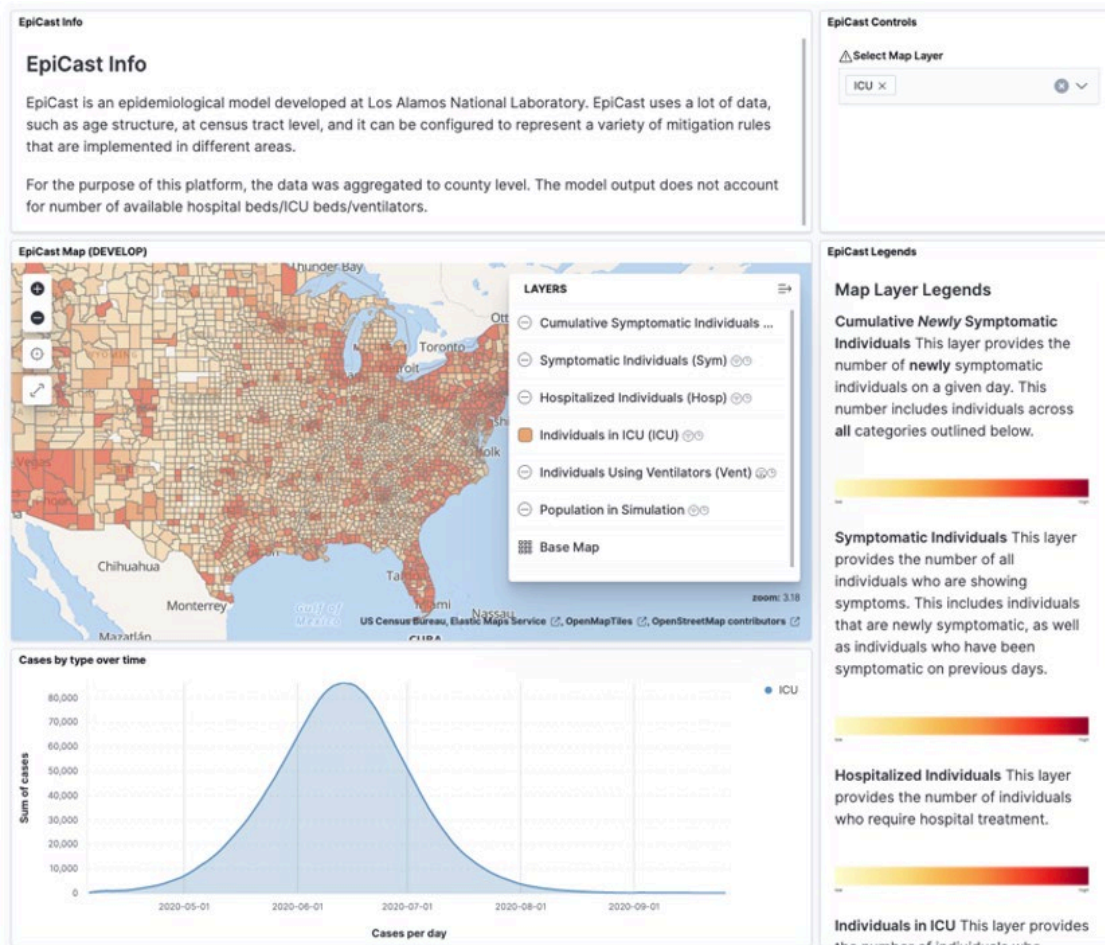


Fig. 3.36. EpiCast epidemiological model data visualization. [Courtesy Oak Ridge National Laboratory]

using the search bar. In addition to the map view, the dashboard also contains a plot displaying each variable over time, as well as a detailed legend with information about each variable.

EpiGrid

The EpiGrid model, also developed by LANL, simulates a virtual population with detailed COVID-19 status based on cell phone mobility data in each respective area. Because EpiGrid is simulated on a rectangular grid, each state includes some counties from surrounding states. The dashboard displays the output as reaggregated to the county and state levels.

EpiGrid produces variables including exposed (but not infectious), infected and quarantined, infected but not quarantined, receiving hospital treatment, requiring hospital care but not receiving it, recovered, and dead. In addition to the model's variables, the number of new cases was provided to enable proper filtering (i.e., sum over time). Figure 3.37, p. 137, shows EpiGrid data visualizations for a number of focus areas. The dashboard contains a map with layers for all variables, displayed at the state or county level depending on zoom settings. Users can down-select to a county or state using interactive controls. Multiple charts allow users to further explore aspects such as a comparison between simulated data and actual cases (using *The New York Times* data), as well as the states and counties with the highest counts for any of the variables.

COVID-19 Recovery Framework Integration

ANL's COVID-19 Recovery Framework provides a system for analyzing various mitigation and recovery concepts. The system integrates data from a variety of sources and provides a flexible environment for displaying and manipulating results. Functionalities that will be developed in the future include tools for assessing demographic, workforce, economic, and disease progression factors under different recovery scenarios. A separate dashboard was created to visualize the highest/

lowest accessibility to grocery stores, hospitals, and pharmacy locations. Figure 3.38, p. 138, shows visualizations from ANL's COVID-19 Recovery Framework.

Ensemble Visualizations

The team designed and implemented ensemble data visualizations to compare future projections and other simulation results produced by models such as EpiGrid, EpiCast, COMBO, Mechanistic, and IHME. Custom Kibana plug-ins were created to integrate these visualizations and user interfaces into the Kibana dashboard, and they serve as a comparative visual analysis tool for evaluating COVID-19 predictive model performance.

The team analyzed a collection of COVID-19 predictions from various epidemiological models using the COVID-19 Forecast Hub dataset (covid19forecasthub.org). As shown in Fig. 3.39, p. 139, the visual interface provides a data-driven workflow to select a COVID-19 model prediction ensemble based on the spatiotemporal overlap of available predictions. Users can quantify the model performance using both the uncertainty of each model prediction ensemble and the error of each ensemble member representing individual model predictions.

3.5 Task 4: COVID-19 Transportation Modeling

The movement of people and goods has been central to managing the response to COVID-19. City leaders and transportation operators are developing strategies and operational plans for safe transportation and the return of full-scale economic activity. DOE's national laboratories have lent deep, world-leading modeling and simulation capabilities to the DOE Office of Energy Efficiency and Renewable Energy's Systems and Modeling for Accelerated Research in Transportation (SMART) Mobility Laboratory Consortium. Under the COVID-19 project, the tools and scientific expertise developed for the consortium were applied to transportation modeling for various cities. With funding from the

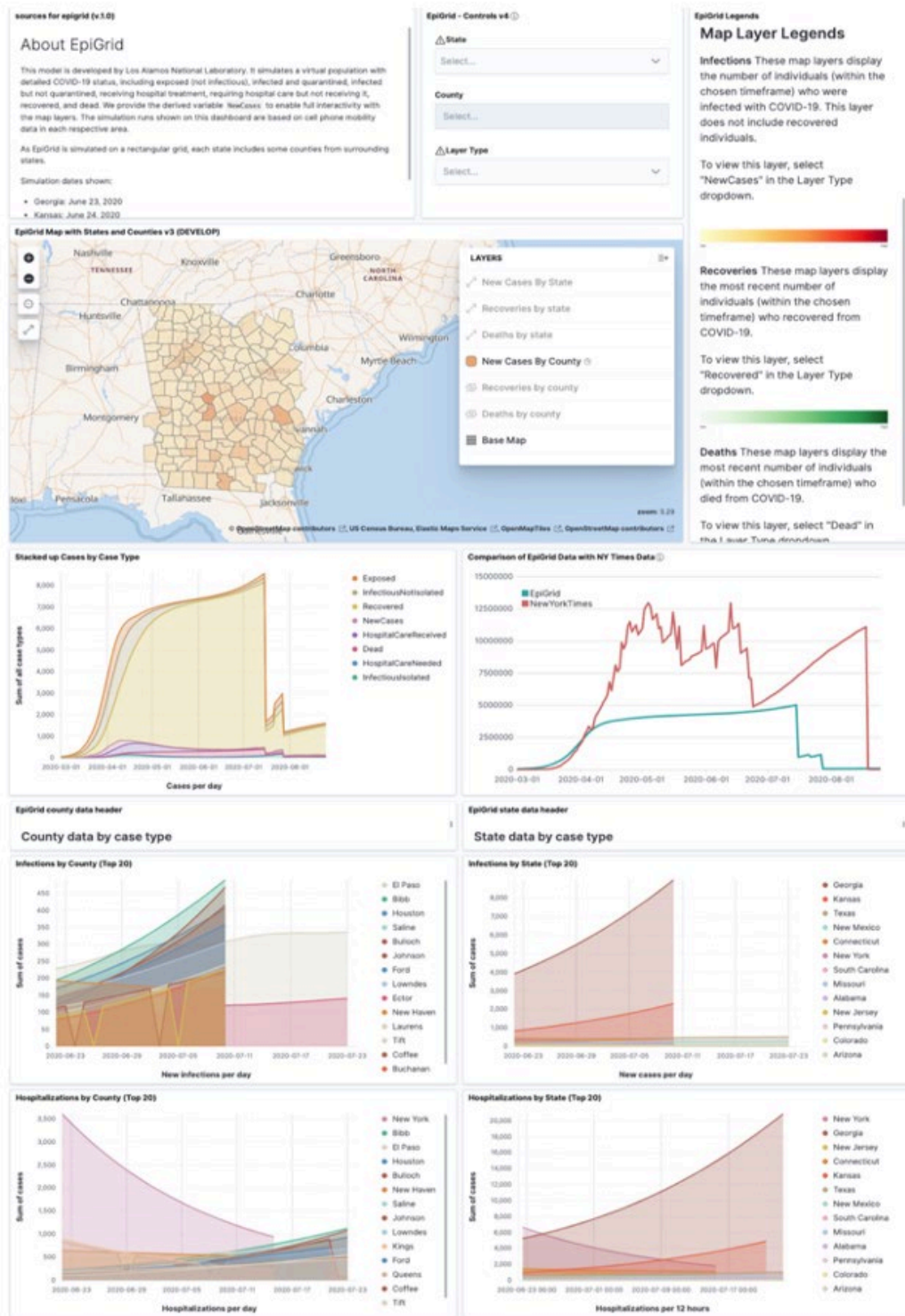


Fig. 3.37. EpiGrid epidemiological model data visualization. [Courtesy Oak Ridge National Laboratory]

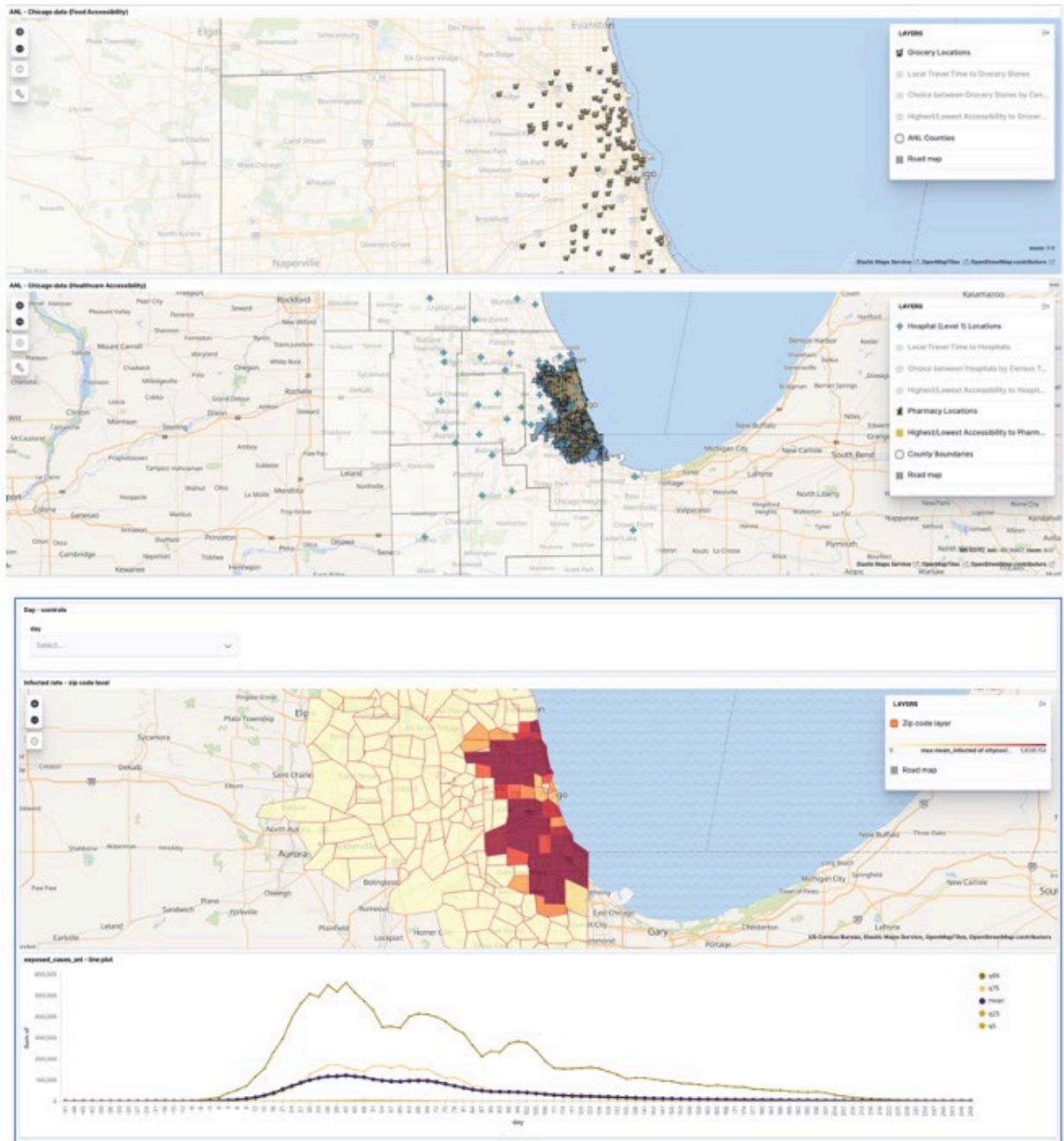


Fig. 3.38. Data visualization from Argonne National Laboratory’s COVID-19 Recovery Framework Integration model. [Courtesy Oak Ridge National Laboratory]

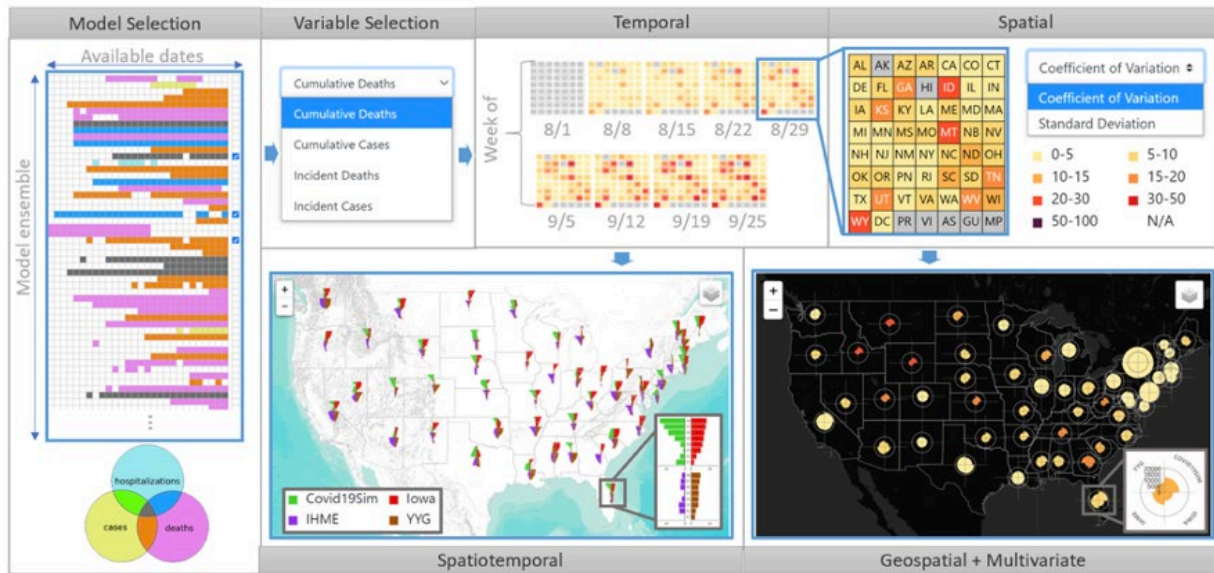


Fig. 3.39. Ensemble data visualization serves as a comparative analysis tool for evaluating COVID-19 predictive model performance. A visualization of the spatiotemporal variability in projection performance of individual models is shown in a textured-tile calendar representing each state as a tile element (top middle panel). Visualizations of differences between selected models are shown using time series leaflet glyphs (bottom left) and multivariate rose charts (bottom right). [Reprinted from Xu, H., et al. EPISembleVis: A geo-visual analysis and comparison of the prediction ensembles of multiple COVID-19 models, *Journal of Biomedical Informatics*. (124) Copyright 2021, with permission from Elsevier.]

federal-level Coronavirus Aid, Relief, and Economic Security (CARES) Act, DOE has directed ANL, Lawrence Berkeley National Laboratory (LBNL), ORNL, and NREL to quickly assist major cities (i.e., Chicago and New York City) with transportation planning and strategies to enable a safe and efficient return to operations. This effort also focuses on analyzing shifting mobility patterns to inform tracking of disease diffusion and progress toward a return to postpandemic operations. This section describes ANL's analysis of Chicago's transportation needs, LBNL's and ORNL's analysis of New York City's transportation needs, and NREL's analysis of road and air travel needs.

3.5.1 Chicago Transportation Analysis

This task, led by ANL, was undertaken to estimate the impact of COVID-19 on multiple transportation and energy metrics in the city of Chicago. The POLARIS Transportation System Simulation Tool, an integrated, large-scale, multiagent,

activity-based travel demand and multimodal traffic and transit assignment software, was used to simulate passenger and freight movement for 24 hours in the Chicago Metropolitan Region under 10 different scenarios developed in close collaboration with the Chicago Transit Authority (CTA). The scenarios consider that certain behaviors, such as telecommuting and shared-mode avoidance, may persist at different levels of severity. Because transit agencies suffered major revenue losses during the pandemic, the model assumed different levels of service cuts (i.e., no cuts, 20%, and 55%).

The scenarios developed with CTA were designed to explore the impact of possible future options based on four factors: (1) operational service cuts, (2) telecommuting, (3) shared-mode risk perception, and (4) transit vehicle load limits. Although the factors were determined from the perspective of transit, their impacts go beyond transit. As a result, the outcome metrics studied included (1) bus and

rail boardings, (2) traffic congestion, (3) fuel/energy consumption, (4) emissions, (5) fuel economy, (6) transit user experience, and (7) equity.

The 10 scenarios defined in collaboration with CTA are described below:

1. No service cut – baseline telecommuting, baseline risk perception, no load limits
2. No service cut – low telecommuting, low risk perception, no load limits
3. No service cut – moderate telecommuting, moderate risk perception, no load limits
4. 20% service cut – baseline telecommuting, baseline risk perception, no load limits
5. 20% service cut – low telecommuting, low risk perception, no load limits
6. 20% service cut – moderate telecommuting, moderate risk perception, no load limits
7. 55% service cut – baseline telecommuting, baseline risk perception, no load limits
8. 55% service cut – low telecommuting, low risk perception, no load limits
9. 55% service cut – moderate telecommuting, moderate risk perception, no load limits
10. No service cut – high telecommuting, high risk perception, half vaccinated, load limits

POLARIS synthesizes a population of households and individuals and includes home, school, and work location choices. Person- and household-level socioeconomic details help generate activities for each individual for a 24-hour period. Activity generation is followed by start time, duration, location, mode, and travel party choice for each agent in the model. The routing of each trip is accomplished with a time-dependent intermodal A* algorithm within a dynamic transit and traffic assignment framework. When combined with Autonomie and GREET (Greenhouse gases, Regulated Emissions, and Energy use in Transportation) models, the workflow provides a complete picture including mobility, energy, emissions, and cost.

The existing POLARIS traveler telecommuting behavior model, based on the probability of a person working from home, is influenced by the industry, job type, and commute characteristics, as well as additional details on industry and job types. To model risk perceptions related to public transportation and ride-sharing services, data was used from a recent “stated preference–revealed preference” survey from the University of Illinois at Chicago. A bivariate ordered probit model was used to determine an individual’s likelihood of being in risk perception categories. Four scenarios were defined for telecommuting and risk perception measures: baseline (prepandemic), low, moderate, and high.

Results of ANL’s Chicago transportation scenario analysis (see Fig. 3.40, p. 141) demonstrate that continued COVID-19 risk perception related to virus variants, vaccine duration, and other diseases has the potential to disrupt transit ridership more than deep service cuts or telecommuting. Even without transit service cuts, expected growth in telecommuting and lingering risk concerns around transit will increase roadway use and thus congestion, resulting in an average of 1.5–8.5 more minutes of drive time per person. Additionally, the analysis showed a ~20% to 40% decline in transit ridership over a 24 hour period and up to a \$3.7 billion economic impact at the regional level.

Moreover, while service cuts directly impact CTA service and jobs, they also cause ripple effects in the economy (see Table 3.1, p. 142). The expected economic loss to shopping, dining, and entertainment industries already severely impacted by COVID-19 is estimated between \$112 million and \$327 million, as well as thousands of lost jobs. The expected combined economic impact is between \$1 billion and \$3.4 billion. When risk perception remains high, employees continue to telecommute at least once per week, service cuts take place, traffic worsens, and road speeds decrease by up to 33%. The increase in fuel use and greenhouse gas emissions reverse substantial recent gains in vehicle efficiency. Under worst-case scenarios, the economic impact is expected to be between

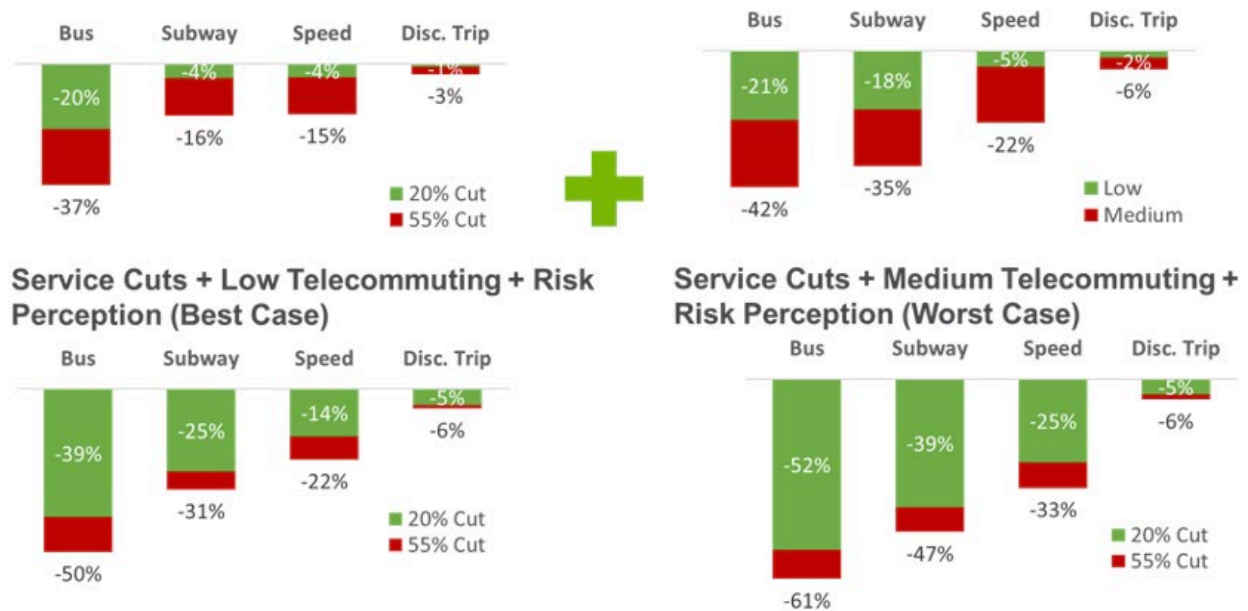


Fig. 3.40. Best case (left) and worst case (right) impacts of service cuts, transportation behavioral changes, and COVID-19 risk perception on key transportation metrics in Chicago, Ill. [Courtesy Verbas et al., 2022]

\$4.7 billion and \$7.2 billion. Transit user experience generally degrades as service is cut. However in the case of COVID, the lower demand still led to improved user experience due to reduced vehicle congestion. Geographical analysis shows that traffic congestion and transit vehicle congestion is higher in disadvantaged communities when service cuts take place.

3.5.2 New York City Transportation Analysis

The COVID-19 pandemic has put the functioning of urban transportation systems at risk. This is especially true in New York City and the surrounding region, which was an early epicenter of the disease and has the greatest reliance on public transit than other urban areas in the U.S. The New York City transportation analysis, led by LBNL and ORNL, focused on applying advanced transportation simulation tools developed at the two national laboratories to achieve rapid response modeling of pandemic impacts and reopening plans for the

New York Metropolitan Transportation Authority (MTA) and other local transportation providers. Stakeholders were concerned with providing safe and useful public transit service as travel restrictions were lifted. Maximizing the amount of transportation services that can be provided safely is critical to economic recovery, as public transit provides mobility to individuals while freeing capacity on the road network for freight movement and other modes. Balancing the need to provide essential mobility services while avoiding overcrowding requires an understanding of the interactions between traveler choices, transportation system performance, and mitigation measures. The team used BEAM-centric transportation modeling and PanTrans modeling to perform this subtask.

BEAM-Centric Transportation Modeling

To guide decision-makers on strategies enabling the transportation system to operate despite drastic changes to behavioral patterns, LBNL's high-performance agent-based transportation demand model, BEAM (Behavior, Energy, Autonomy,

Table 3.1. Impact of Different Scenarios on Transit Ridership, Traffic, Energy Use, Emissions, and the Economy in Chicago, Ill.

| Scenario/ Metric | Subway Boardings | Bus Boardings | Average Daily Speed | Energy Use | GHG Emissions | Discretionary Trips | Economic Impact |
|---|---------------------|------------------|------------------------|---------------|------------------|------------------------|--------------------|
| No cut – low demand change | –18.0% | –21.0% | –5.0% | 1.8% | 2.9% | –2.1% | –\$0.8B |
| No cut – moderate demand change | –35.0% | –42.0% | –22.1% | 19.0% | 20.3% | –5.8% | –\$3.7B |
| 20% cut – no demand change | –4.0% | –20.0% | –4.1% | 4.9% | 6.1% | –1.0% | –\$1.0B |
| 20% cut – low demand change | –25.0% | –39.0% | –14.4% | 10.5% | 12.3% | –4.8% | N/A |
| 20% cut – moderate demand change | –39.0% | –52.0% | –25.4% | 20.4% | 21.8% | –5.1% | –\$4.7B |
| 55% cut – no demand change | –16.0% | –37.0% | –15.3% | 11.8% | 13.1% | –3.2% | –\$3.4B |
| 55% cut – low demand change | –31.0% | –50.0% | –21.5% | 13.5% | 14.7% | –6.0% | N/A |
| 55% cut – moderate demand change | –47.0% | –61.0% | –33.2% | 31.7% | 33.1% | –6.3% | –\$7.2B |
| No cut – high demand change and load limits | –53.0% | –58.0% | –19.5% | 16.9% | 18.2% | –5.1% | N/A |

Mobility), was deployed to analyze the New York City metropolitan area, calibrated to prepandemic and in-pandemic travel patterns, and then used to analyze a set of scenarios of future travel demand and transit service. BEAM, a core capability developed under DOE's SMART Mobility Laboratory Consortium, simulates the mode, route, time, and destination choices of millions of individual travelers and the performance of the transportation system, including road speeds and transit crowding, given

those choices. BEAM simulates private car travel, all transit modes, nonmotorized travel, ride-hailing, and multimodal trips. For this project, researchers at LBNL developed an initial set of realistic scenarios and meaningful performance measures with which to evaluate them, informed by stakeholders in the New York City metropolitan area.

To represent the various evolving timelines within the pandemic, the team developed a baseline

Table 3.2. Scenario Development Parameters Used in BEAM-Centric Transportation Modeling of the New York City Metropolitan Area

| Scenario | Work from home | Fear factor (transit aversion) |
|---------------------|-------------------------------------|--------------------------------|
| Baseline (February) | Baseline | None |
| Phase-1 (April) | High (50%) | High (80%) |
| Phase-4 (September) | Moderate (30%) | Moderate (40%) |
| New normal | Moderate (varies by industry types) | Moderate (40%) |

Table 3.3. Systems-Level Scenario Results of BEAM-Centric Transportation Modeling of the New York City Metropolitan Area

| Scenario | Passenger miles of travel (millions) | Passenger hours of travel (millions) | Energy (million gallons) | Work trips (millions) | Nonwork trips (millions) | Percent work trips |
|-------------------------------|--------------------------------------|--------------------------------------|--------------------------|-----------------------|--------------------------|--------------------|
| Baseline (February) | 96 | 10.5 | 1.9 | 8.5 | 6.6 | 56% |
| Phase-1 (April) | 12 | 0.9 | 0.2 | 0.7 | 0.7 | 48% |
| Phase-4 (September) | 44 | 4.6 | 1.1 | 2.7 | 3.8 | 42% |
| New normal | 75 ($\pm 8\%$) | 8.0 | 1.6 | 6.9 | 4.3 | 61% |
| Percent change from September | 69% | 74% | 47% | 153% | 15% | |
| Percent change from base | -22% | -24% | -15% | -19% | -35% | |

scenario that represented onset conditions of the pandemic in early February 2020. Later phases of reopening considered by stakeholders (i.e., Reopen1 to Reopen4) and an emerging new normal scenario were included in the team's analysis. Each scenario was defined based on the parameters identified as having primarily dictated the early onset of pandemic trends within the transportation system in New York City and the surrounding region. Parameters for scenarios included work from home (i.e., telecommuting) and fear factor (i.e., transit aversion); levels of these parameters are shown in Table 3.2, this page. Systems-level scenario results for the BEAM modeling subtask are provided in Table 3.3, this page.

At the end of the project, LBNL researchers delivered to local stakeholders an initial set of scenario analysis results exploring potential new normal travel patterns, defined as economic activity

beginning to increase with risk aversion remaining above baseline levels (Fig. 3.41, p. 144). For example, passenger miles of travel were forecasted at 75% ($\pm 8\%$) under the new normal scenario, a 69% change from September 2020 passenger miles of travel. Results showed travel behavior continuing to rebound past levels observed in fall 2020, with work-related travel growing at a faster rate than nonwork travel, but with those levels showing high sensitivity to assumptions of risk aversion. Under all reopening scenarios, transit service levels were assumed to continue from those provided in fall 2020; under this assumption, congestion levels did not grow worse than prepandemic levels despite continued avoidance of mass transit modes. These results reinforced the importance of public transit to the functioning of New York City, even if transit must operate at reduced capacity and with reduced ridership. The fact that the model did not find

Percent difference from Baseline (February)

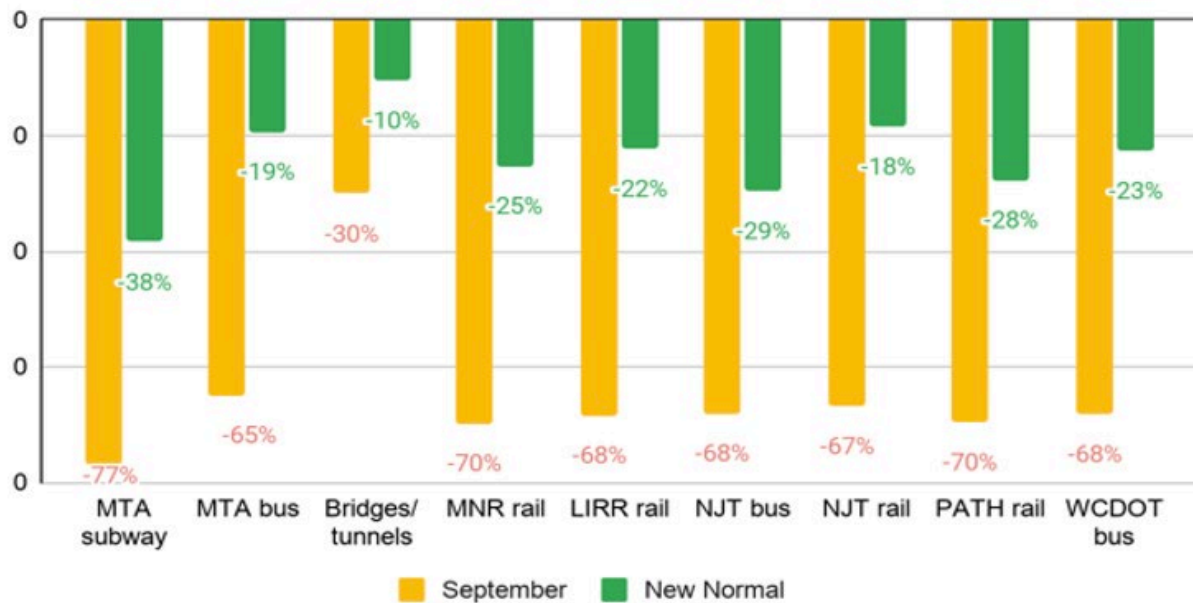


Fig. 3.41. Percent difference in transit ridership by mode of transport between February 2020 and September 2020 (yellow) and a projected post-pandemic new normal (green). [Courtesy Wenzel et al., 2021]

massive increases in traffic congestion indicates that interventions focused on increasing the capacity of the road network for private vehicles may be unnecessary. This research also provided line-by-line and stop-by-stop ridership and crowding data under different scenarios.

The team presented the results of the BEAM transportation modeling effort to MTA and other local stakeholders in a series of meetings in fall 2020, and detailed data on transit ridership and crowding were shared with MTA for verification and use in schedule planning. These results were also shared with the transportation modeling community at the 100th annual meeting of the Transportation Research Board (Needell 2021b).

This project built important core modeling capabilities that will continue to be useful in improving COVID-19 response and many other projects going forward. This effort is the first known case in which

a fully integrated activity-based travel demand model was deployed, calibrated, and used for scenario analysis in a new city in just three months using only publicly available data. The deployment pipeline and experience gained in this process will make agent-based transportation modeling more accessible for future users. The project also developed several capabilities that have been adopted for continuing SMART Mobility transportation system modeling efforts: sensitivity of agents to crowding on transit modes, ability of travelers to work from home, implementation of bike lanes (and associated behavioral responses), and modification of transit schedules.

PanTrans Modeling

In response to the need for transportation analysis under the rapidly evolving dynamics of the COVID-19 response in New York City, ORNL adapted two existing software tools to create an interactive system

called PanTrans for estimating commuting demand and mode choice. This task was undertaken to allow transportation planners and policymakers to understand the implications of economic and social factors on the demand for various modes of transportation at each location in the city. The economic and social factors included changes in the demand for workers by various industries due to layoffs, the move to working from home, and reluctance to use the transit system. This interactive system was designed to screen potential plans or scenarios and identify where resources are likely to be severely stressed. It also helps understand the demographics of groups affected by loss of transit or other transportation modes.

The two software systems that formed the basis of this interactive tool were developed originally in 2018 with LDRD funding. The first software tool was a synthetic U.S. population created by the UrbanPop system. The tool provides a dataset at the person level using demographics including age, race, income level, vehicle ownership, and household structure. The synthetic individuals are located in block groups and are linked to jobs in specific industries in other block groups. While the individuals in the synthetic population do not represent specific individuals in the real population, the synthetic population statistically matches census and other demographics. In this case, the synthetic population was ~3 million commuters living and working in New York City. The individuals were considered agents with independent choices of transportation mode for their daily work trip (i.e., walk, bike, car, transit).

The transportation mode choice for each individual was determined by the second of the two LDRD-funded software systems, CommuterSim, an agent-based simulation running in an HPC environment. CommuterSim models the agents, their interactions with others in their home and work locations, and their interactions with the built environment (e.g., sidewalks and bike lanes). CommuterSim was transferred to a new HPC computer, Rhea, during the project and can now generate a years'

worth of commuting patterns in a few minutes. CommuterSim generated a first-choice transportation mode for each agent and then a second choice for all agents whose first choice was transit. The combination of these two choices allowed the team to develop an interactive mode choice modeling tool. The user begins by setting assumptions about industry work percentages. These can be estimated based on media reports or survey data on the status of the pandemic or on an assumption of the ability and tendency of workers to commute to work in various phases of the multiple waves of the pandemic. Figure 3.42, p. 146, shows the interface for setting assumptions on commuting percentages by industry.

CommuterSim automatically updates a set of maps showing home and workplace density. Fig. 3.43, p. 147, shows commuter density by home and work location under the 50% transit aversion condition and transportation mode data underlying the maps. Traffic levels also consider the level of transit "fear factor," which decreases transit use by commuters who have a choice.

Fig. 3.44, p. 147, shows the demand for transit at subway stations based on where commuters live and a 50% fear factor. While the model does not route travelers from point to point on the subway, it shows demand at home and work locations. Time of day for commuting trips is not included, so demands are daily totals; however, they could easily be translated into time of day with appropriate data.

Commuters who do not have a car and their commute is too long to walk or bike are considered "captive to transit." Demographics from the agent-based model enable determination of the number of affected groups by race, gender, income level, industry, and general location. Figure 3.45, p. 148, shows which riders remain on public transit when the "fear factor" is increased to 100% and everyone with an alternative transit choice leaves. The demographic breakdown of this group of commuters shows that women of color make up the highest percentage of

Set Commuting by Industry

| Industry Text | Brooklyn | | Manhattan | | Queens | | Staten Island | | The Bronx | | Grand Total | |
|----------------|--------------------|------------------|--------------------|------------------|--------------------|------------------|--------------------|------------------|--------------------|------------------|--------------------|------------------|
| | Number BaselinePop | Number Commuting | Number BaselinePop | Number Commuting | Number BaselinePop | Number Commuting | Number BaselinePop | Number Commuting | Number BaselinePop | Number Commuting | Number BaselinePop | Number Commuting |
| Construction | 7,404 | 2,970 | 4,057 | 1,642 | 14,537 | 5,949 | 2,107 | 807 | 3,162 | 1,294 | 31,267 | 12,662 |
| Education | 81,274 | 16,385 | 40,285 | 8,191 | 71,626 | 14,481 | 15,390 | 3,094 | 40,778 | 8,071 | 249,354 | 50,222 |
| Entertainment | 82,824 | 8,255 | 88,602 | 8,805 | 89,197 | 9,007 | 15,891 | 1,637 | 41,710 | 4,199 | 318,224 | 31,903 |
| F.I.R.E. | 62,921 | 12,601 | 69,099 | 13,876 | 66,537 | 13,445 | 11,231 | 2,274 | 27,950 | 5,523 | 238,338 | 47,719 |
| Healthcare | 255,057 | 255,057 | 142,839 | 142,839 | 234,118 | 234,118 | 56,786 | 56,786 | 125,369 | 125,369 | 814,169 | 814,169 |
| Information | 14,443 | 5,744 | 17,297 | 6,920 | 14,784 | 5,933 | 1,896 | 748 | 5,231 | 2,124 | 53,651 | 21,469 |
| Manufacturing | 16,408 | 9,947 | 8,286 | 4,992 | 19,047 | 11,326 | 2,504 | 1,489 | 6,899 | 4,129 | 53,144 | 31,883 |
| Other | 111,055 | 111,055 | 79,182 | 79,182 | 106,480 | 106,480 | 20,251 | 20,251 | 45,392 | 45,392 | 362,360 | 362,360 |
| Professional | 108,557 | 10,921 | 113,026 | 11,304 | 108,209 | 10,695 | 20,944 | 2,094 | 38,672 | 3,880 | 389,408 | 38,844 |
| Retail | 89,900 | 53,862 | 64,710 | 38,849 | 89,283 | 53,621 | 19,157 | 11,473 | 45,744 | 27,488 | 308,794 | 185,293 |
| Transportation | 32,987 | 26,520 | 7,547 | 6,007 | 32,478 | 26,019 | 7,008 | 5,647 | 9,518 | 7,601 | 89,538 | 71,794 |
| Wholesale | 13,892 | 11,186 | 9,473 | 7,582 | 12,902 | 10,280 | 2,661 | 2,156 | 4,785 | 3,809 | 43,713 | 35,013 |
| Grand Total | 876,722 | 524,503 | 645,004 | 330,189 | 859,198 | 501,354 | 175,826 | 108,456 | 395,210 | 238,829 | 2,951,960 | 1,703,331 |

Commuters by Home Selected vs Baseline

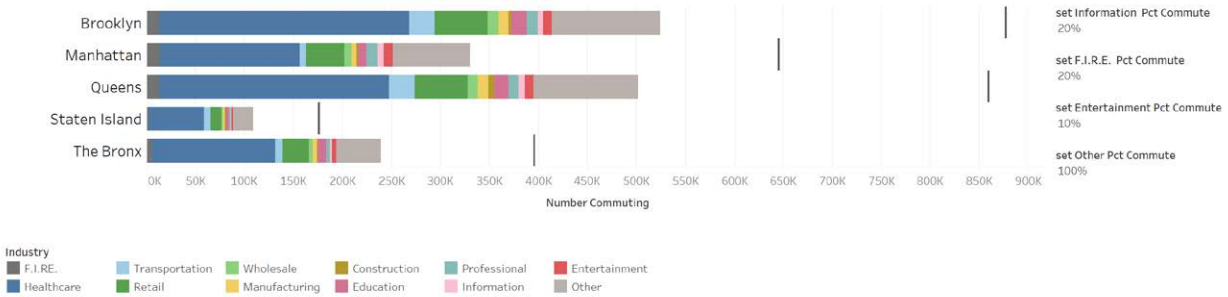


Fig. 3.42. Interface for setting assumptions on commuting percentages by industry for the five New York City boroughs. [Courtesy Oak Ridge National Laboratory]

commuters with no option but transit. Thus, PanTrans begins to provide a tool to consider equity issues in potential responses to transit disruptions.

The PanTrans system does not attempt to model all the routing and detailed timing conditions that a microsimulation tool provides. Instead, it attempts to provide as much analysis capability as possible, focusing on the transportation mode choice of a large population of individuals with detailed demographic characteristics. This interactive tool can be useful to planners and policy analysts determining which scenarios need further analysis with a more detailed model.

3.5.3 Road and Air Travel Trends and Vaccine Administration Siting Analysis

A multipronged, data-informed mobility modeling and analysis effort led by a crosscutting team at NREL identified pandemic-related travel behavior changes—on the road and in the air—and informed

regional vaccine administration site planning. This work culminated in several publications and presentations, including a feature article in *The New York Times* (Badger, June 11, 2021) identifying how long-term changes in remote work and work flexibility might affect travel patterns across the nation.

Several aspects of this research were informed by access to national-level industry data from provider INRIX, with a dataset larger than 1 terabyte reflecting travel behavior. Key findings included: (1) mobility drastically decreased across all transportation modes at the onset of the pandemic, (2) within a few months, personal vehicle travel rebounded to 80% but with different temporal patterns, and (3) shared transportation modes (e.g., transit, air) continue to suffer from COVID-19 risk aversion, with traditional transit modes taking the longest to move toward recovery. Figure 3.46, p. 149, provides sample data outputs using INRIX and represents shifts in U.S. mobility patterns by month for January to June 2020, using trips per hour per day.

50% avoid transit if possible

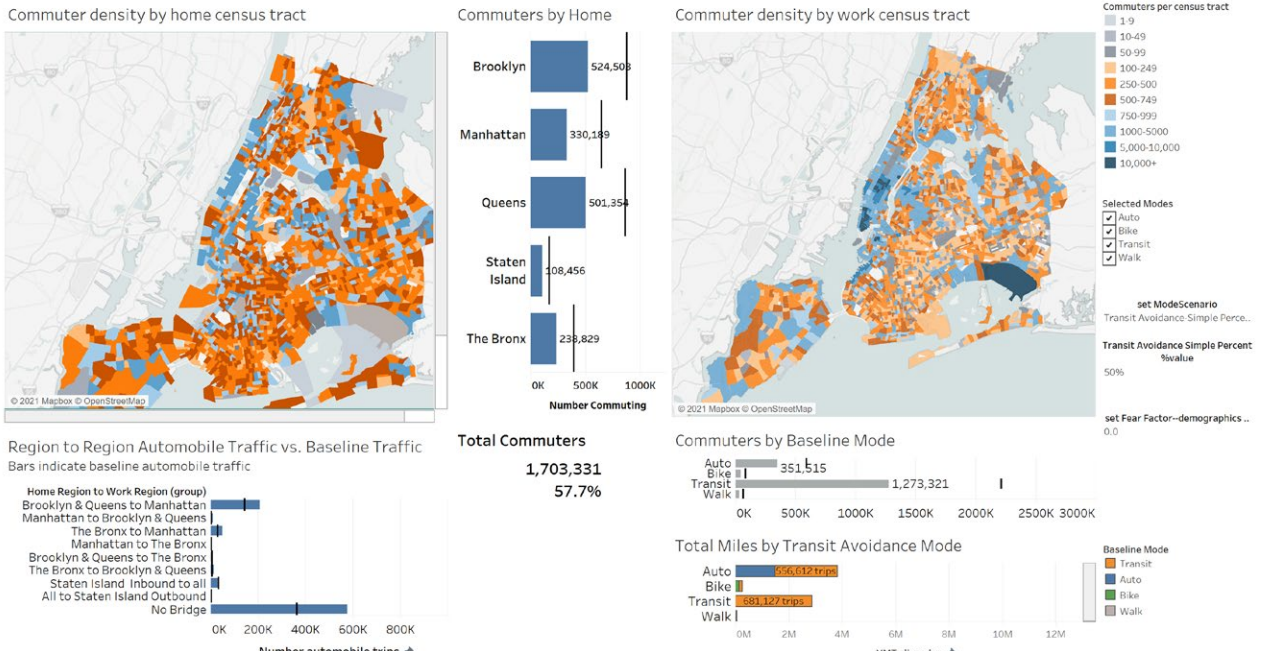


Fig. 3.43. Home and work maps show the density of commuters by census tract, and graphics below the maps indicate where car traffic demand is expected to exceed normal limits. [Courtesy Oak Ridge National Laboratory]

Home Subway Stations by Commuter Number

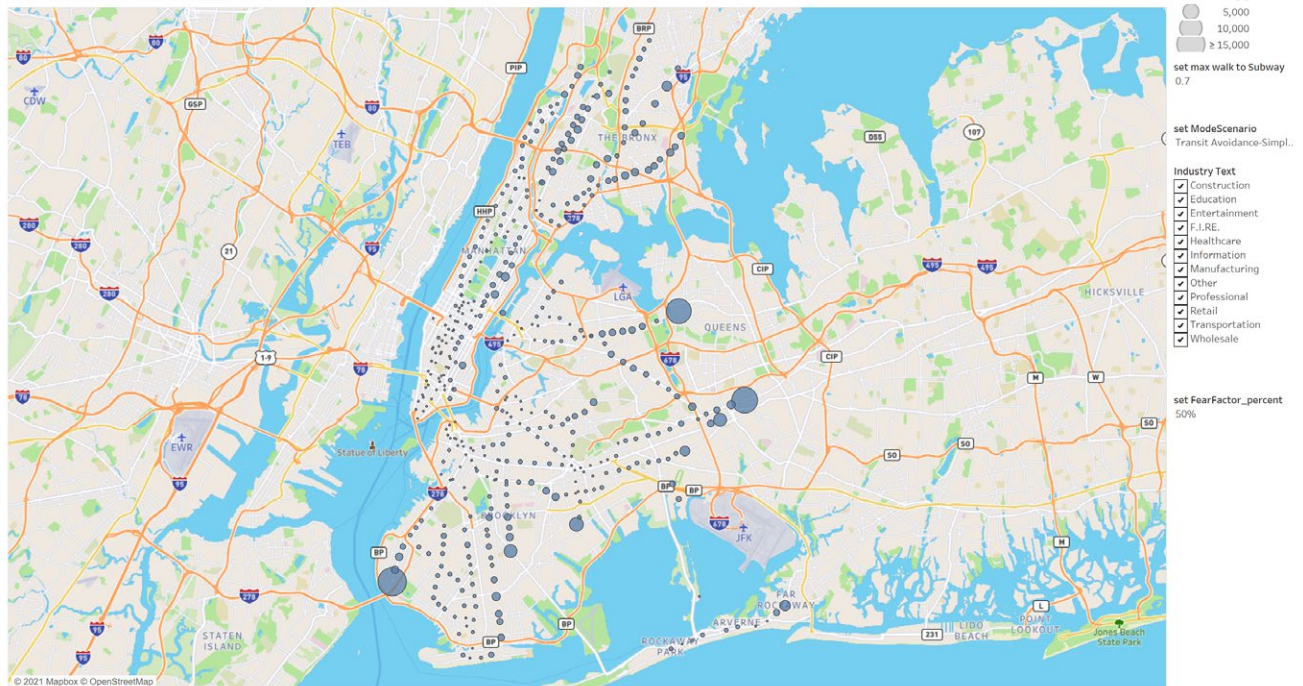


Fig. 3.44. Subway demand based on home locations and a 50% fear factor. [Courtesy Oak Ridge National Laboratory]

100% avoid transit if possible

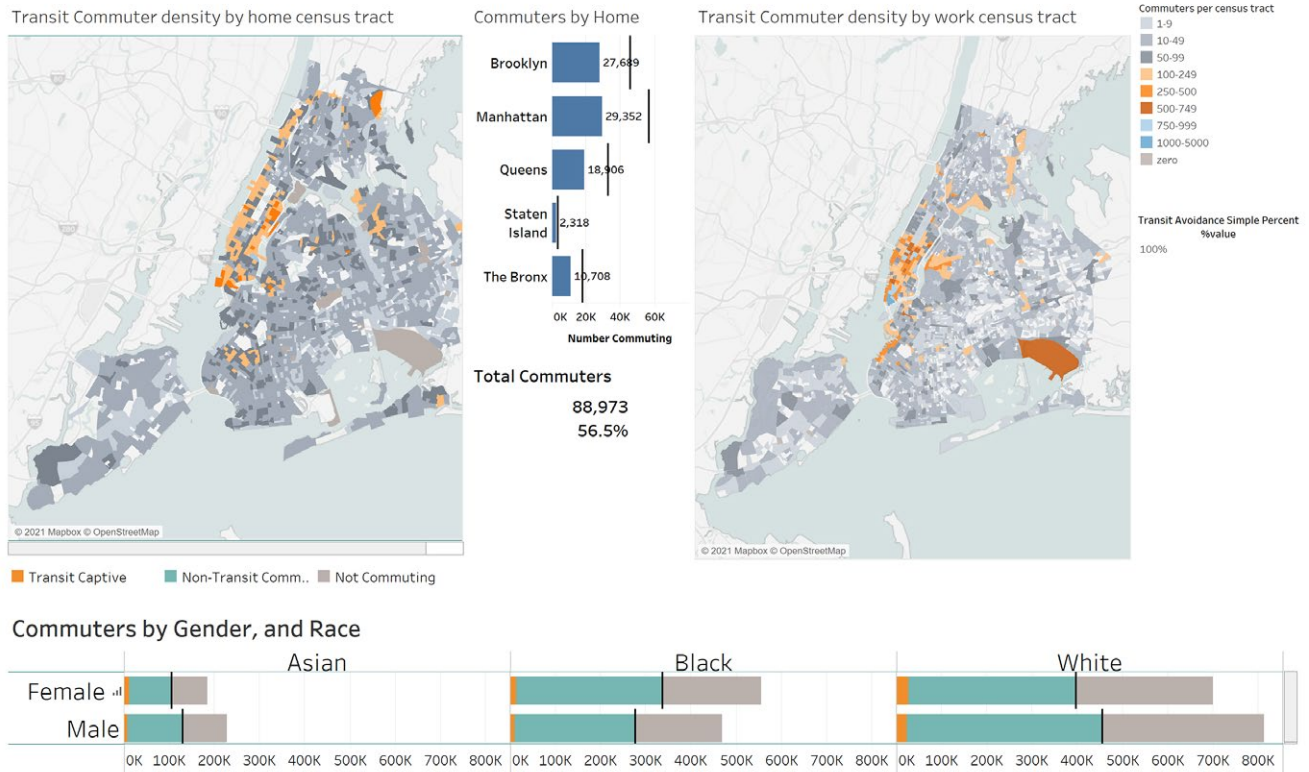


Fig. 3.45. Commuter density by home and work location under the 100% transit aversion condition and demographic data underlying the maps. [Courtesy Oak Ridge National Laboratory]

Travel Changes: On the Road and In the Air

Changes in When and Where People Are Spending Time

The team employed two newly developed metrics to analyze the INRIX high-resolution trip data to quantify behavioral shifts in driving as a function of time, enabling comparisons of patterns before and after the pandemic began. The resulting technical report (Reinicke et al., 2021) explored three MSAs with significantly different labor markets: Denver, Colorado; Louisville, Kentucky; and Des Moines, Iowa. Although certain unique behavioral shifts emerged, common trends surfaced in the three seemingly unique locations. For example, drivers in all three cities spent more time at residential locations and less time in workplaces after the pandemic started. In addition, workplaces that

may be incompatible with remote working, such as hospitals and retail stores, retained much of their prepandemic travel activity. Figure 3.47, p. 149, shows the significant differences in prepandemic and in-pandemic travel behavior for retail vs. educational workplaces. Travel behavior associated with workplaces unable to move online (e.g., hospitals and retail) remained relatively unchanged whereas travel behavior associated with workplaces able to move online (e.g., schools and universities) changed significantly.

The New York Times used the team’s analysis of INRIX data to explore how a continued shift to less workplace-related travel could result in less traffic congestion and reduced system energy, thus improving energy efficiency for all users, including those who must commute (Badger, June 11, 2021).

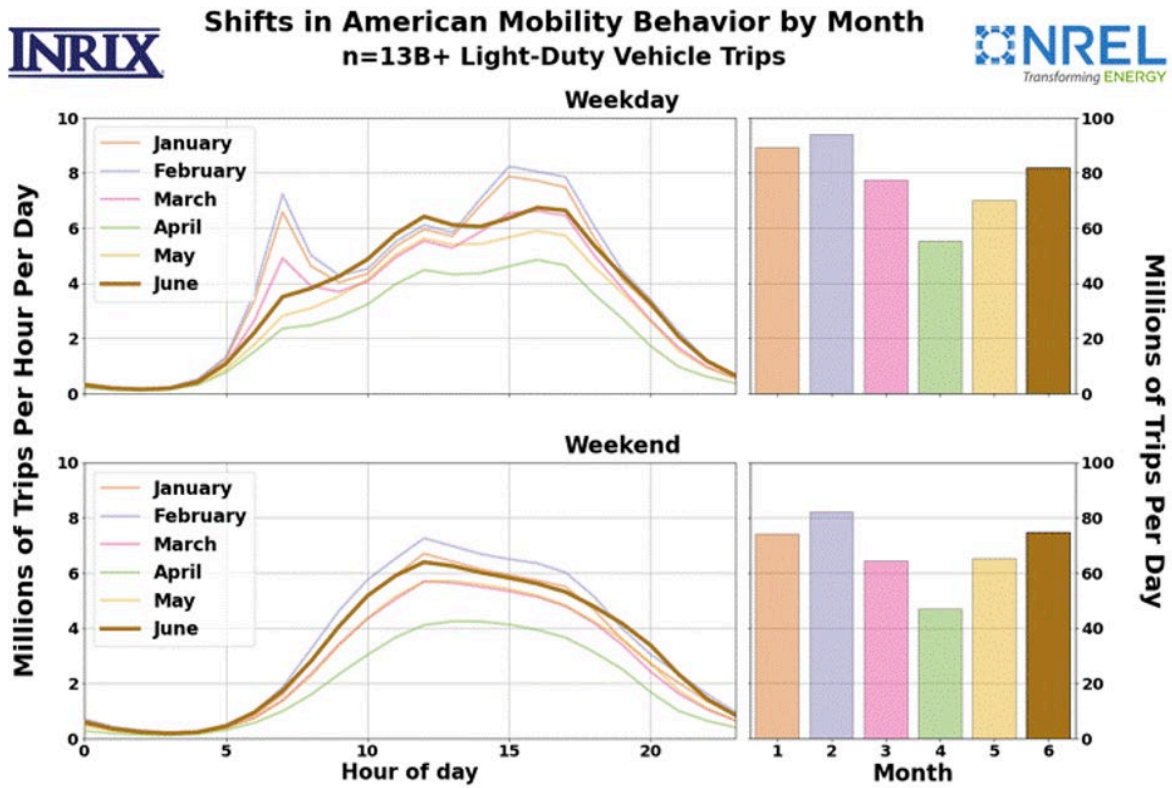


Fig. 3.46. Sample data outputs using INRIX. [Courtesy National Renewable Energy Laboratory]

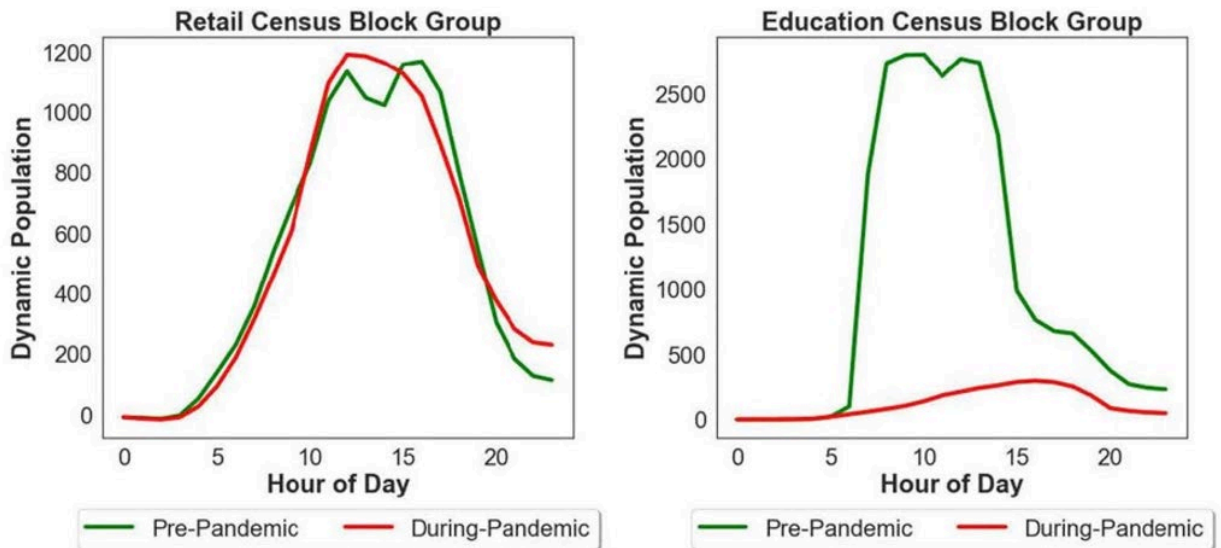


Fig. 3.47. Changes in travel behavior for retail stores (left) and educational institutions (right). Pre-pandemic trends are shown in green, and in-pandemic trends are shown in red. [Courtesy National Renewable Energy Laboratory]

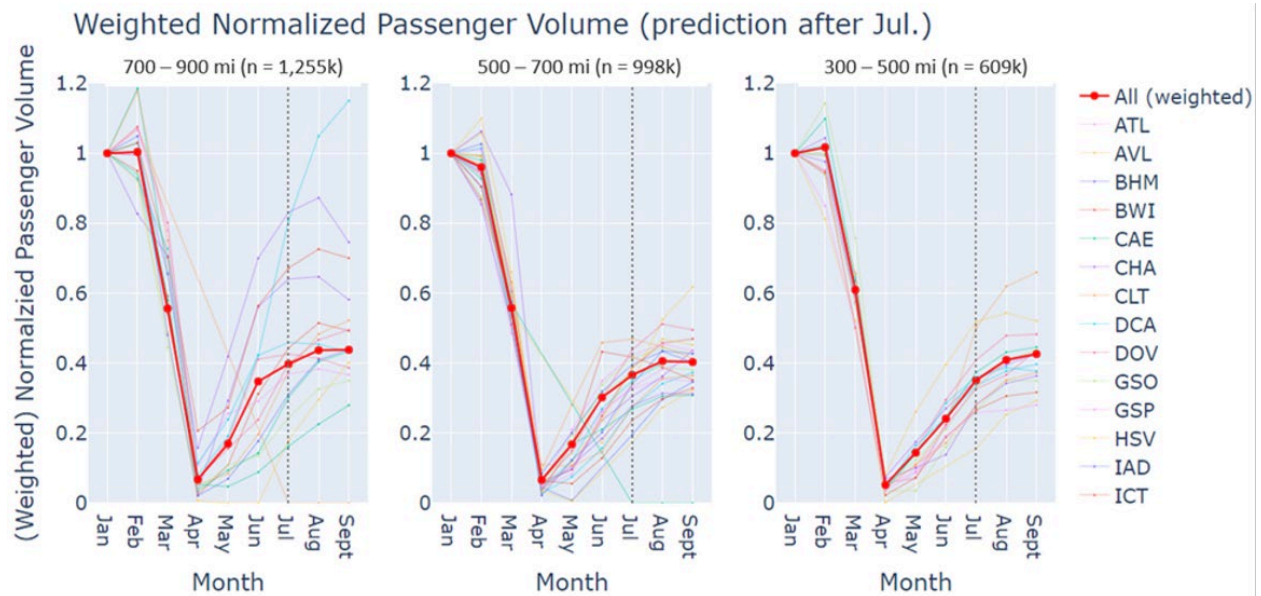


Fig. 3.48. Estimated passenger volumes using the NREL-developed PITA model. The heavy red line shows the weighted normalized passenger volume; thin lines on each plot represent trends between Chicago O’Hare International Airport and other airports. [Courtesy National Renewable Energy Laboratory]

Predicting Long-Distance Air Travel Characteristics

Because air travel data typically is available only after 1 to 3 months, the team developed a model to predict air travel characteristics for time-proximate decision-making. The Point-in-Time Air Travel (PITA) model enables timely and accurate predictions of inbound traffic volumes for all domestic airports.

Due to the lack of publicly accessible, real-time data on the number of passengers traveling by air, researchers tapped into two national datasets to estimate current airline passenger volumes between any two domestic airports. Using a combination of historical passenger count data from the Bureau of Transportation Statistics and near-real-time passenger departure data from the Transportation Security Administration, researchers can now use PITA to estimate current air travel passenger counts for a given city or metropolitan area.

To demonstrate the feasibility of using PITA to understand air travel behavior, the team used

Chicago O’Hare International Airport as an example destination, providing estimated inbound traffic volumes from domestic airports for a 9-month period. Passenger volumes at trip distances of 700 to 900 miles, 500 to 700 mi, and 300 to 500 mi all dropped sharply beginning in March, reached a minimum in April 2020, then rebounded over the remainder of the period (see Fig. 3.48, this page).

Vaccination Site Planning

Analyzing the Relative Ease of Accessing a Vaccination Site

NREL’s Mobility Energy Productivity (MEP) metric quantifies the ability of an area’s transportation system to connect individuals to goods, services, employment opportunities, and other activities while accounting for time, cost, and energy. Using a modified version of MEP, the team quantified the relative ease of accessing certain vaccine administration sites via a variety of travel modes—walking, biking, public transit, and driving—from any given location in the Denver metro area.

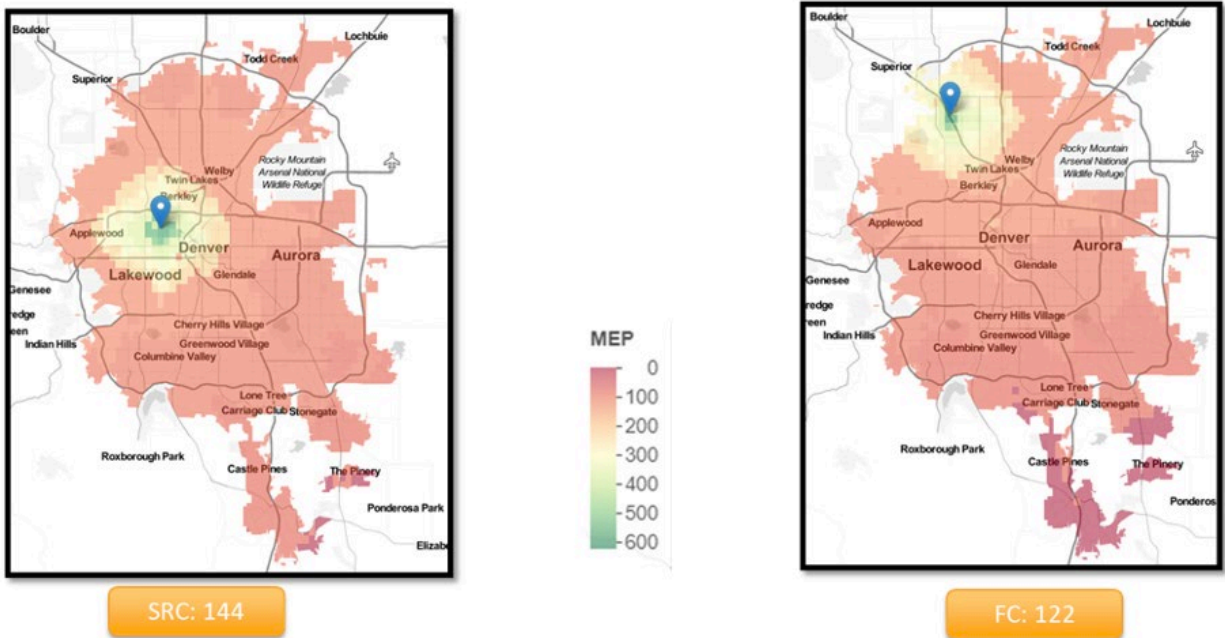


Fig. 3.49. Site-specific MEP scores for two locations in the Denver area under consideration as vaccination sites. The Senior Resource Center (left) has a higher MEP score than the Fat Cats Fun Center (right) in Westminster because it is more centrally located in the state. [Courtesy National Renewable Energy Laboratory]

Mode-specific MEP scores can help identify vaccination sites offering equitable access. For example, NREL's analysis showed that the Senior Resource Center near downtown Denver had a greater level of accessibility via walking, biking, taking public transit, or driving compared to the location at Fat Cats Fun Center in Westminster,

Colorado. A higher MEP score indicates better accessibility. The team's analysis (see Fig. 3.49, this page) suggests that the downtown Denver site is more accessible than the Westminster site because the downtown site, being more centrally located, can be reached from more parts of the city and via a greater variety of transportation modes.

3.6 Publications and Research Output

Publications

Klise, K.; Beyeler, W.; Acquesta, E.; Deangelis, H.; Makvandi, M.; Finley, P. Vaccine Prioritization Strategies Based on Analysis of Community Networks. *Spatial and Spatio-temporal Epidemiology*. Manuscript submitted.

Beyeler, W.; Acquesta, E.; Klise, K.; Makvandi, M.; Finley, P. *Adaptive Recovery Model: Designing Systems for Testing, Tracing, and Vaccination to Support COVID-19 Recovery Planning*; SAND2020-11014; Sandia National Laboratories: Albuquerque, NM, 2020. DOI: 10.2172/1684646

Beyeler, W.; Frazier, C.; Krofcheck, D.; Swiler, L. P.; Portone, T.; Klise, K. *Uncertainty Analysis Framework for the Hospital Resource Supply Model for COVID-19*; SAND2020-5569; Sandia National Laboratories: Albuquerque, NM, 2020. DOI: 10.2172/1763544

Blonigan, P.; Chowdhary, K.; Ray, J.; Safta, C. *PRIME – A Software Toolkit for the Characterization of Partially Observed Epidemics in a Bayesian Framework*; SAND2020-133310; Sandia National Laboratories: Albuquerque, NM, 2020. <https://sandialabs.github.io/PRIME> (accessed 2022-04-20).

Blonigan, P.; Ray, J.; Safta, C. Forecasting Multi-Wave Epidemics Through Bayesian Inference. *Arch. Computat. Methods Eng.* **2021**, *28*, 4169–4183. DOI: 10.1007/s11831-021-09603-9

Brelsford, C.; Barnard, M.; Daughton, A.; Erwin, S. Co-evolution of COVID-19 Attention, Mitigation Behavior, and Cases. *Ecology and Society*. Manuscript submitted.

Brelsford, C.; Moehl, J.; Weber, E. COVID-19 Associated School Closures in U.S. Counties. *Nature Scientific Data*. Manuscript submitted.

Brelsford, C.; Moehl, J.; Weber, E.; Sparks, K.; Rose, A. Spatial and Temporal Measurements of the Shopper-Worker Ratio, 2019–2020. *Nature Scientific Data*. Manuscript submitted.

Castro, L. A.; Shelley, C. D.; Osthus, D.; Michaud, I.; Mitchell, J.; Manore, C. A.; Del Valle, S. Y. How New Mexico Leveraged a COVID-19 Case Forecasting Model to Preemptively Address the Health Care Needs of the State: Quantitative Analysis. *JMIR Public Health Surveill.* **2021**, *7* (6), e27888. DOI: 10.2196/27888

Fair, J. M.; LeClaire, R. J.; Dauelsberg, L. R.; Ewers, M.; Pasqualini, D.; Cleland, T.; Rosenberger, W. Systems Dynamics and the Uncertainties of Diagnostics, Testing and Contact Tracing for COVID-19. *Methods* **2021**, *195*, 77–91. DOI: 10.1016/j.ymeth.2021.03.008

Frazier, C. R.; Krofcheck, D. J.; Gearhart, J. L.; Beyeler, W. E. *Integrated Resource Supply-Demand-Routing Model for the COVID-19 Crisis*; SAND2020-5277; Sandia National Laboratories: Albuquerque, NM, 2020. DOI: 10.2172/1763531

Hotton, A. L.; Ozik, J.; Kaligotla, C.; Collier, N.; Stevens, A.; Khanna, A. S.; MacDonell, M. M.; Wang, C.; LePoire, D. J.; Chang, Y.-S.; Martinez-Moyano, I. J.; Mucenic, B.; Pollack, H. A.; Schneider, J. A.; Macal, C. M. Impact of Changes in Protective Behaviors and Out-of-Household Activities by Age on COVID-19 Transmission and Hospitalization. *Public Health Reports*. Manuscript submitted.

Kaligotla, C.; Ozik, J.; Collier, N. T.; Macal, C. M.; Stevens, A.; Mucenic, B.; Hutton, A.; Choe, K. Development of Large-Scale Synthetic Population to Simulate COVID-19 Transmission and Response. In *Proceedings of the 2020 Winter Simulation Conference*, Virtual, December 14–8, 2020; Bae, K.-H., Feng, B., Kim, S., Lazarova-Molnar, S., Zheng, Z., Roeder, T., Thiesing, R., Eds. 2020. <https://informatics-sim.org/wsc20papers/088.pdf> (accessed 2021-11-16).

Kaufman, J.; Grant, J.; Sorokine, A.; Stewart, R. N.; Piburn, J.; Root, E.; Bhaduri, B. The Challenges of COVID-19 Data Collection during the Emerging Pandemic. Manuscript in preparation.

Klise, K.; Beyeler, W.; Finley, P.; Makvandi, M. Analysis of Mobility Data to Build Contact Networks for COVID-19. *PLoS One* **2021**, *16* (4), e0249726. DOI: 10.1371/journal.pone.0249726

Klise, K. A.; Bynum, M. L. *Facility Location Optimization Model for COVID-19 Resources*; SAND-2020-4693R; Sandia National Laboratories: Albuquerque, NM, 2020. DOI: 10.2172/1617839

Korber, B.; Fischer, W. M.; Gnanakaran, S.; Yoon, H.; Theiler, J.; Abfalterer, W.; Hengartner, N.; Giorgi, E. E.; Bhattacharya, T.; Foley, B.; Hastie, K. M.; Parker, M. D.; Partridge, D. G.; Evans, C. M.; Freeman, T. M.; de Silva, T. I.; Angyal, A.; Brown, R. L.; Carrilero, L.; Green, L. R.; Groves, D. C.; Johnson, K. J.; Keeley, A. J.; Lindsey, B. B.; Parsons, P. J.; Raza, M.; Rowland-Jones, S.; Smith, N.; Tucker, R. M.; Wang, D.; Wyles, M. D.; McDanal, C.; Perez, L. G.; Tang, H.; Moon-Walker, A.; Whelan, S. P.; LaBranche, C. C.; Saphire, E. O.; Montefiori, D. C. Tracking Changes in SARS-CoV-2 Spike: Evidence that D614G Increases Infectivity of the COVID-19 Virus. *Cell* **2020**, *184* (4) 812-817.e19. DOI: 10.1016/j.cell.2020.06.043

Lewis, L. P.; Petit, F.; Hummel, J. R.; Bergerson, J. D.; Schlueter, S. O.; Smith, B. J.; Wagner, A. M.; Feffer, K. A.; Macal, C. M. Understanding Disparities in COVID-19 Public Health Outcomes as a Function of Socioeconomic Exposure: A Framework for Assessing the Risks Presented by Inequities in Workforce Vulnerability, Infrastructure Accessibility, and Community Resilience. Chapter 4, *United Nations Global Assessment Report (GAR) 2022*. Manuscript accepted.

Lin, Y. T.; Neumann, J.; Miller, E.; Posner, R.; Mallela, A.; Safta, C.; Ray, J.; Thakur, G.; Chinthavali, S.; Hlavacek, W. Daily Forecasting of Regional Epidemics of Coronavirus Disease with Bayesian Uncertainty Quantification, United States. *Emerging Infect. Dis.* **2021**, *27* (3), 767–778. DOI: 10.3201/eid2703.203364

Macal, C. M.; Ozik, J.; Collier, N. T.; Kaligotla, C.; MacDonell, M. M.; Wang, C.; LePoire, D. J.; Chang, Y.-S.; Martinez-Moyano, I. J. CityCOVID: A Computer Simulation of COVID-19 Spread in a Large-Urban Area. In *Proceedings of the 2020 Winter Simulation Conference*, Virtual, December 14–8, 2020; Bae, K.-H., Feng, B., Kim, S., Lazarova-Molnar, S., Zheng, Z., Roeder, T., Thiesing, R., Eds. 2020. <https://informatics-sim.org/wsc20papers/087.pdf> (accessed 2021-11-16).

Makvandi, M.; Wallis, L. D.; West, C. N.; DeAngelis, H. E.; VanWinkle, Z.; Halkjaer-Knudsen, V.; Acquesta, E.; Beyeler, W. E.; Klise, K. A.; Finley, P. D. *Modeling Efficient and Equitable Distribution of COVID-19 Vaccines*; SAND2020-11973; Sandia National Laboratories: Albuquerque, NM, 2020. DOI: 10.2172/1718986

Martinez, C.; Jones, J. E.; Levin, D.; Trask, N. A.; Finley, P. D. *Physics-Informed Machine Learning for Epidemiological Models*; SAND2020-11933R; Sandia National Laboratories: Albuquerque, NM, 2020. DOI: 10.2172/1706217

Ozik, J.; Wozniak, J.M.; Collier, N. T.; Macal, C. M.; Binois, M. A Population Data-Driven Workflow for COVID-19 Modeling and Learning. *International Journal of High Performance Computing Applications* **2021**, 35 (5), 483–499. DOI: 10.1177/10943420211035164

Peluso, A.; Christian, B.; Stewart, R. N.; Bhaduri, B. Spatio-temporal Ensemble Tools for the Analysis of COVID-19 Positive Cases in the United States. Manuscript in preparation.

Piburn, J.; Kaufman, J.; Sorokine, A.; Axley, E. *DOE COVID-19 Data Curation Effort: An Initial Analysis of the Data*; ORNL/TM-2021/2329; Oak Ridge National Laboratory: Oak Ridge, TN, 2020.

Reinicke, N.; Borlaug, B.; Moniot, M. *Changes in When and Where People are Spending Time in Response to COVID-19*; NREL/TP-5400-78473; National Renewable Energy Laboratory: Golden, CO, 2021. DOI: 10.2172/1808276

Safta, C.; Ray, J.; Sargsyan, K. Characterization of Partially Observed Epidemics through Bayesian Inference - Application to COVID-19. *Computational Mechanics* **2020**, 66, 1109-1129. DOI:10.1007/s00466-020-01897-z

Sanche, S.; Lin, Y.; Xu, C.; Romero-Severson, E.; Hengartner, N.; Ke, R. High Contagiousness and Rapid Spread of Severe Acute Respiratory Syndrome Coronavirus 2. *Emerging Infectious Diseases* **2020**, 26 (7), 1470-1477. DOI: 10.3201/eid2607.200282

Spannaus, A.; Papamarkou, T.; Erwin, S.; and Christian, B. Bayesian State Space Modeling for COVID19: With Tennessee and New York Case Studies. Manuscript in preparation.

Stewart R. N.; Erwin, S.; Piburn, J.; Nagle, N.; Kaufman, J.; Peluso, A.; Christian, B.; Grant, J.; Sorokine, A.; Bhaduri, B. The COVID County Situational Awareness Tool: COVID-19 Near-Term Monitoring and Forecasting for Decision Support. Manuscript in preparation.

Swiler, L.; Portone, T.; and Beyeler, W. *Uncertainty Analysis of Hospital Resource Demand Model for COVID-19*; SAND2020-4900; Sandia National Laboratories: Albuquerque, NM, 2020. DOI: 10.2172/1630395

Thakur, G.; Sparks, K.; Berres, A.; Tansakul, V.; Chinthavali, S.; Whitehead, M.; Schmidt, E.; Xu, H.; Fan, J.; Spears, D.; Cranfill, E. COVID-19 joint pandemic modeling and analysis platform. In *Proceedings of the 1st ACM SIGSPATIAL International Workshop on Modeling and Understanding the Spread of COVID-19*, November 2020, pp. 43-52.

Xu, H.; Berres, A.; Thakur, G.; Sanyal, J.; Chinthavali, S. EPIsembleVis: A geo-visual analysis and comparison of the prediction ensembles of multiple COVID-19 models. *Journal of Biomedical Informatics* **2021**, 124, 103941.

Presentations

Auld, J.; Verbas, O.; Rousseau, A.; Wainwright, S.; Fissinger, M. R. Impact of Service Cuts, Telecommuting, and COVID Risk Perception on Ridership and Congestion. Presentation to Chicago Transit Authority President. Virtual, February 15, 2021.

Auld, J.; Verbas, O.; Rousseau, A.; Wainwright, S.; Fissinger, M. R. Modeling the Transportation System Impacts of COVID Mitigation and Recovery in the Chicago Metro Area Using POLARIS. Presentation at the 100th Annual Meeting of the Transportation Research Board, Pandemics and Public Health in Integrated Transport Modeling Workshop. Virtual, January 22, 2021.

Duvall, A. Research Overview on Mobility during the Pandemic. Presentation to the COVID Mobility Task Force for the Denver Department of Transportation and Infrastructure. August 26, 2020.

Duvall, A.; Sperling, J.; Wilson, A.; Young, S.; Zimny-Schmitt, D. Assessing U.S. Current and Future Impacts of Telework during the COVID-19 Pandemic. Poster no. TRBAM-21-04064. Presentation at the 2021 Transportation Research Board Annual Meeting, Poster Session 1214—Changes in Activity Patterns, Use of ICT, and Advanced Mobility During the COVID-19 Pandemic. Virtual, January 26, 2021.

Finley, P.; Finley, M.; Beyeler, W.; Kroccheck, D.; Frazier, C.; Swiler, L.; Portone, T.; Acquesta, E.; Austin, P.; Levin, D.; Taylor, R.; Tremba, K.; Makvandi, M.; DeRosa, S.; Hammer, A.; Davis, C. COVID-19 Medical Resource Demands. Presentation no. SAND2020-6849PE. Sandia National Laboratories. Virtual, May 12, 2020.

Macal, C. M. Modeling Chicago for the COVID-19 Pandemic. Presentation to U.S. Department of Homeland Security S&T Working Group. Virtual, April 28, 2021.

Macal, C. M. Epidemiological Modeling on Speed Dial. Presentation to the Pandemic Prediction and Forecasting S&T Working Group. Virtual, February 9, 2021.

Macal, C. M. Modeling Chicago for the COVID-19 Pandemic. Presentation to the Chicago Council on Science and Technology. Virtual, February 2, 2021. <https://www.c2st.org/event/modeling-chicago-for-the-covid-19-pandemic/> (accessed 2022-5-2).

Macal, C. M. Epidemiological Modeling on Speed Dial. Keynote presentation at Resilience Week 2020. Virtual, October 2020.

Macal, C. M.; Ozik, J.; Collier, N.; Kaligotla, C.; MacDonell, M. CityCOVID: Modeling COVID19 Spread and Effectiveness of Interventions. Presentation to the Centers for Disease Control and Prevention. Virtual, August 28, 2020.

Martinez, C.; Jones, J.; Levin, D. Initial Comorbidity Analysis. Presentation no. SAND2020-10206PE. Sandia National Laboratories. May 2020.

Moehl, J.; Trombley, N.; Morton, A.; Rose, A. High-Resolution and Demographically Detailed Population Database for the United States, Epidemiology Package. UrbanPop Dataset. *Oak Ridge National Laboratory*. 2020.

Needell, Z. Best Practices in Transportation Policy: Opportunities and Risks for Decarbonizing the Transportation System. Presentation at the American Chemical Society Annual Meeting: Climate Public Policy Session. Virtual, April 6, 2021a.

Needell, Z. Integrated Transportation System Modeling of the New York City Metropolitan Area under COVID-19 Response Using BEAM. Presentation at Workshop on Pandemics and Public Health in Integrated Transportation Modeling, 100th Annual Meeting of the Transportation Research Board. Virtual, January 22, 2021b.

Needell, Z. and Davies, R. Integrated Transportation System Modeling of the NYC Metro Area under COVID-19 Response: Lessons Learned and Next Steps. Presentation to the U.S. Departments of Energy and Transportation and the U.S. Environmental Protection Agency, Information Exchange on Connected, Autonomous, Shared, Electric Vehicles. Virtual, April 28, 2021c.

Needell, Z.; Wenzel, T.; Ravulaparthi, S.; Kirchstetter, T.; Laraabi, H.; Waraich, R. Integrated Transportation System Modeling of the NYC Metro Area under COVID-19 Response Using BEAM. Presentation to the COVID-19 HPC Consortium Webinar. Virtual, June 16, 2021d.

Needell, Z.; Wenzel, T.; Ravulaparthi, S.; Kirchstetter, T.; Laraabi, H.; Waraich, R. Integrated Transportation System Modeling of the NYC Metro Area under COVID-19 Response Using BEAM. Presentation at the SMART Mobility Consortium All Hands Meeting. Virtual, March 2, 2021e.

Needell, Z.; Wenzel, T.; Ravulaparthi, S.; Kirchstetter, T.; Laraabi, H.; Waraich, R. Integrated Transportation System Modeling of the NYC Metro Area under COVID-19 Response Using BEAM. Presentation at the 100th Annual Meeting of the Transportation Research Board, Session 1036–Pandemics and Public Health in Integrated Transport Modeling. Virtual, January 22, 2021f.

Rimer, S. P.; Macal, C. M.; Kaligotla, C. Developing a Large-Scale Synthetic Population of Persons for Simulating COVID-19 Transmission and Response. Presentation at the 89th Military Operations Research Society Symposium. Virtual, June 21–25, 2021.

Vargas, V. COVID-19 Pandemic Economic Impacts Study–May 2020. Presentation no. SAND2020-5052PE. Sandia National Laboratories. May 2020.

Verbas, O.; Auld, J.; Fissinger, M. R.; Wainwright, S. Impact of Service Cuts, Telecommuting, and COVID-19 Risk Perception on Transit Ridership, Traffic Congestion, Energy, Emissions, and Equity. Presentation no. TRBAM-22-01372. 101st Annual Meeting of the Transportation Research Board, Washington, D.C. January 10, 2022. <https://annualmeeting.mytrb.org/OnlineProgram/Details/17357> (accessed 2022-5-2).

Verbas, O.; Auld, J.; Rousseau, A. Impact of Service Cuts, Telecommuting and COVID Risk Perception on Ridership and Congestion. Presentation to the U.S. Department of Energy/American Physical Therapy Association: CARES Act COVID Transit Modeling. Virtual, April 14, 2021.

Verbas, O.; Auld, J.; Rousseau, A.; Wainwright, S.; Fissinger, M. R. Impact of Service Cuts, Telecommuting, and COVID Risk Perception on Ridership and Congestion. Presentation to the U.S. Departments of Energy and Transportation and the U.S. Environmental Protection Agency Information Exchange: Connected, Autonomous, Shared, Electric Vehicles. Virtual, March 31, 2021.

Verbas, O.; Auld, J.; Rousseau, A.; Wainwright, S.; Fissinger, M. R. Impact of Service Cuts, Telecommuting, and COVID Risk Perception on Ridership and Congestion. Presentation to Transit Authorities Monthly Meeting. Virtual, March 5, 2021.

Wenzel, T. Agent-Based Modeling of Potential Mobility Futures Using BEAM. Presentation at the Networking and Information Technology Research and Development Computer-Enabled Networked Physical Systems Interagency Working Group. Virtual, September 2, 2020.

Wenzel, T.; Needell, Z.; Ravulaparthi, S.; Kirchstetter, T.; Laarabi, H.; Waraich, R. Mobility Systems Analysis for COVID-19 Response in NYC. Presentation at the U.S. Department of Homeland Security Virtual Booth, Consumer Electronics Show. January 11–14, 2021.

Young, S.; Duvall, A.; Moniot, M.; Zhong, G.; Borlaug, B.; Wilson, A.; Reinicke, N.; Sun, B.; Perr-Sauer, J.; Jeong, K. Mobility Behavior during COVID-19 Pandemic Revealed through Data. Presentation at the Eastern Transportation Coalition – The Changing World of Optimal Traffic Monitoring Web Meeting. Virtual, December 10, 2020.

Software Disclosures

Argonne National Laboratory. *CityCOVID*. SF-21-101. September 13, 2021.

Argonne National Laboratory. *The Chicago Social Interaction Model (ChiSIM) Framework*. SF-21-104. Revision 0.3 for chi_sim, Ver. 0.4.2; <https://github.com/Repast/chiSim> (accessed 2021-11-16).

Argonne National Laboratory. *Repast for High-Performance Computing (RepastHPC)*. SF-21-100. Ver. 2.3.1. <https://github.com/Repast/repast.hpc> (accessed 2021-11-16).

Sandia National Laboratories. PRIME. Ver. 1. <https://sandialabs.github.io/PRIME/> (accessed 2021-12-01).

Media Mentions

Acquesta, E.; Beyeler, W.; Finley, P.; Klise, K.; Makvandi, M.; Stanislawski, E. Modeling Resource Demands and Constraints for COVID-19 Intervention Strategies. *SIAM News (Philadelphia, PA)*, vol. 53, no. 09, November 2, 2020). <https://sinews.siam.org/Details-Page/modeling-resource-demands-and-constraints-for-covid-19-intervention-strategies> (accessed 2022-04-25).

Badger, E. A Little More Remote Work Could Change Rush Hour a Lot. *New York Times (New York, NY)*, June 11, 2021. <https://www.nytimes.com/2021/06/11/upshot/rush-hour-remote-work.html> (accessed 2022-04-25).

CHAPTER 4

Viral Fate and Transport

| | |
|--|------------|
| 4.1 Project Overview | 156 |
| 4.2 Introduction | 156 |
| 4.3 Task 1: Improving Understanding of the Drivers of Airborne Transport and Fate Impacting SARS-CoV-2 Transmission in the Built Environment | 157 |
| 4.3.1 Overview | 157 |
| 4.3.2 Objectives | 157 |
| 4.3.3 Outcomes | 158 |
| 4.3.4 Results: Topic 1 | 158 |
| 4.3.5 Results: Topic 2 | 165 |
| 4.3.6 Results: Topic 3 | 172 |
| 4.3.7 Results: Topic 4 | 180 |
| 4.4 Task 2: Understanding the Roles of Surface Chemistry and Materials Science for Viral Transmission and Spread | 185 |
| 4.4.1 Overview | 185 |
| 4.4.2 Objectives | 185 |
| 4.4.3 Outcomes | 185 |
| 4.4.4 Results: Topic 1 | 186 |
| 4.5 Task 3: Analyzing and Modeling SARS-CoV-2 Transport and Emergence from Environmental Reservoirs Contributing to Human Transmission of COVID-19 | 192 |
| 4.5.1 Overview | 192 |
| 4.5.2 Objectives | 193 |
| 4.5.3 Outcomes | 196 |
| 4.5.4 Results: Topic 1 | 196 |
| 4.5.5 Results: Topic 2 | 200 |
| 4.6 Publications and Research Output | 209 |

Team Leadership

Katrina Waters (Team Lead), Pacific Northwest National Laboratory; **Viktor Balema**, Ames Laboratory; **Cristina Negri**, Argonne National Laboratory; **Robert McGraw**, Brookhaven National Laboratory; **Ryszard Michalczyk**, Los Alamos National Laboratory; **Thomas Kirchstetter**, Lawrence Berkeley National Laboratory; **Michael Dillon**, Lawrence Livermore National Laboratory; **Jack Cahill**, Oak Ridge National Laboratory; **Liz Dobitz**, SLAC National Accelerator Laboratory; **Brady Lee**, Savannah River National Laboratory; **Oscar Negrete**, Sandia National Laboratories

4.1 Project Overview

The NVBL Viral Fate and Transport Team included researchers from 11 DOE national laboratories and utilized unique experimental facilities combined with physics-based and data-driven modeling and simulation to study the transmission, transport, and fate of SARS-CoV-2. The team focused on understanding and ultimately predicting SARS-CoV-2 viability in varied environments with the goal of rapidly informing strategies that guide the nation's resumption of normal activities. The primary goals of this project included (1) prioritizing administrative and engineering controls that reduce the risk of SARS-CoV-2 transmission within an enclosed environment, (2) identifying the chemical and physical properties that influence binding of SARS-CoV-2 to common surfaces, and (3) understanding the contribution of environmental reservoirs and conditions on transmission and resurgence of SARS-CoV-2.

Key research activities and accomplishments include:

- **Improving understanding of the drivers of airborne transport and fate impacting SARS-CoV-2 transmission in the built environment.** The team leveraged highly instrumented, configurable facilities and computational capabilities resident in DOE national laboratories to provide robust and quantitative information about how behavioral, environmental, and operational conditions affect the risk of airborne transmission of COVID-19.
- **Understanding the roles of surface chemistry and material science for viral transmission and spread.** The team designed new antiviral materials with a low potential toxicity to humans as well as those with high binding potential that could be used to trap virus particles. Direct imaging of virus-surface interactions was conducted using a range of imaging techniques available at DOE's scientific user facilities.
- **Analyzing and modeling SARS-CoV-2 transport and emergence from environmental reservoirs contributing to human transmission of**

COVID-19. The team analyzed existing datasets to produce validated models for SARS-CoV-2 fate and transport in wastewater and groundwater. Scenarios of particular interest were seepage of sewer water or septic tanks into groundwater and associated subsurface transport and potential exposure routes and population risks. Fate and infectivity of SARS-CoV-2 associated with genomic change was also analyzed by comparing sequences from wastewater and groundwater sites.

4.2 Introduction

The NVBL Viral Fate and Transport Team included researchers from eleven DOE national laboratories and utilized unique experimental facilities combined with physics-based and data-driven modeling and simulation to study the transmission, transport, and fate of SARS-CoV-2. The resulting information provided key insights required to understand factors involved in emergence, circulation, and resurgence of pathogenic microbes and support the response to the COVID-19 pandemic. SARS-CoV-2 was originally thought to be passed principally between humans through inhalation of expelled droplets and aerosolized particles, although the potential for transmission through contact with contaminated surfaces, circulating air, and wastewater were poorly described. Data suggested aerosolized SARS-CoV-2 could persist in enclosed environments (especially in poorly ventilated environments) for several hours and that the virus could persist on some surfaces for days. A lack of understanding of the transport and fate of the virus and associated particles in the environment, including air, water, and surfaces, forced regulators to rely on data from different viral outbreaks and limited their ability to devise strategies to reduce virus uptake and prevent infection considering unique properties of SARS-CoV-2. Controlling spread within communities and workplaces required understanding the factors regulating COVID-19 viability, transmission, and transport as well as the prevalence of the virus in the environment. Organized under three tasks, the team's research activities were designed to predict

SARS-CoV-2 prevalence in varied environments and enable economic recovery through the generation of data-driven guidelines for optimized safe reopening of businesses, schools, restaurants, and recreation.

- Task 1: Improving understanding of the drivers of airborne transport and fate impacting SARS-CoV-2 transmission in the built environment.
- Task 2: Understanding the roles of surface chemistry and material science in viral transmission and spread.
- Task 3: Analyzing and modeling SARS-CoV-2 transport and emergence from environmental reservoirs contributing to human transmission of COVID-19.

Summarized in the task-specific sections below are team accomplishments, including manuscripts that are published, currently in review, or in preparation for future submission.

4.3 Task 1: Improving Understanding of the Drivers of Airborne Transport and Fate Impacting SARS-CoV-2 Transmission in the Built Environment

4.3.1 Overview

Pandemic management requires understanding how the virus responds to different environmental conditions, stressors, and dynamics, and how these responses translate into risk to exposed populations and mitigation strategies. It is thought that most SARS-CoV-2 transmissions occur within the built environment, where people commonly come into close contact, exchange air with each other, and touch the same surfaces. A range of environmental factors control the dispersion and transport of aerosols that contain virus particles. Masking and physical distancing reduce virus transfer rates by intercepting expelled respiratory fluid and reducing exhalation momentum and deposition; but, a substantial fraction of the aerosol expelled from coughing, talking, and exhalation can travel tens of meters at common indoor air speeds, and smaller aerosol

droplets remain airborne for up to hours, until they are removed by ventilation or filtration. A study by four leading infectious disease laboratories found that SARS-CoV-2 retained infectiousness in simulated respiratory aerosols over 16 hours for common indoor environmental conditions (Fierce et al. 2021). Early in the pandemic, over 200 of the world's leading bioaerosol and indoor air quality scientists urged public health agencies to acknowledge this important transmission route and provide guidance on risk reduction, noting that "current measures do not adequately protect the population from the small virus-carrying particles exhaled by infected people and inhaled by others who share the same not-well-ventilated environments" (NASEM 2020).

Through this research, the Viral Fate and Transport team set out to fill critical gaps in understanding processes and systems within the built environment that impact the risk of airborne disease transmission, with the aim of informing risk-based assessments of controls for classrooms, transit vehicles, and other shared, enclosed spaces of priority for a return to new normal operations. Environmental drivers impact emissions, dispersion, transport, fate, and human exposure to virus-containing droplets and particles at varied scales in controlled environments and in conditions extensible to atmospheric conditions. Investigations of these drivers informed prioritization of administrative and engineering controls (e.g., physical distancing, face masks, occupant density in buildings and transit compartments, ventilation, and filtration) for individual and group exposure reduction.

Reducing exposure risk based on solid scientific findings remains important, as many areas of the U.S. and the world look to resume educational and commercial activities while protecting the most vulnerable members of society and reducing disease spread.

4.3.2 Objectives

The Viral Fate and Transport team prioritized the study of environments with high-risk exposure populations, hard-to-reduce occupancy, and operations that enable resumption of high priority

economic and educational activities. The team leveraged national laboratory expertise in numerical physics-based modeling and unique experimental facilities and set out to develop a common framework for evaluating the transport and fate of airborne particles.

Near-Field (Direct) Viral Transport Within Enclosed Spaces

This research intended to provide information related to the effectiveness of measures to reduce direct virus transfer between occupants in enclosed structures, including distancing, face coverings, barriers between individuals, and air distribution management. The proposed approach included physical experiments and physics-based modeling [e.g., computational fluid dynamics (CFD) and network-zonal models] that simulated droplet and aerosol emissions and airborne transport to determine spatially and temporally resolved concentrations and fate of virus-containing droplets and aerosols within occupied enclosed spaces. Experiments and models included deposition to surfaces, removal by ventilation or filtration, and reductions achieved from interventions.

Transmission Between Occupants Throughout a Building and Other Structures

This research intended to establish quantitative estimates of relative benefits of measures to reduce average concentration of virus-containing particles in individual rooms, enclosed transit spaces (e.g., buses), and connected spaces up to the building scale. Additionally, the study proposed to provide information on the most effective risk reduction measures, including the following: occupancy limits, outdoor air ventilation rates, airflow management between spaces, and filtration. This was to include simulation of aerosol transport within and between rooms and in heating, ventilation, and air conditioning (HVAC); building ventilation systems; filtration; deposition and other loss rates; occupant density; potential number of infected persons; and emission characteristics (i.e., aerosol size distribution, droplet concentrations, and distribution of virus by droplet size).

4.3.3 Outcomes

1. Conducted physical experiments of dispersion and fate of expelled respiratory fluids during breathing, talking, and coughing in the near-field and in buildings.
2. Performed numerical experiments using computational fluid dynamics and whole-building models to describe aerosol dispersion and fate and conducted exposure assessment in a room or other shared environments.
3. Evaluated effectiveness and relative risk reduction for physical barriers, including masks and partitions, and for interventions to building ventilation, filtration, and occupancy.

4.3.4 Results: Topic 1

Transmission Within Classrooms and Meeting Rooms and Throughout Buildings

- Performed Large-Eddy Simulation of Isothermal and Nonisothermal Turbulent Flows in Ventilated Classrooms
- Measured Influence of Overhead HVAC on Exposure to Airborne Contaminants from Simulated Speaking in a Meeting and a Classroom
- Investigated Potential Aerosol Transmission and Infectivity of SARS-CoV-2 Through Central Ventilation Systems
- Conducted Experimental Evaluation of Respiratory Droplet Spread to Rooms Connected by a Central Ventilation System
- Examined Size-Dependent Infectivity of SARS-CoV-2 via Respiratory Droplets Spread through Central Ventilation Systems
- Characterized Indoor Near-Field and Far-Field Aerosol Transmission in a Model Commercial Office Building

Large-Eddy Simulation of Isothermal and Nonisothermal Turbulent Flows in Ventilated Classrooms

Presentation

Balakrishnan, R.; Kotamarthi, R.; Fischer, P. Large Eddy Simulation of Isothermal and Non-isothermal

Turbulent Flows in Ventilated Classrooms. 13th International European Research Community on Flow, Turbulence and Combustion (ERCOFTAC) Virtual Symposium: Engineering, Turbulence, Modelling and Measurements (ETMM13), Rhodes, Greece, September 15–17, 2021.

Practical Implications

- Ventilation pathways commonly seen in school classrooms, which are often of the kind where cool/hot air flows into the room from an inlet high up on a wall, create a thermal stratification layer (in winter) that inhibits mixing of air.
- Thermal stratification exacerbates the formation of dead zones where aerosols get trapped and cannot be expelled from rooms merely by increasing the air changes per hour (ACH).
- Results showed that mixing of air could be improved less expensively by redesigning the ventilation pathway (as opposed to the expensive solution of increasing ACH by increasing the ventilation flow rate). The use of isolated fans in dead zone regions could also improve mixing.
- From a simulation standpoint, the study demonstrated that it is possible to use large-eddy simulation (LES) as an effective design tool to explore a wider parameter space, on CPU+GPU computing platforms, to improve classroom ventilation in existing buildings and to design new classrooms.

Summary

Over the last year, interest was renewed in simulating flows-particle interactions in enclosed spaces to (1) assess the length of time for which aerosol particles continue to remain in a ventilated room and (2) estimate the deposition of aerosol particles around people in a room. Due to the computational cost of doing resolved simulations of the flow-field, which is inherently unsteady by nature, the vast majority have been steady state simulations with Reynolds Averaged Navier-Stokes models. Examples include the $k - \epsilon$ model (with known limitations for predicting separated and recirculating flows), LES on coarse meshes, and very diffusive sub-grid scale models. Therefore, the goal of this

research at Argonne National Laboratory (ANL) was twofold: (1) to advance the understanding of turbulent flows in enclosed rooms via well-resolved LES of the isothermal and nonisothermal flows at realistic ventilation rates and (2) to demonstrate the use of LES as a viable tool for designing indoor ventilation systems on heterogeneous computing platforms (i.e., CPU + GPU). This study considered isothermal and nonisothermal flows in a classroom setting with different placements of ventilation outlets and different layouts of student units within the classroom. Simulation results indicated that the locations and extents of dead zones—regions with very low velocity and turbulent kinetic energy—can be altered quite significantly with changes in the ventilation pattern. Dead zone locations and extents can also be altered with changes in the temperature of the ventilation jet and could, in turn, become highly infectious zones if aerosol particles with significant virion density tend to accumulate preferentially in these regions (see Figs. 4.1 and 4.2, p. 160).

Measured Influence of Overhead HVAC on Exposure to Airborne Contaminants from Simulated Speaking in a Meeting and a Classroom

Publication

Singer, B. C.; Zhao, H.; Preble, C. V.; Delp, W. W.; Pantelic, J.; Sohn, M. D.; Kirchstetter, T. K. Measured Influence of Overhead HVAC on Exposure to Airborne Contaminants from Simulated Speaking in a Meeting and a Classroom. *Indoor Air* **2022**, *32* (1), e12917. DOI: 10.1111/ina.12917

Practical Implications

- Overhead HVAC systems, which are common in schools and office buildings, can create thermally stratified conditions during heating.
- Stratification interferes with dilution and reduces the effectiveness of ventilation to remove expelled respiratory aerosols that can carry infectious agents.

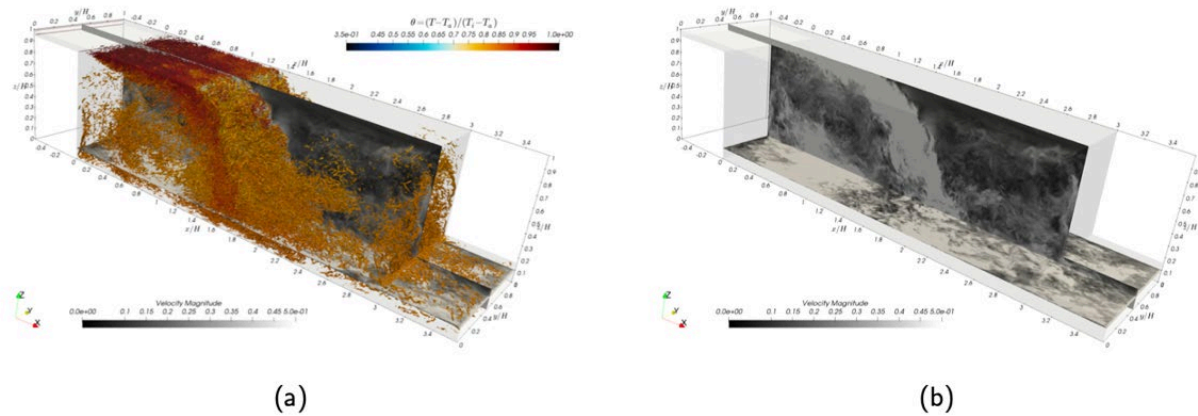


Fig. 4.1. Nonisothermal results with the inlet temperature 5°C cooler than ambient. **(a)** λ_2 isosurface colored by the nondimensional temperature (θ). **(b)** Instantaneous velocity indicates the extent of the dead zones in the room. [Courtesy Argonne National Laboratory]

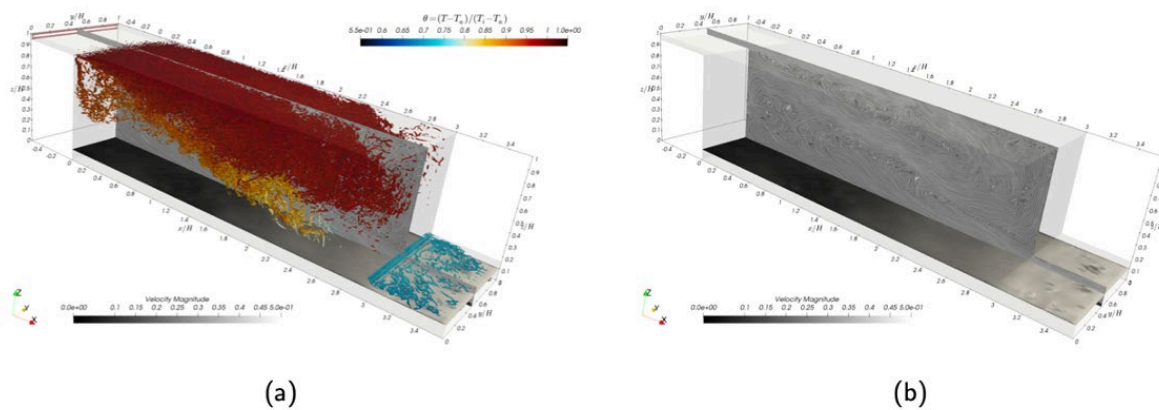


Fig. 4.2. Nonisothermal results with the inlet temperature 5°C warmer than ambient. **(a)** λ_2 isosurface colored by the nondimensional temperature (θ). **(b)** Instantaneous velocity indicates the extent of the dead zones in the room. [Courtesy Argonne National Laboratory]

- Ceiling diffusers can achieve good mixing for effective dilution and ventilation of bioeffluents when supplying cooled or thermally neutral air.
- Fans, including portable air filters, can break up stratification and improve ventilation performance during the heating season.

Summary

Tracer gas experiments were conducted at Lawrence Berkeley National Laboratory's (LBNL) FLEX-LAB facility in a 158 m³ room with overhead supply

diffusers to study dispersion of contaminants from simulated speaking in physically distanced meeting and classroom configurations. The room was contained within a 237 m³ cell with open plenum return to the HVAC system. Heated manikins at desks and a researcher operating the tracer release apparatus presented 8–9 thermal plumes. Experiments were conducted under conditions of no forced air and neutral, cooled, or heated air supplied at 980–1100 m³h⁻¹, and with/out 20% outdoor air. CO₂ was released at the head of one manikin in

each experiment to simulate small ($<5 \mu\text{m}$ diameter) respiratory aerosols. The metric of exposure relative to perfectly mixed (ERM) was introduced to quantify impacts, based on measurements at manikin heads and at three heights in the center and corners of the room. Chilled or neutral supply air provided good mixing with ERMs close to one. Thermal stratification during heating produced higher ERMs at most manikins: 25% were ≥ 2.5 and the highest were $>5 \times$ perfectly mixed conditions. Operation of two within-zone air cleaners together moving $\geq 400 \text{ m}^3\text{h}^{-1}$ vertically in the room provided enough mixing to mitigate elevated exposure variations (see Fig. 4.3, this page).

Investigation of Potential Aerosol Transmission and Infectivity of SARS-CoV-2 through Central Ventilation Systems

Publication

Pease, L. F.; Wang, N.; Salsbury, T. I.; Underhill, R. M.; Flaherty, J. E.; Vlachokostas, A.; Kulkarni, G.; James, D. P. Investigation of Potential Aerosol Transmission and Infectivity of SARS-CoV-2 Through Central Ventilation Systems. *Building and Environment* **2021**, *197*, 107633. DOI: 10.1016/j.buildenv.2021.107633

Practical Implications

- Well-mixed multizone model evaluated COVID-19 infection probabilities under different system operating scenarios for internal and external exposure sources.
- This study showed for internal sources that: (1) more filtration lowered the probability of infection in connected spaces, (2) higher air change rates increased infection probabilities in connected rooms, and (3) increasing outdoor air decreased virus concentration.

Summary

The COVID-19 pandemic raised concern of viral spread within buildings. Although the near-field transmission and the infectious spread within individual rooms have been well studied, the impact of aerosolized spread of SARS-CoV-2 via air handling

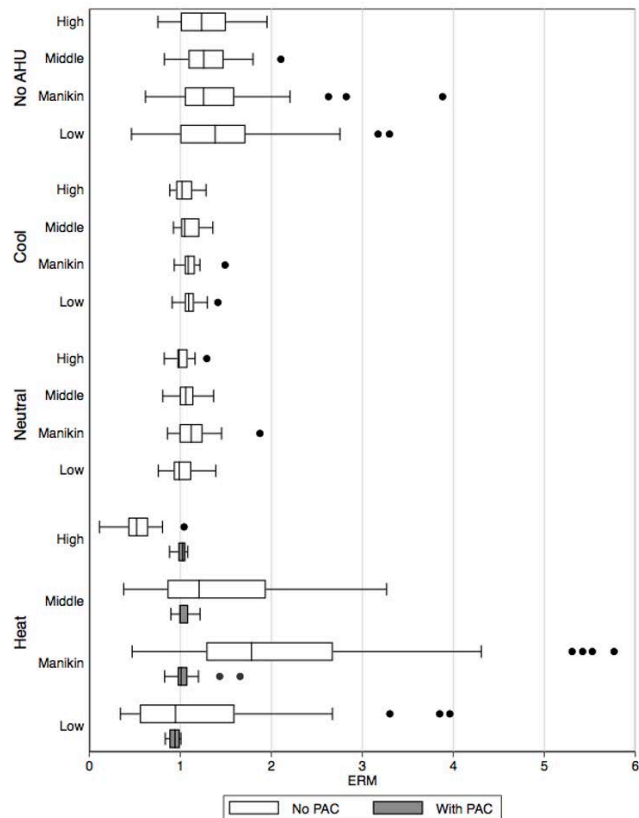


Fig. 4.3. Exposures relative to perfectly mixed (ERM) at each vertical level of the room under each HVAC condition in meeting room experiments with no outdoor air. PAC refers to the operation of portable air cleaners. Boxes show median and interquartile range (IQR) and whiskers extend to $1.5 \times$ IQR. Measurement heights: low = 30 cm; manikins mostly seated at 105 cm; standing teacher at 121 cm; middle = 137 cm; high = 244 cm. [Reprinted with permission from Singer, B. C. et al. Measured Influence of Overhead HVAC on Exposure to Airborne Contaminants from Simulated Speaking in a Meeting and a Classroom. *Indoor Air* **2022**, *32* (1), e12917. DOI: 10.1111/ina.12917. Copyright 2022 John Wiley and Sons.]

systems within buildings remains unexplored. This study at Pacific Northwest National Laboratory (PNNL) evaluated the concentrations and probabilities of infection for both building interior and exterior exposure sources using a well-mixed model of a multiroom building served by a central air handling system (without packaged terminal air conditioning). In particular, the Viral Fate and

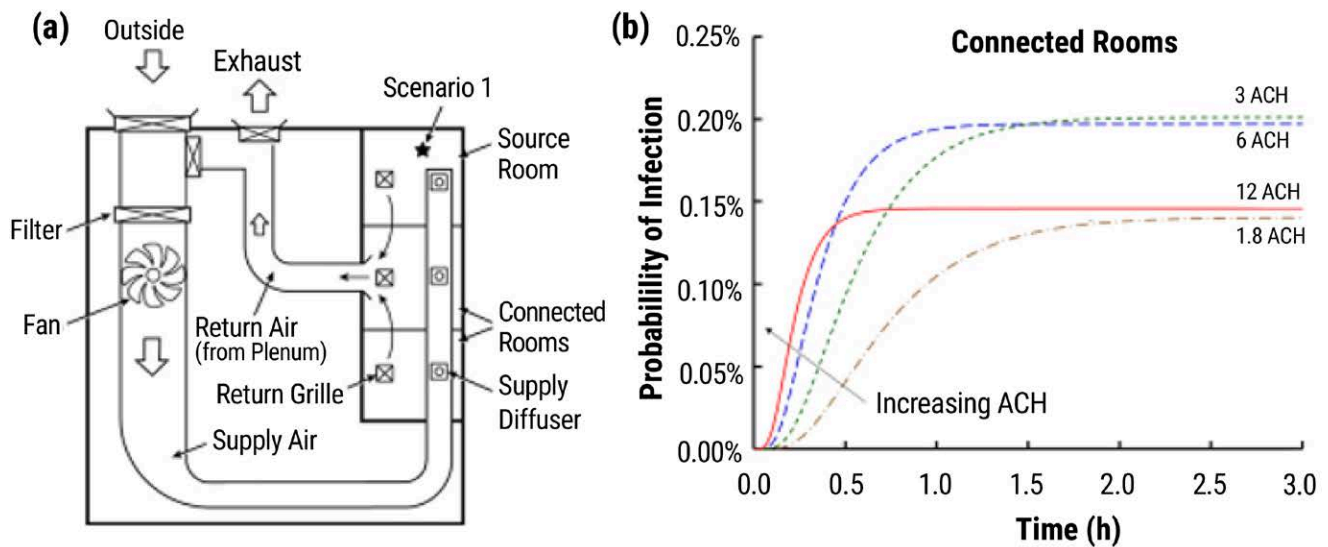


Fig. 4.4. (a) Essential elements of a central air handling system in a generic small building. The virus spreads to the connected rooms via a centrally connected plenum and air handling unit (AHU). (b) Cumulative probability of infection versus time for the connected rooms for air change rates of 1.8, 3, 6, and 12 air changes per hour (ACH). Reprinted from Pease, L.F., et al. Investigation of Potential Aerosol Transmission and Infectivity of SARS-CoV-2 through Central Ventilation Systems. *Building and Environment* **2021**,197, 107633. DOI: 10.1016/j.buildenv.2021.107633. Copyright 2022, with permission from Elsevier.]

Transport team compared the influence of filtration, air change rates, and the fraction of outdoor air. When the air supplied to the rooms comprised both outdoor air and recirculated air according to typical guidelines, filtration had the largest impact on lowering the concentration and probability of infection in both source and connected rooms. Increasing the air change rate removed virus from the source room faster but also increased the rate of exposure in connected rooms. Therefore, slower air change rates reduced infectivity in connected rooms at shorter durations. Furthermore, increasing the fraction of virus-free outdoor air was helpful unless outdoor air was infective, in which case pathogen exposure inside persisted for hours after a short-term release. Increasing the outdoor air to 33% or the filter to MERV-13 decreased infectivity in connected rooms by 19% or 93% respectively, relative to a MERV-8 filter with 9% outdoor air based on 100 quanta/h of 5 μm droplets, a breathing rate of 0.48 m^3/h , and for the building

dimensions and air handling system considered (see Fig. 4.4, this page).

Experimental Evaluation of Respiratory Droplet Spread to Rooms Connected by a Central Ventilation System

Publication

Vlachokostas, A.; Burns, C. A.; Salisbury, T. I.; Daniel, R. C.; James, D. P.; Flaherty, J. E.; Wang, N.; Underhill, R. M.; Kulkarni, G.; Pease, L. F. Experimental Evaluation of Respiratory Droplet Spread to Rooms Connected by a Central Ventilation System. *Indoor Air* **2022**, 32 (1), e12940. DOI: 10.1111/ina.12940

Practical Implications

- This study presented experimental results showing how transmissions of airborne viral particles that mimic SARS-CoV-2 are affected by HVAC operations, including airflow rate, outdoor air fraction, and filtration.

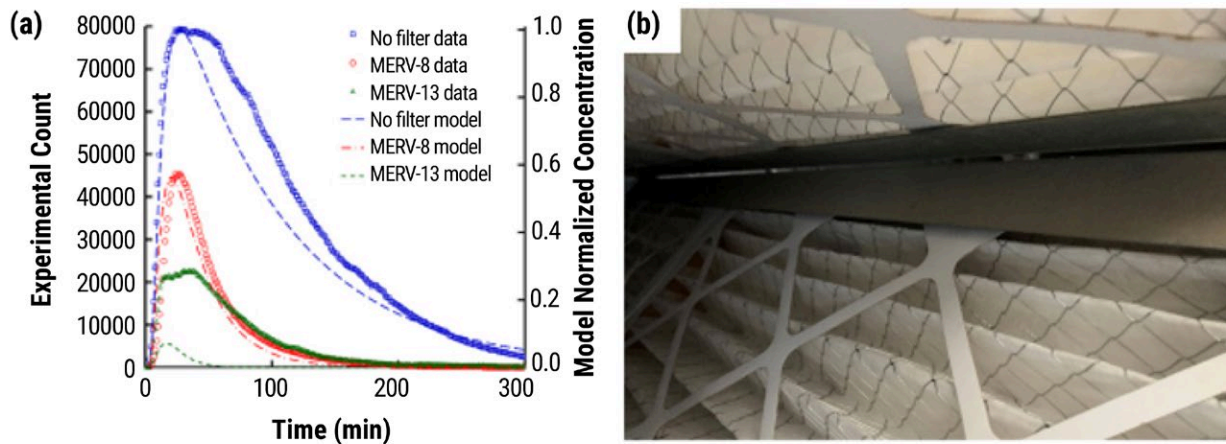


Fig. 4.5. (a) Differential particle counts averaged across two rooms connected to a source room via a central ventilation system versus time from respiratory droplet release for no filter, a MERV-8 filter, and a MERV-13 filter for size bins of 1-2 μm with corresponding model predictions. Secondary axis aligned to match the tallest peak magnitude. **(b)** Small gap (>1 mm) at the intersection of two filters arranged in a “V” configuration within a larger filter housing that permits respiratory droplets to bypass the filter. [Reprinted with permission from Vlachokostas, A., et al. Experimental Evaluation of Respiratory Droplet Spread to Rooms Connected by a Central Ventilation System. *Indoor Air* **2022**, 32 (1), e12940. DOI: 10.1111/ina.12940. Copyright 2022 John Wiley and Sons.]

- Experimental data was used to validate the utility of simplified models, such as those based on a well-mixed assumption.
- Data from physical experiments provided evidence for researchers and practitioners to develop effective building operation strategies that not only assure a safer reopening after the COVID-19 pandemic but also protect building occupants from other airborne pathogens.

Summary

An experimental study by PNNL ascertained SARS-CoV-2 virus transmissibility between rooms in a building connected by a central ventilation system. Respiratory droplet surrogates made of mucus and virus mimics were released in one room in a test building, and measurements of concentration levels were made in other rooms connected through the ventilation system. Experimental results were obtained for different ventilation system configurations, including ventilation rate, filtration level (up to MERV-13), and fractional outdoor air intake. The most important finding was that respiratory droplets can and do transit through central ventilation

systems, suggesting a mechanism for viral transmission (and COVID-19 specifically) within the built environment in reasonable agreement with well-mixed models. Deposition of these droplets on room walls was found to be negligibly small (see Fig. 4.5, this page).

Size Dependent Infectivity of SARS-CoV-2 via Respiratory Droplets Spread through Central Ventilation Systems

Publication

Pease, L. F.; Wang, N.; Salsbury, T. I.; Underhill, R. M.; Flaherty, J. E.; Vlachokostas, A.; Kulkarni, G.; James, D. P. Investigation of Potential Aerosol Transmission and Infectivity of SARS-CoV-2 Through Central Ventilation Systems. *Building and Environment* **2021**, 197, 107633. DOI: 10.1016/j.buildenv.2021.107633

Practical Implications

- Bronchiole and larynx droplets readily transit central ventilation systems.
- Oral droplets rarely transit central ventilation systems.

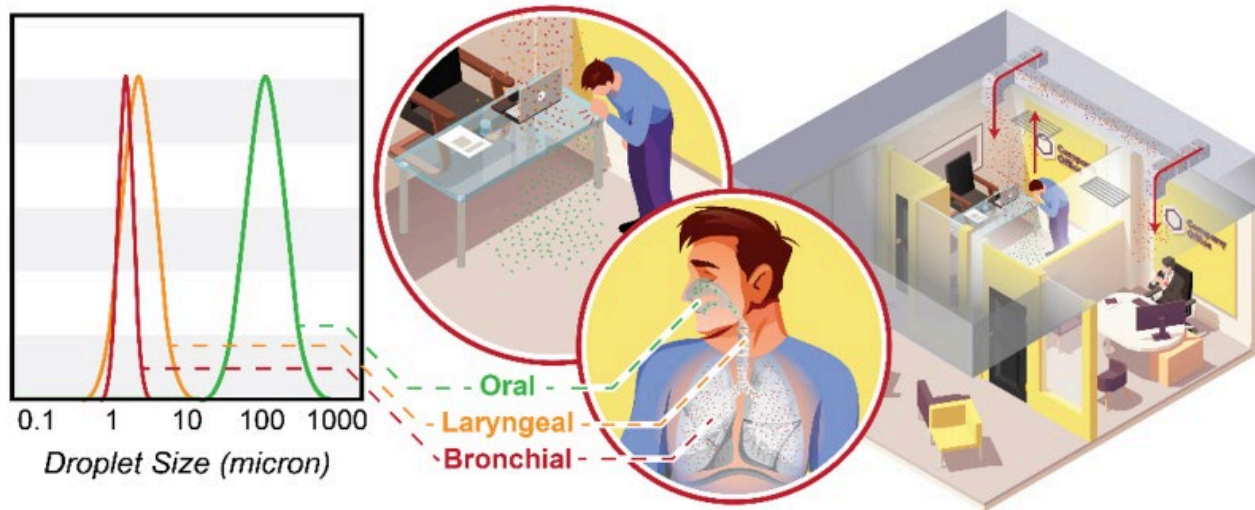


Fig. 4.6. The fate and transport of respiratory droplets through buildings with central ventilation systems depends on the droplet sizes. The larger droplets dominated the infectivity of the room in which they were released, but the small droplets transmitted through the air handling systems to adjacent rooms. [Reprinted from Pease, L. F., et al. Size Dependent Infectivity of SARS-CoV-2 via Respiratory Droplets Spread through Central Ventilation Systems. *International Communications in Heat and Mass Transfer* **2021**, 105748. DOI: 10.1016/j.icheatmasstransfer.2021.105748. Copyright 2022, with permission from Elsevier.]

- The probability of lower respiratory or deep lung infection will be higher than upper respiratory infections when viral particles are spread between rooms via a central air handling system.
- Raising humidity and temperature in air handlers reduced infectivity risk modestly.

Summary

A PNNL study evaluated the transport of respiratory droplets that carry SARS-CoV-2 through central air handling systems in multiroom buildings. Respiratory droplet size modes arise from the bronchioles representing the lungs and lower respiratory tract, the larynx representing the upper respiratory tract including vocal cords, or the oral cavity. The size distribution of each mode remains largely conserved, although the magnitude of each droplet mode changes as infected individuals breathe, speak, sing, laugh, cough, and sneeze. This study evaluated how each type of respiratory droplet transits central ventilation systems and the implications thereof for infectivity of COVID-19. Results showed that while larger oral droplets can transmit through the air handling systems, their size and concentration were greatly reduced, with but few

oral droplets leaving the source room. In contrast, the smaller droplets that originated from the bronchioles and larynx were much more effective in transiting through the air handling system into connected rooms (see Fig. 4.6, this page). These findings suggested that the ratio of lower respiratory or deep lung infections increased relative to upper respiratory infections in rooms connected by central air handling systems. Also, increasing the temperature and humidity in the range considered after the droplets have achieved an equilibrium size reduced the probability of infection.

Characterization of the Indoor Near-Field and Far-Field Aerosol Transmission in a Model Commercial Office Building

Publication

Chien, C. H.; Cheng, M. D.; Im, P.; Nawaz, K.; Fricke, B.; Armstrong, A. Characterization of the Indoor Far-Field Aerosol Transmission in a Model Commercial Office Building. *Int. Comm. Heat Mass Transfer* **2021**, 105744. DOI: 10.1016/j.icheatmasstransfer.2021.105744

Practical Implications

- In the near-field study, a well-mixed condition was established under the effect of HVAC in the test building with multiple zones at ORNL.
- Within the source zone in the test building, the analysis of aerosol concentrations showed the return air fraction dominated compared to other factors, such as outside air ratio, filtration, transport loss in ventilation duct, and particle deposition.
- In the far-field study, the fraction of aerosol transmitted was <16% and <11% for submicron and micron aerosol, respectively, with doors closed.
- Opening interior doors that connect different zones could greatly enhance the aerosol transmission for zones close to the source but appeared to have less impact on those farther away.

Summary

Aerosol transmission under the effect of HVAC was studied in a multizone small office test building at Oak Ridge National Laboratory (ORNL). For the near-field campaigns, nine measurement points in a single zone using active aerosol impactors reported that the coefficient of variation of the time-averaged concentration over one hour was <10% in two campaigns and <15% in one campaign, indicating a nearly well-mixed condition. To understand the effect of the building HVAC system operation on the concentration of aerosols in office spaces, an aerosol transport model that included factors such as outside air ratio, filtration, return air fraction, transport loss in duct, and particle deposition was developed. The model fitting results demonstrated excellent agreement with experimental data. This investigation found that the return air fraction outweighed other mechanisms for the aerosol recirculation, and the air change rate (ACR) was more important than the small particle deposition for aerosol removal. Because ACR dominated the aerosol transport, the full model could be simplified to just one factor, the ACR, while maintaining acceptable representation of the experimental data. For the far-field study, data showed higher submicron-aerosol transmission than that for the larger ones. In campaigns with the doors closed,

the submicron aerosol transmission was less than 16% and less than 11% for micron aerosol transmission. Opening the interior doors that connect different zones could significantly enhance the aerosol transmission for zones close to the source but appeared to have less impact on those farther away (see Fig. 4.7, p. 166).

4.3.5 Results: Topic 2

Airborne Exposure Risk in Buses, Semi-Enclosed Dining Environments, and Outdoor Spaces

- Airborne Exposure Risk of Modeled Indoor and Outdoor Dining Environments Using a Rapid Response Model
- Regional Relative Risk: A Physics-Based Metric for Characterizing Airborne Infectious Disease Transmission
- Modeling and Mitigating Airborne Pathogen Risk Factors in School Buses
- High-Fidelity Large-Eddy Simulation Using a Directly Coupled Eulerian and Point-Lagrangian Tool: Coupling CFD with Dose-Response Modeling Airborne Exposure Risk of Modeled Indoor and Outdoor Dining Environments Using a Rapid Response Model

Practical Implications

- Different outdoor dining configurations at restaurants can be assessed using the Quick Urban and Industrial Complex (QUIC) fast-running high-resolution 3D wind and plume model to reduce the risk of airborne viral transmission.
- Airborne viral plume residence time within different courtyard areas depends on the area of the courtyard, the height of the surrounding walls, whether the walls are the same height or different heights, the wind speed and direction, and the location of the emitter within the courtyard.
- Partially enclosed dining areas should be designed to maximize air flow, taking into consideration different layouts, including wind breaks

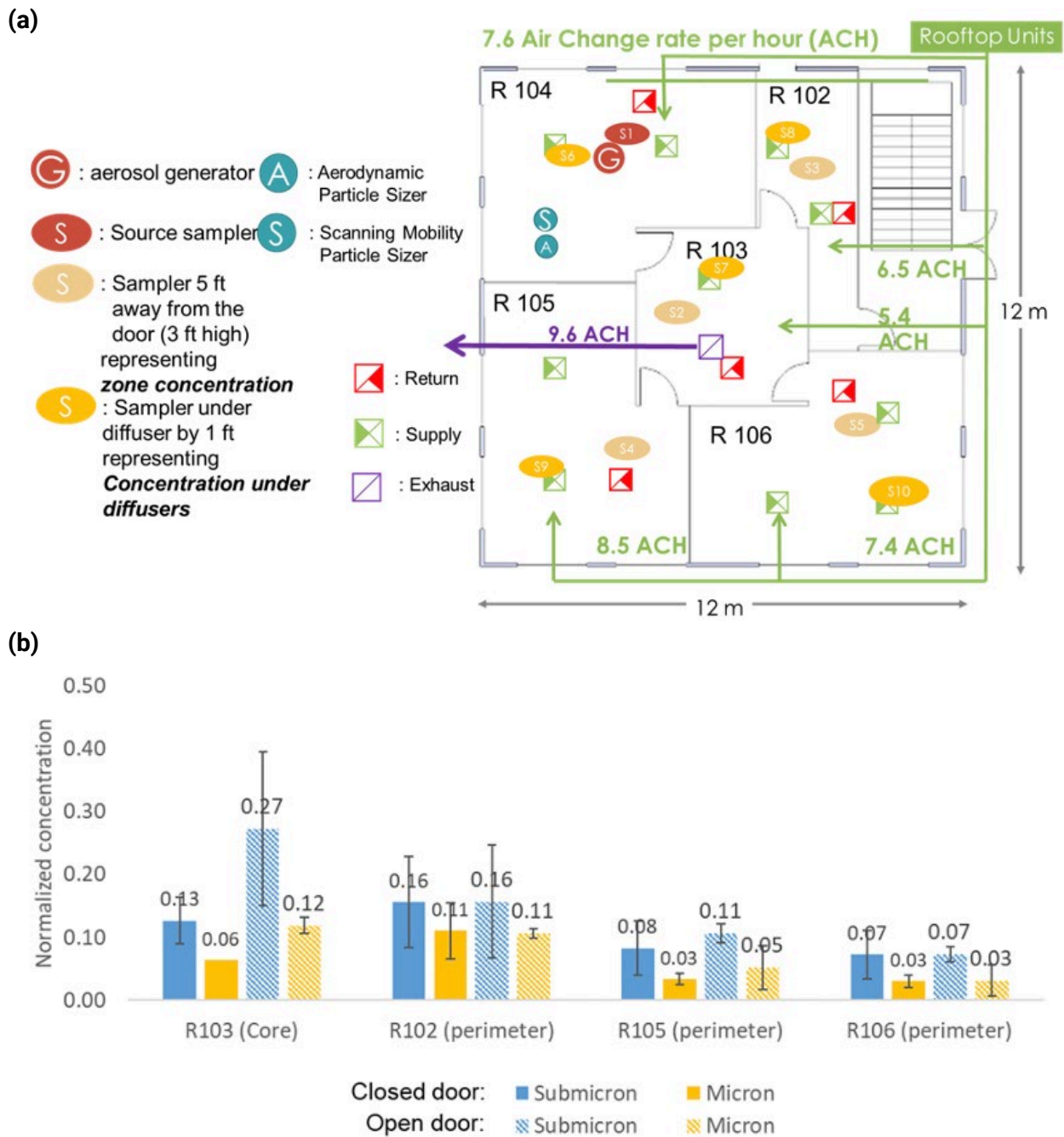


Fig. 4.7. (a) Ventilation and sampler deployment in the far-field campaigns. **(b)** Comparison of cross-zone aerosol transmission: closed door vs. open door. [Reprinted from Chien, C.H., et al. Characterization of the Indoor Far-Field Aerosol Transmission in a Model Commercial Office Building. *International Communications in Heat and Mass Transfer* **2021**, 105744. DOI: 10.1016/j.icheatmasstransfer.2021.105744.105748. Copyright 2022, with permission from Elsevier.]

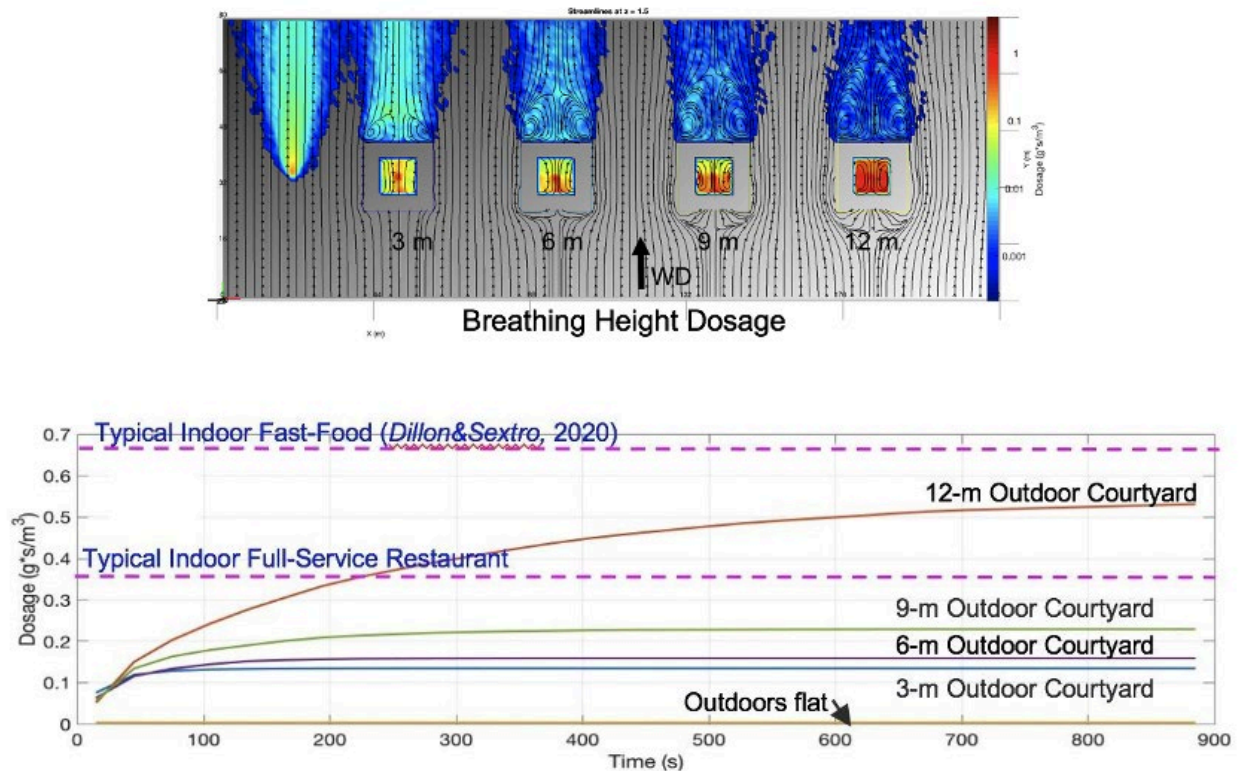


Fig. 4.8. Plan view of 3D courtyard plume simulation with an emitter at the center of the courtyard. The droplet emissions get transported and mixed out of the courtyard for shorter wall heights and trapped near the surface as the building height increases. Note that dosage (i.e., time-integrated concentration) levels are on a log scale. Streamlines show wind patterns and are denoted by black lines (top). For deeper courtyards, QUIC dispersal calculations suggest weaker ventilation, leading to time-integrated airborne concentrations that are similar to those found in indoor fast-food restaurants (bottom). [Courtesy Los Alamos National Laboratory]

like interior dividers, shade canopies, trees, and bushes.

- For deeper outdoor courtyards, QUIC dispersal calculations suggest weaker ventilation, leading to airborne concentrations that are similar to those found in indoor fast-food restaurants.

Summary

At Los Alamos National Laboratory (LANL), the QUIC chemical, biological, and radiological (CBR) Plume Modeling System was used to simulate droplet emissions from a single infected diner sitting in an outdoor courtyard dining environment. A tracer gas, solid particles, and evaporating droplets of different sizes were used to assess the residence time and peak concentrations reached inside of different

sized courtyards with walls of different heights. Model results showed that small courtyards with tall walls of the same height generally resulted in the largest residence time of gas, particles, and evaporating droplets. With wall height and wind conditions fixed, contaminants were flushed out more rapidly in larger area courtyards. Walls of different height generally acted to produce more ventilation in the courtyard, leading to lower airborne concentrations. The exposure levels in a tall square outdoor courtyard were somewhere between levels found in a typical fast-food restaurant and in a typical full-service indoor restaurant, while those with shorter walls were within a factor of two or three of the levels in a full-service indoor restaurant (see Fig. 4.8, this page). These modeling results suggest

that some outdoor dining spaces are not well ventilated and could result in heightened risk of infection if masks are not worn.

Regional Relative Risk: A Physics-Based Metric for Characterizing Airborne Infectious Disease Transmission

Publication

Dillon, Charles F.; Dillon, M. B. Regional Relative Risk: A Physics-Based Metric for Characterizing Airborne Infectious Disease Transmission. *Appl. Environ. Microbiol.* **2021**, *87* (21), e01262-21. DOI: 10.1128/AEM.01262-21

Practical Implications

- Regional Relative Risk (RRR) is a new epidemiological metric that compares the risk between two geographic regions, which can range from individual rooms to large areas. Minimal information is required to use the RRR for distances ranging from 50 m to 20 km downwind.
- This work could enhance airborne disease outbreak assessment and management, as well as the control of chronically occurring airborne exposures.
- This work predicted a signature of single particle, airborne infection events.
- This work could inform future updates to remediation clearance and biosafety criteria (i.e., how clean is clean enough).
- This work demonstrated that even when infectivity is lost rapidly, 10 h^{-1} , infection probabilities were minimally impacted 100s of meters downwind.

Summary

Airborne infectious disease transmission events occur over a wide range of spatial scales and can be an important means of disease transmission. Physics- and biology-based models can assist in predicting airborne transmission events, overall disease incidence, and disease control strategy efficacy. Lawrence Livermore National Laboratory (LLNL) developed a new theory that extends current approaches for the case in which an individual

is infected by a single airborne particle, including the scenario in which numerous infectious particles are present in the air but only one causes infection (see Fig. 4.9, p. 169). A single infectious particle can contain more than one pathogenic microorganism and be physically larger than the pathogen itself. This approach allows robust relative risk estimates even when there is wide variation in (1) individual exposures and (2) the individual response to that exposure (the pathogen dose-response function can take any mathematical form and vary by individual). Based on this theory, this study proposed the Regional Relative Risk – a new metric, distinct from the traditional relative risk metric that compares the risk between two regions (in theory, these regions can range from individual rooms to large geographic areas). This research applied the Regional Relative Risk metric to outdoor disease transmission events over spatial scales ranging from 50 m to 20 km, demonstrating that in many common cases, minimal input information was required to use the metric. Results also demonstrated consistency with data from prior outbreaks. Future efforts could apply and validate this theory for other spatial scales, such as indoor environments. This work provides context for (1) the initial stages of an airborne disease outbreak and (2) larger scale disease spread, including unexpected low probability disease sparks that potentially affect remote populations, a key practical issue in controlling airborne disease outbreaks.

Modeling and Mitigating Airborne Pathogen Risk Factors in School Buses

Publication

Ho, C. K.; Binns, R. Modeling and Mitigating Airborne Pathogen Risk Factors in School Buses. *Int. Comm. Heat Mass Transfer* **2021**, *129*, 105663. DOI: 10.1016/j.icheatmasstransfer.2021.105663

Practical Implications

- For stationary bus scenarios, including at least one set of openings when the heater is on is recommended to promote ventilation, dilution, and through-flow conditions.

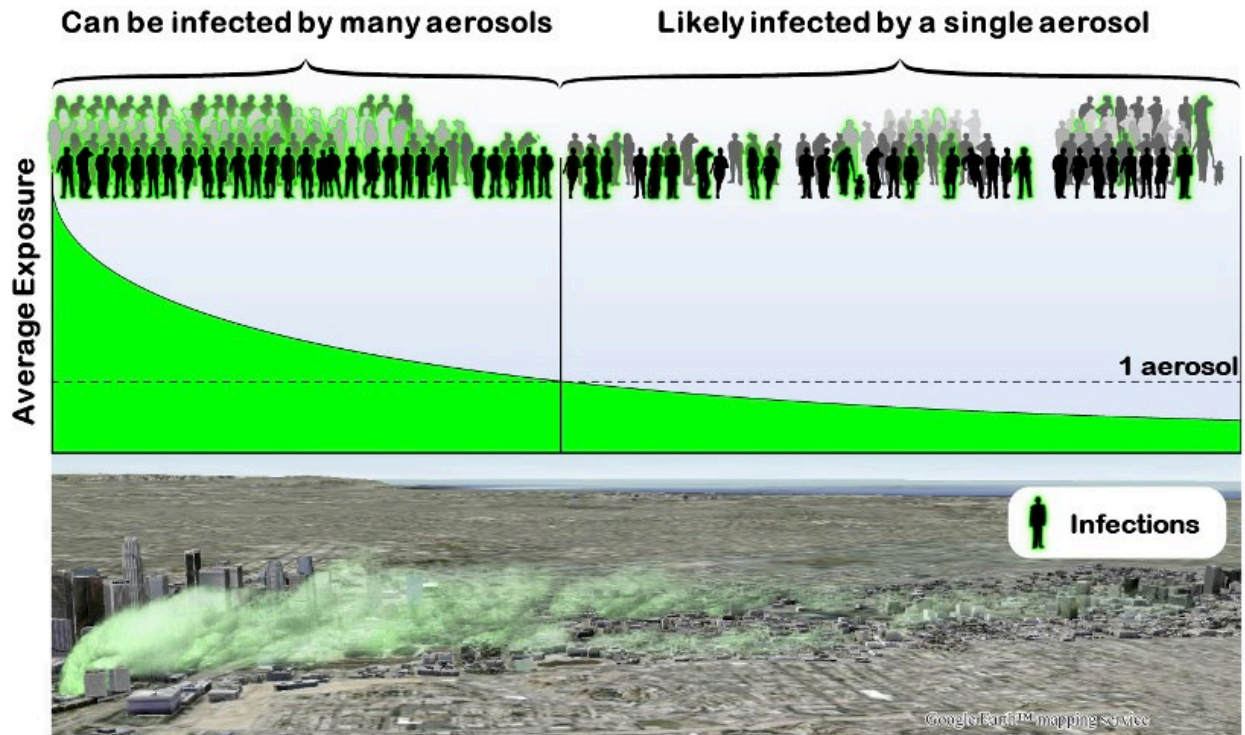


Fig. 4.9. Illustration of locations in which people can be infected by many (top left) or a single (top right) airborne particle. Single particle infections can occur far downwind (bottom). This illustration assumes that the inhalation of a single particle is sufficient to cause infection. [Reprinted with permission from ASM Journals. Articles of Significant Interest in this Issue. *Applied Environmental Microbiology* **2021**, 87 (21), e01747-21. DOI: 10.1128/AEM.01747-21. Copyright 2022 American Society for Microbiology.]

- For moving bus scenarios, opening just the emergency hatch on top of the bus is not recommended. At least two sets of openings (e.g., hatch and back windows, front and back windows) are recommended to promote through-flow conditions, increase ventilation, and reduce exposure risks while maintaining thermal comfort. Opening every other window or all windows is recommended if environmental conditions allow it.
- In a moving bus with the front and back windows open, air tends to enter the bus toward the rear opening(s), move toward the front of the cabin, and leave the cabin through the front opening(s). Placing at-risk individuals near openings toward the rear of the vehicle may reduce the risks of exposure from upstream passengers.
- Recommendations from this study were implemented in new safety and operating procedures

by the Albuquerque Public Schools Transportation Center.

Summary

Sandia National Laboratories (SNL) developed computational fluid dynamic models to simulate the impact of different ventilation scenarios on airborne exposure risks in a 72-passenger school bus resulting from an infected student exhaling aerosolized pathogens. Scenarios and factors that were investigated included (1) a moving vs. stationary bus, (2) impacts of a heating unit within the bus, and (3) impacts of alternative ventilation scenarios with different combinations of openings (e.g., windows, door, emergency hatch). The models were compared against a limited set of tests that measured transient temperatures and air speeds when the heater was turned on to gain confidence in the methods and simulations. Simulation results

showed that when the bus was stationary, use of the heater increased receptor pathogen concentrations unless there was another opening. When the bus was moving, simulations with at least two sets of openings separated from each other in the forward and aft directions produced a through-flow condition that reduced pathogen concentrations via dilution from outside air by a factor of ten or more. A single opening in a moving bus generally increased pathogen concentrations throughout the cabin due to increased mixing with minimal ventilation. The cumulative exposure risk (time-averaged concentrations) was found to be inversely correlated to the air exchange rate. Stationary and moving-bus scenarios that yielded above ~20 air changes per hour resulted in the lowest cumulative exposures (see Fig. 4.10, p. 171).

Recommendations from this study were implemented in new safety and operating procedures by the Albuquerque Public Schools Transportation Center, which consisted of opening the front windows, rear windows, and hatches on buses while transporting students during the winter months. The heaters were on, and the students wore extra layers to compensate for the additional cold air flow. During seasons with warmer temperatures, all windows were opened together with the roof hatch to create the necessary air flow and ventilation, and disinfection of the bus was maintained after each run.

High-Fidelity Large-Eddy Simulation Using a Directly Coupled Eulerian and Point-Lagrangian Tool: Coupling CFD with Dose-Response Modeling

Publication

Domino, S. P. A Case Study on Pathogen Transport, Deposition, Evaporation and Transmission: Linking High-Fidelity Computational Fluid Dynamics Simulations to Probability of Infection. *International Journal of Computational Fluid Dynamics* **2021**. DOI: 10.1080/10618562.2021.1905801

Practical Implications

- This study deployed a high-fidelity, computational fluid dynamics approach that coupled Eulerian/

Lagrangian (fluids and particles) to simulate exposure risks in a common outdoor public configuration with and without environmental wind conditions.

- Close proximity to the coughing source (i.e., within 1 m) demonstrated the greatest risk for all configurations tested. Results indicated that with the added wind flow configurations, there exists a finite, nonzero risk even at distances more than 10 m from the cough source.
- Simulations for open-space social distance guidelines (10-foot diameter, 8-foot offsets) were shown to be effective for reduction of primary droplet deposition. However, aerosols containing pathogens persisted for long length and time scales in all configurations.

Summary

SNL developed a high-fidelity, Sierra/Fuego low-Mach computational fluid dynamics simulation tool that includes evaporating droplets and variable-density turbulent flow coupling. This simulation tool is well-suited to ascertain transmission probability and support risk mitigation methods development for airborne infectious diseases, such as COVID-19. A multiphysics, LES-based paradigm was used to explore droplet and aerosol pathogen transport from a synthetic cough emanating from a kneeling humanoid. For an outdoor configuration that mimics the recent open-space social distance strategy of San Francisco, maximum primary droplet deposition distances were shown to approach 8.1 m in a moderate wind configuration, with the aerosol plume transported more than 15 m. In quiescent conditions, the aerosol plume extended to approximately 4 m before the emanating pulsed jet became neutrally buoyant. A dose-response model, based on previous SARS coronavirus (SARS-CoV) data, was exercised on the high-fidelity aerosol transport database to establish relative risk at 18 virtual receptor probe locations (see Fig. 4.11, p. 172).

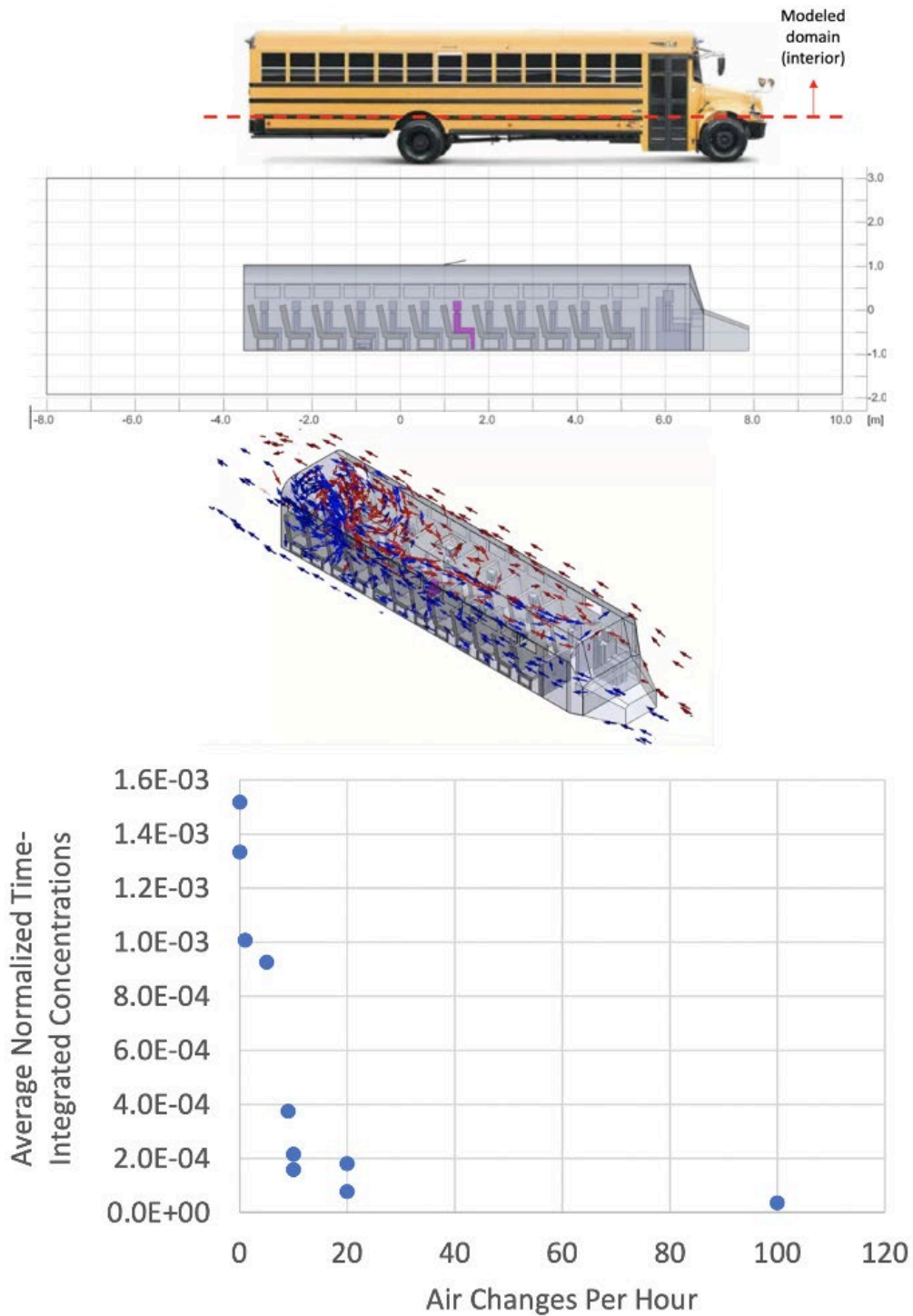


Fig. 4.10. CFD simulations of airflow and cumulative exposures in a school bus for different window openings and ventilation configurations (top). Plot of time-integrated concentrations after 30 min as a function of air changes per hour resulting from different ventilation scenarios within the school bus (bottom). [Reprinted from Ho, C. K., et al. Modeling and Mitigating Airborne Pathogen Risk Factors in School Buses. *International Communications in Heat and Mass Transfer* **2021**, 129, 105663. DOI: 10.1016/j.icheatmas-transfer.2021.105663. Copyright 2022, with permission from Elsevier.]

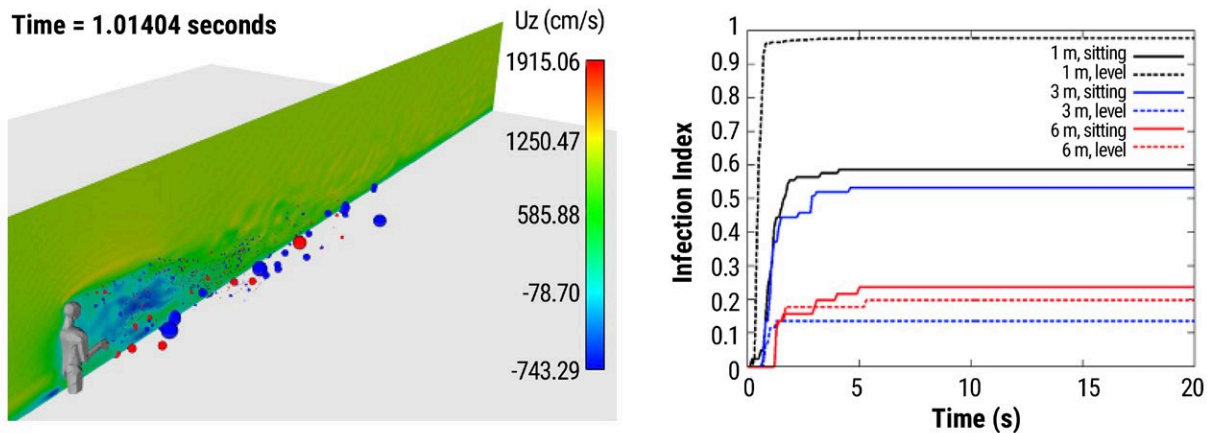


Fig. 4.11. (Left) Kneeling humanoid coughing simulation with a 10 m/s crossflow (from the back) illustrating the velocity shading recirculation zone (blue). Also included are the point-Lagrangian evaporating droplets that are found within the recirculation zone and deposited at long distances (roughly 8 m) from the source. The droplet cloud consisting of roughly 5000 droplets evaporates to form a persisting aerosol that is transported out of the full domain (> 10 m). Above, the red droplets represent those that include pathogen (roughly 30% of the droplets that emanate from the cough). (Right) Sample infection index for a set of virtual probes 1, 3, and 6 m from the cough source; 10 m/s crosswind in the streamwise direction. The plot showcases that the highest risk is directly level with the emanating cough 1 m from the cough source. The figure also captures the finding that sitting positions at large downwind locations have a higher infection index than at the level position, possibly due to crossflow and bluff body interactions effects along with boundary layer phenomena, such as turbophoresis. [Courtesy Sandia National Laboratories. See also Domino, S.P. A Case Study on Pathogen Transport, Deposition, Evaporation and Transmission: Linking High-Fidelity Computational Fluid Dynamics Simulations to Probability of Infection. *International Journal of Computational Fluid Dynamics* **2021**. DOI: 10.1080/10618562.2021.1905801

4.3.6 Results: Topic 3

Numerical Simulation of Expiratory Event and Impact of Aerosol Physics and Environmental Conditions on Dispersion and Infectivity

- Quantifying the Effect of Size, Release Location and Evaporation on HVAC-Induced Respiratory Aerosol Dispersion using High-Resolution Large-Eddy Simulations
- Direct Numerical Simulation of the Turbulent Flow Generated During a Violent Expiratory Event
- Direct Numerical Simulation of Turbulent Dispersion of Evaporative Aerosol Clouds Produced by an Intense Expiratory Event
- Simulating Near-Field Enhancement in Transmission of Airborne Viruses with a Quadrature-Based Model

- The Missing Layer in COVID-19 Studies: Transmission of Enveloped Viruses in Mucus-Rich Droplets
- Sensitivity of Airborne Transmission of Enveloped Viruses to Seasonal Variation in Indoor Relative Humidity

Quantifying the Effect of Size, Release Location and Evaporation on HVAC-Induced Respiratory Aerosol Dispersion using High-Resolution Large-Eddy Simulations

Publications

Dutta, S.; Obabko, A.; Balakrishnan, R.; Feng, Y.; Kotamarthi, R. Quantifying the Effect of Size and Release Location on HVAC Induced Respiratory Aerosol Dispersion in Using High-Resolution Large Eddy Simulations. In preparation for submission to *Phys. Fluids*.

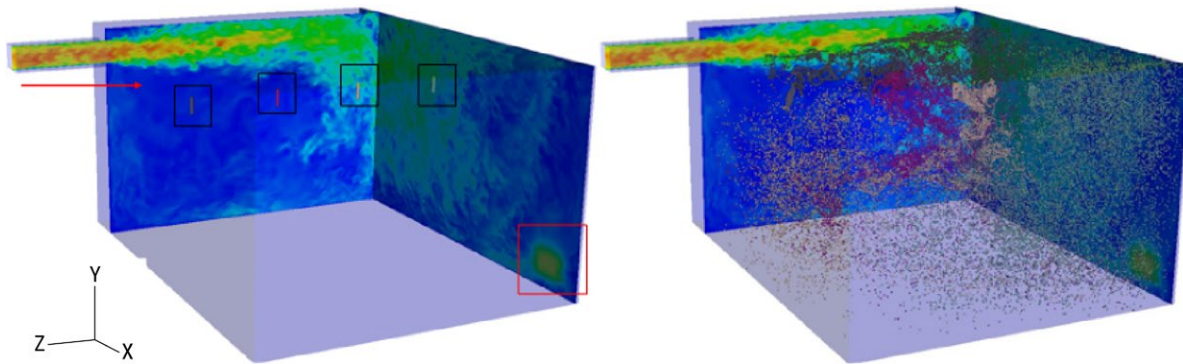


Fig. 4.12. The HVAC inflow is at the edge of the roof and outflow at the opposite corner of the room near the floor, and the layout corresponds to a single hospital room. The simulated flow is shown in the left-hand side figure and the four colored bars are release locations of 5 micro-meter (uniform size) particles. The right-hand figure shows locations of the particles due to dispersion within the room. Variation of particle dispersion within the room and rate at which they go out of the HVAC outlet was found to be highly dependent on their release location. [Courtesy Argonne National Laboratory]

Dutta, S.; Obabko, A.; Balakrishnan, R.; Feng, Y.; Kotamarthi, R. (2021). Quantifying the Effect of Evaporation on HVAC Induced Respiratory Aerosol Dispersion. In preparation for submission to *Phys. Fluids*.

Practical Implications

- This research provided accurate quantification of the turbulence in a mid-sized room, providing benchmark data to validate and test Reynolds Averaged Navier-Stokes model simulations.
- The sweeping out time of aerosols was not directly correlated with distance from outlet, with aerosols released farthest from the outlet not taking the most time to leave the room.

Summary

Using high-resolution LES, ANL investigated respiratory aerosol transport induced by HVAC (at six air changes per hour) in a 2.3 m x 4.3 m x 3.6 m empty room. These simulations are one of the first at this scale that strived to resolve all the important scales of turbulence accurately, including the turbulence property of the flow entering the room. The simulations were conducted using Nek5000, a computational fluid dynamics code that simulates fluid flow with thermal and passive scalar transport,

with aerosols being modeled using the Lagrangian particle tracking approach. Aerosols of the sizes 0.5–32 μm were released at four different locations in the room, helping to quantify the effect size and position on aerosol dispersion (see Fig. 4.12, this page). The simulations provided unprecedented information about deposition patterns and dispersal mechanisms of aerosols of different sizes. The study also quantified the effect of evaporation on the aerosols' deposition and dispersion patterns.

Publication

Fabregat, A.; Gisbert, F.; Vernet, A.; Dutta, S.; Mittal, K.; Pallarès, J. Direct Numerical Simulation of the Turbulent Flow Generated during a Violent Expiratory Event. *Phys. Fluids* **2021**, 33 (3), 035122. DOI: 10.1063/5.0042086

Practical Implications

- One of the first fully resolved turbulent simulations of an idealized cough.
- Differences between the actual buoyant turbulent puff dispersion process and the theoretical model of a cough are illustrated (see Fig. 4.13, p. 174).
- The fully resolved hydrodynamics could be used to inform new analytical models, leading to

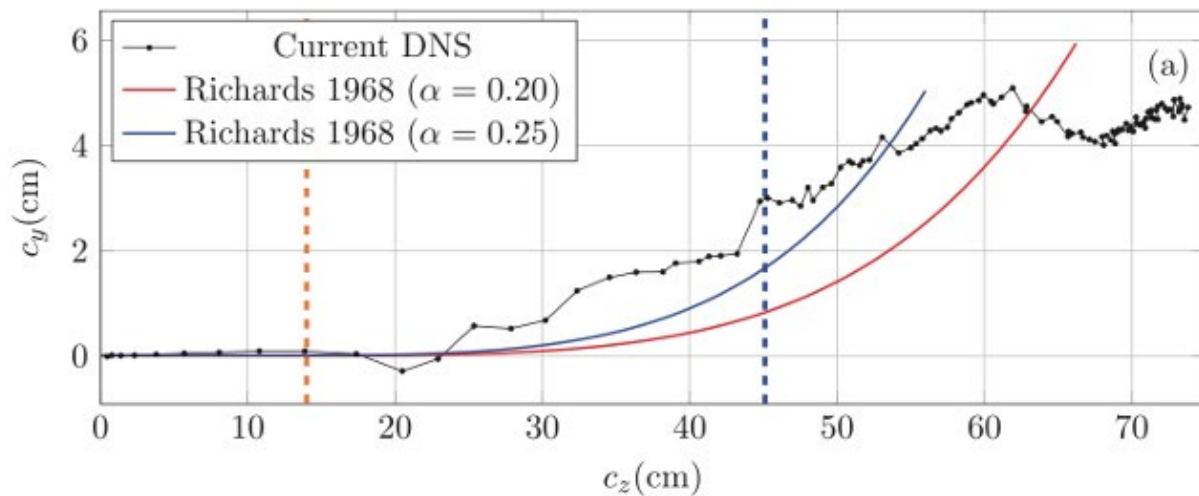


Fig. 4.13. Comparison of the puff front trajectory centroid from the DNS (thin dotted black) against the theoretical model for different values of the entrainment coefficients 0.20 (red) and 0.25 (blue). This comparison shows that the theoretical model does not capture the evolution of the cough. [Reproduced from Fabregat, A., et al. Direct Numerical Simulation of the Turbulent Flow Generated during a Violent Expiratory Event. *Phys. Fluids*. **2021**, 33 (3), 035122. DOI: 10.1063/5.0042086, with the permission of AIP Publishing.]

improved prediction of cough-induced pathogen-laden aerosol dispersion.

Summary

ANL investigated the hydrodynamics produced by a violent expiratory event resembling a mild cough. Coughs can be split into an initial jet stage during which air is expelled through the mouth and a dissipative phase over which turbulence intensity decays as the puff penetrates the environment. Time-varying exhaled velocity and buoyancy due to temperature differences between the cough and the ambient air affect the overall flow dynamics. The direct numerical simulation (DNS) of an idealized isolated cough was used to characterize the jet/puff dynamics using the trajectory of the leading turbulent vortex ring and extract its topology by fitting an ellipsoid to the exhaled fluid contour. The three-dimensional structure of the simulated cough showed that the assumption of a spheroidal puff front failed to capture the observed ellipsoidal shape. Numerical results suggested that, although analytical models provided reasonable estimates of the distance traveled by the puff, trajectory predictions exhibited larger deviations from the

DNS. The fully resolved hydrodynamics presented in this study can be used to inform new analytical models, leading to improved prediction of cough-induced pathogen-laden aerosol dispersion.

Direct Numerical Simulation of Turbulent Dispersion of Evaporative Aerosol Clouds Produced by an Intense Expiratory Event

Publication

Fabregat, A.; Gisbert, F.; Vernet, A.; Ferré, J. A.; Mittal, K.; Dutta, S.; Pallarès, J. Direct Numerical Simulation of Turbulent Dispersion of Evaporative Aerosol Clouds Produced by an Intense Expiratory Event. *Phys. Fluids*. **2021**, 33 (3), 033329. DOI: 10.1063/5.0045416

Practical Implications

- One of the first fully resolved turbulent simulations of an expiratory event with evaporative respiratory aerosols.
- Modeled the transport of different sized aerosols (4–256 μm), illustrating the effect of evaporation and turbulence on transport of respiratory aerosols. The study clearly showed that aerosols

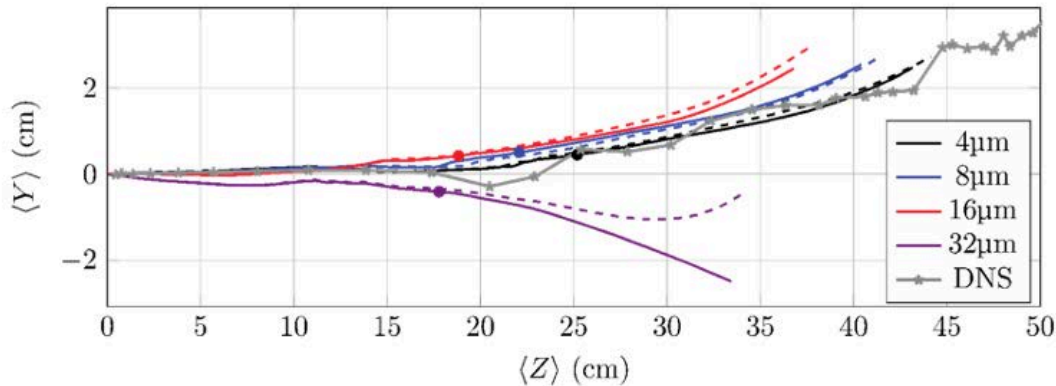


Fig. 4.14. Trajectory of particle cloud centroid for evaporative (dashed) and nonevaporative (solid) aerosols for four different aerosol sizes (4–32 μm), compared against the centroid of the buoyant air puff (DNS). [Courtesy Argonne National Laboratory and Utah State University]

of sizes 4–32 μm show maximum effect due to evaporation (see Fig. 4.14, this page).

- The probability density function generated from the simulation showed that the largest aerosols/droplet sizes (>128 μm) are transported the furthest longitudinally.
- Longitudinal and vertical spread of different sized droplets/aerosols clearly showed three different regimes based on aerosol/droplet size: first is less than or equal to 16 μm , second regime is 32–128 μm , and third is larger than 128 μm (see Fig. 4.15, this page).

Summary

ANL investigated the aerosol/droplet transport during a violent expiratory event resembling a mild cough. While the dynamics of the largest droplets are dominated by gravitational effects, the smaller aerosol particles, mostly transported by means of hydrodynamic drag, form clouds that can remain afloat for long times. In sub-saturated air environments, the dependence of pathogen-laden particle dispersion on their size is complicated due to evaporation of the aqueous fraction. Particle dynamics can significantly change when ambient conditions favor rapid evaporation rates that result in a transition from buoyancy- to drag-dominated dispersion regimes.

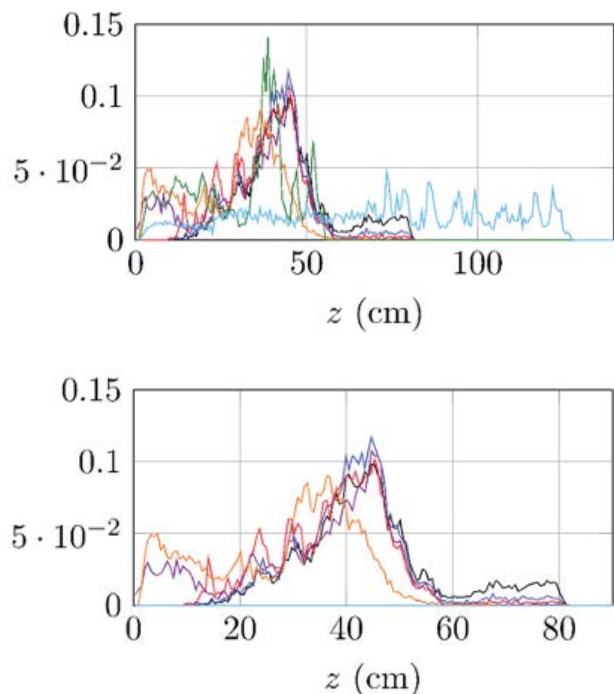


Fig. 4.15. Probability density distribution (PDF) of the terminal spatial location in each coordinate for evaporative particles: all sizes (top), 4–64 μm (bottom). [Courtesy Argonne National Laboratory and Utah State University]

To investigate the effect of particle size and evaporation on pathogen-laden cloud evolution, a direct numerical simulation of a mild cough was coupled with an evaporative Lagrangian particle advection model. Results suggested that while the dispersion of cough particles in the tails of the size distribution were unlikely to be disrupted by evaporative effects, preferential aerosol diameters (30–40 μm) might exhibit significant increases in the residence time and horizontal range under typical ambient conditions (see Figs. 4.14 and 4.15). Estimations of the viral concentration in the spewed fluid and the number of ejected particles in a typical respiratory event provided a map of viral load per volume of air at the end of the cough and the number of virus copies per inhalation in the emitter vicinity.

Simulating Near-Field Enhancement in Transmission of Airborne Viruses with a Quadrature-Based Model

Publication

Fierce, L.; Robey, A. J.; Hamilton, C. Simulating Near-Field Enhancement in Transmission of Airborne Viruses with a Quadrature-Based Model. *Indoor Air* **2021**, *31* (6), 1843–1859. DOI: 10.1111/ina.12900

Practical Implications

- The risk of airborne transmission was orders of magnitude greater in the expiratory jet of an infectious person than in a well-mixed room.
- The horizontal extent of near-field airborne transmission extended beyond the travel distance of large droplets.
- Variability in the horizontal extent of near-field effects was driven primarily by variability in expiration velocity.

Summary

Particles carrying airborne viruses are created in the respiratory system through expiratory activities, such as sneezing, coughing, talking, or breathing. A particle's size at the time of expulsion dictates the distance traveled before settling to the ground. If a particle is transported to another

individual and inhaled, its size influences if and where in the respiratory system it is most likely to deposit. For this reason, the Quadrature-based model of Respiratory Aerosols and Droplets (QuaRAD) was designed to accurately and efficiently represent the size distribution of expelled particles and their evolution through evaporation, transport, and removal. Transmission of airborne viruses depends on factors that are inherently variable and, in many cases, poorly constrained. Quantifying this uncertainty requires large ensembles of model simulations that span the variability in input parameters. However, models that are well-suited to simulate the near-field evolution of respiratory particles are also computationally expensive, which limits the exploration of parametric uncertainty. To perform many simulations that span the wide variability in factors governing airborne transmission, scientists at Brookhaven National Laboratory (BNL) developed the QuaRAD model. Quadrature methods have a long and productive history of development at BNL for the representation of aerosol and cloud droplets in atmospheric models. Their application in this model introduced a highly efficient framework for simulating the airborne fate and transport of virus-laden particles, from their expiration from an infectious person to their deposition in the nasal cavity of a susceptible person, and the subsequent risk of initial infection (see Fig. 4.16, p. 177). Using this model, scientists simulated 10,000 scenarios to quantify the risk of initial infection through airborne transition of the particular virus SARS-CoV-2.

Data Availability Statement

The QuaRAD source code, input files, and processing script are available for download at github.com/lfierce2/QuaRAD/. Simulation ensembles were created using Latin hypercube sampling with pyDOE (pythonhosted.org/pyDOE/). The sensitivity analysis was performed using the Sensitivity Analysis Library in Python, which is available at salib.readthedocs.io/en/latest.

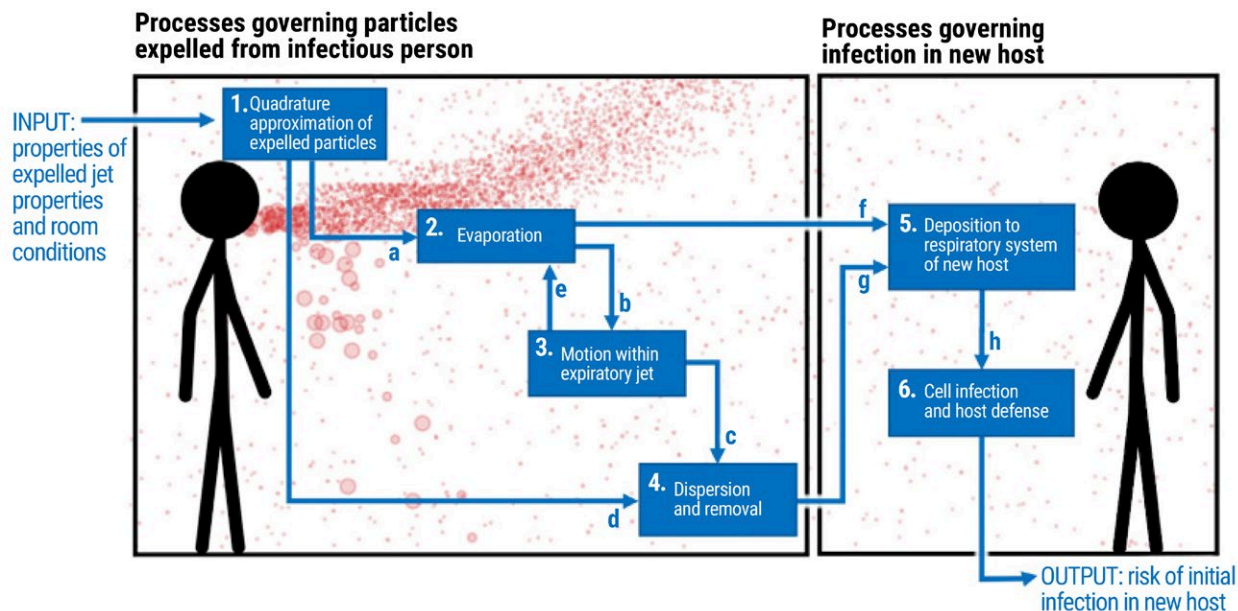


Fig. 4.16. A schematic depiction of processes represented in the Quadrature-based model of Respiratory Aerosols and Droplets (QuaRAD). These include key processes governing the evolution of expelled particles (left) and processes governing infection in a new host (right) for statistical ensembles of exposure conditions. [Reprinted under a Creative Commons Attribution 4.0 International License (CC BY 4.0) from Fierce, L., et al. Simulating Near-Field Enhancement in Transmission of Airborne Viruses with a Quadrature-Based Model. *Indoor Air* **2021**, 31 (6), 1843–1859, 2021. DOI: 10.1111/ina.12900]

The Missing Layer in COVID-19 Studies: Transmission of Enveloped Viruses in Mucus-Rich Droplets

Publication

Pease, L. F.; Wang, N.; Kulkarni, G.; Flaherty, J. E.; Burns, C. A. A Missing Layer in COVID-19 Studies: Transmission of Enveloped Viruses in Mucus-Rich Droplets. *Int. Comm. Heat and Mass Transfer* **2021**, 131, 105746. DOI: 10.1016/j.icheatmasstransfer.2021.105746

Practical Implications

- Analysis showed that mucus shells increased the drying time by orders of magnitude so that enveloped virions might remain well hydrated and thus, fully infective at substantial distances.
- Aerosolized particles that remain infectious could potentially be transmitted through ventilation systems in buildings.
- Analysis could help guide public health policies, such as social distancing.

Summary

PNNL evaluated the influence of mucus layers on the evaporation time and transport of enveloped viruses, including SARS-CoV-2. Enveloped viruses must remain moist to be fully infective. Yet, the simple but enduring Wells model, which is based on water droplets, divides respiratory droplets into two categories: (1) droplet nuclei, or quickly evaporated aerosolized particles (<10 s) or (2) liquid droplets that fall to the nearest surface. The Wells model division leaves no physical mechanism for airborne transmission of fully infective enveloped viruses over large distances (greater than a few meters). Yet, the role of mucus layers on evaporation times has not been considered even though the formation of mucus shells around liquid cores of respiratory droplets has been shown experimentally. This study showed that mucus shells increased the drying time by orders of magnitude so that enveloped virions might

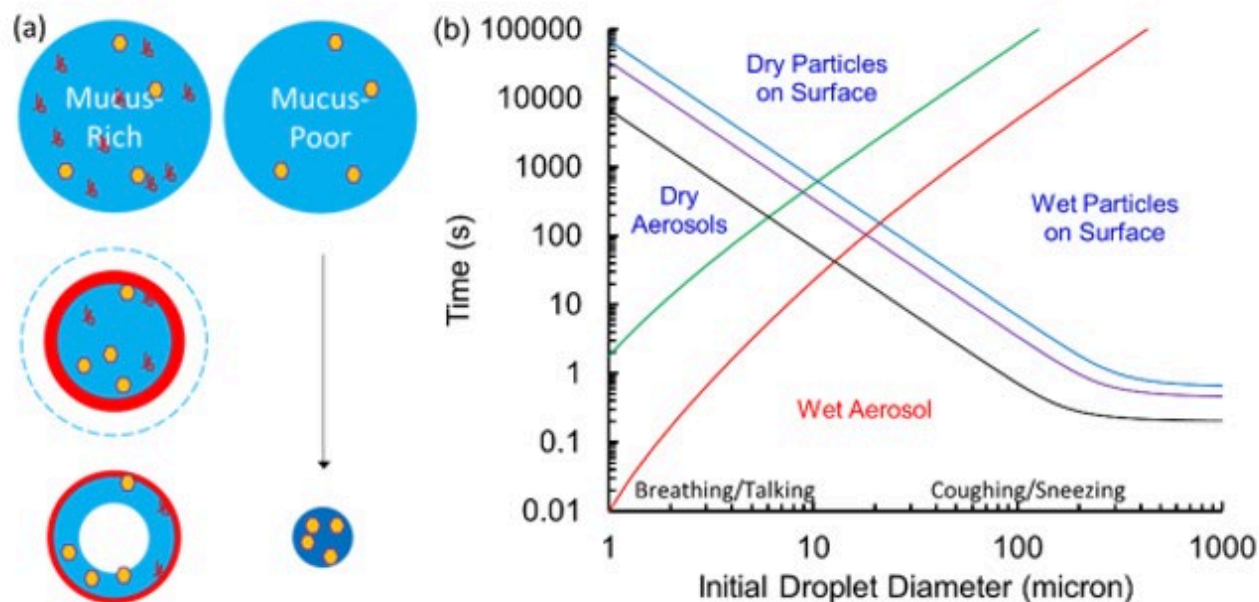


Fig. 4.17. (a) Comparison of mucus-rich droplets that form mucus shells around liquid cores and mucus-poor droplets that do not. Mucus-poor droplets dry disrupting the enveloped coating of enveloped viruses. (b) Time to complete drying of a core-shell mucus particle with a wet shell as a function of initial droplet diameter for gelation to initial concentration ratios of 5 (green) and 50 (red), along with fall times corresponding to fall distances of 2 m (blue), 1 m (purple), and 0.2 m (black) at 25°C at standard temperature and pressure under quiescent conditions. Relative humidity values (20–80% RH) collapse on the same curves. [Reprinted from Pease, L. F., et al. A Missing Layer in COVID-19 Studies: Transmission of Enveloped Viruses in Mucus-rich Droplets. *Int. Comm. Heat and Mass Transfer* **2021**, *131*, 105746. DOI: 10.1016/j.icheatmasstransfer.2021.105746. Copyright 2022, with permission from Elsevier.]

remain well hydrated and, thus, fully infective at substantial distances (see Fig. 4.17, this page). Results provided a mechanism by which infective enveloped virus particles could be transmitted as aerosols within buildings and between buildings over extended distances. This analysis is important because public health agencies typically follow the Wells model to establish health policies, including social and physical distancing guidelines.

Sensitivity of Airborne Transmission of Enveloped Viruses to Seasonal Variation in Indoor Relative Humidity

Publication

Robey, A. J.; Fierce, L. Sensitivity of Airborne Transmission of Enveloped Viruses to Seasonal

Variation in Indoor Relative Humidity. *Int. Comm. Heat and Mass Transfer* **2022**, *130*, 105747. DOI: 10.1016/j.icheatmasstransfer.2021.105747

Practical Implications

- Dry indoor conditions typical of the winter season led to slower virion inactivation rates compared to the more humid summer season. This effect increased the concentration of active virions when the susceptible person was farther than 2 m downwind of the infectious person.
- Process analysis revealed that the greater virion exposure at RH = 40% than at RH = 65% was caused by differences in virion inactivation rate and not by RH-induced changes in particle removal rates through gravitational settling and deposition.

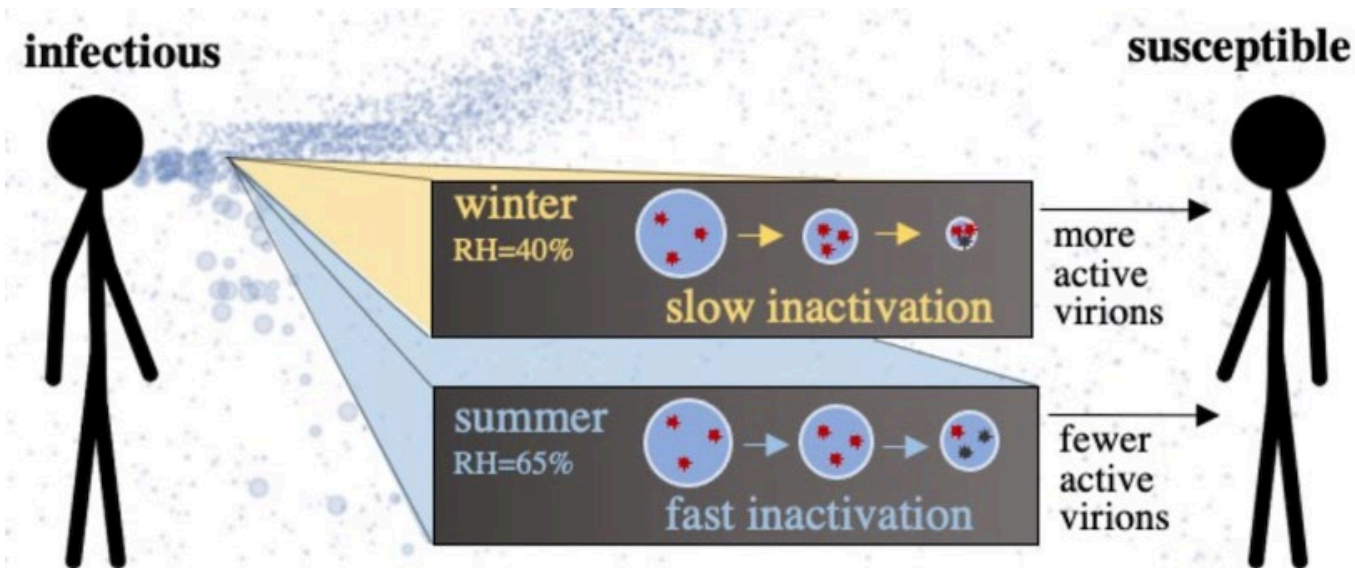


Fig. 4.18. Study results showed that a lower relative humidity (RH), typical of the winter season, increased airborne virion exposure by slowing the virion inactivation rate, not by increasing the travel distance or residence times of respiratory particles due to changes in particle settling velocity. [Reprinted from Robey, A. J., et al. Sensitivity of Airborne Transmission of Enveloped Viruses to Seasonal Variation in Indoor Relative Humidity. *Int. Comm. Heat and Mass Transfer* **2022**, 130, 105747. DOI: 10.1016/j.icheatmasstransfer.2021.105747. Copyright 2022, with permission from Elsevier.]

Summary

While outdoor temperatures and humidity levels vary dramatically throughout the year, humans spend around 90% of their time indoors where temperatures remain stable, but relative humidity (RH) displays consistent summer highs and winter lows. Several mechanisms pertinent to the airborne transmission of viruses are sensitive to this variability in RH, such as faster inactivation of enveloped virions at extreme RH levels and shorter travel distance of mid-sized particles at high RH levels due to changes in growth rate and equilibrium particle size. However, it is unclear which mechanism—RH-mediated differences in droplet removal or RH-mediated virion inactivation—drives the seasonality of enveloped viruses.

BNL used the Quadrature-based model of Respiratory Aerosol and Droplets (QuaRAD) to explore whether the seasonal variation in enveloped viruses, specifically SARS-CoV-2, is driven by

differences in particle removal rates or in the rate at which virions are inactivated. A large ensemble of simulations revealed that the dry indoor conditions typical of the winter season led to slower inactivation relative to the more humid summer season. In poorly ventilated spaces, this reduction in inactivation rates increased the concentration of active virions when the susceptible person was farther than 2 m downwind of the infectious person. On the other hand, changes in particle settling velocity with relative humidity did not significantly affect the removal or travel distance of virus-laden particles (see Fig. 4.18, this page).

Data Availability Statement

The QuaRAD source code, input files, and processing script are available for download at github.com/lfierce2/QuaRAD. Simulation ensembles were created using Latin hypercube sampling with pyDOE (pythonhosted.org/pyDOE/).

4.3.7 Results: Topic 4

Efficacy of Controls for Reducing Exposure to Airborne Pathogens

- High Efficacy of Layered Controls for Reducing Exposure to Airborne Pathogens
- Control of Airborne Infectious Disease in Buildings: Evidence and Research Priorities
- Protecting Building Occupants Against the Inhalation of Outdoor-Origin Aerosols
- Simplified Screening Method to Measure Indoor Airborne Particle Removal Rates
- Multiscale Airborne Infectious Disease Transmission

High Efficacy of Layered Controls for Reducing Exposure to Airborne Pathogens

Publication

Fierce, L.; Robey, A. J.; Hamilton, C. High Efficacy of Layered Controls for Reducing Exposure to Airborne Pathogens. *Indoor Air* **2022**, 32 (2), e12989. DOI: 10.1111/ina.12989

Practical Implications

- Focusing on SARS-CoV-2, thousands of scenarios with QuaRAD were simulated to quantify the efficacy of individual and combined controls on airborne transmission.
- Each scenario compared the risk of initial infection in the susceptible person for cases without controls (low ventilation, no masks) and for cases with different combinations of controls.
- This study showed that layered controls were highly effective in reducing transmission of airborne pathogens like SARS-CoV-2. The combination of social distancing, masking, and increasing ventilation led to a reduction in the median risk of infection by more than 99%.

Summary

Controls on airborne transmission may reduce the number of virus-laden particles inhaled by a susceptible person and depositing to the infection site, but the efficacy of any given control depends on factors that are inherently variable and, often, poorly

constrained. For example, while the size-resolved collection efficiencies of different types of face masks have been measured, the reduction in the risk of infection also depends on highly variable factors, such as rates of viral shedding, characteristics of expiratory jets, room conditions, and immune responses. Uncertainty due to these variables can be represented in models by simulating ensembles of scenarios, but models well-suited for simulating the evolution of respiratory particles in indoor spaces are often computationally expensive, limiting their ability to represent uncertainty. To optimize strategies for curbing the transmission of airborne pathogens, the efficacy of three key controls—face masks, ventilation, and physical distancing—must be well understood. In this study, BNL scientists used QuaRAD to quantify the efficacy of controls across thousands of scenarios that represent the tremendous variability in factors governing airborne transmission. While the efficacy of any individual control was highly variable among scenarios, combining universal mask-wearing with distancing of 1 m or more reduced the median exposure by more than 99% relative to a close, unmasked conversation, with further reductions if ventilation was also enhanced (see Fig. 4.19, p. 181). These findings suggest that layering controls is highly effective for reducing transmission of airborne pathogens and will be critical for curbing outbreaks of novel viruses in the future.

Data Availability Statement

The QuaRAD source code, input files, and processing script are available for download at github.com/lfierce2/QuaRAD/. Simulation ensembles were created using Latin hypercube sampling with pyDOE (pythonhosted.org/pyDOE/). The sensitivity analysis was performed using the Sensitivity Analysis Library in Python, which is available at salib.readthedocs.io/en/latest/.

Control of Airborne Infectious Disease in Buildings: Evidence and Research Priorities

Publication

Bueno de Mesquita, P. J.; Delp, W. W.; Chan, W. R.; Bahnfleth, W. P.; Singer, B. C. Control of Airborne

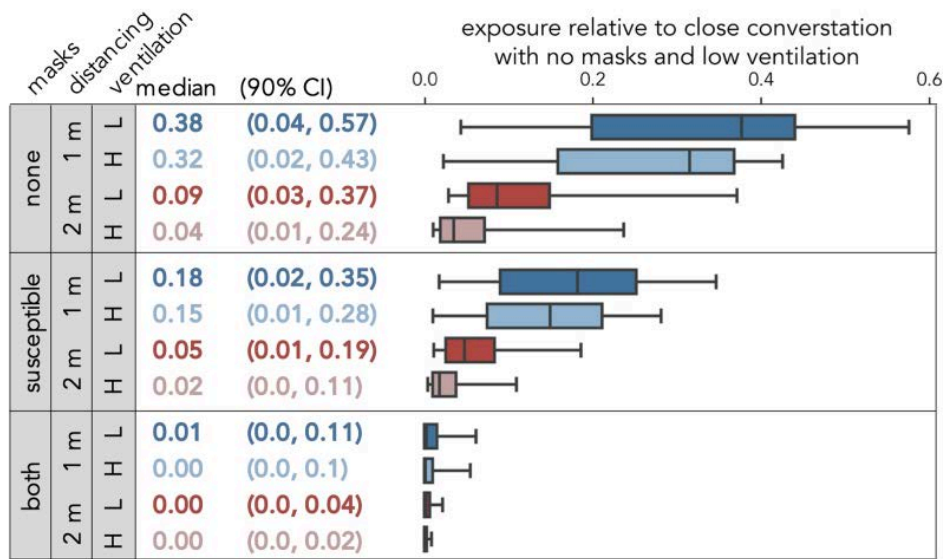


Fig. 4.19. Efficacy of layered controls. Median (solid line), quartiles (boxes), and 90% confidence interval (whiskers) of the fraction of airborne pathogens reaching the infection site when different combinations of controls were employed in comparison with a close (0.5 m) conversation at the baseline (low) ventilation rates. Median and 90% confidence intervals of relative exposure are also shown. [Reprinted with permission from Fierce, L., et al. High Efficacy of Layered Controls for Reducing Exposure to Airborne Pathogens. *Indoor Air* **2022**, 32 (2), e12989. DOI: 10.1111/ina.12989. Copyright 2022 John Wiley and Sons.]

Infectious Disease in Buildings: Evidence and Research Priorities. *Indoor Air* **2022**, 32 (1), e12965. DOI: 10.1111/ina.12965

Practical Implications

- Emerging variants of SARS-CoV-2 have led to increased infectivity by the aerosol inhalation mode and increasing infection incidence.
- Even in the absence of symptoms, people infected with respiratory viruses can exhale infectious aerosols that could be inhaled, deposited in the respiratory tract, and initiate infection.
- Indoor environments are the predominant settings for respiratory infection transmission because people spend most of their time indoors and concentrations of infectious aerosols can accumulate, resulting in hazardous inhalation exposure at close-interactive, room (even at distances much greater than two meters), and building scales.

- This study illustrated the relative respiratory aerosol transfer and exposure at these scales, provided an overview of the scientific basis of engineering controls that could be deployed in buildings to reduce transfer between people, and outlined priority research directions to guide widespread implementation of controls in buildings.

Summary

The evolution of SARS-CoV-2 virus resulted in variants more readily transmitted through respiratory aerosols, underscoring the increased potential for indoor environmental controls to mitigate risk. Use of tight-fitting face masks to trap infectious aerosols in exhaled breath and reduce inhalation exposure to contaminated air is of critical importance for disease control. Administrative controls, including the regulation of occupancy and interpersonal spacing, are also important, while presenting social and economic challenges. Indoor engineering controls, including ventilation, exhaust, air flow control, filtration,

and disinfection by germicidal ultraviolet irradiation, can reduce reliance on stringent occupancy restrictions. However, the effects of controls—individually and in combination—on reducing infectious aerosol transfer indoors remain to be clearly characterized to the extent needed to support widespread implementation by building operators. In this study, LBNL reviewed aerobiologic and epidemiologic evidence of indoor environmental controls against transmission and presented a quantitative aerosol transfer scenario, illustrating relative differences in exposure at close-interactive, room, and building scales (see Fig. 4.20, this page). Results identified an overarching need for investment to implement building controls and evaluate their effectiveness on infection in well-characterized and real-world settings, supported by specific, methodological advances. Improved understanding of engineering control effectiveness guides implementation at scale while considering occupant comfort, operational challenges, and energy costs.

Protecting Building Occupants Against the Inhalation of Outdoor-Origin Aerosols

Publication

Dillon, M. B.; Sextro, R. G.; Delp, W. W. Protecting Building Occupants against the Inhalation of Outdoor-Origin Aerosols. *Atmos. Environ.* **2022**, *268*, 118773. DOI: 10.1016/j.atmosenv.2021.118773

Practical Implications

- Study estimated the protection that existing U.S. building stock provides their occupants from outdoor-origin airborne particulate hazards, such as infectious aerosols and wildfire smoke.
- Study compiled published deposition, penetration, filtration, and building operation data. This data was used in subsequent research (not presented in this paper) that assessed the indoor-origin aerosol exposure risk and mitigation measure efficacy of U.S. building stock.
- Building protection varied widely by occupancy type, particle-size, and airborne loss rate.

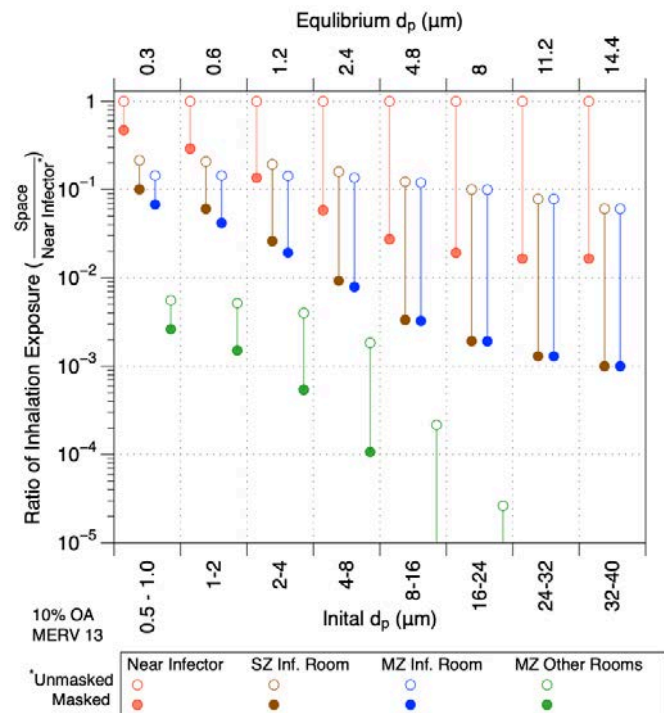


Fig. 4.20. Relative inhalation exposure attributed to aerosols at different exposure scales compared with close-interactive exposure in the SZ Inf. Room. SZ Inf. Room = Single-zone HVAC system serving 93 m² with an infector in the room. MZ = mixed-zone HVAC system serving a total 929 m² with infector in the room. d_p = aerosol diameter. OA = outdoor air. [Reprinted with permission from Bueno de Mesquita, P. J., et al. Control of Airborne Infectious Disease in Buildings: Evidence and Research Priorities. *Indoor Air* **2022**, *32* (1), e12965. DOI: 10.1111/ina.12965. Copyright 2022 John Wiley and Sons.]

- Furthermore, variability within a given building type—due to variability in weather, building construction, and operating conditions—was similar to variability between different building types.

Summary

During normal operations, buildings can protect their occupants from outdoor airborne particle hazards of all types, including airborne pollutants. A long-term international research effort has advanced knowledge of building protection physics. Recently, an operationally efficient, regional-scale methodology—Regional Shelter

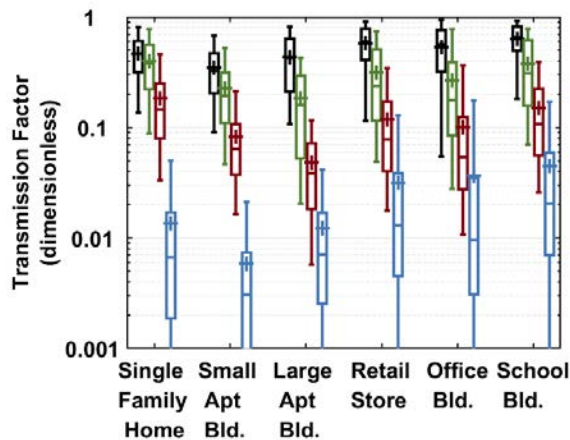


Fig. 4.21. Distribution of transmission factor (ratio of indoor to outdoor exposure) for select building types by particle size for the no airborne loss case. Box and whisker plot shows the median (line), interquartile (box), 5 and 95 percentiles (whiskers), and mean (+ symbol). Particle diameter varied from left to right for each building type: black, 0.1 μm ; green, 1 μm ; red, 3 μm ; and blue, 10 μm . [Reprinted from Dillon, M. B., et al. Protecting Building Occupants against the Inhalation of Outdoor-Origin Aerosols. *Atmos. Environ.* **2022**, 268, 118773. DOI: 10.1016/j.atmosenv.2021.118773. Copyright 2022, with permission from Elsevier.]

Analysis—was developed to account for both building protection effects and the typical distribution of people in and among buildings. To provide input to this capability, LLNL and LBNL partnered to estimate the degree of protection afforded by currently existing U.S. building stock. Scientists first assembled and summarized the published literature relevant to indoor particle losses, including (1) deposition to indoor surfaces, (2) losses that occur when particles penetrate through the building envelope, and (3) HVAC system filtration efficiencies, as well as general building operating conditions. Building protection against inhaling particulate hazards varied strongly, by orders of magnitude, according to building use (occupancy), particle-size, and airborne particle loss rate. Protection increased modestly as particle size increases from 0.1 to 1 μm and significantly as particle size increased

from 1 to 10 μm (see Fig. 4.21, this page). Model results were placed in context with previously reported measurements. Suggestions for future work, including enhanced validation datasets, were provided.

Simplified Screening Method to Measure Indoor Airborne Particle Removal Rates

Publication

Dillon, M. B.; Frank, M; Wheeler, E. K. Simplified Screening Method to Measure Indoor Airborne Particle Removal Rates. Manuscript submitted to *J. Occup. Environ. Hyg.*

Practical Implications

- This study demonstrated an approach that rapidly assesses overall airborne particle removal rates.
- This method could be used to quickly screen if indoor environments pose a notable exposure risk and evaluate mitigation measure efficacy.
- This method could be used in occupied spaces.

Summary

There is increasing evidence that COVID-19 can be spread at distances ≥ 2 m indoors through the inhalation of infectious airborne particles. To reduce disease spread, U.S. governmental and industrial standards setting groups have emphasized increasing outdoor air ventilation and the use of various air cleaning technologies, including filtration. While a method exists to assess overall aerosol removal rates (including ventilation and filtration), its use can be time-consuming and/or costly. This study demonstrated the use of an alternative, faster approach often used in research. Particulate matter was injected into room air, raising airborne particle concentrations well above ambient levels, and the aerosol removal rate was directly estimated from the resulting decay in aerosol concentration with time (see Fig. 4.22, p. 184). This method, either by itself or in conjunction with established ventilation assessment methods, provides an opportunity to quickly screen indoor

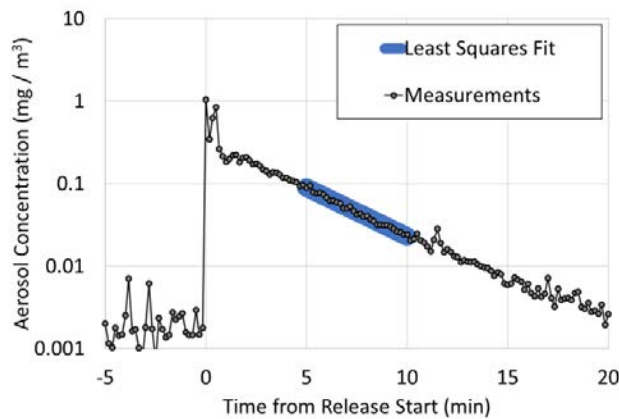


Fig. 4.22. Time series of measured (symbol) airborne particle concentrations with corresponding least squares fit (line). The slope corresponds to the overall aerosol removal rate. [Courtesy Lawrence Livermore National Laboratory]

environments to rapidly identify those that may pose a notable exposure risk (e.g., poorly ventilated or filtered rooms), with respect to particle emissions within the same room. This approach could be used in occupied buildings, as was done with this demonstration. It could also be employed to evaluate mitigation efficacy.

Multiscale Airborne Infectious Disease Transmission

Publication

Dillon, C. F.; Dillon, M. B. Multiscale Airborne Infectious Disease Transmission. *Appl. Environ. Microbiol.* **2021**, *87* (4), e02314-20. DOI: 10.1128/AEM.02314-20

Practical Implications

- The overall importance of airborne disease transmission is underappreciated in the scientific literature, although the cumulative body of knowledge across the scientific disciplines is large. Consequently, airborne precautions may not be taken when airborne transmission is important, but unrecognized.
- This literature review demonstrated, through well-established examples, that airborne viruses, bacteria, and fungal pathogens can cause disease in plants, animals, and humans over

distance scales ranging from a few meters to continental.

- The overall airborne disease burden may be underreported, particularly for opportunistic pathogens that can spread through multiple pathways.

Summary

Airborne disease transmission is central to many scientific disciplines including agriculture, veterinary biosafety, medicine, and public health. Legal and regulatory standards are in place to prevent agricultural, nosocomial, and community airborne disease transmission. However, the overall importance of the airborne pathway is underappreciated. For example, U.S. National Library of Medicine's Medical Subjects Headings (MESH) thesaurus lacks an airborne disease transmission indexing term. This underappreciation has practical consequences, as airborne precautions to control epidemic disease spread may not be taken when airborne transmission is important, but unrecognized. Publishing clearer, practical methodological guidelines for surveillance studies and disease outbreak evaluations could help address this situation.

To inform future work, this study by LLNL highlighted selected, well-established airborne transmission events—largely cases replicated in multiple, independently conducted scientific studies. Methodologies included field experiments, modeling, epidemiology studies, disease outbreak investigations and mitigation studies. Collectively, this literature demonstrated that airborne viruses, bacteria, and fungal pathogens have the capability to cause disease in plants, animals, and humans over multiple distances – from near range (<5 m) to continental (>500 km) in scale. The plausibility and implications of undetected airborne disease transmission were discussed, including the notable underreporting of disease burden for several airborne transmitted diseases.

4.4 Task 2: Understanding the Roles of Surface Chemistry and Materials Science for Viral Transmission and Spread

4.4.1 Overview

The current COVID-19 pandemic was caused by a SARS-type enveloped coronavirus wrapped in a lipid bilayer membrane, bearing glycoproteins directed outward. These spike proteins enable the virus to attach itself to surfaces of abiotic objects. This attachment allows the viral particles on such surfaces to serve as reservoirs for further viral transmission. Like other coronaviruses, SARS-CoV-2 can spread human-to-human mainly via respiratory droplets, although other mechanisms remain possible. Early in the pandemic, the stability of the virus under various conditions, transmission routes, and many other properties related to virus-material interaction were unknown. Despite previous research on SARS and other related pathogens, the mechanism of their attachment to abiotic surfaces and the factors that drive their adherence to different types of materials are not known. Furthermore, the role of virus-surface interactions in the viral transport within enclosed spaces also remains unknown, as well as how such interactions may impact key exposure pathways and scenarios. Therefore, there was a need to understand the ability of various materials to bind SARS-CoV-2 to provide information on how the virus might be transferred and/or reside on common surfaces. Additionally, identification of materials with selective adsorption of viruses have important potential uses in technological applications, such as in novel personal protective equipment (PPE) or diagnostics.

4.4.2 Objectives

Critical, multidisciplinary approaches were needed to generate datasets that address the persistence of enveloped coronaviruses on nonbiological surfaces. Supporting this research, direct imaging of virus-surface interactions was conducted using a range of imaging technologies available at

DOE's scientific user facilities. Ultimate goals of Task 2 included (1) understanding various materials interactions that may define fate and transmission of coronaviruses in the built environment and (2) investigating the ability of surface-bound viruses to serve as a reservoir for airborne transmission, which is complementary to Task 1 of this project.

A library of materials, including metals/alloys, oxides and polymers with different surface chemistries and degrees of roughness, were assembled to assess the impact of surface chemistry and morphology on retention, transmission, and stability of coronaviruses. To explore materials features and their interactions with spike proteins of coronaviruses, the team used diverse imaging approaches, including cryo-electron microscopy (cryo-EM) at SLAC; scanning electron microscopy (SEM) and scanning transmission electron microscopy (STEM) at Ames, PNNL, and ORNL; atomic force microscopy (AFM) at PNNL; as well as direct visualization in near-native environments using correlative fluorescence microscopy and electron microscopy in liquid phase at Ames. A limited number of materials were tested at biosafety level 3 (BSL-3) with SARS-CoV-2 (SNL) as needed. The research determined a range of materials' properties responsible for repelling or trapping SARS-CoV-2 and enabled development of mitigation approaches preventing virus transmission and spread in the built environment.

4.4.3 Outcomes

1. Selected surrogate viral test system, initial set of materials for testing, and most appropriate material characterization techniques for materials.
2. Assessed virucidal behavior of selected man-made and natural materials, including metals (stainless steel, copper, brass) and oxide (iron oxides, clay-like and complex oxides) as well as polymeric materials.
3. Determined material composition/surface morphologies with enhanced or reduced affinity to viral proteins that contributed to the ability of surface-bound pathogens to serve as reservoirs for viral transmission.

4.4.4 Results: Topic 1

Generation and Screening of Materials Commonly Found in the Built Environment

- S/TEM Imaging of Materials' Interactions with Virus-Like Nanoparticles and Inactivated SARS-CoV-2 Virus Nanoparticles
- Evaluation of COVID-19 Spike Protein Adhesion to Common Surfaces with Atomic Force Microscopy and Infrared Nanospectroscopy
- Profiling Material-Virus Interactions for Selective Adsorption of SARS-CoV-2 using Vesicular Stomatitis Virus (VSV)–Based Pseudoviruses
- Imaging SARS-CoV-2 on Substrates with FIB/HRSEM
- Towards Correlative Spatio-Chemical Imaging of SARS-CoV-2 Virus-Like Particles Bound to Common Surfaces

Publications

O'Callahan, B.; Qafoku, O.; Balema, V.; Negrete, O. A.; Passian, A.; Engelhard, M. H.; Waters, K. M. Atomic Force Microscopy and Infrared Nanospectroscopy of COVID-19 Spike Protein for the Quantification of Adhesion to Common Surfaces. *Langmuir* **2021**, *37* (41), 12089–12097. DOI: 10.1021/acs.langmuir.1c01910

Negrete, O.; Singh, A.; Hlova, I. Z.; Balema, V. Profiling Materials for Selective Adsorption to SARS-CoV-2 Using Vesicular Stomatitis Virus (VSV) Based Pseudoviruses. In preparation for *ChemComm*.

Dobisz, E. A.; Thompson, W.; Phadke, K.; Bellaire, B.; Sakdinawat, A. Dual Beam Focused Ion Beam: Scanning Electron Microscope Imaging and Cross-Sectioning on SARS-CoV-2. In preparation for *Nat. Nanotechnol.*

Passian, A.; et al. Viral Stability on Surfaces: A Brief Review of Surface Characterization. In preparation for *ACS Nano*.

S/TEM Imaging of Materials' Interactions with Virus-Like Nanoparticles and Inactivated SARS-CoV-2 Virus Nanoparticles

Practical Implications

- Developed and optimized scanning transmission electron microscopy imaging of material interactions with virus-like nanoparticles and inactivated SARS-CoV-2 virus nanoparticles. The developed procedure of imaging of biological specimens with inherently poor contrast incubated with the high-contrast inorganic particles is expected to be broadly applicable to imaging and characterization of materials-virus interactions for a wide variety of inorganic materials.
- Aqueous suspension of ball-milled ceria particles and alumina nanospheres were incubated with virus-like nanoparticles, inactivated SARS-CoV-2 virus nanoparticles, and imaged using BF-TEM and HAADF-S/TEM imaging modes, utilizing staining.

Summary

An aqueous suspension containing ceria nanoparticles was incubated with a spike protein trimer solution for 30 minutes at room temperature before proceeding with S/TEM imaging.

The sample was drop-casted on a grid. Following the 30-minute incubation with ceria suspension, a microvolume of sample incubated inactivated virus nanoparticles solution was deposited on a hydrophilized ultrathin carbon support grid. The samples were allowed to stay on a grid for 3 minutes, after which they were washed with copious amounts of water and stained with UraniLess for 20 seconds (see Fig. 4.23, p. 187).

Evaluation of COVID-19 Spike Protein Adhesion to Common Surfaces with Atomic Force Microscopy and Infrared Nanospectroscopy

Practical Implications

- To aid the understanding of SARS-CoV-2 spread and persistence on commonplace surfaces and help mitigate future outbreaks of coronaviruses

and other pathogens, this study examined the binding and interaction of viral proteins with nonbiological surfaces. To achieve this objective, the team used a combination of IR scattering-type scanning near-field optical microscopy (s-SNOM) and an approach based on atomic force microscopy (AFM).

- This study provided insight into attachment and binding of SARS-CoV-2 spike glycoproteins on common selected inorganic materials, such as aluminum-, copper-, iron-, silica-, and ceria-oxides, as well as metallic gold.

Summary

This study showed the topography of spike proteins acquired by AFM and phase image acquired by s-SNOM at 1650 cm^{-1} and included a plot summarizing adhesion forces measured by AFM based on the interaction of the spike protein with metal or metal oxide coated tips (see Figs. 4.24 and 4.25, p. 188). The measured forces between spike proteins and metal or metal oxides-coated AFM tips varied over an order of magnitude from the lowest 1-2 nanonewtons (nN) for cerium oxide (CeO_2) and iron oxide, to the highest $\sim 20\text{-}25\text{ nN}$ for gold (Au). Normalized forces were plotted by radius per each coated tip, for spike proteins as well as for ferritin (Fe) coated surface and for silicon dioxide (SiO_2) surface using the same AFM tips. Results indicated that except for copper (Cu) oxide, the adhesion forces between spike protein and metal or metal oxides were similar to that of ferritin. The Cu oxide adhesion measurements showed a factor of three times weaker adhesion of spike protein compared to ferritin or Si-substrate. Most significantly, for both ferritin and spike glycoproteins, the data indicated much stronger adhesion forces on Au. It is noted that orientations of the spike proteins in this study were not controlled and were expected to be random. The conformational state of the proteins could be open or closed, which played a key role in the infectivity properties of the virus. The conformational state of the protein was expected to be a mixture of both the open and closed states or partially denatured protein. Nevertheless, these measurements aimed to emulate real-world adhesion of the SARS-CoV-2 virus in workplace and

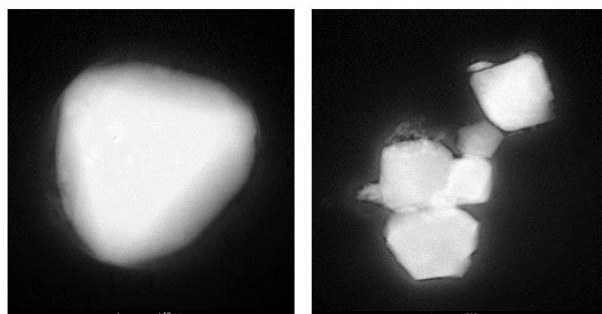


Fig. 4.23. HAADF-S/TEM images of ceria particles incubated with inactivated SARS-CoV-2 virus nanoparticles. (Left) Heat-inactivated virus. (Right) Glutaraldehyde-inactivated virus. [Courtesy Ames Laboratory and Iowa State University]

household environments, which may be determined by nonsite-specific interactions.

Profiling Material-Virus Interactions for Selective Adsorption of SARS-CoV-2 Using Vesicular Stomatitis Virus (VSV)–Based Pseudoviruses

Practical Implications

- Gained better understanding of the ability of various materials to bind SARS-CoV-2 to provide information on how the virus might be transferred and/or reside on common surfaces.
- Identified materials with selective adsorption of viruses that have important potential uses in technological applications, such as in novel personal protective equipment or diagnostics.

Summary

To profile materials for their ability to bind and/or inactivate SARS-CoV-2 pseudoviruses, this study coupled a rapid adsorption method to an infection assay (see Fig. 4.26a, p. 189). A set concentration of purified vesicular stomatitis virus (VSV)-SARS particles was incubated with various materials sent from Ames Laboratory, rotated for 1 hour, and then centrifuged to pellet the material. As these low centrifugation rates were not capable of pelleting the virus alone, materials that bound the virus allowed for analysis of viral titers from pellet and nonpelleted mix. Comparison of the fold titer

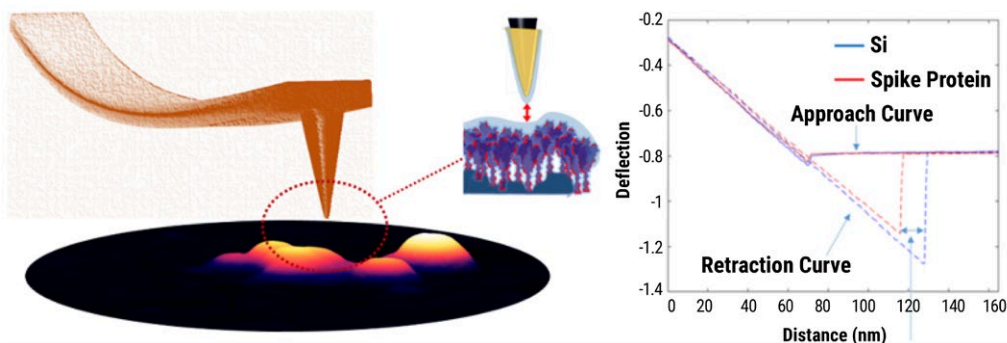


Fig. 4.24. Schematic of a gold coated AFM cantilever probe tip interacting with spike proteins deposited on an Si substrate. Forces of interaction are shown on the right insert. Force-curve measurements were analyzed to extract the adhesion force between the spike protein and the tip material. [Reprinted (adapted) with permission from O’Callahan, B., et al. Atomic Force Microscopy and Infrared Nanospectroscopy of COVID-19 Spike Protein for the Quantification of Adhesion to Common Surfaces. *Langmuir* **2021**, 37 (41), 12089–12097. DOI: 10.1021/acs.langmuir.1c01910. Copyright 2022 American Chemical Society.]

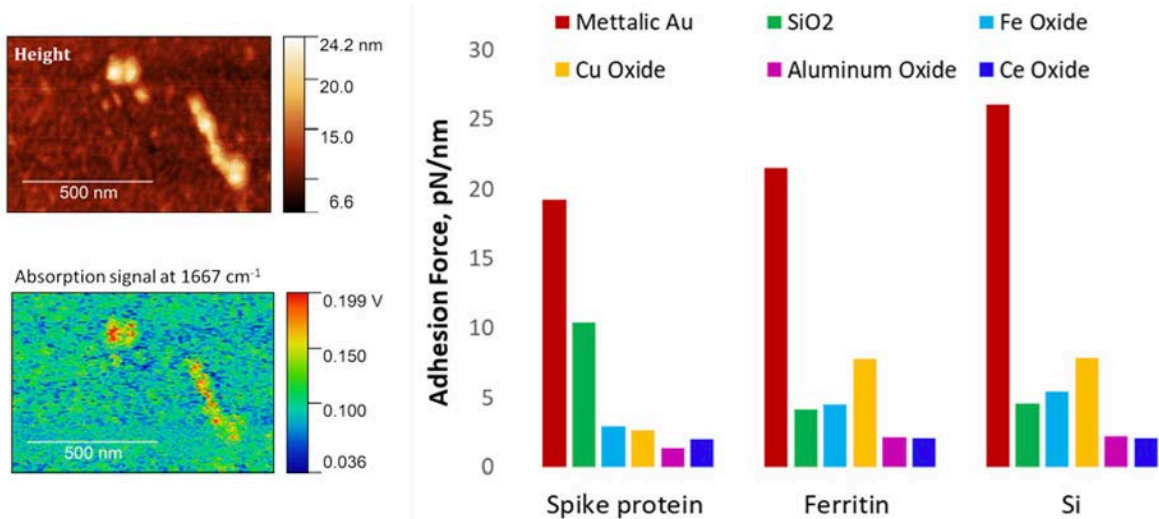


Fig. 4.25. AFM topography of SARS-CoV-2 spike protein on a gold substrate (top left) and corresponding s-SNOM phase image acquired at 1650 cm⁻¹ (bottom left). Relative adhesion forces between AFM tips coated with different metals and spike protein (blue) and ferritin (red) [right]. [Reprinted (adapted) with permission from O’Callahan, B., et al. Atomic Force Microscopy and Infrared Nanospectroscopy of COVID-19 Spike Protein for the Quantification of Adhesion to Common Surfaces. *Langmuir* **2021**, 37 (41), 12089-12097. DOI: 10.1021/acs.langmuir.1c01910. Copyright 2022 American Chemical Society.]

changes between the mixed sample (virus-material slurry) to the pelleted samples allowed for a rapid understanding if the virus remained active after material interactions and, additionally, the relative binding strength of the materials. As a control, VSV was also used to understand the selective material adsorption properties. Upon profiling various metal

oxides, cellulose, and others, the study found that CeO₂ was highly active in adsorption of both VSV and VSV-SARS2 pseudoviruses using this rapid screening assay (see Fig. 4.26b, p. 189).

To verify the strong binding properties of CeO₂ to both VSV and VSV-SARS2, a western blot analysis

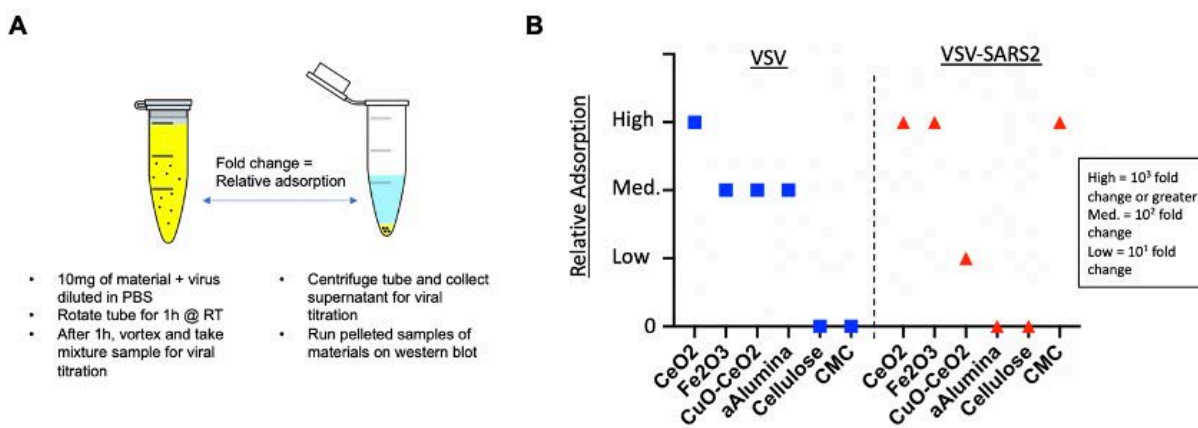


Fig. 4.26. (A) Pseudovirus-based infection assay used to profile material-virus interactions. **(B)** This rapid screening assay showed CeO₂ was highly active in adsorption of both VSV and VSV-SARS2 pseudoviruses. [Courtesy Sandia National Laboratories]

was performed on the pellet samples from the profiling assay (see Fig. 4.27, this page). The samples were blotted using either antibodies against VSV-G or the spike protein of SARS-CoV-2 (SARS2-S).

Results confirmed the strong binding properties of CeO₂ to the surface glycoproteins of these viruses and the lack of their binding to cellulose. However, for the other samples, the results from the screening assay compared with the western blot differed for reasons that were not fully characterized. As CeO₂ bound these pseudoviruses with high affinity without inactivation, the study set out to characterize time- and concentration-dependent adsorption to SARS-CoV-2 pseudoviruses.

The team then determined that there was a concentration-dependent adsorption of VSV-SARS2 to CeO₂, with 10 mg serving as the highest-level binding per 10⁷ plaque forming units (pfu) of virus (see Fig. 4.28, this page). Also, adsorption occurred quickly, as it was measurable within 10 minutes of incubation with CeO₂—a nontoxic and biocompatible material suitable for applications in virology. Although the full potential of CeO₂ in technological applications remains to be understood, this study identified a novel material-virus interaction that can be further pursued in the future. Confirmation with live SARS-CoV-2 under BSL-3 containment will follow.

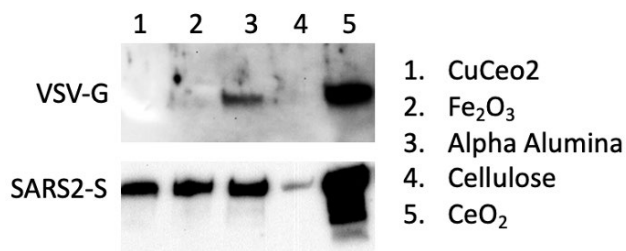


Fig. 4.27. Western blot analysis of material-virus interactions. [Courtesy Sandia National Laboratories]

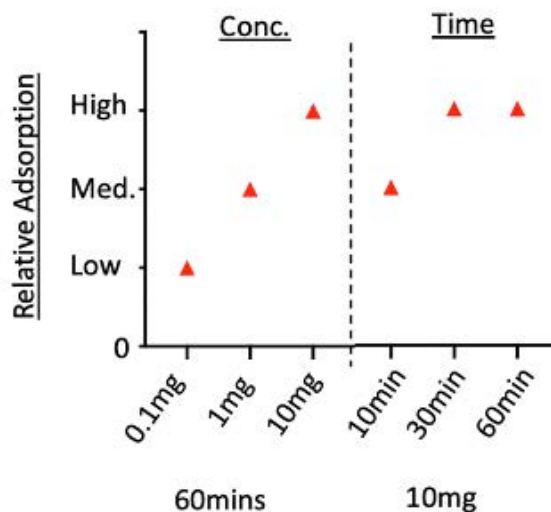


Fig. 4.28. Time- and concentration-dependent binding properties for CeO₂ against VSV-SARS2. [Courtesy Sandia National Laboratories]

Imaging SARS CoV-2 on Substrates with FIB/HRSEM

Practical Implications

- Identified procedures and guidelines for imaging small virions on surfaces by SEM.
- Demonstrated the ability to image SARS-CoV-2 at room temperature with SEM.
- Demonstrated methods to cross section the virus and the viral surface interface with substrate materials.

Summary

Because the size of SARS-CoV-2 virions are of the order of ~100 nm or less, imaging requires very high resolution only obtainable by electron microscopy, primarily by transmission electron microscopy (TEM). TEM imaging of viral and cellular materials is limited to thin slices that are transparent to electrons. Little or no work has been done on virus imaging on surfaces outside of an organism. Due to the dry nature of the viral interaction with dry substrates and the limited water content within the virus, rapid freeze and cryogenics may not be necessary. Room temperature SEM imaging has many advantages in ease of preparation and handling over cryo-EM. SEM observation of biological materials is attractive in ease of sample preparation, larger available area of view, and 3-dimensionality of view, as compared to TEM. When combined with a focused ion beam (FIB) in a dual beam system, one can cross-section very localized selected regions of material. By combined FIB slicing and SEM imaging, one can image 3-dimensional viral interactions with the substrate and adjacent virions in a cluster. Only recently has high resolution low voltage SEM become an available tool to be applied to biological samples. SARS and many other viruses are typically much smaller (1–2 orders of magnitude) than biological cells and tissue and require much higher resolution. This project examined SARS-CoV-2 on a variety of surfaces to develop procedures for understanding the virus outside of organisms and to aid in the selection of surfaces to limit virus spread.

Figure 4.29 (p. 191) shows micrographs of SARS-CoV-2 on different substrates. The substrate

(a) and (b) was carbon membrane (C), (c) and (d) was copper (Cu) grid, (e) and (f) was aluminum (Al) stub, and (g) was gold (Au) grid. Comparing (a) and (b) revealed more indications of viral clusters merging in planar clusters on C than a vertical cluster (b). The base of the virions on the Cu grid appeared to be spreading at the substrate and difficult to image. Fine particles of size 20 nm and below were seen over the substrate surface. The small particles on the substrate were particular to the Cu substrate. The size of isolated virions on C and Al were ~60 nm, while the isolated virions on Cu and Au were >100 nm.

To investigate the internal structure of the virus, virus to virus interaction, and viral substrate interaction, methods for cross sectioning the virus were developed, such as the FIB cross-sectional methods (see Fig. 4.30, p. 192). Samples were sputter coated with ~2–4 nm of platinum (Pt) in a sputter coater tool for conductivity and protection of the virus during FIB etching. It would have been desirable to deposit a thicker layer of Pt for protection, but virus location became more difficult with increasing metal thickness. Figure 4.30 shows a cross-section of a viral cluster coated with 2 nm of Pt and dropped on a silicone (Si) surface. An entire cluster of virions is visible beneath a small bump on the surface. Virion sizes ranged from 100 nm to 500 nm, indicating virion merging at some points in viral storage or the sample processing. The p-RNA complexes became more apparent with e-beam scanning of the cross section, indicating some viral interaction with the e-beam. In the micrograph, none of the virions were observed to be in contact with the Si wafer surface. Dried carrier fluid occupied the 100 nm space directly in contact with the Si surface.

Towards Correlative Spatio-Chemical Imaging of SARS-CoV-2 Virus-Like Particles Bound to Common Surfaces

Practical Implications

- Investigated the morphological and chemical effects expressed by SARS-CoV-2 when adsorbed onto common surfaces.

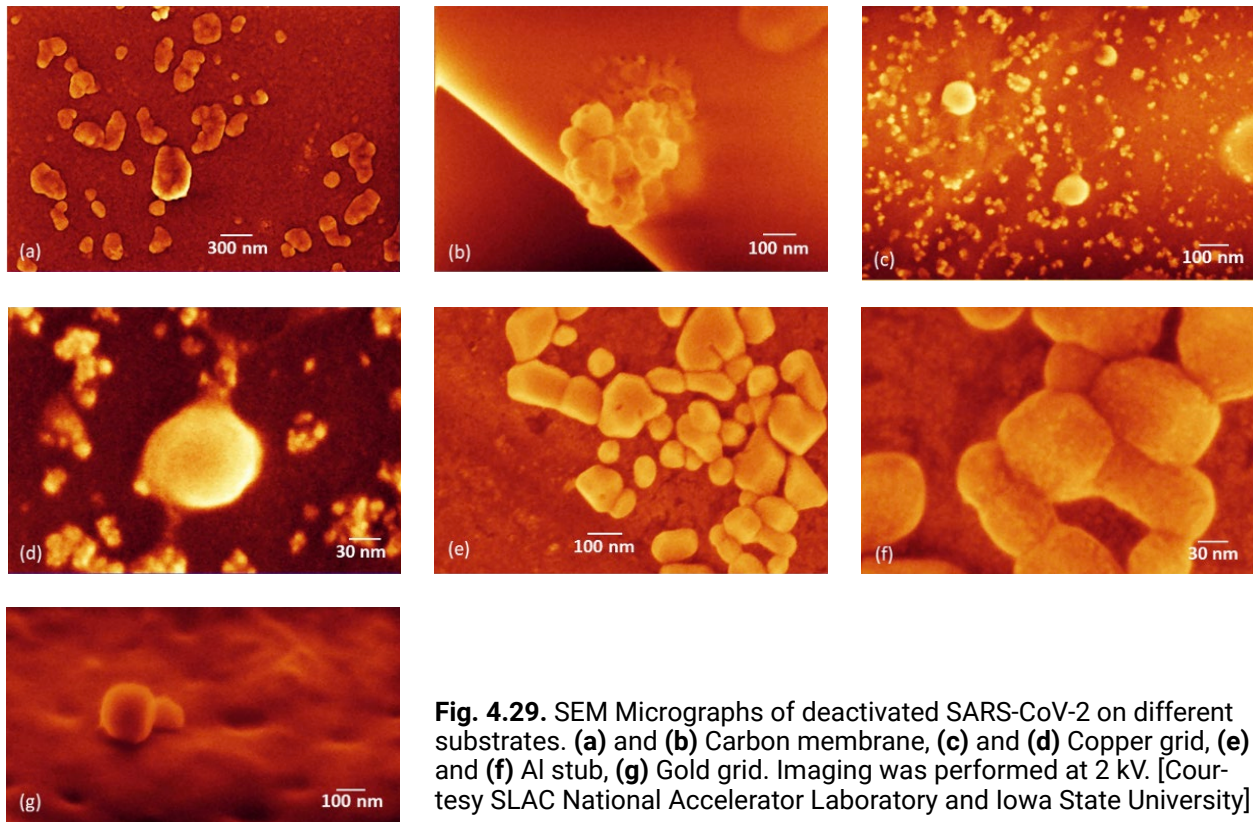


Fig. 4.29. SEM Micrographs of deactivated SARS-CoV-2 on different substrates. (a) and (b) Carbon membrane, (c) and (d) Copper grid, (e) and (f) Al stub, (g) Gold grid. Imaging was performed at 2 kV. [Courtesy SLAC National Accelerator Laboratory and Iowa State University]

- Identified and characterized acceptable surrogates.
- Investigated interaction of surrogates with infrared radiation to understand limitation of spectroscopic characterization and their deactivation and thermo-optic effects on viruses.
- Contributed toward addressing the following question: Can determination of the nanoscale physical and chemical properties of deposited virus-laden particles provide a viable methodology for understanding how COVID-19 spreads through contact transmission?

Summary

When a virus approaches a surface, multiphysics interactions occur as the distance is reduced. Therefore, spectroscopic and microscopic characterization of surfaces are required independently of the virus but under ambient conditions. Upon surrogate adsorption to a given material surface, the virus-surface properties may vary sufficiently to

characterize attachment, detachment, and deactivation physics and chemistry for different materials. The Viral Fate and Transport team sought to establish a framework for optimizing surrogate preparation, chemical identification, and morphochemical analysis of viruses at high spatial and spectral resolutions using scanning probe microscopy and infrared spectroscopy. Developing this framework requires obtaining baseline measurements, so this study began by addressing the following details:

- Focused on three surrogate systems: (1) bacteriophage MS2, (2) *Escherichia coli* C3000, and (3) *Bacillus thuringiensis* subsp. israelensis (BGS-CID 4Q7) spores (see Fig. 4.31, p. 192).
- Measured infrared microspectra of surrogates to guide nanoscale-resolution chemical mapping (see Figs. 4.32–4.35, beginning on p. 193).
- Tested measurements via AFM of *E. coli* and spike proteins on Au substrates, along with X-ray

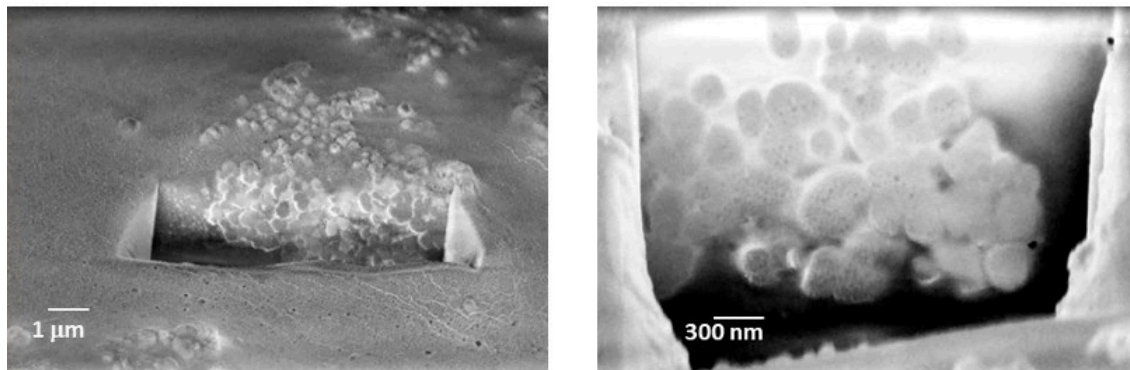


Fig. 4.30. FIB cross-sections of SARS in solution dropped onto a Si wafer. [Courtesy SLAC National Accelerator Laboratory and Iowa State University]

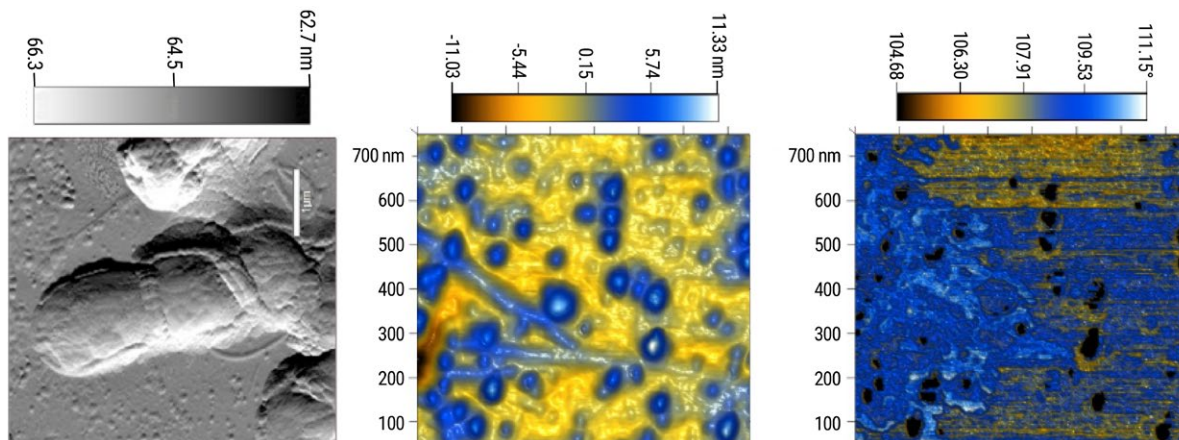


Fig. 4.31. Preliminary AFM of *E. coli* (left) and MS2 (middle and right), paving the way to improve sample preparation to isolate surrogates. [Courtesy Oak Ridge National Laboratory]

photoelectron spectroscopy (XPS) analysis of test substrates.

- Developed computational model to predict photo-thermal response of surface-adsorbed virus-like particles (see Fig. 4.36, p. 195).

4.5 Task 3: Analyzing and Modeling SARS-CoV-2 Transport and Emergence from Environmental Reservoirs Contributing to Human Transmission of COVID-19

4.5.1 Overview

Viral agents are known to survive in water for varying periods of time. The viral species may

persist in standing pools, natural water with organic material, sewage, or wastewater with biosolids. Because SARS-CoV-2 has been isolated from human feces, fecal transmission may represent a significant form of environmental contamination through aerosolized dispersions from wastewater treatment plants, septic system failure resulting in groundwater contamination, and sewer overflow triggered by extreme weather events. Characterization and quantification of SARS-CoV-2 present in wastewater may not only define or be an indicator for potential routes of transmission but may also reveal previously unknown hot spots of transmission and possibly new genotypes. Several reports of SARS-CoV-2

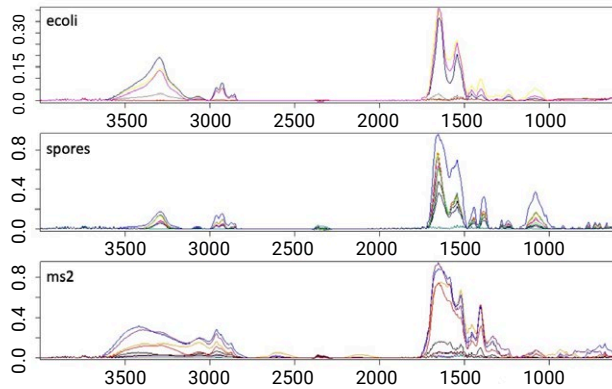


Fig. 4.32. Infrared spectra of surrogates to guide AFM-based nanospectroscopy. Common spectral features likely received contributions from the buffer. [Courtesy Oak Ridge National Laboratory]

identification in wastewater streams have raised questions about the potential for enteric transmission of COVID-19, similar to observations made during the 2003 outbreak of SARS, as reported by the World Health Organization. SARS-CoV-2 can enter groundwater through leaching of virus contaminated surface water or leaking of septic systems. Once in the groundwater, potential exists for contamination of wells and oral ingestion by humans or animals. Transport in groundwater is contingent on virus-specific adsorption and inactivation rate, water chemistry, flow rate, and soil properties, including content and temperature, meaning that the potential for virus transport may change due to climatic shifts in future years. While SARS-CoV-2 has not yet been identified in groundwater, microbial contamination of water sources from wastewater have been documented; coronaviruses have been shown to survive several days in water sources; and wells in certain types of aquifers are more susceptible to enhanced virus transport.

4.5.2 Objectives

This research established a modeling framework to understand how results from monitoring of SARS-CoV-2 in U.S. wastewater and surface waters conducted by others can help understand

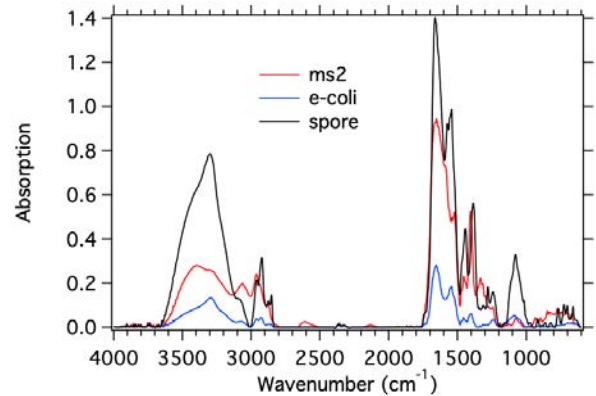


Fig. 4.33. Spectral comparison of considered surrogates. [Courtesy Oak Ridge National Laboratory]

the spatial and temporal features of SARS-CoV-2 community spread. The modeling framework also could be used as a source-tracking methodology regionally and nationwide. This task had the potential for cost-effective source tracking of community spread, including from symptomatic and asymptomatic carriers, as hypothesized by others. This project was distinct from efforts by the U.S. Environmental Protection Agency (EPA) to monitor and detect wastewater virus, in that this study performed no measurements for identification, infectivity, persistence, or treatment efficacy and only utilized data from EPA studies where available to parameterize the models.

Virus Fate and Transport Monitoring and Modeling in Water and Wastewater Systems

This task developed a system for evaluating SARS-CoV-2 presence in sewerage, wastewater, and surface waters sources that varied as a function of population infection loading and environmental factors. To establish fundamental proof-of-concept understanding of viral fate and transport in wastewater systems, the Viral Fate and Transport team leveraged current, ongoing SARS-CoV-2 studies and associated data from the Centers for Disease Control and Prevention (CDC), EPA, and other sources related to wastewater fate and transport measurements. The team leveraged the raw data available and team members'

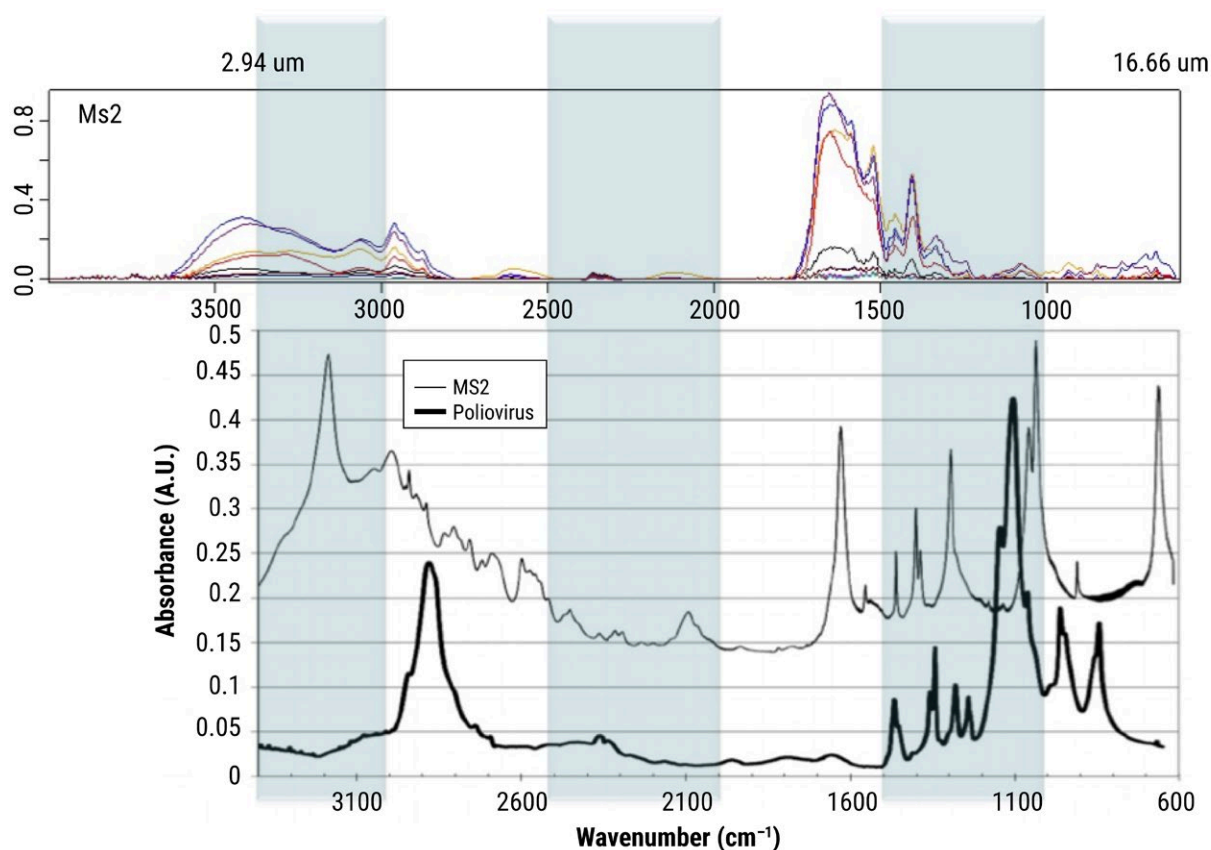


Fig. 4.34. Measured spectral features agree in part with Vargas, et al. Integrated Capture and Spectroscopic Detection of Viruses. *Appl. Environ. Microbiol.* **2009**, 75(20), 6431–40. However, further work is needed to isolate the MS2 features from the buffer. [Courtesy Oak Ridge National Laboratory]

understanding of wastewater processing and chemistry, including real-time virus data, to create unique theoretical models targeted to quantitatively determine SARS-CoV-2 load, detection, transport behavior, and correlation to predicted clinical outcomes on the populace. The team analyzed data from multiple datasets for generating models from several regional areas in the United States. A hydraulic model of the sewer and wastewater system was developed, and initial literature and historical data (e.g., chemical and physical water analysis, flow rates, and weather and water consumption data) was used to understand virus transport behavior, quantitative viral presence, and resilience. A data-based modeling method was developed to improve regional assessment

of virus signal quantification, potential locations of virus transport, degrees of infection prevalence, and virus emergence. This method could also be used for identifying potential spread scenarios and routes. The modeling tool helped understand virus transport in wastewater system, improve predictions, and identify potential spread scenarios and routes.

SARS-CoV-2 Viability in Groundwater and Implications for the Current Outbreak and Potential Resurgence

The development of a refined groundwater and subsurface transport model that can predict the movement of SARS-CoV-2 and the potential for viable virus spread is a key tool in understanding

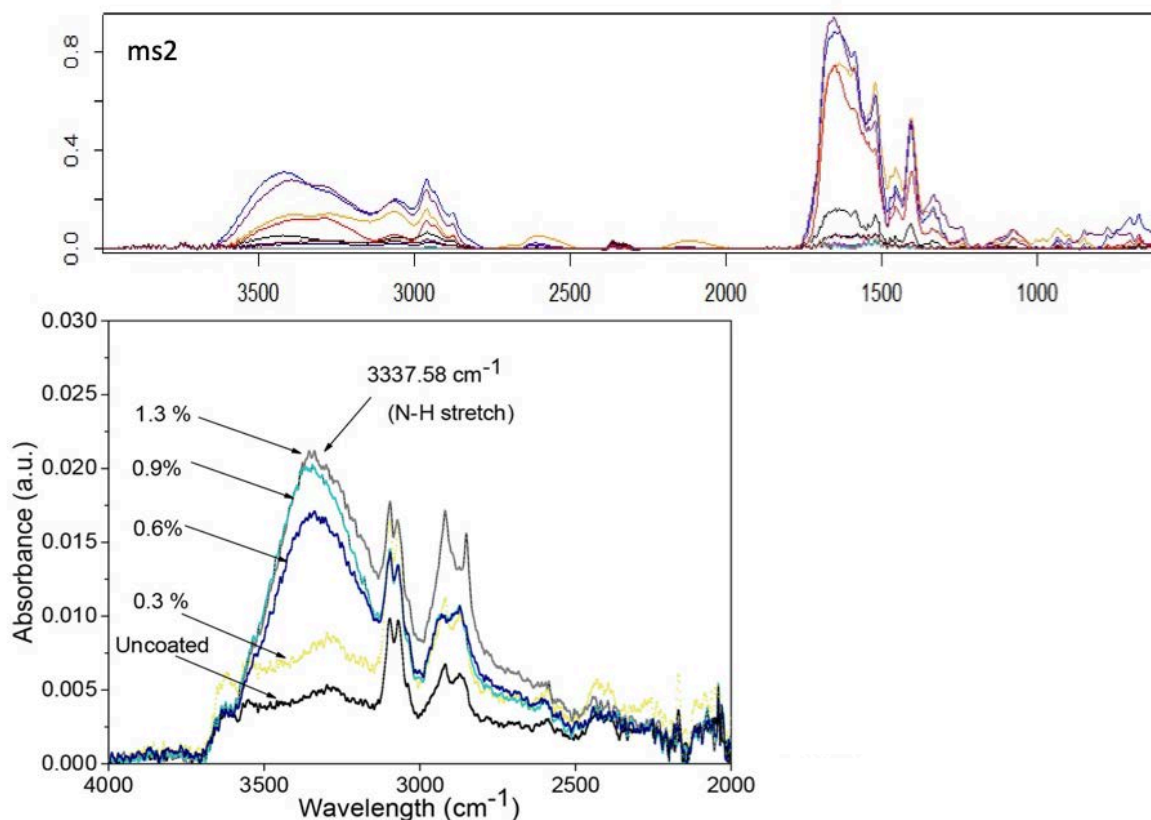


Fig. 4.35. Measured NIR spectra (top) agree with spectrum reported by Sinclair, et al. Virus Reduction Through Microfiltration Membranes Modified with a Cationic Polymer for Drinking Water Applications. *Colloids and Surfaces A: Physicochemical and Engineering Aspects* **2018**, 551 (20), 33–41.

whether this vector of spread requires further examination, both for the current pandemic and for potential future pandemics. This task combined existing groundwater and subsurface transport modeling to create a modeling framework to assess the potential for contamination of groundwater by SARS-CoV-2, as well as the potential for future resurgence of the virus. This research intended to identify existing relationships and data, as well as the results of recent and upcoming studies regarding the factors contributing to SARS-CoV-2 viability, to assess whether viable virus can exist and be sustained in groundwater. The Viral Fate and Transport team utilized the existing subsurface transport model and refined it by incorporating new transport parameters from recent publications to develop a model that simulates

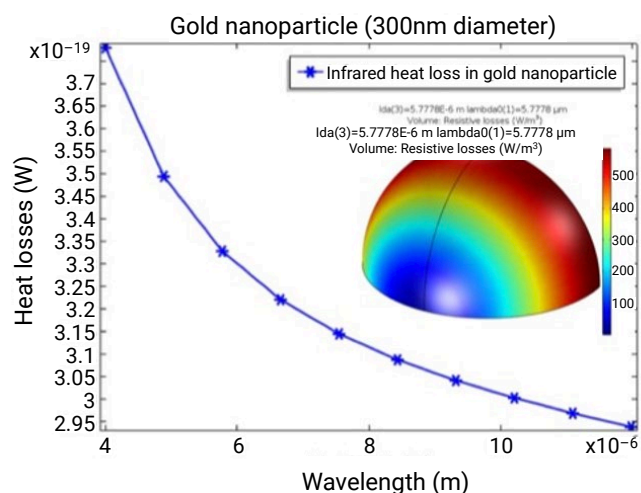


Fig. 4.36. Preliminary computational model developed to investigate virus photothermal effects due to infrared radiation of particle (shown) and planar substrates. [Courtesy Oak Ridge National Laboratory]

virus transport behavior, including virus loading, adsorption, inactivation rate, and travel time under various scenarios.

4.5.3 Outcomes

1. Advanced understanding of the relationship among infection rates, environmental factors, water chemistry, wastewater plan processing, and genetic signal using AI tools.
2. Assessed virus transport behavior in wastewater and sewage systems using hydraulic modeling.
3. Improved infection prevalence quantification, hot spot identification, and early detection of re-emergence using the modeling tool coupled with bioinformatics.
4. Identified potential exposure scenarios and routes from wastewater and sewage, as well as contributing factors for virus reduction, using the modeling tool and developed relationships contributing to virus transport.
5. Improved the understanding of controlling factors for SARS-CoV-2 viability in groundwater. Relationships between SARS-CoV-2 and environmental factors, including subsurface temperature, moisture and organic contents, water chemistry, and soil properties, were established to refine and improve the modeling framework. This work focused on those relationships that will affect virus loading, adsorption, and inactivation rate, which control SARS-CoV-2 viability while it migrates through groundwater systems.
6. Used the refined model to perform analyses that assessed the potential for subsurface transport of SARS-CoV-2 in groundwater. The team also assessed how predicted changes to the climate may impact future viral transport vectors. Specific scenarios were simulated to provide real-world examples of quantitative viability measures of virus in groundwater for urban and rural regions.

4.5.4 Results: Topic 1

Virus Fate and Transport Monitoring and Modeling in Water and Wastewater Systems

- The Small World Network Model for SARS-CoV-2 Wastewater Sewershed Fate and Transport
- The Extended Susceptible-Exposed-Infectious-Removed (SEIR) Small World Sewershed Model
- Genomic Sequencing of SARS-CoV-2 in Wastewater

Publications

- Brigmon, R. L.; Hamm, L.; Dichosa, A. SARS-CoV-2 Wastewater Fate and Transport: A Model to Estimate Outbreaks and Infected Sewersheds. Manuscript in preparation.
- Dichosa, A.; Hamm, L.; Brigmon, R. L. Methods for Sampling-to-qPCR-to-Sequencing and Establishing a “Genomic Stamp” for Multiple WWTP Sites. Manuscript in preparation.

The Small World Network Model for SARS-CoV-2 Wastewater Sewershed Fate and Transport

Practical Implications

- Attained data from several Southeast communities (e.g., in South Carolina, Georgia, and Virginia). This data will provide specific information associated with viral history at wastewater treatment facilities (WWTFs) along with other critical data (e.g., population demographics and potential super spreader events).
- Development Phase — Created a FORTRAN-based algorithm (i.e., a forward running working model). This model stochastically predicted disease spread coupled to a sewershed model to ultimately predict the viral content entering a WWTF.
- Benchmarking Phase — To assist in parameter calibration of this working model, a few WWTF-specific databases were chosen in a down-selection process for use in a benchmarking activity. Given the scarcity of data associated with certain key COVID-19 viral aspects, open literature information supplemented these databases.

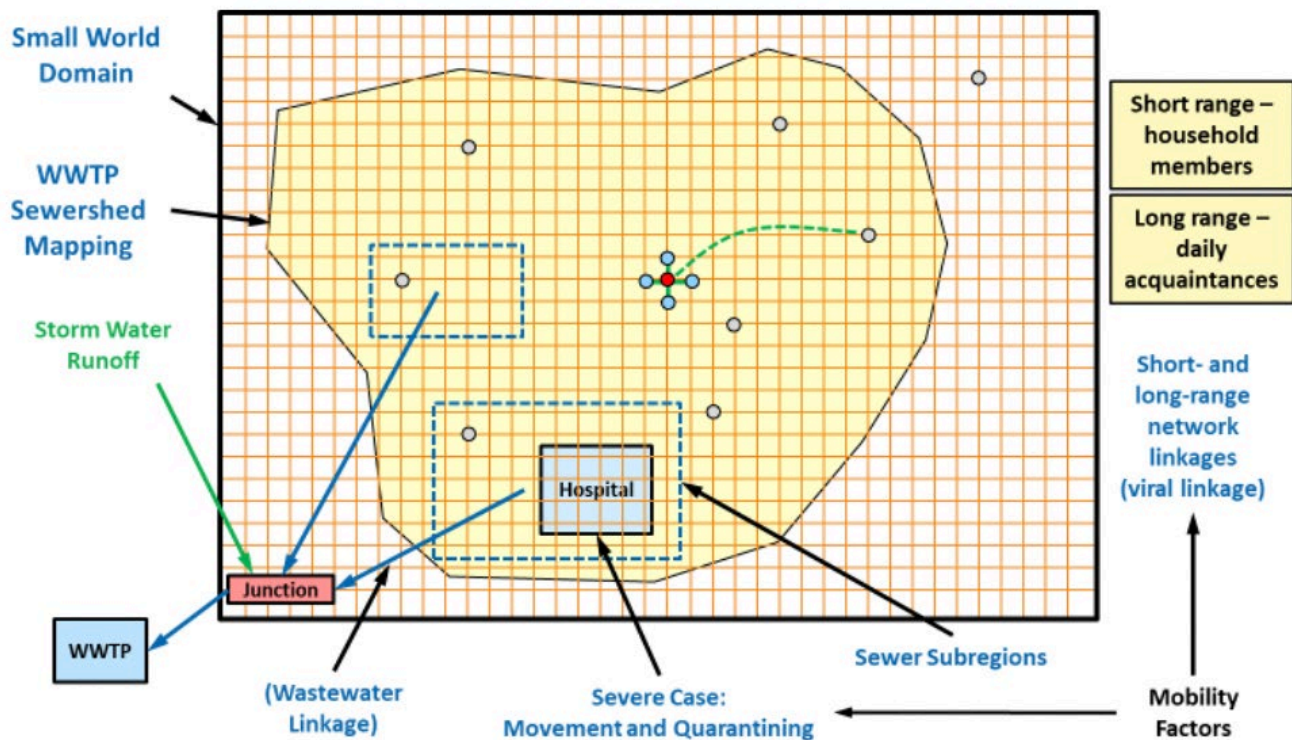


Fig. 4.37. Small world network grid overlaid onto a sewer system. [Courtesy Savannah River National Laboratory and Los Alamos National Laboratory]

Summary

Based on the most recent successes within the open literature associated with disease spreading dynamics of SARS-CoV-2 within communities, a small world approximation method was chosen to address the viral source term entering a specific sewershed system's WWTF. This small world approximation employed a regular undirected weighted nodal network to represent individuals within its domain, where the more traditional stochastic epidemic algorithms were utilized. This approach was ideal for addressing a viral source term supplying fecal material to a local specific WWTF of a small community.

This study's small world network approximation conformed to basic graph theory geometric restrictions. Both the fate and transport model and the stochastic network epidemic source term model

were introduced. Both models relied on a geometric nodal network scheme. In this section, the two models were coupled on a common nodal network layout. Generally, the term "a small world network" implies a closed system, which, in this case, represented a fixed population size. An overview of the two models being overlaid onto one nodal network diagram is shown in Figure 4.37 (this page).

For the viral source term perspective, at each of the vertices, a single individual person resided (typically at their residence or at a hospital). Transmission events were the key processes assumed to occur by a Markovian process where:

- **Short range** – Household members who interacted frequently. The number of household members was an inputted number that was fixed during a given set of runs.

- **Long range** – Daily acquaintances who interacted less frequently (e.g., workplace or shopping). The average number of daily acquaintances was an inputted number that could be fixed during a given set of runs or varied.

Individuals who resided within this small world domain could, in principle, come into contact with any other individual within this domain. These potential contacts occurred based on the long-range daily acquaintance's linkages. However, fecal material associated with any given individual was limited to occur only at that person's household location. The transport timing associated with each node location was related to its physical distance from the entrance point for its WWTF and average tortuosity factor. Travel times were generally only approximations where the highly time-dependent volumetric flow rates were time-averaged and transport velocities were assumed based on systems design guidelines (e.g., 1 to 3 feet/hour phasic water velocities in open-channel flow conditions). The following travel time variations are shown for the two-sewer example in Figure 4.38 (this page). Based on an average water consumption of ~100 gallons of daily (EPA estimate), 10,000 people within a single sewer system would be sending ~1 million gallons per day to a WWTF. Thus, travel times were related to population density and sewer-shed footprint size.

The Extended Susceptible-Exposed-Infectious-Removed (SEIR) Small World Sewershed Model

Practical Implications

- Integrated SEIR epidemic model overlay with small world sewershed fate and transport model.
- Modeled outbreak dynamics from a sewershed exposure event and estimated the numbers of infected individuals based on wastewater RNA concentrations.

Summary

To accomplish the objectives above, a small world approximation approach was selected in which the viral source term used a stochastic-based (i.e., Markovian processes) extended SEIR model. This

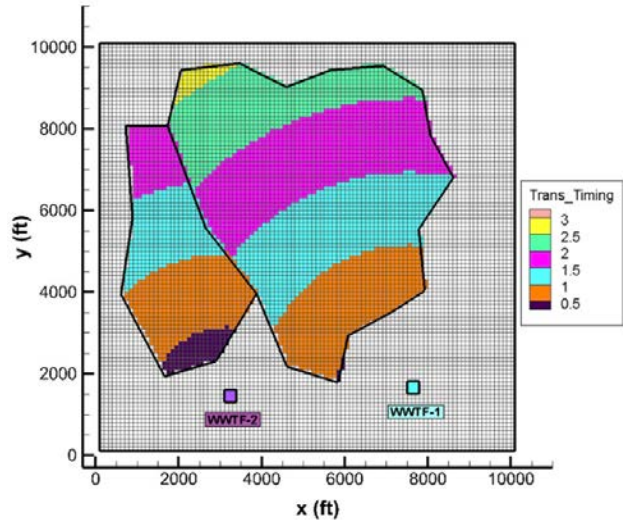


Fig. 4.38. An example of a small world nodal network illustrating travel time variations associated with two sewersheds. [Courtesy Savannah River National Laboratory and Los Alamos National Laboratory]

viral source term model was applied on a nodal network that defined the small world and was coupled to a simplified viral transport equation that was also overlaid on the same nodal network. Each realization used a Markovian process model where randomly chosen seeds locations started the process, and the subsequent, randomly selected SEIR parameter settings progressed over time. Multiple realizations were then run in a Monte Carlo fashion until convergence of key measures of merit was achieved. For the conditions specified, the series of plots in Figure 4.39 (p. 199), illustrate the source term model's behavior for a single realization (i.e., the first one). Each rectangle shown represents a specific individual and has been colored coded, (i.e., class/status of individuals being either [S], [E], [I], or [R]). The specific extended SEIR model did not distinguish between symptomatic and asymptomatic individuals.

At time zero (0 d), two observation regions highlighted by dashed, red circles were watched to see how household contacts behaved (circle on the

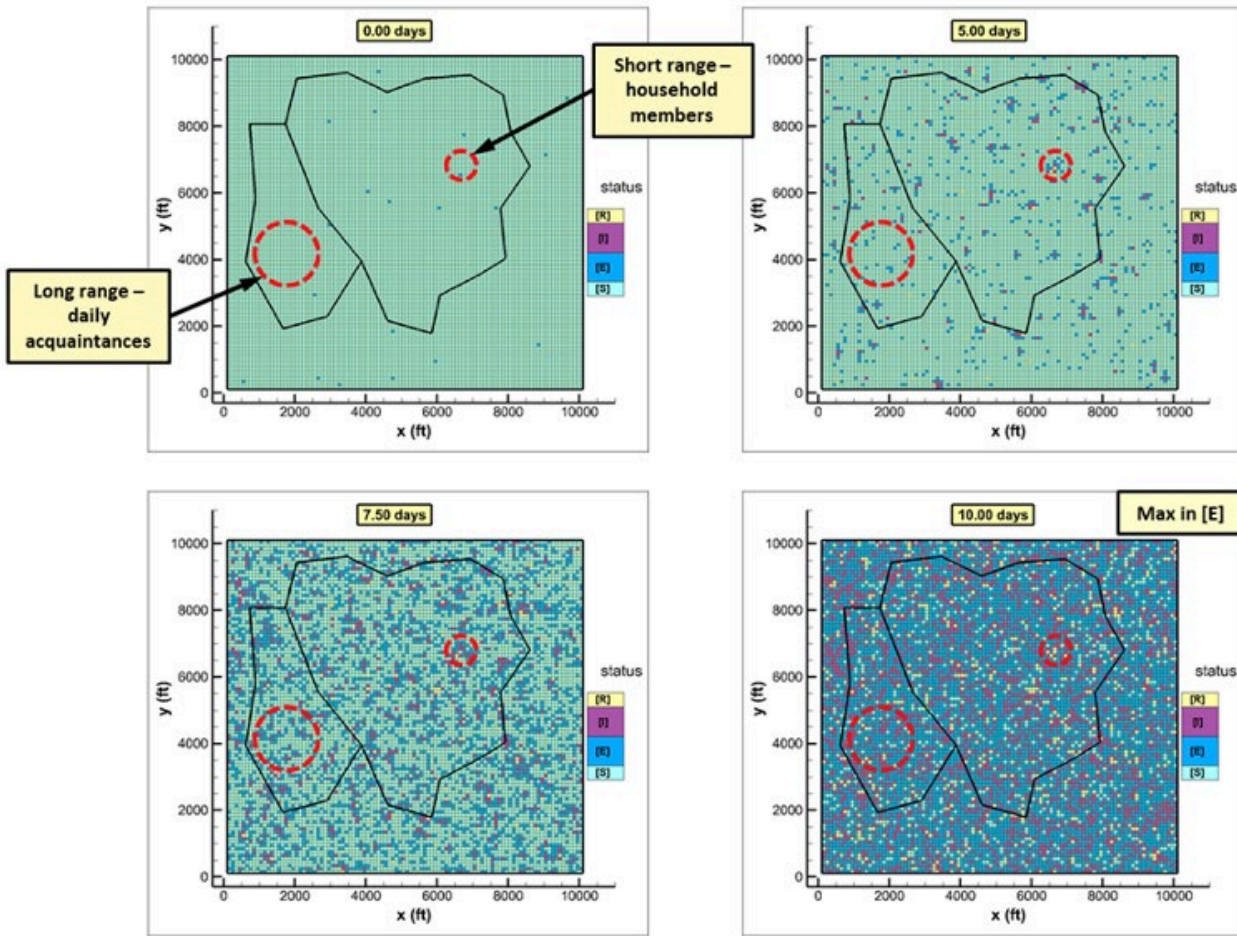


Fig. 4.39. Extended SEIR status on the nodal network. Time = 0 days (top left), 5 days (top right), 7.5 days (bottom left), or 10 days (bottom right). [Courtesy Savannah River National Laboratory and Los Alamos National Laboratory]

right), while the other was watched to see how long-range contacts behaved (circle on the left). Prior to time zero, all individuals were set to [S]. As can be seen in the figure, one initial [E] seed was placed within the right circle, while no [E] seeds were placed in the left circle. After 5 days, multiple household contacts generated local pockets of activity, while long-range contacts distributed activity throughout the small world. Infections showed up in both sewersheds, as well as in the surrounding areas. By 7.5 days, a significant number of exposed [E] and infectious [I] individuals were seen. At day 10, a maximum level of totally exposed [E]

individuals was reached where their distribution was relatively uniform over the entire small world domain. Results illustrate that even for a single realization, a very dynamic process of evolution occurs. To reach a converging stochastic-based response, many realizations must be executed (numbers in the 1,000s in many cases).

Genomic Sequencing of SARS-CoV-2 in Wastewater

Practical Implications

- Assessed feasibility of using the wastewater microbiome as an indicator of community-wide SARS-CoV-2 surveillance.

- Established SARS-CoV-2 genomic variation's association with mortality rate of COVID-19 and correlation with WWTF genomic analysis.

Summary

Since the start of the pandemic, public health officials, researchers, and epidemiologists have turned to sewage systems across the country (and the globe) to strategically detect the presence and gauge the prevalence of SARS-CoV-2 RNA signatures. Sampling at specific effluent sewage sites equates to testing up to thousands of potential human shedders at one time. Thus, SARS-CoV-2 viral loads can be compared from one community to another to triage which populations need critical resources more than others. While SARS-CoV-2 detection methods have principally relied on molecular amplification of partial viral genomes (e.g., N1 and N2 markers) via quantitative polymerase chain reaction (qPCR), one significant drawback of this method is the loss of whole genomic information that can identify genomic mutations and critical variants. Genomic variations from the original (wild type) Wuhan strain have been proposed to either increase virulence and/or decrease vaccine efficacy. Therefore, it is vital to concurrently detect and quantify SARS-CoV-2 in the population and identify key genomic variations that may lead to phenotypic alterations.

For the goal of sequencing SARS-CoV-2 genomes from wastewater, the Viral Fate and Transport wastewater team collaborated with Drs. Raul Gonzalez and Jim Pletl from Hampton Roads Sanitation District (HRSD) in Virginia. HRSD has been performing molecular-based/qPCR wastewater monitoring for human respiratory diseases for several years. Team discussions with HRSD targeted nine wastewater facilities from which HRSD extracted DNA/RNA to perform its state dashboard reporting of COVID-19 cases. Upon completion of the sequencing efforts, HRSD sent the data to LANL to perform genomic analysis and mapping of the reads to the SARS-CoV-2 Wuhan genome reference strain (NC045512.2) using EDGE Bioinformatics platform (edgebioinformatics.org).

Using the Wuhan strain as the reference to map Illumina reads sequenced, none of the individual datasets completed a SARS-CoV-2 genome, as each sample uniquely covered varied regions of the genome. By looking at which areas of the reference genome had representation, it appeared that there was no amplification or sequencing bias involved. Rather, targeted amplification across the genome during the library preparation step was random. This could be the result of several events, either alone or in combination: (1) the (dominant) SARS-CoV-2 genome in the extract may have been degraded, (2) inhibitory compounds potentially present in the extract may have limited amplification efficiency during library preparation; (3) the amount of high-quality SARS-CoV-2 RNA template may have been insufficient; and (4) low-quality products may have been derived during the library preparation.

From the datasets derived from all the wastewater sites, the team surmised that if the collective data were combined, a significantly greater coverage of the SARS-CoV-2 genome would have been achieved, albeit short of a complete genome. Another assumption was that, if assembled, the collective data would have revealed no strain variant of the reference Wuhan strain. To address this, the wastewater team used five datasets that individually gave the most coverage of the reference genome: York River (YR), Williamsburg (WB), Atlantic Beach (AT), and unassigned reads (P1 and P2) that possessed sequence data but were not identified via demultiplexing based on the assigned barcodes. This collective analysis greatly improved genome coverage to nearly 60%, but still fell short of a complete mapped genome with no detection of single nucleotide polymorphisms (see Fig. 4.40, p. 201). Analyses of each of these sites strongly suggests that effort on wet lab operations must be improved.

4.5.5 Results: Topic 2

SARS-CoV-2 Viability in Groundwater and Implications for the Current Outbreak and Potential Resurgence

- Effects of Virus Load, Filtration, Inactivation, and Dilution on Virus Transport

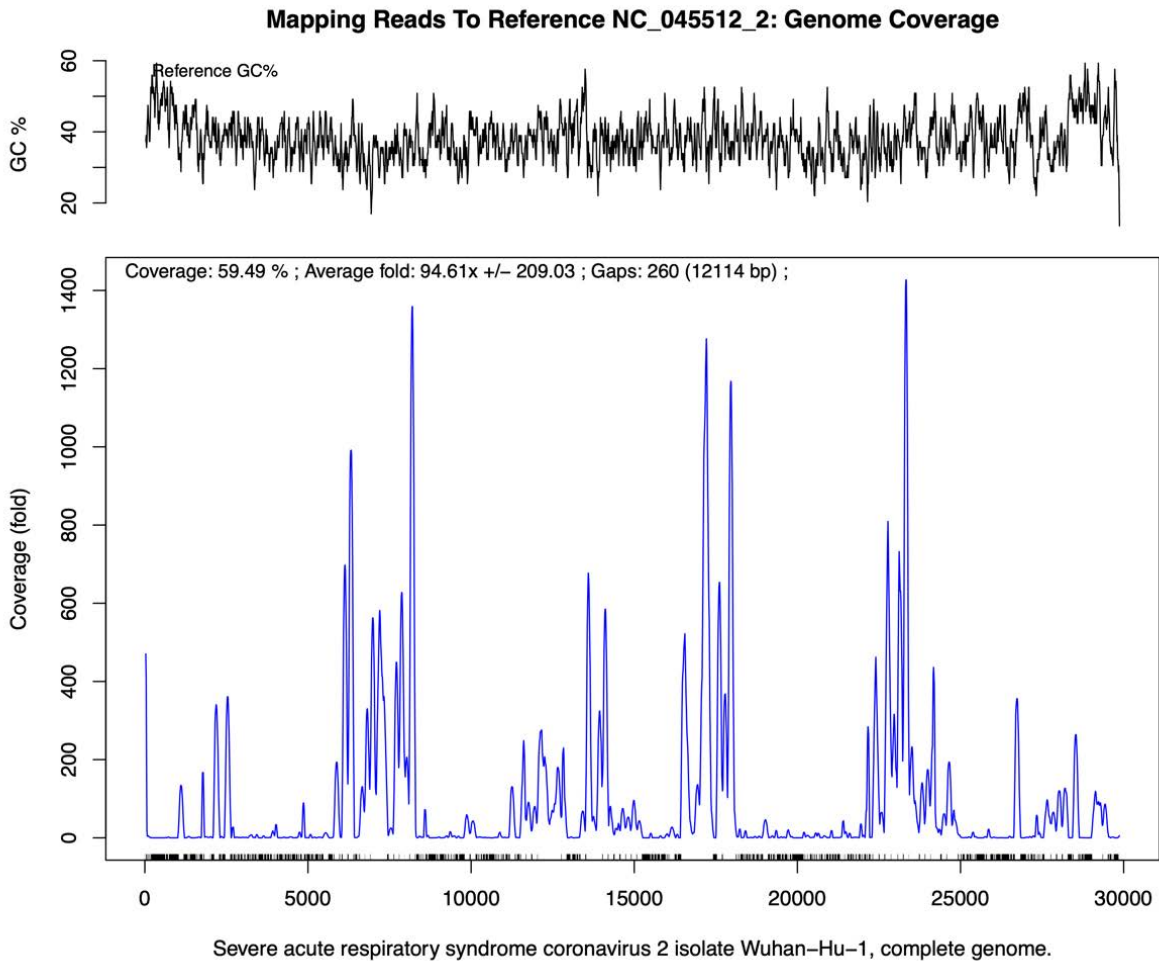


Fig. 4.40. Combining reads from select datasets. Datasets with the most resultant, individual coverage were utilized. These sites were York River (YR), Williamsburg (WB), Atlantic Beach (AT), and unassigned reads (P1 and P2). Although this improved the genome coverage to 59.5%, a complete genome was not obtained. [Courtesy Northwestern University, Argonne National Laboratory, and Savannah River National Laboratory]

- Effects of Hydrogeologic Factors (Permeability, Hydraulic Gradient, Depth to Unconfined Aquifer, and Fractures)
- Effects of Inactivation Rate and Attachment
- Results of Stochastic Modeling and Effects of Uncertainty of Attachment Rate
- Assessment of the Worst-Case Scenarios

Publications

- Saavedra Cifuentes, E.; Mills, R.T.; Nichols, R.; Torres, H. E.; Viner, B.; Yan, E.; Packman, A.

Assessing the Transport of SARS-CoV-2 in Groundwater. Manuscript submitted to *Water Research*.

- Saavedra Cifuentes, E.; Mills, R.T.; Nichols, R.; Torres, H. E.; Viner, B.; Yan, E.; Packman, A. Evaluation of Controlling Factors for Virus Transport in Groundwater. Manuscript in preparation.
- Saavedra Cifuentes, E.; Mills, R.T.; Nichols, R.; Torres, H. E.; Viner, B.; Yan, E.; Packman, A. The Impact of CSO Flow Events on Virus Transport in Surface Water. Manuscript in preparation.

Effects of Virus Load, Filtration, Inactivation, and Dilution on Virus Transport

Practical Implications

- Provided a current understanding of factors influencing groundwater transport of SARS-CoV-2.

Summary

A new module named BIOPARTICLE was developed for PFLOTRAN to simulate virus transport. Figure 4.41 (this page) shows the conceptual model used for the development of BIOPARTICLE, including virus activation; particle filtration; and the combined effects of dilution, inactivation, and filtration on SARS-CoV-2 breakthrough. Since filtration and inactivation were both modeled as first-order reactions, they had a similar effect on the relationship between SARS-CoV-2 breakthrough and travel time: longer travel times resulted in greater removal of infectious viruses. The attachment rate was quantified in experiments using an intermediate value for the collision efficiency = 0.01. Consequently, accounting for filtration resulted in a minimum log-removal that was 0.5 higher than when considering only virus inactivation. While this minimum occurred at a slightly higher water table gradient ($I \sim 1 \times 10^{-2}$), a wide range of I ($5 \times 10^{-3} < I < 5 \times 10^{-2}$) still yielded a SARS-CoV-2 removal that was less than four log-reductions.

Effects of Hydrogeologic Factors (Permeability, Hydraulic Gradient, Depth to Unconfined Aquifer, and Fractures)

Practical Implications

- Provided a current understanding of factors influencing groundwater transport of SARS-CoV-2.
- Provided estimates for virus concentrations at drinking water wells in unconfined alluvial aquifers and identified conditions leading to potentially concerning scenarios.

Summary

A finite-volume numerical model was utilized to solve the governing equations for

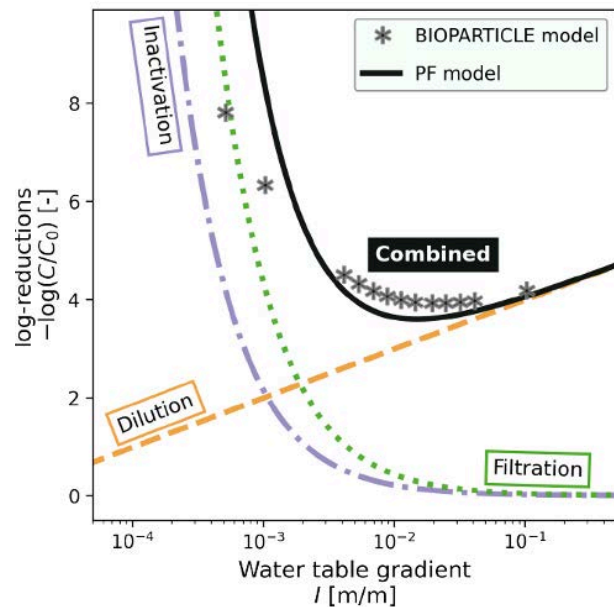


Fig. 4.41. Reduction in SARS-CoV-2 concentration between source and receptor due to the combination of filtration, dilution, and inactivation predicted by PF and BIOPARTICLE model simulations. Results are shown for the effect of filtration only, dilution only, inactivation only, and the combined effect of all three processes. [Courtesy Northwestern University, Argonne National Laboratory, and Savannah River National Laboratory]

nonconservative transport in three-dimensional, variably saturated porous media, as an attempt to investigate the effects of hydrogeologic conditions on virus transport. To identify the impact of hydrogeologic factors on the virus concentration at the domestic well, and the combinations leading to potentially concerning scenarios, 54 scenarios or model variations were defined. These scenarios were built considering variations in three main hydrogeologic factors: (1) the permeability of the aquifer, (2) the hydraulic gradient, and (3) the thickness of the unsaturated zone. Six different permeability values were tested, with three representing homogenous gravel, coarse sand, and fine sand aquifers, and three representing heterogeneity and preferential flow paths within the aquifer through fractures. To model flow through the unsaturated zone, relative

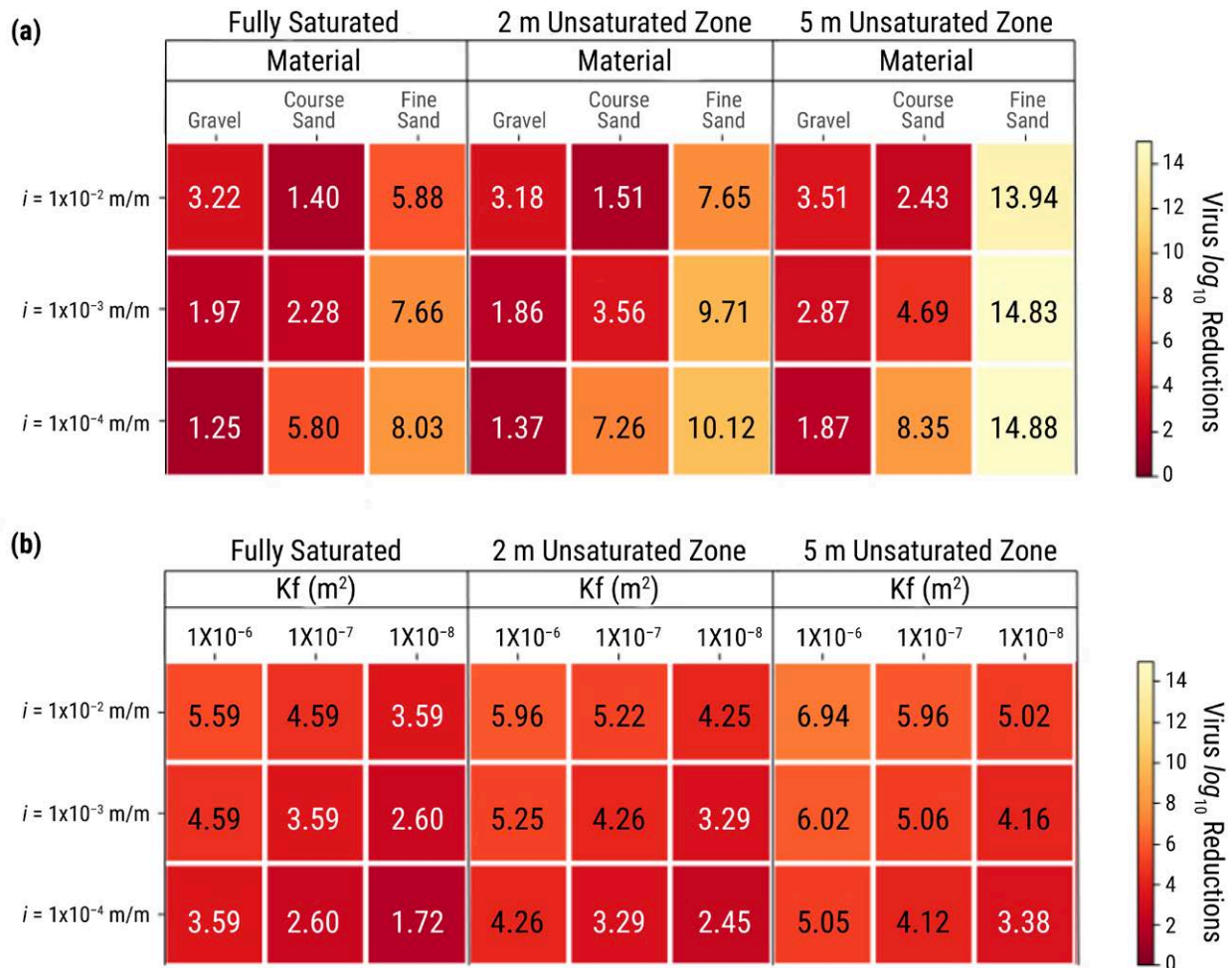


Fig. 4.42. (a) Virus relative concentrations and \log_{10} reductions at the domestic well for models with homogeneous media. Potentially vulnerable scenarios are indicated with a white font. **(b)** Virus relative concentrations and \log_{10} reductions at the domestic well for models with heterogeneous media. Potentially vulnerable scenarios are indicated with a white font. [Courtesy Northwestern University, Argonne National Laboratory, and Savannah River National Laboratory]

permeability and saturation functions had to be associated with each soil material.

The models representing gravel aquifers were found to achieve lower virus reductions below the threshold value among all the tested aquifer materials (e.g., gravel, coarse and fine sands). However, the least \log_{10} reductions observed in the gravel models were achieved under the lower hydraulic gradient (1×10^{-4} m/m) consistently, regardless of the thickness of the unsaturated zone (see

Fig. 4.42a, this page). This result indicated that the combination of high permeability and high hydraulic gradient actually allowed for more dilution of the virus, resulting in increasing virus reduction with faster flow systems, given that the leakage rate was constant. In contrast, for less-permeable aquifer materials (e.g., coarse sand), the lower virus reduction was achieved with the higher hydraulic gradient. This suggested that increasing the flow velocity (combination of the permeability and hydraulic gradient) in the system raised the virus concentration

at the receptor up to an inflection point (as shown in the previous section) controlled by the leakage rate, and, after which, increasing the flow velocity only led to greater dilution and lower viral loads.

Fine sand models were unable to achieve potentially concerning concentrations at the domestic well for $t = 102$ days, even under fully saturated conditions with the higher gradient value (see Fig. 4.42b, p. 203). Since these experiments represented the slower flow systems and would be affected the most by the virus removal processes, fine sand models were not investigated for further analyses under inactivation and filtration scenarios. Increasing the thickness of the unsaturated zone was found to consistently lead to greater virus log₁₀ reductions at the receptor, with a more significant impact on lower permeabilities, since these more effectively reduce the virus leakage into the vadose zone and enhance dilution.

In comparison with the homogeneous media models, the models with multiple continua to represent heterogeneity due to fractures in the aquifer had permeability values equal or higher than the permeability chosen for gravel models. Therefore, dilution was more significant for these scenarios, leading to most of the potentially concerning scenarios, and those with the least virus log₁₀ reductions being found with the lower fracture permeability value (k_f) of 1×10^{-8} m/d (see Fig. 4.42b, p. 203). Additionally, a model with this permeability value was able to achieve virus log₁₀ reductions below the threshold value, even with an unsaturated zone thickness of 5 m in combination with the lower gradient value. Overall, Figure 4.42b shows how greater permeabilities due to preferential flow paths in aquifers did not necessarily result in less virus log₁₀ reductions at potential receptors, supporting the previous observations on permeability, gradient, and unsaturated zone thickness as controlling factors for dilution.

Effects of Inactivation Rate and Attachment

Practical Implications

- Provided a current understanding of factors influencing groundwater transport of SARS-CoV-2.

- Provided estimates for virus concentrations at drinking water wells in unconfined alluvial aquifers considering inactivation rate and attachment and identified conditions leading to potentially concerning scenarios.

Summary

Two inactivation rates were simulated for the modeling systems identified as being vulnerable based on the combination of permeability, hydraulic gradients, and unconfined aquifer depth. Attachment occurring in combination with inactivation decay represents more realistic conditions for virus transport in groundwater. Therefore, several experiments were simulated considering the combination of the two inactivation decay rates, with two different attachment rates intending to represent a range of possible conditions. For cold climate regions with a decay rate of $3.23 \times 10^{-6} \text{ s}^{-1}$, the lower bound attachment rate ($9 \times 10^{-7} \text{ s}^{-1}$) increased the virus log₁₀ reductions for the coarse sand model above the threshold value, while not impacting the rest of the potentially concerning scenarios as significantly (see Fig. 4.43, p. 205). The higher bound attachment rate ($9 \times 10^{-5} \text{ s}^{-1}$) successfully mitigated all concerning scenarios, except for gravel under fully saturated conditions with a gradient of 1×10^{-2} m/m. This combination of hydrogeological conditions seemed to be concerning even for warmer climate regions, where the higher decay rate was found to be insufficient to achieve four or more virus log₁₀ reductions (see Fig. 4.43). Out of the homogeneous media models, those representing gravel aquifers were the only ones considered potentially concerning when accounting for both attachment and decay, with the worst-case scenario being under fully saturated conditions and with a gradient of 1×10^{-3} m/m. However, gravel aquifers with the middle and high gradient were able to achieve less than four virus log₁₀ reductions, even with a 2 m unsaturated zone.

Shorter travel times to the receptor could minimize the possible attenuation, due to removal processes through attachment or inactivation. Therefore, several experiments were simulated to evaluate effects of attachment and inactivation on virus reduction. The low attachment rate ($9 \times 10^{-7} \text{ s}^{-1}$) was found

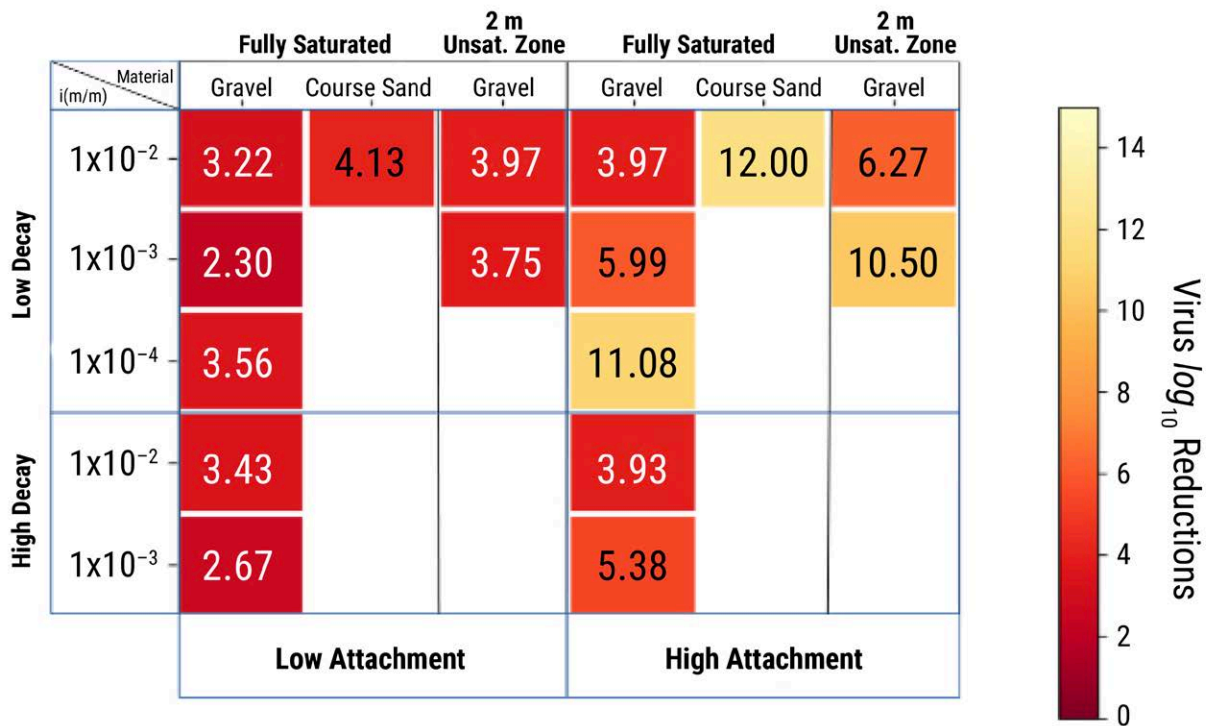


Fig. 4.43. Virus relative concentrations at the domestic well for models with homogeneous media, after the addition of decay and attachment rates. Potentially concerning scenarios are indicated with a white font. [Courtesy Northwestern University, Argonne National Laboratory, and Savannah River National Laboratory]

to be unable to significantly affect virus removal in any of potentially concerning scenarios, despite the climate condition governing decay (see Fig. 4.44, p. 206). Contrarily, the higher bound attachment rate ($9 \times 10^{-5} \text{ s}^{-1}$) was able to significantly reduce virus concentration for all the potentially concerning scenarios with a 2 m depth to unconfined aquifer, and the scenarios with the combination of the low fracture permeability and the low gradient of $1 \times 10^{-4} \text{ m/m}$ in the fully saturated setting (see Fig. 4.44). In summation, the difference between decay rates controlled by groundwater temperatures was too small to result in significant differences of virus inactivation for fractured aquifers in warm and cold climate regions. Additionally, attachment could be the more important removal process for these systems, considering that attachment rates evaluated in these experiments might not be the highest that can be estimated from the range of Darcy velocities analyzed for these systems,

according to colloid filtration theory. With the lower bound attachment rate, the hydrogeological conditions that led to the worst-case scenario were found to be the lower fracture permeability value of $1 \times 10^{-8} \text{ m/d}$ with the lower gradient ($1 \times 10^{-4} \text{ m/m}$) under fully saturated conditions.

Results of Stochastic Modeling and Effects of Uncertainty of Attachment Rate

Practical Implications

- Provided a current understanding of factors influencing groundwater transport of SARS-CoV-2.
- Evaluated sources of uncertainty in the model caused by variations of physical properties of the aquifer.

Summary

Based on the colloid filtration theory, attachment rates are controlled by both physical and chemical

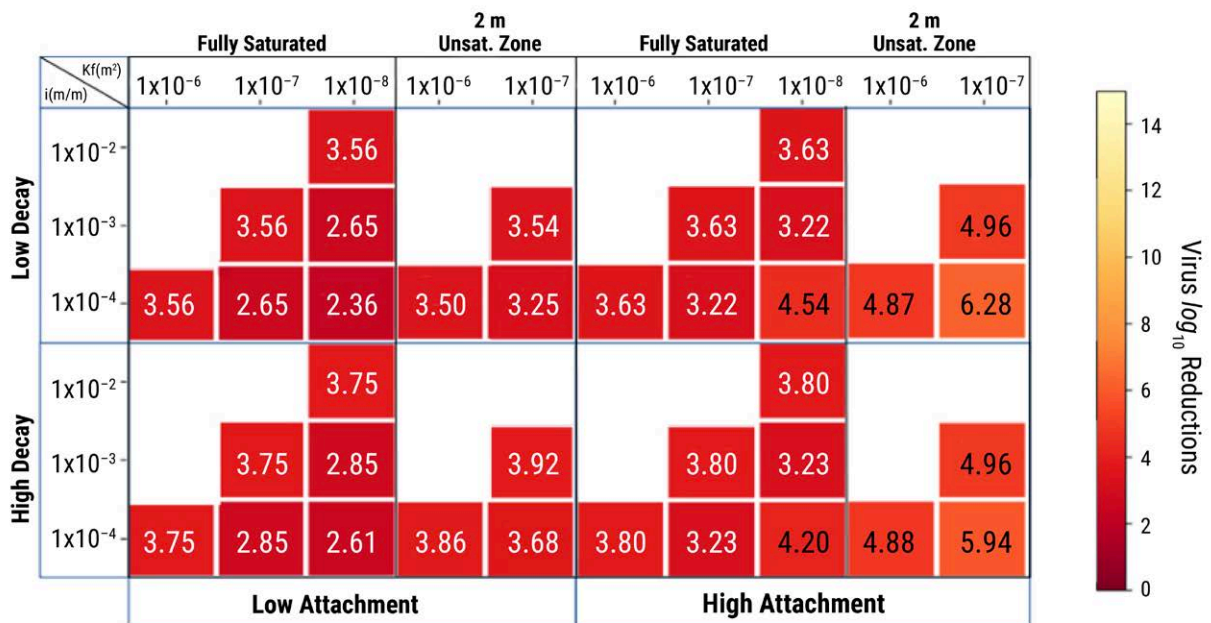


Fig. 4.44. Virus relative concentrations at the domestic well for the models with heterogeneous media after the addition of the inactivation decay and attachment rates. Potentially concerning scenarios are indicated with a white font. [Courtesy Northwestern University, Argonne National Laboratory, and Savannah River National Laboratory]

properties of the aquifer, groundwater, and virus. In this analysis, the physical properties affecting filtration (e.g., the porosity and grain size) were quantitatively linked to the permeability and/or flow velocity to capture the uncertainty caused by variations of physical properties of the aquifer. Variation of chemical properties (i.e., isoelectric point of the virus and pH of the groundwater controlling the charges of the virus and soil particles) was captured by the attachment efficiency (α_{att}) and was allowed to take any value between 0 and 1. Impacts of permeability and attachment efficiency on the attachment rate is shown in Figure 4.45 (p. 207).

A slightly decreasing trend in attachment rates was observed as permeability (tied to the porosity and grain size) increased, indicating that the effect of permeability on the attachment rate was minimal (less than one order of magnitude). Great variability in attachment rates was observed due to the uncertainty of attachment efficiency, especially for

the group with attachment efficiencies equal or less than 0.25.

Another significant source of variability was the hydraulic gradient, which was also randomly sampled and affected the attachment rate by increasing or decreasing the Darcy velocity of the system. To evaluate the impact of hydraulic gradient variability, \log_{10} reductions derived from the 1,000 ensembles were analyzed against flow velocity, calculated from the permeability, porosity, and hydraulic gradient for each ensemble. Figure 4.46 (p. 207) shows that the uncertainty associated with chemical properties of the virus and transport media had significant effects on virus reduction in slower flow systems. For a similar flow system at or less than 10^{-4} m/s, differences greater than 10 \log_{10} reductions were observed over the possible range of attachment efficiencies. Contrarily, for flow velocities above 2×10^{-3} m/s, the drastic changes in the attachment efficiency resulted in very small differences in terms of \log_{10} reductions.

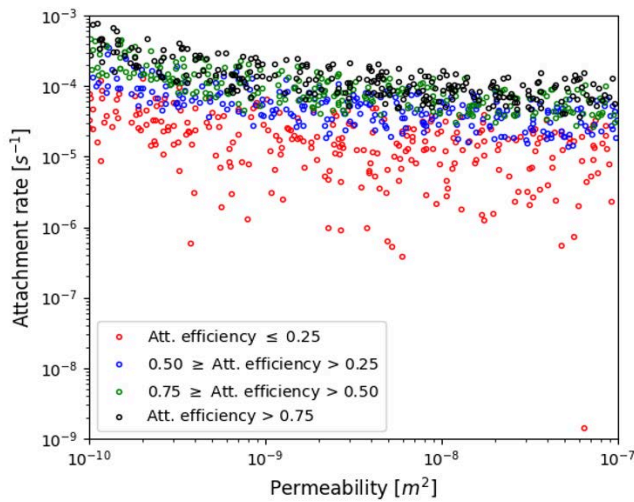


Fig. 4.45. Effects of a possible range of attachment efficiencies and permeabilities on attachment rate. [Courtesy Northwestern University, Argonne National Laboratory, and Savannah River National Laboratory]

These results suggested that the uncertainty associated with the attachment rate was not as significant for fast flow systems, as it was also observed for the inactivation decay rate. Overall, the virus reductions were found to decrease as flow velocity increased, and the number of potentially concerning scenarios significantly increased with flow velocities between 1×10^{-3} and 1×10^{-2} m/s, supporting that certain hydrogeological conditions had minimal virus removal.

Assessment of the Worst-Case Scenarios

Practical Implications

- Assessed the impact of setback difference on virus removal needed to achieve acceptable risk of transmission based on worst-case scenarios for virus transport identified in the previous sections.

Summary

Given that gravel under fully saturated conditions was found to achieve the least virus log₁₀ reductions at the receptor, this combination of hydrogeological conditions was selected as the worst-case scenario to evaluate the impact of additional

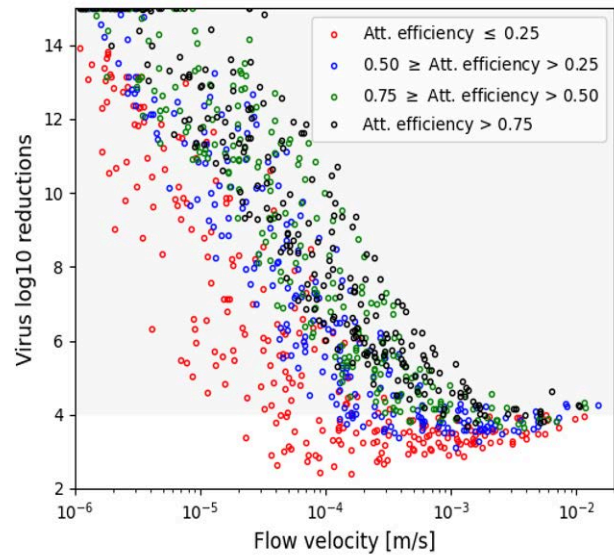


Fig. 4.46. Effects of a possible range of attachment efficiencies and flow velocities on virus reduction. [Courtesy Northwestern University, Argonne National Laboratory, and Savannah River National Laboratory]

considerations on virus reduction. Similarly, the worst-case scenarios for evaluation used the low decay rate value of $3.23 \times 10^{-6} \text{ s}^{-1}$ for cold climate regions, as it represented lower virus attenuation and resulted in more concerning scenarios. Four additional gradients, for a total of seven, were applied to the models constructed for the worst-case scenarios, and the virus log₁₀ reductions achieved after 30 days of pumping and constant leakage are presented in Figure 4.47 (p. 208).

Focusing on the worst-case scenario assumed for the domestic well setting, Figure 4.47a shows how the least virus log₁₀ reductions were found at different hydraulic gradients depending on the attachment rate. Gradients greater than the inflection point resulted in greater attenuation due to dilution, while gradients lower than the inflection point resulted in greater virus removal. The virus reduction reached the lowest at the inflection point. However, the inflection point in the high virus attachment environment occurred at higher hydraulic gradient conditions (10^{-1} to 10^{-2}), while the

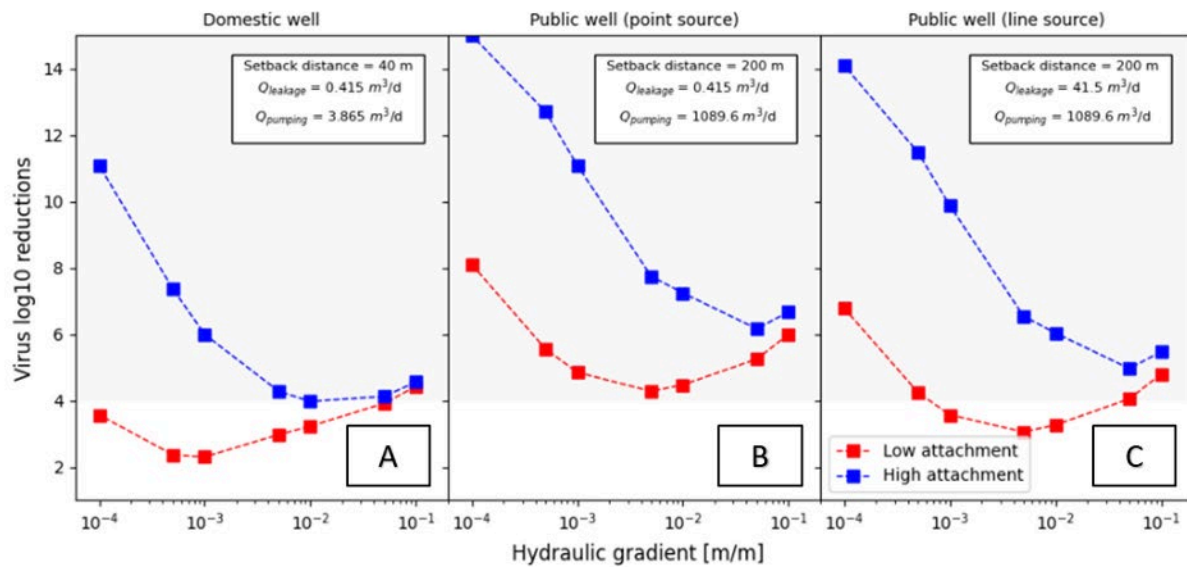


Fig. 4.47. Comparison of the worst-case scenario under the following configurations: **(A)** domestic well, **(B)** public well with a point leakage source, and **(C)** public well with a line leakage source. [Courtesy Northwestern University, Argonne National Laboratory, and Savannah River National Laboratory]

inflection point in the low attachment environment shifted to lower hydraulic gradient conditions (10^{-3}).

In comparison with the public well setting with point source leakage (see Fig. 4.47b), a greater setback distance resulted in significant virus removal even at high gradients. Virus reduction above the threshold of 4 log₁₀ suggested that the worst-case scenarios would not be concerns for both low- and high-virus attachment environments. Combined with a greater pumping rate, the virus reductions observed were expectedly higher, since increased pumping leads to more dilution considering that the leakage rate is the same.

To assess the impact of the ratio of leakage rate to pumping rates, without the influence of other factors (e.g., different setback distances or a larger well

screen), the experiments were simulated assuming increased leakage rate due to leaking sewer lines or combined sewer overflow (see Fig. 4.47c). Comparing Figures 4.47b to c, increasing the leakage rate—thus increasing the ratio of leakage rate to the pumping rates—resulted in a shift of the virus reduction curve toward less virus reductions without changing its shape. This suggested that increasing the ratio of leakage rate to the pumping rate would raise the potential of viral loads at the receptor, regardless of the conditions. However, even under this higher leaking to pumping ratio scenario, virus removal remains significant if the system was under the high virus attachment environment. The vulnerable areas identified from the worst-case assessment could potentially be used for groundwater and surface water sampling for validation.

4.6 Publications and Research Output

Publications

Brigmon, R. L.; Hamm, L.; Dichosa, A. SARS-CoV-2 Wastewater Fate and Transport: A Model to Estimate Outbreaks and Infected Sewersheds. Manuscript in preparation.

Bueno de Mesquita, P. J.; Delp, W. W.; Chan, W. R.; Bahnfleth, W. P.; Singer, B. C. Control of Airborne Infectious Disease in Buildings: Evidence and Research Priorities. *Indoor Air* **2022**, *32* (1), e12965. DOI: 10.1111/ina.12965

Chien, C. H.; Cheng, M. D.; Im, P.; Nawaz, K.; Fricke, B.; Armstrong, A. Characterization of the Indoor Far-Field Aerosol Transmission in a Model Commercial Office Building. *Int. Comm. Heat Mass Transfer* **2021**, 105744. DOI: 10.1016/j.icheatmasstransfer.2021.105744

Dichosa, A.; Hamm, L.; Brigmon, R. L. Methods for Sampling-to-qPCR-to-Sequencing and Establishing a “Genomic Stamp” for Multiple WWTP Sites. Manuscript in preparation.

Dillon, C. F.; Dillon, M. B. Multiscale Airborne Infectious Disease Transmission. *Appl. Environ. Microbiol.* **2021**, *87* (4), e02314-20. DOI: 10.1128/AEM.02314-20

Dillon, Charles F.; Dillon, M. B. Regional Relative Risk: A Physics-Based Metric for Characterizing Airborne Infectious Disease Transmission. *Appl. Environ. Microbiol.* **2021**, *87* (21), e01262-21. DOI: 10.1128/AEM.01262-21

Dillon, M. B.; Frank, M.; Wheeler, E. K. Simplified Screening Method to Measure Indoor Airborne Particle Removal Rates. Manuscript submitted.

Dillon, M. B.; Sextro, R. G.; Delp, W. W. Protecting Building Occupants against the Inhalation of Outdoor-Origin Aerosols. *Atmos. Environ.* **2022**, *268*, 118773. DOI: 10.1016/j.atmosenv.2021.118773

Dobisz, E. A.; Thompson, W.; Phadke, K.; Bellaire, B.; Sakdinawat, A. Dual Beam Focused Ion Beam: Scanning Electron Microscope Imaging and Cross-Sectioning on SARS-CoV-2. Manuscript in preparation.

Domino, S. P. A Case Study on Pathogen Transport, Deposition, Evaporation and Transmission: Linking High-Fidelity Computational Fluid Dynamics Simulations to Probability of Infection. *International Journal of Computational Fluid Dynamics* **2021**. DOI: 10.1080/10618562.2021.1905801

Dutta, S.; Obabko, A.; Balakrishnan, R.; Feng, Y.; Kotamarthi, R. Quantifying the Effect of Size and Release Location on HVAC Induced Respiratory Aerosol Dispersion in Using High-Resolution Large Eddy Simulations. Manuscript in preparation.

Dutta, S.; Obabko, A.; Balakrishnan, R.; Feng, Y.; Kotamarthi, R. (2021). Quantifying the Effect of Evaporation on HVAC Induced Respiratory Aerosol Dispersion. Manuscript in preparation.

Fabregat, A.; Gisbert, F.; Vernet, A.; Dutta, S.; Mittal, K.; Pallarès, J. Direct Numerical Simulation of the Turbulent Flow Generated during a Violent Expiratory Event. *Phys. Fluids* **2021**, *33* (3), 035122. DOI: 10.1063/5.0042086

Fabregat, A.; Gisbert, F.; Vernet, A.; Ferré, J. A.; Mittal, K.; Dutta, S.; Pallarès, J. Direct Numerical Simulation of Turbulent Dispersion of Evaporative Aerosol Clouds Produced by an Intense Expiratory Event. *Phys. Fluids* **2021**, *33* (3), 033329. DOI: 10.1063/5.0045416

Fierce, L.; Robey, A. J.; Hamilton, C. Simulating Near-Field Enhancement in Transmission of Airborne Viruses with a Quadrature-Based Model. *Indoor Air* **2021**, *31* (6), 1843–1859. DOI: 10.1111/ina.12900

Fierce, L.; Robey, A. J.; Hamilton, C. High Efficacy of Layered Controls for Reducing Exposure to Airborne Pathogens. *Indoor Air* **2022**, *32* (2), e12989. DOI: 10.1111/ina.12989

Ho, C. K.; Binns, R. Modeling and Mitigating Airborne Pathogen Risk Factors in School Buses. *Int. Comm. Heat Mass Transfer* **2021**, *129*, 105663. DOI: 10.1016/j.icheatmasstransfer.2021.105663

Negrete, O.; Singh, A.; Hlova, I. Z.; Balema, V. Profiling Materials for Selective Adsorption to SARS-CoV-2 Using Vesicular Stomatitis Virus (VSV) Based Pseudoviruses. Manuscript in preparation.

O’Callahan, B.; Qafoku, O.; Balema, V.; Negrete, O. A.; Passian, A.; Engelhard, M. H.; Waters, K. M. Atomic Force Microscopy and Infrared Nanospectroscopy of COVID-19 Spike Protein for the Quantification of Adhesion to Common Surfaces. *Langmuir* **2021**, *37* (41), 12089-12097. DOI: 10.1021/acs.langmuir.1c01910

Passian, A.; et al. Viral Stability on Surfaces: A Brief Review of Surface Characterization. Manuscript in preparation.

Pease, L. F.; Salsbury, T. I.; Anderson, K.; Underhill, R. M.; Flaherty, J. E.; Vlachokostas, A.; Burns, C. A.; Wang, N.; Kulkarni, G.; James, D. P. Size Dependent Infectivity of SARS-CoV-2 via Respiratory Droplets Spread through Central Ventilation Systems. *Int. Comm. Heat and Mass Transfer* **2021**, 105748. DOI: 10.1016/j.icheatmasstransfer.2021.105748

Pease, L. F.; Wang, N.; Salsbury, T. I.; Underhill, R. M.; Flaherty, J. E.; Vlachokostas, A.; Kulkarni, G.; James, D. P. Investigation of Potential Aerosol Transmission and Infectivity of SARS-CoV-2 Through Central Ventilation Systems. *Building and Environment* **2021**, *197*, 107633. DOI: 10.1016/j.buildenv.2021.107633

Pease, L. F.; Wang, N.; Kulkarni, G.; Flaherty, J. E.; Burns, C. A. A Missing Layer in COVID-19 Studies: Transmission of Enveloped Viruses in Mucus-Rich Droplets. *Int. Comm. Heat and Mass Transfer* **2021**, *131*, 105746. DOI: 10.1016/j.icheatmasstransfer.2021.105746

Robey, A. J.; Fierce, L. Sensitivity of Airborne Transmission of Enveloped Viruses to Seasonal Variation in Indoor Relative Humidity. *Int. Comm. Heat and Mass Transfer* **2022**, *130*, 105747. DOI: 10.1016/j.icheatmasstransfer.2021.105747

Saavedra Cifuentes, E.; Mills, R.T.; Nichols, R.; Torres, H. E.; Viner, B.; Yan, E.; Packman, A. Assessing the Transport of SARS-CoV-2 in Groundwater. Manuscript submitted.

Saavedra Cifuentes, E.; Mills, R.T.; Nichols, R.; Torres, H. E.; Viner, B.; Yan, E.; Packman, A. Evaluation of Controlling Factors for Virus Transport in Groundwater. Manuscript in preparation.

Saavedra Cifuentes, E.; Mills, R.T.; Nichols, R.; Torres, H. E.; Viner, B.; Yan, E.; Packman, A. The Impact of CSO Flow Events on Virus Transport in Surface Water. Manuscript in preparation.

Singer, B. C.; Zhao, H.; Preble, C. V.; Delp, W. W.; Pantelic, J.; Sohn, M. D.; Kirchstetter, T. K. Measured Influence of Overhead

HVAC on Exposure to Airborne Contaminants from Simulated Speaking in a Meeting and a Classroom. *Indoor Air* **2022**, *32* (1), e12917. DOI: 10.1111/ina.12917

Vlachokostas, A.; Burns, C. A.; Salsbury, T. I.; Daniel, R. C.; James, D. P.; Flaherty, J. E.; Wang, N.; Underhill, R. M.; Kulkarni, G.; Pease, L. F. Experimental Evaluation of Respiratory Droplet Spread to Rooms Connected by a Central Ventilation System. *Indoor Air* **2022**, *32* (1), e12940. DOI: 10.1111/ina.12940

Presentations

Balakrishnan, R.; Kotamarthi, R.; Fischer, P. Large Eddy Simulation of Isothermal and Non-isothermal Turbulent Flows in Ventilated Classrooms. 13th International European Research Community on Flow, Turbulence and Combustion (ERCOFTAC) Virtual Symposium: Engineering, Turbulence, Modelling and Measurements (ETMM13), Rhodes, Greece, September 15–17, 2021.

CHAPTER 5

Materials and Manufacturing of Critical Supplies

| | |
|---|------------|
| 5.1 Project Overview | 212 |
| 5.2 Introduction | 213 |
| 5.2.1 Capabilities | 213 |
| 5.2.2 Technical Highlights | 214 |
| 5.3 Task 1: Personal Protective Equipment | 218 |
| 5.3.1 Overview | 218 |
| 5.3.2 Face Shields | 218 |
| 5.3.3 Scaling N95 Production | 219 |
| 5.3.4 Reusable Respirators | 228 |
| 5.3.5 Homemade Masks | 233 |
| 5.4 Task 2: Ventilators | 236 |
| 5.4.1 Overview | 236 |
| 5.4.2 Ventilator Supply Chain Analysis Tool Development | 236 |
| 5.4.3 Lung Modeling | 243 |
| 5.4.4 Rapid Development and Commercialization of a Ventilator | 251 |
| 5.4.5 Accelerated Modernization of Monitoring and Alarm Systems | 253 |
| 5.4.6 Development of Advanced Ventilation Techniques | 254 |
| 5.5 Task 3: Consumables | 256 |
| 5.5.1 Overview | 256 |
| 5.5.2 Printed Swabs | 256 |
| 5.5.3 Coke Bottle Preforms | 262 |
| 5.5.4 Thermo Fisher Test Tubes | 263 |
| 5.5.5 Thermo Fisher 96-Well Plates | 265 |
| 5.6 Publications and Research Output | 266 |

Team Leadership

Lonnie Love (Team Lead), Oak Ridge National Laboratory; **Thomas Lograsso**, Ames Laboratory; **Santanu Chaudhuri**, Argonne National Laboratory; **Amy Marschilok**, Brookhaven National Laboratory; **Robert O'Brien**, Idaho National Laboratory; **Matthew Koetting**, Kansas City National Security Campus; **Toni Taylor**, Los Alamos National Laboratory; **Deepti Tanjore**, Lawrence Berkeley National Laboratory; **Christopher Spadaccini**, Lawrence Berkeley National Laboratory; **Randall Gentry**, National Energy Technology Laboratory; **Panos Datskos**, National Renewable Energy Laboratory; **Rebecca Erikson**, Pacific Northwest National Laboratory; **Mojtaba Safabakhsh**, Princeton Plasma Physics Laboratory; **Steve Eglash**, SLAC National Accelerator Laboratory; **Randy Schunk**, Sandia National Laboratories; **Ralph James**, Savannah River National Laboratory

5.1 Project Overview

Fifteen NVBL laboratories formed a Manufacturing team to address significant research and development (R&D) gaps in the COVID-19 manufacturing supply chain. Beginning in March 2020, the team developed an R&D agenda, worked with DOE and other agencies to set priorities, and collaborated to deliver timely results.

The rapid spread of COVID-19 resulted in significant supply chain shortages regarding critical medical supplies and medical equipment, including N95 respirators, surgical masks, face shields, and ventilators. A critical shortage of personal protective equipment (PPE) put medical professionals at risk and may have resulted in a slower effective response to the emerging crisis. A *New York Post* article suggested that the U.S. would need 3.5 billion N95 masks during a serious pandemic¹; however, prior to the pandemic, 3M was only manufacturing around 600 million masks per year². Further, the shortfall of face shields led some hospital workers to build their own using office supplies.³ Another shortfall was the lack of ventilators; it was initially estimated that the U.S. would need 740,000 ventilators if the outbreak reached the same level as the 1918 Spanish Flu,⁴ but the U.S. had an inventory of only 160,000 (62,000 full capacity, 98,000 basic) plus 20,000 in emergency stockpile.

DOE national laboratories have extensive capabilities in advanced manufacturing technologies,

¹ Steinbuch, Y. "3M Doubles Output of N95 Respirator Masks Amid Coronavirus Outbreak." *New York Post*, 20 March 2020. <https://nypost.com/2020/03/20/3m-doubles-output-of-n95-respirator-masks-amid-coronavirus-outbreak/>

² Gruley, B.; Clough, R. "How 3M Plans to Make More Than a Billion Masks By End of Year." *Bloomberg*, 25 March 2020. <https://www.bloomberg.com/news/features/2020-03-25/3m-doubled-production-of-n95-face-masks-to-fight-coronavirus>

³ Elgin, B.; Tozzi, J. "U.S. Hospital Workers Are Making Masks, Protective Gear From Office Supplies Amid Equipment Shortage." *Time*, 18 March 2020. <https://time.com/5805557/homemade-medical-face-mask-shortage/>

⁴ Kenen, J. "Local Officials Alarmed by Dearth of Ventilators, Hospital Beds." *Politico*, 14 March 2020. <https://www.politico.com/news/2020/03/14/health-system-coronavirus-preparation-129066>

including tooling infrastructure, support for logistics and supply chain management, and broad design capabilities that enable manufacturing improvements relevant to addressing COVID-19-related supply chain issues. These capabilities include design (mechanical parts, materials, chemical processes, and electronics), 3D printing (additive manufacturing), conventional manufacturing (injection molding, compression forming, machining), digital and data technologies, characterization (biological and inorganic samples), sensing, metrology, and project management. Many of these capabilities are relevant to supporting COVID-19 manufacturing efforts at U.S. companies. Efforts conducted by the fifteen laboratories comprising the NVBL COVID-19 Manufacturing team were divided into three tasks:

- PPE focused on masks and respirators (see "Task 1," p. 215)
- Ventilators, focused on modeling, new designs, and retrofits (see "Task 2," p. 217)
- Consumables, focused on developing components for test kits (see "Task 3," p. 217)

NVBL has been an exceptionally effective contributor to the nation's COVID-19 response, quickly marshaling unique national laboratory expertise and capabilities to meet critical supply chain needs. For example, NVBL supported manufacturers addressing key shortages in medical supply chains, creating nearly 1,500 new medical manufacturing jobs. NVBL worked closely with other federal agencies including the U.S. Department of Health and Human Services (HHS), the Centers for Disease Control and Prevention (CDC), the Strategic National Stockpile, and state and regional decision-makers to provide solutions to a range of COVID-19 challenges. The manufacturing impacts of this collaborative effort are summarized as follows:

- Enabled production of up to 10 million test kits per week.
- Enabled expanded N95 production to more than 3 million masks per day.

- Validated additive manufacturing swabs, enabling production of up to 250,000 swabs per day.
- Supported commercialization of a BioMed-Innovations ventilator and secured U.S. Food and Drug Administration (FDA) Emergency Use Authorization (EUA) approval.
- Participated in creating more than 1,500 new jobs in the U.S. medical manufacturing sector.

These accomplishments demonstrate the game-changing resource represented by DOE's national laboratories working together within the integrated NVBL framework. NVBL can bring these resources to bear on future national and international needs and emergencies.

5.2 Introduction

In March 2020, the NVBL Manufacturing team was formed, composed of experts from 15 DOE national laboratories: Ames National Laboratory (Ames), Argonne National Laboratory (ANL), Brookhaven National Laboratory (BNL), Idaho National Laboratory (INL), Kansas City National Security Campus (KCNSC), Los Alamos National Laboratory (LANL), Lawrence Berkeley National Laboratory (LBNL), Lawrence Livermore National Laboratory (LLNL), National Energy Technology Laboratory (NETL), National Renewable Energy Laboratory (NREL), Oak Ridge National Laboratory (ORNL), Pacific Northwest National Laboratory (PNNL), Sandia National Laboratories (SNL), SLAC National Accelerator Laboratory (SLAC), and Savannah River National Laboratory (SRNL). They jointly submitted to DOE a concept paper titled "DOE Strategy on Materials and Manufacturing to Address Supply Chain Issues Related to COVID-19." DOE approved the project by the first week in April 2020, and efforts were initiated at the laboratories. At the end of May 2020, the team responded to a DOE request for a proposed Phase 2 for the project. The project goals, now accomplishments, are summarized below. Since its beginning, the project has benefited from close connections with the private sector to help rapidly transition laboratory discoveries and

technologies to the medical industry. During the project, the team established collaborations with other government entities including HHS, CDC, the Strategic National Stockpile, and others.

DOE's strategy to mitigate real and anticipated medical supply and device shortages was to support the existing U.S. industrial manufacturing base by providing resources, expertise, and a distributed manufacturing and repair/sterilization infrastructure ready to deploy nationally, regionally, and locally. The Manufacturing team combined resources to rapidly identify and solve manufacturing supply chain challenges; it also assessed the needs of local healthcare ecosystems (hospitals and healthcare providers) and evaluated manufacturing ecosystems to understand their capabilities. The team shared lessons learned, designs, manufacturing processes, material suppliers, and manufacturing partners and established subgroups of subject matter experts for each of the project's initial technical challenge area and others as they become apparent. The objective for the project's task teams was to enable rapid and effective collaboration across the DOE complex to establish viable solutions in days rather than weeks and months. To accelerate the distribution of data, the laboratories agreed to avoid, whenever possible, executing Cooperative Research and Development Agreements (CRADAs) or user agreements. For cases in which this was not possible, CRADAs and field-office approvals were expedited. All information generated by the team was published in weekly reports and open-access literature and made available for replication by anyone in industry and government due to the nature of the national and global healthcare crisis.

5.2.1 Capabilities

Many DOE laboratories have metal powder bed systems that can be used for rapid tooling production, with specific applications in injection mold tooling (see Fig. 5.1, p. 214). For rapid testing and low-volume production, many laboratories offer experimental injection molding (see Fig. 5.2, p. 214) and compression forming systems that can be leveraged for rapid validation.

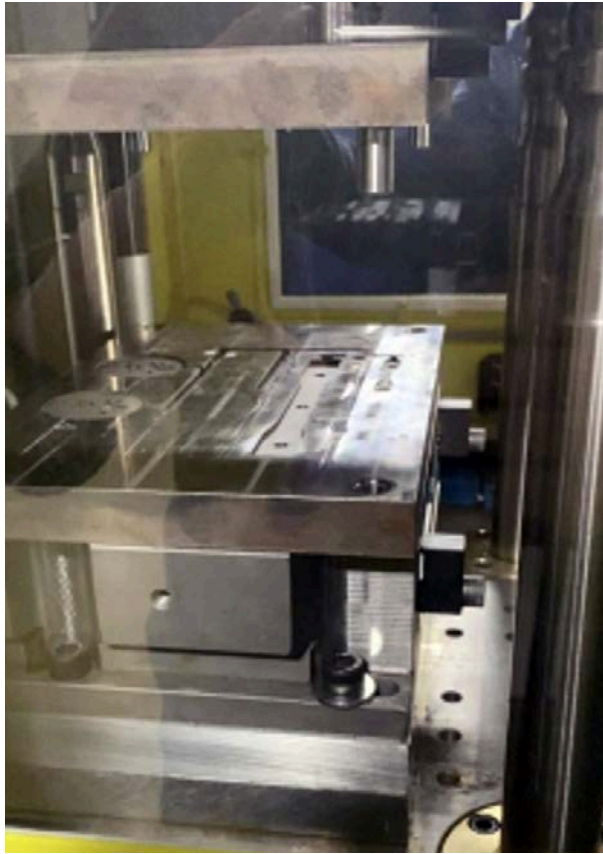


Fig. 5.1. Additive manufacturing tooling installed on an injection mold system. [Courtesy Oak Ridge National Laboratory]

In addition, the national laboratories can reverse engineer critical parts rapidly, manufacture tooling, and verify performance on a pilot-scale production system. Once the tooling is proven on the pilot-scale system, it can be replicated and transitioned to full-scale production in days rather than weeks or months. However, even with this growth in production, some regions in the U.S. will likely need rapid scaling of production. The national laboratories can quickly evaluate materials and methods for locally manufactured ventilators as well as modify existing ventilators to support more than one person simultaneously.⁵

⁵ Neyman, G.; Irvin, C. "A Single Ventilator for Multiple Simulated Patients to Meet Disaster Surge." *Society for Academic Emergency Medicine* **13** (11), 1246-1249 (2006). DOI: 10.1197/j.aem.2006.05.009



Fig. 5.2. Prototype injection molding system [Courtesy Oak Ridge National Laboratory]

5.2.2 Technical Highlights

The tasks described in this chapter were designed with very short timelines and intense efforts to address critical supply shortages in support of the national response to the COVID-19 crisis. Project duration was approximately 8 months, from April to December 2020. The full team and each sub-team held virtual meetings at least weekly. Every Friday, participating laboratories provided written reports that were compiled and delivered to NVBL leadership by the close of business the following Tuesday. Over the project's duration, 34 technical reports were submitted ranging from 22 to 43 pages in length. The following is a sampling of the technical highlights achieved within the Manufacturing team's three tasks.



Fig. 5.3. Peter Tsai, inventor of N95 filter media, holds a sample of the material produced at the Oak Ridge National Laboratory's Carbon Fiber Technology Facility (CFTF). [Courtesy Oak Ridge National Laboratory]

Task 1: Personal Protective Equipment

N95 Masks

A critical shortage of N95 masks, broadly used by healthcare workers, was identified early in the pandemic. These masks are manufactured by 3M and other companies, but most are manufactured overseas. The masks use a polymer-based fabric that generally captures large droplets but is also electrostatically charged to capture much smaller virus particles with diameters in the low micron range. The NVBL Manufacturing team partnered with Peter Tsai, materials scientist and inventor of the N95 mask filter material, to develop a new electrostatic charging system that could be used on a melt-blown polymer line at ORNL's Carbon Fiber Technology Facility (see Fig. 5.3, this page).

Sample materials were distributed to multiple laboratories for rapid characterization and refinement, including characterization of particle transmission through the masks. The charging system design was transferred to Cummins Inc., an automotive filtration company in Nashville, Tenn., that converted an oil filter production line to N95 fabric production, enabling enough material to manufacture millions of N95 respirators per day.⁶

The Manufacturing team subsequently collaborated with DemeTECH, a medical manufacturer

⁶ Cummins Newsroom. "Cummins Inc. and Oak Ridge National Laboratory Collaboration Enables Capability to Produce Millions of Face Masks." *Cummins Inc.*, 31 August 2020. <https://www.cummins.com/news/releases/2020/08/31/cummins-inc-and-oak-ridge-national-laboratory-collaboration-enables>



Fig. 5.4. DemeTECH Factory where N95 masks and respirators are produced. [Courtesy DemeTECH]

based in Miami Lakes, Fla., and developed tooling to support establishment of a new manufacturing facility in Tampa, Fla., for production of N95 respirators and surgical masks (see Fig. 5.4, this page). Later, when DemeTECH was experiencing manufacturing issues, the Manufacturing team leveraged DOE's synchrotron light sources to identify and correct production issues; DemeTECH received its National Institute for Occupational Safety and Health (NIOSH) certification on October 7, 2020, only six months after the project began. By the end of the project, DemeTECH was producing 500,000 N95 respirators and 3 million surgical masks per day and had created more than 1,500 new manufacturing jobs.

Face Shields

Early in the COVID-19 pandemic, multiple universities and companies deployed 3D printing capabilities to produce clips and bands for face shields that could be clipped to the brim of a hat. However, printing these supplies individually would not have met national demand. To enable significant scaling and rapid deployment, the Manufacturing team partnered with DeRoyal Industries (Powell, Tenn.) to design, print, and machine a mold for



Fig. 5.5. Face shield and reusable N95 respirator produced by DeRoyal Industries. [Courtesy Oak Ridge National Laboratory]

industry-scale production within three days, enabling production of over 40,000 face shields per day (see Fig. 5.5, this page). The team also worked

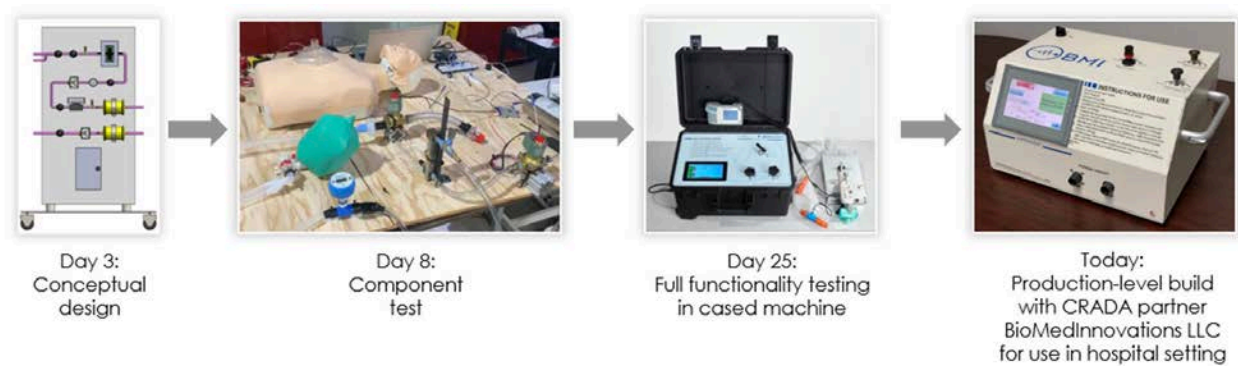


Fig. 5.6. Twelve-week timeline of ventilator development by Lawrence Livermore National Laboratory. [Courtesy Lawrence Livermore National Laboratory and BioMedInnovations, LLC]

with DeRoyal to develop molds to produce reusable N95 respirators.

Task 2: Ventilators, Small Part Production, and Repair

Major highlights from the ventilator task include development of high-fidelity models of the lungs and how they respond to ventilator controls to accelerate mucus removal, development of a pathogen management system for converting bilevel positive airway pressure (BiPAP) units to ventilators, and development of sensors and electronics for oxygenation/CO₂ scrubbing in advanced liquid ventilators. To highlight the strength of leveraging laboratory expertise, LLNL developed an FDA-EUA approved ventilator with components sourced outside commercial ventilator companies in 12 weeks (see Fig. 5.6, this page).

Task 3: Consumables for Testing

One of the biggest supply chain challenges at the beginning of the pandemic was the shortage of test tubes for COVID-19 testing. Within weeks, the Manufacturing team collaborated with The Coca-Cola Company (Atlanta, Ga.) to validate the integrity and sterility of their bottle preforms as a surrogate supply chain for test tubes (see Fig. 5.7, this page). These preforms are typically blown with hot air to form the thin-walled bottles for soft drinks and water. The team helped develop protocols to clean and sterilize the tubes to meet medical supply



Fig. 5.7. A Coke bottle preform with Coke lids used as substitutes for sample collection tubes. [Courtesy Oak Ridge National Laboratory]

requirements. Within two weeks of initial contact, the Manufacturing team had worked with contacts at HHS, Coca-Cola, and Longhorn Vaccines and Diagnostics (Bethesda, Md.) to initiate delivery of two million sample test collection tubes per week.



Fig. 5.8. Thermo Fisher Scientific test facility in Lenexa, Kan., (left) that manufactures COVID-19 sample collection test kits (right). [Courtesy Thermo Fisher Scientific]

In parallel, LLNL and ORNL worked with Thermo Fisher Scientific (Waltham, Mass.) to scale and accelerate testing by designing a new test tube ideally suited for automation. LLNL used additive manufacturing to develop prototype test tubes for Thermo Fisher while ORNL used metal additive manufacturing capabilities to manufacture injection mold tooling. The tooling and tooling design were delivered to Thermo Fisher. Thermo Fisher replicated the tooling, built a new \$40M factory in Lenexa, Kan., hired 300 new employees, and initiated production of 10 million test kits per week (see Fig. 5.8, this page).

5.3 Task 1: Personal Protective Equipment

5.3.1 Overview

The goal of the PPE efforts was to ensure that first responders and the general public had adequate access to PPE to slow the spread of COVID-19. Major thematic areas included development of tooling to scale production of face shields, development of reusable N95 respirators, production expansion of N95 meltblown fabric, and evaluating the efficacy of homemade masks used by the general public. The project drew on primary expertise in materials synthesis and characterization and advanced manufacturing systems for rapid prototyping and tooling, and, most importantly, scientific

and technical expertise in rapidly solving evolving technical challenges.

5.3.2 Face Shields

Early in the pandemic, first responders faced significant shortages of face shields. Many universities and companies leveraged their plastic 3D printers to rapidly manufacture adjustable head bands for use with disposable face shields. While this organic approach is viable, it could not guarantee a secure supply of face masks to all 6,000 U.S. hospitals.

The Manufacturing team's strategy was to work with the medical supply community and leverage metal additive manufacturing capabilities to rapidly manufacture injection mold tooling. ORNL staff worked with DeRoyal Industries, a global medical manufacturing company that provides products to every U.S. hospital. First, the team designed and used additive manufacturing to rapidly prototype head bands for disposable face shields. Next, the team designed injection mold tooling and used metal additive manufacturing capabilities at the ORNL Manufacturing Demonstration Facility (MDF)⁷ to produce the tooling and deliver it to DeRoyal's facility in less than five days. Each mold in an injection molding system could produce 40,000 head bands per day. The tooling design was transferred to DeRoyal for replication, but the face shield components (injection molded band, foam

⁷ www.ornl.gov/facility/mdf

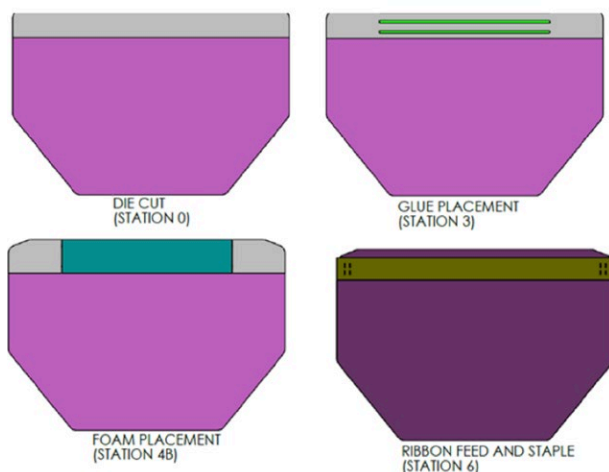


Fig. 5.9. Four-step process for face shield assembly. [Courtesy Oak Ridge National Laboratory]

strip, and clear shield) had to be manually assembled (see Fig. 5.9, this page). During the first weeks of production, DeRoyal outfitted a company basketball arena with tables and recruited all their sales team and management staff to manually assemble the face shields.

ORNL worked with the Manufacturing team to rapidly develop fixtures that could initially be used to speed up the assembly process and then could be reconfigured for automation. The team used polymer additive manufacturing systems to rapidly produce the assembly system in two days and delivered it to DeRoyal for testing and evaluation. After a few refinements, the team transferred the design to DeRoyal for replication (see Fig. 5.10, this page).

5.3.3 Scaling N95 Production

In the 1990s, materials scientist Peter Tsai was examining different methods to create filtration material. By inducing an electrical charge on meltblown plastic, he achieved an approximately 95% efficiency in capturing particulates greater than 3 microns in size with very low air resistance, thereby reducing breathing labor while protecting the wearer from airborne particulates. In 1995, Tsai received a patent for this process and 3M licensed the technology to make nonwoven polypropylene

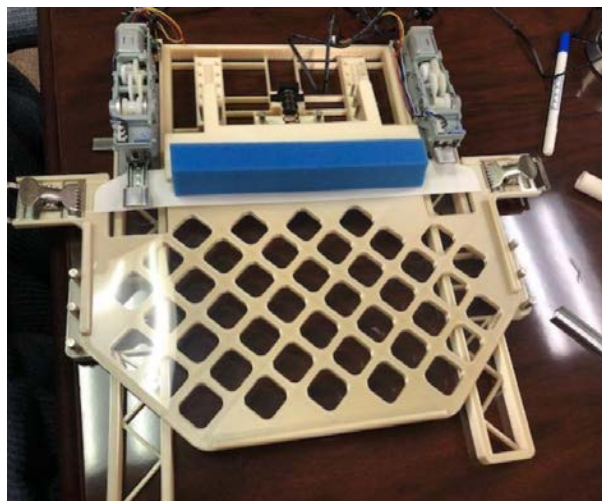


Fig. 5.10. Automated face mask assembly fixture [Courtesy Oak Ridge National Laboratory]

masks for industrial use (e.g., mining, construction, painting). The value of these new face coverings became evident for medical first responders, providing significant protection over the standard surgical mask.

Early in the pandemic, N95 respirators were in significantly short supply. The Manufacturing team recruited Tsai to help retrofit existing meltblown production facilities in the United States with charging systems to significantly increase the domestic supply of N95 material. The first step was retrofitting ORNL's meltblown line with a prototype system Tsai brought from his lab at the University of Tennessee, Knoxville (see Fig. 5.11, p. 220). ORNL manufactured the prototype material (see Fig. 5.12, p. 220) and provided samples to six different laboratories for advanced characterization.

Baseline Filtration Performance Assessment

BNL and ANL used advanced characterization tools to assess baseline filtration performance and material requirements. BNL compared the 3M Particulate Respirator 8210 N95, the VWR Advanced Protector Mask, and Filti Face Mask Material.

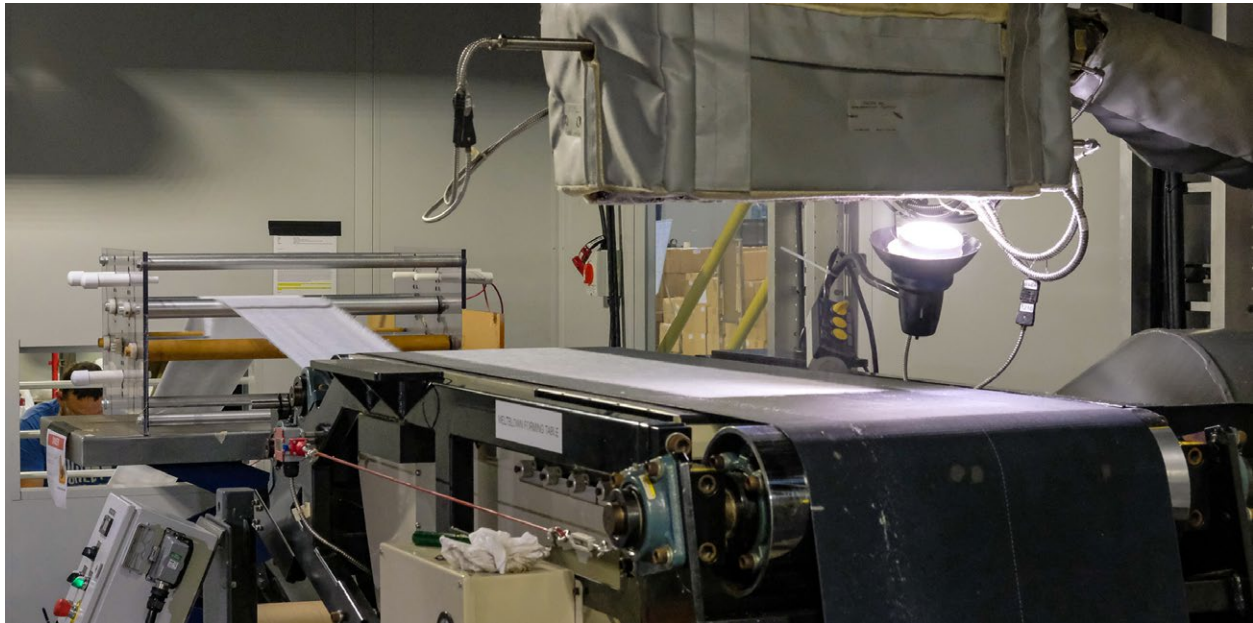


Fig. 5.11. Initial charging system installed at Oak Ridge National Laboratory. [Courtesy Oak Ridge National Laboratory]

A particle generator was used to deliver NaCl aerosol through two stacked layers of meltblown filter media at an air flow rate of 50 liters per minute. Filtration efficiency was characterized by measuring the penetration of the filter media.

The 3M 8210 comprises four layers of nonwoven materials: outer layer, first meltblown layer, second meltblown layer, inner layer. The outer layer is approximately 200 microns thick and comprises polyester microfibers approximately 20 microns in diameter. The first meltblown layer is approximately 400 microns thick and comprises polypropylene microfibers ranging from 1 to 10 microns in diameter. The second meltblown layer is 200 microns thick and comprises polypropylene microfibers from 1 to 10 microns in diameter. The inner layer is approximately 200 microns thick and comprises polyester microfibers approximately 30 microns in diameter (see Fig. 5.13, p. 221).

The VWR mask is constructed from three layers of nonwoven material. The outer and inner layers are approximately 200 microns thick comprising patterned 20-micron diameter microfibers. The middle



Fig. 5.12. First supply of N95 material produced at Oak Ridge National Laboratory. [Courtesy Oak Ridge National Laboratory]

meltblown layer is approximately 100 microns with 2- to 10-micron-diameter microfibers (see Fig. 5.14, p. 222).

The Filti Face Mask Material was reported as the most effective cloth mask material for blocking

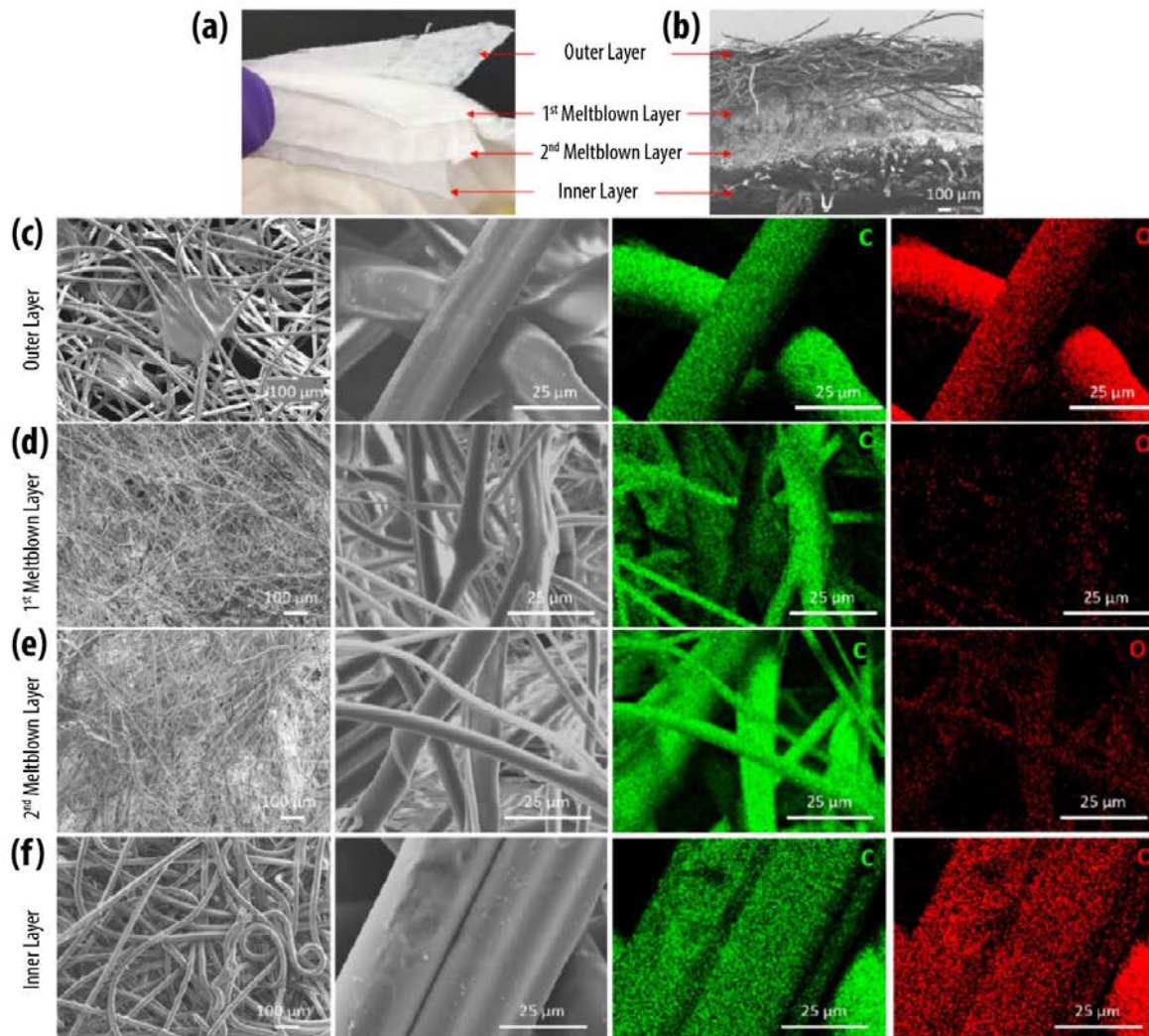


Fig. 5.13. Brookhaven National Laboratory scanning electron microscopy (SEM) and energy dispersive X-ray spectroscopy (EDS) characterization of the 3M™ Particulate Respirator 8210 N95. **(a)** Peeling apart 8210 N95 reveals four layers of nonwoven materials. **(b)** SEM cross section image reveals the outer layer, first and second middle meltblown layer and inner layer. **(c)** SEM and EDS mapping images of top-down view of the outer layer. **(d)** SEM and EDS mapping images of top-down view of the first meltblown layer. **(e)** SEM and EDS mapping images of top-down view of the second meltblown layer. **(f)** SEM and EDS mapping images of inner layer. [Reprinted with permission from Chavis, A., et al. Characterization of Materials Used as Face Coverings for Respiratory Protection. *ACS Applied Materials & Interfaces* **2021** 13 (40), 47996-48008. Copyright 2021 American Chemical Society.]

0.3-micron particles with 84% filtration efficiency. The filter material is composed of two layers. The support outer layer comprises 10-micron diameter microfibers. The meltblown layer of the outer layer has fibers in the range of 200 to 500 nm. The inner layer comprises 10-micron-diameter microfibers (see Fig. 5.15, p. 223).

Materials Characterization Development

ANL optimized nanoscale computed tomography (nanoCT) characterization methods of soft nano-fiber filter medium samples. At the nanoscale, they tend to shrink under X-ray illumination. To overcome this limitation, a new reconstruction algorithm was developed. Antibacterial testing for

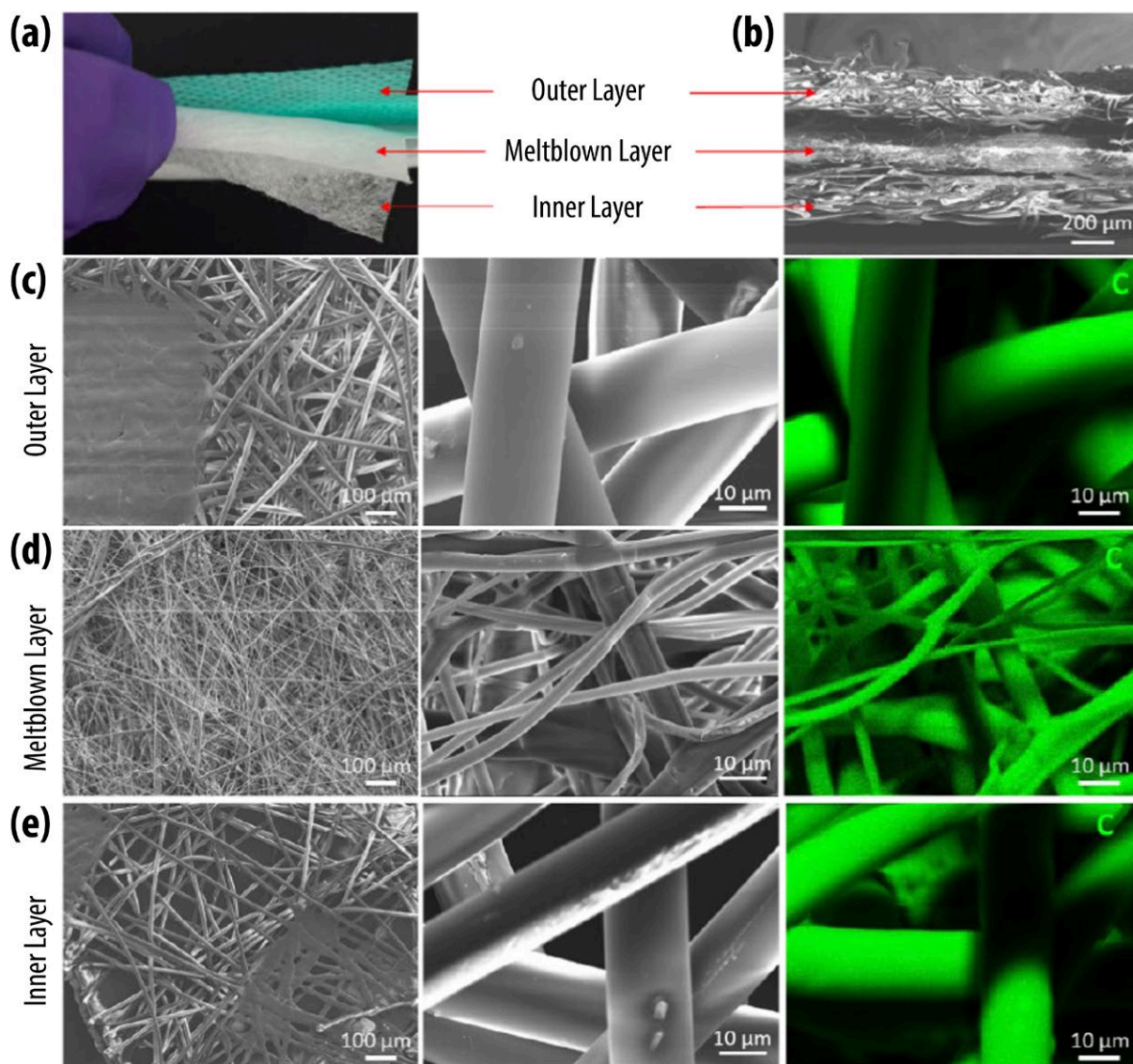


Fig. 5.14. Brookhaven National Laboratory SEM/EDS characterization of the VWR Advanced Protector Mask. **(a)** Peeling apart the mask reveals three layers of nonwoven materials. **(b)** SEM cross section image reveals the outer layer, middle meltblown layer, and inner layer. **(c)** SEM and EDS mapping images of top-down view of the outer layer. **(d)** SEM and EDS mapping images of top-down view of the middle meltblown layer. **(e)** SEM and EDS mapping images of inner layer. [Reprinted with permission from Chavis, A., et al. Characterization of Materials Used as Face Coverings for Respiratory Protection. *ACS Applied Materials & Interfaces* **2021** 13 (40), 47996-48008. Copyright 2021 American Chemical Society.]

anti-microbial nanofibers synthesized by electrospinning showed high efficacy against *E. coli* (see Fig. 5.16, p. 223).

Corona Charging System Development

While materials characterization was being developed, ORNL focused on the design of a

new electrostatic charging system. The system was integrated and tested at the ORNL MDF (see Fig. 5.17, p. 224) with a battery of different feedstocks. The feedstocks were shared with the other national laboratories for rapid characterization. ORNL delivered N95 material made at its Carbon Fiber Technology Facility to BNL, SNL, SRNL, LANL,

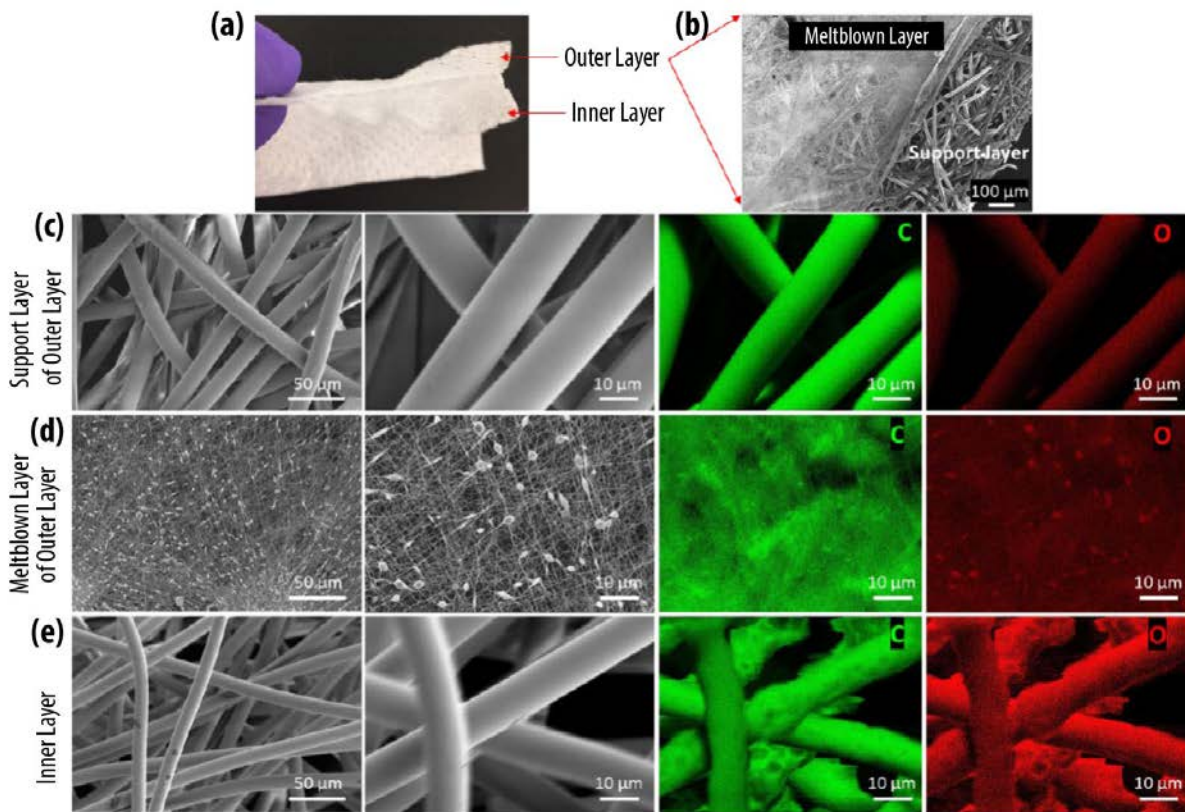


Fig. 5.15. Brookhaven National Laboratory SEM/EDS characterization of the Filti Face Mask Material. (a) peeling apart the material reveals two layers of nonwoven materials. (b) SEM images reveal a support layer and a meltblown layer at the outer layer. (c) SEM and EDS mapping images of top-down view of the support layer of outer layer. (d) SEM and EDS mapping images of top-down view of the meltblown layer of outer layer. (e) SEM and EDS mapping images of inner layer. [Reprinted with permission from Chavis, A., et al. Characterization of Materials Used as Face Coverings for Respiratory Protection. *ACS Applied Materials & Interfaces* **2021** 13 (40), 47996-48008. Copyright 2021 American Chemical Society.]

and PNNL for characterization. Once the system was validated, it was established at the Cummins Inc. facility (see Fig. 5.18, p. 224).

Identification of Manufacturing Defects

ORNL worked with DemeTECH to identify manufacturing defects in their original production of N95 respirators, which failed to achieve NIOSH qualification. The flaws were identified using optical microscopy, which revealed areas with large amounts of light passing through (see Fig. 5.19, p. 224). The team at ORNL discovered leakage around ultrasonic bonding areas, with additional

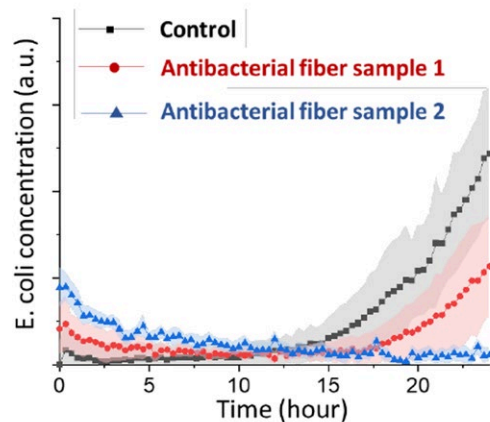


Fig. 5.16. Antibacterial test for ANL anti-microbial electrospun fibers. [Courtesy Argonne National Laboratory]



Fig. 5.17. Corona charging system assembled at ORNL. [Courtesy Oak Ridge National Laboratory]



Fig. 5.18. Corona charging system integrated at Cummins Inc. [Courtesy Oak Ridge National Laboratory]

testing at SNL showing that the average filtration efficiency was 84% and the average resistance 1.14 inches of water. It was assumed that that the low efficiency was due to processing and not the material (see Fig. 5.19 and 5.20, this page,

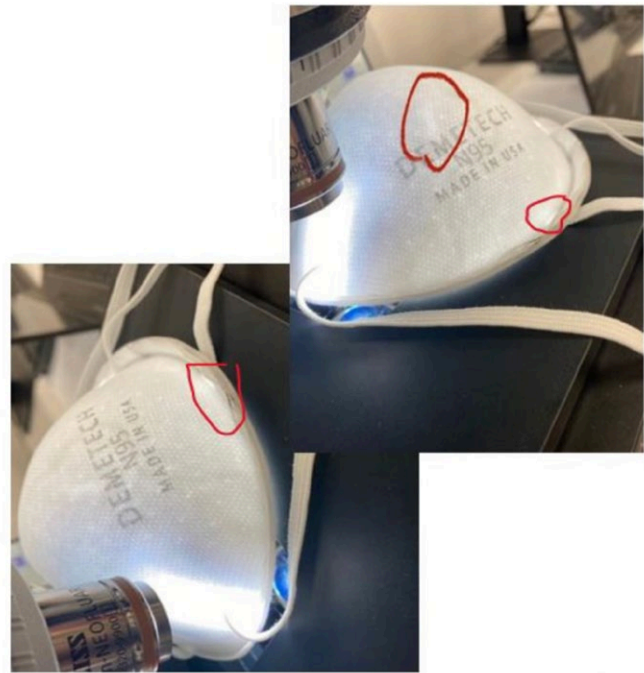


Fig. 5.19. Identified leakage paths at ultrasonic welding positions. [Courtesy Oak Ridge National Laboratory]

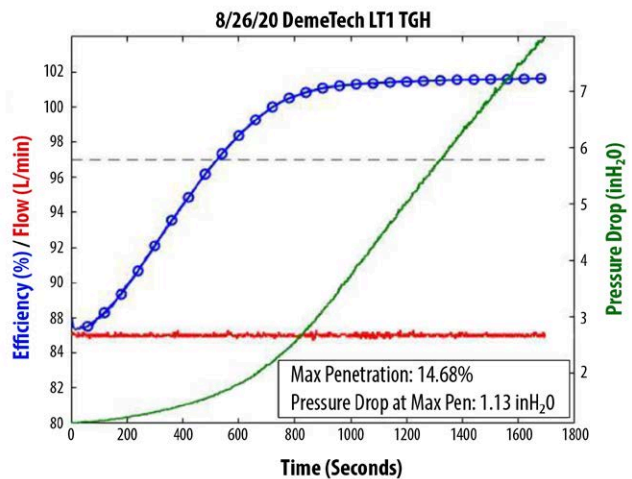


Fig. 5.20. Testing efficiency plots. [Courtesy Sandia National Laboratories]

and Table 5.1, p. 225). The ORNL and SNL teams reported the findings to DemeTECH, and modifications were made to their production line. The resulting modifications were critical to achieving successful NIOSH certification.

Table 5.1. Testing Data

| DemeTECH | | | | |
|---------------------------|------------------|-----------------------|---|-------------------|
| Run Number | Test Type | Preconditioned | Resistance (in. of H₂O) | Efficiency |
| 1 | Load | No | 1.13 | 85.3177% |
| 2 | Load | No | 1.08 | 85.2970% |
| 3 | Load | No | 1.10 | 80.5810% |
| 4 | Load | High Humidity | 1.17 | 86.8340% |
| 5 | Load | High Humidity | 1.04 | 85.6170% |
| 6 | Load | High Humidity | 1.09 | 90.1430% |
| 7 | Load | High Humidity | 1.09 | 86.3910% |
| 8 | Penetration | No | 1.06 | 80.7990% |
| 9 | Penetration | No | 1.06 | 77.6430% |
| 10 | Penetration | No | 1.13 | 84.1650% |
| 11 | Penetration | No | 1.00 | 80.2920% |
| 12 | Penetration | No | 1.32 | 81.7090% |
| 13 | Penetration | No | 1.11 | 87.0510% |
| 14 | Penetration | No | 1.03 | 86.8890% |
| 15 | Penetration | No | 1.13 | 83.4560% |
| 16 | Penetration | No | 1.43 | 78.0340% |
| 17 | Penetration | No | 1.02 | 89.0080% |
| 18 | Penetration | No | 1.11 | 83.4700% |
| 19 | Penetration | No | 1.51 | 80.6920% |
| Average | | | 1.14 | 83.9% |
| Standard Deviation | | | 0.13 | 3.5% |
| Minimum | | | 1.00 | 77.6430% |
| Maximum | | | 1.51 | 90.1430% |

Polymer Manufacturing

ANL explored another approach to making N95 by electrospinning the fibers. Filter efficiency tests on nanofiber media using 0.3 μm Most Penetration Particle Size (MPPS) NaCl particulates showed 99.1% efficiency with a large pressure drop, indicating that the samples effectively blocked particles but their thickness needed to be reduced. Antibacterial testing of the anti-microbial coatings deposited on commercial N95 masks by atomic layer deposition (ALD) and sequential infiltration synthesis (SIS) technologies using *E. coli* as a bio-agent showed very high efficacy (see Fig. 5.21, p. 226).

N95 Filtration Efficiency

Members of the Manufacturing team at SLAC utilized beamlines 10-2 and 11-3 at the Linac Coherent Light Source (LCLS) to conduct scattering experiments on N95 materials. A new *in situ* cell design was transferred to a computer-aided design (CAD) program, 3D printed, and tested using a prototype setup for *in situ* experiments (see Fig. 5.22, p. 226). The first prototype was printed out of polylactic acid (PLA) and used to test flow and N95 material seal. The test verified that the expected >95% rejection of 0.3 mm particles could be achieved. The final version shown in Fig. 5.21(c) will be printed out of polyetheretherketone (PEEK)

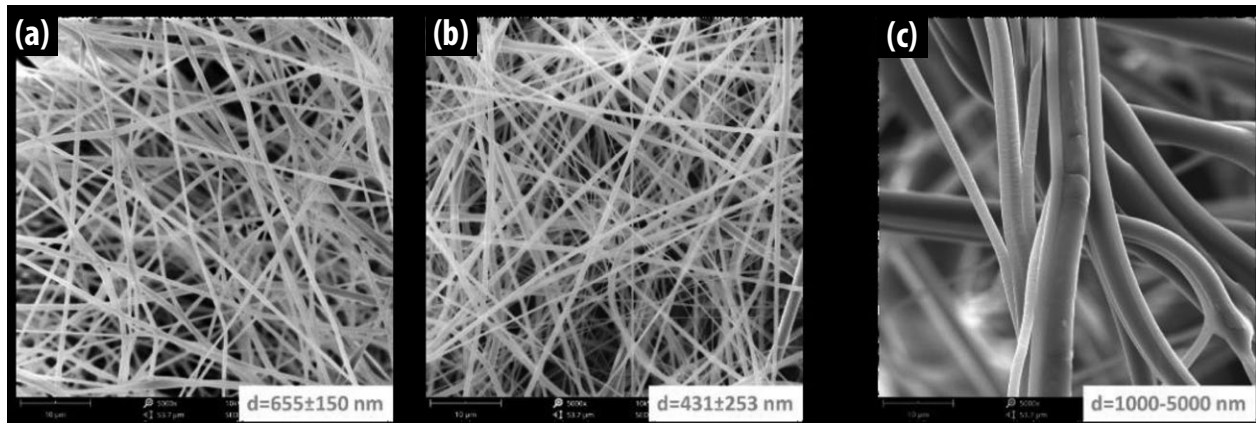


Fig. 5.21. SEM images of (a) Argonne National Laboratory nanofiber filter medium materials produced by electrospinning contain coarse and fine fibers; and (b) 3M N95 microfiber filter media 1 to 5 microns in diameter. (c) Polyetheretherketone (PEEK) material. [Courtesy Argonne National Laboratory]

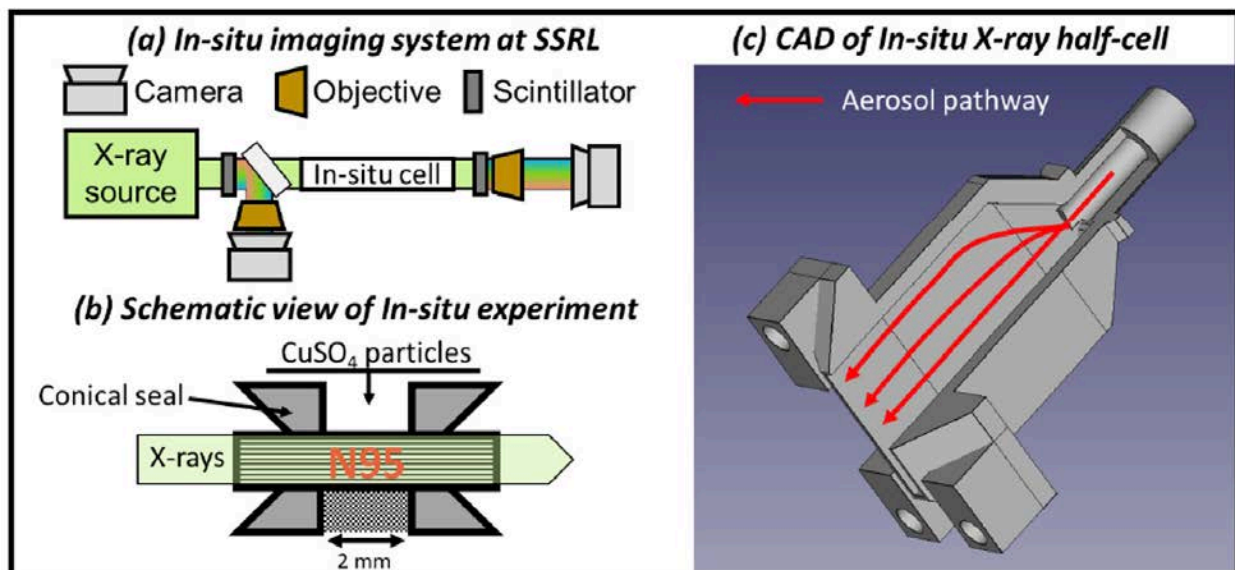


Fig. 5.22. (a) Scattering system designed to examine N95 materials at LCLS. The imaging system utilized at beamline 10-2. (b) X-rays are transmitted through the N95 material to image the progression of aerosols through the material. (c) CAD design of the latest version of the *in situ* cell. [Courtesy SLAC National Accelerator Laboratory]

material. The cell utilizes a conical seal to compress the N95 filter and prevents leakage of air and particulate. This seal design has been successfully used for liquid and air-based *in situ* experiments at SLAC's Stanford Synchrotron Radiation Lightsource.

Virus Filtration Mechanism

The SLAC team began attaching viruses to N95 mask polymer fibers to develop process protocols for further studies of the virus filtration mechanism and the effects of disinfection. Human coronavirus NL63 was selected for the first tests because a

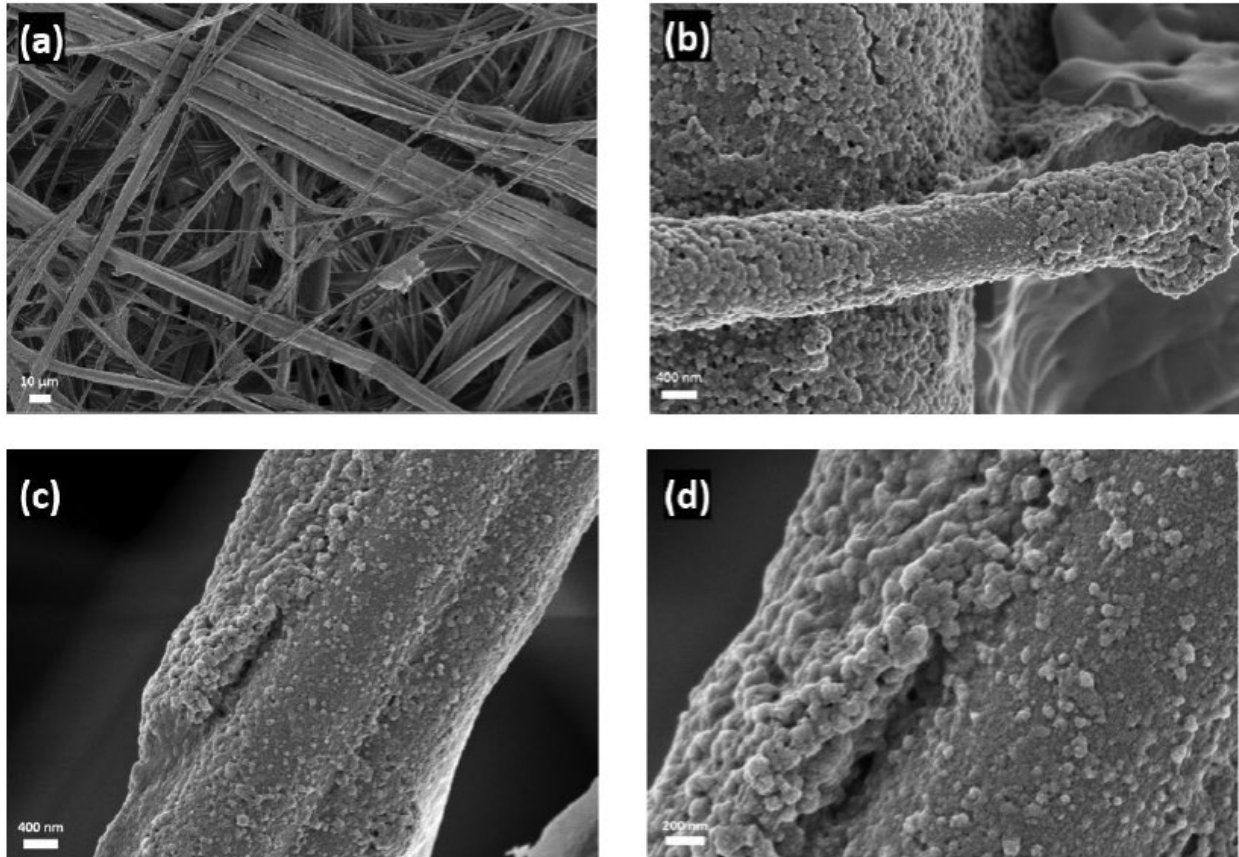


Fig. 5.23. SLAC SEM images of N95 polymer fibers contaminated with a high viral load of human coronavirus NL63, which were inactivated and air dried for observation. [Courtesy SLAC National Accelerator Laboratory]

virus process protocol had already been developed and NL63 is similar to SARS-CoV-2 in size and structure. Virus growth, purification, and application were performed by collaborator Jing Jin at Vitalant Research Institute in San Francisco.

To compare contamination morphology with a high versus low viral load, the face mask material was fully submerged and soaked for one hour in 500 microliters of HCoV-NL63 virus extracted from virus-infected cells after three rounds of dry-ice freeze-thaw. Next, 200 microliters of HCoV-NL63 virus were added in 5-microliter drops onto one side of the mask and dried at room temperature for about two hours. The viruses were subsequently inactivated by heating at 75°C for 30 minutes and the material air-dried overnight in a low humidity

chamber. Small (10 x 10 mm) pieces of material were then mounted onto a standard 12 mm SEM pin stub, sputter-coated with a 6 nm conductive layer of Au/Pd using a Leica EM ACE600 sputter-coater (Leica Microsystems, Germany), and visualized with a Zeiss Crossbeam 550 Field Emission Scanning Electron Microscope (Carl Zeiss Microscopy, USA) operated at 2-5 kV using 100 pA beam current and secondary electron detection. In samples with a high viral load, the virus aggregated onto individual fibers and also adhered in large clusters in the pores between fibers (see Fig. 5.23 a–b, this page) and could potentially change the porosity of the fibrous material. Virus particles appear as spheres approximately 100 nm in diameter adhering closely to the fiber surface (see Fig. 5.23 c–d, this page). In samples with a low

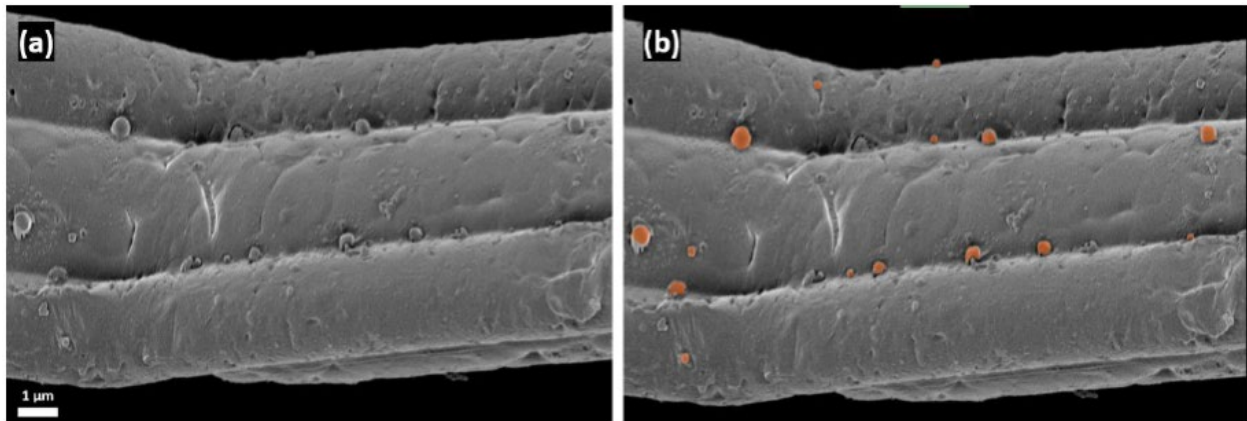


Fig. 5.24. SLAC SEM image (a) of N95 polymer fibers contaminated with a low viral load of human coronavirus NL63 and (b) its virus annotated image (orange color indicates virus). [Courtesy SLAC National Accelerator Laboratory]

viral load the virus appears as spheres sparsely distributed along the surface of individual fibers (see Fig. 5.24, this page).

5.3.4 Reusable Respirators

The onset of the pandemic saw significant shortages of surgical masks and N95 respirators. Initial efforts to address these shortages focused on developing reusable respirators that minimized use of N95 or surrogate filtration materials (see Fig. 5.25, p. 229). A reusable mask design from ORNL, developed with DeRoyal Industries, attempted to reduce injection molding to a single part. The projected cost was between \$5 and \$8 per mask, with filters costing between \$0.15 to \$0.20 each. Typically, 100 filters are provided with each mask, bringing the cost to \$0.56 per use, which is considerably lower than the cost of disposable N95 masks.

ORNL delivered tooling models to SNL, which manufactured prototypes and scaled to three different sizes for improved fit. SNL developed a human head test fixture that allows full masks to be tested (see Fig. 5.26, p. 229) and partnered with Lovelace Hospital in Albuquerque to perform fit tests using a variety of facial forms. The fit data drove expanded tooling designs by ORNL for the silicone injection

molding to scale production. The designs were shared with multiple laboratories for replication. Both metal and polymer molds could be made for rapid replication. SNL is developing mask reuse procedures for the ORNL design including proper decontamination/sterilization approaches in high-resource and low-resource environments.

NETL used design files for the ORNL face mask with a silicone inner mask to 3D print example masks and demonstrated a cast mold that reduced fabrication times (30-minute production) compared to 3D printing (6-hour production). A contact was established with the PPE project lead at West Virginia University's Center for Inhalation Toxicology (WVU-CIT). This group is responsible for addressing PPE requirements for WVU Medicine/J. W. Ruby Memorial Hospital in Morgantown, W.Va. Ruby Memorial is a level 1 trauma center that has treated numerous COVID-19 patients and thus has a good understanding of the PPE needs within the medical community.

Dialogue between WVU-CIT and NETL has helped drive the design process for alternative open-source PPE for the medical community and the population at large to re-open America. Discussion with physicians within the Department of Ophthalmology and Visual Sciences at WVU highlighted

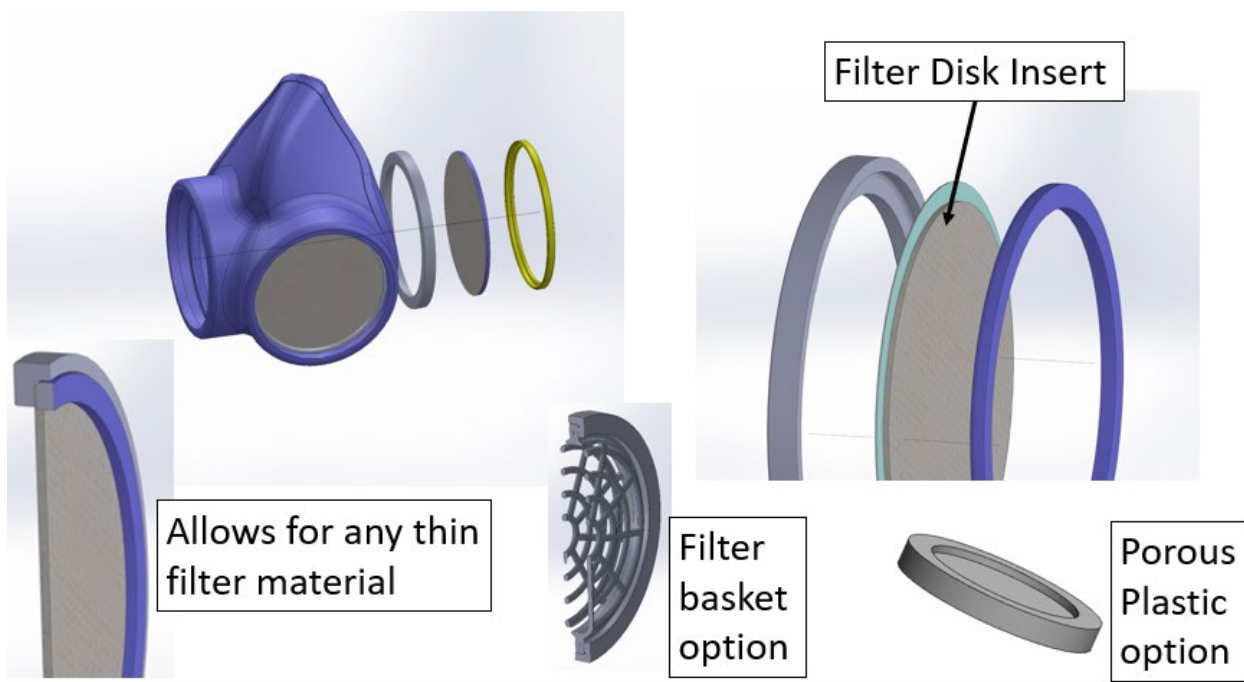


Fig. 5.25. Conceptual design of reusable respirator. [Courtesy Oak Ridge National Laboratory]

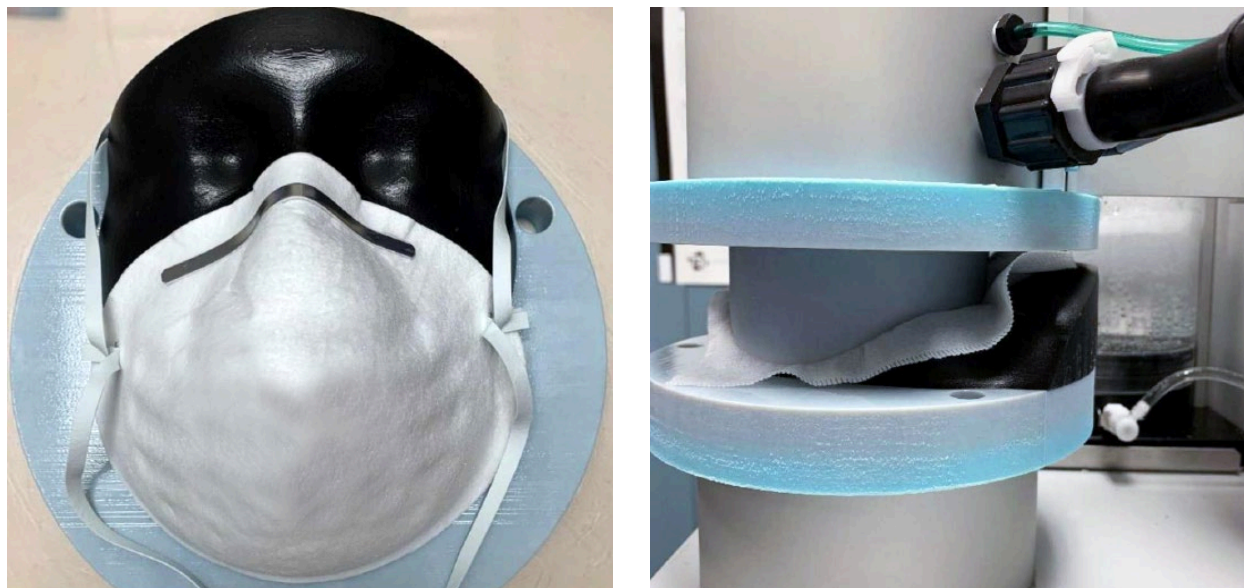


Fig. 5.26. Sandia National Laboratories human head test fixture for the ATI 100Xs automated filter tester. [Reprinted from Omana, M. A., et al. *A Parameterization Study of Sew-EZ Materials: Types #6 and #8*. 2020. Sandia National Laboratories. DOI: 10.2172/1646968.]

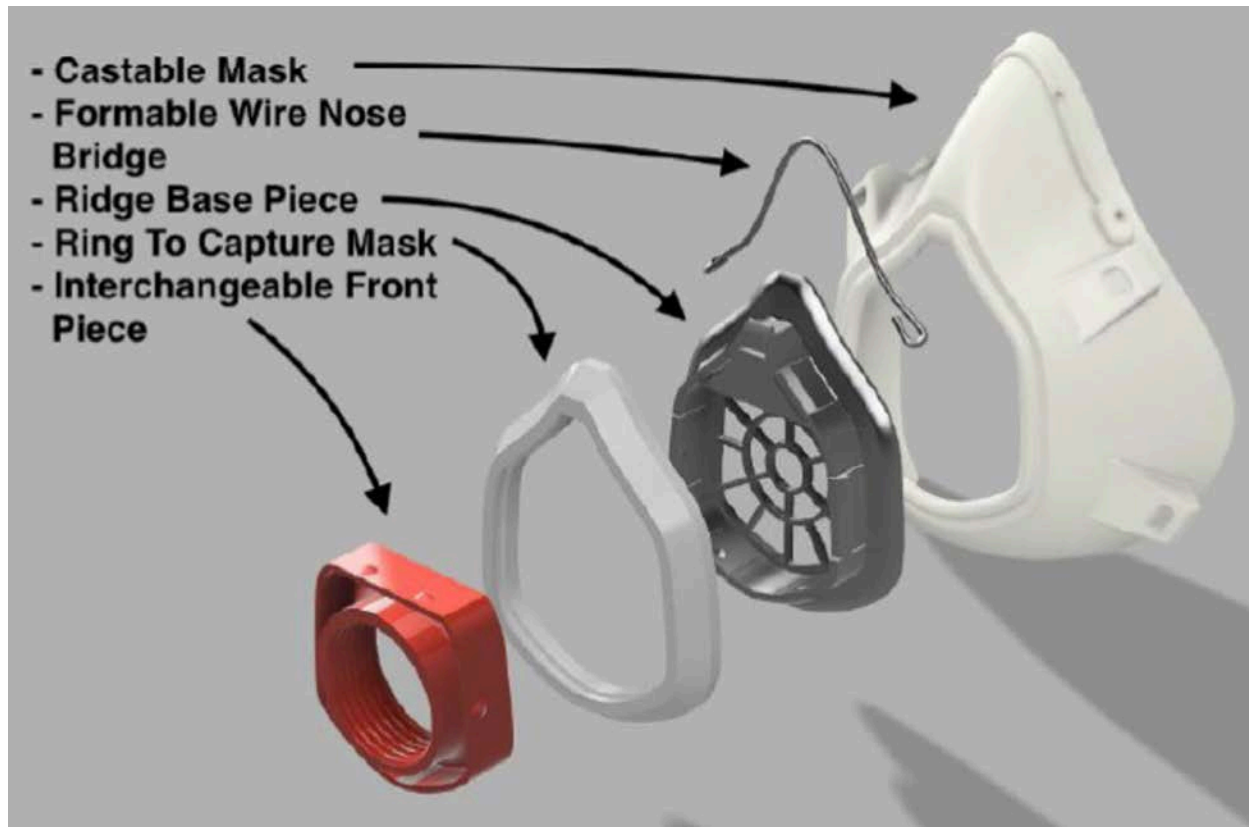


Fig. 5.27. Lawrence Berkeley National Laboratory castable design for reusable masks. [Courtesy Lawrence Berkeley National Laboratory]

the need for greater breathability for face masks that are designed for extended continuous usage. This could lead to modifications of the ORNL design that would incorporate multiple air flow passages as opposed to the existing single passage. NETL met with Brady Gibbons, Associate Dean for Research at Oregon State University (OSU), regarding the university's participation in the DOE open-source respirator project. OSU has significant 3D printing capability and wants to participate in the project if local mask mold printing and deployment of these materials becomes needed in the Corvallis and Albany, Ore., areas. NETL, located in Pittsburgh, Pa., has begun contacting local vendors to establish partnerships for injection molding and mask fabrication in the region. Quotes were received from two vendors in the Pittsburgh area for injection molding parts. One firm that NETL

contacted had idle capacity to manufacture the masks once the molds were fabricated and wanted to help get masks distributed locally.

LBNL evaluated the design of a castable design for reusable face masks. As a test platform to develop new filter technologies, the design is modeled from pre-existing masks proven to seal onto the face and be comfortable and easy to wear. For initial prototyping, the front of the mask was modified to easily accept snap-together pieces to simplify the prototyping process. This interface, with the filtering technologies being developed, is the simplest to remove, replace, or modify (see Fig. 5.27, this page).

PNNL developed vacuum-formed masks using inexpensive flexible material (see Fig. 5.28, p. 231). Ethylene-vinyl acetate (EVA) rubber readily

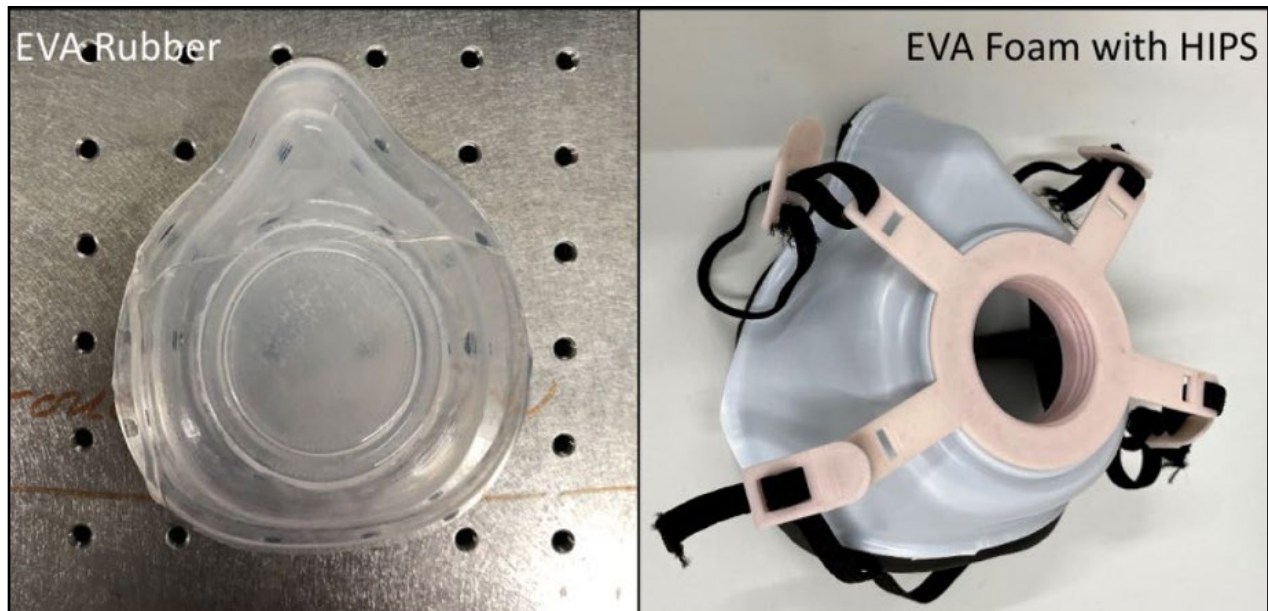


Fig. 5.28. Ethylene-vinyl acetate (EVA) respirators developed by Pacific Northwest National Laboratory. [Courtesy Pacific Northwest National Laboratory]

vacuforms and provides enough structural stability to hold shape when held to the face. EVA foam also easily vacuforms but requires another thin layer of more ridged plastic to maintain its shape during wear. EVA rubber provides the additional benefit of being mostly transparent, which could enable designs that provide visibility of the mouth, enabling lip reading and better communication with individuals who have hearing loss.

Ames Laboratory conducted a survey on face coverings that identified mask fit and comfort as the areas of greatest concern. Gaps at the nose were the top concern with fit, followed by too small size and gaps at the top. The top concerns with comfort were fogging glasses, coverings being too hot, difficulty breathing, and the covering touching the face or mouth while talking and breathing. Survey results can help identify and modify designs tailored to laboratory employees and the broader community. The first 3D-printed face mask frames (see Fig. 5.29, this page) were built and assembled based on the

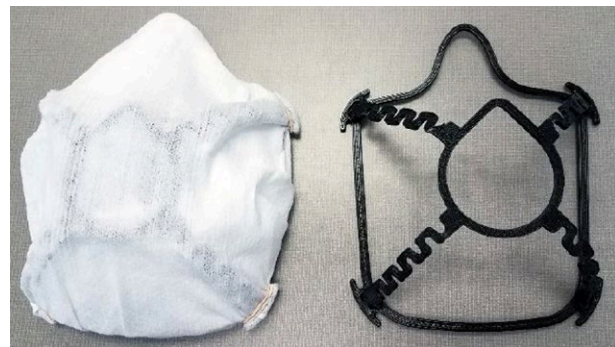


Fig. 5.29. 3D-printed face mask frame. [Courtesy Ames Laboratory]

University of Delaware's Hen's Nest frame.⁸ Issues with these initial frames were brittle plastic (acrylonitrile butadiene styrene), frames/x-ribs breaking during assembly, frame too large for smaller faces, incompatibility with existing cloth masks, and parts not nesting efficiently for 3D printing.

⁸ University of Delaware. *The HensNest v2*. Model 3DPX-013674. NIH 3D Print Exchange, 8 April 2020. <https://3dprint.nih.gov/discover/3dpx-013674>



Fig. 5.30. Experimental setup for testing microbial deactivation as part of efforts to develop filtration systems for breathing hoods. [Courtesy Savannah River National Laboratory]

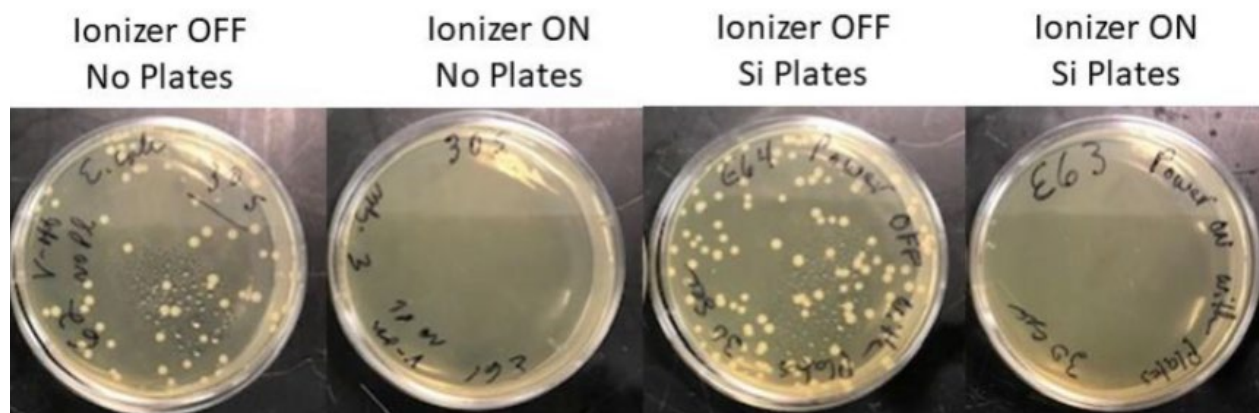


Fig. 5.31. *E. coli* colonies observed during tests of electrostatic precipitator. [Courtesy Savannah River National Laboratory]

SRNL focused on the design and development of a new filtration system for breathing hoods. Research included understanding microbial deactivation using an electrostatic precipitator. An electrostatic precipitator system developed under a prior SRNL project was used to test new

deactivation concepts for the Office of Science. Figure 5.30, this page, shows the current experimental assembly.

Figure 5.31, this page, shows how the ionizer in the electrostatic precipitator affects the growth of

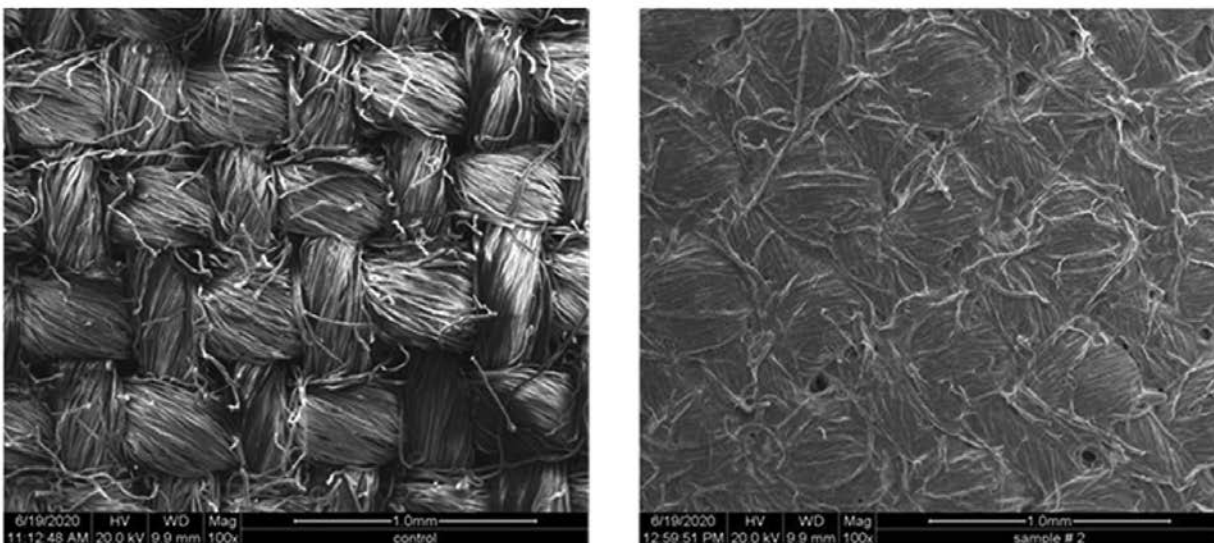


Fig. 5.32. Scanning electron micrographs of original cotton fabric (left) and fabric impregnated with cellulose nanofibrils (right). [Courtesy National Renewable Energy Laboratory. U.S. Patent Application No. 17/477,195: Peter Ciesielski, Michael Himmel, and Todd Vinzant, “Cellulose-Containing Filtration Materials and Methods of Making the Same.”]

E. coli colonies. The effects of silicon collection plates in the system were also tested. The data strongly suggest that *E. coli* bacteria were deactivated after the ionizer was turned on.

5.3.5 Homemade Masks

Shortages of surgical masks and N95 respirators spurred the use of homemade masks. NREL studied the effectiveness of these masks and the degradation of the filtration efficiency through repeated use and washings. NREL also examined masks treated with cellulose nanofibrils (CNF).

The first trials of cotton mask fabric impregnated with CNF showed promising results. Scanning electron microscopy of cotton fabric with various concentrations of CNF (see Fig. 5.32, this page) revealed expected reductions in apparent porosity and a low density of remarkably conserved macropores.

An initial concentration study was performed to assess the impact of CNF loading on the filtration efficiency of cotton fabric. Aqueous CNF slurries were prepared with weight percentages of 0.5, 0.05,

0.01, and 0.005. The deposition was performed by placing a 4.7-centimeter section of cotton fabric over the filter of a Buchner funnel, 10 milliliters of the slurry was poured into the top of the funnel, and vacuum was applied. The samples air dried in ambient conditions overnight. SEM images of the samples are presented in Fig. 5.33, p. 234. At the highest CNF concentration (0.5 weight %), nearly complete coverage of CNF was observed with little remaining porosity. As the concentration decreased, more of the original porosity of the cotton fabric became visible. CNF matrix was present in many of the gaps between the woven fibers, reducing macroporosity and likely increasing the tortuosity of the remaining pores. The higher-magnification view of the sample prepared with 0.005 weight % CNF reveals the nanoscale dimensions of the CNF and indicates intimate integration of the CNF and cotton microfibrils. The image also shows that CNF can aggregate into semi-continuous films with little porosity in some regions. We hypothesize that freeze-drying the material (rather than air drying) may help mitigate this aggregation and better preserve the micro- and nanoscale features of the fibrils.

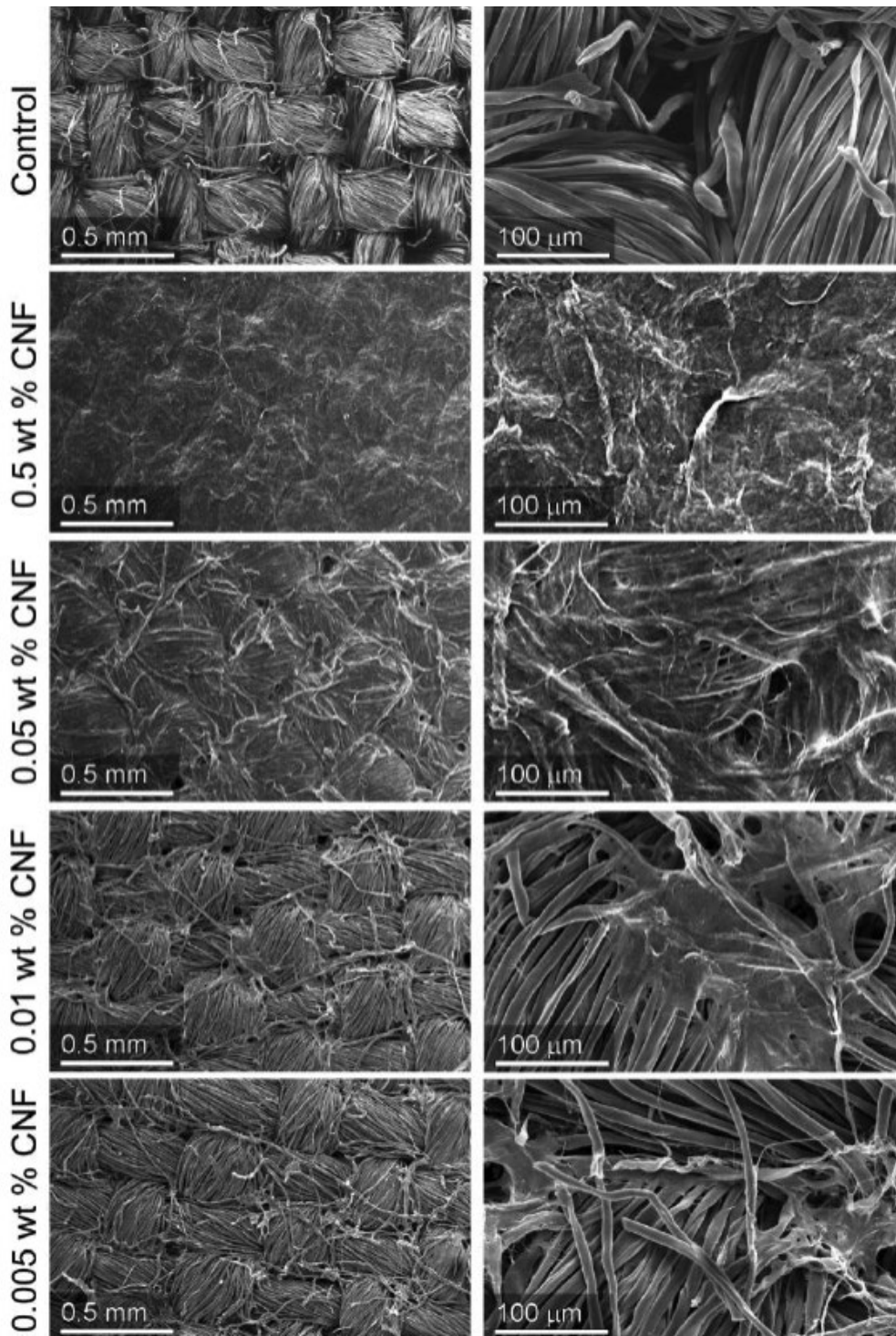


Fig. 5.33. Scanning electron micrographs of cotton fabric modified by cellulose nanofibrils (CNF). [Courtesy National Renewable Energy Laboratory. U.S. Patent Application No. 17/477,195: Peter Ciesielski, Michael Himmel, and Todd Vinzant, "Cellulose-Containing Filtration Materials and Methods of Making the Same."] [Courtesy National Renewable Energy Laboratory. U.S. Patent Application No. 17/477,195: Peter Ciesielski, Michael Himmel, and Todd Vinzant, "Cellulose-Containing Filtration Materials and Methods of Making the Same."]

| Table 5.2. Filter Efficiency After Washing | | | | |
|--|---|---------------------------------|-----------------------------------|---|
| Sample | Average Filtration Efficiency (\pm standard deviation) | | | Average Inhalation Resistance (\pm standard deviation) |
| | In terms of particle mass at 300 nm | In terms of total particle mass | In terms of total particle number | |
| 0 wash cycle | 14% \pm 1% | 20% \pm 1% | 27% \pm 1% | 3.3 \pm 0.3 mm H ₂ O |
| 1 hot wash/dry cycle | 15% \pm 2% | 20% \pm 1% | 28% \pm 2% | 3.8 \pm 0.8 mm H ₂ O |
| 7 hot wash/dry cycle | 15% \pm 4% | 21% \pm 1% | 32% \pm 2% | 4.3 \pm 0.1 mm H ₂ O |
| 14 hot wash/dry cycle | 14% \pm 7% | 20% \pm 1% | 32% \pm 2% | 4.9 \pm 0.6 mm H ₂ O |
| 21 hot wash/dry cycle | 21% \pm 2% | 22% \pm 1% | 32% \pm 1% | 5.6 \pm 0.3 mm H ₂ O |
| 28 hot wash/dry cycle | 15% \pm 2% | 23% \pm 2% | 31% \pm 2% | 7.8 \pm 0.7 mm H ₂ O |

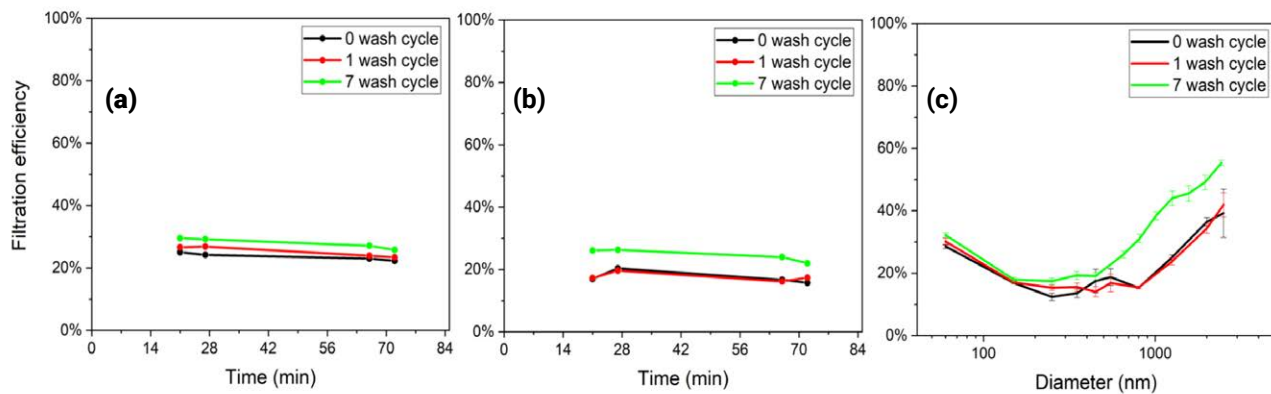


Fig. 5.34. Filtration efficiency plotted over time as a function of (a) particle number; (b) particle mass; and (c) particle number distribution. [Courtesy National Renewable Energy Laboratory]

NREL also investigated the effects of washing and drying on the filtration behavior of the fabric. Filtration characterization tests were performed on the seven wash/dry cycle samples (see Table 5.2, this page). The results indicate that filtration efficiency increased slightly after seven washing cycles. The sample coupon was first pre-conditioned at $85 \pm 5\%$ relative humidity and $38 \pm 2.5^\circ\text{C}$ for 25 ± 1 hours. After conditioning, the sample was sealed in a gas-tight container and tested within 10 hours. Filtration efficiency and size-resolved filtration efficiency were plotted over time as a function of particle number and particle mass (see Fig. 5.34, and 5.35, this page).

Mass-based efficiency increased for the seven-cycle hot wash/dry sample compared with the

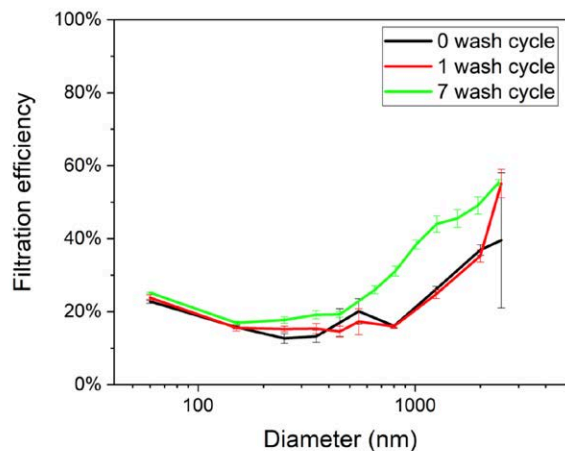


Fig. 5.35. Size-resolved filtration efficiency calculated as a function of particle mass distribution. [Courtesy National Renewable Energy Laboratory]

zero and one wash cycle samples. However, the Aerodynamic Particle Sizer was used to measure particles >500 nm for the zero and one wash cycles, whereas an Optical Particle Counter was used for the seven-cycle wash sample. The observation might therefore be due to instrument differences.

5.4 Task 2: Ventilators

5.4.1 Overview

Five fundamental contributions were made by the ventilator team.

- INL developed a ventilator supply chain analysis tool (1) to analyze the supply chain for existing ventilators, (2) to support industry partners' ability to locate critical components, and (3) to support market prediction and order fulfilment.
- INL and LANL worked with the Percussionaire Corporation to evaluate the benefits of using less common ventilation methods such as intrapulmonary percussive ventilation (IPV). LANL used this assessment to develop high fidelity lung models, which inform ventilator controls aimed at breaking up mucus and accelerating the healing process.
- SNL developed a Pathogen Management Kit to convert a Phillips Respironics V60 BiPAP to a full-scale ventilator that was FDA-EUA approved. LLNL developed a low cost, FDA-approved ventilator made of easily sourced components and not requiring parts from different ventilator suppliers. The system was licensed by a U.S. manufacturer.
- INL worked with Percussionaire on advanced controls for IPV ventilator systems that reduce production costs by 70% and increase supply chain availability through modernization.
- INL and LLNL evaluated advanced ventilation techniques, including liquid ventilation of the lungs and gastrointestinal oxygenation, both using perfluorocarbons (PFCs).

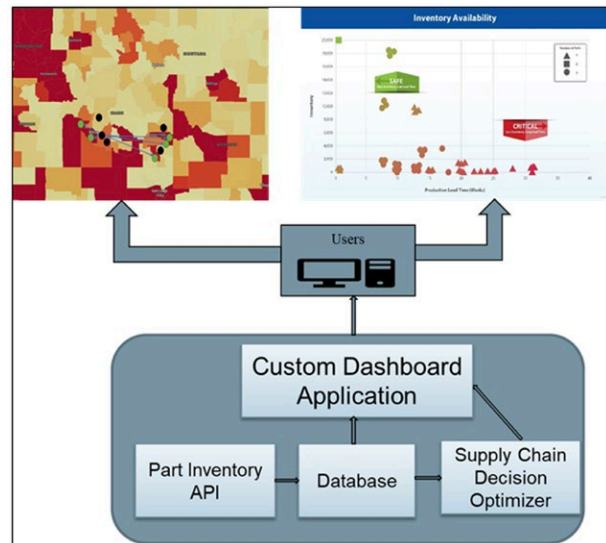


Fig. 5.36. Visual framework of ventilator supply chain tool. [Courtesy Idaho National Laboratory]

5.4.2 Ventilator Supply Chain Analysis Tool Development

INL developed a machine-learning tool to analyze specific ventilator parts lists and evaluate parts availability, location, and supply lead time. A visual framework for the ventilator supply chain analysis tool (VSCT) prototype is presented in Fig. 5.36, this page. The tool integrates various data sources, supply chain modeling, and visualization of analysis. Data flow among different components of the tool. Data sources and tool components are described below.

Potential Hot Spot and Ventilator Demand

The VSCT incorporates hot spot and demand data. Potential hot spots are regions projected to have a high demand for ventilators. Based on the number of hospitals and intensive care unit (ICU) beds in the hot spot region, the tool projects ventilator demand for each hospital in the hot spot. For example, Fig. 5.37, p. 237, shows critical hot spots and hospitals in the state of Idaho. Predicted ventilator demand needs to be assigned to each hospital in the hot spot area.

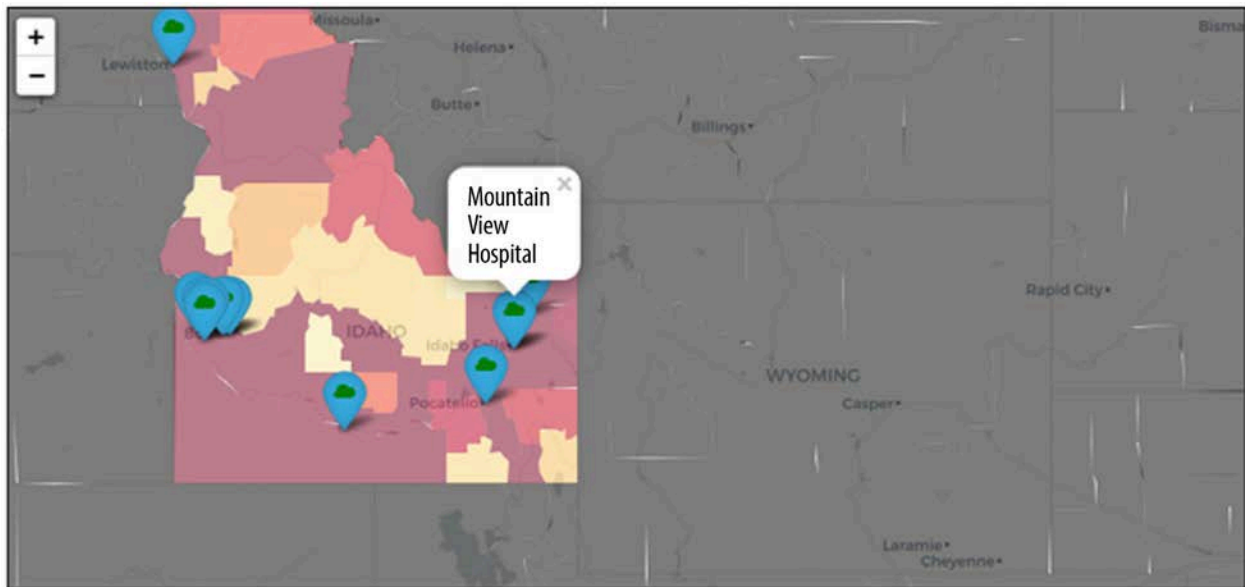


Fig. 5.37. An example of hot spots and hospitals (blue markers) in the affected areas in Idaho. [Courtesy Idaho National Laboratory]

Parts Location and Inventory

Parts locations and availability are input into the VSCT model. For example, Fig. 5.38, p. 238, shows the physical location (black markers) of ventilator air pressure regulators and solenoid valves. The location information also includes manufacturer, vendor, and third-party warehouse.

Candidate Locations for Ventilator Assembly

The supply chain analysis assumed that all ventilator parts were shipped to a temporary assembly location; hence, candidate locations for ventilator assembly were input into the model. Candidate locations were pre-selected based on the existence of manufacturers requiring highly skilled workers in the affected area. For example, Fig. 5.38, p. 238, shows such manufacturers (red markers) in the hot sport region along with hospitals (blue markers) and parts locations (black markers). Routine query development was performed to identify alternative mechanical and electronic parts to add to the inventory input into the VSCT model. Hardware design specifications, manufacturing instructions, ventilator-design documents (including

manufacturing fixtures, printed circuit-board drawings, bills of materials, and 3D CAD files) for ventilators are widely available. The goal was to identify traditional mechanical and electronic parts that can be utilized for a given ventilator design. Inventories of traditional parts can be retrieved from private companies that distribute electronic components commercially (e.g., Digi-key or Octopart). A custom search routine was developed to match parts specifications with an application programming interface (API) to provide information on traditional mechanical and electronic parts suppliers.

Digi-Key is a long-established electronics parts supplier headquartered in Thief River Falls, Minn. In addition to having a sizeable collection of electronics parts, it offers a free-to-use API that enables customers to design and execute custom search and parts-matching algorithms against the parts catalog. In addition to listing standard catalog entries such as part names, descriptions, inventories, and prices, the API permits in-depth searches using parametric parts descriptors (e.g., length, form factor, resistance,

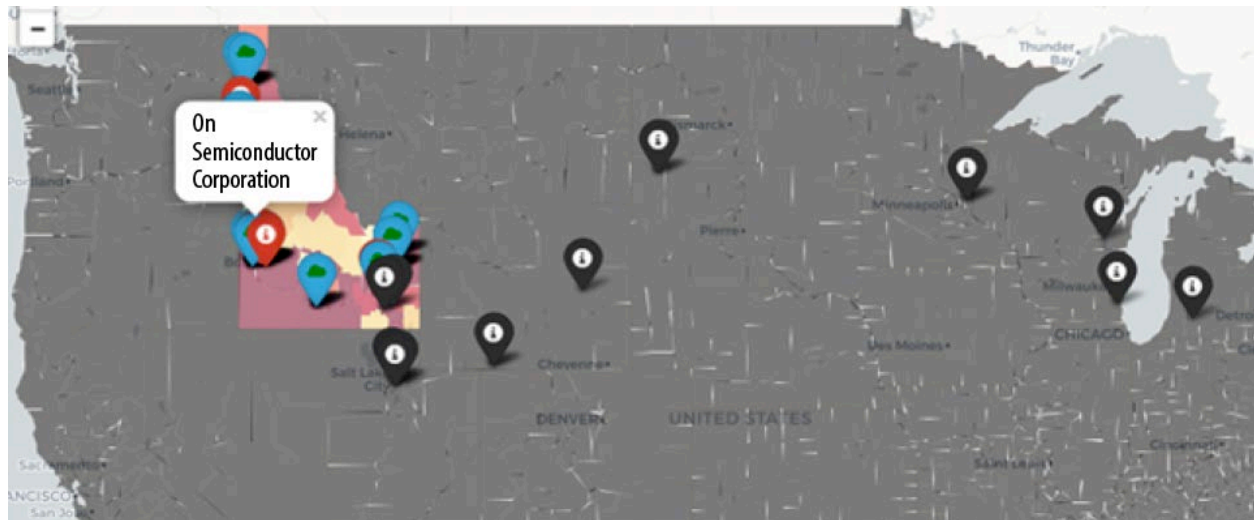


Fig. 5.38. An example of U.S. locations where ventilator parts such as solenoid valves and air pressure regulators can be sourced (black markers), along with hospitals (blue markers) where the ventilators are needed, and candidate temporary locations for ventilator assembly (red markers) in the hot sport region. [Courtesy Idaho National Laboratory]

voltage). This enables designers to efficiently create a bill of materials (BOM) based on operative specifications for the part rather than using a strict SKU-based search. The key benefit is that search results update as new parts come to market or older parts are deprecated and removed.

As an initial test case, a Microsoft Windows application was created wherein users could specify their own BOM for a hypothetical ventilator design. The application would then reach out to the Digi-Key API and return a listing of matching parts, inventories, and factory production lead-times. The inventories and lead times could be tracked to identify the limiting components in the overall manufacturing process. The parts lists could be saved and retrieved as needed so that multiple designs could be independently tracked. The primary limitation to this approach is that it did not deploy well to a web-based platform. In addition, although the Digi-Key catalog has a wide variety of electronic components, it lacks many of the mechanical and pneumatic components that are also required for a ventilator.

The team therefore adjusted the approach to use a different online catalog system along with a web-based user interface. The Octopart API is a search engine tool for finding and comparing electronic components quickly. Octopart provides data for millions of electronic components at a granular level such as availability, pricing, technical and physical specifications, images, data sheets, lead time, CAD models, reference design, and component architecture. The Octopart API paid subscription functionality was utilized to gather data for key components. An Enterprise level subscription was purchased to conduct a higher number of queries and track bills of materials for multiple designs. A post subscription with a gateway API key from Octopart databases was downloaded using Python and GraphQL. A custom Python filtering functionality was developed to get metadata for key dimensions including images, operating voltage, material, etc. Python filtering functionality was used to narrow down the search to a small dataset close to the required specifications, which was arranged in a tabular format. Fig. 5.39, p. 239, shows the sequence of operations for retrieving data from the Octopart API.

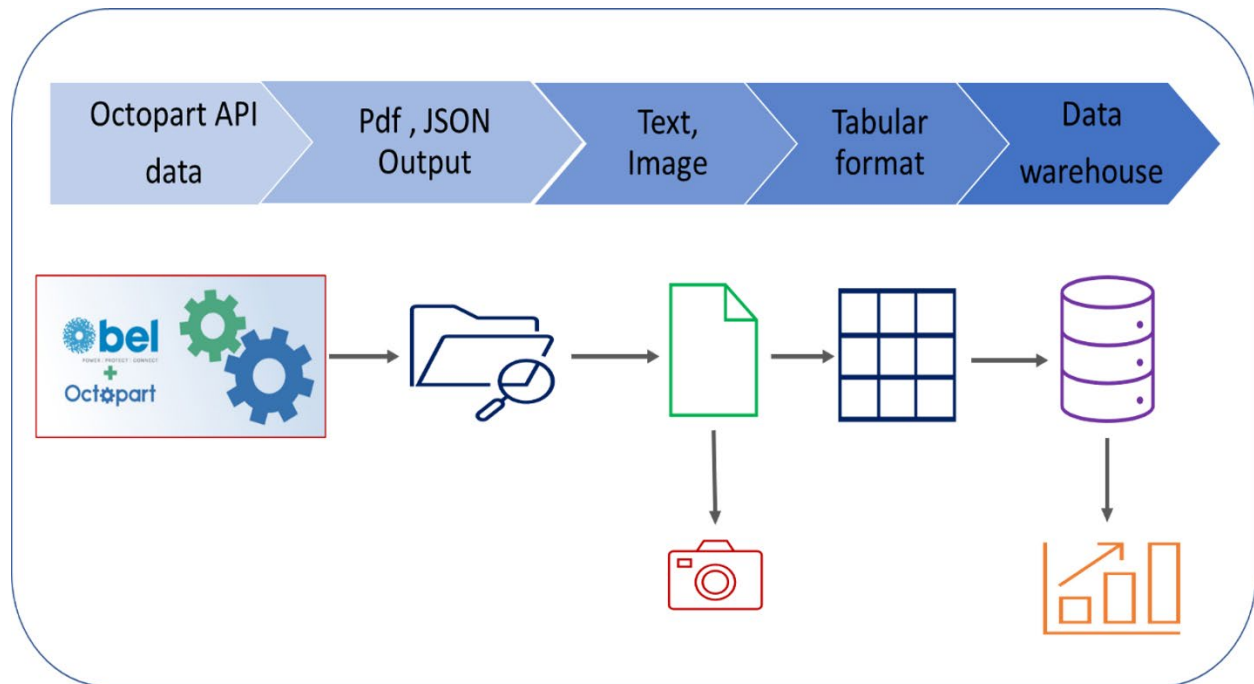


Fig. 5.39. Octopart API data gathering architecture. [Courtesy Idaho National Laboratory]

Optimization Model Development

Given a set of demand locations, parts locations, and ventilator assembly locations, a supply chain network optimization model is needed to optimize decisions regarding parts sourcing and ventilator assembly location to ensure rapid ventilator production and distribution. The optimization model was implemented with VSCT (coded in Python using CPLEX as an optimization solver) to provide rapid supply chain analysis. The VSCT utilized a mixed-integer linear programming (MILP) model to understand where the parts would be coming from and how much to expedite ventilator production. MILP is a method of mathematical optimization in which some of the decision variables are restricted to integer values. The optimization model was used to understand parts sourcing decisions under the following constraints: physical location of hospital, parts supplier and ventilator assembly, supply availability, ventilator demand, and

transportation distance. The model can be updated with evolving conditions and new operational challenges.

Visualization and Dashboard Development

A web-based supply chain dashboard was developed to improve scalability and to separate key user functionalities (i.e., BOM specification and parts availability tracking). As is typical practice for website design, the user interface and data processing tools were built separately, with data being passed through a commonly used database.

Database Design

The database design largely followed the schema for the Octopart search results, with a few extra tables added to hold search specifications. The tables and relations were loaded into a hosted SQL server instance to ensure maximum uptime and to permit communications with users inside and outside the host enclave.

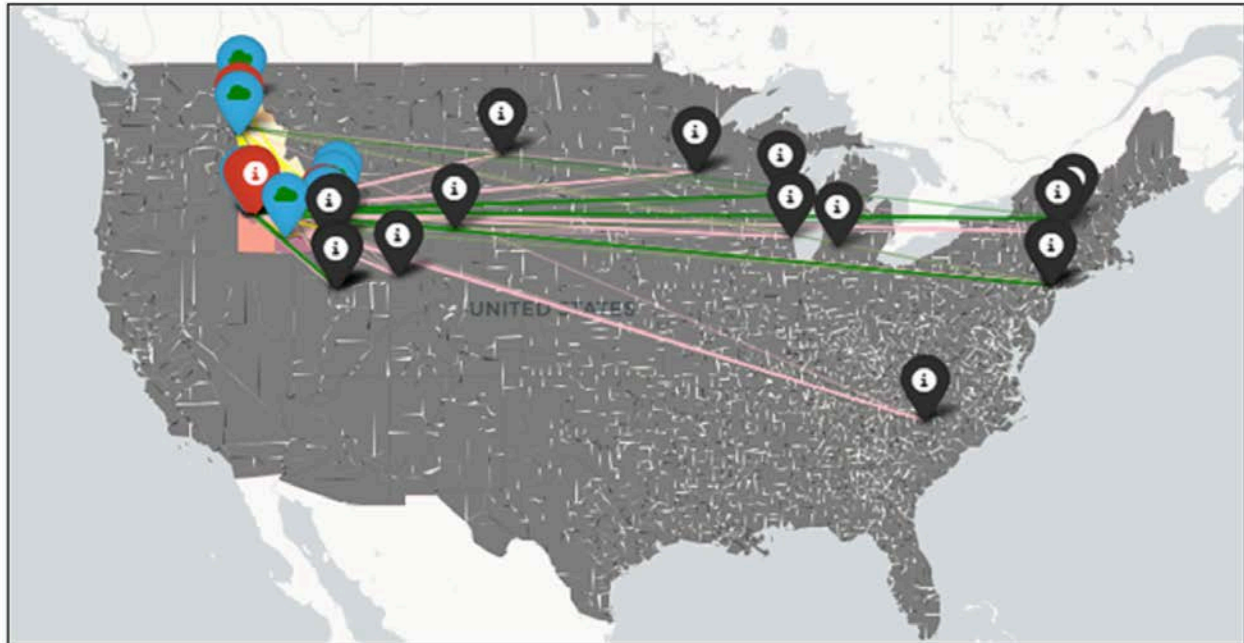


Fig. 5.40. Example supply chain paths based on different elements input into the optimization model. [Courtesy Idaho National Laboratory]

Data-Scraping Tools

To determine which parts pose critical supply chain limitations, it is necessary to track available inventories at regular intervals. This was accomplished using a standalone query script set to run automatically once per day. The script retrieves a list of BOMs from the database and feeds it through the Octopart API, which returns parts inventory data. The data are then returned to the database where they can be accessed by the web frontend. Separating the repetitive data queries from the web frontend improves utilization of the limited number of permitted queries to the Octopart API. This enables a greater number of parts to be tracked for a given subscription level, potentially reducing costs.

The website utilized PHP on the backend and HTML, CSS, and JavaScript on the frontend. Bootstrap and JavaScript libraries (e.g., Moment.js, Chart.js, jQuery, and Popper.js) were utilized on the frontend for styling. SQL Server was used alongside StarUML to create the database schema. Database interactivity

was accomplished via Ajax calls to SQL Server, which in turn returned Ajax that was parsed and used inside Chart.js to graph the data and display various U.S. information about the data.

Use Cases

VSCT generates two types of output: (1) supply chain analysis and (2) a dashboard that tracks critical inventory of nontraditional mechanical and electronic parts needed to manufacture ventilators.

Supply Chain Analysis

The inputs to VSCT are the supply chain networks that link parts locations, ventilator assembly locations, and ventilator demand locations (see Fig. 5.40, this page). The figure illustrates how different supply chain paths can be used to meet ventilator demands at hospitals in affected areas and how parts can be sourced from same location or widely distributed vendors. Based on input data, the optimization model within VSCT decides the best supply chain to meet ventilator demand.

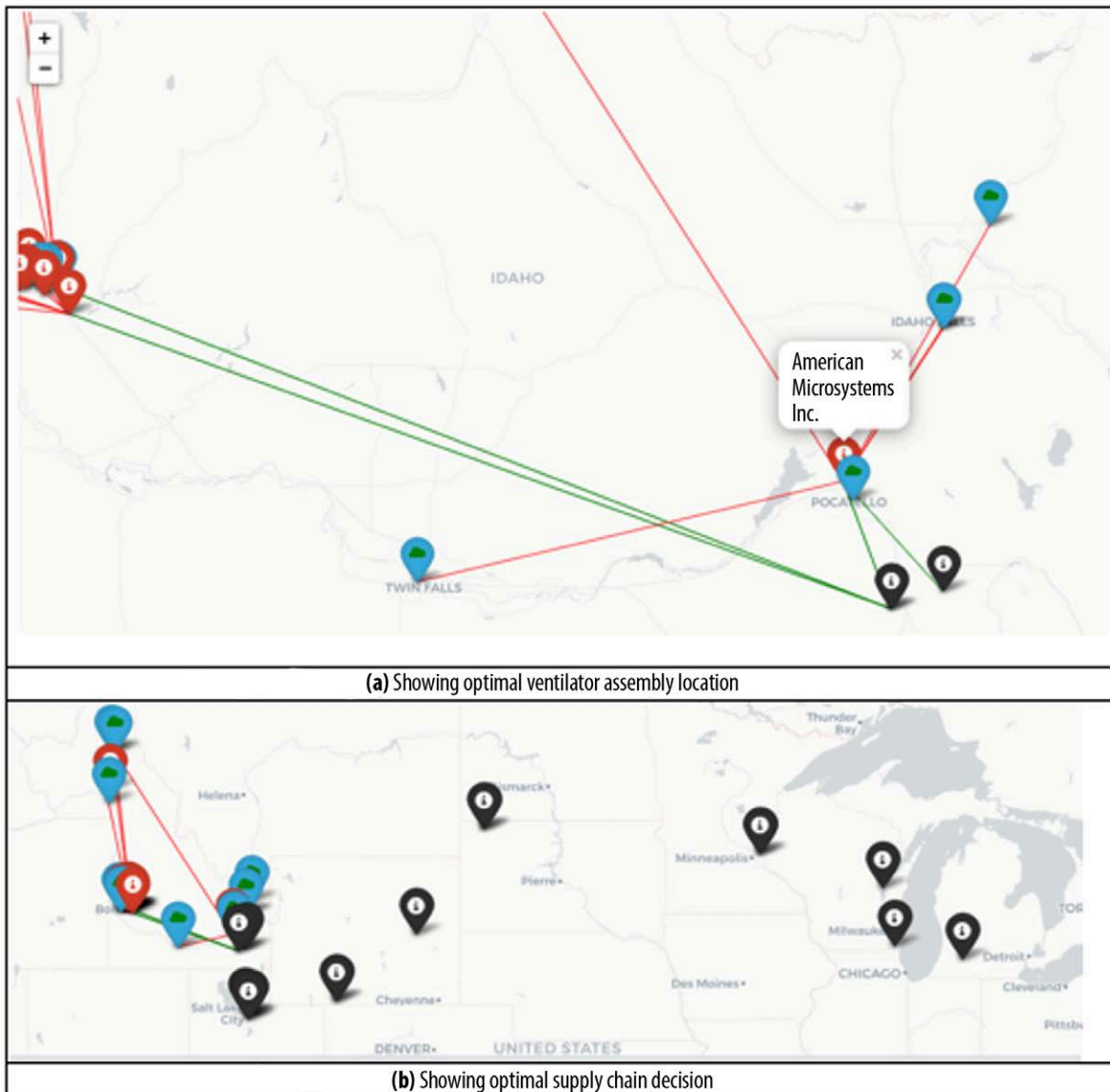


Fig. 5.41. An example of optimization output showing where to source parts and locate ventilator assembly to meet predicted ventilator demand. [Courtesy Idaho National Laboratory]

For example, if supply chains are optimized based on physical distance, the optimization model identifies supply chains that minimize the total distance between hospital, parts supplier, and ventilator assembly locations (see Fig. 5.41, this page).

Supply Chain Dashboard

Figures 5.42 and 5.43, p. 242, show the concept for the supply chain dashboard interface. The home

page displays a list of saved parts with links to their manufacturer web page and saved inventory and pricing data. Individual parts can be more closely inspected by selection of the plots. This allows a comparison of prices and inventories across custom date ranges.

Regional, state, and national stakeholders, including industry, can use this framework to expedite

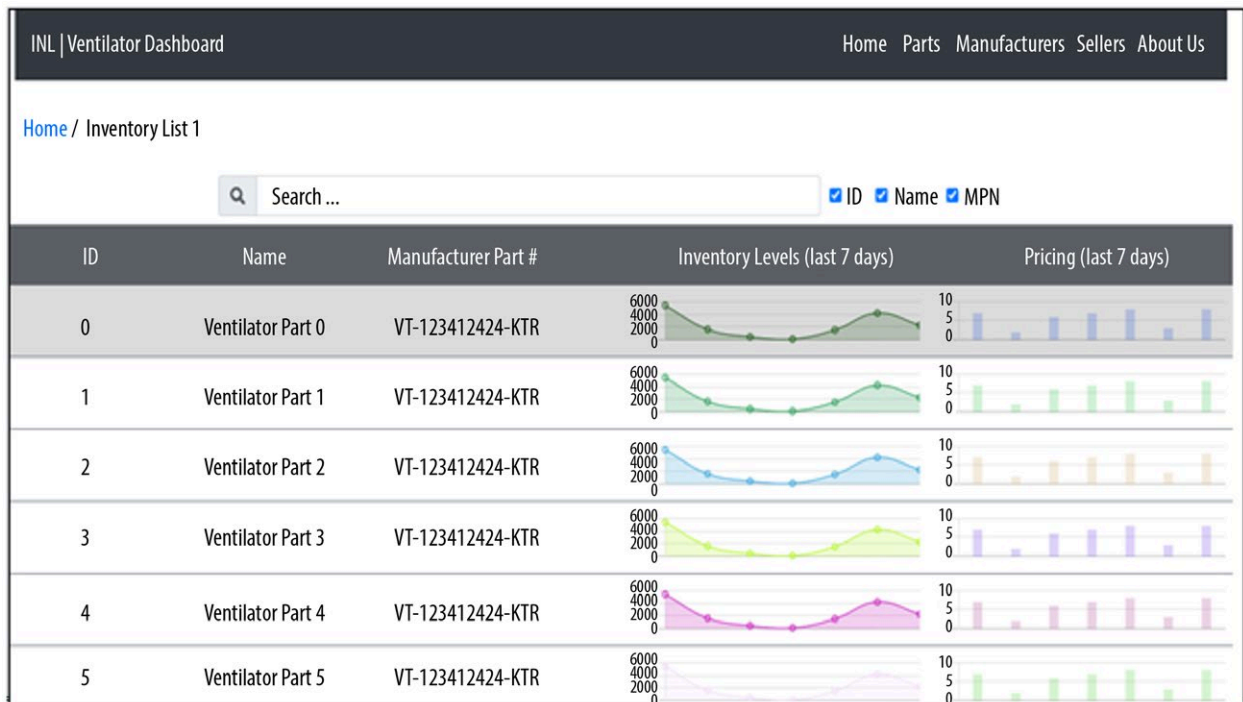


Fig. 5.42. Dashboard displaying inventory and pricing data [Courtesy Idaho National Laboratory]

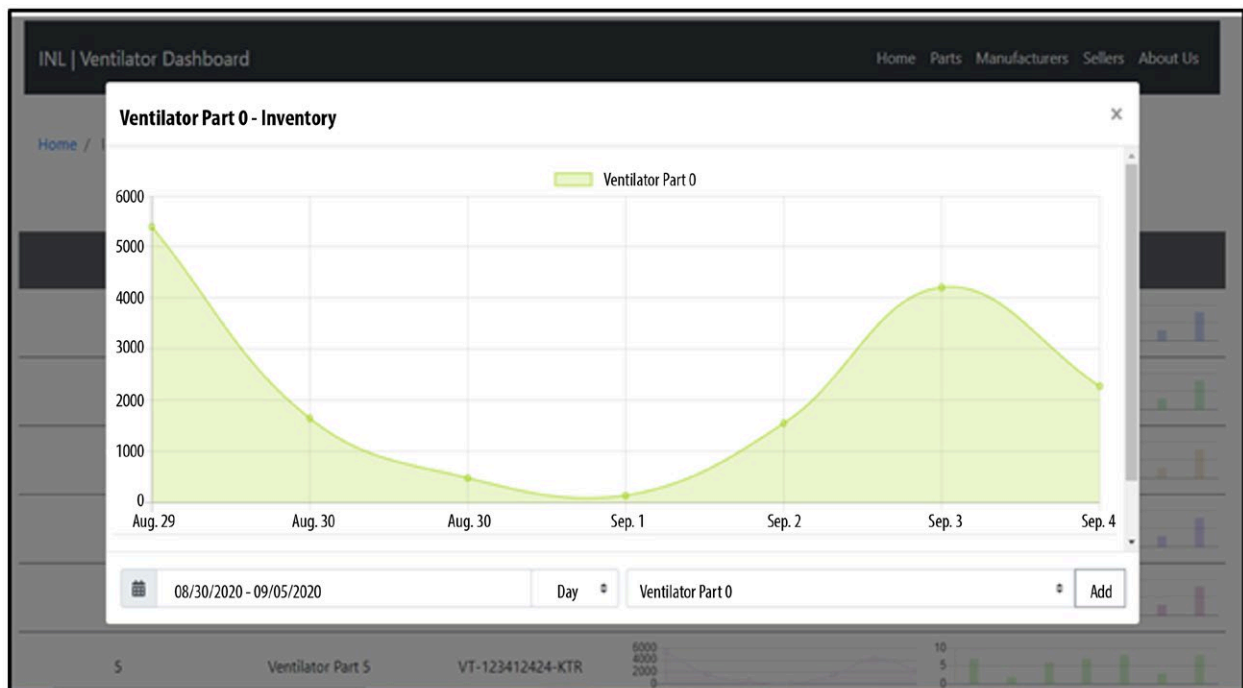


Fig. 5.43. Dashboard displaying individual parts inventory over time. [Courtesy Idaho National Laboratory]

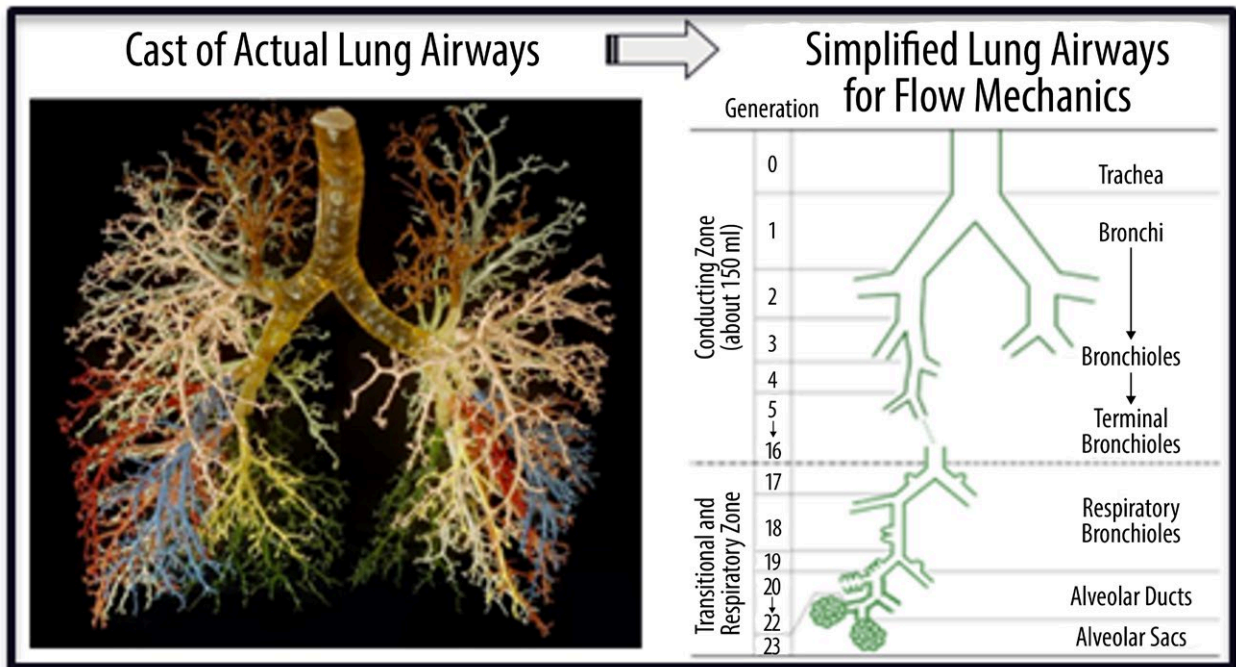


Fig. 5.44. A cast of actual lung passages and a simplified geometrical summary of the 24 lung pathways, also referred to as generations. [Courtesy Los Alamos National Laboratory]

manufacturing of ventilators that utilize nontraditional mechanical and electronic parts suppliers. This first-generation tool requires further development to reach its full capabilities. Specifically, data flow within the dashboard, API, and the optimization model need to be automated; the algorithm for retrieving matching parts requires further refinement; and a user-friendly interface is needed before deploying the tool for use by nonexperts.

Although this tool was designed for ventilator parts and the corresponding supply chain, it can be used to provide strategic supply chain analyses in other areas. Data are a critical component of such analyses, and the query development methodology described here can retrieve data for these analyses. Specialty knowledge about mechanical parts and manufacturing technology can be used in various analyses as well. Also, the dashboard architecture developed for this tool can be utilized to disseminate data and critical analysis into public or restricted domains.

5.4.3 Lung Modeling

The human lung is a complex series of flow passages starting at the trachea and bisecting down to smaller and more numerous passages (referred to as generations), ending with alveolar sacs for oxygen and CO₂ exchange (see Fig. 5.44, this page). Mucus is routinely generated in the lungs to remove everyday dust and other impurities. During certain illnesses, especially those involving the lungs and blood, mucus production increases to aid in the removal of pathogens and waste products as the body fights infection. COVID-19 patients can accumulate excessive amounts of mucus in the air passages, which can greatly restrict or even cut off air flow to portions of the lung, ultimately risking death without mechanical breathing assistance or ventilation to improve air flow. However, ventilation by itself is often inefficient as excessive mucus can cut off airways and prevent fresh air from reaching the alveolar sacs.

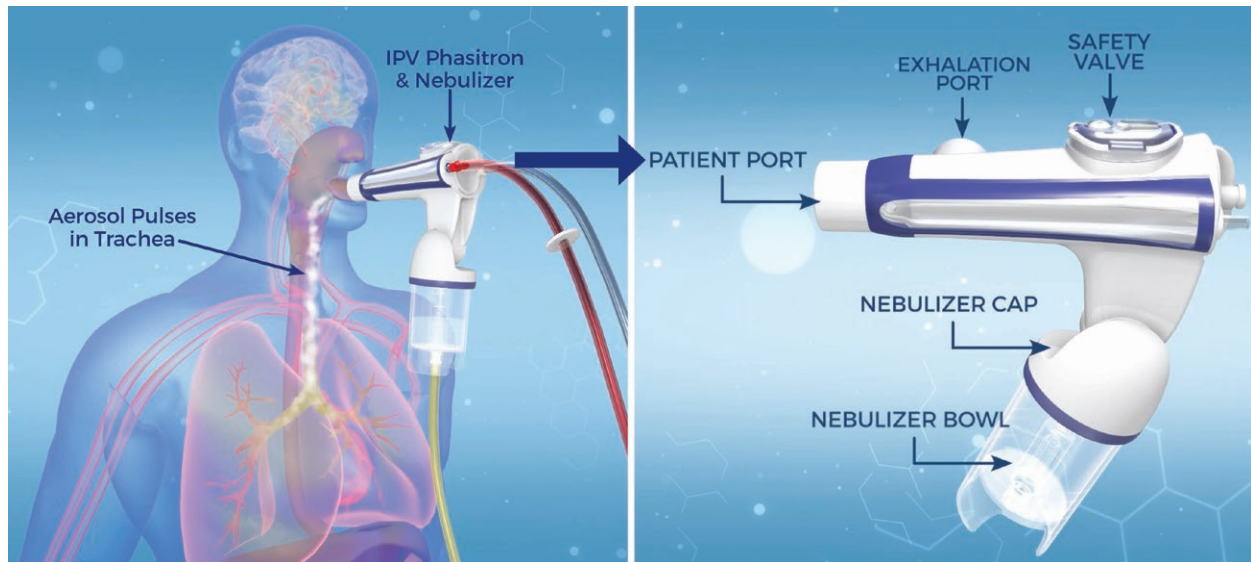


Fig. 5.45. Schematic showing the IPV Phasitron and nebulizer and their application in creating a pulsing stream of aerosol into a patient's lungs during inhalation [Courtesy Percussionaire Corporation]

Ventilated COVID-19 patients need assistance with mucus breakup and removal and thus IPV was explored to remove mucus and aid patients in recovery. IPV uses periodic bursts of air to nebulize a liquid and create pulses of aerosol that can be injected into a patient's mouth for various forms of lung treatments (see Fig. 5.45, this page). IPV, when combined with traditional ventilation, delivers rapid pulses of aerosol to deposit medication and, as claimed, to break up mucus films and open mucus-clogged lung passages.

The effort merged numerical and experimental approaches with machine learning algorithms to form a predictive model of lung behavior under IPV therapy. Acoustic, computational fluid dynamics (CFD), and lung compliance structural models were developed to simulate transient air flow and pressure distributions as a function of lung passage conditions for both healthy and infected lungs. Pulmonary lung cells were used to study alveoli response to IPV pressure pulsations and look for damaging over-pressure conditions. Three-dimensional-printed simulated lung flow channels and sheep lungs were combined with humidified ventilator machines and a large assortment of

measurement methods to observe air velocities and volumetric flow rates, trachea pressure conditions, aerosol size distribution and flow characteristics, and mucus breakup. These numerical and experimental approaches covered different lung generations as depicted in Fig. 5.46, p. 245. When combined with the machine learning algorithm, this integrated research system formed a complete modeling tool to predict the performance of IPV and mechanical ventilation in the treatment of COVID-19 lung infections.

The three questions this research attempted to answer included:

- Can IPV enhance volumetric ventilation by aiding removal of mucus from lungs?
- What are the underlying physics of IPV and what are the influential variables?
- Can an integrated and efficient model be developed to predict how IPV would improve a ventilated COVID-19 patient's recovery?

Several challenges, both logistical and technical, were recognized early on in modeling efforts. A realistic lung geometry is necessary to execute

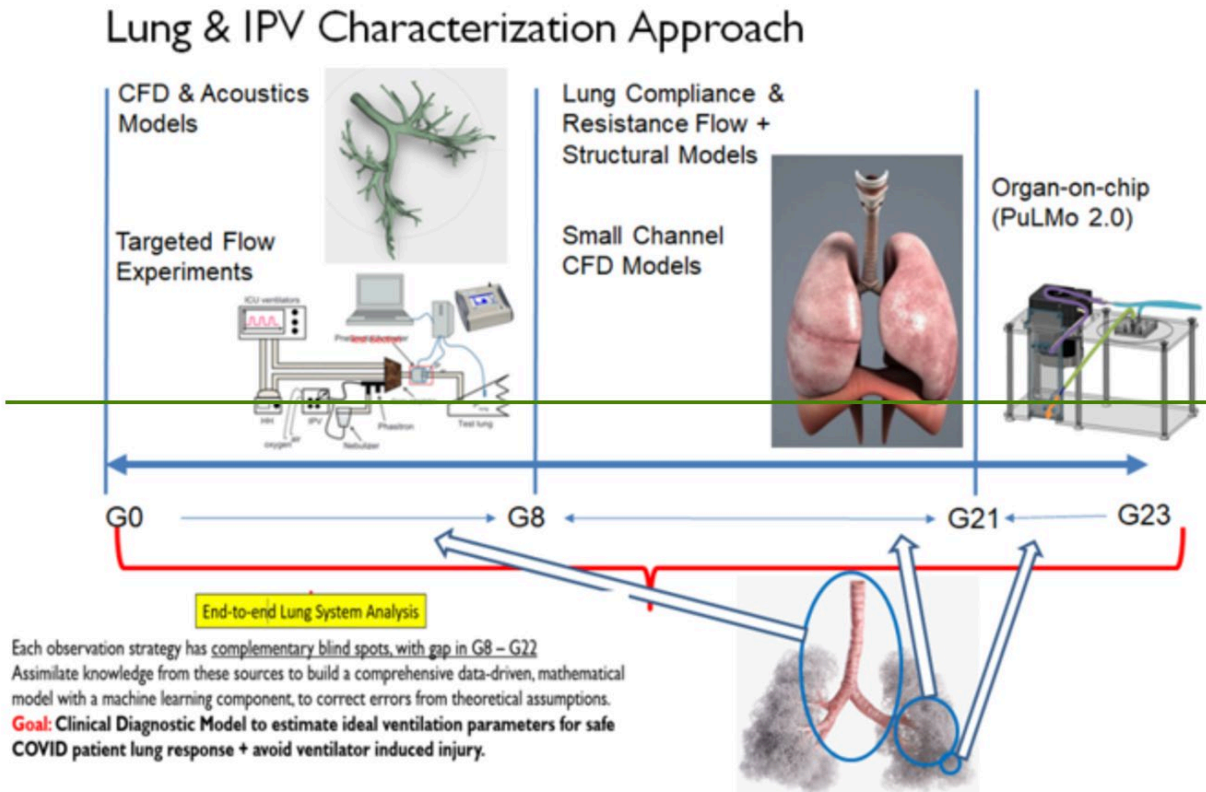


Fig. 5.46. A representation of combined experimental and numerical modeling approaches with a machine-learning algorithm to form a smart model to characterize the performance of IPV and mechanical ventilation in the treatment of lungs infected with COVID-19. The branching level of the lung pathways is indicated by G0 through G23. [Courtesy Los Alamos National Laboratory]

high fidelity CFD simulations and acoustic simulations. It was necessary to procure a lung geometry file obtained through CT scans and preprocess the complex geometry rapidly. In addition to challenges surrounding geometric complexity, state-of-the-art approaches using CFD derive a great deal of data but cost a significant amount of time. Novel machine learning approaches significantly reduced the time required to understand flow behavior in the deep lung from weeks to seconds. Finally, it was recognized that even with current high-fidelity computational models, the lungs can only be captured down to generation 6 to 8 out of 23, and there is currently no means of directly connecting CFD models to behavior at the cellular level. Combining CFD modeling, experimental manufacturing of pulmonary cells, and machine learning enables a

comprehensive model of the human lung that can provide predicted alveolar response in real time.

A CT scanned lung geometry was rapidly pre-processed using engineering software. The final geometry (see Fig. 5.47, p. 246) was subsequently used for high fidelity CFD and acoustic modeling. Surfaces along the lung wall were smoothed and a total of 77 outlets were produced consisting of generations 5 through 8 of the overall lung. The engineering CAD software SpaceClaim was used to reduce preprocessing time from months to weeks. The final geometry was then imported into various engineering software (ANSYS CFX, COMSOL, etc.) for analysis.

A high-fidelity CFD model (see Fig. 5.48, p. 247) using large eddy simulation (LES) to capture

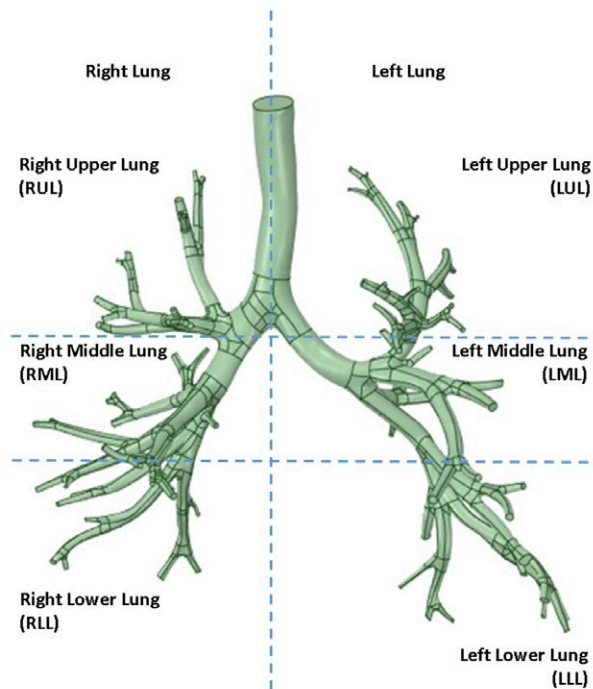


Fig. 5.47. Defeatured computational lung geometry. [Courtesy Los Alamos National Laboratory]

the turbulent kinetic energy was constructed to observe flow fields and to look for regions of high shear stress along the walls of the first nine generations of lung passages. These regions of high shear stress are more likely to present lung damage due to the influence of mechanical ventilation. In addition to regions of high shear stress, air velocity behavior was observed in the upper generations of the lungs. A design scope ranging from 0 to 60 liters per minute peak inflow and an IPV frequency of 0 to 15 Hz was selected to align with expected IPV conditions. Data generated from simulations within this design scope helped influence sensor locations for the experimental lung setup and served as training data for the novel machine learning approach. The resulting lung model captured over 80% of the turbulent kinetic energy (TKE) existing within the lung and in many instances over 90%. This high percentage of resolved TKE provides a high level of confidence in the resulting velocity, shear stress, and turbulence generated in

the lower generations. Ultimately, the confidence in these parameters inherently increases confidence in the surrogate model produced through application of the machine learning algorithms trained on the LES data. Figure 5.48 shows example air velocity fields (including predicted rotational flow in the upper generations) and expected peak shear stress in the lung passages.

Next, an analytical model was generated to investigate lung viscoelastic compliance and resistance in the presence of mucus. This model predicted lung volume during exhalation and inhalation as a function of air pressure in the trachea (see 5.49, p. 247). The analytical model enables more inclusive boundary conditions based upon compliance and resistance that can be directly applied to the outlets within the lung model. The analytical model enables flexibility to capture a wide variety of lung conditions based upon factors such as mucus content, lung health, and viscoelasticity of the lung wall.

Biological studies were performed to create a simulated human mucus for use in aerosol breakup studies. The aerosol breakup studies showed how pressure pulsations could disrupt mucus layers in simulated lung passages, causing them to loosen up and dislodge (see Fig. 5.50, p. 248).

Numerical acoustics models were used to study air pulsations in the human lung and how they coupled in resonance with the lung passages, suggesting that much higher frequencies were needed to couple energy deep in the lungs to dislodge mucus (see Fig. 5.51, p. 248).

Experiments (see Fig. 5.52, p. 249) were set up to observe IPV aerosol flows. A mechanical ventilator forced air through a humidifier and a Fluke gas analyzer (analyzing air flow rate, humidity level, peak inspiratory pressure (PIP), positive end-expiratory pressure (PEEP), and breathing rate), then through a 3D-printed instrumented lung test section (representing the trachea and the two subsequent lung generations) and into a spring-loaded bellows representing the breathing compliance of a human lung. A Percussionaire IPV unit was

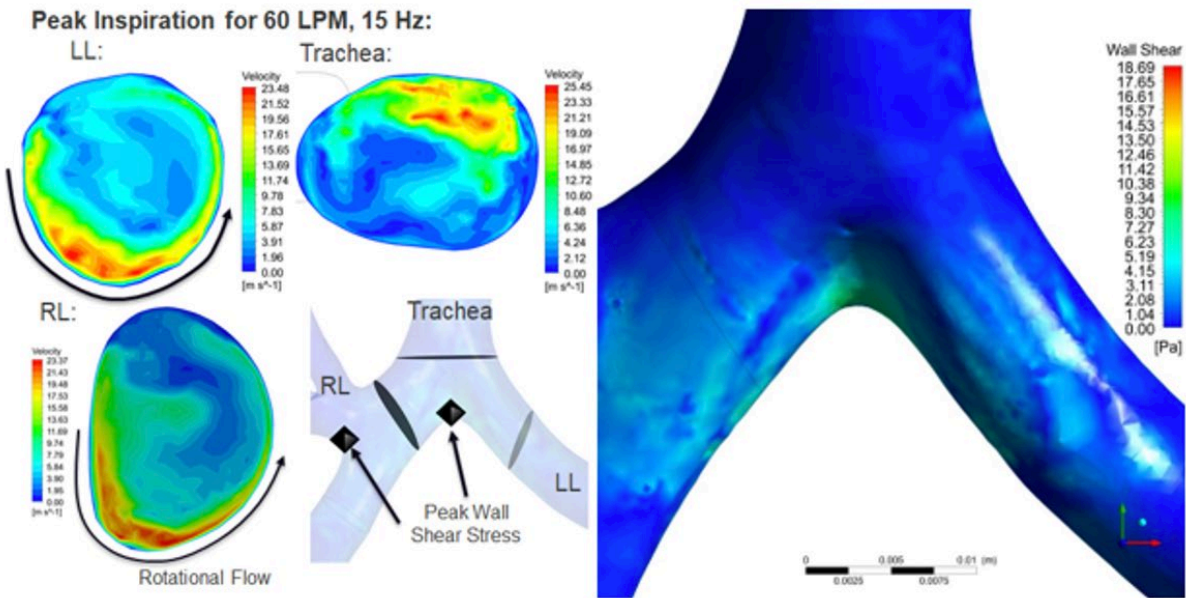


Fig. 5.48. Large eddy simulation (LES) flow predictions and wall shear stress predictions at ventilation conditions of 60 liters per minute inflow and an IPV frequency of 15 Hz. [Courtesy Los Alamos National Laboratory]

connected in parallel with the mechanical ventilator to pulse aerosolized water into the ventilated airflow upstream of the test section. A TSI 3321 aerodynamic particle sizer, connected to ports on the lung test section, monitored the aerosol size distribution as it flowed along the flow passage. Optical sensors (see Fig. 5.52, p. 249), consisting of an LED light source and photodiode detector, measured aerosol density along the flow passage test section. Pressure transducers were mounted along the test section and a hot wire anemometer upstream of the test section monitored air velocity and volumetric flow rate. A National Instruments data acquisition instrument and LabVIEW program collected and stored all the empirical data.

These experiments revealed that humidity and volumetric flow rate had a strong effect on aerosol concentration (see Fig. 5.53, p. 249). Several experiments correlated aerosol density and size distribution with humidity, air flow rate, breathing rate, and lung compliance.

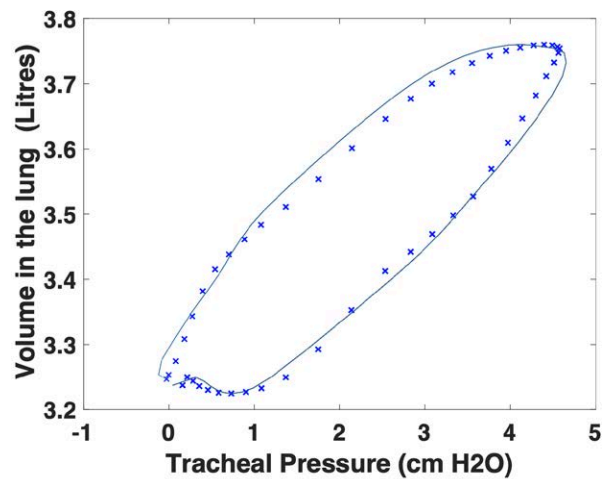


Fig. 5.49. Analytical model of lung viscoelastic compliance and resistance. [Courtesy Los Alamos National Laboratory]

The experimental system was reconfigured to test the IPV system on lung tissue harvested from sheep carcasses (see Fig. 5.54, p. 250), which is highly representative of a human lung. In these

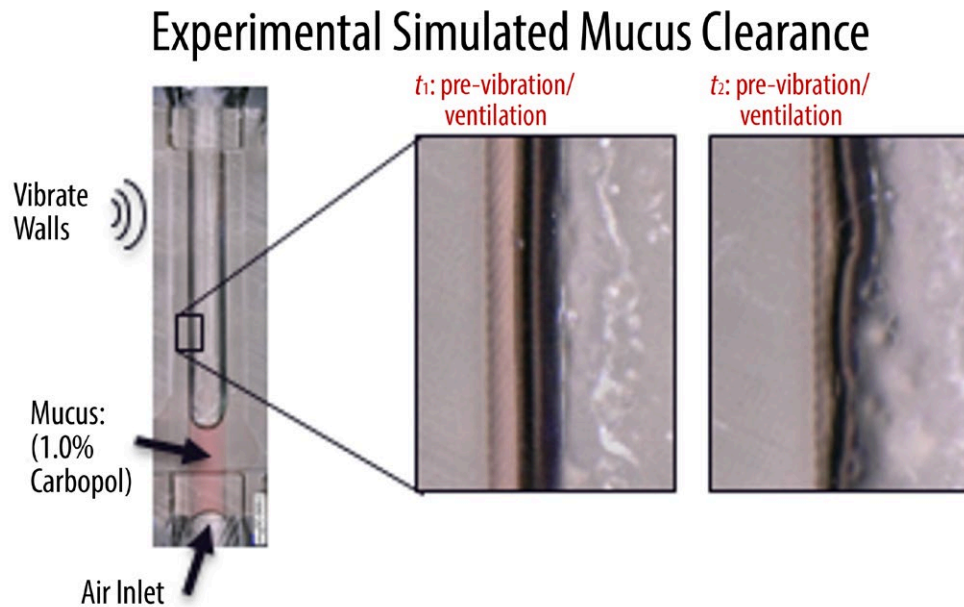


Fig. 5.50. Experimental validation of human mucus. [Courtesy Los Alamos National Laboratory]

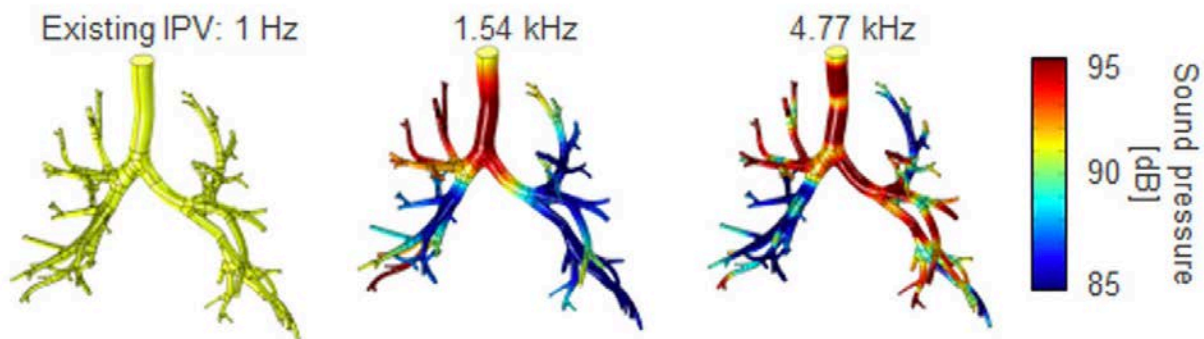


Fig. 5.51. Numerical acoustic models showing acoustic sound pressure level contours in a simplified model of the lung under three distinct drive frequencies. [Courtesy Los Alamos National Laboratory]

tests, the liquid for the IPV was dyed with food coloring to track the aerosol deposition within the lung. A complete set of empirical data including plots and correlations describing the data relationships and a more thorough description of the sheep lung data analysis is available upon request.

Most state-of-the-art lung pressure models rely on relatively simplified piping and engineering-based approximations, where several aspects such

as turbulence and flow separation are ignored. Human lungs are asymmetric and exceptionally complex in geometry, making the piping models severely limited in clinical use. To overcome this, a unique integrated model combining the numerical and experimental data for lung breathing dynamics under ventilated-assist IPV was developed. Tying together these disparate data sources was challenging and accomplished with the help of

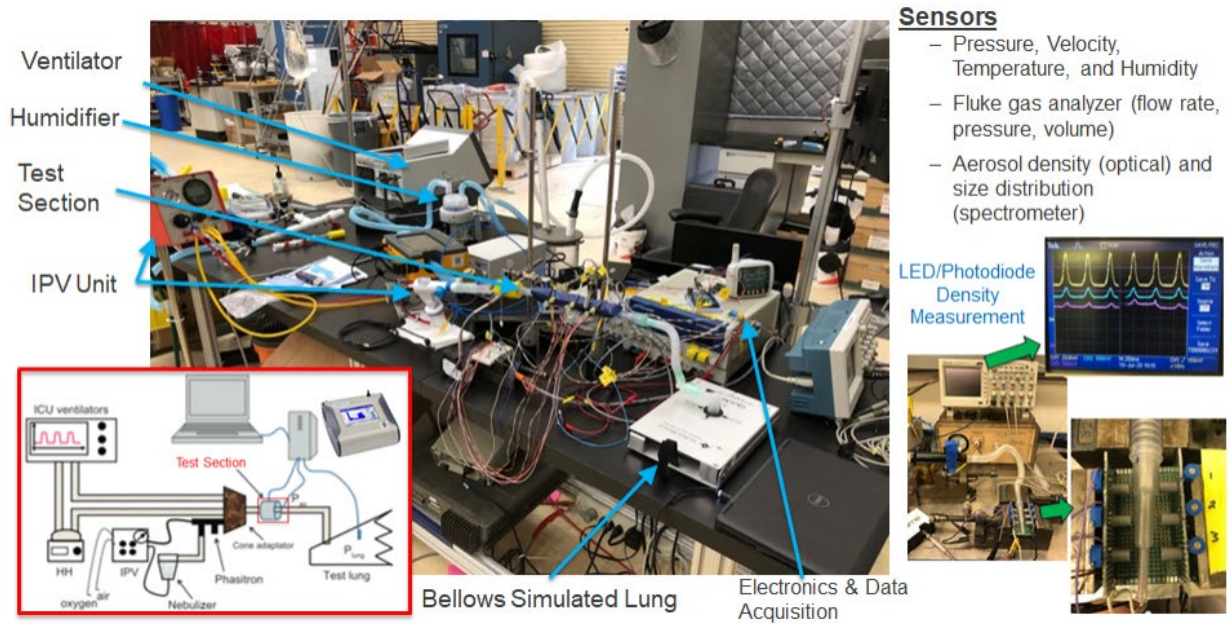


Fig. 5.52. Experimental validation of models. [Reprinted with permission from Riffard, G., et al. Intrapulmonary Percussive Ventilation Superimposed on Conventional Mechanical Ventilation: Comparison of Volume-Controlled and Pressure-Controlled Modes. *Respiratory Care* **2014**, 59 (7). 1116–1122. DOI: 10.4187/respcare.02727 and Los Alamos National Laboratory]

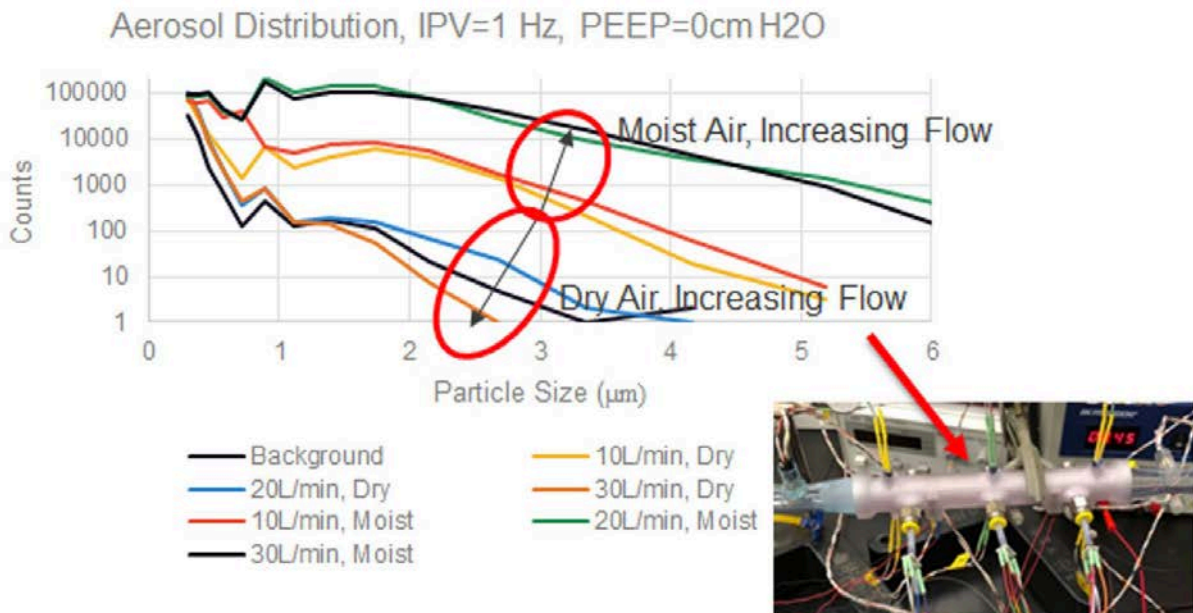


Fig. 5.53. Aerosol distribution as a function of particle size at a location along the simulated lung passage. [Courtesy Los Alamos National Laboratory]

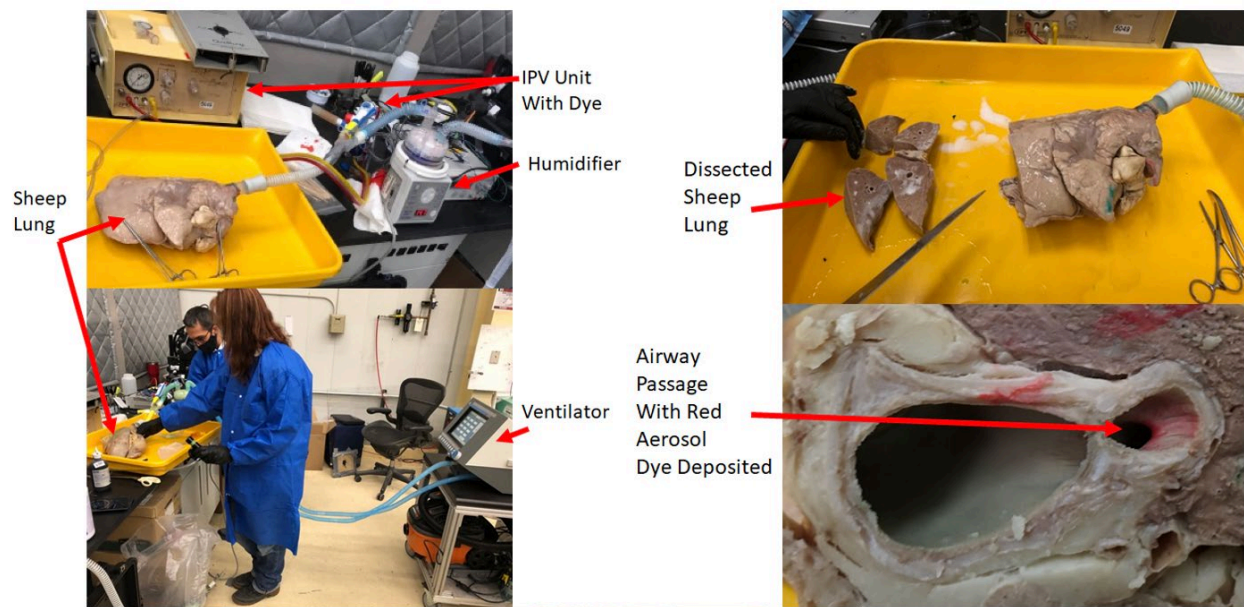


Fig. 5.54. IPV ventilation testing of lung tissue harvested from sheep carcasses (left); red dye deposited via aerosol transport during IPV ventilation testing (right). [Courtesy Los Alamos National Laboratory]

a probabilistic machine learning model. To our knowledge, this is the first-ever attempt in the literature to provide an integrated surrogate model for lung-ventilator interactions. The goal of this model was to provide a real time patient analysis tool that a respiratory therapist and doctor could use to improve treatment and recovery of ventilated COVID-19 patients (see Fig. 5.55, this page).

Fig. 5.56, p. 251, shows a schematic of the integrated data analytics and machine-learning approach for the surrogate models. While more work is needed to adapt this approach for clinical datasets, it shows considerable potential because it leverages advances in the latest machine learning and artificial intelligence techniques to address issues in lung modeling that were historically out of reach.

Intermediate conclusions to the three primary research questions are as follows:

- Can IPV enhance volumetric ventilation by aiding removal of mucus from lungs?

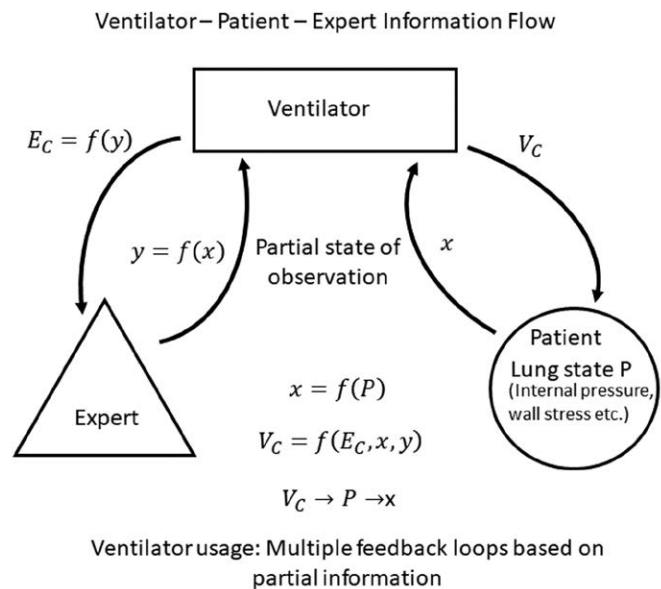


Fig. 5.55. Schematic relationship of a machine learning tool that integrates patient lung behavior, a ventilator and lung model, and a clinical expert. [Courtesy Los Alamos National Laboratory]

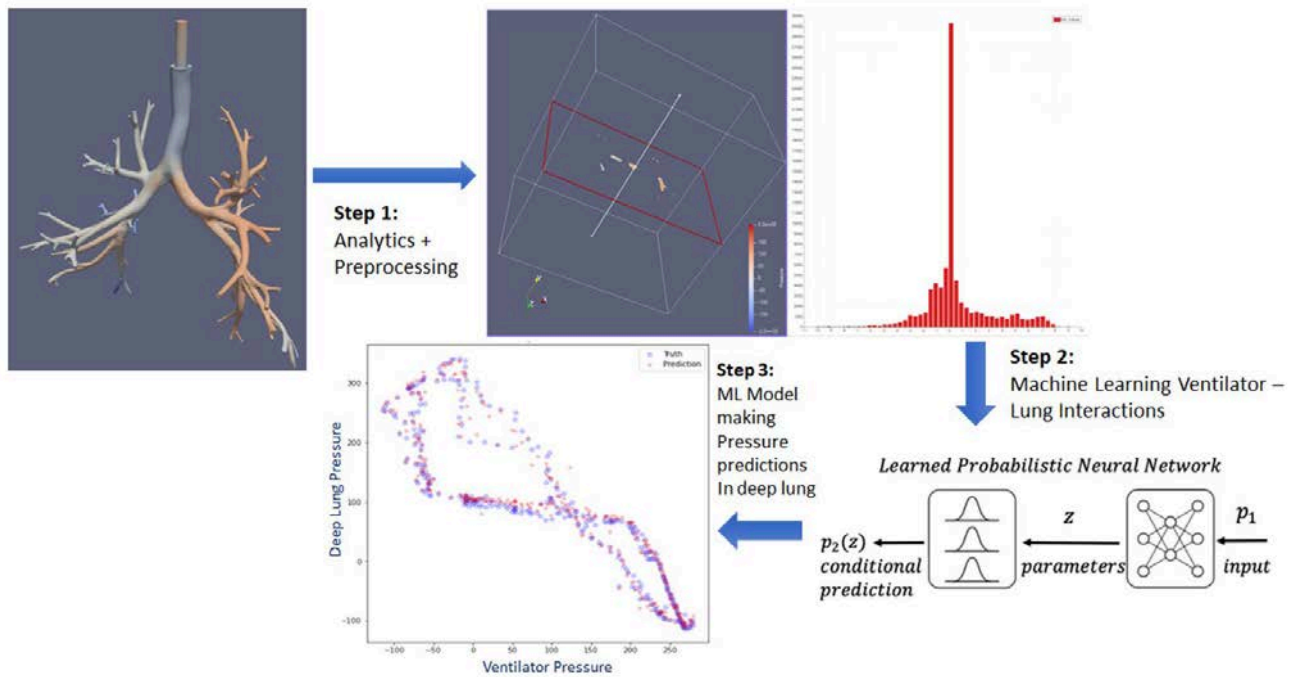


Fig. 5.56. Lung pressure as a function of ventilator pressure as determined by a machine learning algorithm after processing and learning from numerical and empirical input data. [Courtesy Los Alamos National Laboratory]

- Initial acoustic experiments reveal mucus films distorted and dislodged by mechanical disturbances.
- Mucus viscosity is highly frequency dependent.
- What are the underlying physics of IPV? What are the influential variables?
 - Turbulence and secondary flows may impact aerosol flow.
 - Lung compliance and resistance significantly influence lung tidal volume.
 - Initial aerosol propagation tests show strong dependence on humidity and IPV/ventilator synchronization.
- Can an integrated and efficient model be developed to predict how IPV would improve a ventilated COVID-19 patient's recovery?

- A preliminary machine learning algorithm for lung pressure was developed and merged with CFD model results.

5.4.4 Rapid Development and Commercialization of a Ventilator

To address the potential shortage of ventilators, LLNL successfully designed, prototyped, and tested a ventilator (see Fig. 5.6, p. 217) based on discussions and feedback from physicians, engineers, and respiratory therapists using parts that were not sourced from traditional ventilator supply chains (see 5.57, p. 252). With this ventilator design, a CRADA was established with BioMedInnovations, LLC, in preparation for submission to the FDA for an EUA. The ventilator contains 14 components and can control PIP, PEEP, breath rate, and tidal volume. A user interface enables setting the parameters and displays real-time graphs of pressure during ventilation.

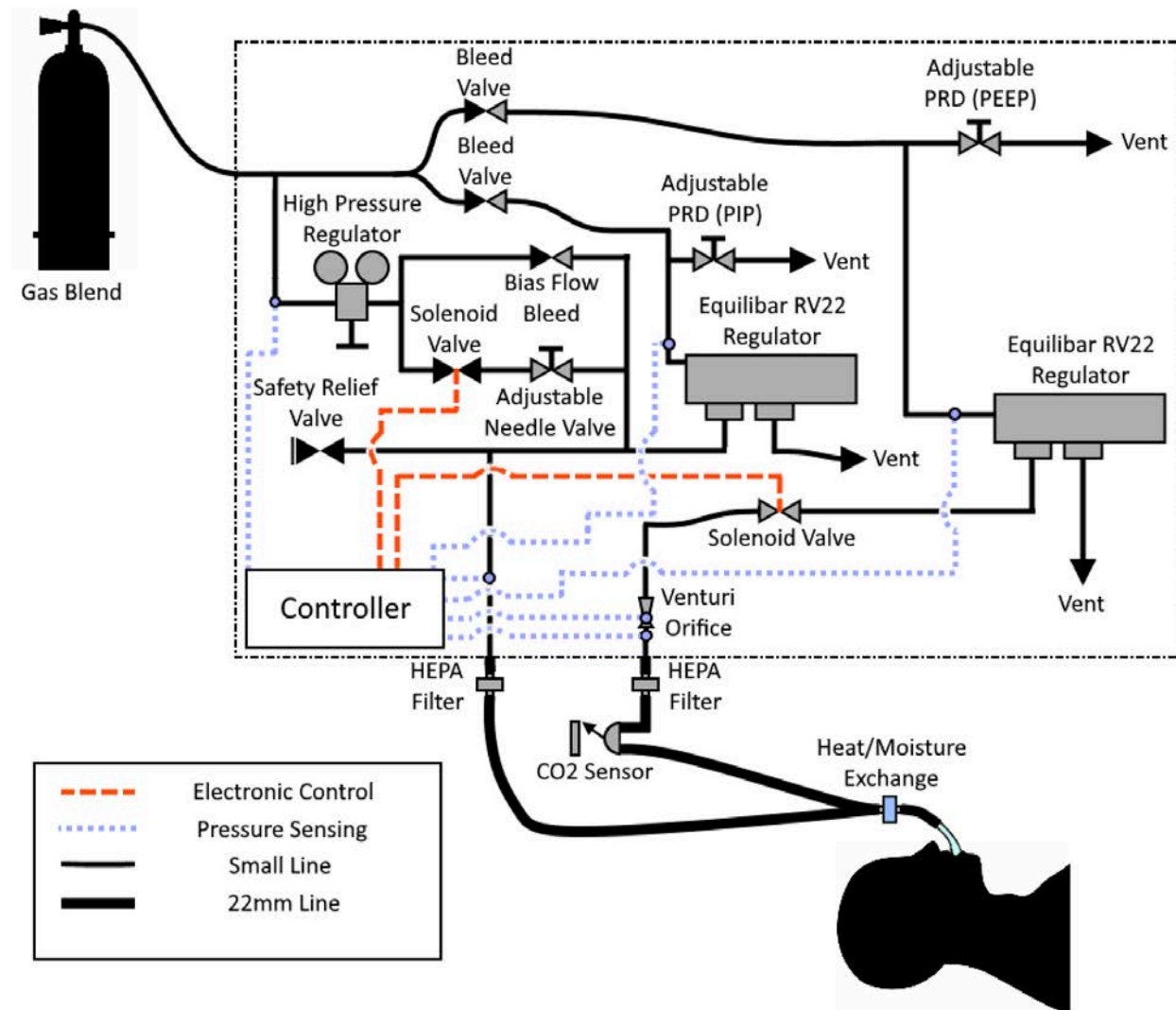


Fig. 5.57. Schematic showing components of the ventilator and path of gas delivery to a patient. [Courtesy Lawrence Livermore National Laboratory]

Through the approval process with the FDA, additional tests of the ventilator were performed to demonstrate consistency and biocompatibility. One test requested by the FDA was to run the ventilator for 24 hours and measure the pressure and flow rate to determine robustness during continuous long-term use; the ventilator exhibited little drift in pressure and flowrate waveforms. Additionally, biocompatibility tests measured particulate concentrations and volatile organic compound concentrations in the ventilated air, satisfying

safety limits set by ISO safety standards (see Fig. 5.58, p. 253).

These results led the FDA to grant an EUA for the final version of the ventilator (see Fig. 5.59, p. 253). The touchscreen user interface on the front-facing panel enables doctors and nurses to monitor breathing waveforms and adjust breathing parameters accordingly. This form-factor was designed to be portable and was based on feedback from clinicians.

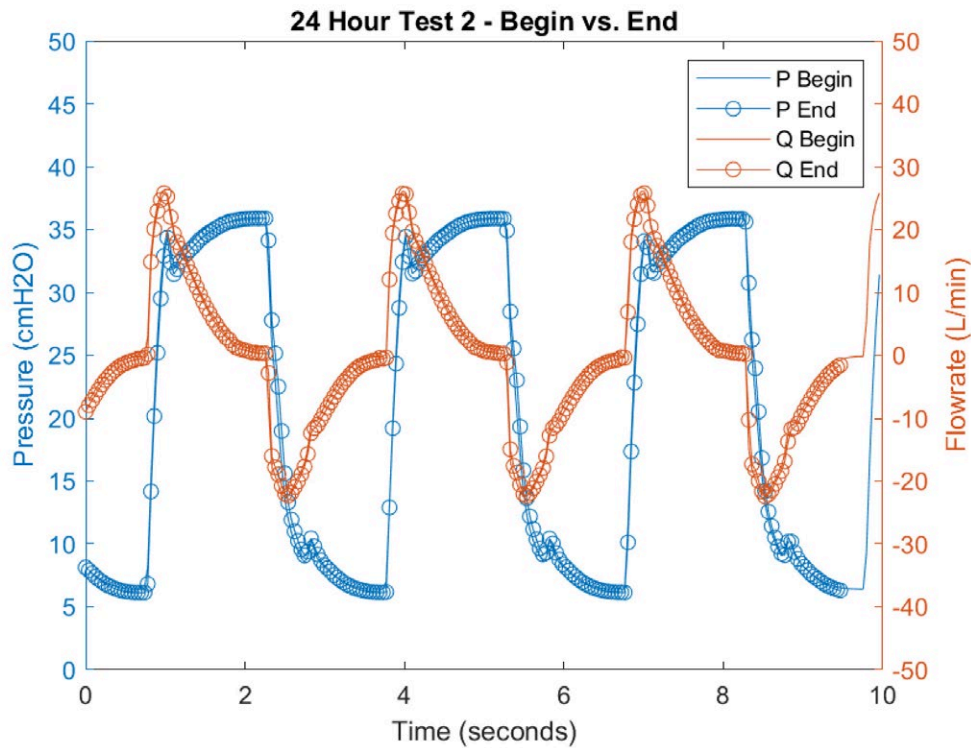


Fig. 5.58. Pressure and flowrate waveforms for the ventilator at the beginning and end of a 24-hour run period. [Courtesy Lawrence Livermore National Laboratory]

5.4.5 Accelerated Modernization of Monitoring and Alarm Systems

INL worked with Percussionaire on advanced controls for IPV ventilator systems that can reduce the cost of production by 70% and increase supply chain availability through modernization. During the early stages of this research, the INL team determined that IPV ventilator manufacturing readiness could be rapidly accelerated for the patient breathing circuit components in partnership with industry. However, the IPV alarm monitors were not ready for mass production due to the need to modernize the design that had been used by Percussionaire for two decades. Specifically, the computation functions of the IPV monitors were performed using an obsolete Windows CE™ computer module circuit board. This obsolete board also required external analogue-to-digital signal conditioning and communications interfacing. The



Fig. 5.59. The final ventilator product showing the user interface and knobs to control power, flow, PIP, and PEEP. The blue tubes are the air pathways to and from the patient. [Courtesy BioMedInnovations, LLC]

INL team integrated a total of five circuit boards into a single circuit board with a readily available open-source Unix computation module (Raspberry Pi) in mass quantities (see Fig. 5.60, this page). Software development continued to improve user interfacing and included elimination of membrane switches still present in the first prototype (see Fig. 5.61, p. 255). Following this prototyping activity, INL transferred the design to Percussionaire for production. At the close of the project, INL and Percussionaire expect to continue development and explore future collaborations under a Strategic Partnerships Project.

5.4.6 Development of Advanced Ventilation Techniques

LLNL and INL investigated alternative pathways for oxygenation, including improvements to extracorporeal membrane oxygenation (ECMO) systems and oxygenation through the gastrointestinal system. Use cases include COVID-19 patients with scarred lungs for whom ventilators would not be an effective treatment.

The team studied the oxygenation of PFCs, which can hold high concentrations of dissolved oxygen and are biocompatible, by initiating discussions with physicians and industry partners who identified the need for new membrane technologies for ECMO oxygenation of blood in parallel to adaptation of IPV ventilator technologies to enhance removal of mucous and reduce lung damage under ventilation.

The team also investigated the delivery of oxygen gas into the small intestine via diffusion across the wall of tubing material or direct delivery via intermittent bubbling. Comparisons of oxygen concentrations in PFCs and delivery rates of diffused oxygen versus oxygen gas revealed that oxygen gas delivered higher concentrations of oxygen at a faster rate than diffusion of oxygen across silicone tubing walls. Initial *ex vivo* porcine models show ready uptake of oxygen from the lumen of the small intestine. With introduction of oxygen, the tissue's oxygen saturation and coloration both show

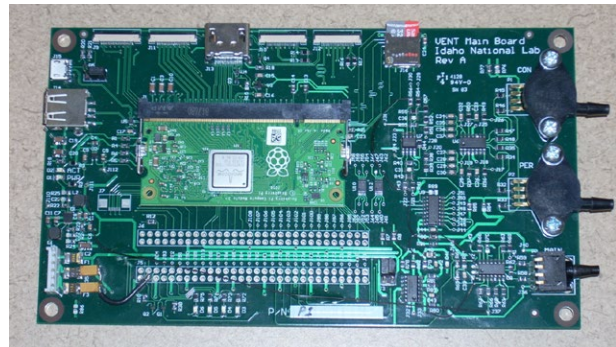


Fig. 5.60. Final prototype of the Idaho National Laboratory Wavetron computation, monitoring, and alarm board that replaced five printed circuit boards in legacy hardware. [Courtesy Idaho National Laboratory]

clear signs of improvement. Organ longevity issues and application of oxygen to the *ex vivo* model suggest an *in vivo* model is preferred to reliably quantify oxygen uptake and enhance survivability of patients failing on ventilators.

In parallel, the INL team began adapting IPV ventilation techniques to a liquid breathing circuit that could leverage PFCs to improve delivery of pharmaceuticals to the surfaces of the lungs while minimizing peak lung pressures experienced by patients with widely used volumetric ventilation (see Fig. 5.62, p. 255). Traditional volumetric ventilation was previously evaluated by the U.S. Navy and several industrial ventures with extension to liquid ventilation techniques. The team's evaluation revealed that volumetric ventilation required high flow rates for PFCs in the breathing circuit to successfully ventilate a subject. High flow rates reduced tolerance and caused discomfort in conscious patients, requiring use of general anesthesia. One challenge was removal of CO₂ from stagnant regions of the lungs. The team's evaluation of intrapulmonary percussive liquid ventilation (IPLV) sought to resolve this problem at low flow rates.

INL began developing IPLV hardware while LANL began extending modeling and simulation to the use of PFC with Percussionaire's Model TXP5

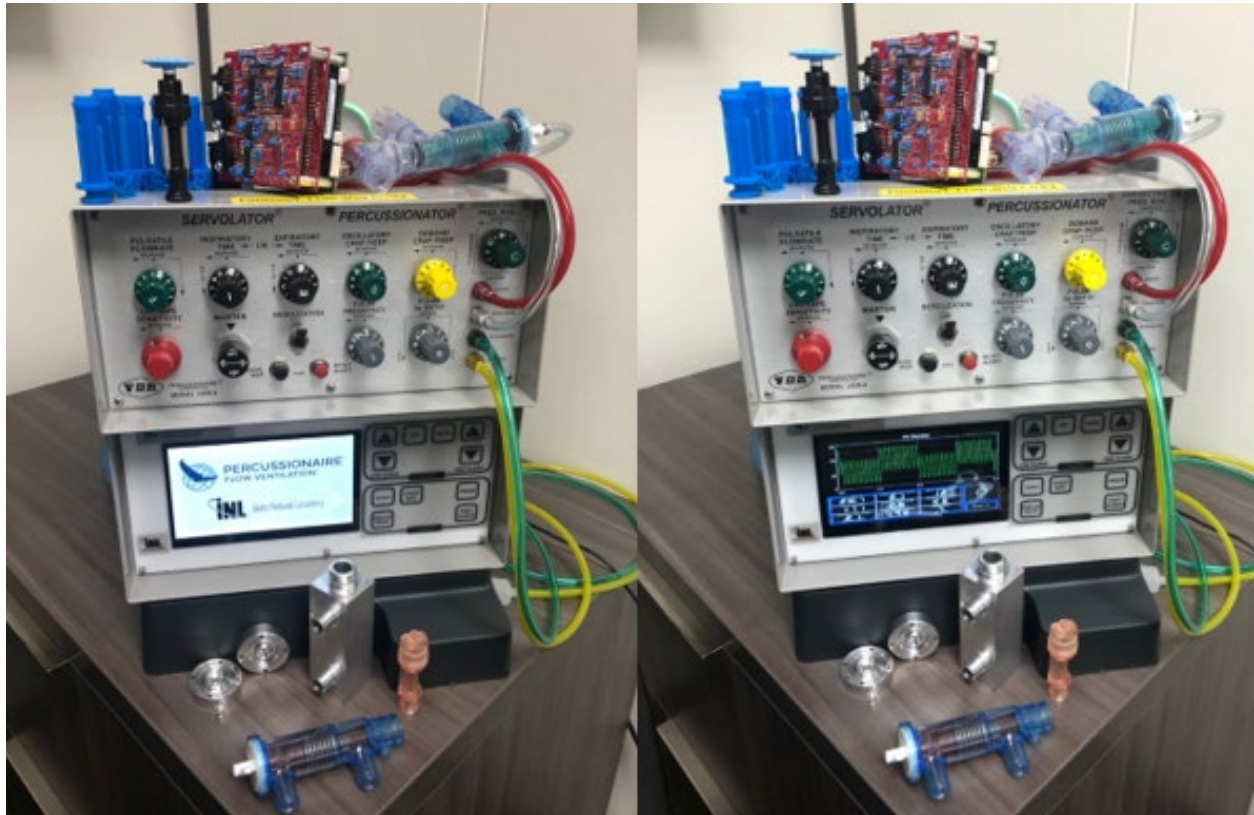


Fig. 5.61. Wavetron with prototype touch screen under Percussionaire VDR4 ventilator. Other components and molds shown. [Courtesy Idaho National Laboratory]

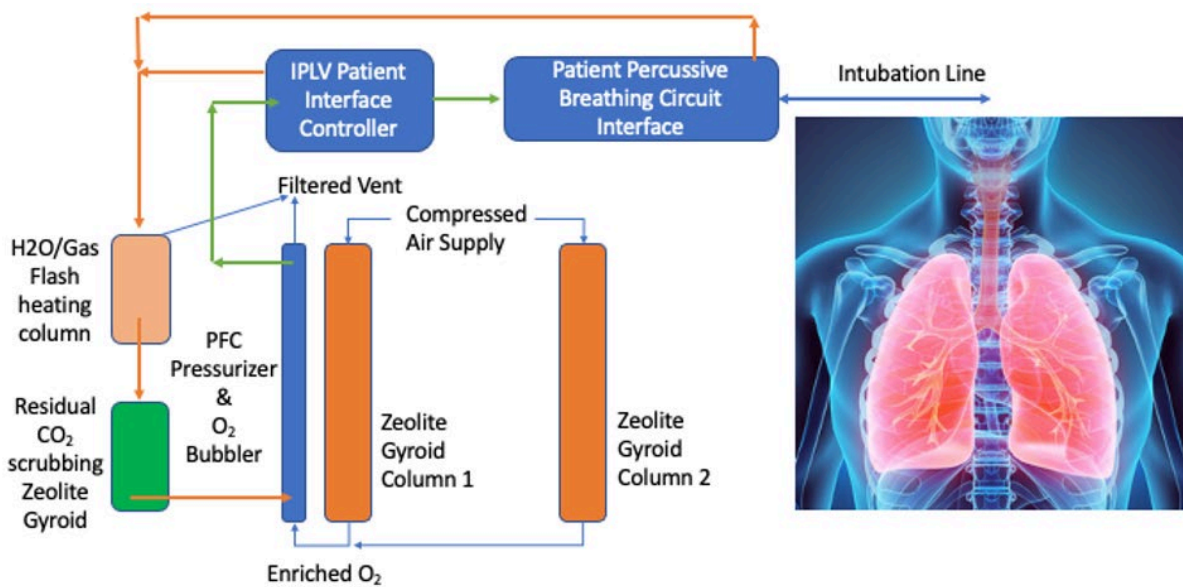


Fig. 5.62. Conceptual intrapulmonary percussive liquid ventilation (IPLV) system schematic. [Courtesy Idaho National Laboratory]

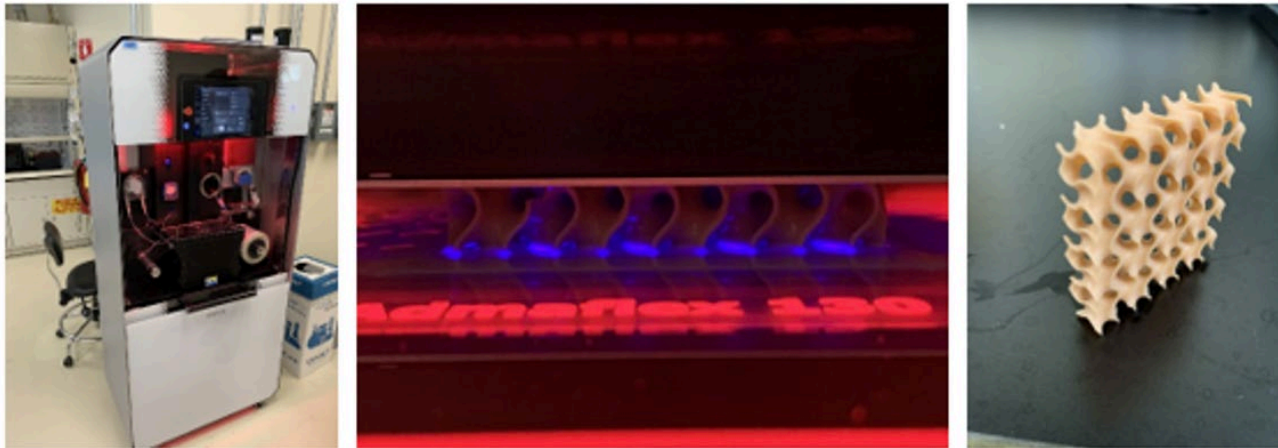


Fig. 5.63. Admaflex A130 digital light processing (DLP) ceramic printer (left), zeolite gyroid during printing (middle), and CO₂ scrubbing gyroid after printing (right). [Courtesy Idaho National Laboratory]

high frequency ventilator system to support the INL design and manufacturing of new venturi jets inside the IPV Phasitron patient interface. To oxygenate the PFC fluid and scrub CO₂ from the PFC within the breathing circuit, INL developed a gyroid structure of zeolite that would be stable under atmospheric conditions within the PFC fluid while being regenerable by application of heat. INL collaborated with Admatec and Lapmaster Wolters to deploy a prototype Digital Light Processing additive manufacturing system at INL to facilitate the development of this zeolite structure. The results of the manufacturing process were successful, leading to INL's application (BA-1269) for a provisional patent for zeolite manufacturing via this process (see Fig. 5.63, this page).

5.5 Task 3: Consumables

5.5.1 Overview

Early in the pandemic, the need for testing was extremely critical. In April 2020, the Manufacturing team was contacted by HHS. The White House had an initial target of 10 million tests per week that it soon raised to 20 million tests per week, with an ultimate goal of enabling every person in the U.S. to be tested at least once a month. This presented some significant supply chain challenges. First,

there was a shortage of nasal swabs and LLNL led an effort to develop and validate 3D-printed swabs. Second, there was a significant shortage of test tubes and ORNL, LLNL, and SNL collaborated to develop approaches to produce test tubes.

5.5.2 Printed Swabs

At the beginning of the COVID-19 pandemic, nationwide shortages surfaced in consumables used for testing. These shortages in the various components of viral testing kits, including nasopharyngeal swabs, were due to the simultaneous increase in demand and the decrease in supply, as temporary shutdowns of many production facilities reduced suppliers' production capabilities. To bridge the gap between the demand and supply of nasopharyngeal swabs, temporary alternative manufacturing methods and sources quickly turned to 3D printing. Ultimately, five different 3D-printed nasopharyngeal swabs were produced and sold to various hospitals and clinics for COVID-19 testing (Table 5.3, p. 257, and Fig. 5.64, p. 257). These printed swabs utilized several different printing processes, materials, and design methodologies for sample collection. Presented here is a framework for bench-testing nasopharyngeal swabs on mechanical and sample collection performance using standard and widely available material testing equipment. The aim was to develop quantitative

Table 5.3. Summary of the 3D-printed and traditional nasopharyngeal swabs commercially available for COVID-19 testing

| 3D-Printed Swab | Printing Process | Material | Design |
|-----------------------|--|-------------------------------|--------------------|
| Abiogenix FAST Spiral | HP Multi Jet Fusion | Polyamide 11 (Nylon) | Spiral |
| Formlabs–USF | Formlabs’ Stereolithography | Formlabs Surgical Grade Resin | Bulbous |
| Formlabs–Northwell | Formlabs’ Stereolithography | Formlabs Surgical Grade Resin | Bulbous with Holes |
| EnvisionTEC | EnvisionTEC’s Continuous Digital Light Manufacturing | E-Guide Soft C-29C Resin | Lattice |
| Resolution Medical | Carbon’s Digital Light Synthesis | KeySplint Soft Clear Resin | Lattice |
| Traditional Swabs | Printing Process | Material | Design |
| Fosun Pharma NP Swab | N/A | Nylon | Flocked |
| Copan FLOQSwab | N/A | Nylon | Flocked |

tests for nasopharyngeal swabs, covering the normal usage performance metrics and allowing for comparisons between the traditional and the newly manufactured 3D-printed swabs.

Testing

Both 3D-printed and traditional nasopharyngeal swabs were tested for mechanical performance, sample collection efficiency, and other preclinical metrics (summarized below and in Fig. 5.65, p. 258). The mechanical test protocols were designed to emulate the clinical use of the nasopharyngeal swabs and to evaluate potential failure modes. The effects of sterilization and shelf-aging on mechanical performance were also evaluated. Sample collection efficiency and other preclinical metrics were designed to ensure the swabs collected sufficient sample to test for the presence of the virus without injuring the patient (e.g., epistaxis).

Mechanical Performance

- Tensile – To mimic the worst-case scenario of the swab being caught on an obstruction upon being pulled from the nasopharyngeal space. The two ends of the swab were clamped between two pneumatic grips and pulled apart until the swab broke.

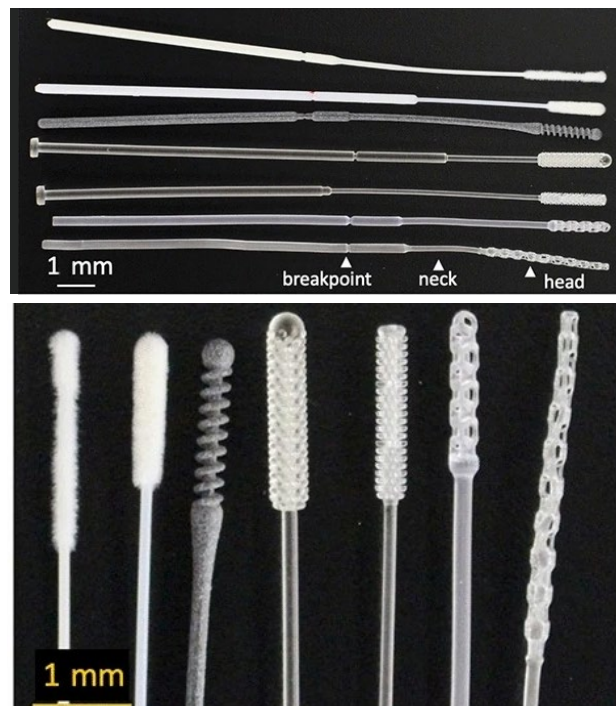


Fig. 5.64. Images of the traditional and 3D-printed nasopharyngeal swabs commercially available for COVID-19 testing. From top to bottom (top image) and left to right (bottom image): Fosun (traditional), Copan (traditional), Abiogenix (3D), Formlabs–USF (3D), Formlabs–Northwell (3D), EnvisionTEC (3D), and Resolution (3D). [Reprinted from Tooker, A., et al. Performance of Three-Dimensional Printed Nasopharyngeal Swabs for COVID-19 Testing *2021 MRS Bulletin* 46, 813–821. DOI: 10.1557/s43577-021-00170-9]

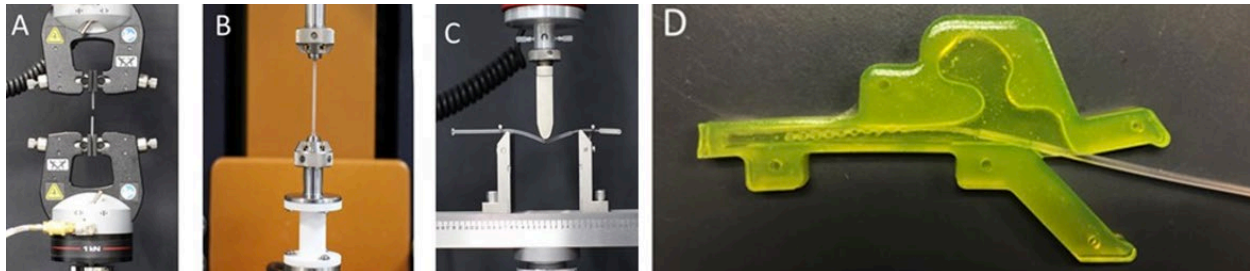


Fig. 5.65. Images of swabs in different test setups: (A) tensile, (B) torsion, (C) break, and (D) abrasion. A nasal cavity mold similar to that shown in (D) was 3D-printed and used for a combined torsion and flexure test. [Reprinted from Tooker, A., et al. Performance of Three-Dimensional Printed Nasopharyngeal Swabs for COVID-19 Testing *2021 MRS Bulletin* 46, 813–821. DOI: 10.1557/s43577-021-00170-9]

- Torsion — To mimic the worst-case scenario of the swab being caught on an obstruction upon being rotated within the nasopharyngeal space. The two ends of the swab were clamped between two grips and one end of the swab was held stationary while the other end was rotated in a counterclockwise direction until the swab broke.
- Combined torsion and flexure — To mimic the actual use case during swabbing. Swabs were flexed and inserted into a 3D-printed nasal cavity (filled with a mucus mimic) and twisted for 25 rotations.
- Flexure — To determine the flexibility of the joint between the head and neck of the swab. The head of the swab was clamped between pneumatic grips and a load was applied on the neck to flex it 90° at the joint between the head and the neck.
- Effect of sterilization and aging on mechanical performance — To evaluate the effects of sterilization on the mechanical performance of the swabs. Manufacturer-sterilized swabs or in-house sterilized swabs (within 6 hours of sterilization) were evaluated using the tensile test. For aging tests, in-house sterilized swabs only were stored for up to 7 days in unopened sterilization pouches prior to testing. Swabs were sterilized in-house, using protocols recommended by the manufacturer (see Table 5.4, p. 259).

Sample Collection

- Uptake/release — To quantify sample amount collected by the swabs, a simplified uptake/release test was performed. Swabs were first weighed prior to fully immersing the head of swab into a solution containing mucus mimic with FITC-labeled dextran as a tracer. Swabs were rotated clockwise for 15 seconds, quickly weighed, and then placed in Hank's Balanced Salt Solution (HBSS). Swabs were kept in solution for 2.5 hours and then vortexed vigorously. The amount of FITC-dextran released was measured.
- Viral RNA recovery — To determine the ability of swabs to retain and release viral samples, swabs were used to collect samples from virus-infected mucus mimic, as well as from virus-infected cells. Swabs were immersed in 1.5 mL mucus mimic spiked with 1×10^6 PFU murine coronavirus and rotated for 15 seconds. A second set of swab samples was used to swab a monolayer of virus-infected 17CL-1 mouse epithelial cells immersed in mucus mimic. Infected swabs were placed in a fresh tube containing 2mL of media and allowed to incubate at room temperature for 2.5 hours for the mucus mimic or overnight at 4°C for the infected cells. Viral RNA was eluted and quantitated in triplicate using a One Step PrimeScript RT-PCR Kit (Takara) and MHV nsp2 specific primers and probes using cycling conditions.

Table 5.4. Summary of Autoclave Sterilization Protocols

| | Description | Swabs Tested |
|-------------|--|---|
| Protocol #1 | 121°C for 30 minutes | Abiogenix Formlabs–USF Formlabs–Northwell EnvisionTEC. |
| Protocol #2 | 132°C for 4 minutes | Abiogenix Formlabs–USF Formlabs–Northwell |
| Protocol #3 | 132°C for 4 minutes, pre-vacuum sterilization with four preconditioning pulses and a 30-minute, 20inHg vacuum dry time with three pulses | Resolution |

- Abrasion – To determine the abrasiveness of the swabs, 3D nasal cavity tissue mimics were molded using agarose with FITC-dextran. Swabs were inserted into the 3D agarose nasal cavity and rotated clockwise for 15 seconds. Swabs were then immersed in HBSS and vigorously vortexed to allow for release of material scraped from nasal cavity. The amount of FITC-dextran released was measured.

Performance

A summary of the results for all tests performed is shown in Table 5.5, p. 260, and Table 5.6, p. 260.

Mechanical Performance

Understanding the mechanical performance is important for patient comfort as well as for safety (e.g., understanding break limits). All the 3D-printed swabs showed higher tensile strength (preferred) in both tensile tests than the traditional swabs. Similarly, all the 3D-printed swabs had higher torques to break (preferred) compared to traditional swabs in the both the torsion and the combined torsion and flexure tests, except for the Abiogenix and Resolution swabs, which did not perform significantly differently from the traditional swabs in the torsion test. It should be noted that although both Formlabs swabs designs had higher torque loads compared to traditional swabs in the torsion tests, they shattered into pieces

upon breaking, which is an undesirable outcome. Although the 3D-printed swabs were stronger than the traditional swabs, they were less flexible and showed higher loads to flex than the traditional swabs. Despite increased loads to flex, none of the swabs broke during this testing.

Abiogenix, Formlabs, and EnvisionTEC swabs showed statistically significant differences in tensile strength before and after autoclave sterilization, although for EnvisionTEC, there were significant differences only in swabs sterilized in the laboratory but not for those sterilized by the manufacturer. The type of autoclave sterilization protocol also resulted in significant differences for both Abiogenix and Formlabs swabs. For all the 3D-printed swabs, except for the Resolution swabs, there were significant differences in tensile strength after aging. For Abiogenix, Formlabs, and EnvisionTEC the interaction between sterilization protocol and aging was significant, indicating that the samples tended to be more susceptible to aging when autoclaved. Nonetheless, shelf-life stability is indicated to play a role in tensile strength for post-sterilization.

Sample Collection

For the uptake/release test, larger uptake and release amounts are preferred to ensure sufficient material is available for PCR viral testing. Given the difference in head designs and materials, we

Table 5.5. Summary of the testing results for the 3D-printed nasopharyngeal swabs, with a comparison to the traditional swabs

| Test | Fosun | Copan | Abiogenix | Formlabs-USF | Formlabs-Northwell | Envision TEC | Resolution |
|--|-------------|-----------------|---------------|---------------|--------------------|---------------|--------------|
| Tensile (N) | 41±4.8# | 33±2.4* | 76±8.6*# | 103±2.4*# | 74±1.2*# | 62±5.0*# | 56±4.7# |
| Torsion (mN*m) | 11±0.8 | N/A | 24±4.3 | 47±3.9* | 25±2.4* | 24±2.5* | 23±1.6 |
| Combined Torsion and Flexure (mN*m) | 2±0.2# | 4±0.7* | 6±1.1* | 10±1.2*# | 7±1.2*# | 9±1.6*# | 8±0.7*# |
| Flexure (N) | 0.6±0.2 | 0.7±0.1 | 4.5±0.9*# | 3.0±0.2*# | 1.4±0.1*# | 2.0±0.1*# | 2.8±0.4*# |
| Uptake (mg) | 104±7.0# | 118±3.9* | 60±1.1*# | 62±4.8*# | 59±4.2*# | 50±5.4*# | 84±3.2*# |
| Release FITC-Dextran (mg/mL) | 0.067±0.004 | 0.081±0.005 | 0.035±0.004*# | 0.043±0.010*# | 0.033±0.004*# | 0.027±0.006*# | 0.054±0.003# |
| RNA Extracted from virus-spiked solution (Ct values) | 31±0.9 | NA | 31±0.2 | 30±0.3 | 31±0.7 | 31±0.1 | 31±0.1 |
| RNA Extracted from virus-infected cells (Ct values) | 30±1.5 | N/A | 35±1.3* | 36±1.3* | 33±2.1 | 31±1.1 | 32±0.5 |
| Abrasion (Normalized Fluorescence) | 1.0±0.3 | 1.0±0.4 | 2.1±0.5*# | 1.8±0.9*# | 0.6±0.4 | 1.4±0.5 | 0.7±0.2 |
| Not Ideal | | Standard | | | Improved | | |

* Significant from Fosun; # Significant from Copan

Table 5.6. Summary of the tensile strengths measured before and after sterilization, for different sterilization protocols, and after aging[†]

| | Pre-Sterilization | Post-Sterilization | After Aging * |
|--------------------|-------------------|---|----------------------------|
| Abiogenix | 69±2.2 | AP#1: 67±1.7, AP#2: 62±2.7 | AP#1: 65±2.2, AP#2: 71±2.8 |
| Formlabs-USF | Not Tested | AP#1: 106±4.0, AP#2: 101±2.8 | AP#2: 122±5.2 |
| Formlabs-Northwell | 94±1.3 | AP#1: 80±2.3 AP#2: 66±2.2 | AP#1: 87±5.3 |
| EnvisionTEC | 58±2.5 | AP#1: 51± 2.6 AP#1: 62±5.0 [^] | AP#1: 59±4.4 |
| Resolution | Not Tested | AP#3: 50±2.3 AP#3: 56±4.7 [^] | AP#3: 50±3.0 |

[†] All data are reported in Newtons. Bold font is used to indicate significant difference from pre-sterilized or unaged sterilized samples.

* Swabs were aged for 7 days, except for the Resolution Medical, which were aged 5 days.

[^] Sterilized by the manufacturer.

first tested the contribution of the printed material alone to attract the mucus mimic-FITC-dextran solution. No differences were noted between the different materials, suggesting that fluid uptake in subsequent studies could largely be attributed to swab design. Although traditional swabs took up more material compared to any 3D-printed swabs, the total amount of FITC-dextran released from the Fosun swab was not significantly different than that from the Resolution swab.

While uptake/release data in these tests provide a straightforward quantification across swab designs, more critical is how these results translate to virus collected and RNA extracted. Swabs were tested by either immersing in a virus-spiked mucus mimic or swabbing virus-infected cells and then subjecting to RNA isolation and quantitative RT-PCR. To measure viral load in RT-PCR, the cycle threshold (Ct) value is used to indicate the cycle number at which the signal exceeds background level. Ct values showed no significant difference between the amount of RNA recovered from 3D-printed swabs immersed in virus-spiked mucus mimic as compared to traditional swabs.

Interestingly, in the test case where swabs sampled a monolayer of virus-infected cells, mimicking collection of cells from the nasopharynx during clinical swabbing, RNA amounts recovered from the Formlabs–USF and Abiogenix swabs differed significantly from traditional swabs. Clinical nasal swab specimens consist of both fluid and cells, so it was important to compare RNA recovery from virus-infected cells in addition to virus-spiked mucus mimic. Despite differences observed in some of the 3D-printed swab designs, ultimately the critical question is whether enough material is collected to qualify as a positive test. Ct values used to conclude a positive test vary among different tests since there is no standardization for Ct values across existing RT-PCR platforms, but typically high viral titers are associated with Ct values in the low 30s/high 20s. It is likely that the two printed swabs found to recover significantly different amounts of RNA compared to

traditional swabs may still be suitable for viral capture and RNA extraction.

Although abrasive swabbing is likely to access deep layers of the mucosal barrier, excessive abrasiveness can cause injury to patients (e.g., epistaxis) and must be considered when designing swabs. Except for Abiogenix and Formlabs–USF, the 3D-printed swabs were not significantly different in abrasiveness compared to traditional swabs. These two printed swabs also had the widest heads, and it is likely that this increased the chances of contact and scraping with tissue mimic nasal cavity walls. In addition to head diameter and possibly head design, flexibility of the swabs was noted to influence contact with the nasal cavity wall where less flexible swabs pushed the swab’s head up against the wall. The Abiogenix and Formlabs–USF swabs were less flexible in the flexure test than the other 3D-printed and traditional swabs and this likely also contributed to the increased abrasiveness. Interestingly, abrasiveness for these two designs was inversely related to swab RNA recovery from the swabbed cell monolayers.

The goal in this work was to provide a comprehensive, quantitative set of pre-clinical testing methods for nasopharyngeal swabs, covering the normal usage performance metrics, to glean a better understanding of where improvements are needed. Critical to the function of swabs is their ability to collect sufficient sample for RNA extraction with minimal patient discomfort and without breaking during sample collection. The tensile, torsion, and flexure testing protocols outlined here can be used to assess whether the swabs will break during sample collection. Together, the flexure and abrasion testing protocols can be used as metrics toward predicting patient comfort; however, there are no metrics or standards at this time to suggest “x amount of flexibility” or “y amount of abrasiveness” are required for maximal patient comfort. Additional studies are needed to more closely link flexibility and abrasiveness with patient comfort. In summary, no single 3D-printed swab performed exactly as traditional swabs and such results were

expected based on the differences in design and materials. In most of the mechanical testing presented here, the 3D-printed swabs demonstrated increased strength; however, this came at the cost of swab flexibility, which may influence patient comfort, as suggested by the abrasion results. However, regarding their primary function to collect sufficient samples for RNA extraction, 3D-printed swabs performed similarly to traditional swabs.

5.5.3 Coke Bottle Preforms

An early proposed solution to address the shortage of test tubes was to use Coke bottle preforms as an alternate source (see Fig. 5.66, this page). More than 10 million test tubes were needed rapidly. Coca-Cola sells approximately 1.7 billion bottles of soda every day. When the pandemic started to accelerate and companies began working from home, the sale of Coca-Cola products dropped 28% (a net reduction of 476 million bottles per day)⁹, leaving a more than ample supply of preforms for potential use in test kits. ORNL and SNL explored sterilization processes and shared the results with five different testing facilities. Many testing manufacturers had automation equipment that did not accept the standard Coke bottle preforms. One company, Longhorn Therapeutics, tested the preforms and found them ideal for their needs. The prototypes were received safely to the molecular lab in San Antonio. Testing included addition of 2.0 mL PrimeStore Molecular Transport Media (MTM) to tubes followed by upside down centrifugation at maximum speed (12,000 rpm) wrapped in Kimwipes for 10 minutes to check for leaks; all tubes passed. Similarly, the tubes were shaken on their side and upside down to maximum speed vortex for 10 minutes at Longhorn Therapeutics; no leaks were observed and all tubes passed. Tubes with PrimeStore MTM, and later ethanol, were placed into boiling water to evaluate volume loss; full volume was retained and all tubes passed.

⁹ Maloney, J. "Coca-Cola Sales Fall 28%, but It Says the Worst Is Over." *The Wall Street Journal*, 21 July 2020. <https://www.wsj.com/articles/coca-cola-sales-fall-28-with-fewer-products-sold-at-bars-restaurants-11595332395>

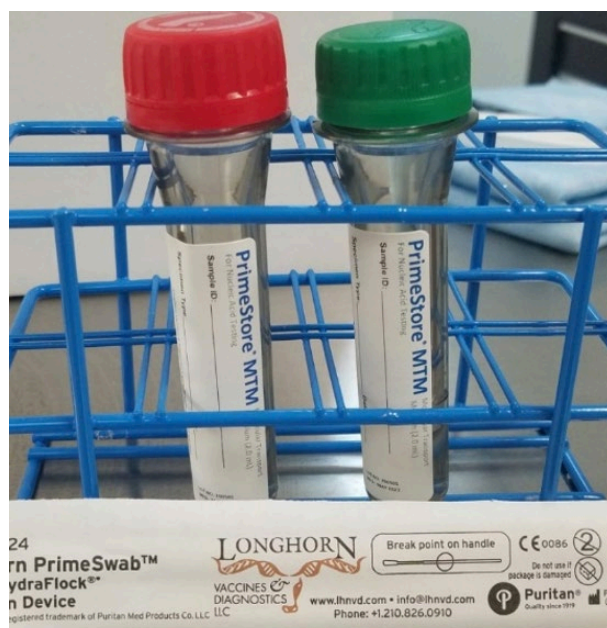


Fig. 5.66. Coke bottle preforms in racks. [Courtesy Oak Ridge National Laboratory]

Tubes containing 2.0 mL PrimeStore were dropped from a fire escape at two stories height onto pavement; no tubes broke or were observed to leak.

Testing revealed several beneficial features of the Coke bottle preforms as potential test tubes:

- In contrast to many cryotube types, the tubes do not leak PrimeStore.
- In contrast to 2.0, 3.0, and 4.0 mL cryotubes, the height of preforms (~110 mm) is optimal. The preforms easily hold the swab head breakpoints for any collection device/swab (oral or nasopharyngeal). This includes the longer nasal swab with breakpoints at 100 mm.
- In contrast to all cryotubes, the inner diameter of the tube is wide enough to accommodate the shafts of all micropipettor sizes (P10, P100, P200, and P1000), enabling laboratory personnel to easily pipette the collected samples during processing.
- The cap seats perfectly on the tube and makes a small sound to indicate when it is properly sealed. This is critical for manual kits.

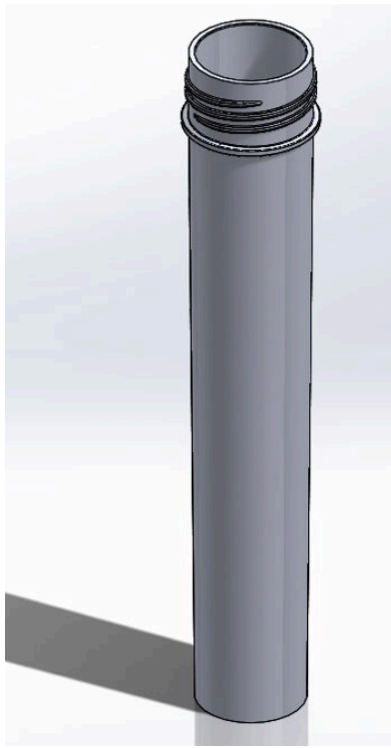


Fig. 5.67. Thermo Fisher test tube. [Courtesy Oak Ridge National Laboratory]

- The team especially liked the tamper-proof seal (inherent to every Coke bottle). This offers assurance that each tube is intact and unused until opened.

On May 1, 2020, ORNL, HHS, Coca-Cola, and Longhorn discussed next steps after testing was completed. Longhorn expressed its desire to use the Coke bottle preforms. In less than 48 hours, Coca-Cola made its first delivery of two million preforms to Longhorn.

5.5.4 Thermo Fisher Test Tubes

Thermo Fisher Scientific was one of the companies in discussions with HHS and the Manufacturing team regarding consumables for test kits. To help scale and accelerate testing results, Thermo Fisher had developed automated sampling systems that could emplace test tubes, remove caps, and extract samples for testing. However, the Coke bottle

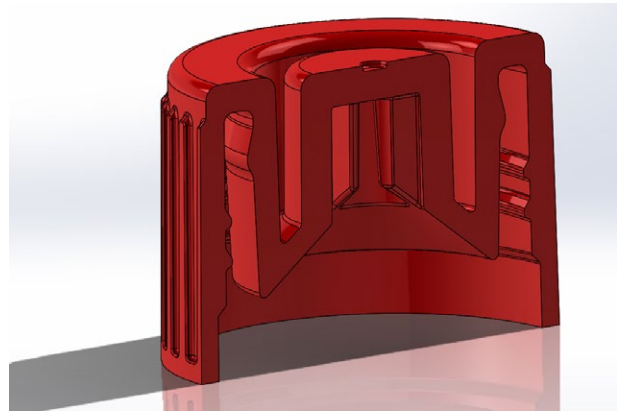


Fig. 5.68. Thermo Fisher cap cross section. [Courtesy Oak Ridge National Laboratory]

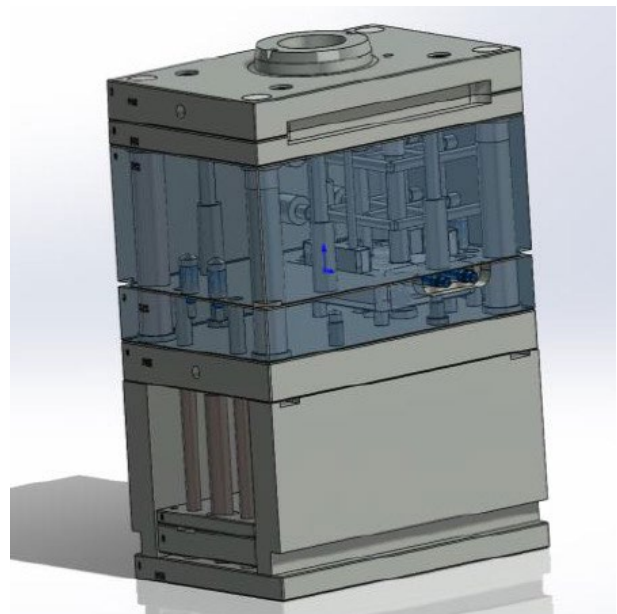


Fig. 5.69. Model of a Thermo Fisher test tube mold. [Courtesy Oak Ridge National Laboratory]

preforms were slightly larger in diameter than the Thermo Fisher equipment, preventing the company from leveraging the preform supply chain.

LLNL and ORNL worked with engineers at Thermo Fisher on a new test tube design. The tube and cap (see Fig. 5.67 and 5.68, this page) were designed to enable automatic capture of the swab and retention of the swab in the cap when it is removed so



Fig. 5.70. Two-cavity injection mold. [Courtesy Oak Ridge National Laboratory]

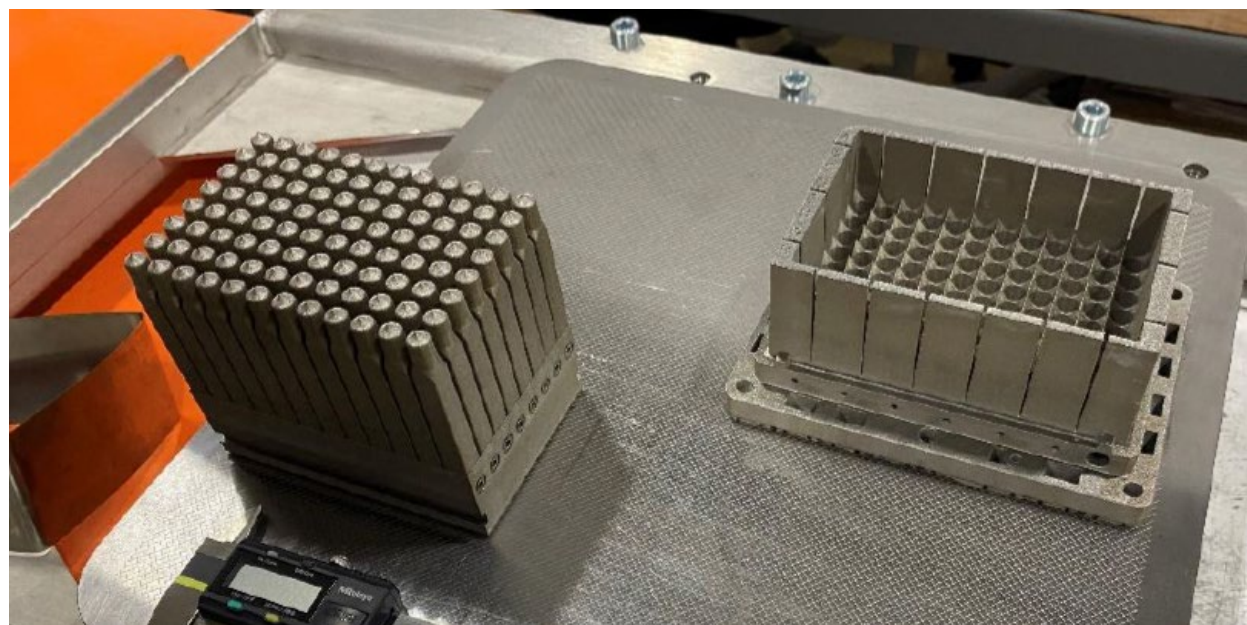


Fig. 5.71. ORNL 3D-printed tooling for Thermo Fisher Kingfisher 96-well plate. [Courtesy Oak Ridge National Laboratory]

that media samples can be automatically extracted from the test tube. LLNL used its rapid prototyping facility to manufacture different designs to test the form, fit, and function of the swab within the test tube and the test tube within the automation equipment. Once a design (see Fig. 5.69, p. 263) was refined and finalized, ORNL designed and used its metal additive manufacturing equipment to rapidly manufacture injection mold tooling (see Fig. 5.70, p. 264). The first tool could produce approximately 10,000 test tubes and caps per day. ORNL provided Thermo Fisher with 10,000 tubes to test and evaluate.

When the process passed acceptance testing (automation, viral transport, etc.), ORNL provided the tool as well as the injection mold tool design to Thermo Fisher to replicate. The original tool had two cavities for two test tubes and caps to be manufactured every cycle (approximately 5 seconds)

on a standard injection molding machine. By late summer, Thermo Fisher had won a \$381 million contract with the U.S. government, built a \$40 million mold production factory in Lenexa, Kan., and created over 300 new manufacturing jobs.

5.5.5 Thermo Fisher 96-Well Plates

Another consumable shortage was the supply of 96-well plates. Once media is extracted from the test tubes, it is placed in 96-well plates for processing. There was a need for hundreds of thousands of these plates every day. The inner geometry of the wells is very complex with tight tolerances. Following the same process that was used for the test tubes, LLNL used its rapid prototyping capabilities to demonstrate the viability of 3D printing the plates. ORNL used its metal additive manufacturing capability to manufacture injection mold tooling (see Fig. 5.71, p. 264). and produce the 3D-printed 96-well plates.

5.6 Publications and Research Output

Publications

DeAngelis, H. E.; Grillet, A. M.; Nemer, M. B.; Wasiolek, M. A.; Hanson, D. J.; Omana, M. A.; Sanchez, A. L.; Vehar, D. W.; Thelen, P. M. Gamma Radiation Sterilization of N95 Respirators Leads to Decreased Respirator Performance. *PLoS One* **2021**, *16* (4), e0248859. DOI: 10.1371/journal.pone.0248859

Kuhne, W. W.; Langan, C. J.; Burckhalter, C. E.; Turick, C. E.; Bobbitt III, J. T.; Villa-Aleman, E. Inactivation of Bioaerosols by Plasma Field Generated Using A Single Wire DC Corona Discharge. Manuscript submitted.

Larsen, G. S.; Cheng, Y.; Daemen, L. L.; Lamichhane, T. N.; Hensley, D. K.; Hong, K.; Meyer, H. M.; Monaco, S. J.; Levine, A. M.; Lee, R. J.; Betters, E.; Sitzlar, K.; Heineman, J.; West, J.; Lloyd, P.; Kunc, V.; Love, L.; Theodore, M.; Paranthaman, M. P. Polymer, Additives, and Processing Effects on N95 Filter Performance. *ACS Appl. Polym. Mater.* **2021**, *3* (2), 1022–1031. DOI: 10.1021/acsp.0c01294

Nikitin, V.; Andrade, V. D.; Slyamov, A.; Gould, B. J.; Zhang, Y.; Sampathkumar, V.; Kasthuri, N.; Gürsoy, D.; De Carlo, D. Distributed Optimization for Nonrigid Nano-Tomography. *IEEE Transactions on Computational Imaging* **2021**, *7*, 272–287. DOI: 10.1109/TCI.2021.3060915

Paranthaman, M.P.; Peroutka-Bigus, N.; Larsen, K. R.; Phadke, K. S.; Summers, T.; Theodore, M.; Hensley, D. K.; Levine, A. M.; Lee, R. J.; Bellaire, B. H. Effective Antiviral Coatings for Deactivating SARS-CoV-2 Virus and South African Variants on N95 Masks or Filters. Manuscript in preparation.

Wang, P. L.; Roschli, A.; Paranthaman, M. P.; Theodore, M.; Cramer, C. L.; Zangmeister, C.; Zhang, Y.; Urban, J. J.; Love, L. Recent Developments in Filtration Media and Respirator Technology in Response to COVID-19. *MRS Bull.* **2021**, *46*, 822–831. DOI: 10.1557/s43577-021-00173-6

Presentations

Love, L.; O'Brien, R.; Spadaccini, C. Testimony to the House Committee on Science, Space, and Technology: NVBL Manufacturing Team's Progress on PPE, Ventilators, and Consumables.

Zhang, Y.; Lee, B.; Powers, D.; Yang, P.; Dahl, E.; Seong, H. J. Scalable Synthesis of Nanofibers for Energy Storage and Filtration Applications. 2021 TMS Annual Meeting and Exhibition, March 2021.

Patents

Zhang, Y.; Powers, D. J.; Pupek, K. Z.; Hryn, J. N.; Krumdick, G. K.; Chaudhuri, S. Nanofiber Filter Medium for Reusable Facemask and Filtering Facepiece Respirator. ANL IN-20-055.

Media Mentions

Boetel, R. Sandia seeks patent, business partners for new N95 masks. *Albuquerque Journal*, April 17, 2021. <https://www.abqjournal.com/2381360/sandia-seeks-patent-business-partners-for-new-n95-masks.html>

Boetel, R. Sandia seeks patent, business partners for new N95 masks. *Yahoo! Finance*, April 18, 2021. <https://finance.yahoo.com/news/sandia-seeks-patent-business-partners-140500543.html>

Crotti, N. Sandia Labs seeks partners to make reusable masks. *Medical Design & Outsourcing*, April 8, 2021. <https://www.medicaldesignandoutsourcing.com/sandia-labs-seeks-partners-to-make-reusable-masks/>

Crotti, N. Sandia Labs seeks partners to make reusable masks. *MassDevice Medical Network*, April 8, 2021. <https://www.massdevice.com/sandia-labs-seeks-partners-to-make-reusable-masks/>

Hall, H. Reusable respirator could ease COVID-19 medical mask shortages. *R&D World*, April 2, 2021. <https://www.rdworldonline.com/reusable-respirator-could-ease-covid-19-medical-mask-shortages/>

Hede, K. COVID-19 Pandemic Sparks 3-D Printing Engineering Innovation. *Pacific Northwest National Laboratory News and Media*, November 2, 2020. <https://www.pnnl.gov/news-media/covid-19-pandemic-sparks-3d-printing-engineering-innovation> (accessed 2022-04-25).

Krabbe, C. Sandia National Laboratories seeks manufacturing partner for new medical device. *Albuquerque Business First*, April 6, 2021. <https://www.bizjournals.com/albuquerque/news/2021/04/06/sandia-labs-looks-to-license-new-mask-design.html>

KRQE Staff. Sandia Labs Reusable Respirator: Replaces N95 Masks. *KOAT Action 7 News (Albuquerque, New Mexico)*, April 1, 2021.

KRQE Staff. Sandia National Labs seek patent for reusable respirators. *KRQE News 13 (Albuquerque, New Mexico)*, April 1, 2021. <https://www.krqe.com/health/coronavirus-new-mexico/sandia-national-labs-look-for-reusable-respirators/> (accessed 2022-05-03).

SMH News. YouTube, July 21, 2021. Sarasota Memorial Hospital Expands 3D Printing during COVID-19 Pandemic and Beyond. <https://www.youtube.com/watch?v=rRnSW7Aohw4&t=119s> (accessed 2022-05-03).

Appendix A

Research Team

Chapter 1: Molecular Design for COVID-19 Therapeutics

Paul Adams*Lawrence Berkeley National Laboratory***Nanda Aduri***SLAC National Accelerator Laboratory***Chase Akins***Argonne National Laboratory***Jonathan Allen***Lawrence Livermore National Laboratory***Marc Alvarez***Los Alamos National Laboratory***Lindsey Anderson***Pacific Northwest National Laboratory***Babak Andi***Brookhaven National Laboratory***Gyorgy Babnigg***Argonne National Laboratory***Yadu Babuji***Argonne National Laboratory***Alexander Batyuk***SLAC National Accelerator Laboratory***Kellon Belfon***Stony Brook University***Debsindhu Bhowmik***Oak Ridge National Laboratory***Benjamin Blaiszik***Argonne National Laboratory***Swen Boehm***Oak Ridge National Laboratory***Peter Bonnesen***Oak Ridge National Laboratory***Jim Brase***Lawrence Livermore National Laboratory***Tom Brettin***Argonne National Laboratory***James Brown***Lawrence Berkeley National Laboratory***Garry Buchko***Pacific Northwest National Laboratory***Seth Carbon***Lawrence Berkeley National Laboratory***Kyle Chard***University of Chicago***Ryan Chard***Argonne National Laboratory***Andrew Chen***Lawrence Berkeley National Laboratory***Julian Chen***Los Alamos National Laboratory***Samuel Chen***Brookhaven National Laboratory***Wah Chiu***SLAC National Accelerator Laboratory***Nicholas Choma***Lawrence Berkeley National Laboratory***Austin Clyde***Argonne National Laboratory***Leighton Coates***Oak Ridge National Laboratory***Matthew (Matt) Coleman***Lawrence Livermore National Laboratory***Connor Cooper***Oak Ridge National Laboratory***Abbigayle (Abby) Cuomo***Stony Brook University***Andy DeGiovanni***Lawrence Berkeley National Laboratory***Thomas Desautels***Lawrence Livermore National Laboratory***Emily Dietrich***Argonne National Laboratory***Peng Ding***Argonne National Laboratory***Mitchel Doktycz***Oak Ridge National Laboratory*

Xiaotian Duan*University of Chicago***Chris Ellis***Oak Ridge National Laboratory***Aidan Epstein***Lawrence Livermore National Laboratory***Daniel Faissol***Lawrence Livermore National Laboratory***Lucy Fallon***Stony Brook University***Yichong Fan***Oak Ridge National Laboratory***Song Feng***Pacific Northwest National Laboratory***William Fischer***Los Alamos National Laboratory***Nicholas (Nick) Fischer***Lawrence Livermore National Laboratory***Ian Foster***Argonne National Laboratory***Magdalena (Magda) Franco***Lawrence Livermore National Laboratory***Stephanie Galanie***Oak Ridge National Laboratory***Carlos Gamboa***Brookhaven National Laboratory***Umamaheswari Ganapathy***Brookhaven National Laboratory***Cornelius Gati***SLAC National Accelerator Laboratory***Sandrasegaram Gnanakaran***Los Alamos National Laboratory***Jose Guerra***Stony Brook University***Mikhail Hameedi***SLAC National Accelerator Laboratory***Brooke Harmon***Sandia National Laboratories***Nomi Harris***Lawrence Berkeley National Laboratory***Darin Hauner***Pacific Northwest National Laboratory***Stewart He***Lawrence Livermore National Laboratory***Martha (Marti) Head***Oak Ridge National Laboratory***Dean Hidas***Brookhaven National Laboratory***Elijah Hoffman***Lawrence Berkeley National Laboratory***Kunlun Hong***Oak Ridge National Laboratory***Zhi Hong***University of Chicago***Naoki Horikoshi***SLAC National Accelerator Laboratory***Kim Hoshin***Pacific Northwest National Laboratory***Mark Hunter***SLAC National Accelerator Laboratory***Stephan Irlle***Oak Ridge National Laboratory***Srinivas Iyer***Los Alamos National Laboratory***Daniel Jacobson***Oak Ridge National Laboratory***Rhema James***Pacific Northwest National Laboratory***Songhao Jiang***Argonne National Laboratory***Marcin Joachimiak***Lawrence Berkeley National Laboratory***Jessica Johnson***Argonne National Laboratory***Rajendra Joshi***Pacific Northwest National Laboratory***Ai Kagawa***Brookhaven National Laboratory***Richard Keith***Lawrence Berkeley National Laboratory***Michael Kent***Sandia National Laboratories***Vilmos Kertesz***Oak Ridge National Laboratory***Kerstin Kleese van Dam***Brookhaven National Laboratory***Daniel Kneller***Oak Ridge National Laboratory*

Bette Korber
Los Alamos National Laboratory

Andrii Kovalevskyi
Oak Ridge National Laboratory

Kristen (Kris) Kulp
Lawrence Livermore National Laboratory

Neeraj Kumar
Pacific Northwest National Laboratory

Audrey Labbé
Oak Ridge National Laboratory

Joshua Ladau
Lawrence Berkeley National Laboratory

Edmond Lau
Lawrence Livermore National Laboratory

Joseph Laureanti
Pacific Northwest National Laboratory

Wellington Leite
Oak Ridge National Laboratory

Zhouzhao Li
University of Chicago

Felice Lightstone
Lawrence Livermore National Laboratory

Xuefeng Liu
Argonne National Laboratory

Heng Ma
Argonne National Laboratory

Carla Mann
Argonne National Laboratory

Irimpan Mathews
SLAC National Accelerator Laboratory

Stefan Maxwell
Sandia National Laboratories

Sean McCorkle
Brookhaven National Laboratory

Jason McDermott
Pacific Northwest National Laboratory

Kevin McLoughlin
Lawrence Livermore National Laboratory

Sean McSweeney
Brookhaven National Laboratory

Ryszard Michalczyk
Los Alamos National Laboratory

Chris Mungall
Lawrence Berkeley National Laboratory

Daniel Murphy-Olson
Argonne National Laboratory

Oscar Negrete
Sandia National Laboratories

Peter Nugent
Lawrence Berkeley National Laboratory

Carlos Olivares-Reboredo
University of Chicago

Hugh O'Neill
Oak Ridge National Laboratory

Swati Pant
Oak Ridge National Laboratory

Jerry Parks
Oak Ridge National Laboratory

Alexander Partin
Argonne National Laboratory

Jose Pereira
Lawrence Berkeley National Laboratory

Gwendalyn Phillips
Oak Ridge National Laboratory

Sai Venkatesh Pingali
Oak Ridge National Laboratory

Martin Purschke
Brookhaven National Laboratory

Emily Purvine
Pacific Northwest National Laboratory

Shuo Qian
Oak Ridge National Laboratory

Xiaohui Qu
Brookhaven National Laboratory

Lauren Raguette
Stony Brook University

Maksim Rakitin
Brookhaven National Laboratory

Arvind Ramanathan
Argonne National Laboratory

Simone Raugei
Pacific Northwest National Laboratory

Justin Reese
Lawrence Berkeley National Laboratory

Yihui Ren
Brookhaven National Laboratory

Andria Rodrigues
Lawrence Berkeley National Laboratory

Nickolaus Saint*Argonne National Laboratory***Kenneth Sale***Sandia National Laboratories***Brian Sanders***Oak Ridge National Laboratory***Anthony Savushkin***Argonne National Laboratory***Jürgen Schmidt***Los Alamos National Laboratory***Joe Schoeniger***Sandia National Laboratories***Ashka Sha***University of Chicago***Carlos Simmerling***Stony Brook University***Suhas Somnath***Oak Ridge National Laboratory***Chris Stanley***Oak Ridge National Laboratory***Darya (Dasha) Stepanenko***Stony Brook University***Rick Stevens***Argonne National Laboratory***Jacob Sumner***Oak Ridge National Laboratory***Li Tan***Brookhaven National Laboratory***Oleg Tchoubar***Brookhaven National Laboratory***Marisa Torres***Lawrence Livermore National Laboratory***Anda Trifan***Argonne National Laboratory***Deepak Unni***Lawrence Berkeley National Laboratory***Hubertus van Dam***Brookhaven National Laboratory***Van Vuong***Oak Ridge National Laboratory***Rick Wagner***University of California San Diego***Soichi Wakatsuki***SLAC National Accelerator Laboratory***Yuzhang Wang***Stony Brook University***Logan Ward***Argonne National Laboratory***Katrina Waters***Pacific Northwest National Laboratory***Amber Webb***Oak Ridge National Laboratory***Bobbie-Jo Webb-Robertson***Pacific Northwest National Laboratory***Kevin Weiss***Oak Ridge National Laboratory***Kelly Williams***Sandia National Laboratories***Sergio Wong***Lawrence Livermore National Laboratory***Yulun Wu***Lawrence Berkeley National Laboratory***Yue Yang***Lawrence Livermore National Laboratory***Hyunseung Yoo***Argonne National Laboratory***Qiu Zhang***Oak Ridge National Laboratory***Mowei Zhou***Pacific Northwest National Laboratory***Fangqiang Zhu***Lawrence Livermore National Laboratory***Ying Zhu***Pacific Northwest National Laboratory*

Chapter 2: COVID-19 Testing

Rebecca Abergel*Lawrence Berkeley National Laboratory***Paul Adams***Lawrence Berkeley National Laboratory***Dion Antonopoulos***Argonne National Laboratory***Gyorgy Babnigg***Argonne National Laboratory***Scott Baker***Pacific Northwest National Laboratory***Daniel Bedinger***Carterra*

Monica Borucki
Lawrence Livermore National Laboratory

Steven B. Bradfute
University of New Mexico

Thomas Bunt
Lawrence Livermore National Laboratory

Chris Daum
Lawrence Livermore National Laboratory

Patrick Fitch
Los Alamos National Laboratory

Vince Gerbasi
Pacific Northwest National Laboratory

Paul Gilna
Oak Ridge National Laboratory

David Graham
Oak Ridge National Laboratory

Michael Guarnieri
National Renewable Energy Laboratory

Sally Hall
Lawrence Livermore National Laboratory

Nathan Hillson
Lawrence Berkeley National Laboratory

Elizabeth Hong-Geller
Los Alamos National Laboratory

Greg Hura
Lawrence Berkeley National Laboratory

Crystal Jaing
Lawrence Livermore National Laboratory

Ramesh Jha
Los Alamos National Laboratory

Andrzej Joachimiak
Argonne National Laboratory

Bishoy Kamel
Lawrence Berkeley National Laboratory

Jeff Kimbrel
Lawrence Livermore National Laboratory

Antonietta M. Lillo
Los Alamos National Laboratory

Betty Mangadu
Sandia National Laboratories

Robert Meagher
Sandia National Laboratories

Joseph Moon
Lawrence Livermore National Laboratory

Nigel Mouncey
Lawrence Berkeley National Laboratory/DOE Joint Genome Institute

Michael Morrison
Lawrence Livermore National Laboratory

Nisha Mulakken
Lawrence Livermore National Laboratory

Hau Nguyen
Los Alamos National Laboratory

Marit Nilsen-Hamilton
Ames Laboratory

Kristin Omberg
Pacific Northwest National Laboratory

Hugh O'Neal
Oak Ridge National Laboratory

Jerry Parks
Oak Ridge National Laboratory

Lili Pasa-Tolic
Pacific Northwest National Laboratory

Christa Pennacchio
Lawrence Berkeley National Laboratory

Dave Rakestraw
Lawrence Livermore National Laboratory

Scott Retterer
Oak Ridge National Laboratory

Marc Salit
SLAC National Accelerator Laboratory

Blake Simmons
Lawrence Berkeley National Laboratory

Anup Singh
*Sandia National Laboratories,
now Lawrence Livermore National Laboratory*

Jess Sustarich
Sandia National Laboratories

James Thissen
Lawrence Livermore National Laboratory

Nileena Velappan
Los Alamos National Laboratory

Geoff Waldo
Los Alamos National Laboratory

Kelly Williams
Sandia National Laboratories

Jesse Wilson
Pacific Northwest National Laboratory

Chunyan Ye
University of New Mexico

Malin Young
Pacific Northwest National Laboratory

Yuko Yoshinaga
Lawrence Berkeley National Laboratory

Mowei Zhou
Pacific Northwest National Laboratory

Chapter 3: Epidemiological Modeling

Erin Acquesta
Sandia National Laboratories

James Ahrens
Los Alamos National Laboratory

Joshua Auld
Argonne National Laboratory

Paula Austin
Sandia National Laboratories

Ryan Aydelott
Argonne National Laboratory

Andrew Bartlow
Los Alamos National Laboratory

Joshua Bergerson
Argonne National Laboratory

Anne Berres
Oak Ridge National Laboratory

Walter Beyeler
Sandia National Laboratories

Budhendra Bhaduri
Oak Ridge National Laboratory

Alec Biehl
Oak Ridge National Laboratory

Patrick Blonigan
Sandia National Laboratories

Brennan Borlaug
National Renewable Energy Laboratory

Christa Brelsford
Oak Ridge National Laboratory

Benjamin Brodsky
Sandia National Laboratories

Lauren Castro
Los Alamos National Laboratory

Youngsoo Chang
Argonne National Laboratory

Supriya Chinthavali
Oak Ridge National Laboratory

Blair Christian
Oak Ridge National Laboratory

Timothy Cleland
Los Alamos National Laboratory

Nicholson Collier
Argonne National Laboratory

Scott Collis
Sandia National Laboratories

Jessica Conrad
Los Alamos National Laboratory

Elton Cranfill
Oak Ridge National Laboratory

Leticia Cuellar-Hengartner
Los Alamos National Laboratory

Chad Davis
Sandia National Laboratories

Lori Dauelsberg
Los Alamos National Laboratory

Rich Davies
Oak Ridge National Laboratory

Haedi DeAngelis
Sandia National Laboratories

Sean DeRosa
Sandia National Laboratories

Sara Del Valle
Los Alamos National Laboratory

Bradley Dickerson
Sandia National Laboratories

Andrew Duvall
National Renewable Energy Laboratory

Samantha Erwin
Oak Ridge National Laboratory

Mary Ewers
Los Alamos National Laboratory

Jeanne Fair
Los Alamos National Laboratory

Geoffrey Fairchild
Los Alamos National Laboratory

John Farrell
National Renewable Energy Laboratory

Kyle Feffer
Argonne National Laboratory

Paul Fenimore
Los Alamos National Laboratory

Melissa Finley*Sandia National Laboratories***Patrick Finley***Sandia National Laboratories***Joseph Fish***National Renewable Energy Laboratory***Michael Ford***Sandia National Laboratories***Christopher Frazier***Sandia National Laboratories***Venu Garikapati***National Renewable Energy Laboratory***Jared Gearhart***Sandia National Laboratories***Timothy German***Los Alamos National Laboratory***Dax Gerts***Los Alamos National Laboratory***Phwey (Danny) Gil***Argonne National Laboratory***Morgan Gorris***Los Alamos National Laboratory***Josh Grant***Oak Ridge National Laboratory***Ann Hammer***Sandia National Laboratories***Desmond Harmon***Sandia National Laboratories***Nicolas Hengartner***Los Alamos National Laboratory***Michael Hilliard***Oak Ridge National Laboratory***William Hlavacek***Los Alamos National Laboratory***Rossitza Homan***Sandia National Laboratories***John Hummel***Argonne National Laboratory***Aundre Huynh***Sandia National Laboratories***Ho-Ling Hwang***Oak Ridge National Laboratory***Brian Ingram***Argonne National Laboratory***Dean Jones***Sandia National Laboratories***Jessica Jones***Sandia National Laboratories***Kyungsoo Jeong***National Renewable Energy Laboratory***Chaitanya Kaligotla***Argonne National Laboratory***Jason Kaufman***Oak Ridge National Laboratory***Thomas Kirchstetter***Lawrence Berkeley National Laboratory***Katherine Klise***Sandia National Laboratories***Daniel Krofcheck***Sandia National Laboratories***Haitam Laarabi***Lawrence Berkeley National Laboratory***Diane Lauderdale***Argonne National Laboratory***Rene LeClaire***Los Alamos National Laboratory***David LePoire***Argonne National Laboratory***Drew Levin***Sandia National Laboratories***Lawrence Paul Lewis***Argonne National Laboratory***Yen Ting Lin***Los Alamos National Laboratory***Charles Macal***Argonne National Laboratory***Margaret MacDonell***Sandia National Laboratories***Monear Makvandi***Sandia National Laboratories***Carrie Manore***Los Alamos National Laboratory***Carianne Martinez***Sandia National Laboratories***Ignacio Martinez-Moyano***Argonne National Laboratory***Taylor McKenzie***Sandia National Laboratories*

Benjamin McMahon*Los Alamos National Laboratory***Isaac Michaud***Los Alamos National Laboratory***Mike Mills***Lawrence Berkeley National Laboratory***Jacob Miner***Los Alamos National Laboratory***Jessica Moehl***Oak Ridge National Laboratory***Matthew Moniot***National Renewable Energy Laboratory***Judith Maurant***Los Alamos National Laboratory***Aaron Myers***Oak Ridge National Laboratory***Zach Needell***Lawrence Berkeley National Laboratory***David Osthus***Los Alamos National Laboratory***Jonathan Ozik***Argonne National Laboratory***Byung Park***Oak Ridge National Laboratory***Nidhi Parkh***Los Alamos National Laboratory***Alina Peluso***Oak Ridge National Laboratory***Jordan Perr-Sauer***National Renewable Energy Laboratory***Sinem Perk***Argonne National Laboratory***Frederic Petit***Argonne National Laboratory***Jesse Piburn***Oak Ridge National Laboratory***Teresa Portone***Sandia National Laboratories***Julia Potter***Sandia National Laboratories***Rosalyn Rael***Los Alamos National Laboratory***Phillip Rauscher***Argonne National Laboratory***Srinath Ravulaparthi***Lawrence Berkeley National Laboratory***Jaideep Ray***Sandia National Laboratories***Nicholas Reinicke***National Renewable Energy Laboratory***Sara Rimer***Argonne National Laboratory***Mark "Danny" Rintoul***Sandia National Laboratories***Amy Rose***Oak Ridge National Laboratory***William Rosenberger***Los Alamos National Laboratory***Aymeric Rousseau***Argonne National Laboratory***Angelika Saeger***Los Alamos National Laboratory***Cosmin Safta***Sandia National Laboratories***Erik Schmidt***Oak Ridge National Laboratory***Scott Schlueter***Argonne National Laboratory***Courtney Shelley***Los Alamos National Laboratory***Anup Singh***Sandia National Laboratories***Nagendra Singh***Oak Ridge National Laboratory***Braeton Smith***Argonne National Laboratory***Asael Sorensen***Sandia National Laboratories***Alex Sorokine***Oak Ridge National Laboratory***Tina Sowers***Oak Ridge National Laboratory***Kevin Sparks***Oak Ridge National Laboratory***Pamela Spetz***Argonne National Laboratory***Anna Spurlock***Lawrence Berkeley National Laboratory*

Abby Stevens*Argonne National Laboratory***Robert Stewart***Oak Ridge National Laboratory***Bingrong Sun***National Renewable Energy Laboratory***Laura Swiler***Sandia National Laboratories***Varisara Tansakul***Oak Ridge National Laboratory***Robert Taylor***Sandia National Laboratories***Kirsten Taylor-McCabe***Los Alamos National Laboratory***Gautam Thakur***Oak Ridge National Laboratory***Katherine Tremba***Sandia National Laboratories***Lawrence Trost***Sandia National Laboratories***Majbah Uddin***Oak Ridge National Laboratory***Vanessa Vargas***Sandia National Laboratories***Omer Verbas***Argonne National Laboratory***Sarah Voter***Los Alamos National Laboratory***Amanda Wagner***Argonne National Laboratory***Laurie Wallis***Sandia National Laboratories***Cheng Wang***Argonne National Laboratory***Ross Wang***Oak Ridge National Laboratory***Rashid Waraich***Lawrence Berkeley National Laboratory***Chrysm Watson***Los Alamos National Laboratory***Eric Webber***Oak Ridge National Laboratory***Tom Wenzel***Lawrence Berkeley National Laboratory***Celine West***Sandia National Laboratories***Matthew Whitehead***Oak Ridge National Laboratory***Kristen Wilding***Los Alamos National Laboratory***Alana Wilson***National Renewable Energy Laboratory***Murray Wolinsky***Los Alamos National Laboratory***Justin Wozniak***Argonne National Laboratory***Fei Xie***Oak Ridge National Laboratory***Haowen Xu***Oak Ridge National Laboratory***Stanley Young***National Renewable Energy Laboratory***Zijia Zhong***National Renewable Energy Laboratory*

Chapter 4: Viral Fate and Transport

Jesse Ahlquist*Lawrence Livermore National Laboratory***Allison Aiken***Los Alamos National Laboratory***Kevin Anderson***Pacific Northwest National Laboratory***Ramesh Balakrishnan***Argonne National Laboratory***Viktor Balema***Ames Laboratory***Bryan Bellaire***Iowa State University***Robin Brigmon***Savannah River National Laboratory***Michael J. Brown***Los Alamos National Laboratory***Carolyn Burns***Pacific Northwest National Laboratory***Jules Cacho***Argonne National Laboratory***Jack Cahill***Oak Ridge National Laboratory*

Andrew Costinett*Pacific Northwest National Laboratory***Richard Daniel***Pacific Northwest National Laboratory***William Delp***Lawrence Berkeley National Laboratory***Armand Dichosa***Los Alamos National Laboratory***Michael Dillon***Lawrence Livermore National Laboratory***Liz Dobitz***SLAC National Accelerator Laboratory***Stefan Paul Domino***Sandia National Laboratories***Mavendra Dubey***Los Alamos National Laboratory***Som Dutta***Utah State University***Anne Marie Erler***Lawrence Livermore National Laboratory***Yan Feng***Argonne National Laboratory***Laura Fierce***Brookhaven National Laboratory, now Pacific Northwest National Laboratory***Paul Fischer***University of Illinois at Urbana-Champaign***Julia Flaherty***Pacific Northwest National Laboratory***Erika Fong***Lawrence Livermore National Laboratory***Laura Forde***Lawrence Livermore National Laboratory***Matthias Frank***Lawrence Livermore National Laboratory***Brian Fricke***Oak Ridge National Laboratory***Brad Fritz***Pacific Northwest National Laboratory***Jamie George***Pacific Northwest National Laboratory***Andrew Glen***Sandia National Laboratories***Kyle Gorkowski***Los Alamos National Laboratory***Larry Hamm***Savannah River National Laboratory***Ihor Hlova***Ames Laboratory***Clifford Ho***Sandia National Laboratories***Dan James***Pacific Northwest National Laboratory***Staci Kane***Lawrence Livermore National Laboratory***Thomas Kirchstetter***Lawrence Berkeley National Laboratory***Rao Kotamarthi***Argonne National Laboratory***Gourihar Kulkarni***Pacific Northwest National Laboratory***Brady Lee***Savannah River National Laboratory***Patricia Lee***Savannah River National Laboratory***Robert Lutes***Pacific Northwest National Laboratory***Naila Mahdi***Argonne National Laboratory***Simo Makiharju***University of California, Berkeley***Bob McGraw***Brookhaven National Laboratory***Richard Mills***Argonne National Laboratory***Kashif Nawaz***Oak Ridge National Laboratory***Oscar Negrete***Sandia National Laboratories***Cristina Negri***Argonne National Laboratory***Ralph Nichols***Savannah River National Laboratory***Aleks Obabko***Argonne National Laboratory***Brian O'Callahan***Pacific Northwest National Laboratory***Ronald Ott***Oak Ridge National Laboratory*

Aaron Packman*Northwestern University***Jovan Pantelic***University of California, Berkeley***Ali Passian***Oak Ridge National Laboratory***Leonard Pease***Pacific Northwest National Laboratory***Kruttika-Suhas Phadke***Iowa State University***Chelsea Preble***University of California, Berkeley***Tanya Prozorov***Ames Laboratory***Odeta Qafoku***Pacific Northwest National Laboratory***John Quinn***Argonne National Laboratory***Edwin Saavedra***Northwestern University***Anne Sakdinawat***SLAC National Accelerator Laboratory***Timothy Salsbury***Pacific Northwest National Laboratory***Andres Lorenzo Sanchez***Sandia National Laboratories***Callen Schwefler***Lawrence Livermore National Laboratory***Brett Singer***Lawrence Berkeley National Laboratory***Rajesh Singh***Pacific Northwest National Laboratory***Michael Sohn***Lawrence Berkeley National Laboratory***Eric Thacher***University of California, Berkeley***Bill Thompson***SLAC National Accelerator Laboratory***Ronald Underhill***Pacific Northwest National Laboratory***Evan Variano***University of California, Berkeley***Brian Viner***Savannah River National Laboratory***Alex Vlachokostas***Pacific Northwest National Laboratory***Nora Wang***Pacific Northwest National Laboratory, now American Council for an Energy-Efficient Economy***Katrina Waters***Pacific Northwest National Laboratory***David Werth***Savannah River National Laboratory***Elizabeth Wheeler***Lawrence Livermore National Laboratory***Annmarie Wood-Zika***Lawrence Livermore National Laboratory***Eugene Yan***Argonne National Laboratory***Haoran Zhao***Lawrence Berkeley National Laboratory*

Chapter 5: Materials and Manufacturing of Critical Supplies

Samantha Adikari*Los Alamos National Laboratory***Daniel Akerib***SLAC National Accelerator Laboratory***Andrew Ames***SLAC National Accelerator Laboratory***Marie Arrowsmith***Sandia National Laboratories***Shaine Athey***Lawrence Livermore National Laboratory***Celeste Atkins***Oak Ridge National Laboratory***William Bachman***Sandia National Laboratories***Teresa Barnes***National Renewable Energy Laboratory***Abby Barnes***Oak Ridge National Laboratory***Todd Barrick***Sandia National Laboratories***Katherine Barrick***Sandia National Laboratories***Andy Beasley***Idaho National Laboratory*

Clint Bedick
National Energy Technology Laboratory

Bryan Bellaire
Ames Laboratory

Donald Benza
Savannah River National Laboratory

John Bernardin
Los Alamos National Laboratory

Emma Betters
Oak Ridge National Laboratory

Randy Bewley
Idaho National Laboratory

Beth Boardman
Los Alamos National Laboratory

John Bobbitt
Savannah River National Laboratory

David Bock
Brookhaven National Laboratory

Yannick Bomble
National Renewable Energy Laboratory

Martin Breidenback
SLAC National Accelerator Laboratory

Michael Bressack
SLAC National Accelerator Laboratory

Pieter Breur
SLAC National Accelerator Laboratory

Kevin Byerly
National Energy Technology Laboratory

Rafael Campos
SLAC National Accelerator Laboratory

James Carney
Sandia National Laboratories

Alberta Carpenter
National Renewable Energy Laboratory

Eric Charles
SLAC National Accelerator Laboratory

Santanu Chaudhuri
Argonne National Laboratory

Victor Chavez
Sandia National Laboratories

Phillip Chesser
Oak Ridge National Laboratory

Wah Chiu
SLAC National Accelerator Laboratory

Josef Christ
Pacific Northwest National Laboratory

Steven Chu
SLAC National Accelerator Laboratory

Peter Ciesielski
National Renewable Energy Laboratory

Kyle Cluff
Los Alamos National Laboratory

Bruce Cohen
Lawrence Berkeley National Laboratory

Adam Cook
Sandia National Laboratories

Cody Corbin
Sandia National Laboratories

Andres Cortez
Los Alamos National Laboratory

Corson Cramer
Oak Ridge National Laboratory

Jun Cui
Ames Laboratory

Yi Cui
SLAC National Accelerator Laboratory

Jeremy Danielson
Los Alamos National Laboratory

Nitin Daphalapurkar
Los Alamos National Laboratory

Panos Datskos
National Renewable Energy Laboratory

Jack Dean
Lawrence Livermore National Laboratory

Vincent DeAndrade
Argonne National Laboratory

Haedi Deangelis
Sandia National Laboratories

Ryan Dehoff
Oak Ridge National Laboratory

Patrick Dempsey
Lawrence Livermore National Laboratory

Alexander Dudchenko
SLAC National Accelerator Laboratory

Eric Duoss
Lawrence Livermore National Laboratory

Steve Eglash
SLAC National Accelerator Laboratory

Jeffrey Elam
Argonne National Laboratory

Amy Elliott
Oak Ridge National Laboratory

Ken Enstrom
Lawrence Livermore National Laboratory

Rebecca Erikson
Pacific Northwest National Laboratory

Tom Feldhausen
Oak Ridge National Laboratory

Michelle Fenn
Pacific Northwest National Laboratory

Don Ferguson
National Energy Technology Laboratory

Patrick Finnegan
Sandia National Laboratories

Matthew Folsom
Savannah River National Laboratory

Dennis Freeman
Lawrence Livermore National Laboratory

William Fuger
Idaho National Laboratory

Nathan Fuller
Sandia National Laboratories

Jon Fulton
National Energy Technology Laboratory

David Gaga
SLAC National Accelerator Laboratory

Kumkum Ganguly
Los Alamos National Laboratory

Randall Gentry
National Energy Technology Laboratory

Kevin Gervais
Pacific Northwest National Laboratory

Jeremy Gleick
Lawrence Livermore National Laboratory

Andrew Glen
Sandia National Laboratories

John Greenhall
Los Alamos National Laboratory

Lisa Gribble
Sandia National Laboratories

Anne Grillet
Sandia National Laboratories

Lorenzo Gutierrez
Sandia National Laboratories

Steven Guzorek
Lawrence Livermore National Laboratory

Ryan Haggerty
Sandia National Laboratories

Michael Ham
Los Alamos National Laboratory

Razi Haque
Lawrence Livermore National Laboratory

Jennifer Harris
Los Alamos National Laboratory

Marcus Hays
Argonne National Laboratory

Ryan Herbst
SLAC National Accelerator Laboratory

Chris Hershey
Oak Ridge National Laboratory

Michael Himmel
National Renewable Energy Laboratory

Andrew Honeycutt
Oak Ridge National Laboratory

Nick Horvath
Oak Ridge National Laboratory

Peter Hosemann
Lawrence Berkeley National Laboratory

Peter Hsieh
National Energy Technology Laboratory

Christina Ignarra
SLAC National Accelerator Laboratory

Ralph James
Savannah River National Laboratory

Todd Jankowski
Los Alamos National Laboratory

Dale Jenne
National Renewable Energy Laboratory

Jing Jin
SLAC National Accelerator Laboratory

Joel Johnson
Idaho National Laboratory

Robert Johnston
Sandia National Laboratories

Mike Kirka
Oak Ridge National Laboratory

Matthew Koetting
Kansas City National Security Campus

Jeffrey Koplow
Sandia National Laboratories

Jack Kotovsky
Lawrence Livermore National Laboratory

Gary Krugger
Los Alamos National Laboratory

Gregory Krumdick
Argonne National Laboratory

Wendy Kuhne
Savannah River National Laboratory

Ian Ladner
Lawrence Livermore National Laboratory

Justin Lajoie
Ames Laboratory

Candace Langan
Savannah River National Laboratory

Greg Larsen
Oak Ridge National Laboratory

Matthew Lee
Los Alamos National Laboratory

Thomas Lewis
Idaho National Laboratory

John Lindahl
Oak Ridge National Laboratory

Peter Lloyd
Oak Ridge National Laboratory

Thomas Lograsso
Ames Laboratory

Lonnie Love
Oak Ridge National Laboratory

Steffen Luitz
SLAC National Accelerator Laboratory

Leah Lujan
Los Alamos National Laboratory

Therese Lujan
Los Alamos National Laboratory

Monear Makvandi
Sandia National Laboratories

Dan Manha
Lawrence Livermore National Laboratory

Ruben Manzanares
Los Alamos National Laboratory

Alex Marchi
Los Alamos National Laboratory

Amy Marschilok
Brookhaven National Laboratory

Adam Martinez
Los Alamos National Laboratory

Mathew Mate
SLAC National Accelerator Laboratory

Chris Matranga
National Energy Technology Laboratory

Michael Maxwell
Savannah River National Laboratory

Sean McGaughey
Pacific Northwest National Laboratory

Eric Miller
SLAC National Accelerator Laboratory

Doug Modlin
Lawrence Livermore National Laboratory

Marwan Mohamed
Los Alamos National Laboratory

Arvind Mohan
Los Alamos National Laboratory

Brian Mong
SLAC National Accelerator Laboratory

Patrick Moo
Idaho National Laboratory

Murray Moore
Los Alamos National Laboratory

Robert Morgan
Los Alamos National Laboratory

Monica Moya
Lawrence Livermore National Laboratory

Elvin Munoz
Pacific Northwest National Laboratory

Du Nguyen
Lawrence Livermore National Laboratory

Greg Norton
Lawrence Livermore National Laboratory

David Nuttall
Oak Ridge National Laboratory

Andrzej Nycz
Oak Ridge National Laboratory

Austin Nye
Lawrence Livermore National Laboratory

Robert O'Brien*Idaho National Laboratory***Michael Omana***Sandia National Laboratories***Scott Paap***Sandia National Laboratories***Cristian Pantea***Los Alamos National Laboratory***Parans Paranthaman***Oak Ridge National Laboratory***Phil Paul***Lawrence Livermore National Laboratory***Jeremy Payton***Los Alamos National Laboratory***Martin Perraglio***Los Alamos National Laboratory***Matt Pharr***Lawrence Livermore National Laboratory***Brian Post***Oak Ridge National Laboratory***Krzysztof Pupek***Argonne National Laboratory***Samantha Reese***National Renewable Energy Laboratory***Steve Richardson***National Energy Technology Laboratory***Bryce Ricken***Sandia National Laboratories***Jacob Riglin***Los Alamos National Laboratory***Jason Roadman***National Renewable Energy Laboratory***Larry Rodriguez***Los Alamos National Laboratory***Mohammad Roni***Idaho National Laboratory***Alex Roschli***Oak Ridge National Laboratory***Alexander Rose***Los Alamos National Laboratory***Michael Sabo***Sandia National Laboratories***Bradley Salzbrenner***Sandia National Laboratories***Andres Sanchez***Sandia National Laboratories***Daniel Schabacker***Argonne National Laboratory***Andrew Schmalzer***Los Alamos National Laboratory***Patrick Scholl***Lawrence Livermore National Laboratory***Eric Shaner***Sandia National Laboratories***Maxim Shusteff***Lawrence Livermore National Laboratory***Randall Schunk***Sandia National Laboratories***Tom Shutt***SLAC National Accelerator Laboratory***Graham Simmons***SLAC National Accelerator Laboratory***Michael Sinclair***Sandia National Laboratories***Julie Slaughter***Ames Laboratory***Denver Smith***Los Alamos National Laboratory***Scott Smith***Oak Ridge National Laboratory***Brittnee Smith***Pacific Northwest National Laboratory***David Soscia***Lawrence Livermore National Laboratory***Christopher Spadaccini***Lawrence Livermore National Laboratory***Dusan Spernjak***Los Alamos National Laboratory***Aaron Sperry***Lawrence Livermore National Laboratory***Mike Steinzig***Los Alamos National Laboratory***Christopher Takacs***SLAC National Accelerator Laboratory***Deepti Tanjore***Lawrence Berkeley National Laboratory***Bryce Tappan***Los Alamos National Laboratory*

Antionette Taylor*Los Alamos National Laboratory***Paul Thelen***Sandia National Laboratories***Merlin Theodore***Oak Ridge National Laboratory***Angela Tooker***Lawrence Livermore National Laboratory***Katherine Tremba***Sandia National Laboratories***Michael Triplett***Lawrence Livermore National Laboratory***Jacob Trueblood***Lawrence Livermore National Laboratory***Charles Turick***Savannah River National Laboratory***Jeffrey Urban***Lawrence Berkeley National Laboratory***Victor Vargas***Lawrence Livermore National Laboratory***Vanessa Vargas***Sandia National Laboratories***Joshua Vaughan***Oak Ridge National Laboratory***Eliel Villa-Aleman***Savannah River National Laboratory***Lei Wang***Brookhaven National Laboratory***Peter Wang***Oak Ridge National Laboratory***Scott Weaver***SLAC National Accelerator Laboratory***Nina Weisse-Bernstein***Los Alamos National Laboratory***Dora Wiemann***Sandia National Laboratories***Brian Wihl***Lawrence Livermore National Laboratory***Zachary Wilson***Sandia National Laboratories***Edward Winrow***Sandia National Laboratories***Matthias Wittgen***SLAC National Accelerator Laboratory***Shan Yan***Brookhaven National Laboratory***Allison Yorita***Lawrence Livermore National Laboratory***Qinghui Yuan***Argonne National Laboratory***Yuepeng Zhang***Argonne National Laboratory*

Appendix B

Acronyms and Abbreviations

| | | | |
|--------------------------|---|-----------------|---|
| 1D, 2D, 3D | one-, two-, three-dimensional | CCSAT | COVID County Situational Awareness Tool |
| 3CL^{pro} | 3 chymotrypsin-like protease | CDC | Centers for Disease Control and Prevention |
| Å | angstrom | CDPH | California Department of Public Health |
| ACE2 | angiotensin-converting enzyme 2 | CE | capillary electrophoresis |
| ACH | air changes per hour | CFD | computational fluid dynamics |
| ACR | air change rate | CFR | case fatality rate |
| ADRP | ADP ribose phosphatase | CLIA | Clinical Laboratory Improvement Amendments |
| AFM | atomic force microscopy | CNF | cellulose nanofibrils |
| AHU | air handling unit | COVID-19 | Coronavirus disease 2019 |
| AI | artificial intelligence | CPE | cytopathic effect |
| ALD | atomic layer deposition | CPU | central processing unit |
| ALS | Advanced Light Source | CRADA | Cooperative Research and Development Agreement |
| Ames | Ames Laboratory | cryo-EM | cryo-electron microscopy |
| ANL | Argonne National Laboratory | CSGID | Center for Structural Genomics of Infectious Diseases |
| APCF | Advanced Protein Characterization Facility | Ct | cycle threshold |
| API | application programming interface | CTA | Chicago Transit Authority |
| ARM | Adaptive Recovery Model | DARPA | Defense Advanced Research Projects Agency |
| ATOM | Accelerating Therapeutic Opportunities for Medicine | DDMD | DeepDrive Molecular Dynamics |
| BEI | Biodefense and Emerging Infections | DHS | U.S. Department of Homeland Security |
| BF-TEM | bright-field transmission electron microscopy | DMF | disposable digital microfluidic |
| BLADE | Berkeley Lab Automated Diagnostics Extension | DMSO | dimethyl sulfoxide |
| BLAST | Basic Local Alignment Search Tool | DNS | direct numerical simulation |
| BNL | Brookhaven National Laboratory | DoD | U.S. Department of Defense |
| BOM | bill of materials | DOE | U.S. Department of Energy |
| BSL-3 | biosafety level 3 | DTT | dithiothreitol |
| CAD | computer-aided design | E | SARS-CoV-2 viral envelope protein |
| CARES Act | Coronavirus Aid, Relief, and Economic Security Act | EBVSV | Ebola glycoprotein labeled VSV virions |
| CBR | chemical, biological, and radiological | | |

| | | | |
|-------------------|---|-------------------|---|
| EC50 | half-maximal effective concentration | HT | high-throughput |
| ECMO | extracorporeal membrane oxygenation | HT-SAXS | high-throughput small angle X-ray scattering |
| EDS | energy dispersive X-ray spectroscopy | HTVS | high-throughput virtual screening |
| EDTA | ethylenediamine tetra-acetic acid | HVAC | heating, ventilation, and air conditioning |
| ELISA | enzyme-linked immunosorbent assay | IC50 | half-maximal inhibitory concentration |
| EnTK | RADICAL-Ensemble Toolkit | ICU | intensive care unit |
| EPA | Environmental Protection Agency | IgG | immunoglobulin G |
| EpiCast | Epidemiological Forecasting | IGV | Integrative Genomics Viewer |
| ERM | exposure to perfectly mixed | IHME | Institute for Health Metrics and Evaluation |
| ESMACS | enhanced sampling of molecular dynamics with approximation of continuum solvent | IMPECCABLE | Integrated Modeling PipEline for COVID Cure by Assessing Better LEads |
| EUA | Emergency Use Authorization | INL | Idaho National Laboratory |
| EVA | ethylene-vinyl acetate | IPLV | intrapulmonary percussive liquid ventilation |
| Fabs | human antigen-binding fragments | IPV | intrapulmonary percussive ventilation |
| Fc | crystallizable fragment | IQR | interquartile range |
| FDA | U.S. Food and Drug Administration | IR | infrared |
| FEMA | Federal Emergency Management Agency | IRB | Institutional Review Board |
| FF | force field | JGI | DOE Joint Genome Institute |
| FIB | focused ion beam | KBase | DOE Systems Biology Knowledgebase |
| FLISA | fluorescence-linked immunosorbent assay | KCNSC | Kansas City National Security Campus |
| FRET | fluorescence resonance energy transfer | Kd | binding affinity |
| GC | guanine-cytosine | KG | knowledge graph |
| GP1,2 | Ebola virus glycoprotein | Ki | inhibitor constant |
| GPU | graphics processing unit | LANL | Los Alamos National Laboratory |
| HAADF-STEM | high-angle annular dark-field scanning transmission electron microscopy | LBNL | Lawrence Berkeley National Laboratory |
| HEK | human embryonic kidney | LDRD | Laboratory Directed Research and Development |
| HHS | U.S. Department of Health and Human Services | LES | large eddy simulation |
| HILIC | hydrophilic liquid interaction chromatography | LIMS | laboratory information management system |
| HPC | high-performance computing | LLMDA | Lawrence Livermore Microbial Detection Array |
| HRSD | Hampton Roads Sanitation District | LLNL | Lawrence Livermore National Laboratory |
| HRSEM | high resolution scanning electron microscopy | | |

| | | | |
|-----------------|---|-----------------|---|
| LOD | limits of detection | PAC | portable air cleaners |
| mAbs | monoclonal antibodies | PBD | Protein Data Bank |
| MALS | multi-angle light scattering | PBS | phosphate-buffered saline |
| MDF | Manufacturing Demonstration Facility | PE | phycoerythrin |
| MEP | Mobility Energy Productivity | PEEK | polyetheretherketone |
| MERS | Middle East respiratory syndrome | PEEP | positive end-expiratory pressure |
| MERS-CoV | Middle East respiratory syndrome-related coronavirus | PF | phase-field |
| MERV | minimum efficiency reporting value | PFU | plaque forming units |
| MeSH | Medical Subject Headings | PIP | peak inspiratory pressure |
| MILP | mixed-integer linear programming | PITA | Point-in-Time Air Travel model |
| ML | machine learning | PLA | polylactic acid |
| MNP | magnetic nanoparticle | PLpro | papain-like protease |
| MPPS | Most Penetration Particle Size | PMCMC | particle Markov chain Monte Carlo |
| MSA | multiple sequence alignment (Ch. 2) | PMIx | Process Management Interface for Exascale |
| MSA | metropolitan statistical area (Ch. 3) | PNNL | Pacific Northwest National Laboratory |
| MTA | New York Metropolitan Transportation Authority | PNNL-MTS | PNNL Medical Test Site |
| MUSCLE | MUltiple Sequence Comparison by Log-Expectation | PPE | personal protective equipment |
| N gene | SARS-CoV-2 nucleocapsid gene (N1 and N2) | PRIME | Partially obseRved epldeMics – Bayesian InferenceE |
| NCBI | National Center for Biotechnology Information | QC | quality control |
| NETL | National Energy Technology Laboratory | qPCR | quantitative polymerase chain reaction |
| NIAID | National Institute of Allergy and Infectious Diseases | QuadRAD | Quadrature-based model of Respiratory Aerosols and Droplets |
| NIH | National Institutes of Health | QUASR | quenching of unincorporated amplification signal reporters |
| NIOSH | National Institute for Occupational Safety and Health | QUIC | Quick Urban and Industrial Complex |
| NLP | Natural Language Processing | R0 | replicative number/basic reproduction number |
| NP | nasopharyngeal | R&D | research and development |
| NPX | neutron protein crystallography | RAPTOR | RAAdical-Pilot Task OverLay |
| NREL | National Renewable Energy Laboratory | RBD | receptor binding domain |
| NSLS-II | National Synchrotron Light Source II | RCT | RADICAL Cybertools |
| Nsp15 | SARS-CoV-2 endoribonuclease | RdRp | RNA polymerase |
| NVBL | National Virtual Biotechnology Laboratory | REST | representational state transfer |
| ORNL | Oak Ridge National Laboratory | RH | relative humidity |
| OSU | Oregon State University | ROX | carboxyrhodamine |
| | | RP | RADICAL-Pilot |
| | | RRR | regional relative risk |
| | | RTC | RNA transcription complex |

| | | | |
|----------------------|---|-----------------|---|
| RT-LAMP | Reverse Transcription Loop-mediated isothermal AMplification | s-SNOM | scattering-type scanning near-field optical microscopy |
| RT-PCR | reverse transcription polymerase chain reaction | STEM | scanning transmission electron microscopy |
| RT-qPCR | reverse transcription quantitative polymerase chain reaction | STEM-EDS | scanning transmission electron microscopy–energy-dispersive X-ray spectroscopy |
| SANS | small-angle neutron scattering | TCEP | tris(2-carboxyethyl)phosphine |
| SARS-CoV-1 | severe acute respiratory syndrome coronavirus 1 | TEM | transmission electron microscopy |
| SARS-CoV-2 | severe acute respiratory syndrome coronavirus 2 | TIES | thermodynamic integration with enhanced sampling |
| SAXS | small-angle X-ray scattering | TKE | turbulent kinetic energy |
| SBC | Argonne’s Advanced Photon Source Structural Biology Center | TMB | 3,3',5,5'-Tetramethylbenzidine |
| scFv | human single chain antibody | TNA | total nucleic acid |
| SEC-MALS-SAXS | size exclusion chromatography and multi-angle light scattering coupled SAXS | UTHSC | University of Tennessee Health Science Center |
| SEIR | susceptible-exposed-infectious-removed | V&A | velocity and acceleration |
| SEM | scanning electron microscopy | VAMP | variational approaches for Markovian processes |
| Sf | super folder | VHH-huFc | nanobodies (VHH) fused to the crystallizable fragment (Fc) domain of a human IgG1 |
| SIBYLS | Structurally Integrated BiologY for the Life Sciences | VH | scFv’s variable heavy regions |
| SIR | Susceptible-Infections-Recovered | ViPR | Virus Pathogen Database and Analysis Resource |
| SIS | sequential infiltration synthesis | VL | scFv’s variable light regions |
| SLAC | SLAC National Accelerator Laboratory | VSCT | ventilator supply chain analysis tool |
| SMILES | simplified molecular-input line-entry system | VSV | vesicular stomatitis virus |
| SNL | Sandia National Laboratories | VSV-G | vesicular stomatitis virus G protein |
| SNRL | Savannah River National Laboratory | VTM | viral transport medium |
| SPR | surface plasmon resonance | WSTAMP | World SpatioTemporal Analytics and Mapping Project |
| S-protein | SARS-CoV-2 surface spike glycoprotein | WVU-CIT | West Virginia University’s Center for Inhalation Toxicology |
| | | WWTF | wastewater treatment facility |

